SEISMIC BEHAVIOUR OF RECTANGULAR REINFORCED CONCRETE WALLS UNDER BI-DIRECTIONAL LOADING

A thesis submitted in partial fulfilment of the

requirements for the Degree of

Doctor of Philosophy in Civil Engineering

by

Arsalan Niroomandi

Supervised by

Professor Stefano Pampanin

Professor Rajesh Dhakal

Dr Mohammad Soleymani Ashtiani

Department of Civil and natural Resources Engineering

University of Canterbury

Christchurch, New Zealand

November 2018

ABSTRACT

Current seismic design codes of practice specify the earthquake loadings independently in each direction of the structure's principal axis. However, the lateral earthquake excitations could be simultaneous in both directions or in a skewed direction to the principal axis. Therefore, if the seismic design or performance is based on the inelastic behaviour of the structure up to the ultimate limit state, then the deformation capacity of the structure in the skewed direction must be ensured from another point of view.

Columns as elements which are under flexural and axial actions were recognized by researchers as members that are under the influence of bi-directional loading. Several experimental and analytical studies were carried out on bi-axially loaded columns and magnification factors for the column actions were also introduced in recent seismic design of reinforced concrete (RC) structures. On the other hand, due to the good performance of RC structural walls in the past earthquakes, the need for relatively advanced investigations and considerations such as the effects of bi-directional loading were not justifiable. Over the past several decades, a large number of studies (experimental and numerical) were conducted on the seismic behaviour of RC walls. Most of the walls were subjected to in-plane cyclic lateral loading and gravity loads simulating the calculated response of actions in a proto-type structure during an earthquake, while a small number of these walls were tested under bi-directional loading. Therefore, the effect of bi-directional loading on rectangular RC shear walls is not yet fully understood by researchers. However, unexpected failure modes observed in RC walls in the 2010 Chile and 2011 New Zealand earthquakes raised a global concern on the contribution of bi-directional loading to these failure modes.

This thesis aims to provide a better understanding on the seismic performance of rectangular RC walls subjected to a more realistic loading regime (bi-directional loading). Due to lack of experimental data on rectangular RC walls under bi-directional loading especially for slender walls, a series of experiments were conducted to cover some of the key research questions on the seismic performance of rectangular RC walls subjected to bi-directional loading. To complement the experimental investigation, a comprehensive numerical study was carried out targeting the key research gaps that were not investigated in the laboratory due to the limitations with the number of specimens.

The experimental programme included two main phases. In the first phase, three identical walls subjected to different lateral loading patterns were tested to investigate the effects of various lateral loading patterns on the seismic behaviour of rectangular RC walls which was not investigated before. In the second phase of experiments, three rectangular walls designed for different section detailing ductility based on NZS3103:2006-A3 (2017) were investigated under high axial load ratio and bi-directional loading targeting a failure mode suspected to be a product of bi-directional loading (out-of-plane shear failure). Out-of-plane shear failure was captured in the laboratory which significantly helped with understanding the mechanism of this failure mode. One of the main challenges with the experimental phase was the test setup which had seven hydraulic actuators. Second phase of the experimental study was even more challenging with the combination of high axial load and bi-directional loading.

There were challenges with the numerical phase as well, as there was limited number of numerical studies on rectangular RC walls subjected to bi-directional loading. Therefore, a finite element (FE) model had to be developed and validated for RC walls subjected to bi-directional loading. New experimental data provided by the current study significantly helped with the development of the FE model. The FE software DIANA was used for the numerical phase of the study. The FE model was validated extensively against 7 rectangular RC walls with 4 different lateral loading patterns and complex failure modes such as lateral instability and out-of-plane shear failures. Using the validated FE model, failure mode of a rectangular RC wall collapsed in the 2011 NZ earthquake in out-of-plane shear was successfully captured. The last part of the numerical phase was to identify the key parameters contributing to the development of out-of-plane shear failure. Each parameter was investigated comprehensively. Using the numerical parametric results, a matrix of walls was formed based on the two most influential parameters in causing vulnerability in rectangular RC walls to out-of-plane shear failure. An analytical method was proposed using the matrix results which can be used for identifying RC walls prone to out-of-plane shear failure in practice for both design and assessment purposes.

ACKNOWLEDGEMENTS

The research described in this thesis was carried out in the Department of Civil and Natural Resources Engineering, University of Canterbury, under the overall guidance of Professor Stefano Pampanin.

I would like to express my profound gratitude to my primary supervisor, Professor Stefano Pampanin who gave me a new vision and a level of understanding in structural engineering that I'm not sure I would have been able to achieve if it wasn't for him.

I wish to acknowledge the great debt of gratitude I owe to my co-supervisor Professor Rajesh Dhakal who was there for me when I needed him and was more than a co-supervisor under my special circumstances.

I am also grateful to my second co-supervisor Dr Mohammad Soleymani Ashtiani who supported me and believed in me during the course of this work, even during the darkest moments.

The financial assistance provided by the Ministry of Business, Innovation and Employment managed by the University of Canterbury quake centre is gratefully acknowledged. Without the financial aids from these organisations, my PhD research and experience would not have been possible.

I would like to thank all the Civil and Natural Resources Engineering academics who were involved in this work, especially Professor Roger Nokes for his kind and modest help with the particle tracking measurement used in the experimental phase of this project.

I would like to thank the technicians and staff of the Department of Civil and Natural Resources Engineering who helped me in this project. Special thanks to Alan Thirlwell for his constant support in the lab. I am grateful to Peter Coursey for his key role in revising the software controlling the hydraulic actuators that allowed the complex test setup to work. The

assistance of Russell McConchie, Mosese Fifita, Gavin Keats, Tim Perigo and John Maley during the experimental phase of the study has also been much appreciated. Thanks also to Elizabeth Ackerman, Ricardo Bello Mendoza and David MacPherson for their assistance over the years.

My thanks are extended to my fellow postgraduate students who made this four and half years journey memorable. Special thanks to Saeid Alizadeh for his kind help during the project. My gratitude goes to Chris De la Torre for taking care of the displacement response of the Canterbury 2010 and 2011 earthquakes.

Lastly but most importantly, this dissertation and my whole engineering career would not have been possible without the unwavering support from my family. In the darkest moments, you all were there for me. My deepest gratitude goes to my wife, Sara, to my mom and dad and to my brothers, Siamak and Arash for their endless love and support. This thesis is dedicated to you all.

TABLE OF CONTENTS

LIST OF FIGURES

LIST OF TABLES

1. INTRODUCTION

1.1. BACKGROUND AND RESEARCH MOTIVATION

Several experimental and analytical/numerical studies were carried out on Reinforced Concrete (RC) columns subjected to bi-directional loading (Padilla-Mora and Schnobrich 1974, Pecknold 1974, Lai et al. 1984, Maruyama et al. 1984, Umehara and Jirsa 1984, Low and Moehle 1987, Oliva and Clough 1987, Li et al. 1988, Mahin 1988, Zeris and Mahin 1991, Wong et al. 1993, Bousias et al. 1995, Kim and Lee 2000, Lai and Chang 2001, Marante and Flórez-López 2002, Qiu et al. 2002, Bonet et al. 2005, Boys et al. 2008, Pallarés et al. 2008, Bonet et al. 2011, Rodrigues et al. 2013, Wang et al. 2013). On the other hand, although a large number of experimental and numerical studies were conducted on the seismic behaviour of rectangular RC walls over the past several decades, most of them were subjected to cyclic in-plane uni-directional loading. Only a small number of rectangular RC walls were tested under bi-directional loading (Tatsuya 1996, Kabeyasawa et al. 2014, Almeida et al. 2017). Therefore, the effect of bi-directional loading on rectangular RC walls is not yet fully understood for researchers. However, in recent earthquakes in Chile (2010) and New Zealand (2011), some unexpected failure modes in RC walls were observed which were not previously seen in earthquakes. Following these observations, several researchers started investigating different aspects of these new observations (Acevedo et al. 2010, Johnson 2010, Constantin and Beyer 2012, Wallace and Moehle 2012, Alarcon et al. 2014, Behrouzi et al. 2014, Dashti et al. 2014, Hilson et al. 2014, Parra and Moehle 2014, Yamamoto et al. 2014, Constantin and Beyer 2016, Junemann et al. 2016b, Almeida et al. 2017, Brueggen et al. 2017, Segura and Wallace 2017, Shegay et al. 2017). One of the concerns the researchers had was the contribution of bi-directional loading to these failure modes. In this chapter, firstly, the recent observations from Chile and New Zealand earthquakes were discussed. Then, the previous studies conducted on RC structural elements such as column, beam-column joints and structural walls subjected to bi-directional loading were presented. Finally, the research gaps in the subject of rectangular slender RC walls subjected to bi-directional loading were presented and the research objectives of the thesis were introduced.

Seismic performance of RC structural walls in the 2010 Chile and 2011 New Zealand Earthquakes

Due to the relatively good performance of RC structural walls in the earthquakes prior to 2010, the need for deeper investigations such as the effects of bi-directional loading were not of interest for most researchers in the field of RC structural walls. However, recent earthquakes in Chile (Maule, February 2010, M_w 8.8) and New Zealand (Canterbury, February 2011, M_L=6.3) have provided new information that can challenge the conventional methods of seismic assessment and design of structures that use RC walls as the main lateral resisting system. Some of the observed damage in Chile 2010 earthquake was included buckling of longitudinal reinforcement at wall boundaries, lateral instability (out-of-plane buckling) of walls (Figure 1-1), damage from coupling of walls through slabs and other elements and damage concentrated at wall discontinuities.

Figure 1-1 Lateral instability of walls from the 2010 Maule earthquake Chile (NIST 2014)

Similar failure modes were also observed in the 2011 Christchurch (Lyttelton) earthquake, indicating that these vulnerabilities of structural walls are not limited to the 2010 Chile earthquake (Figure 1-2). Figure 1-3 shows a diagonal web crushing in the first storey of a slender wall that extended downward from the damaged boundary element. Kam et al. (2011) suggested that considering the diagonal pattern of the web crushing, high shear stresses may have also contributed to the observed damage. Another unexpected failure mode observed in 2011 New Zealand earthquake was an out-of-plane shear failure which was not observed before in an earthquake (Figure 1-4). In a preliminary study by Dunning Thornton (2011), contribution of bi-directional loading to this failure mode was mentioned. Partial out-of-plane shear failure was observed in an experimental study by Paulay and Goodsir (1985) on a rectangular thin wall with high axial load ratio ($0.26A_g f_c'$) subjected to cyclic in-plane

loading (Figure 1-5). The main reason for the partial out-of-plane shear failure to happen was the combination of high axial load and out-of-plane buckling as a consequence of high slenderness ratio (H_w/t) of the wall. However, the wall failed in lateral instability and only partial out-of-plane shear was observed.

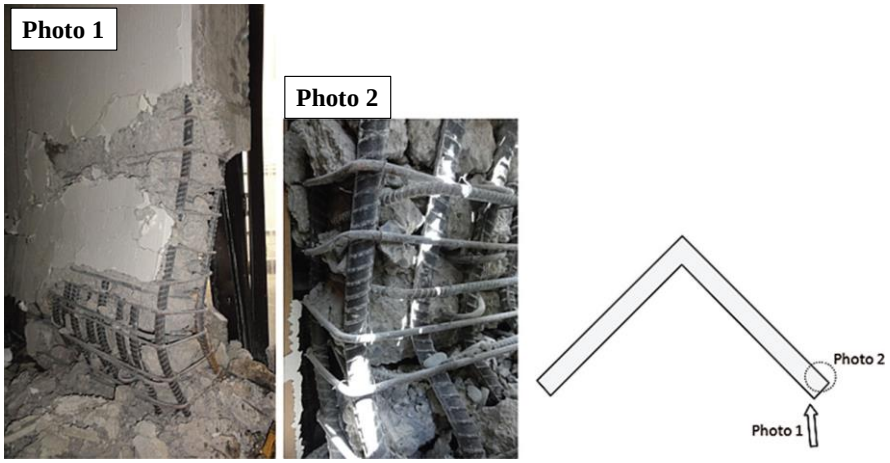

Figure 1-2 Web buckling of well-confined wall (Elwood 2013)

Figure 1-3 Web crushing of a slender wall in the 22 Feb 2011 Canterbury earthquake (Kam et al. 2011)

Figure 1-4 Out-plane Shear failure observed in 2011 New Zealand (Dunning Thornton 2011)

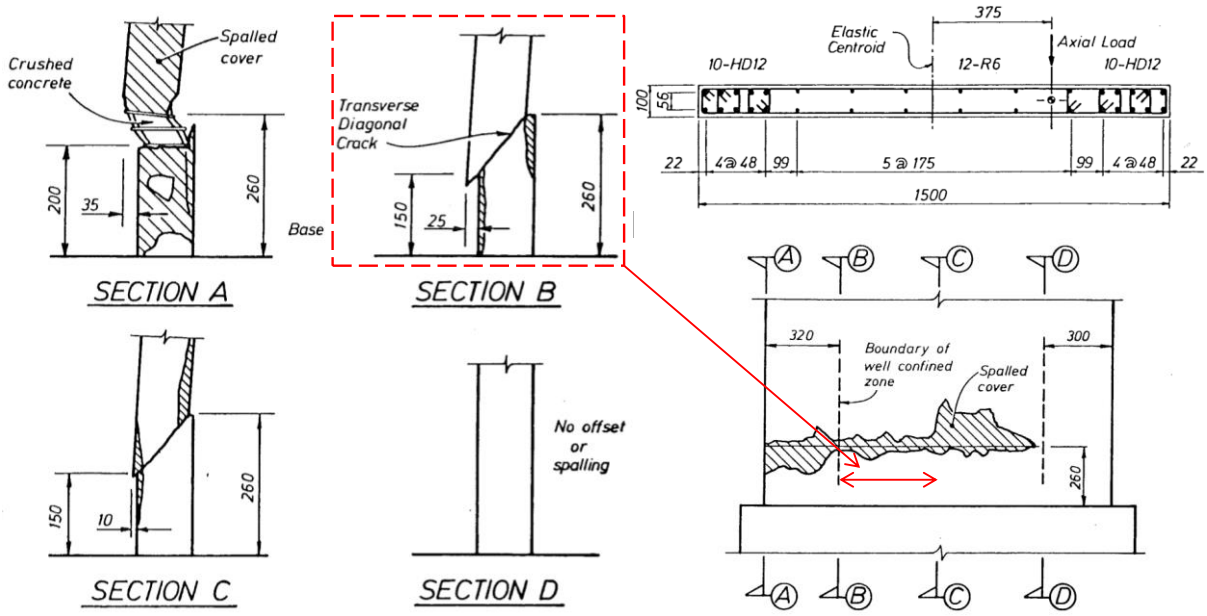

Figure 1-5 Description of the failure mode of Wall 1 tested by Paulay and Goodsir (1985)

1.2.BI-DIRECTIONAL LOADING DEFITITION

This section tries to briefly explains what bi-directional loading in RC walls means. Right now to design a RC wall, for example the one shown in blue in Figure 1-6, it will be designed for the gravity load and the earthquake forces in the in-plane direction of the wall. However, in reality not only earthquake forces might occur in the out-of-plane direction, but also with an angle to the whole structure that can be any angle. One might argue that the walls in the out-of-plane direction like the one shown in red in Figure 1-6 will take care of the out-of-plane earthquake forces and the walls in the in-plane direction will take care of the in-plane forces and there's no issue. But it is important to understand that regardless of what is taking care of which force in which direction, the wall shown in blue would undergo a certain drift in its out-of-plane direction in case of an earthquake in that direction which is basically the out-of-plane drift of the structure. Therefore, it is crucial to understand that it is not just about the forces but more importantly the deformation capacity of the wall under earthquake actions with different loading angles. What happened to Wall D5-6 from Grand Chancellor Hotel in the February 2011 earthquake is an example of bi-directional loading effects on the behaviour of structural walls. This will be discussed in more details in Chapter 7.

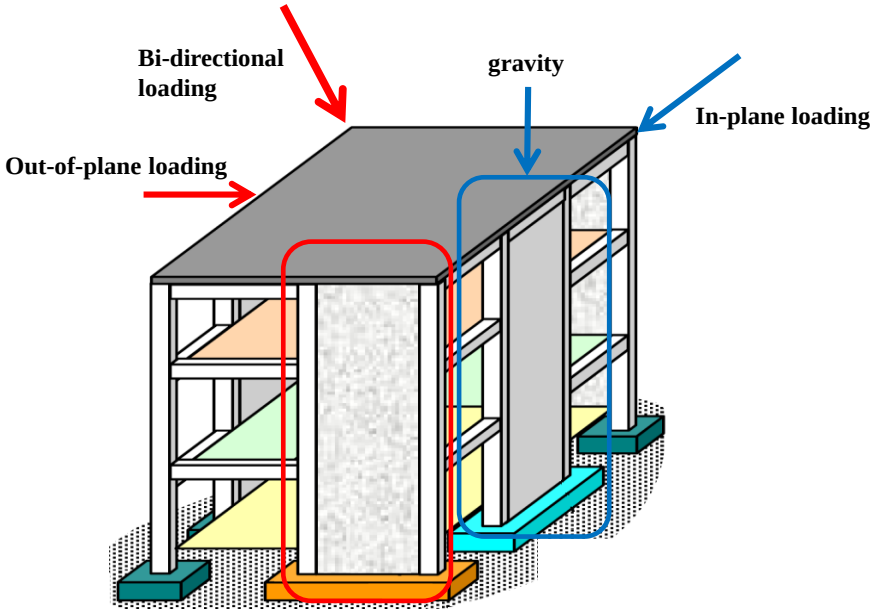

Figure 1-6 Bi-directional loading effects on RC walls

1.3. BI-DIRECTIONAL LOADING EFFECTS ON RC STRUCTURAL ELEMENTS

The behaviour of a large number of RC buildings during earthquakes was significantly different from the intended one (Japan, 1978; Algeria, 1980; Italy, 1980; Greece, 1981; Mexico, 1985; Taiwan, 1999; Turkey, 1999 and 2002; Italy, 2009; Chile, 2010; and New Zealand, 2011). One of the key parameters led to the changes in the behaviour of the structure compared to the expected one was the bi-directional nature of earthquake excitations. In this section, previous studies conducted on structural elements were discussed in three main categorized of columns, beam-column joints and structural walls.

1.3.1. Columns

The damage observed in the corner columns of Hachinohe Library in the 1968 Tokachi-oki earthquake, Oliva View Hospital in the 1971 San Fernando Earthquake, and Imperial County Services building (Figure 1-7a) in the 1979 Imperial Valley earthquake, are good examples for detrimental effects of bi-directional loading. As seen in Figure 1-7a, as a result of considerable inertia forces developed in the two principal directions (shown with arrows), the corner columns experienced significant bi-directional loading demand. However, the final failure of the corner column was due to inadequate confinement of concrete and lack of shear reinforcement in the column (Figure 1-7b).

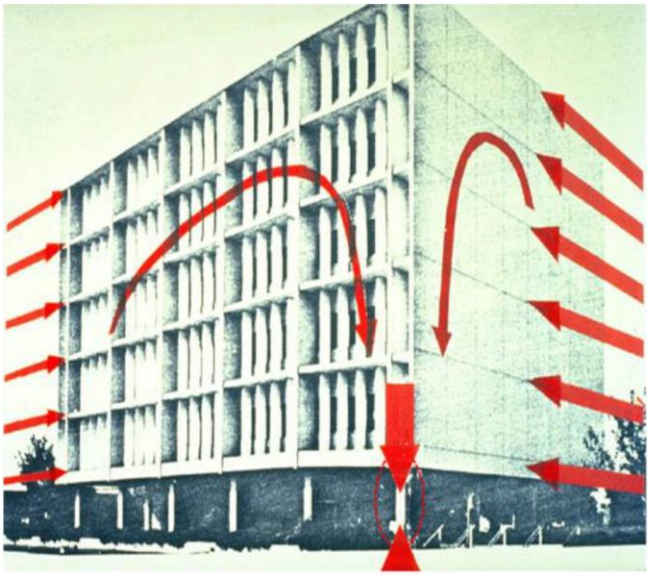

a) Imperial County Services Building – before earthquake

b) Close-up of the failure at the bottom of a corner column

Figure 1-7 Photograph of Imperial County Services building and failed corner column (Earthquake Image Information System: Karl V. Steinbrugge Collection NISEE, University of California, Berkeley)

These observations provided motivations for many researchers to investigate the bi-axial bending behaviour of RC columns (Padilla-Mora and Schnobrich 1974, Pecknold 1974, Lai et al. 1984, Maruyama et al. 1984, Umehara and Jirsa 1984, Low and Moehle 1987, Oliva and Clough 1987, Li et al. 1988, Mahin 1988, Zeris and Mahin 1991, Wong et al. 1993, Bousias et al. 1995, Kim and Lee 2000, Lai and Chang 2001, Marante and Flórez-López 2002, Qiu et al. 2002, Bonet et al. 2005, Boys et al. 2008, Pallarés et al. 2008, Bonet et al. 2011, Rodrigues et al. 2013, Wang et al. 2013). The key findings of some of these studies are presented in this section.

In an experimental and analytical study by Low and Moehle (1987) on RC columns subjected to constant/varied axial load and different lateral load path including skewed and clover leaf loading patterns, it was shown that bi-directional loading reduces strength and flexural stiffness of RC columns (Figure 1-8).

In another study by Zeris and Mahin (1991), they concluded that as a result of bi-directional loading, higher strains will be induced at the critical section level (such as in the corner reinforcement) which are greater than those result under severe uni-directional loading under equal imposed drifts. Therefore, local concentrations of damage at the critical regions will be higher when subjected to bi-directional excitations compared to uni-directional ones for comparable drift demands. Bi-directional response also affects the hysteretic and post-ultimate softening characteristics of columns.

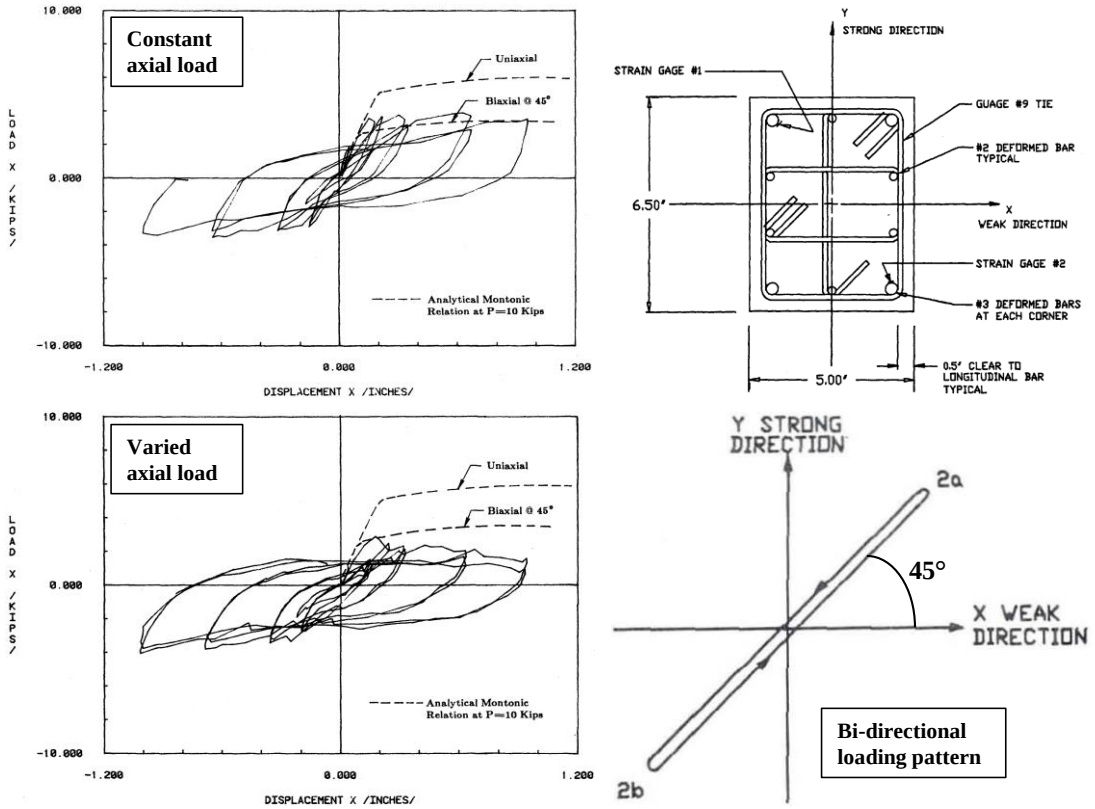

Figure 1-8 Hysteresis relations of RC columns under uni- and skewed loadings (Low and Moehle 1987)

In a comprehensive experimental study by Wong et al. (1993) in the University of Canterbury, sixteen RC columns with different spiral reinforcement configurations were tested under various lateral loading patterns and axial load ratios. They found that bi-directional loading on columns would lead to more severe degradation of strength and stiffness in comparison with the same column subjected to uni-directional loading. Ultimate drift capacity of the wall was also decreased significantly as can be seen in Figure 1-9.

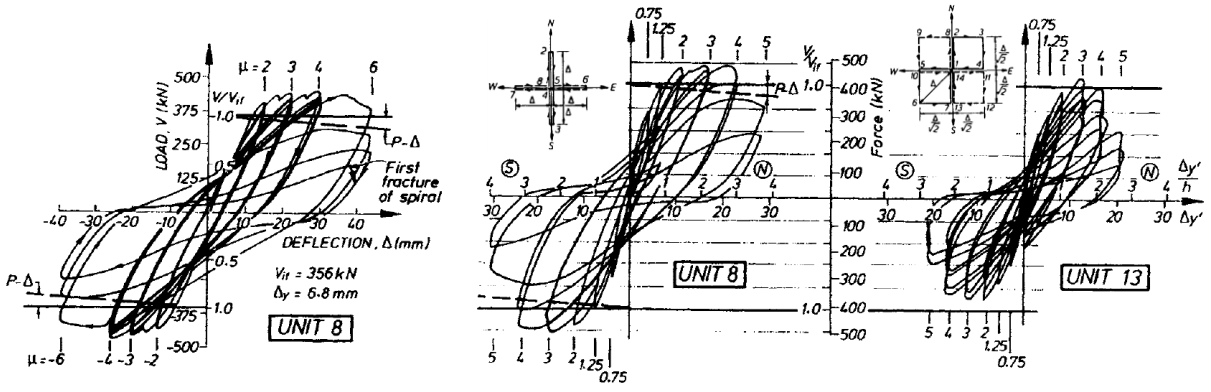

(a) Unixial [8] (b) Biaxial 'b' pattern (c) Biaxial 'S' Pattern

Figure 1-9 Hysteresis loops for identical units tested with different displacement patterns (Wong et al. 1993)

Bonet et al. (2005) proposed a method for determining the capacity of rectangular RC sections with doubly symmetrical reinforcement subjected to axial load and bi-directional loading. The method was based on the simplification to an increased uni-axial bending analysis. Their method allows reinforced concrete sections to be checked and designed in a simple but accurate way, which is very interesting for practising engineers.

In an experimental study, Boys et al. (2008) tested inadequately detailed RC columns subjected to bi-directional loading and found that bi-directional loading results in a significant reduction in the displacement capacity when compared to uni-directional loading (Figure 1-10). Figure 1-10 also shows the observed damage when the column was under uni- and bi-directional loadings at the same drift level of 1.5%. Boys et al. (2008) observed that at 1-1.5% drift, some specimens were losing gravity bearing capacity under bi-directional loading which would lead to partial or total collapse of the building.

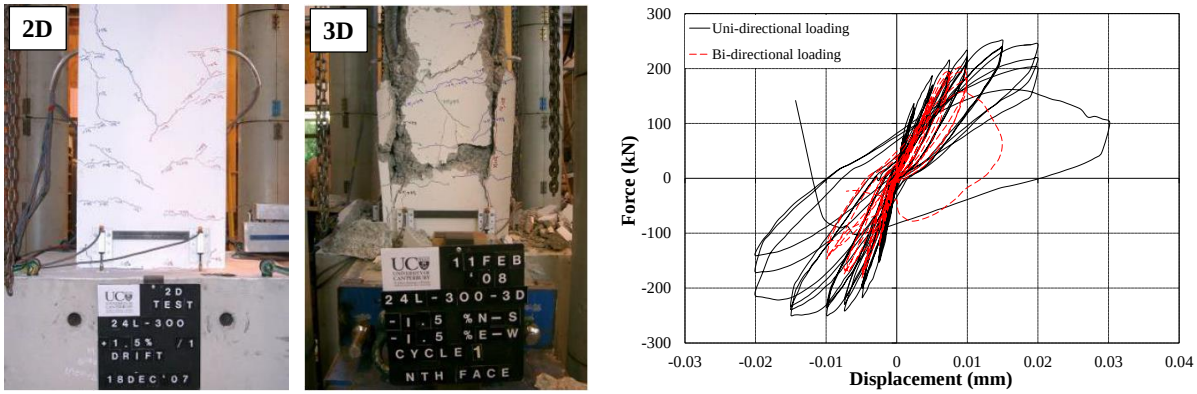

Figure 1-10 Damage observed at 1.5% drift for 2D and 3D tests (Boys et al. 2008)

Pallarés et al. (2008) tested several high strength RC columns to investigate the seismic performance of this type of columns under uni- and bi-directional loadings. some of the failure types that they observed are shown in Figure 1-11.

Bousias et al. (1995), Qiu et al. (2002) and Rodrigues et al. (2013) tested several specimens subjected to different bi-axial loading paths to investigate the effect of loading pattern on the seismic behaviour of RC columns. Figure 1-12 shows the bi-directional loading path investigated by Qiu et al. (2002) and the envelope of the hysteresis curves of the specimens subjected to these load paths. They have shown that different bi-directional loading patterns can significantly affect the force-displacement curves as well as the failure mode of RC columns.

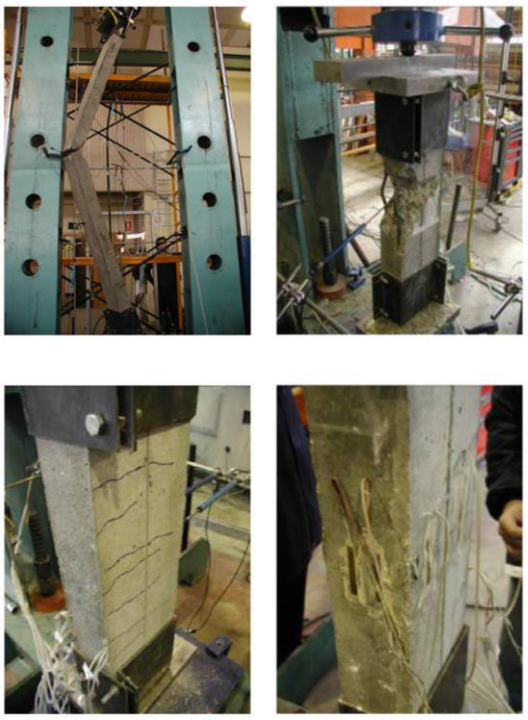

Figure 1-11 RC columns under bi-directional loading (Pallarés et al. 2008)

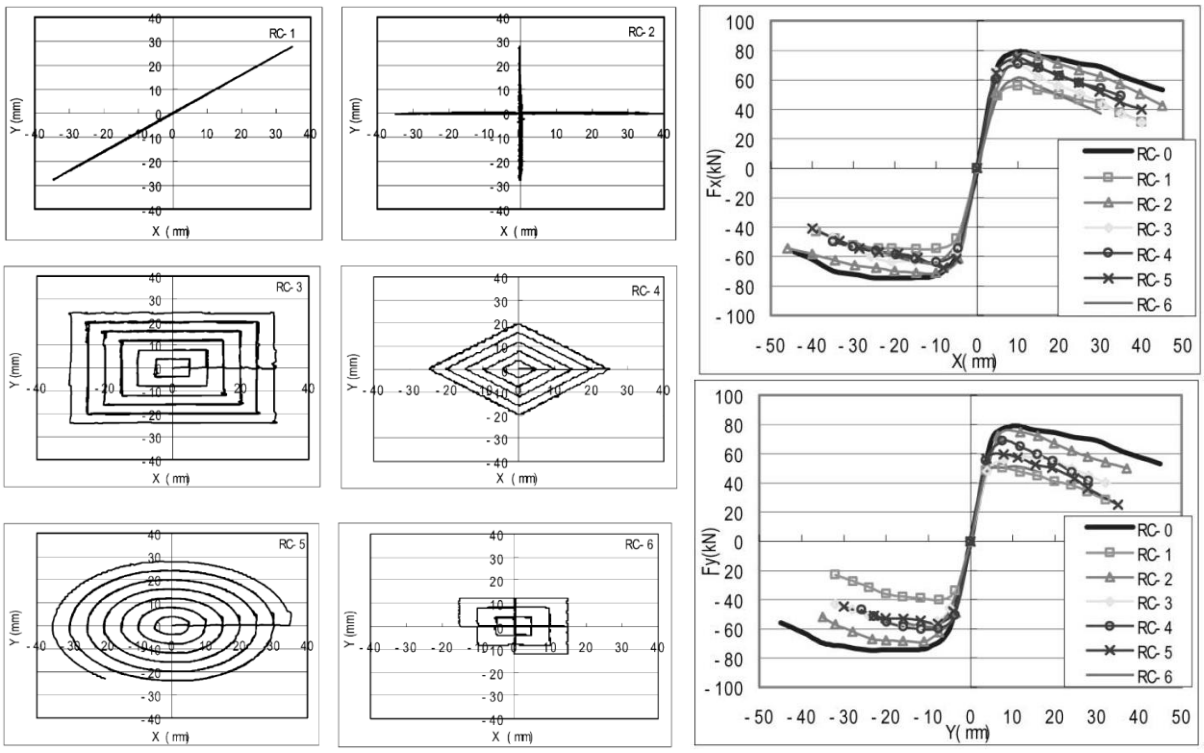

Figure 1-12 Loading path and load displacement peak envelopes of the specimens (Qiu et al. 2002)

1.3.2. Beam-column joints

Several researchers investigated the effects of bi-directional loading on the seismic performance of RC beam-column joints (Beckingsale 1980, Leon and Jirsa 1986, Bolong and Yuzhou 1991, Kurose et al. 1991, Akguzel and Pampanin 2010). Some of these studies are described briefly here.

Beckingsale (1980) conducted experimental investigations on the behaviour of new-designed beam-column joints under uni- and bi-directional loadings. Although some stiffness degradation was observed under bi-directional loading, the beam strength capacity attained at the same drift level did not reduce considerably.

In an experimental parametric study by Leon and Jirsa (1986), the effects of bi-directional loading on the joint behaviour were investigated. Experimental results showed that bi-directional loading significantly affects the joint behaviour due to the deterioration of column strength. They have concluded that the effects of bi-directional loading should be considered in the analysis and design of space ductile moment resisting frames. Figure 1-13 shows the specimen, lateral load path and the typical crack patterns observed in the test.

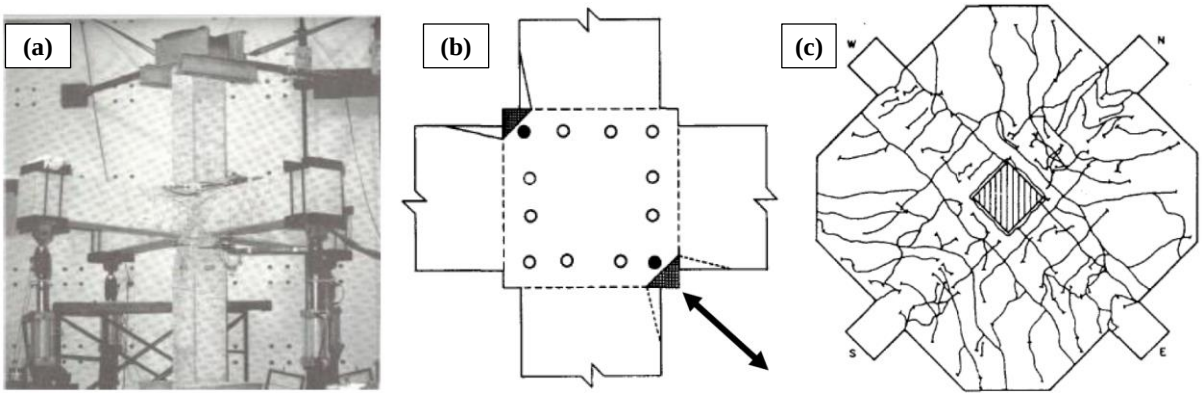

Figure 1-13 Experimental study by Leon and Jirsa (1986): (a) specimen view, (b) lateral load path and (c) typical distribution of crack patterns

In a comprehensive experimental study, Akguzel and Pampanin (2010) investigated the effects of bi-directional loading on the seismic performance of RC beam-column joints. Test setup and the bi-directional loading patterns used for this study were shown in Figure 1-14. Lateral force-top displacement of one the specimens under uni- and bi-directional loadings were shown in Figure 1-15. The experimental results showed that neglecting the effects of varied axial load and bi-directional loading would lead to unconservative results when assessing the behaviour of existing beam-column joints. The test results confirmed that bi-directional loading on the corner joints can reduce the strength and drift capacities of the

beam-column joints considerably and consequently affect the efficiency of a retrofit solution designed based on a uni-directional loading.

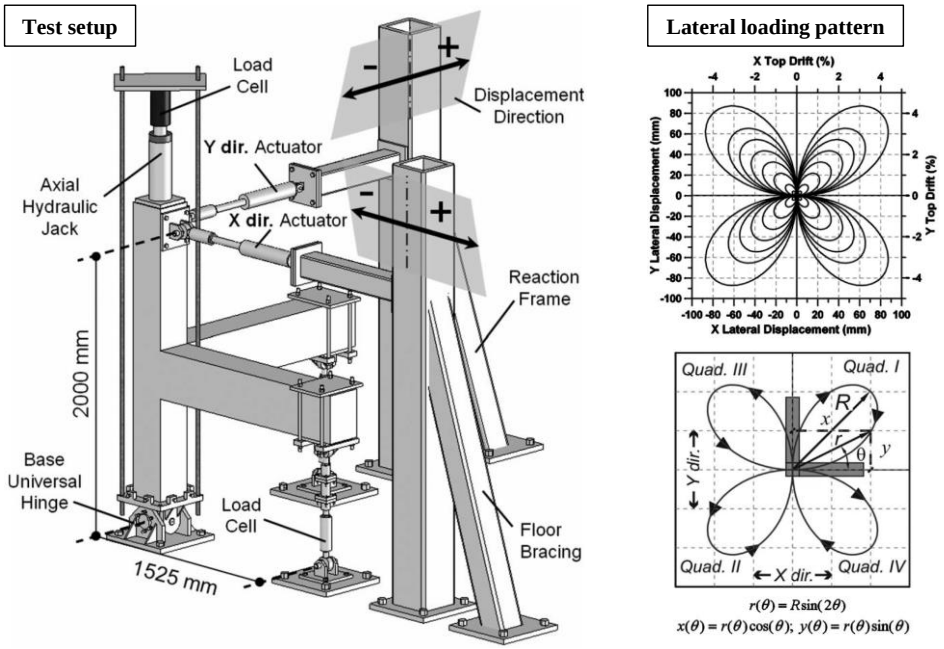

Figure 1-14 Test setup and lateral loading patterns used for specimens subjected to uni- and bi-directional loadings (Akguzel and Pampanin 2010)

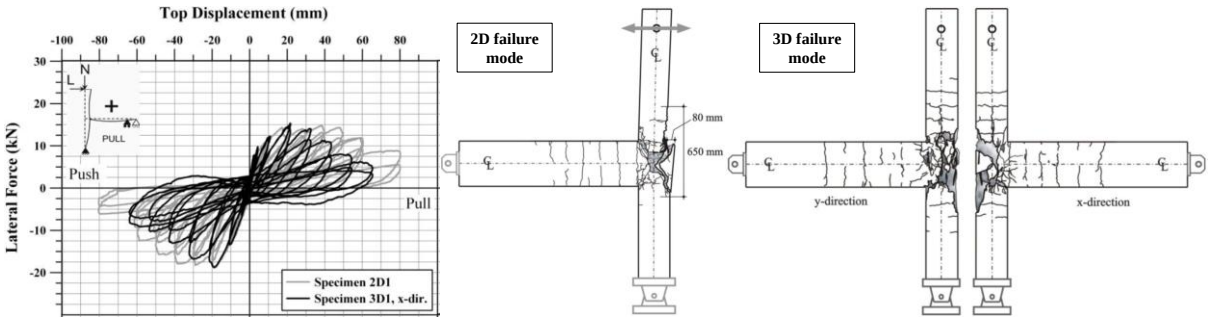

Figure 1-15 Lateral force-top displacement curve and failure patterns of beam-column joints tested under uni- and bi-directional loadings (Akguzel and Pampanin 2010)

1.3.3. Non-planar walls

There are a few experimental studies conducted on non-planar RC walls such as U-shaped, C-shaped, T-shaped and etc. (Ile and Reynouard 2005, Beyer et al. 2008, Behrouzi et al. 2014, Constantin and Beyer 2016, Brueggen et al. 2017) which some of them were briefly discussed here.

Ile and Reynouard (2005)

Effects of bi-directional loading were investigated on three identical U-shaped RC walls (Figure 1-16) under different lateral loading patterns. The three loading pattern used were cyclic uni-directional loading in the X and Y directions and bi-directional loading

(Figure 1-17). It was found that maximum drift capacity of the wall was reduced by about 33% when it was subjected to bi-directional loading (Figure 1-18). Maximum strength capacity was also reduced in the wall subjected to bi-directional loading in the X-direction (along the web). Based on Ile and Reynouard (2005) experimental results, it can be concluded that a pre-existing displacement in the transverse direction reduces the maximum attainable strength in U-shaped walls (Beyer et al. 2017). Moreover, a shear failure was observed in one of the flanges of the wall subjected to bi-directional loading which was not observed in the case of the wall subjected to uni-directional loading (Figure 1-19).

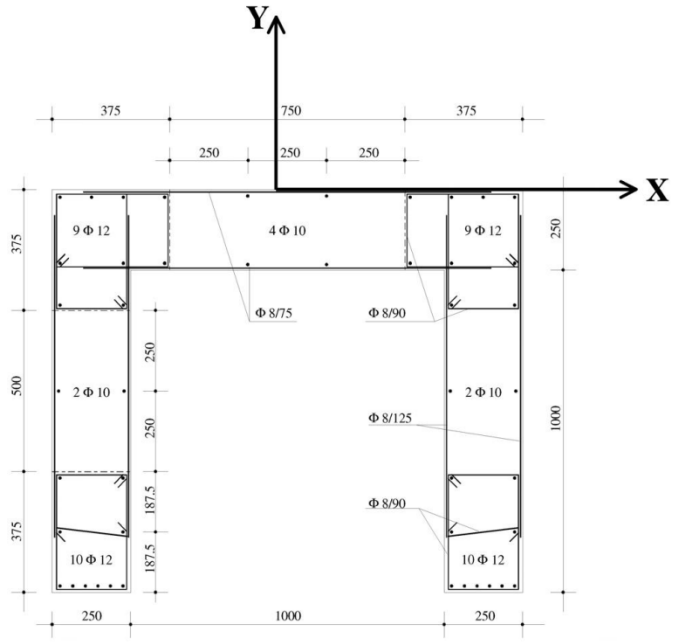

Figure 1-16 section of the test specimen (Ile and Reynouard 2005)

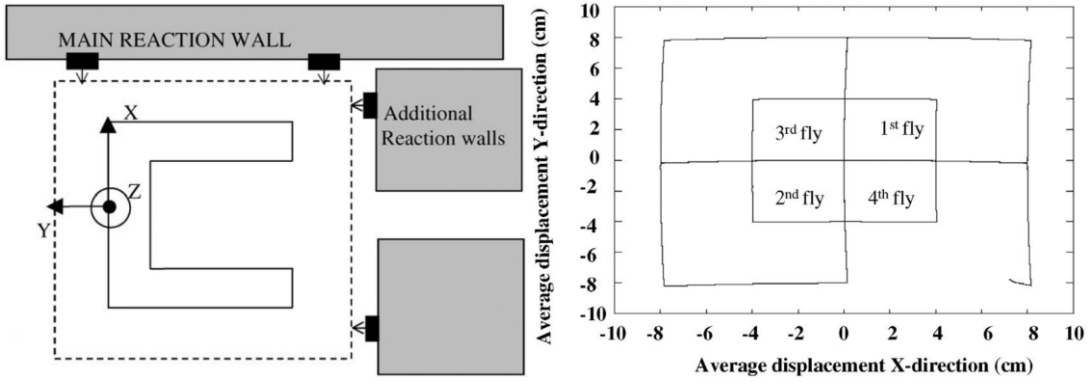

Figure 1-17 Lateral loading pattern of the specimen under bi-directional loading (Ile and Reynouard 2005)

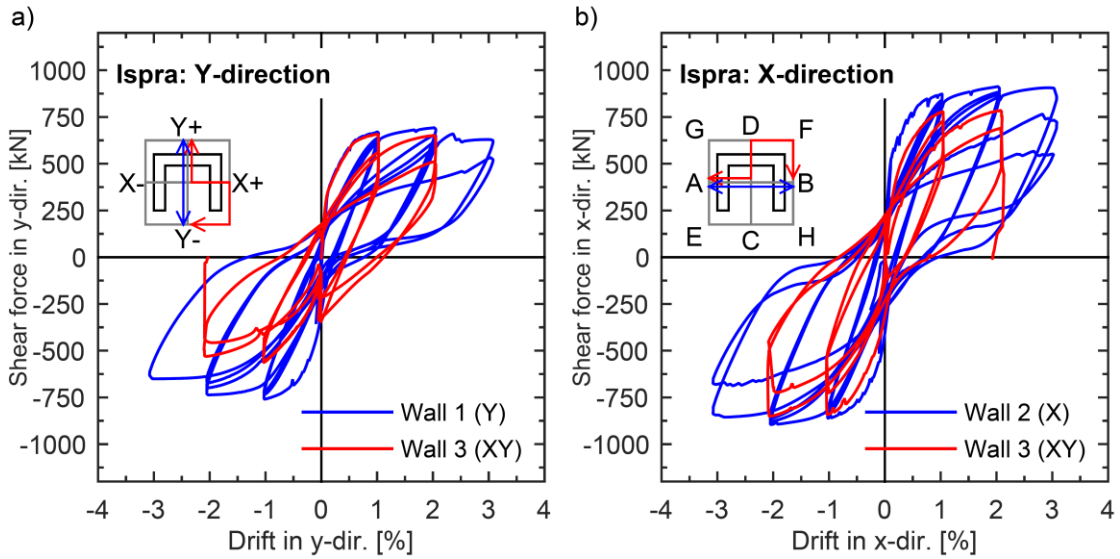

Figure 1-18 Comparison of force-displacement hysteresis for uni-directional loading against force-displacement hysteresis from bi-directional loading (clover leaf pattern): a) Parallel to flanges, b) Parallel to web(Ile and Reynouard 2005, Beyer et al. 2017)

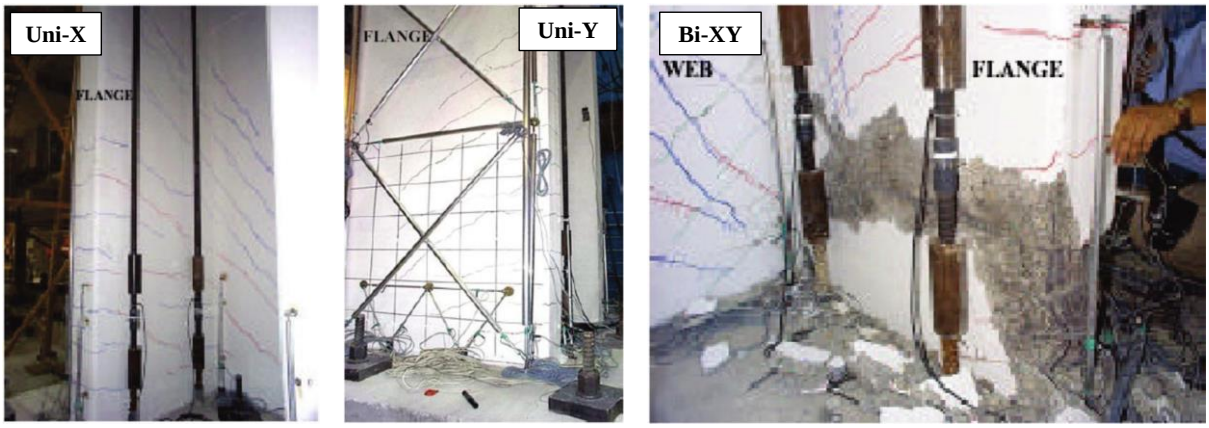

Figure 1-19 Failure pattern of the wall under each loading patterns (Ile and Reynouard 2005)

Beyer et al. (2008)

Two U-shaped RC walls were tested under bi-directional loading at the structural engineering laboratories of the ETH Zurich. The walls were built at half-scale and designed for high ductility. Cross sections of the two specimens are shown in Figure 1-21. The main difference between the two walls was their wall thickness (specimen TUA had larger thickness compare to specimen TUB). Test setup and the lateral loading pattern used for testing the walls under bi-directional loading showed in Figure 1-21 and Figure 1-22, respectively. The main focus of the study was the bending behaviour of the walls in different directions. The experiments showed that the most critical direction in a U-shaped wall is the diagonal one for which the maximum attained moment capacity was less than what section analysis would predict, while at the same time the drift capacity is smallest. Failure pattern of the specimens TUA and TUB were shown in Figure 1-23. Specimen TUA failed due to rupture of the longitudinal

reinforcing bars after buckling and specimen TUB failed due to web crushing. The concrete crushing failure of specimen TUB in the web found to be caused by the reduction of the effective wall thickness due to spalling of the unconfined concrete outside of the boundary elements which was not expected before the experiment. Beyer et al. (2008) concluded that depends on the lateral loading's direction, the ratio of the shear to the total displacements varied greatly between the different wall sections, i.e., the web and the two flanges. It was found that the contribution of the shear displacements was largest when a wall section was under net tension.

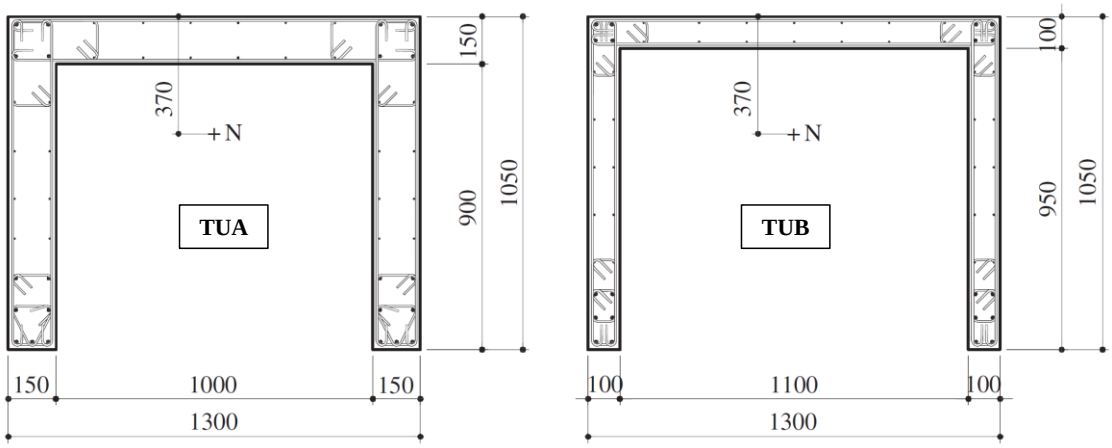

Figure 1-20 Cross sections of TUA, TUB (Beyer et al. 2008)

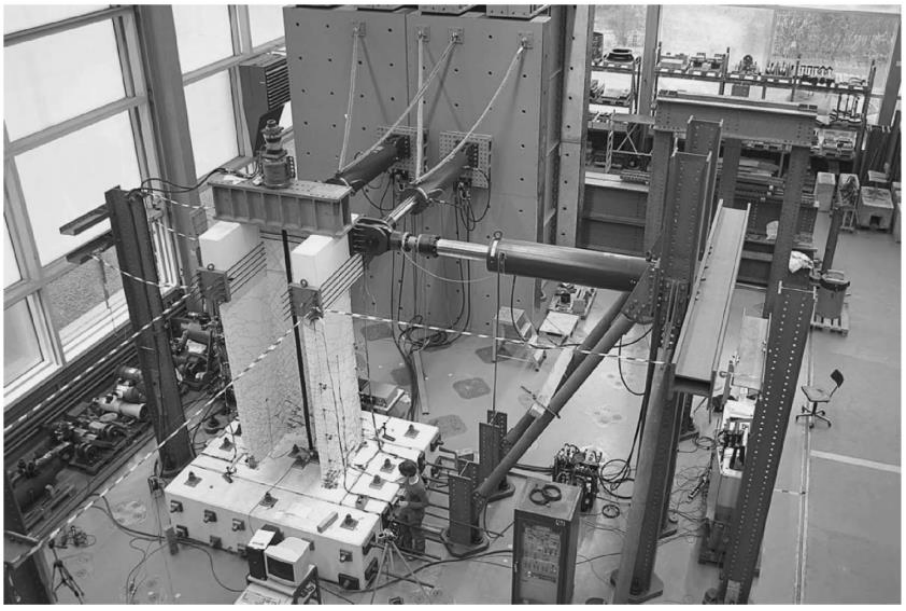

Figure 1-21 Photo of the test setup used for walls under bi-directional loading (Beyer et al. 2008)

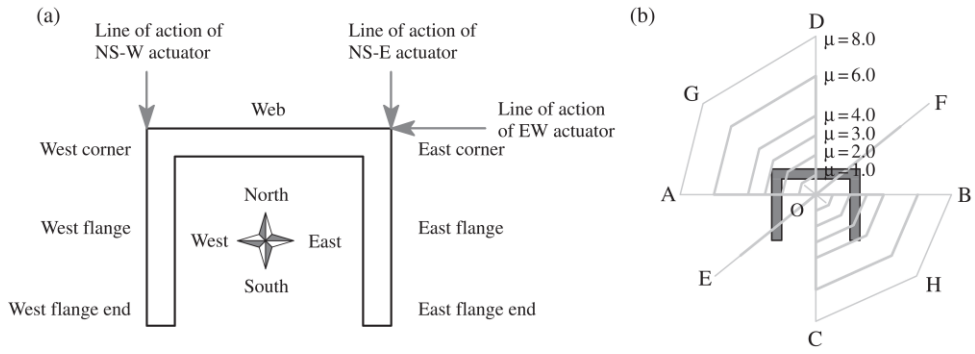

Figure 1-22 (a) Cardinal points and labelling of different wall sections and (b) target displacement pattern (Beyer et al. 2008)

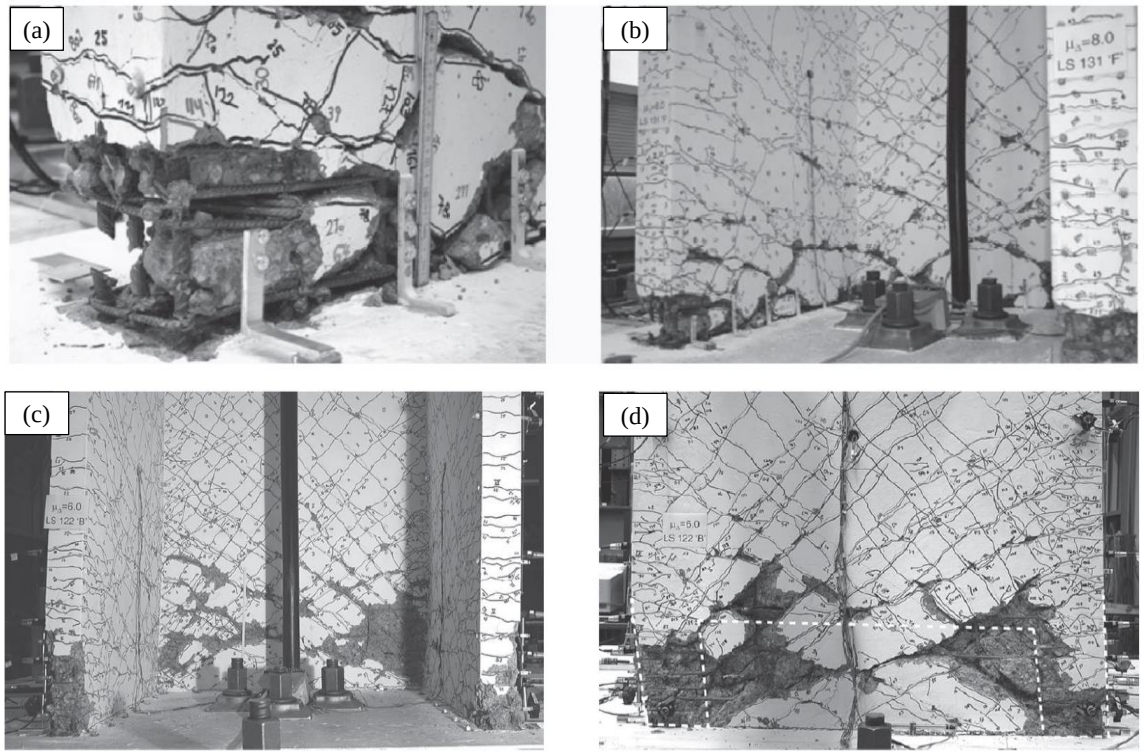

Figure 1-23 (a & b) specimen TUA at failure point (c & d) specimen TUB at failure point (Beyer et al. 2008)

Constantin and Beyer (2016)

Two half-scale RC U-shaped walls were tested at EPFL under skewed lateral loading. The main objective of the experimental study was to investigate the effects of skewed loading on the behaviour of U-shaped walls. Both test units, TUC and TUD had identical longitudinal reinforcement configurations (Figure 1-24) but different axial load ratio and shear reinforcement. TUC was subjected to an axial load ratio of 6% and TUD to an axial load ratio of 15%. Figure 1-25 shows the test setup and the loading patterns used for the experiments. Constantin and Beyer (2016) found that flanges of U-shaped wall subjected to bi-directional loading are prone to out-of-plane buckling (see Figure 1-26). Concrete crushing failure of the specimens TUC and TUD are shown in Figure 1-27 and Figure 1-28, respectively. The axial

load ratio, which was the main varying parameter between the two experiments, affected the wall ultimate drift and the failure mode as can be seen in Figure 1-27 and Figure 1-28. The higher axial load ratio decreased the ultimate drift capacity of the wall as the failure modes of both test units were compression-controlled. It was found that the unconfined concrete of the concentrated layout flange was more damaged than the unconfined concrete of the distributed layout flange (Figure 1-29). It was found that the plane section assumption, which is the basis of section analysis tools for RC walls, does not hold for the U-shaped walls under skewed loading since it fails to capture the presence of additional compression zones at the corners between web and flange.

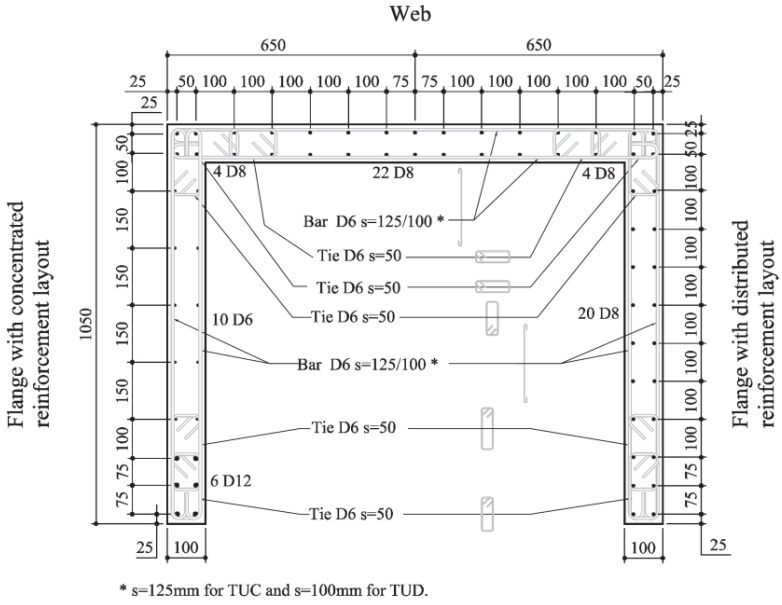

Figure 1-24 cross-section and reinforcement layout of the test units (Constantin and Beyer 2016)

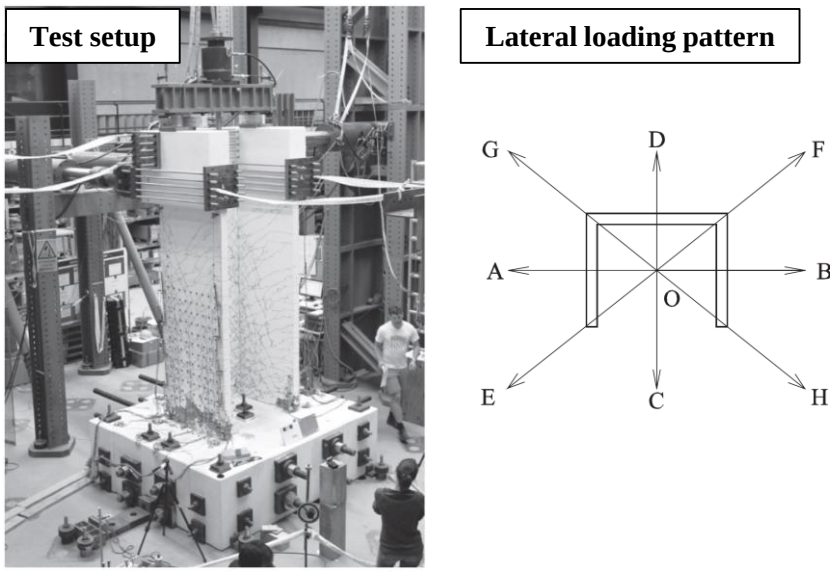

Figure 1-25 Photo of the test setup and the loading positions (Constantin and Beyer 2016)

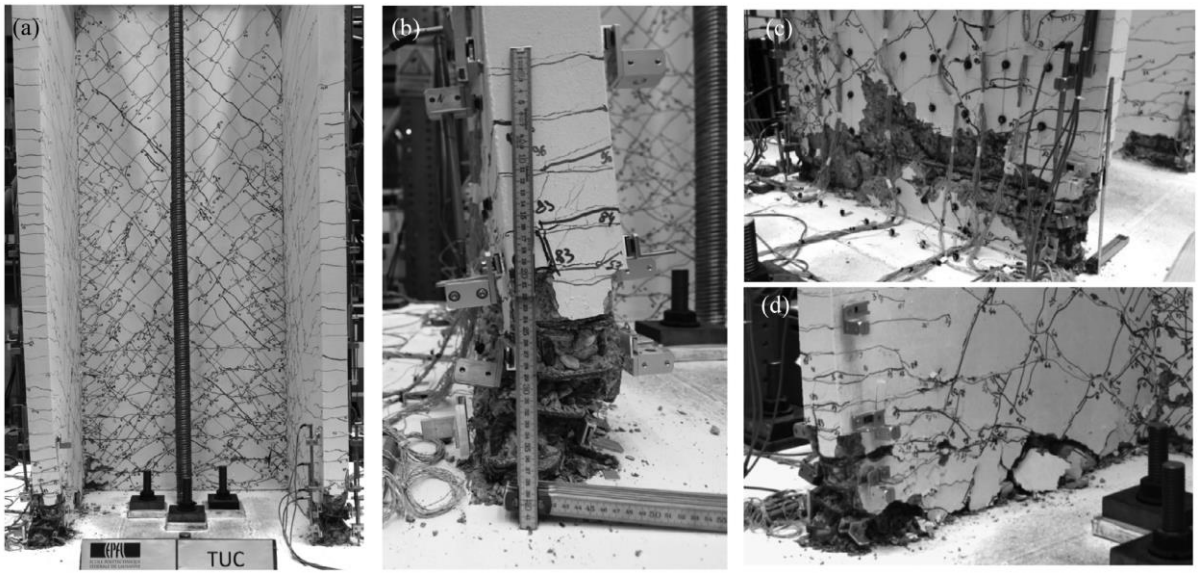

Figure 1-26 Out-of-plane buckling and compression failure of the concentrated reinforcement layout flange of specimen TUC at 1% drift (Constantin and Beyer 2016)

Figure 1-27 Crushing of the concrete in the flange with distributed reinforcement of specimen TUC at 2.5% drift (Constantin and Beyer 2016)

Figure 1-28 explosive compression failure of the distributed reinforcement layout flange of specimen TUD at 1.5% drift (Constantin and Beyer 2016)

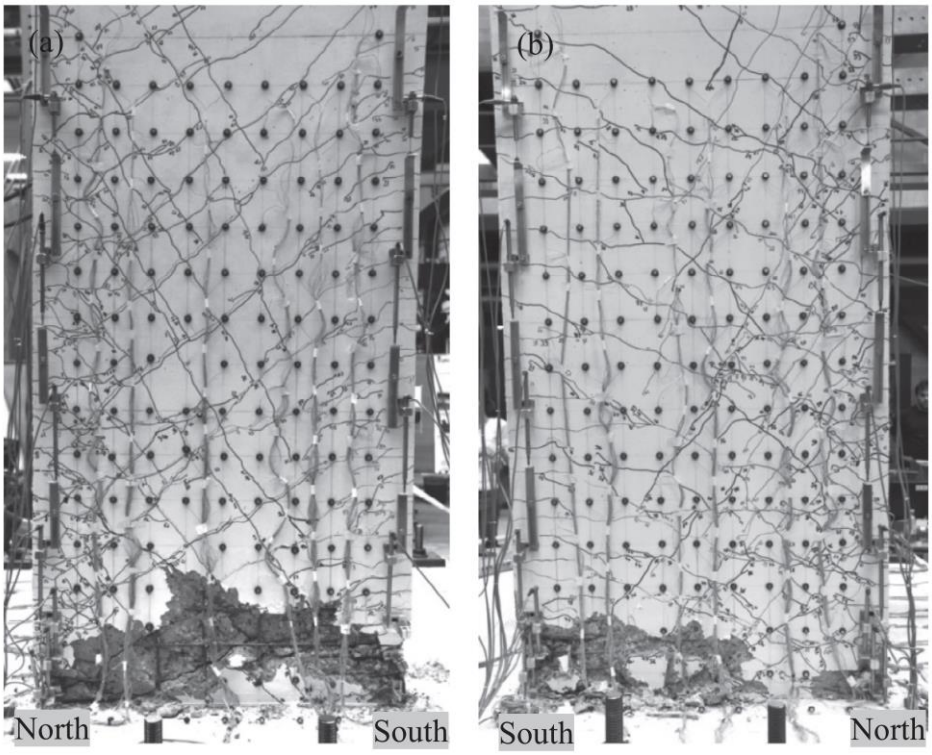

Figure 1-29 Influence of the vertical reinforcement layout on the damage to the unconfined concrete of the wall flanges in specimen TUC (a) concentrated reinforcement layout (West flange) and (b) distributed reinforcement layout (East flange) (Constantin and Beyer 2016)

1.3.4. Rectangular walls

There are a limited number of studies on rectangular RC walls subjected to bi-directional loading (Tatsuya 1996, Kabeyasawa et al. 2014, Almeida et al. 2017) which all of them are discussed here in details.

Tatsuya (1996)

Tatsuya (1996) tested five RC walls with 1/3-scale subjected to uni- and bi-directional loadings (1 under uni- and 4 under bi-directional loadings). The objective of the study was to investigate the deformation capacity of walls under bi-directional loading. Table 1-1 and Table 1-2 summarize the characteristics of the specimens. Specimens MW and M types are shown in Figure 1-30. Test setup and the lateral load path used by Tatsuya (1996) are shown in Figure 1-31. It is worth noting that, the vertical actuators were used to control the axial load and rotational angle at the top of the specimens. It should be noted that the loading started from in-plane direction for all cases.

Table 1-1 Main characteristics of the specimens (Tatsuya 1996)

Specimen	In-plane shear span ratio (H_e/L_w)	Out-of-plane shear span ratio (H_w/t)	Axial load ratio $P/(A_g f'_c)$	Loading path
M35X	2	5	16	In-plane uni-directional
M30H			13.3	Bi-directional (H-shape) Figure 1-31
M35H			17.4	
MW35H			15.1	
P35H			16.9	

Table 1-2 Details of the specimens (Tatsuya 1996)

Specimen	Boundary column				Wall web		
	Width × depth (mm)	Main bar (ρ_g%)	Spiral hoop (ρ_w%)	Sub tie (ρ_w%)	Panel height h_w (mm)	Panel thickness × Panel length (mm)	Wall web bar (ρ_s%)
M35X	200 × 200	12-D10 (2.14)	D6 @60 (0.53)	D6 @60 (0.53	2000	80 × 1300	2-D6 @100 (0.8)
M30H							
M35H							
MW35H							
P35H				----			

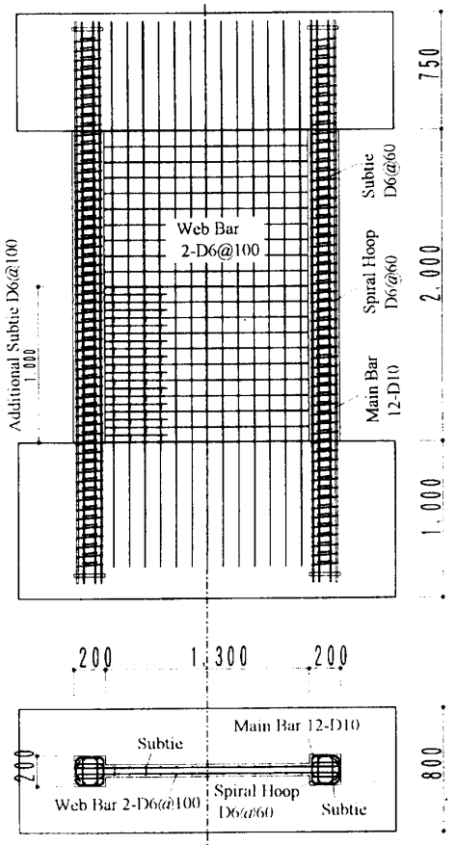

Figure 1-30 Details of the specimens (Tatsuya 1996)

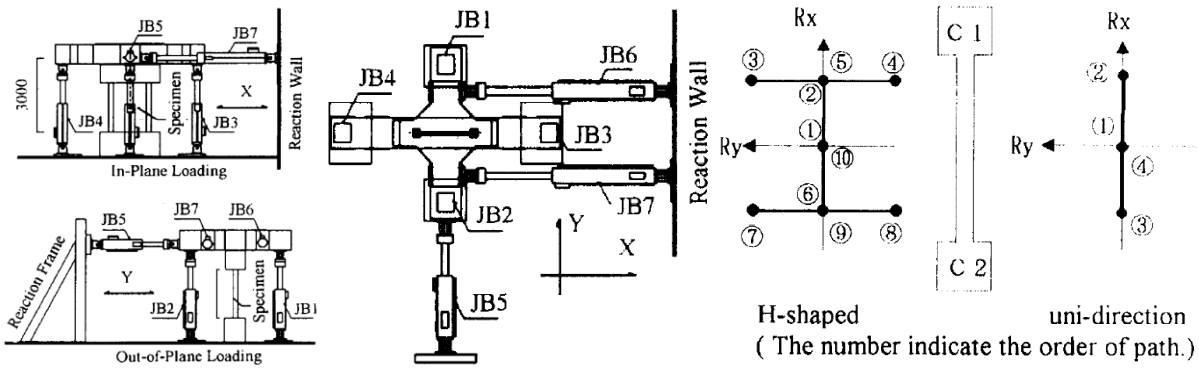

Figure 1-31 The test setup of loading system and the lateral loading protocols (Tatsuya 1996)

Figure 1-32 shows the hysteressis relations for M35X (specimen under uni-directional loading only) and M35H (identical specimen under bi-directional loading). Tatsuya (1996) found that the deformation capacity of the specimens subjected to bi-directional loading was smaller than the one subjected to uni-directional loading. However the same failure mode was observed (web crushing) for both specimens (M35X and M35H). It can be due to relatively high axial load ratio of the specimens (Beyer et al. 2017). Figure 1-33 shows each specimen after web crushing. Not much difference was observed in the wall's strength capacity and flexural stiffness when it was under bi-directional loading compared to the same wall subjected to uni-directional loading.

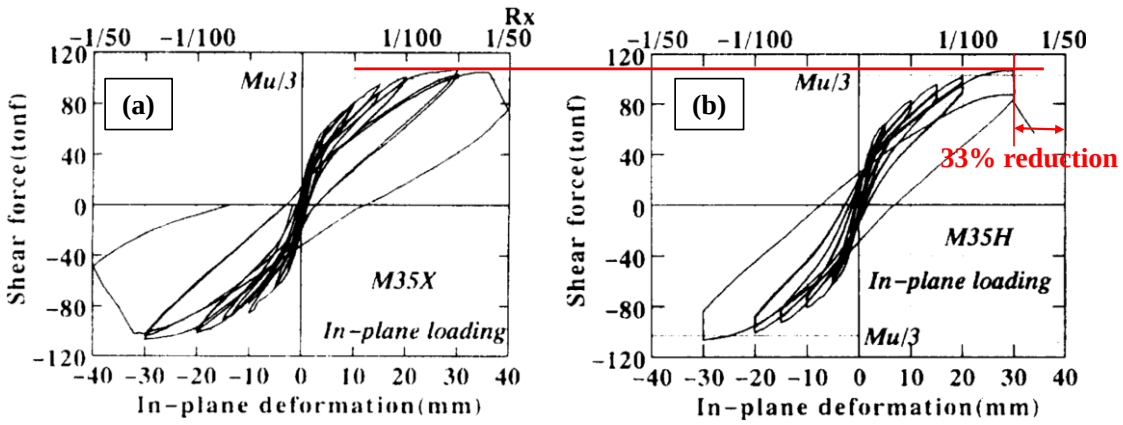

Figure 1-32 Hysteresis relations under (a) Uni- (b) Bi-directional loadings (Tatsuya 1996)

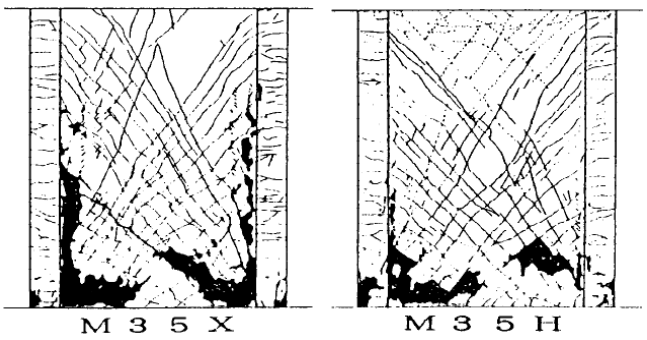

Figure 1-33 Failure mode of the specimens M35X and M35 H (Tatsuya 1996)

Axial strains in the compression side of the boundary elements (columns) and the web is shown in Figure 1-34. As can be seen axial strains started to increase from the very beginning in the boundary elements (columns) when the wall was under bi-directional loading. However, axial strains in the web were almost the same in both cases until the web crushed.

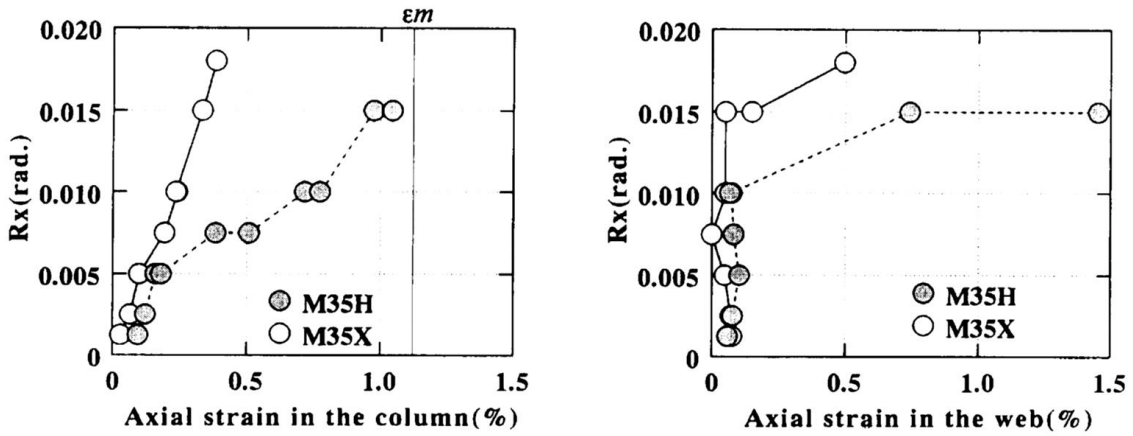

Figure 1-34 Axial strains in the compression-side of the boundary elements (columns) and the web (Tatsuya 1996)

Kabeyasawa et al. (2014)

In another experimental study by Kabeyasawa et al. (2014), eight specimens of about one-third scaled were tested (4 under uni- and 4 under bi-directional loadings). Table 1-3 and Table 1-4 summarize the characteristics of the specimens. One of pair identical specimens was tested under uni-directional and the other under bi-directional loading. Figure 1-35 shows the section details of each specimen.

Table 1-3 Main characteristics of the specimens (Kabeyasawa et al. 2014)

Specimen	In-plane shear span ratio (H_e/L_w)	Out-of-plane shear span ratio (H_w/t)	Axial load ratio $P/(A_g f'_c)$ %	Loading path
WA-1D	1.4	2.5	7.5	In-plane uni-directional
WA-2D			7.6	Bi-directional
WB-1D	1.32	4.17	8.1	In-plane uni-directional
WB-2D			7.6	Bi-directional
WC-1D	1.1	4.17	8.8	In-plane uni-directional
WC-2D			8.4	Bi-directional
WD-1D	1.1	6.25	12.4	In-plane uni-directional
WD-2D			12	Bi-directional

Table 1-4 Details of the specimens (Kabeyasawa et al. 2014)

	Specimen	WA	WB	WC	WD
Boundary Elements	Section $B_c \times D_c$ (mm)	250×150	150×250	150×300	100×450
	Longitudinal reinforcement	10 D10	10 D10	8 D13	12 D10
	Transverse reinforcement	D4@33	D4@33	D4@33	D4@33
Web	Length (mm)	1350	1250	1150	850
	Thickness (mm)	100	100	150	100
	Longitudinal and transverse reinforcement	2D4@80	2D4@80	2 D4@50	2 D4@75

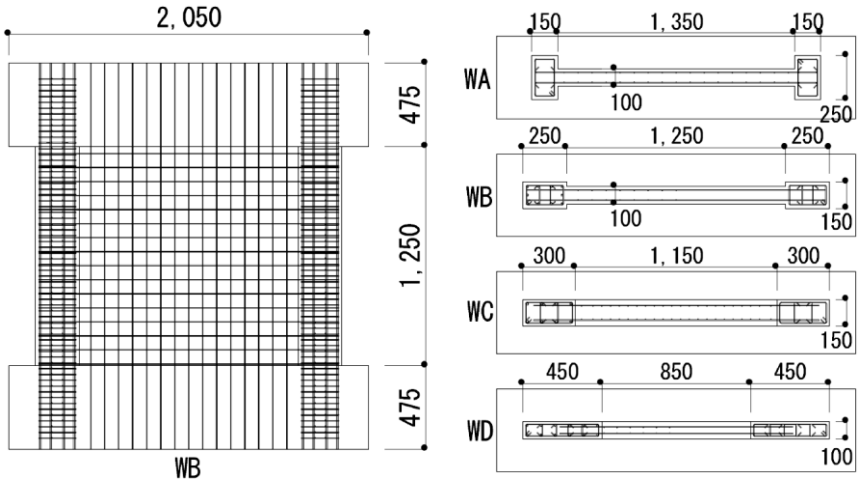

Figure 1-35 Details of tested wall specimens (Kabeyasawa et al. 2014)

Figure 1-36 shows the test setup that Kabeyasawa et al. (2014) used in the laboratory for the experiments. As for the out of plane direction of loading, the hydraulic actuators were set at the height of 625mm, which is the mid-height of the inner column height, so that anti-symmetric bending moment was applied in the orthogonal direction (see Figure 1-36).

The reversed and cyclic loading was controlled for both directions with the deflection measured at the wall top to trace the planned displacement path as shown in Figure 1-37. As can be seen, in the case of specimens under bi-directional loading, loading was started from the out of plane direction.

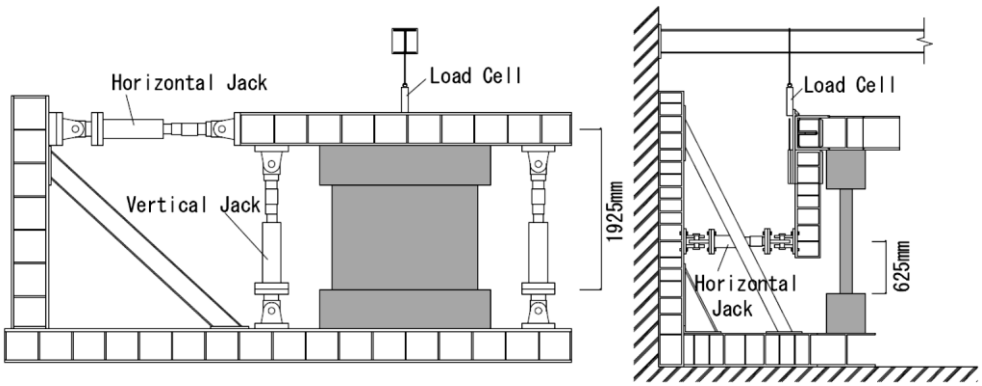

Figure 1-36 Setup for bi-axial loading (Kabeyasawa et al. 2014)

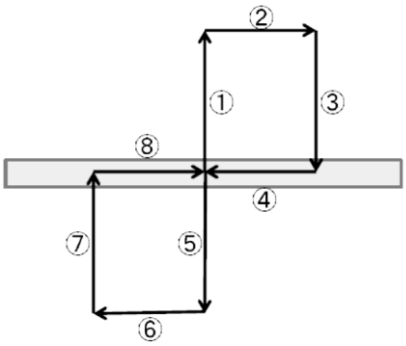

Figure 1-37 Bi-directional loading protocol (Kabeyasawa et al. 2014)

The observed hysteretic relations between the in-plane base shear and in-plane drift ratio of each specimen are shown in Figure 1-38 and Figure 1-39. Kabeyasawa et al. (2014) found that the flexural strengths were not much different for the specimens under uni- and bi-directional loadings. However, the ultimate drift capacity of the wall under bi-directional loading was relatively smaller than those under uni-directional loading in all four cases by 1.2 to 1.33 times.

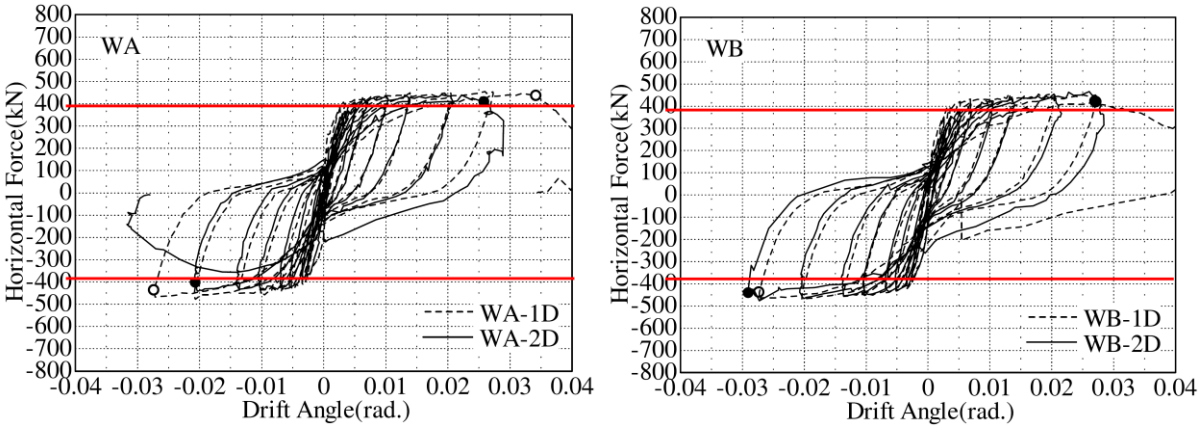

Figure 1-38 In-plane hysteretic relations comparing uni-directional and bi-directional loadings for specimens WA and WB (Kabeyasawa et al. 2014)

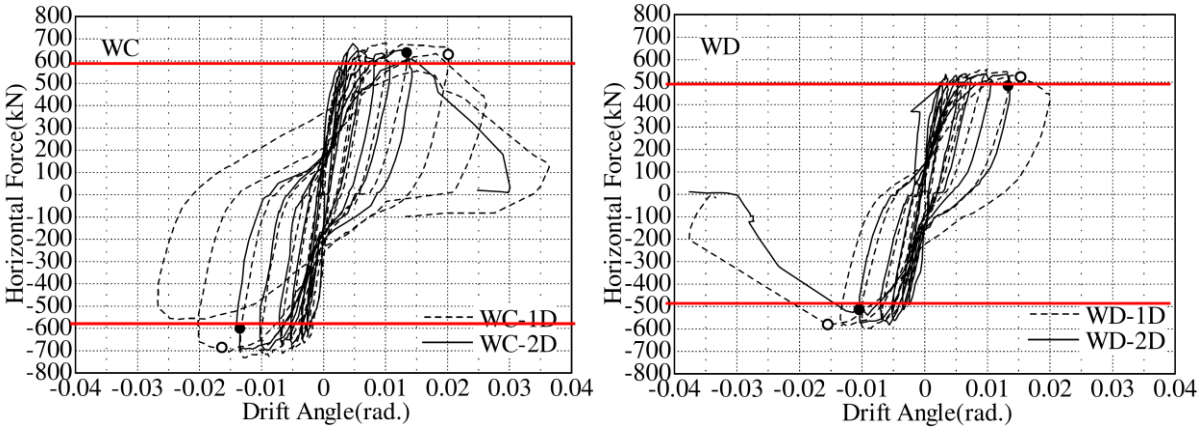

Figure 1-39 In-plane hysteretic relations comparing uni-directional and bi-directional loadings for specimens WC and WD (Kabeyasawa et al. 2014)

Figure 1-40 and Figure 1-41 show each specimen at the failure point. Kabeyasawa et al. (2014) found the diagonal shear tension failure in the wall panel (when under uni-directional loading) was changed to a horizontal sliding shear in the wall panel above the wall base (when under bi-directional loading).

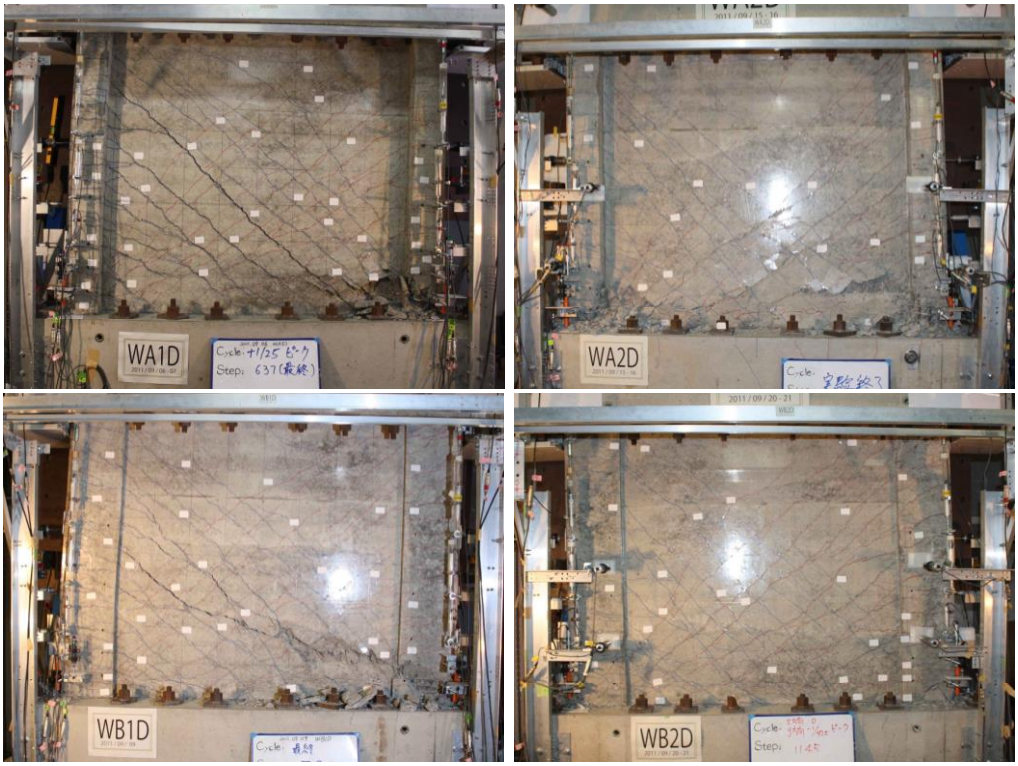

Figure 1-40 Failure mode of specimens WA and WB under uni-and bi-directional loadings (Kabeyasawa et al. 2014)

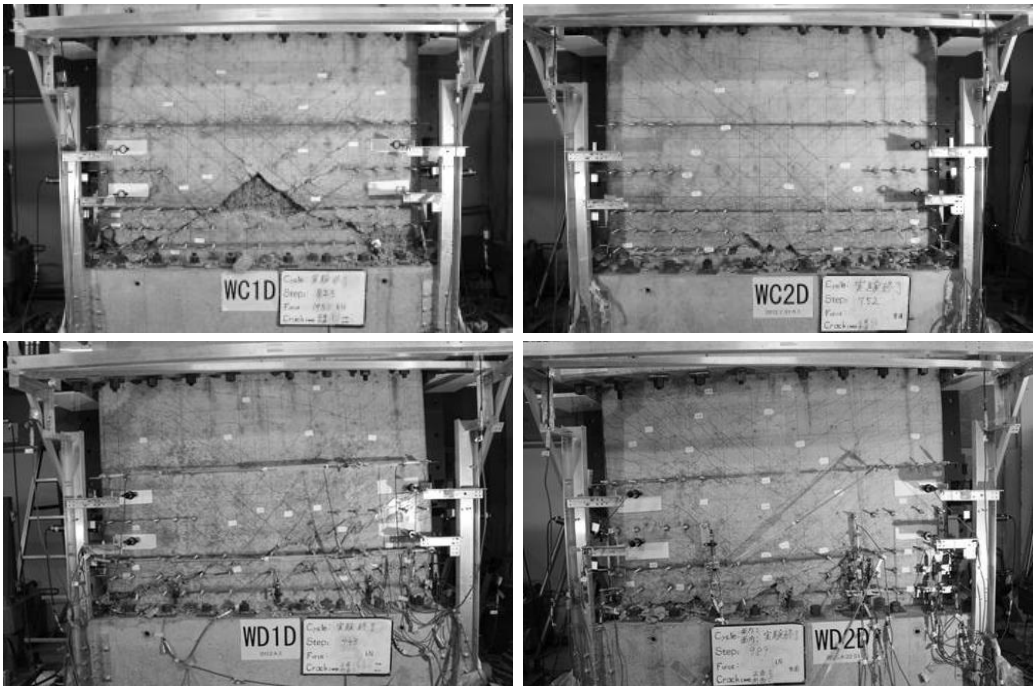

Figure 1-41 Failure mode of specimens WC and WD under uni-and bi-directional loadings (Kabeyasawa et al. 2014)

In the case of WA and WB, Kabeyasawa et al. (2014) observed heavier damage rates (in terms of crack widths and cover concrete spalling) in the specimens under bi-directional loading compared to the same specimen under uni-directional loading during smaller deformations. However, they mentioned that in cases of WC and WD, the observed damage rates under bi-directional loading were not much different from those under uni-directional loading in terms of crack widths. By comparing the behaviour of WC and WD, Kabeyasawa et al. (2014) observed unstable behaviour in the axial load capacity after the shear failure due to out-plane buckling in case of WD.

Almeida et al. (2017)

In a more recent study, Almeida et al. (2017) tested two rectangular (T-shaped wall with a small flange) doubly reinforced concrete walls under uni- and bi-directional loadings. Table 1-5, Table 1-6 and Figure 1-42 show the characteristics and details of the specimens. Test setup used by Almeida et al. (2017) is shown in Figure 1-43.

Table 1-5 Characteristic of the specimens (Almeida et al. 2017)

Specimen	In-plane shear span ratio (H_e/L_w)	Axial load ratio $P/(A_g f'_c)$ %	Loading path
TW2	1.17	3.2	In-plane uni-directional
TW5	2.72	4.8	Bi-directional

Table 1-6 Details of the specimens (Almeida et al. 2017)

Specimen	TW2 and TW5
Length (mm)	2700
Thickness (mm)	120
Total longitudinal reinforcement ratio (%)	0.57%
Web longitudinal reinforcement ratio (%)	0.5%
Boundary element longitudinal reinforcement ratio (%)	0.5%
Transverse reinforcement ratio (%)	0.36%

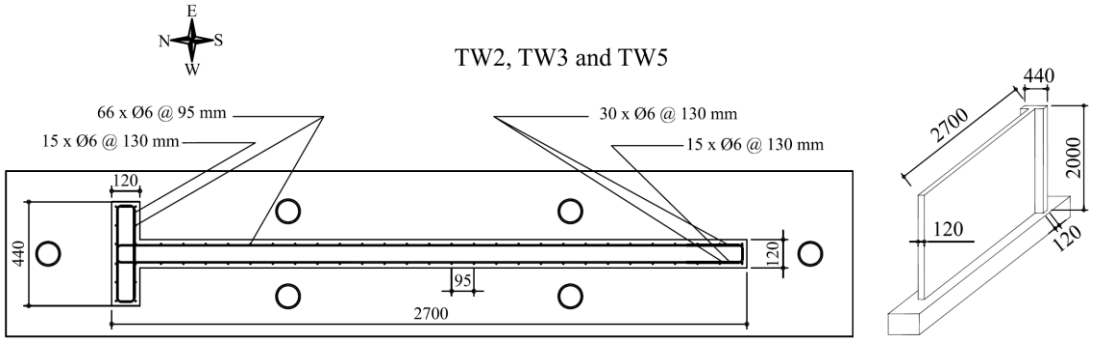

Figure 1-42 Details of the specimen (Almeida et al. 2017)

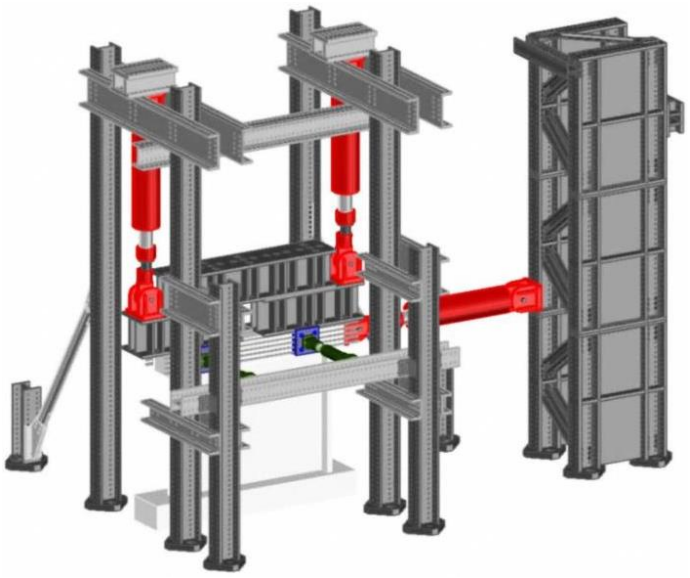

Figure 1-43 Test programme on rectangular walls (Almeida et al. 2017)

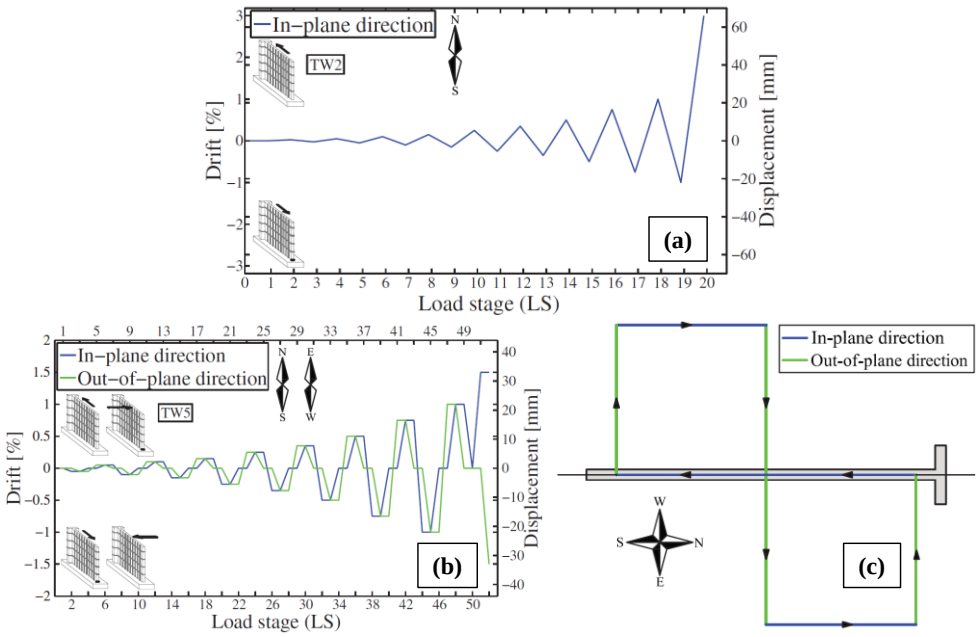

Figure 1-44 Planned drift history throughout load stages for walls: (a) TW2; (b) TW5; (c) Typical loading cycle when bi-directional loading was applied (Almeida et al. 2017)

Figure 1-45 shows the in-plane force-displacement responses of wall TW2 and TW5. Figure 1-46 shows the condition of the test units TW2 and TW5 at the end of the experiment. Almeida et al. (2017) reported that in the case of TW2, the continuation of strength reduction beyond 2% drift was not due to concrete crushing in the flange but can be attributed to the consecutive rupture of longitudinal bars at the (opposite) web edge. Very small out-of-plane displacements were observed in the case of TW2 (less than 1 cm).

Concrete crushing along with bar buckling were the main failure mode of the specimen TW5. Moreover, at larger in-plane drifts, some inclined shear cracks showed up to bridge between the tensile and compressive zones. According to Almeida et al. (2017) apart from the last

drift cycle, the influence of the imposed out-of-plane displacements did not seem to have significantly affected the member response since the load stages corresponding to the application of out-of-plane displacements only minimally influenced the resisting in-plane lateral load, and further produced only a relatively minor increase of pre-existing cracks, concrete crushing and spalling. However, such effect was visible in the flange, suggesting that the study of the effects of out-of-plane loads on barbelled walls may be worth pursuing.

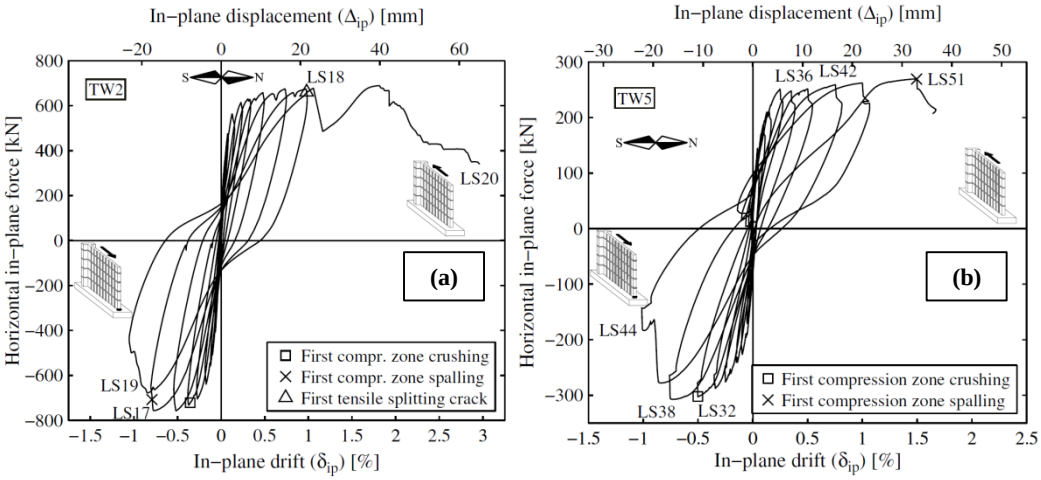

Figure 1-45 In-plane force-displacement response for walls: (a) TW2; (b) TW5 (Almeida et al. 2017)

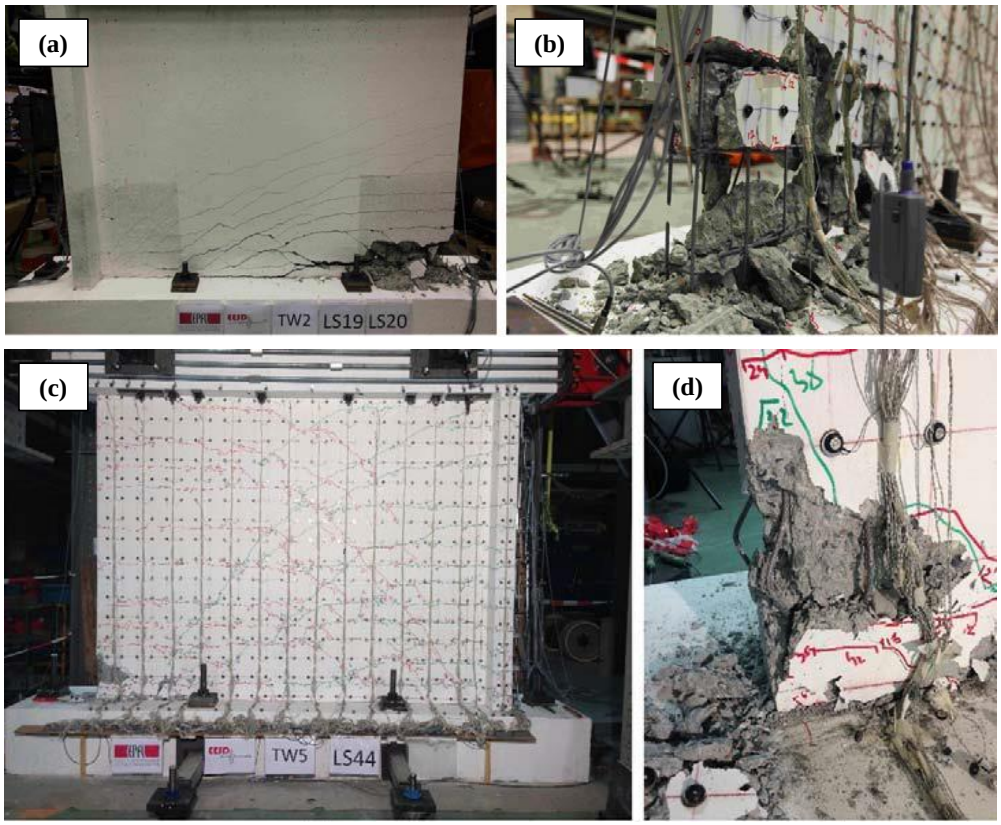

Figure 1-46 (a) Overview of wall TW2 condition at final load stage LS20, (b) Close-ups at web edge, depicting rebar fracture, (c) General condition of wall TW5 at horizontal failure (loading toward the web edge, at load stage LS44), (d) Detail of the crushing zone, with buckling of longitudinal rebars (Almeida et al. 2017)

1.3.5. Summary of the experimental studies on structural walls subjected to bi-directional loading

Table 1-7 summarizes the previous experimental studies conducted on RC walls subjected to bi-directional loading include planar and non-planar walls. Parameters such as in-plane shear span ratio, axial load ratio and applied lateral loading pattern are shown in Table 1-7.

Table 1-7 Summary of the experiments on RC walls subjected to bi-directional loading

Type of walls		Test programme reference	In-plane shear span ratio	Axial load ratio (%)	Lateral loading patterns
Non-planar	U-shaped	(Ile and Reynouard 2005)	2.6-3.12	10-12	Modified Clover leaf (Figure 1-17)
	U-shaped	(Beyer et al. 2008)	2.58-2.81	2-4	Modified Clover leaf (Figure 1-22)
	T-shaped	(Brueggen et al. 2017)	3.2-4	3	Multi-directional
	C-shaped	(Behrouzi et al. 2014)	2.84	5	Cruciform bi-directional
	U-shaped	(Constantin and Beyer 2016)	2.58-2.81	6-15	Skewed (Figure 1-25)
Planar	Rectangular	(Tatsuya 1996)	2	13.3-17.4	Modified Clover leaf (Figure 1-31)
	Rectangular	(Kabeyasawa et al. 2014)	1.1-1.4	7.5-12.4	Modified Clover leaf (Figure 1-37)
	Rectangular	(Almeida et al. 2017)	1.17-2.72	3.2-4.8	Modified Clover leaf (Figure 1-44)

1.4.RESEARCH GAPS

Based on the recent earthquake observations discussed in Section 1.1 and the previous studies conducted on rectangular RC walls subjected to bi-directional loading discussed in Section 1.3.4, the main research gaps were found and discussed below.

1. Lack of experimental data on slender rectangular walls subjected to bi-directional loading as was shown in Section 1.3.5; i.e. walls with shear span ratio higher than 3 (Paulay and Priestley 1992, ASCE41-13 2013).
2. Among several bi-directional loading patterns, until now only one of them has been applied to rectangular RC walls (shown in Figure 1-31, Figure 1-37 and Figure 1-44). Investigating the effects of other types of bi-directional loading patterns on rectangular RC walls is necessary as this parameter could change the results (strength and displacement capacities and failure mode) dramatically as it has for columns.
3. The need to investigate the effects of bi-directional loading on RC walls susceptible to lateral instability failure that was raised after the recent earthquakes in Chile (NIST 2014) and New Zealand (Kam et al. 2011).
4. Although several experimental studies investigated RC walls with high axial load ratio under in-plane uni-directional loading (Paulay and Goodsir 1985, Zhang and Wang 2000,

Su and Wong 2007, Alarcon et al. 2014, Shegay et al. 2017), up to this date, there is no experimental or numerical study on such walls subjected to bi-directional loading.

5. One of the unexpected failure modes that was observed in rectangular RC walls in New Zealand 2011 earthquake was out-of-plane shear failure. This failure mode was not observed in previous earthquakes and therefore its mechanics was not experimentally or numerically studied before. The preliminary results suggested that bi-directional loading contributed to this failure mode (Dunning Thornton 2011).
6. Significant changes have been made to the New Zealand design code of practice regarding RC structural walls since NZS3101:2006. However, these new changes have not yet tested under severe axial load ratio and more realistic lateral loading regimes.
7. New limitations on the maximum axial load ratio of RC walls were added to NZS3101:2006-A3 (2017). However, brittle failure mode of a rectangular wall with high axial load ratio in the 2011 New Zealand earthquake (Figure 1-4) revealed the vulnerability of such walls when subjected to bi-directional loading. These new limitations of axial load ratio need to be validated experimentally and numerically under a more realistic lateral loading regime.
8. Key parameters contributing to the development of out-of-plane shear failure were not identified in previous experimental or numerical studies and therefore, the effects of each of these parameters were not investigated before.
9. Lack of an analytical method for identifying RC walls prone to out-of-plane shear failure that can be used for design and assessment purposes.

1.5.SCOPE AND OBJECTIVES OF THE RESEARCH

As the subject of RC walls under bi-directional loading could be quite broad and include all different types of RC walls, the scope of this study is limited to:

1. In this study the effects of bi-directional loading were investigated only on doubly reinforced concrete walls. Therefore, singly reinforced concrete walls were not investigated here.
2. There are several different shapes for RC walls including L shape, C shape, T shape, barbelled or rectangular. However, this study only covers rectangular walls. This was mainly due to the fact that rectangular shape is the most common type for RC walls in New Zealand.
3. Although squat walls under bi-directional loading could also be an interesting subject that needs to be investigated, since most of the unexpected failure modes observed in

recent earthquakes in Chile and New Zealand were in slender walls, the experimental and numerical phases of this thesis were limited to slender walls only.

Considering the scope of the work and the research gaps addressed in the previous section, this study focuses on gathering a better understanding on the seismic behaviour of rectangular slender doubly reinforced concrete walls under bi-directional loading. Accordingly, the main research objectives of this study are:

1- Identifying the key geometric, mechanical and demand parameters influencing the seismic performance of rectangular RC walls under bi-directional loading and quantitatively estimating their effects on the overall strength and displacement capacity.
2- Assessing whether bi-directional loading (3D response) can change the damage/failure mode expected in uni-directionally (2D) loaded walls, and if so, what the likely changes are.
3- Assessing the effects of various lateral load paths on the seismic performance of rectangular slender walls.
4- Investigating the effects of bi-directional loading on RC walls prone to lateral instability failure.
5- Verifying the newly added limitation to NZS3101:2006-A3 (2017) on maximum axial load ratio for RC walls when subjected to a more realistic loading regime (bi-directional loading).
6- Understanding the mechanics behind out-of-plane shear failure and identifying the key parameters in the development of this failure mode.
7- Developing an analytical method to identify rectangular RC walls prone to out-of-plane shear failure taking into account the effect of bi-directional loading.
8- Verifying the reliability of current New Zealand code-based design requirements, including structural detailing for walls subject to more realistic loading regimes.
9- Suggesting recommendations/guidelines (based on experimental and analytical evidences) to improve current practice (taking into account bi-directional loading/response) for both the design of new walls and the assessment of existing ones to assist engineers in their daily practice.

1.6. ORGANIZATION OF THE THESIS

The thesis is laid out in such a manner that the research objectives presented in Section 1.5 are studied, researched and answered in a logical order. The dissertation is divided into nine chapters including this introductory **Chapter 1**.

Chapter 2 will describe the test programme for the first phase of the experimental study includes three identical rectangular slender RC walls under different lateral loading patterns. In particular, the material properties, testing setup, loading protocol and instrumentations will be described to allow for replication of test by other researchers.

The test result of the first phase of the experimental study will be presented in detail in **Chapter 3**. Particular emphasis will be given to the influences of different loading regimes on the seismic behaviour of rectangular slender RC walls. Moreover, effects of bi-directional loading on the behaviour of walls prone to lateral instability failure will be discussed.

Chapter 4 will describe the test programme for the second phase of the experimental study includes three rectangular slender RC walls designed for different section detailing ductility levels according to NZS3101:2006-A3 (2017) subjected to high axial load ratio and bi-directional loading. The material properties, testing setup, loading protocol and instrumentations will be described.

The test result of the second phase of the experimental study will be presented in detail in **Chapter 5**. Particular emphasis will be given to the detailed failure mode of each wall when subjected to severe axial load and bi-directional loading. Mechanics of out-of-plane shear failure and the key parameters in developing this failure mode will be also described.

The numerical investigations will begin by presenting the FE model in **Chapter 6**, with two distinctive parts. Firstly, the FE model will be presented in details. Then, seven RC walls tested by other researchers and here in this study will be used for verifying the FE model. The numerical validation focuses on replicating the failure mechanism and base shear vs drift ratio of the wall.

In **Chapter 7**, a case study wall collapsed in out-of-plane shear in the 2011 New Zealand earthquake namely Wall D5-6 from Grand Chancellor Hotel is simulated using the FE model presented in Chapter 6. Effects of directionality of the earthquake and out-of-plane boundary condition on the failure mode of the wall will be also presented.

A comprehensive numerical parametric study on rectangular RC walls prone to out-of-plane shear failure is performed in **Chapter 8.** Key parameters in developing out-of-plane shear failure were identified and the effects of each parameter were discussed in details. Based on

the numerical parameter study results, a matrix of walls were formed from which an analytical method for identifying RC walls prone to out-of-plane shear failure is proposed in **Chapter 8.** The proposed method can be used for both design and assessment purposes.

Chapter 9 will summarise the key findings and conclusions for each research objectives introduced in Section 1.5. Suggestions for future research will be presented with emphasis on the limitations of this work and potential for further investigations.

2. EXPERIMENTAL PROGRAMME FOR THE EFFECTS OF LATERAL LOAD PATH ON RECTANGULAR SLENDER WALLS

2.1.INTRODUCTION

As was described in Chapter 1, there are several major research gaps in the subject of rectangular slender walls subjected to bi-directional loading. This chapter describes the first phase of the experimental testing programme investigating some of the major research objectives on the effects of bi-directional loading on rectangular RC walls. These research objectives are:

1. To gather more experimental data on slender walls under bi-directional loading, i.e. walls with shear span ratio higher than 3 (Paulay and Priestley 1992, ASCE41-13 2013).
2. Investigate the effects of different types of lateral loading patterns such as skew or clover leaf on rectangular RC walls.
3. Assess the effects of bi-directional loading on various damage states and failure modes such as cover concrete spalling, bar buckling and concrete crushing in the boundary elements and web.
4. Investigate the effects of bi-directional loading on RC walls susceptible to lateral instability failure that was raised after the recent earthquakes in Chile (2010) and New Zealand (2011).

The test series comprised of three identical cantilever RC walls tested under three different lateral loading patterns. One of the main challenges of this experimental study was the complexity of the test setup (with 7 actuators and 3 loading beams), especially by considering a double bending deformation shape for the out-of-plane direction. The other challenge was controlling the 7 actuators during the test which was done using a special programme written by Peter Coursey, one of the technicians of the Civil and Natural Resources Engineering Department. Geometry of the specimens, material properties, test setup, instrumentation, and loading history are described in the following sections.

2.2. DESCRIPTION OF THE TEST UNITS

In order to make the benchmark susceptible to lateral instability failure, the panel of the wall was constructed identical to specimen RWL tested by Dashti et al. (2017b) which failed in lateral instability under cyclic in-plane loading. Since the test setup was changed compared to that of Dashti et al. (2017b) and a RC cap beam was added to the top of the specimens, the benchmark was prepared and tested again to make sure results are directly comparable. The specimens were 1:2 scale models of the first storey of a RC wall in a four-storey reference building with a total height of 16 m. Figure 2-1 shows the full scale wall, the scaled specimen and the loading pattern. It should be noted that the wall was designed by Dashti et al. (2017b) according to NZS3101:2006 for a ductile level. It is worth noting that it is corresponding to a ductility of at least 3.

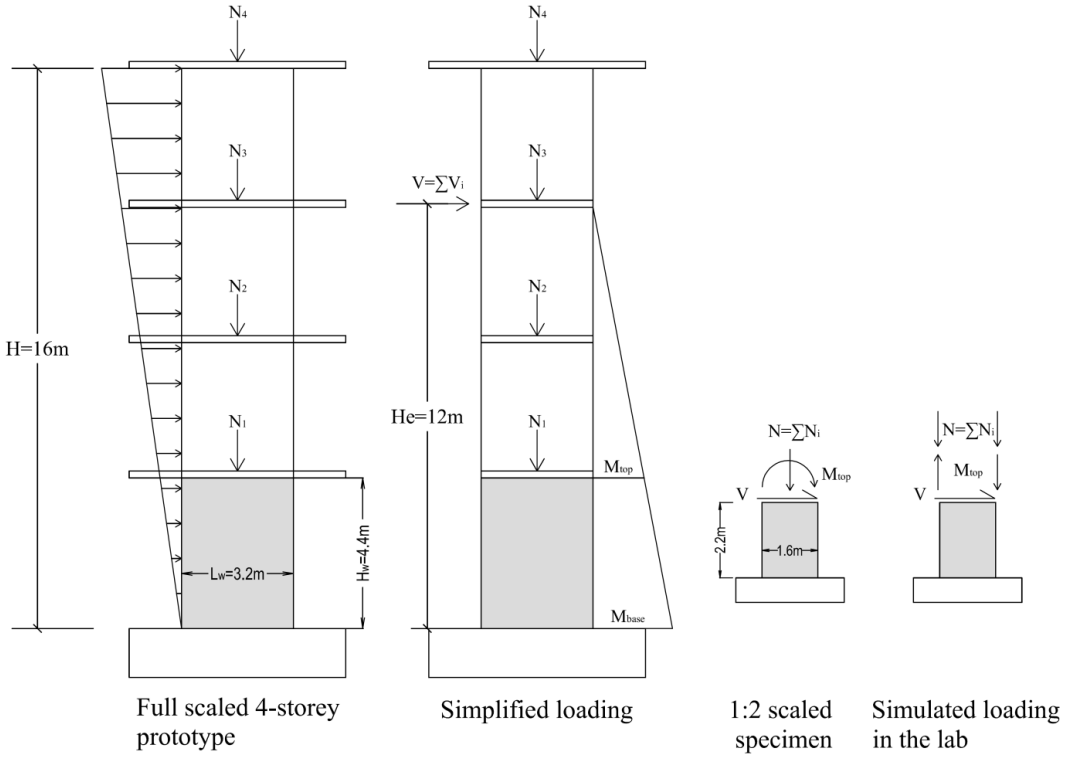

Figure 2-1 Specimen scaling and loading pattern

Three identical specimens, namely SP1-Uni, SP1-Skew and SP1-Clover were constructed. Lateral loading pattern was the only varying parameter between the three specimens. Lateral loading patterns of in-plane uni-directional, skewed uni-directional (with a 45 degree angle) and clover leaf bi-directional were chosen for SP1-Uni, SP1-Skew and SP1-Clover, respectively. A quick summary of the test matrix is given in Table 2-1. Summary of the main geometrical features and reinforcement details are listed in Table 2-2. Some of the notations used in Table 2-1 and Table 2-2 are shown in Figure 2-2 graphically. Cross-section and side-

view of the reinforcement layout are shown in Figure 2-3. Details of the cap beam and foundation of the specimens are shown in Figure 2-4.

Table 2-1 Test matrix of the three RC walls specimens

Name	In-plane shear span ratio (H_e/L_w)	Shear span, H_e (mm) (Figure 2-1)	Axial load ratio, $P/(A_g f'_c)$, using $f'_c = 35\ MPa$	Loading pattern	
				Type	Schematic view
SP1-Uni	3.75	6000	6.26%	In-plane uni-directional	
SP1-Skew				Skewed uni-directional	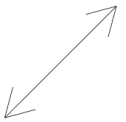
SP1-Clover				Clover leaf	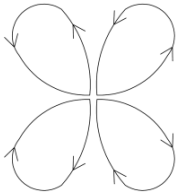

Table 2-2 Details of the specimens (Dashti et al. 2017b)

Specimen	SP1-Uni, SP1-Skew & SP1-Clover
Clear height, H_w (mm)	2200
Length, L_w (mm)	1600
Thickness, t (mm)	125
Total longitudinal reinforcement ratio, $\rho_t = (A_{s,BZ} + A_{s,web}) / (L_w \times t)$	1.95%
Web longitudinal reinforcement ratio	0.55%
Boundary zone (BZ) longitudinal reinforcement ratio	4.15%
BZ transverse reinforcement ratio, $\rho_{sx} = A_{vx} / (s \times t)$	0.75%
BZ transverse reinforcement ratio, $\rho_{sy} = A_{vy} / (s \times l_{BZ})$	0.61%
Web shear reinforcement ratio, $\rho_v = A_{sv} / (s \times t)$	0.84%

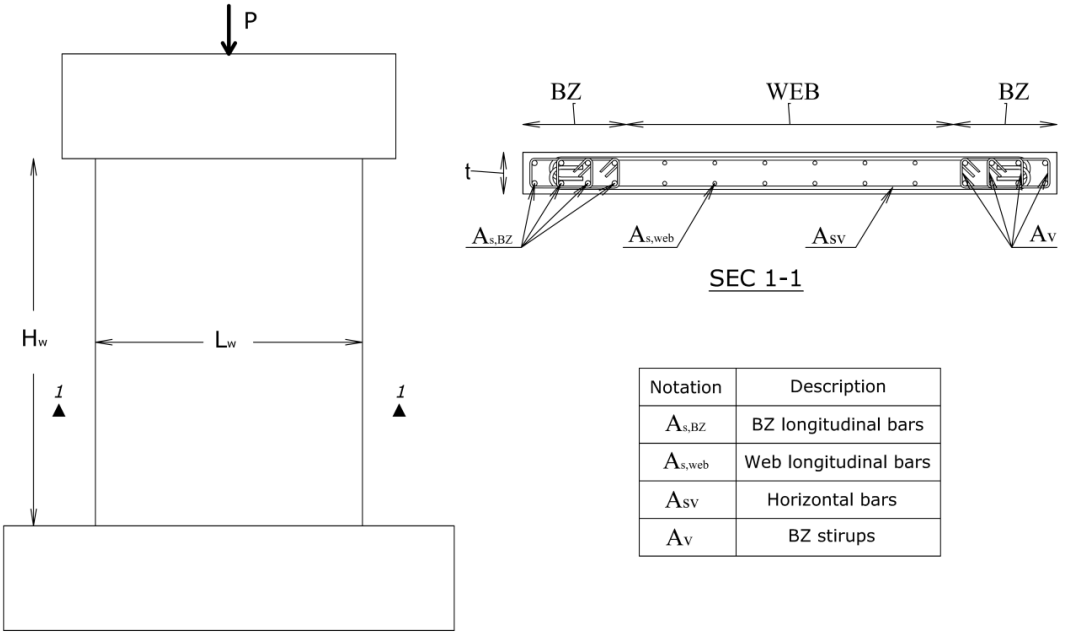

Figure 2-2 Notations used in Table 2-1 and Table 2-2

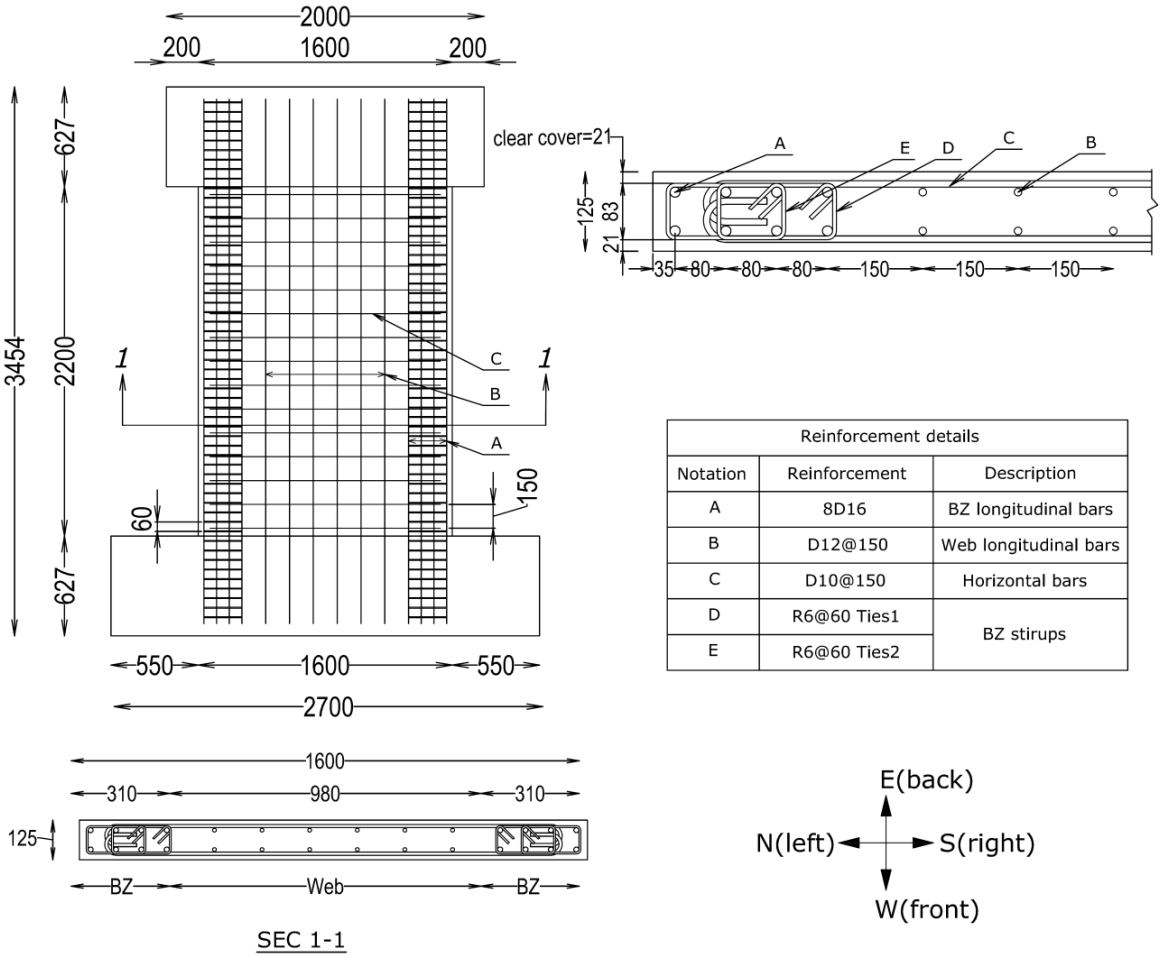

Reinforcement details		
Notation	Reinforcement	Description
A	8D16	BZ longitudinal bars
B	D12@150	Web longitudinal bars
C	D10@150	Horizontal bars
D	R6@60 Ties1	BZ stirups
E	R6@60 Ties2	

Figure 2-3 Details of the section and side view of the reinforcement layouts of the specimens

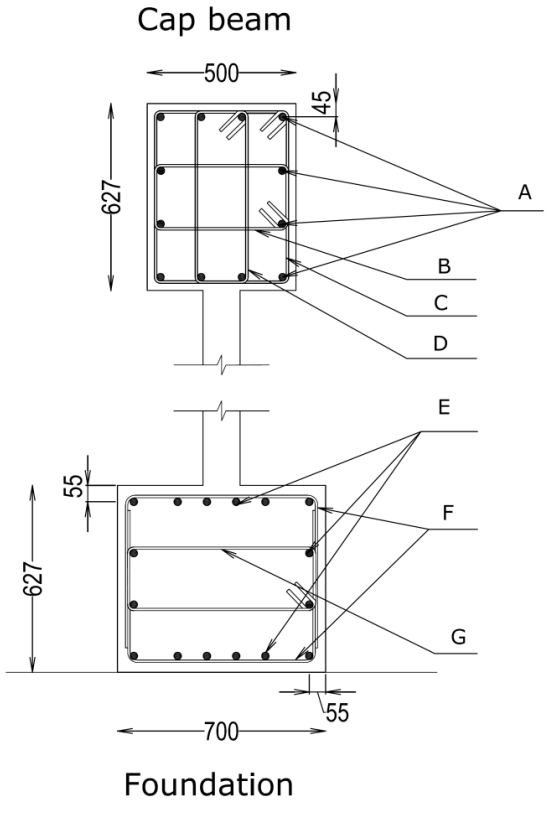

REINFORCEMENT SCHEDULE	
Mark	Reinforcement
A	12D25
B	D12@100
C	D12@100
D	D12@100

REINFORCEMENT SCHEDULE	
Mark	Reinforcement
E	16D25
F	D20@100
G	D12@100

Figure 2-4 Details of the cap beam and foundation of the specimens

2.3.MATERIAL PROPERTIES

Specimens were constructed for a concrete compressive strength of 35MPa. However, since the specimens were tested about six month after they were cast; their compressive strength was relatively higher on the test day. The average concrete compressive strength of each specimen on the test day is shown in Table 2-3.

The steel reinforcing bars used for the specimens were NZ Grade 300 except R6 which was close to Grade 500. Typical stress-strain curves of the steel rebars are shown in Figure 2-5. Table 2-4 shows the material properties of the steel reinforcement.

Table 2-3 Average concrete compressive strength of each specimen

Specimen	Average concrete compressive strength (MPa)
SP1-Uni	47.3
SP1-Skew	50.4
SP1-Clover	52.7

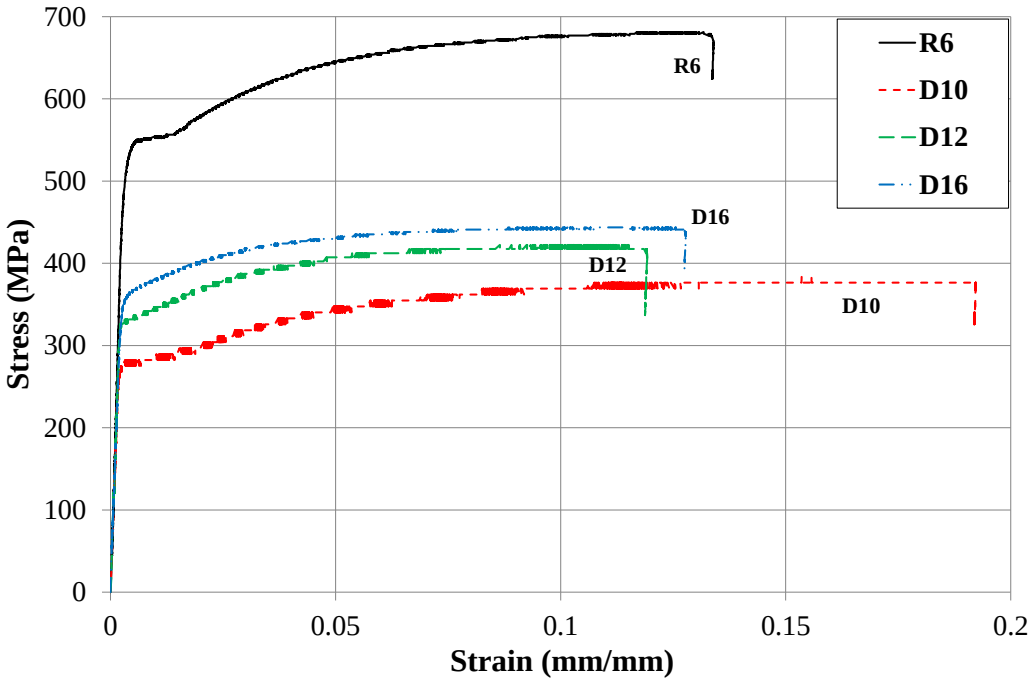

Figure 2-5 Typical monotonic behaviour of the rebars

Table 2-4 Material properties of the steel reinforcement

Bars	E_s (MPa)	f_y (MPa)	f_u (MPa)	ε_u
R6	200918	548	681	0.152
D10	180822	278	385	0.193
D12	171387	334	420	0.13
D16	185210	362	445	0.15

2.4.SPECIMENS CONSTRUCTION

The specimens were constructed by Bradford Precast Company. Key process steps include reinforcing cages, formwork, concrete casting and transportation are discussed below.

2.4.1. Reinforcing cages

Steel reinforcing cages were assembled by Complete Reinforcing Company. The cages were first sent to the Structural laboratory of the University of Canterbury (Figure 2-6) for attaching the strain gauges and welded couplers to the bars (Figure 2-7). Then they were sent to Bradford Precast Company for casting.

Figure 2-6 Steel reinforcing cages delivered to the Structural Engineering Laboratory of the University of Canterbury for part of the instrumentation's plan

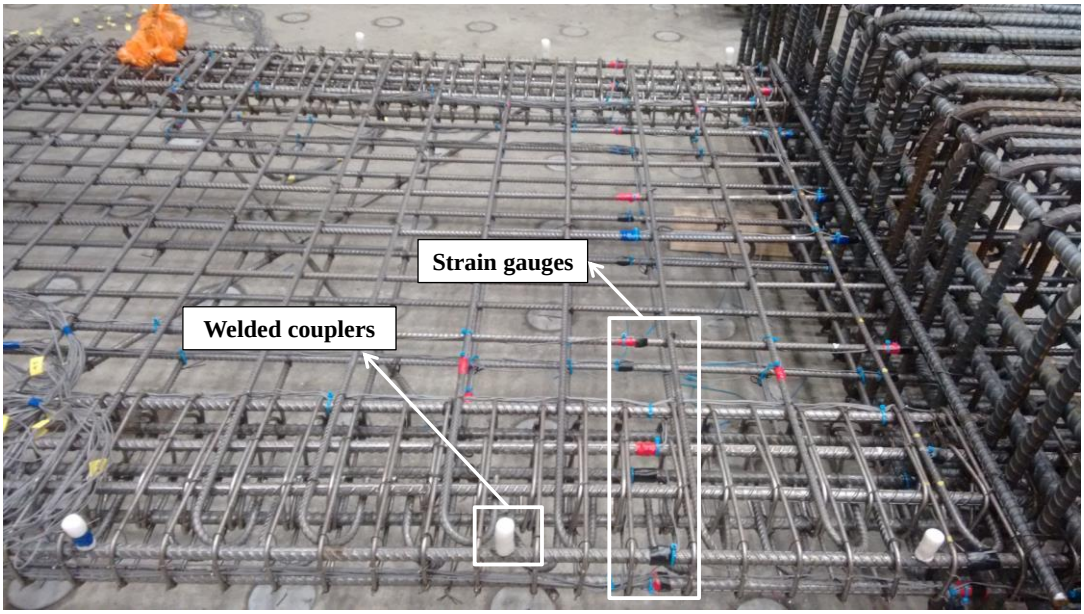

Figure 2-7 Attaching strain gauges and welded couplers in the lab before sending the cages for casting

2.4.2. Formwork

The formwork was manufactured from plywood sheets. One of the challenges of constructing the specimens was designing the formwork. The main challenge was placing 14 drossbachs in the foundation and 32 in the cap beam. These drossbachs are shown in Figure 2-8. As can be seen in Figure 2-9 and Figure 2-10 this was done by using rubbers that hold the drossbachs. The mould was oiled prior to casting to assist removal (Figure 2-11). Upon the placement of the reinforcing cage in the casting mould, plastic spacers were inserted to ensure a 20mm clear cover to the stirrups reinforcement and an approximately 35mm cover to the centroid of longitudinal reinforcement of the wall's boundary zone.

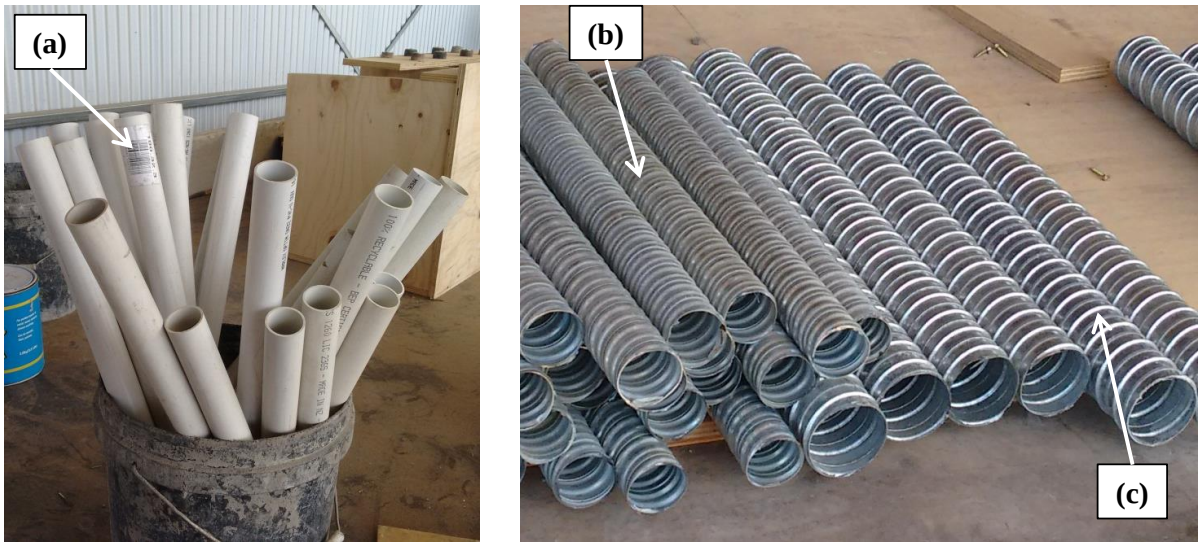

Figure 2-8 Drossbachs (a) 32mm and (b) 40mm and (c) 60mm

Figure 2-9 The formwork used for the specimens, (a) the mould, (b) the rubbers used for cap beam's drossbachs and (c) the rubbers used for the foundation's drossbachs

Figure 2-10 Drossbachs embedded in (a) cap beam and (b) foundation

Figure 2-11 Oiling the formwork for easier removal

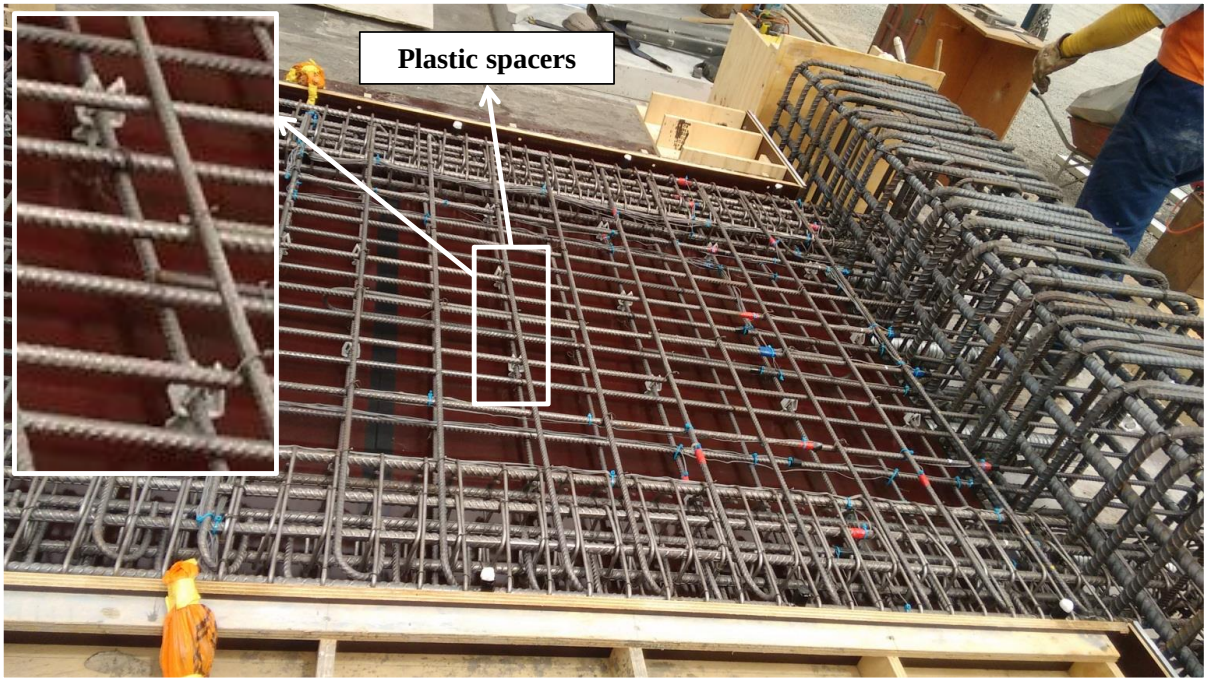

Figure 2-12 Plastic spacers used to ensure the required clear cover

2.4.3. Concrete casting

Specimens were casted horizontally in one single pour (Figure 2-13-Figure 2-15). The maximum aggregate size was 13mm to allow for some concrete micro-structure scaling. For each specimen, some cylinders were prepared for the compressive strength (f'_c) test (Figure 2-16). Finally when the specimens were ready, they have been transported carefully to the lab (Figure 2-17).

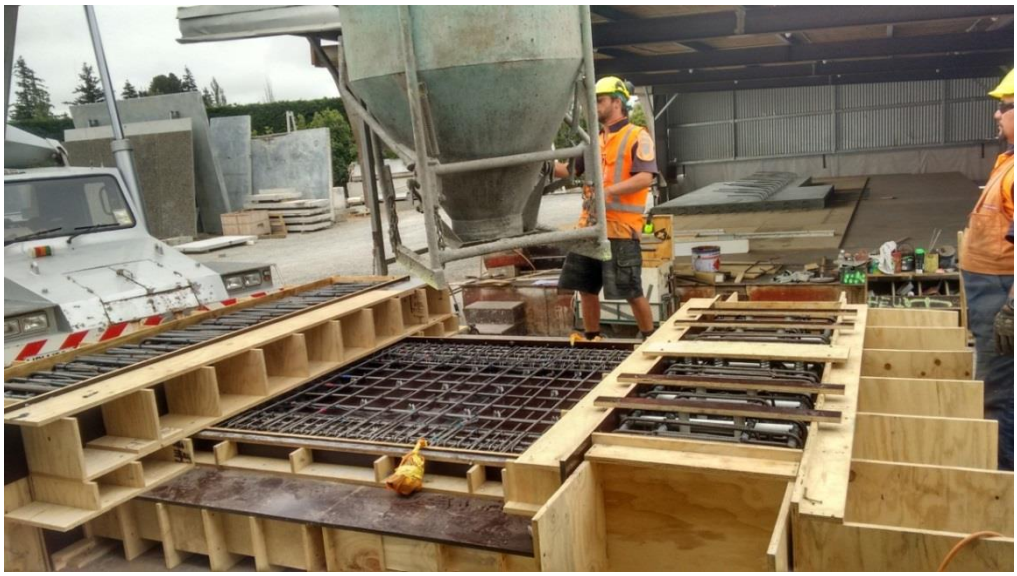

Figure 2-13 Specimen just before casting

Figure 2-14 Specimen after finishing was complete

Figure 2-15 Specimen before its removal from the mould

Figure 2-16 Concrete cylinder units

Figure 2-17 Specimens (a) ready to be sent to the lab and (b) being transported to the lab

2.5.TEST SETUP

A schematic view and a photo of the test setup used in this study to apply both uni- and bi-directional loadings are shown in Figure 2-18 and Figure 2-19, respectively. More details of the test setup are shown in Figure 2-20-Figure 2-22.

This complex test setup consists of an in-plane steel loading beam on top of the specimen and two out-of-plane steel loading beams attached to the specimen's cap beam. Seven hydraulic actuators were used to apply the gravity load and lateral in-plane and out-of-plane cyclic displacements. Out of these seven actuators, three 1000kN actuators were employed for applying the gravity and in-plane displacement (identified as C in Figure 2-18). As shown before (Figure 2-1), only the bottom storey was tested and the effect of omitted higher stories were simulated by the two in-plane 1000kN vertical actuators as demonstrated in Figure 2-1. Therefore, the vertical actuators applied the gravity load and the bending moment corresponding to the chosen shear span ratio through the actuators' lever arm. The third horizontal 1000kN actuator applied the lateral in-plane displacement to the specimen. Out of the four hydraulic actuators left, two horizontal 400kN actuators apply the out-of-plane cyclic displacements (identified as D in Figure 2-18). The other two 400kN vertical actuators in the out-of-plane direction were used to create a double bending deformation in the wall (Also identified as D in Figure 2-18). The double bending deformation shape in the out-of-plane represents the rigidity of the slab compared to the wall's stiffness in the out-of-plane direction. It should be noted that the wall had a cantilever deformation shape in the in-plane direction. Equations 2-1 - 2-3 show how the actuators were controlled during the test.

$$T_{top} = \frac{(6000 - 3070)}{7544} C_1 \qquad 2\text{-}1$$

$$C_2 + C_3 = Axial\ load \qquad 2\text{-}2$$

$$D_3 + D_4 = near\ zero \qquad 2\text{-}3$$

$$\delta_{D3} = \delta_{D4} \qquad 2\text{-}4$$

C_1, C_2, C_3, D_3 and D_4 are shown in Figure 2-18. It is worth mentioning that in order to control and limit the foundation's movement, several jacking bolts were used. These jacking bolts were designed based on the base shear of the wall in each direction. This is shown in Figure 2-23.

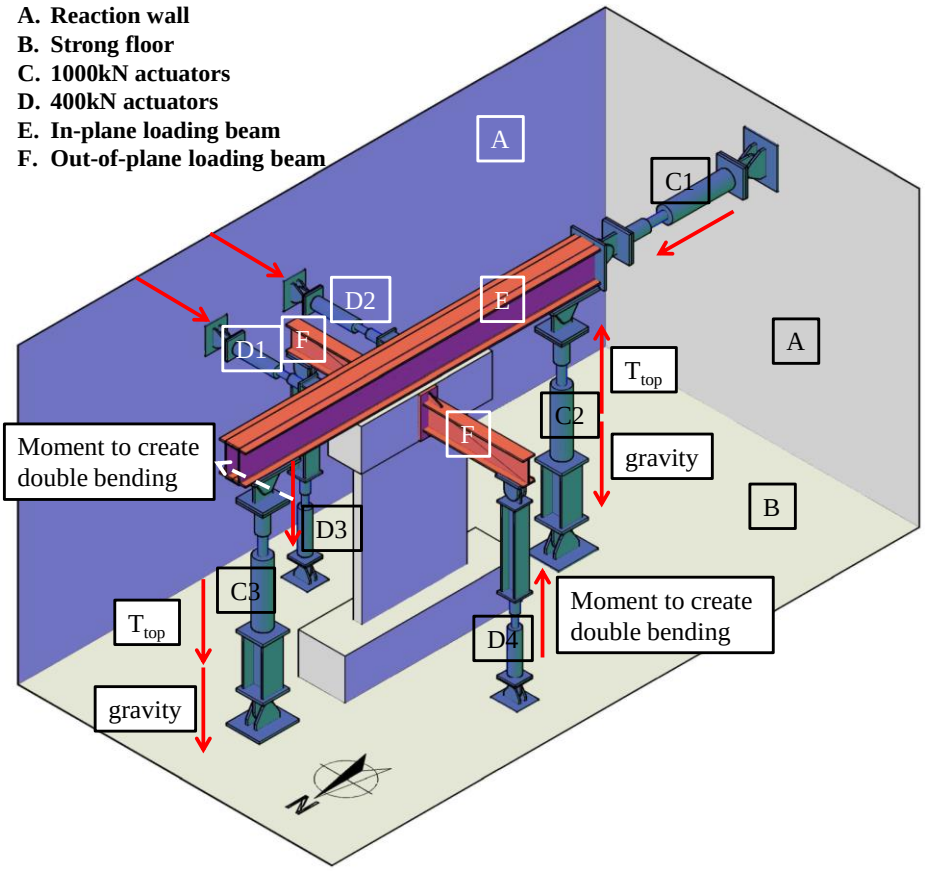

Figure 2-18 Schematic view of the test setup used for the experiments

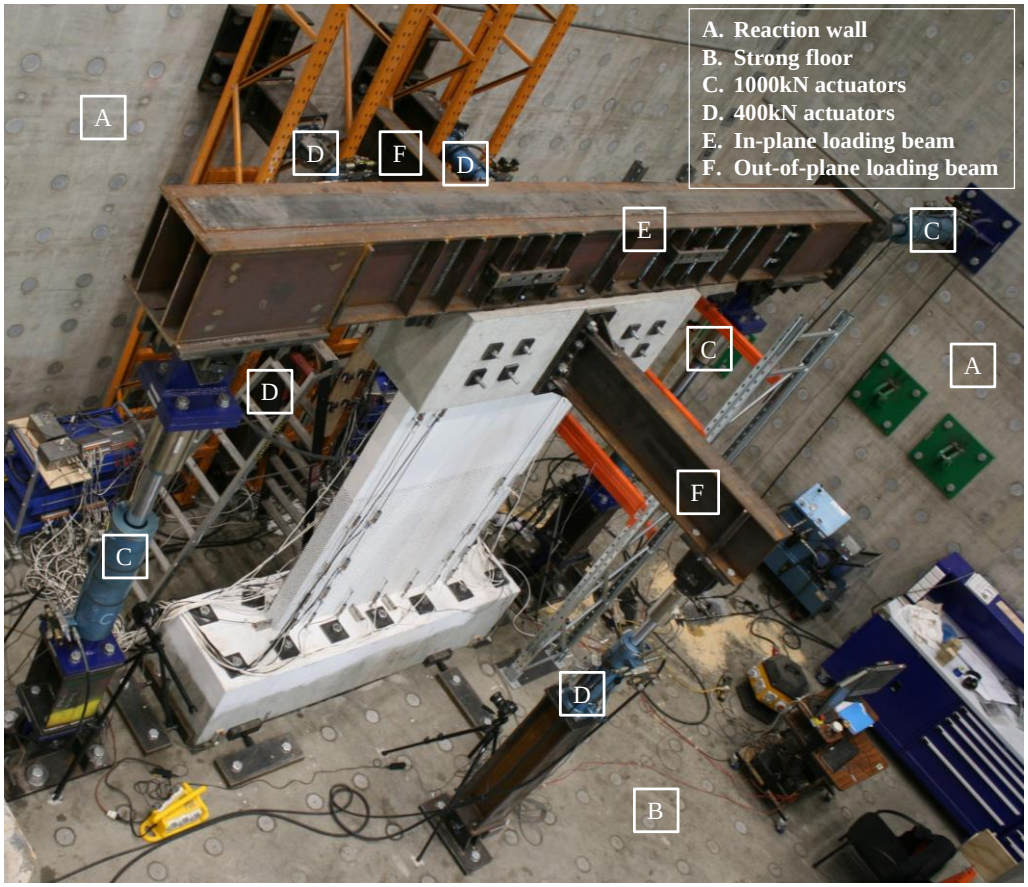

Figure 2-19 Photo of the test setup used for the experiments

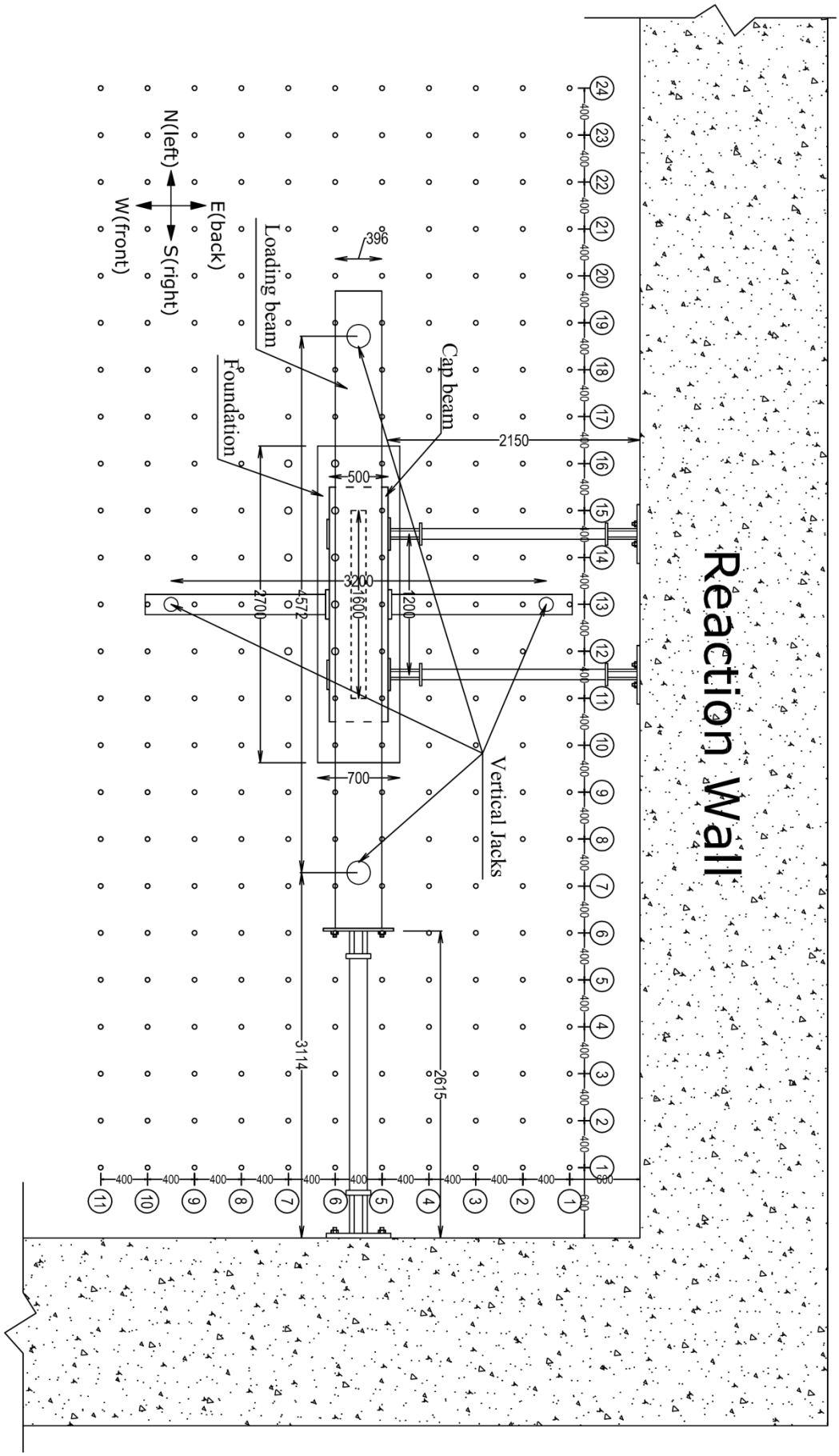

Figure 2-20 Schematic view of the test setup – plan view

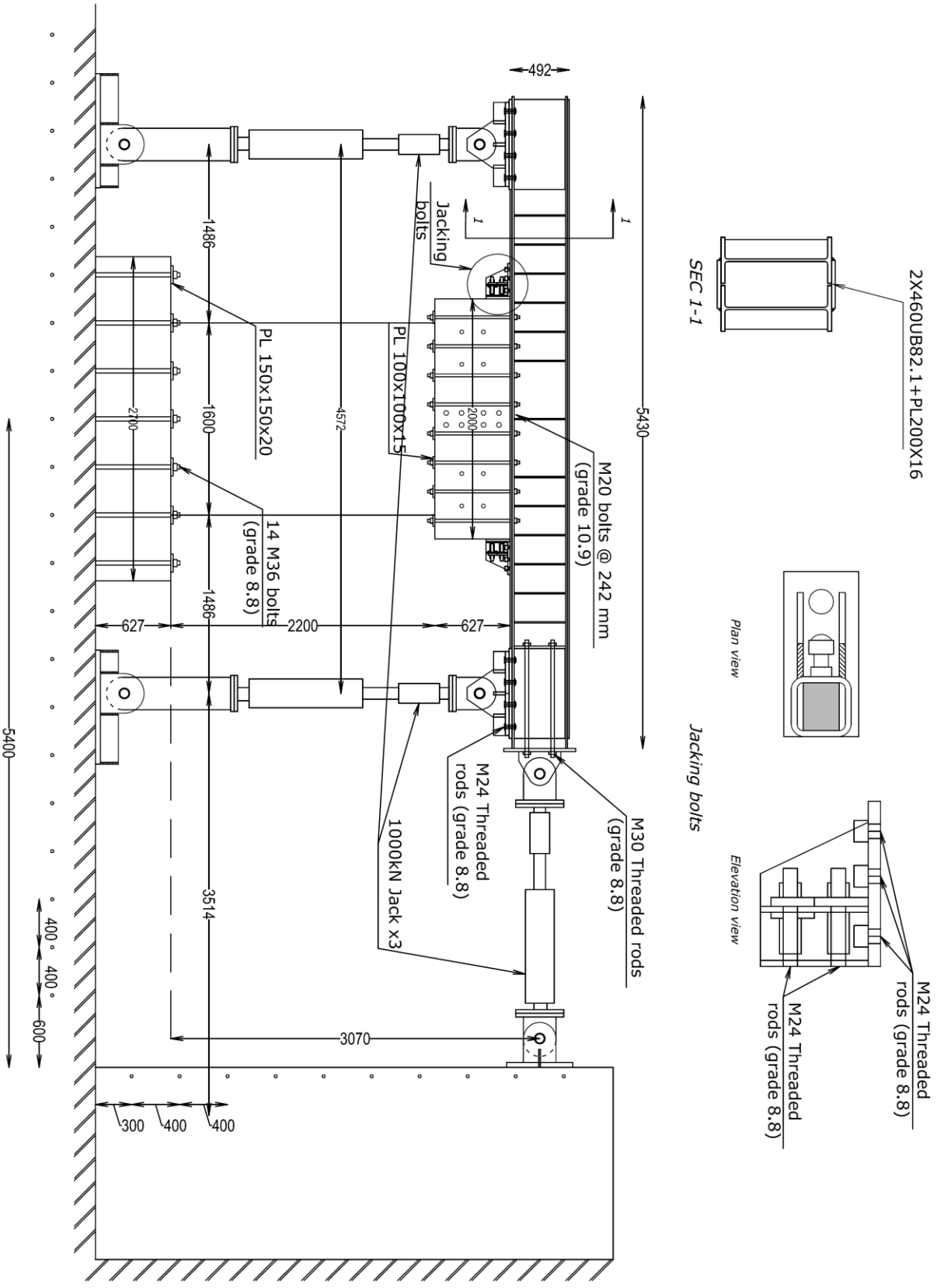

Figure 2-21 Schematic view of the test setup – in-plane view (front/west view)

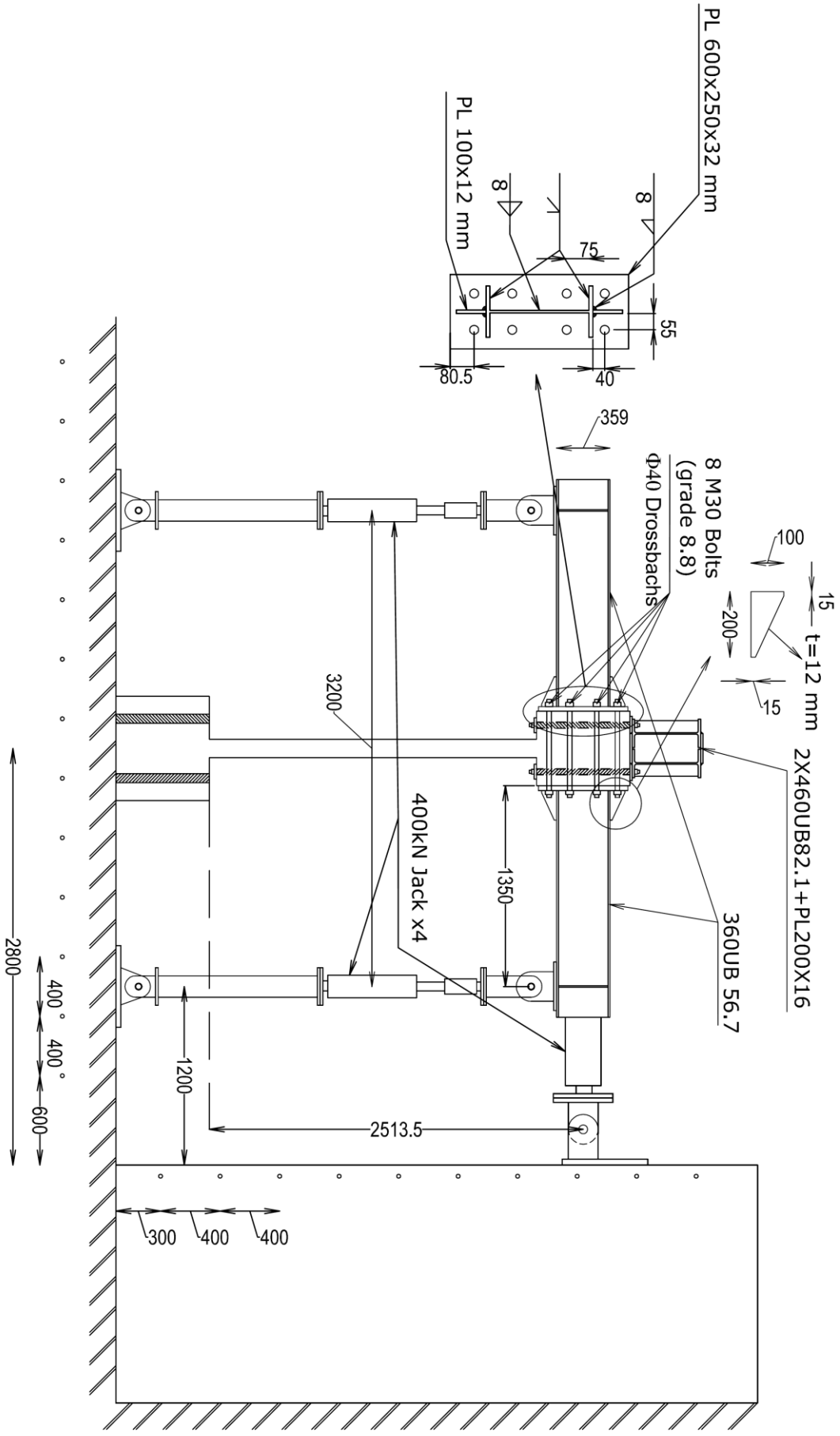

Figure 2-22 Schematic view of the test setup – out-of-plane view (right/south view)

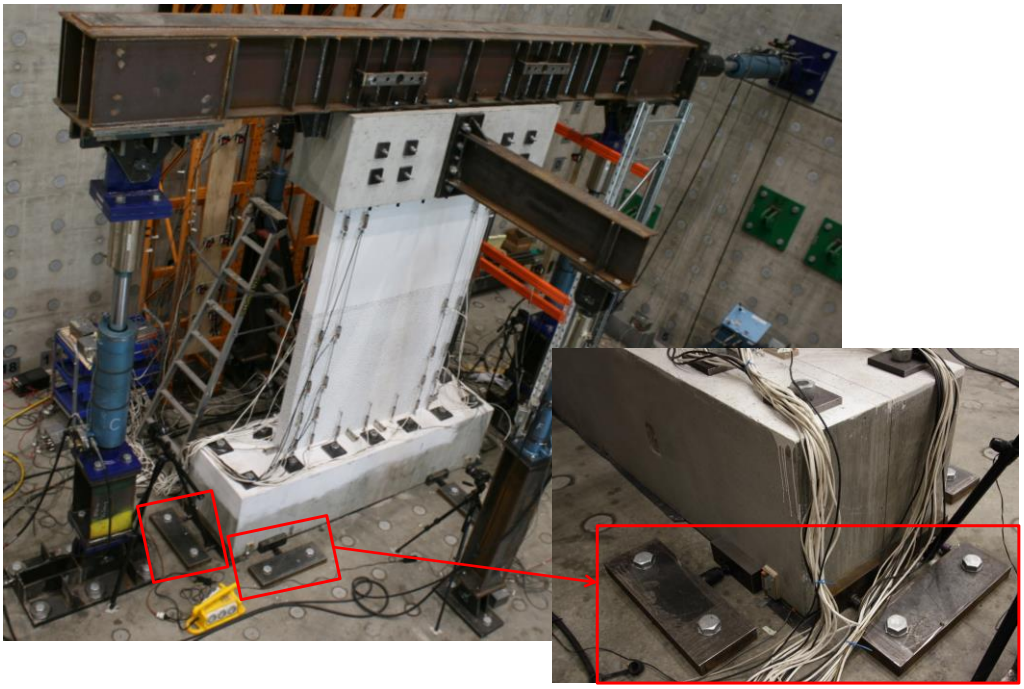

Figure 2-23 Jacking bolts used to limit the movement of the foundation

2.6.LATERAL LOADING PROTOCOL

The three loading protocols used in this study are: 1-in-plane uni-directional, 2-skewed uni-directional (with a 45 degree angle) and 3- clover leaf bi-directional; these are shown in Figure 2-24 and Figure 2-25.

The lateral loading protocol used in this experiment (in both in-plane and out-of-plane directions) consisted of three displacement-controlled cycles at increasing amplitudes: 0.05%, 0.125%, 0.375%, 0.5%, 0.75%, 1.0%, 1.5%, 2.0% and 2.5% inter-storey drift, as shown in Figure 2-24a. As a sign convention for the thesis, in-plane pull loading direction (south/right in Figure 2-3) refers to the negative top wall lateral displacement. In the out-of-plane also the pull loading direction (east/back in Figure 2-3) would be the negative drift ratio.

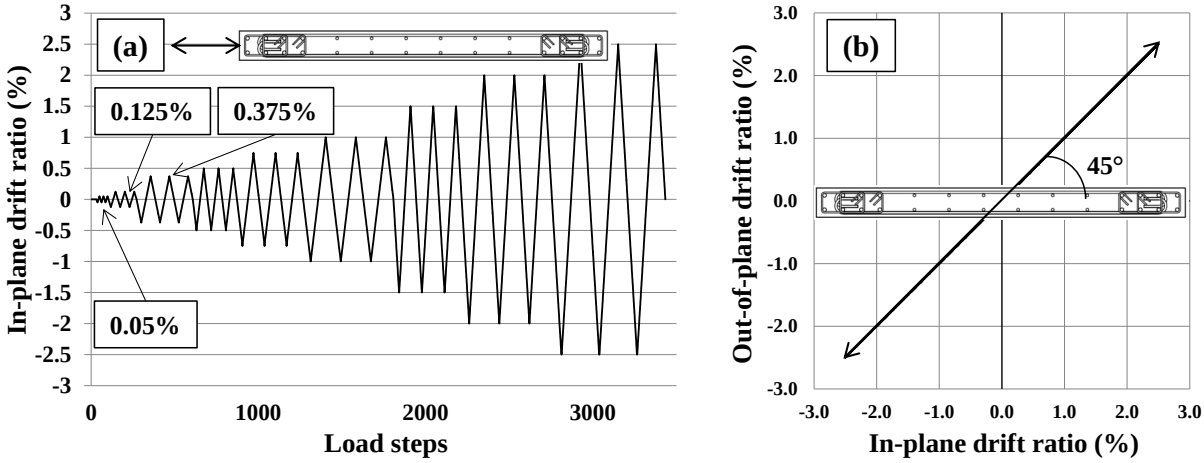

Figure 2-24 Loading protocols of the specimens, (a) SP1-Uni and (b) SP1-Skew

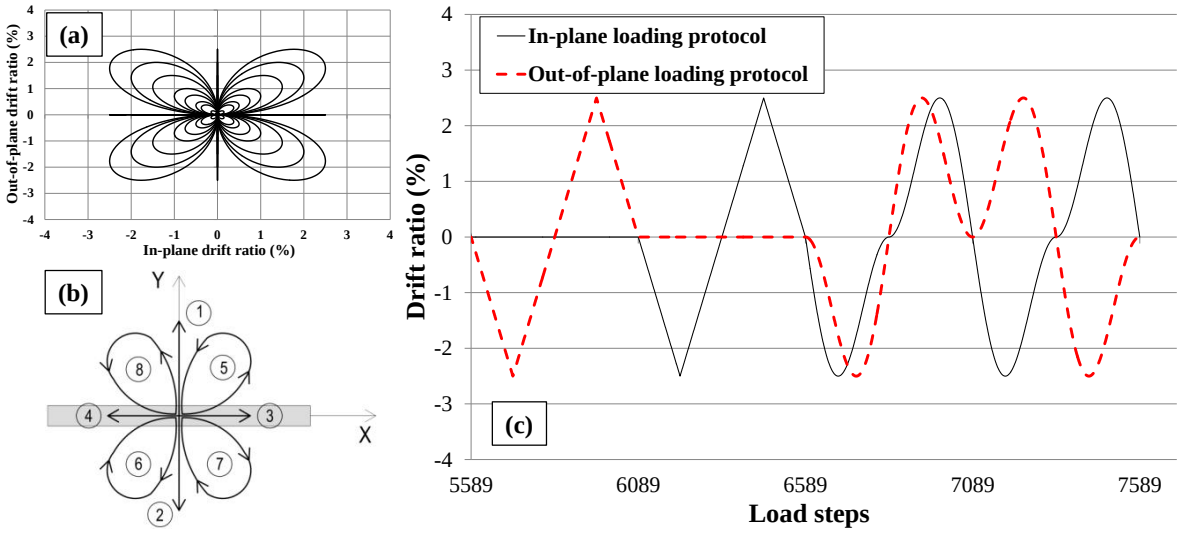

Figure 2-25 Loading protocols of the specimen SP1-Clover, (a) clover leaf, (b) order of each cycle and (c) details of each cycle of the clover leaf

In-plane cyclic displacement was measured at a height of 2250mm from the base for SP1-Uni using a rotary pot as shown in Figure 2-26. However, it was found that the rotary pot is not reliable for the case of the specimens under bi-directional loading as the specimen also move in the out-of-plane direction and the string could slip out of the rotary pot. Therefore, for SP1-Skew and SP1-Clover, a draw wire was used to measure the in-plane displacements (Figure 2-27). It should be noted that in all cases the in-plane cyclic displacement was applied at a height of 3070mm and measured at a height of 2250mm from the base and the out-of-plane cyclic displacements were applied and measured at the midpoint of the cap beam (2513.5mm from the base). It is worth noting that the clover leaf loading pattern was defined such that it matches the other two loading patterns in the in-plane direction (Figure 2-24c). One cycle of out-of-plane and in-plane displacements were applied at the beginning of each clover leaf drift level to match the three cycles of displacements in the skew and in-plane uni-directional loading patterns as a full clover leaf only consists of 2 cycles of loading.

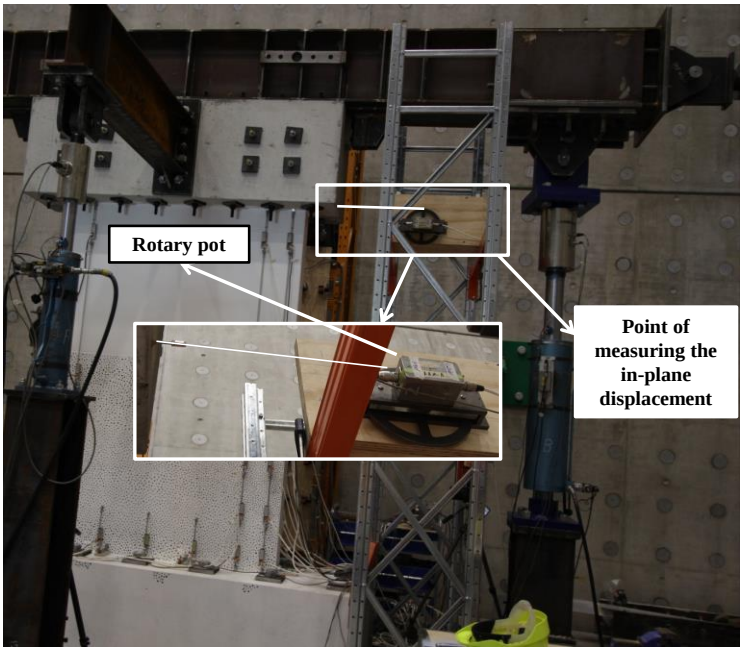

Figure 2-26 Rotary pot used to measure in-plane displacement of SP1-Uni

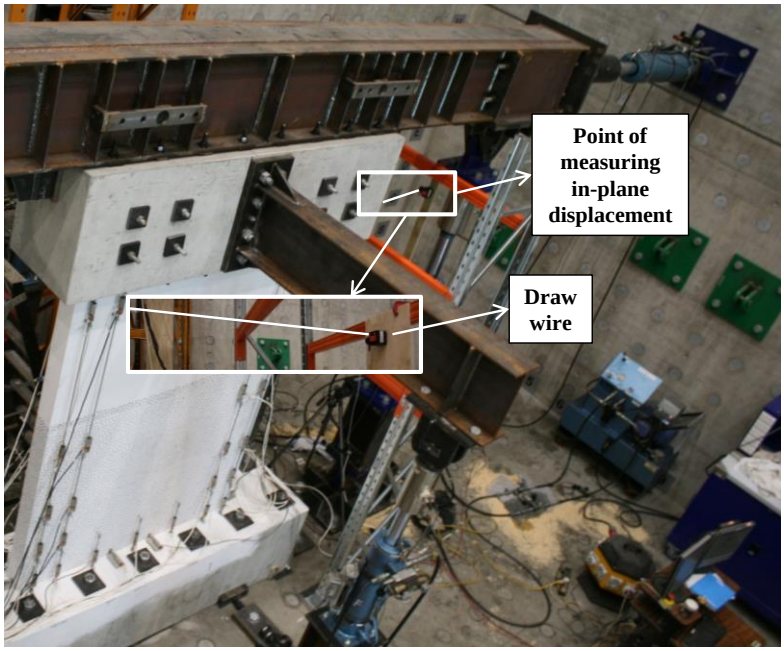

Figure 2-27 Draw wire used to measure the in-plane displacement of SP1-Skew and SP1-Clover

2.7.INSTRUMENTATION

2.7.1. Measurements of loads

Applied loads and reactive forces were measured using load cells, which consisted of hollow cylinders machined from high strength steels and instrumented with two independent sets of full bridge circuits of 350Ω resistance strain gages. Three 1000kN capacity load cells were used to measure the horizontal in-plane load and vertical axial forces, while four 400kN capacity load cells were used to measure the load in the 400kN actuators.

2.7.2. Measurements of displacements

All specimens were instrumented using both conventional instruments and modern particle tracking measurement system. In addition, crack widths were measured at the peak drifts and photos were taken at the end of each displacement step. In order to make it easier when referring to each face of the specimen, as it is shown in Figure 2-3 and Figure 2-18, front face is the western, back face is eastern, right face is southern and left face is northern face of the specimen. To measure the in-plane horizontal displacements of SP1-Uni, rotary potentiometers with a 5kΩ resistance was used (Figure 2-26). As was discussed in section 2.6, a draw wire was used to measure the in-plane displacement of the wall for SP1-Skew and SP1-Clover (Figure 2-27). Table 2-5 presents the description of each instrument and its specifications.

Table 2-5 Displacement instrument description and specifications

Instrument	Description	Stroke	Picture
Strain gauge	Used to measure tensile strain of longitudinal and horizontal bars	up to 0.02 tensile strain	
LVDT	Used to measure the average compressive and tensile strains of concrete	±30 mm	
Spring LVDT	Used to measure the base movement of the wall's panel and the foundation	±30 mm	
Draw wire	Used to measure the in-plane and out-of-plane displacements	±150 mm	
Rotary pot	Used to measure the movement of the actuators	±150 mm	

Strain gauges: 48 strain gauges were used to measure strains in the longitudinal and horizontal steel reinforcement. Figure 2-7 and Figure 2-28 show how these strain gauges were attached to the bars. Positions of the strain gauges on the specimen's cage are also shown in Figure 2-28. It should be noted that strain gauges were attached on both sides (front and back) of the cage as shown in Figure 2-28.

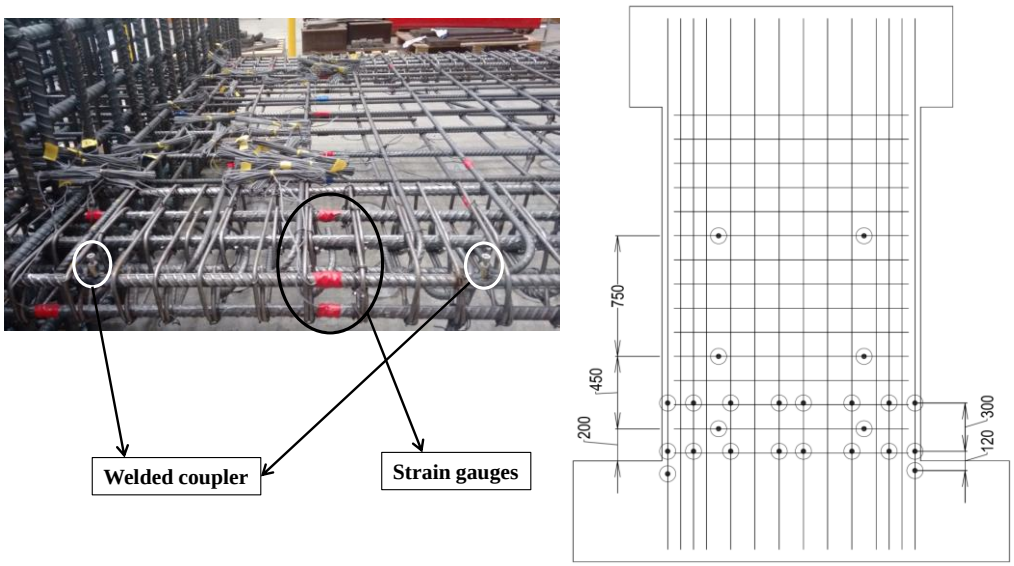

Figure 2-28 Strain gauges and the welded couplers used for instrumentation

Linear variable differential transducer (LVDT): As can be seen in Figure 2-29, 23 vertical LVDTs on the front and 20 on the back faces of the wall were used to measure average strain of concrete. Figure 2-30 shows the LVDTs on the front and back faces of the specimen. In order to measure the average strain of longitudinal bars, 6 couplers were welded directly to the two corner longitudinal bars on the back face. After casting, 4 vertical LVDTs were attached between these couplers allowing measuring the average strains of those reinforcing bars. The positions of these welded couplers are shown in Figure 2-29a. Figure 2-7, Figure 2-28 and Figure 2-30b show how these LVDTs were attached to the specimen.

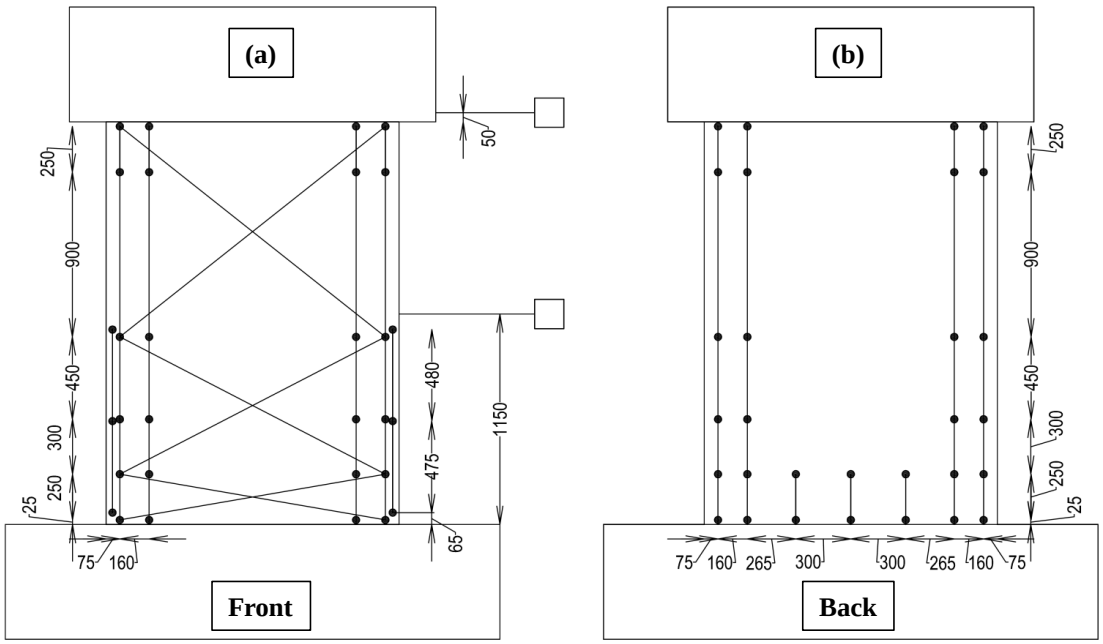

Figure 2-29 Instrumentation, (a) LVDTs on the front face and (b) LVDTs on the back face

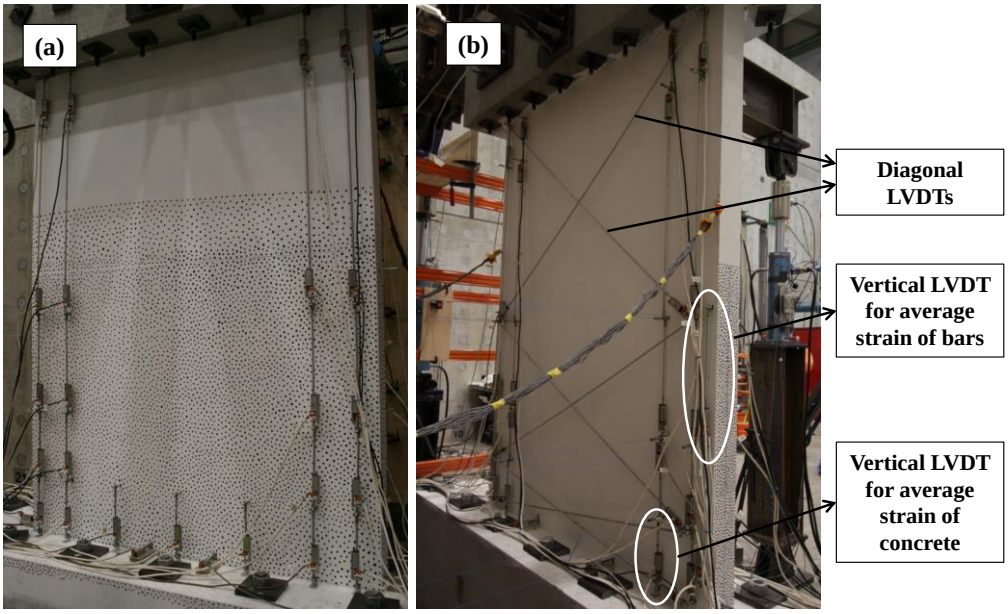

Figure 2-30 Photo of LVDTs, (a) on the front and (b) on the back faces

On the back face, 6 diagonal LVDTs were used to capture the shear deformations of the wall (Figure 2-29a and Figure 2-30b). The shear displacements of the shear panel can be calculated using Equation 2-5 or Equation 2-6 (Beyer et al. 2011).

$$\Delta_s = \frac{1}{4b}((d+\delta_2)^2 - (d+\delta_1)^2 \qquad 2\text{-}5$$

$$\Delta_s = \frac{1}{4b}((d+\delta_2)^2 - (d+\delta_1)^2 - (\alpha - 0.5)\theta(h_{sh})h_{sh} \qquad 2\text{-}6$$

Where b is the width of the shear panel, d is the original length of the diagonal, and δ_i is the change in length of one of the two diagonals (Figure 2-31), $\theta(h_{sh})$ is the difference of rotations at the top and bottom of the panel of height h_{sh} for which the shear deformations are determined, and α is a measure for the variation of the curvature over the height of the panel. The values of α vary between 0.5 and 1 if the point of contraflexure is above the panel for which the shear deformations are determined.

$$\alpha = \frac{\int_0^{h_{sh}} \theta(z)dz}{\theta(h_{sh})h_{sh}} \qquad 2\text{-}7$$

For a constant curvature, α is 0.5, if the curvature distribution is triangular, α equates to 2/3 and if the deformations are concentrated near the base, α tends toward unity. Provided that the base lengths of the LVDTs measuring the elongations of the wall edges are shorter than the height of the shear panel, the value of α can be computed from these LVDT measurements.

As was pointed out by Beyer et al (2011), Equation 2-5 can lead to 5-12% increase in the shear deformation (Figure 2-32). Massone and Wallace (2004) reported up to as 31% differences between Equations 2-5 and 2-6. The obtained difference depends on the curvature profile over the height of the shear panel, the magnitude of the α factor, and the ratio of shear-to-flexural deformations of the shear panel (Beyer et al. 2011). In this study, both methods will be used and compared for shear deformation evaluation.

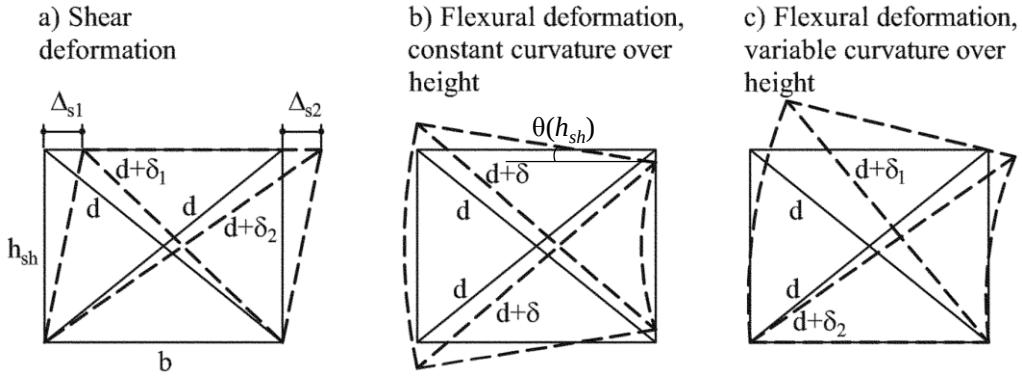

Figure 2-31 Wall shear deformation calculation (Beyer et al. 2011)

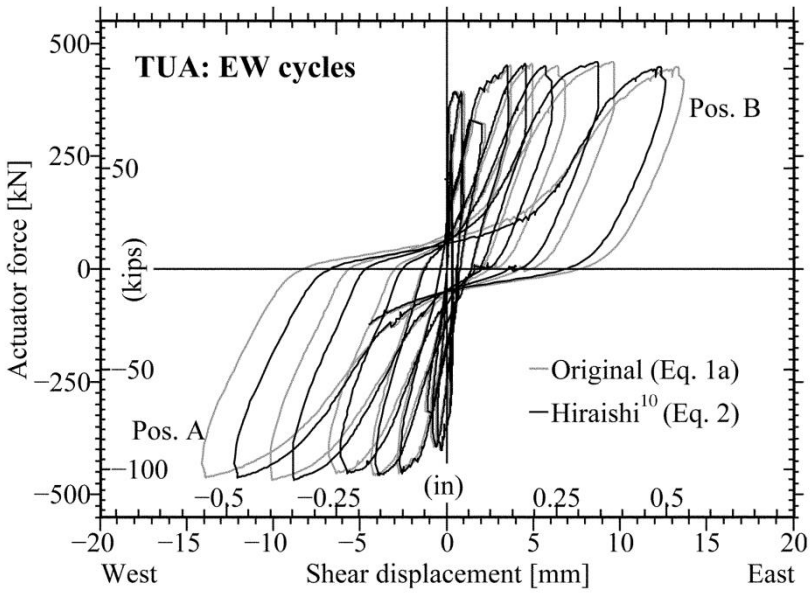

Figure 2-32 Shear displacement-shear force hysteresis curve using Equation 2-5 and Equation 2-6 (Beyer et al. 2011)

Spring LVDT: 4 spring LVDTs were used for monitoring the foundation movement (if any) and 6 spring LVDTs were used to measure the wall-to-foundation sliding in the in-plane and out-of-plane directions. The positions of the spring post are show in Figure 2-33. A typical photo of spring pots attached to the specimen is shown in Figure 2-34.

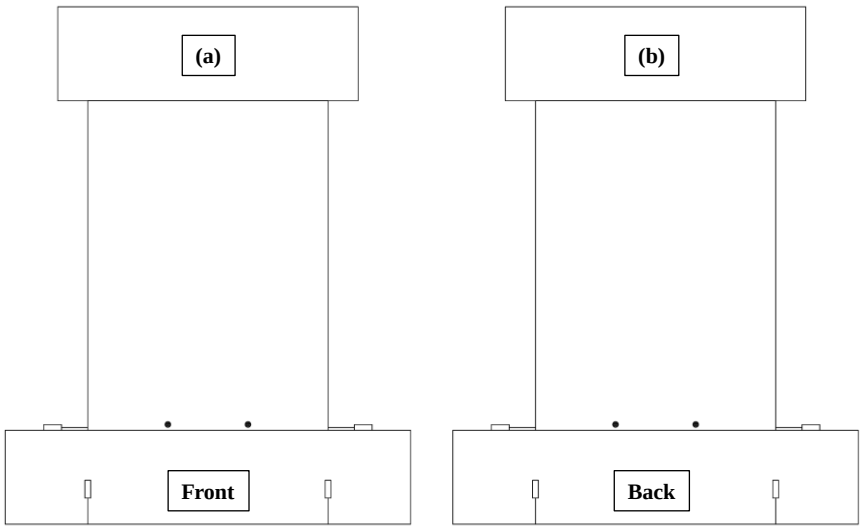

Figure 2-33 Spring pots, (a) front face and (b) back face

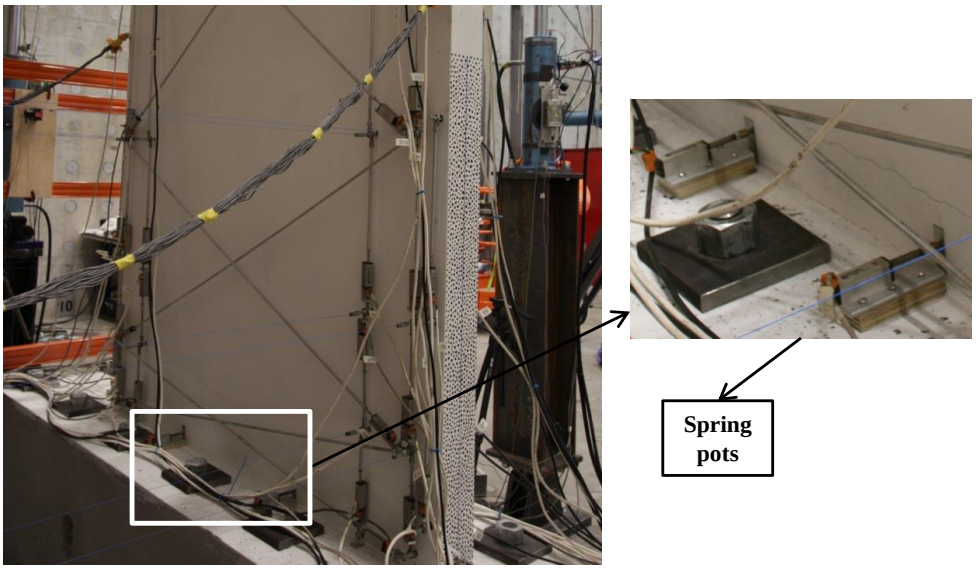

Figure 2-34 spring pots attached to the back face of the specimen

Draw wire: On the back face, 20 draw wires were used to measure out-of-plane deformations of the wall. Figure 2-35 shows typical draw wires attached to the back of the specimen. Two draw wires were also used to measure the in-plane deformations of the specimen (Figure 2-27, Figure 2-30b and Figure 2-35). The positions of the draw wires are also shown in Figure 2-35.

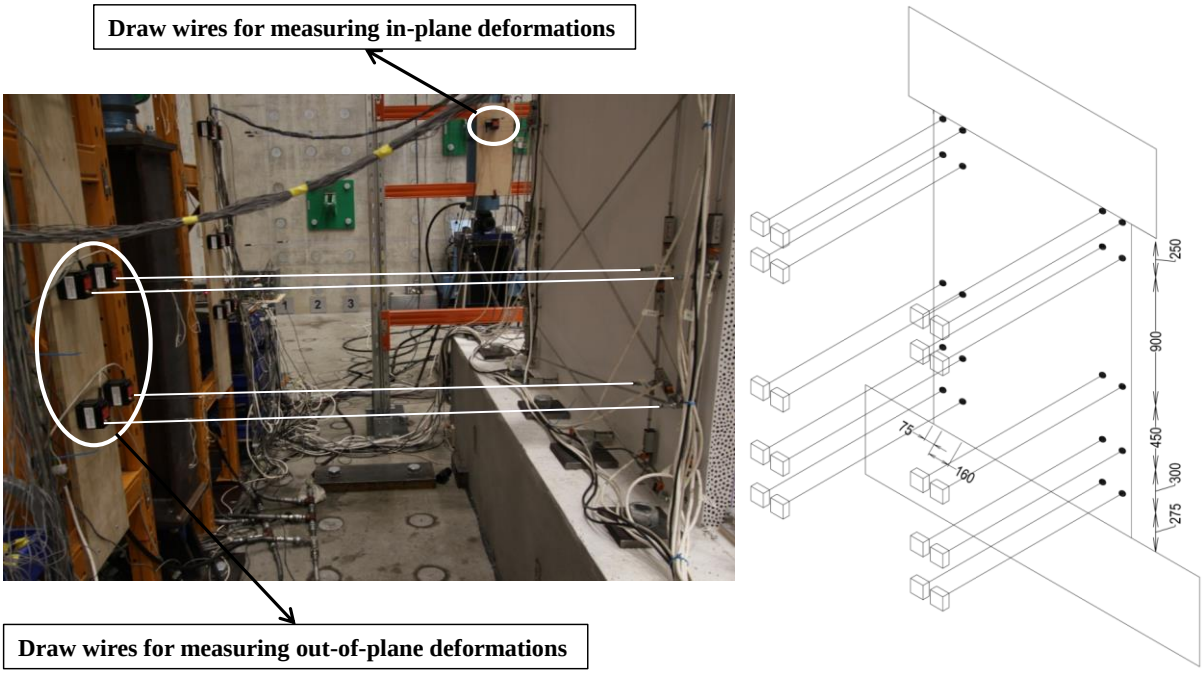

Figure 2-35 Draw wires used to measure the in-plane and out of plane displacements

Particle tracking: Further to these instruments, local deformations of the specimens were also measured on three faces of the specimen (front, left and right) using a Light Attenuation (LA) technique with STREAMS, a software tool developed at the University of Canterbury to support the analysis of images obtained from the experiment (Nokes 2016, Cenedese et al. 2017). The dots painted on three faces of the specimen for particle tracking are shown in Figure 2-36. It should be noted since particle tracking was used for the first time at the University of Canterbury for RC structures, this technique was used as the backup plan and mainly for future development of particle tracking for RC structures.

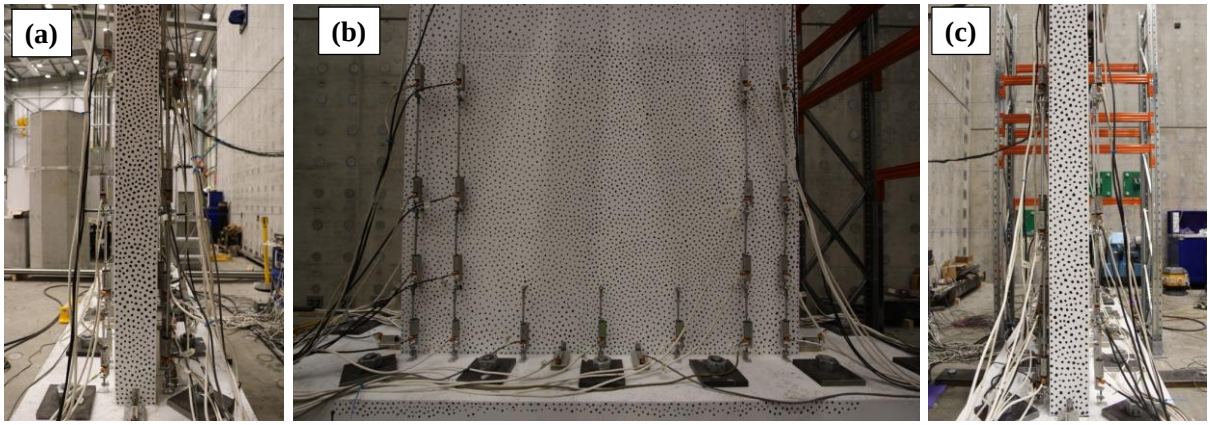

Figure 2-36 Dots painted on the specimen for particle tracking, (a) right, (b) front, (c) left faces

3. TEST RESULTS OF THE EFFECTS OF LOAD PATH ON RECTANGULAR SLENDER WALLS

3.1.INTRODUCTION

In the first part of this chapter the experimental observations of the three specimens described in Chapter 2 were shown along with the base shear vs drift ratio curve of each specimen as well as the crack pattern and failure mode. In the second part, the experimental observations were discussed in terms of effects of bi-directional loading on the failure mode, strength and drift capacity, average strain in concrete, strain profile, crack pattern, out-of-plane displacement evolution pattern and shear deformation for each specimen.

3.2.TEST OBSERVATIONS

Description of damage evolution and the final failure mechanism is provided for each specimen. The in-plane base shear-drift ratio hysteresis curves of each specimen including the key points such as initiation of cover concrete spalling, bar buckling and lateral instability failure were shown in Figure 3-4, Figure 3-8 and Figure 3-13. The out-of-plane base shear vs drift ratio curves of SP1-Skew and SP1-Clover were shown in Figure 3-9 and Figure 3-14. It is worth noting that the in-plane drift ratio was measured for a height of 2.25m (50mm above the panel's height, see Figure 2-26) and out-of-plane drift ratio was measured for a height of 2.51m (at the midpoint of the cap beam).

3.2.1. SP1-Uni

This was the benchmark specimen tested under cyclic in-plane loading protocol. SP1-Uni was mainly used for comparison when investigating the seismic behaviour of specimens subjected to bi-directional loading.

Concrete cover spalling initiated at 0.75% drift ratio, when the compressive strain of concrete reached about 0.003. However, tensile cracks began much earlier than that during 0.375% drift ratio. At 0.75% drift ratio, maximum crack width was about 1mm. Concrete cover spalling increased on the right side during 1.5% drift level. Up to 3mm crack width was observed at 1.5% drift ratio. Concrete cover spalling penetrated the boundary zone (BZ)

during the 2% drift level. Bar buckling initiated at this drift level in the front-right corner bar. By the end of 2% drift cycles, the two corner bars in the left and right faces of the specimen buckled. Concrete crushing in the boundary zone began at 2.5% drift level. SP1-Uni failed in lateral instability mode on its right face during the first 2.5% drift cycle (Figure 3-1).

The failure was relatively sudden. Before the lateral instability happens, the damage was mostly limited to the concrete cover spalling and bar buckling in the corner bars only. Whereas after the lateral instability occurred, all eight BZ longitudinal bars on the right face buckled and most of the BZ area crushed (Figure 3-2). There was no sign of web crushing or bar buckling in the web even after the final failure.

Crack patterns of SP1-Uni at the third cycle of each drift level are shown in Figure 3-3. Cracks were predominantly flexural due to the relatively large in-plane shear span ratio of the specimen.

Figure 3-4 shows the in-plane base shear vs. drift ratio curve of SP1-Uni. Theoretical strength shown in Figure 3-4 was calculated based on a section analysis using SAP2000 software (2015).

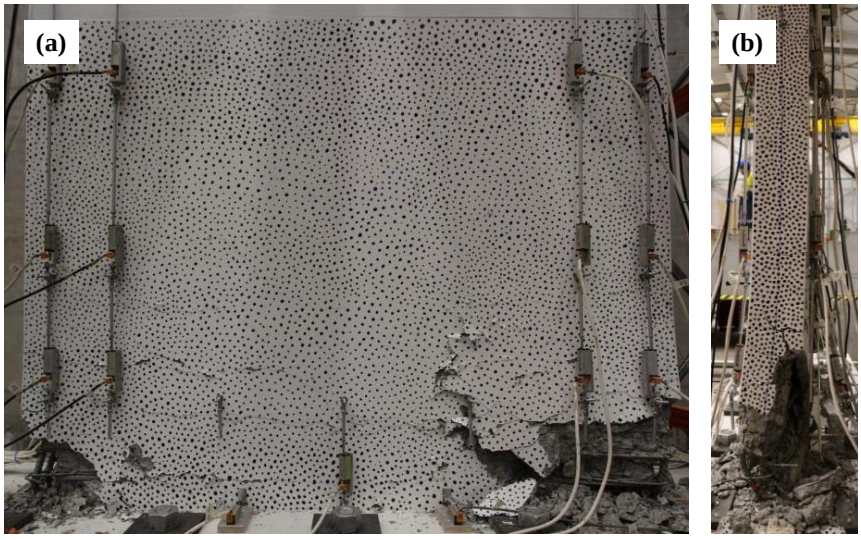

Figure 3-1 SP1-Uni at failure point (a) front face and (b) right face

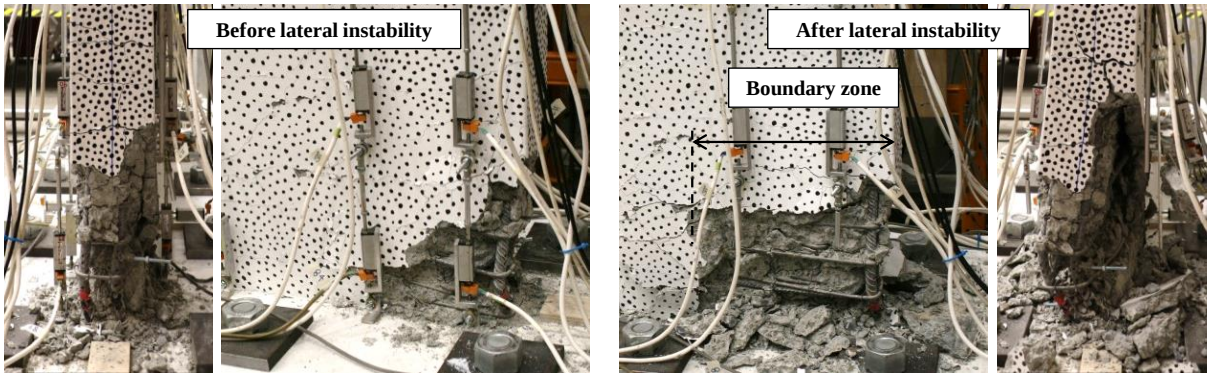

Figure 3-2 SP1-Uni before and after lateral instability occurs

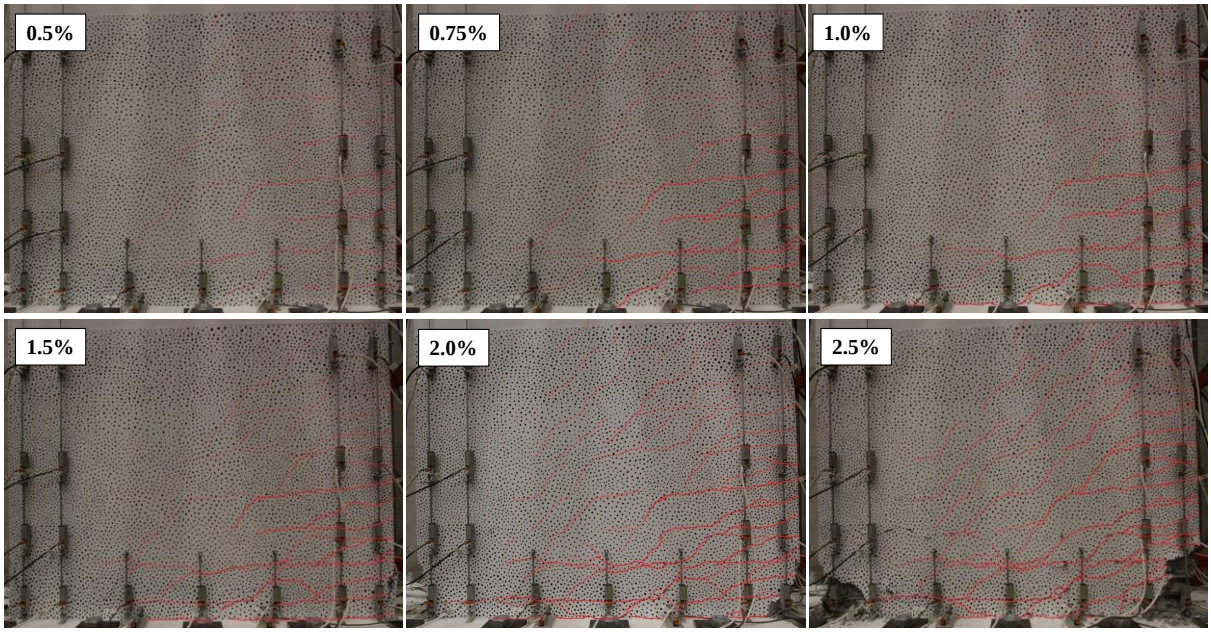

Figure 3-3 Crack pattern of SP1-Uni at each drift level

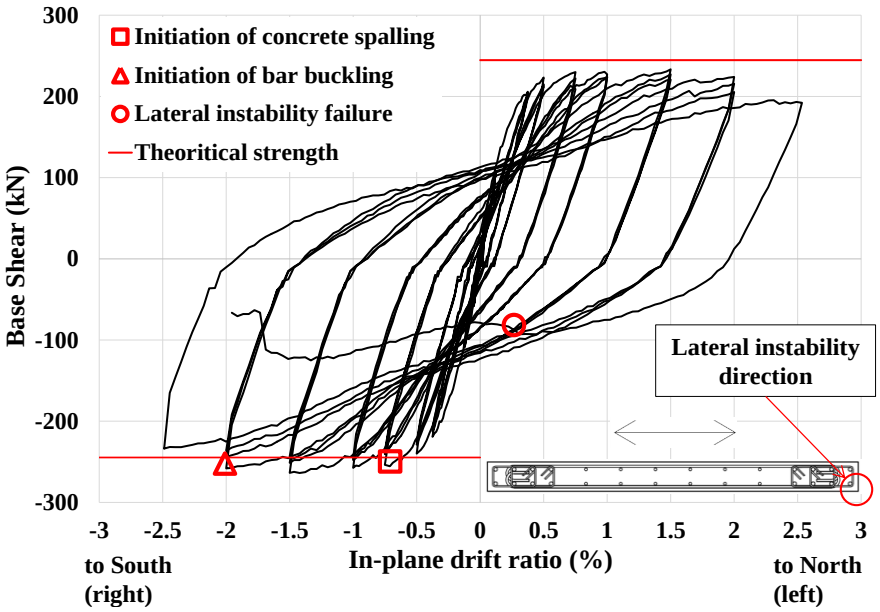

Figure 3-4 In-plane base shear - drift ratio of SP1-Uni

3.2.2. SP1-Skew

As the name suggests, this specimen was tested under skew loading protocol (loading pattern was shown in Figure 2-24b).

Concrete cover spalling initiated on the left side of this specimen during the second cycle of 0.375% drift. At this drift level, maximum crack width was about 0.4mm. Crack width increased to 0.5mm at 0.5% drift. At 0.75% drift, concrete cover spalling initiated on the right side of the wall. Concrete cover spalling penetrated the boundary zone (BZ) on the left face during this drift level. Crack width of about 1.1mm was observed during 0.75% drift cycles. Concrete cover spalling increased significantly on the left face at 1% drift. Maximum crack

width was about 3mm at this stage. During the 1.5% drift cycles, concrete cover spalling took place on the back-left corner; this was delayed due to the skew loading pattern which led to less compressive and tensile strains on that corner. During the second cycle of 1.5% drift, bar buckling was noticed in the front-left corner bar. Maximum crack width was about 6mm at 1.5% drift level. During the first cycle of 2% drift, bar buckling had initiated on the back-left corner bar as well (delayed due to the same reason explained above). By the end of 2% drift cycle, both right face corner bars had also started to buckle. The front-left corner bar snapped during the first cycle of 2.5% drift (Figure 3-5). Concrete crushing penetrated the web from the first cycle of 2.5% drift ratio. Lateral instability occurred in the left side of the specimen during unloading of the first 2.5% drift cycle (Figure 3-5).

All eight BZ bars and four of the web longitudinal bars buckled on the left side after the onset of lateral instability (Figure 3-6). Web crushing that initiated from the first cycle of 2.5% drift, significantly increased after the lateral instability failure.

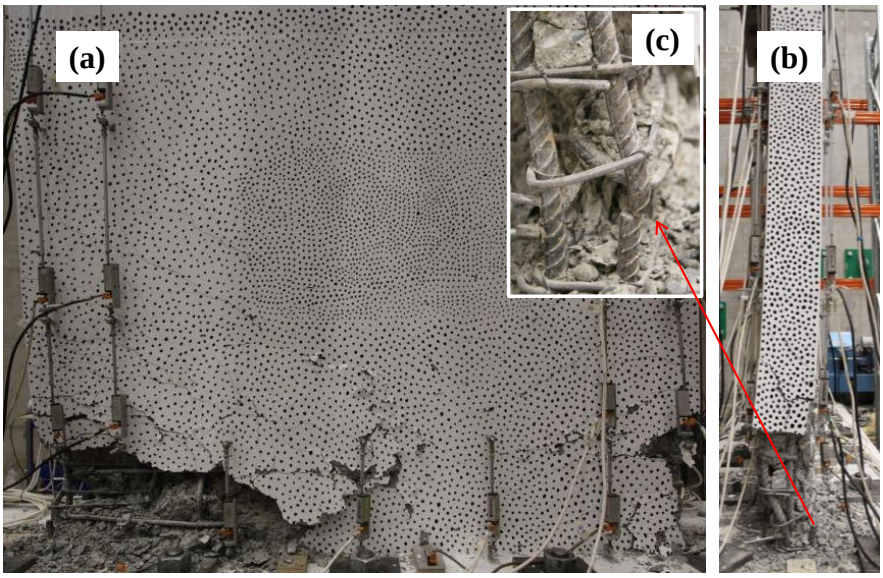

Figure 3-5 SP1-Skew at Failure point (a) front face, (b) left face and (c) bar snapping

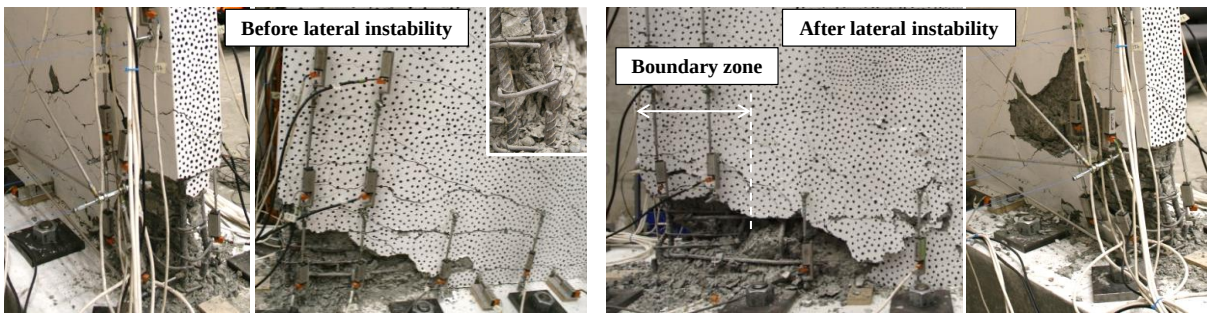

Figure 3-6 SP1-Skew before and after lateral instability occurs

Crack patterns of SP1-Skew at the third cycle of each drift level are shown in Figure 3-7. Some shear cracks were observed in both in-plane and out-of-plane directions in SP1-Skew.

In-plane and out-of-plane base shear-to-drift ratio curves of SP1-Skew are shown in Figure 3-8 and Figure 3-9, respectively. It should be noted that out-of-plane force-displacement curve of SP1-Skew had some minor noises which have been smoothed as shown in Figure 3-9. Data smoothing was carried out using Microsoft Excel Data Analysis using the Exponential Smoothing with a damping factor of 0.6. Theoretical strength was calculated based on a section analysis using SAP2000 software (2015).

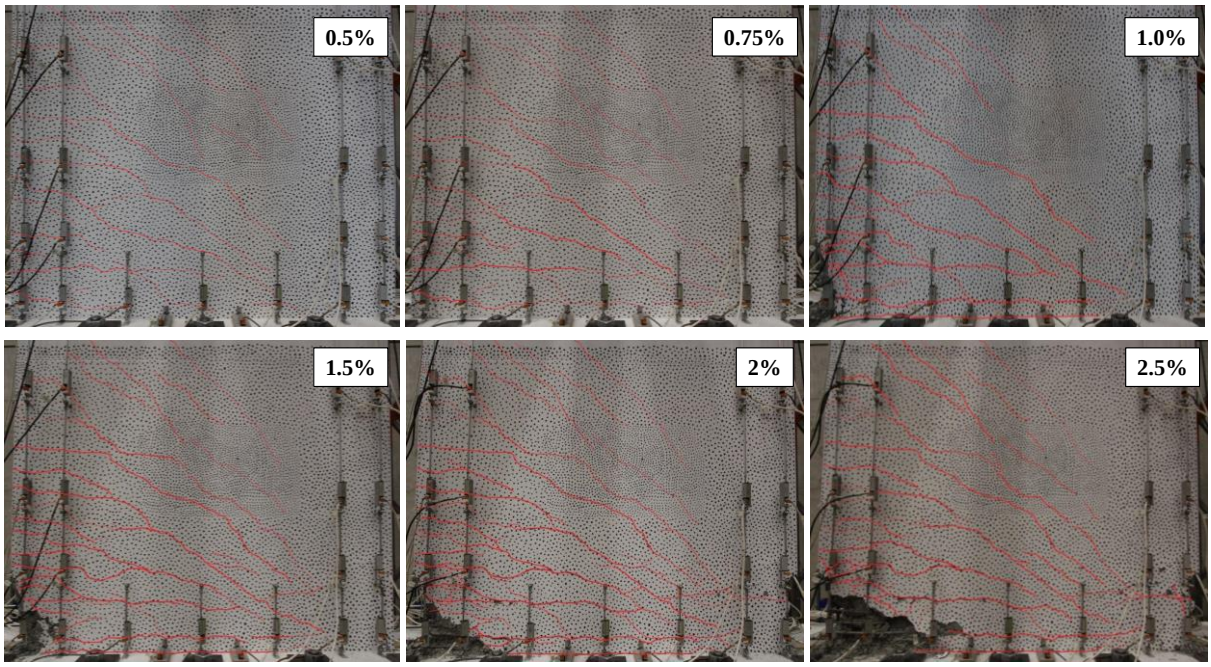

Figure 3-7 Cracking pattern of SP1-Skew at the each drift level

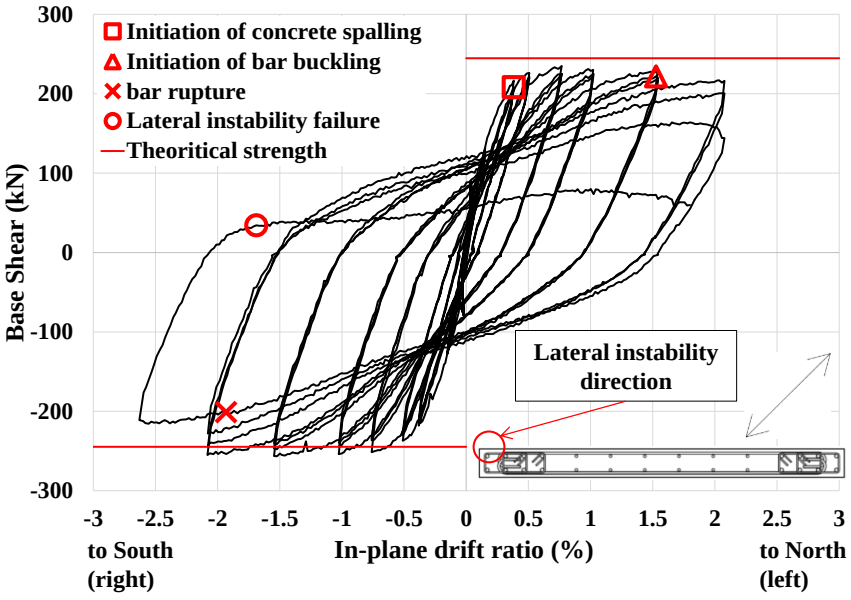

Figure 3-8 In-plane base shear - drift ratio of SP1-Skew

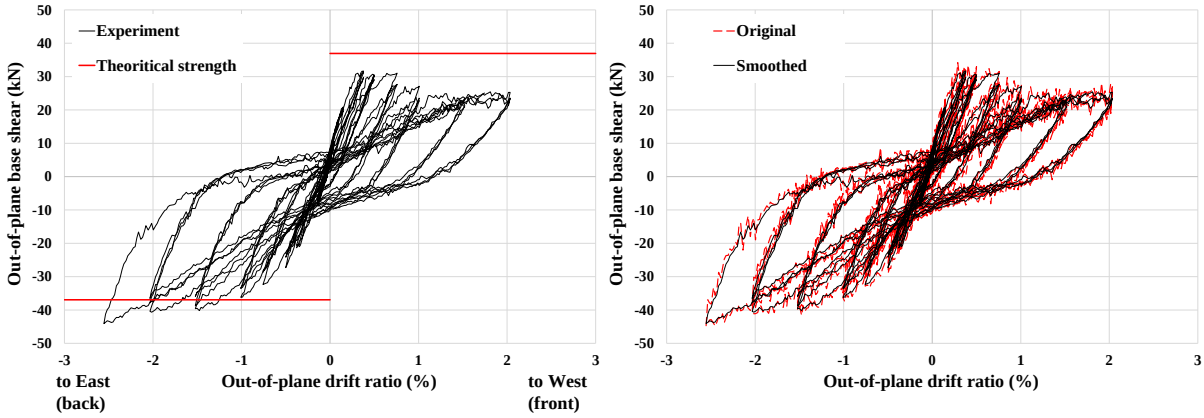

Figure 3-9 Out-of-plane base shear - drift ratio of SP1-Skew

3.2.3. SP1-Clover

SP1-Clover was tested under bi-directional clover leaf loading protocol (See Figure 2-25).

At 0.375% drift, the concrete cover at the wall base started to show the first vertical cracks which appeared before the onset of the cover concrete spalling (on the right face). At this drift level, maximum crack width was about 0.3mm. At 0.75% drift, concrete cover spalling initiated on the left face. During 0.75% drift cycles, concrete cover spalling penetrated the BZ on the left and right faces. Maximum crack width was about 1mm by the end of 0.75% drift cycle. Concrete cover spalling increased significantly on the right side of the specimen at 1% drift. Crack width increased to about 2mm at this drift level.

At 1.5% drift, concrete cover spalling extended to the right face. During the second cycle of 1.5% drift, bar buckling was triggered in the right-back corner bar. The front-right corner bar buckled at the end of 1.5% drift level. Maximum crack width was about 4mm at this stage. During the first cycle of 2% drift, bar buckling was initiated in the left-back corner bar. Lateral instability occurred in the right side of the specimen during unloading in the first cycle of 2% drift (Figure 3-10).

The failure occurred unexpectedly and significantly damaged the wall (Figure 3-11). All eight BZ bars and two of the web longitudinal bars buckled on this face after the lateral instability happened. Concrete crushing in the web only initiated after the lateral instability failure.

Figure 3-10 SP1-Clover at Failure point (a) front face, (b) right face

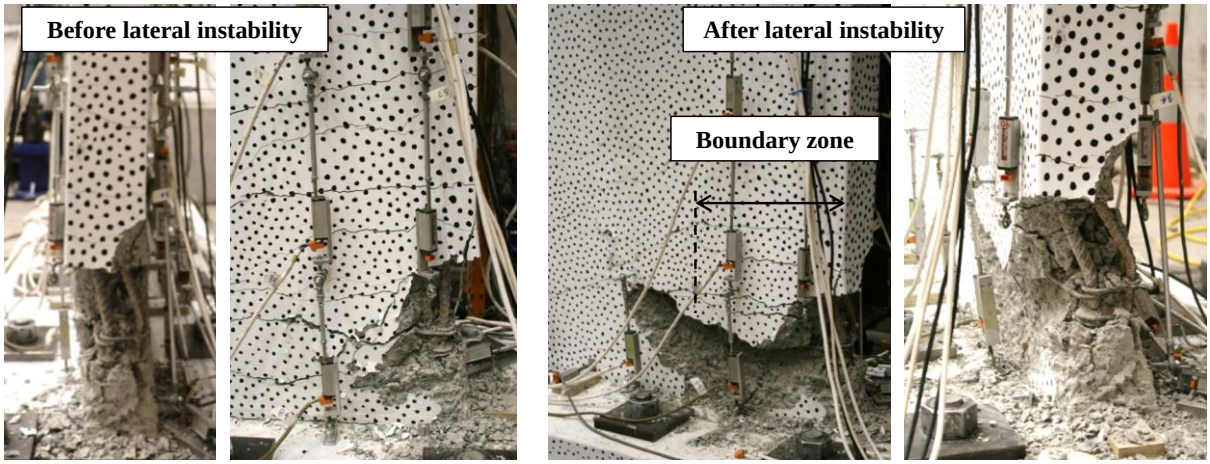

Figure 3-11 SP1-Clover before and after lateral instability occurs

Crack pattern of SP1-Clover at the third cycle of the critical drift ratios is shown in Figure 3-12. SP1-Clover showed some shear cracking in the in-plane direction. However, no out-of-plane shear crack was observed in SP1-Clover.

The in-plane and out-of-plane base shear-to-drift ratio of the specimen are shown in Figure 3-13 and Figure 3-14, respectively. It should be noted that out-of-plane force-displacement curve of SP1-Clover had some minor noises which have been smoothed as is shown in Figure 3-14. Theoretical strength was calculated based on a section analysis using SAP2000 software (2015).

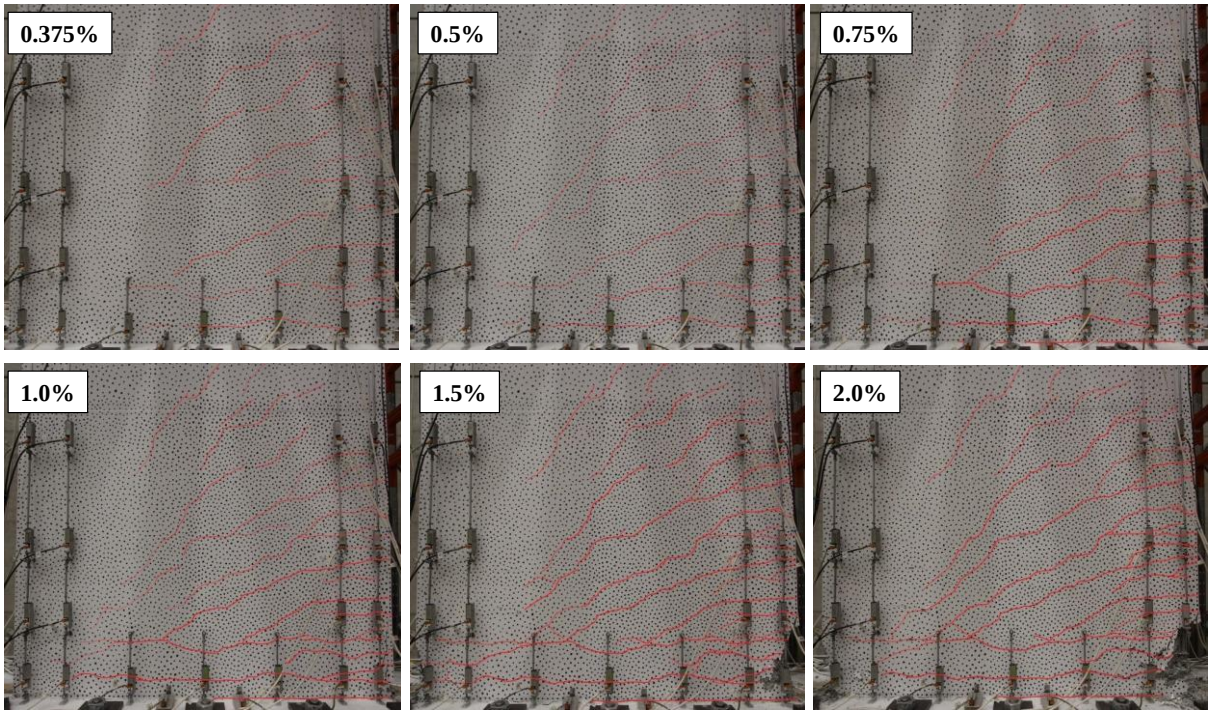

Figure 3-12 Cracking pattern of SP1-Clover at each drift level

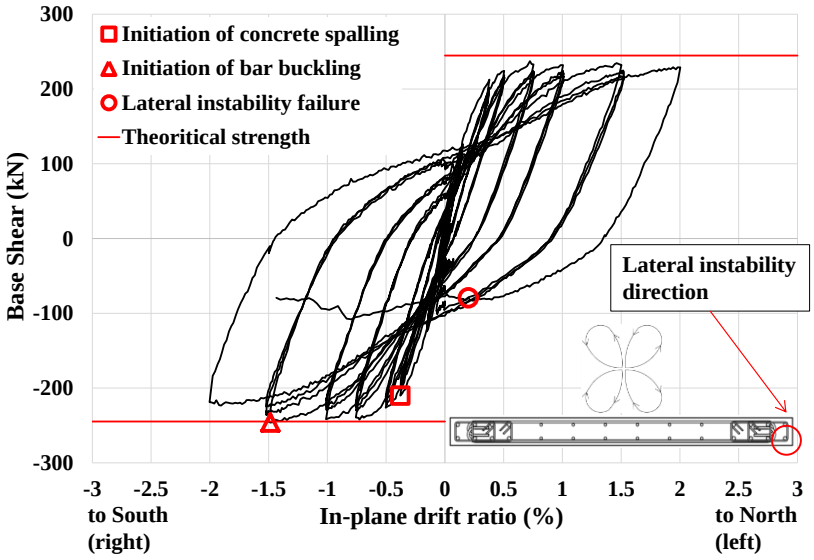

Figure 3-13 In-plane base shear - drift ratio of SP1-Clover

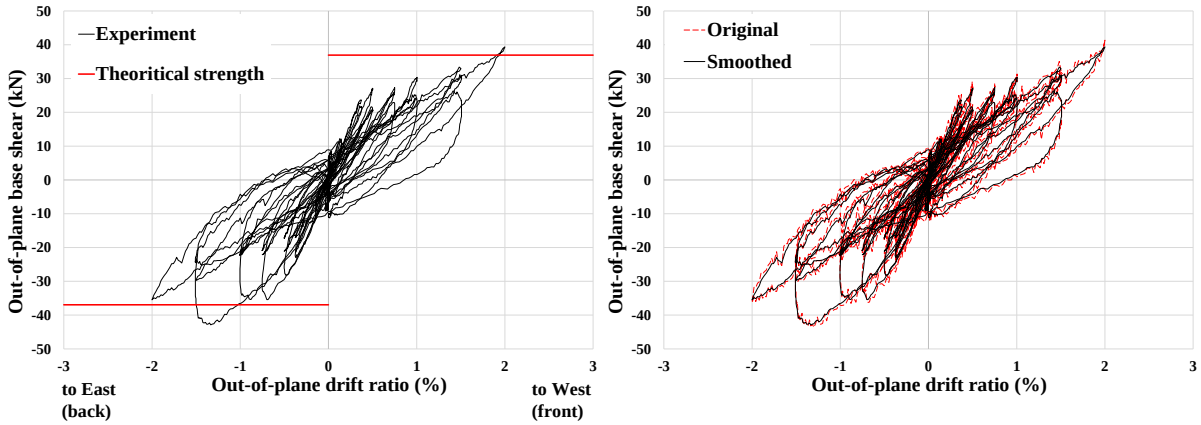

Figure 3-14 Out-of-plane base shear - drift ratio of SP1-Clover

3.3.DISCUSSION OF THE TEST RESULTS

3.3.1. Effects of bi-directional loading on the failure mode

In Section 3.2, the behaviour of the specimens during the experiment was presented in details and the failure mode of each wall was discussed. Table 5-1 shows a summary of the in-plane drift capacity and the types of failure mode observed in each specimen (such as concrete crushing, bar buckling, bar rupture, lateral instability and web crushing). The effects of bi-directional loading on each of these failure modes were summarized in Table 3-2.

Table 3-1 Failure mode and drift capacity of the specimens

Specimen	In-plane drift capacity at failure		Types of failure mode observed
	Right side	Left side	
SP1-Uni	2.5%	2.5%	Bar buckling, concrete crushing, lateral instability
SP1-Skew	2.5%	2%	Bar buckling, concrete crushing, bar rupture, web crushing, lateral instability
SP1-Clover	2%	2%	Bar buckling, concrete crushing, lateral instability, web crushing

Table 3-2 Effects of bi-directional loading on each type of failure

Specimen	Cover concrete spalling initiation	Concrete crushing		Bar buckling initiation		Bar rupture	Lateral instability
		BZ*	Web	BZ*	Web		
SP1-Uni	0.75% drift	2.5% drift	was not observed	2% drift	was not observed	was not observed	2.5% drift
SP1-Skew	0.375% drift	2% drift	2.5% drift	1.5% drift	2.5% drift	2.5% drift	2% drift
SP1-Clover	0.375% drift	2% drift	Initiated with lateral instability failure	1.5% drift	Initiated with lateral instability failure	was not observed	2% drift

* BZ=Boundary Zone

3.3.2. Drift and strength capacities

Figure 3-15 and Figure 3-16 show the in-plane and out-of-plane base shear – drift ratio of the three specimens, respectively. Based on these two curves the drift and strength capacities of the specimens were compared.

Drift capacity: As was also shown in Table 5-1, skew loading decreased the in-plane drift capacity of the specimen compared to the wall subjected to uni-directional loading (on the left face) while it did not change the drift capacity of the right side of the specimen. Clover

leaf loading pattern decreased the total in-plane drift capacity of the wall from 2.5% to 2% compared to uni-directional loading. The main reason for the decrease in the drift capacity was earlier concrete spalling/crushing and bar buckling due to bi-directional loading which decreased the out-of-plane stiffness of the wall. However, for the specimen under skew loading there was a delay in concrete spalling/crushing and bar buckling in one corner due to the asymmetry of skew loading and consequently delayed the ultimate failure of the wall (see Figure 3-17).

Strength capacity: Bi-directional loading did not significantly affect the in-plane strength capacity of the specimens tested in this set of experiments. However, reduction of strength due to bi-directional loading cannot be ruled out completely and needs further investigation on other type of walls and loading patterns. Table 3-3 shows the strength capacity of the three specimens at each drift level. Here the maximum and minimum strengths refer to the maximum strength of the specimen at the first cycle and the third cycle, respectively. It should be noted that the values shown in Table 3-3 are the strength capacity of the specimen on the side that lateral instability occurred (shown in Figure 3-1, Figure 3-5 and Figure 3-10). The only significant decrease in the strength was in the specimen under skew loading. The 33% in-plane strength reduction (on the left side at 2% drift) and 25% out-of-plane one (on the front side from 0.75% drift) in SP1-Skew was due to substantial bar buckling/snapping and concrete crushing resulted from bi-directional loading.

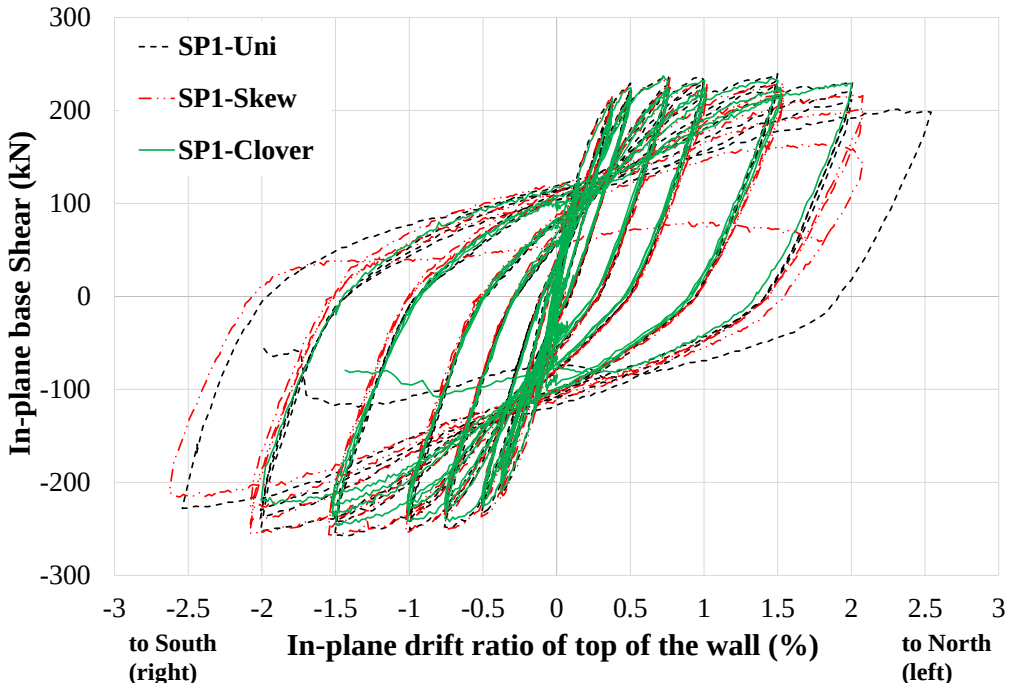

Figure 3-15 Base shear - drift ratio of the three specimens in the in-plane direction

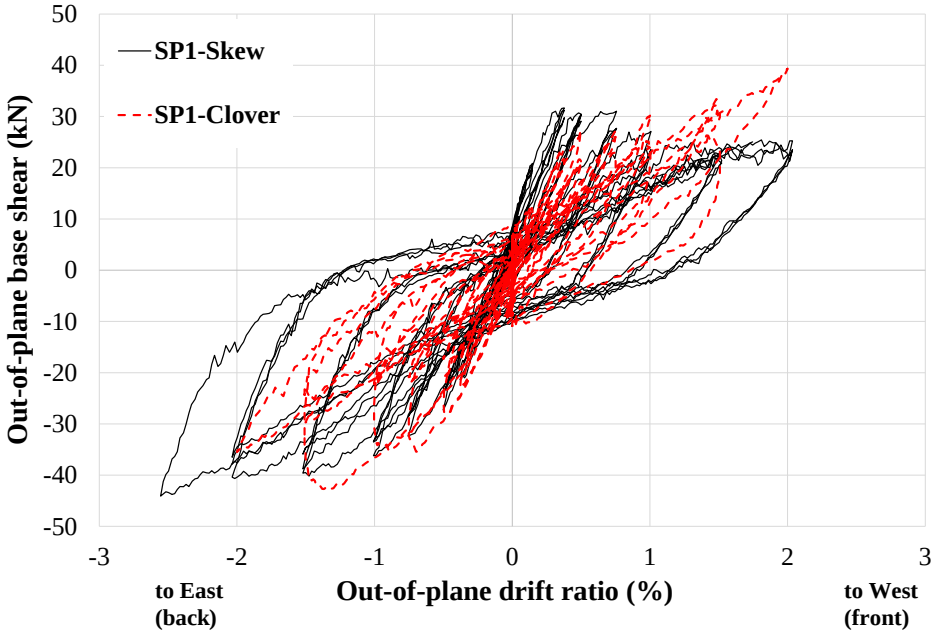

Figure 3-16 Base shear - drift ratio of SP1-Skew and SP1-Clover in the out-of-plane direction

Table 3-3 Strength capacity at each drift level for the three specimens

Drift	SP1-Uni (right side)		SP1-Skew (left side)		SP1-Clover (right side)	
	Max (kN)	Min (kN)	Max (kN)	Min (kN)	Max (kN)	Min (kN)
0.375%	-213.3	-203	216.65	206.6	-210.2	-199.15
0.5%	-233.9	-219.3	226.2	219.8	-226.2	-215.45
0.75%	-249.5	-230.55	234.9	225	-242.3	-226.5
1%	-251.4	-239.9	231.3	221.44	-241.8	-226
1.5%	-257.9	-239.65	229.8	217.1	-246.1	-225.3
2%	-252.1	-230.3	216.9	163.9	-223.4	-
2.5%	-227.9	-	-	-	-	-

3.3.3. Compressive and tensile strains of concrete

Figure 3-17 shows regions of the wall in compression when subjected to each cyclic lateral loading patterns. It can be seen that while under skewed loading a larger length of the wall is in compression, clover leaf loading increase the compression area when compared to uni-directional loading one.

As is shown in Figure 3-18, the strain measured (using LVDTs) in the specimens subjected to bi-directional loading are higher than the actual strain of the specimen due to the curvature of the wall in the out-of-plane direction. Therefore, to solve this issue, the strain measured by the LVDTs were modified assuming a linear variation along the thickness.

Maximum average compressive and tensile strains of the specimens at each drift level are shown in Table 3-4. It should be noted that this average strain was measured for a length of 250mm above the base.

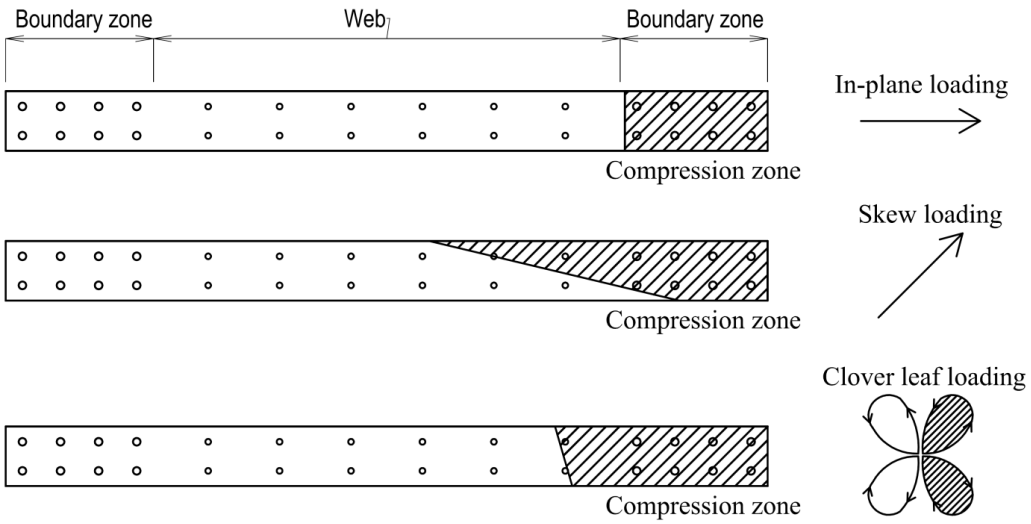

Figure 3-17 Schematic view of the effect of different loading patterns on the compressive strain of the wall

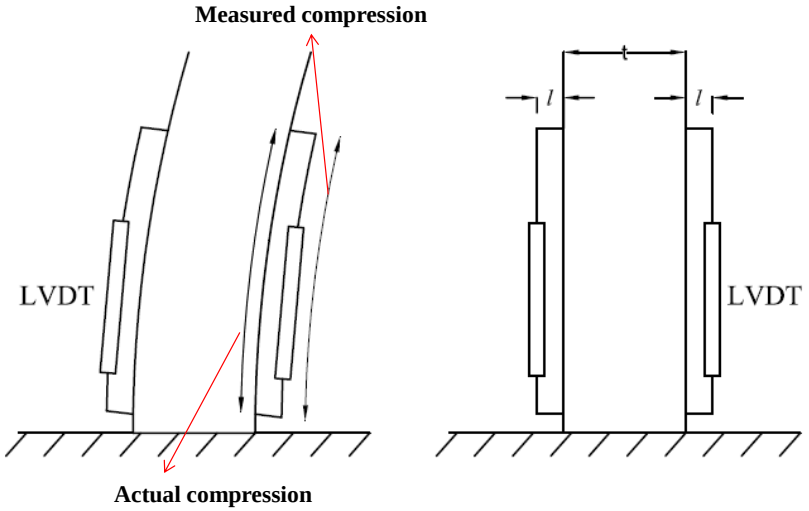

Figure 3-18 Effects of out-of-plane curvature on the strain measurements

Figure 3-19 shows the maximum average compressive and tensile strains of the three specimens at each drift level. Average compressive and tensile strains of concrete along the wall's height at 1% and 1.5% drift are shown in Figure 3-20. It should be noted that the LVDTs measuring the average strain in concrete had to be removed at the end of 2% drift for SP1-Clover due to concrete spalling and in order to avoid damaging the device itself.

As can be seen, the maximum compressive and tensile strains increased significantly at each drift level when the specimen was subjected to bi-directional loading (Figure 3-19a). However, from Figure 3-20, it can be seen that bi-directional loading mostly increased the compressive and tensile strains at the base and not as mush along the height.

Table 3-4 Maximum compressive and tensile strains for each specimen

Specimen	Drift level	Maximum compressive strain		Maximum tensile strain	
		Left side	Right side	Left side	Right side
SP1-Uni	0.375%	-0.192	-0.190	0.393	0.400
	0.5%	-0.234	-0.230	0.575	0.649
	0.75%	-0.293	-0.312	1.159	1.365
	1%	-0.363	-0.358	1.821	2.034
	1.5%	-0.512	-0.575	3.186	3.261
	2%	-1.124	-1.326	4.400	4.400
	2.5%	-2.152	-2.530	5.416	5.272
SP1-Skew	0.375%	-0.372	-0.297	0.482	0.620
	0.5%	-0.477	-0.389	0.680	1.005
	0.75%	-0.731	-0.603	1.447	1.931
	1%	-1.018	-0.866	2.390	2.816
	1.5%	-1.617	-1.560	4.252	4.388
	2%-1st cycle	-3.365	-2.661	6.760	5.584
	2%-3rd cycle	-3.365	-2.661	6.760	5.584
SP1-Clover	0.375%	-0.257	-0.263	0.522	0.456
	0.5%	-0.332	-0.342	0.799	0.721
	0.75%	-0.458	-0.503	1.529	1.421
	1%	-0.697	-0.749	2.310	2.284
	1.5%	-1.183	-1.632	3.743	3.412

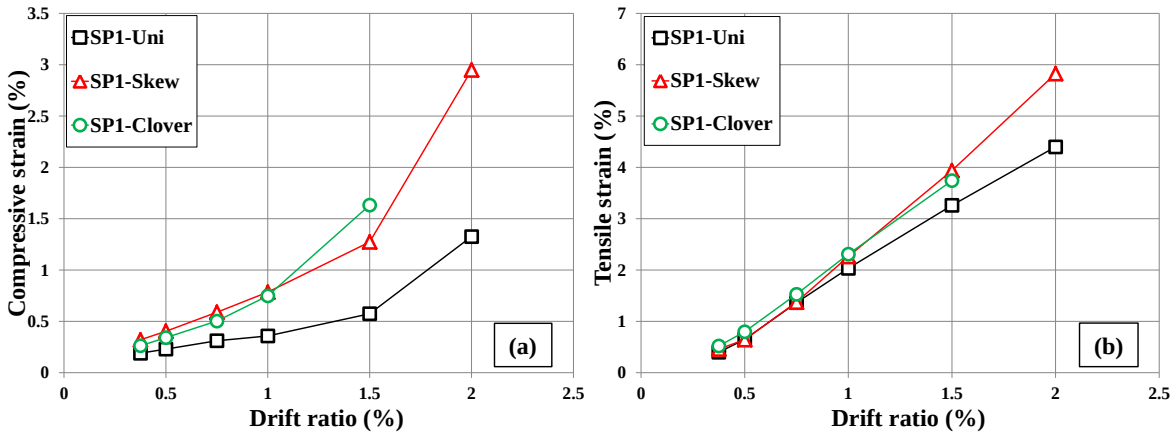

Figure 3-19 Maximum average (a) compressive strains and (b) tensile strains of the specimens at each drift level

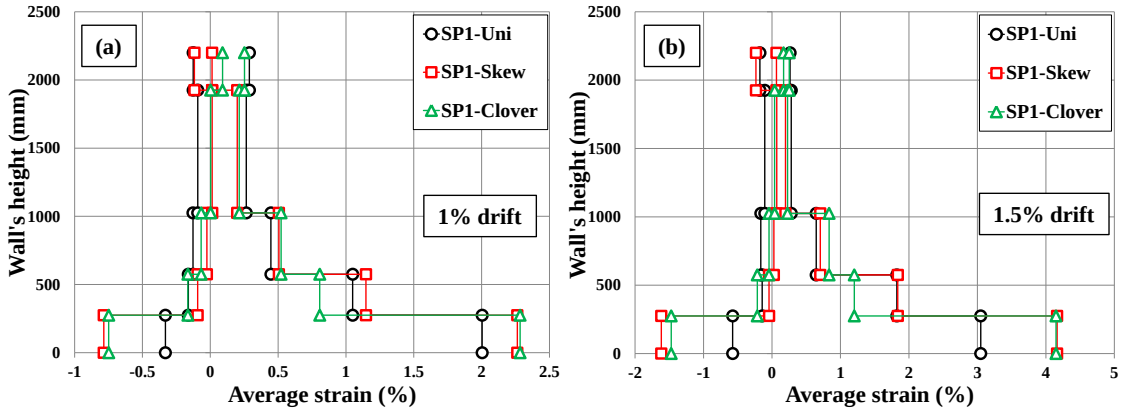

Figure 3-20 Maximum average compressive strains of the specimens along the height of the wall at (a) 1% drift and (b) 1.5% drift

3.3.4. Strain profile

2D strain profile of the three specimens at each drift level is shown in Figure 3-21. It can be seen that under clover leaf bi-directional loading a relatively symmetric area of the wall was in compression by the end of each drift level. This additional damage let to the reduction of out-of-plane stiffness and consequently earlier lateral instability failure. On the other hand, although skew loading affected a larger length of the wall, it was not as effective as clover leaf loading in decreasing the out-of-plane stiffness of the wall as the damages were not symmetric. However, as can be seen in Figure 3-21, neutral axis depth increased significant when the wall was subjected to skew loading which led to considerable concrete crushing and bar buckling in the web of SP2-Skew. 2D strain profile of the wall was drawn for a LVDT with a height of 250mm and between 25-275mm above the base.

Figure 3-22 and Figure 3-23 show the strain profile of SP1-Uni and SP1-Skew at the first cycle of each drift level. Average strain of each point along the wall was measured for two lengths of 250mm and 1000mm above the base.

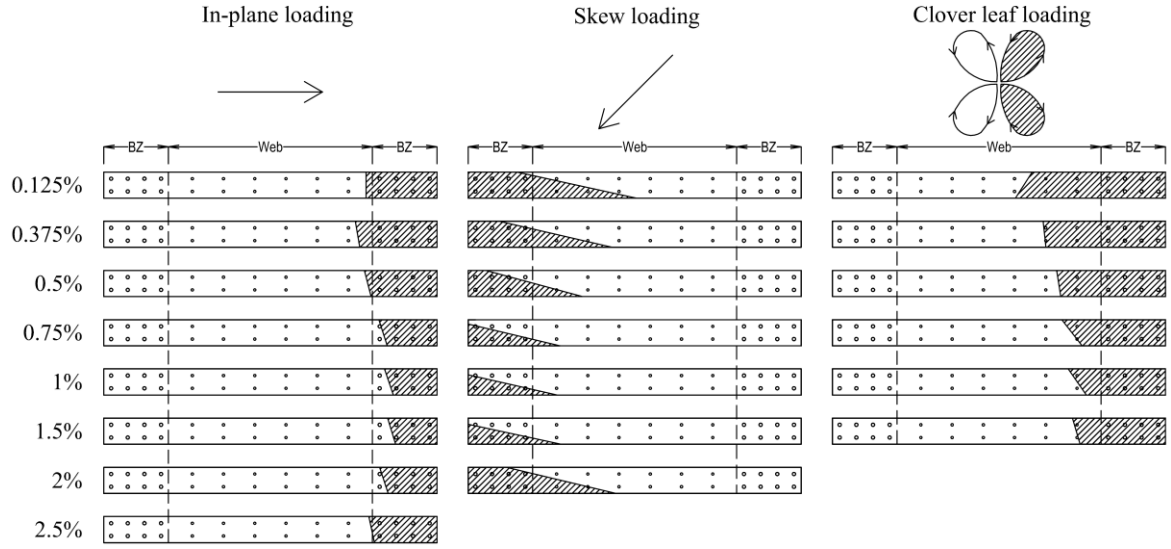

Figure 3-21 2D strain profile of the three specimens for each drift level

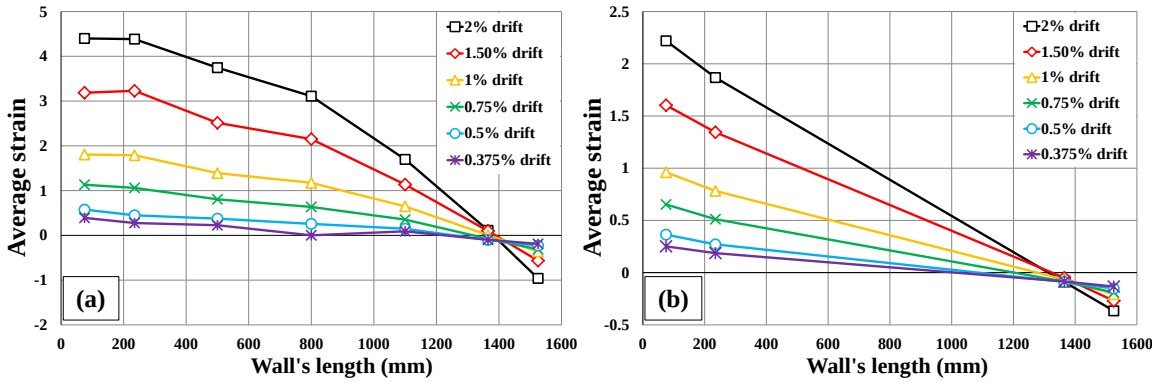

Figure 3-22 Strain profile of SP1-Uni based on an average strain measured for a length of (a) 250mm and (b) 1000mm above the base

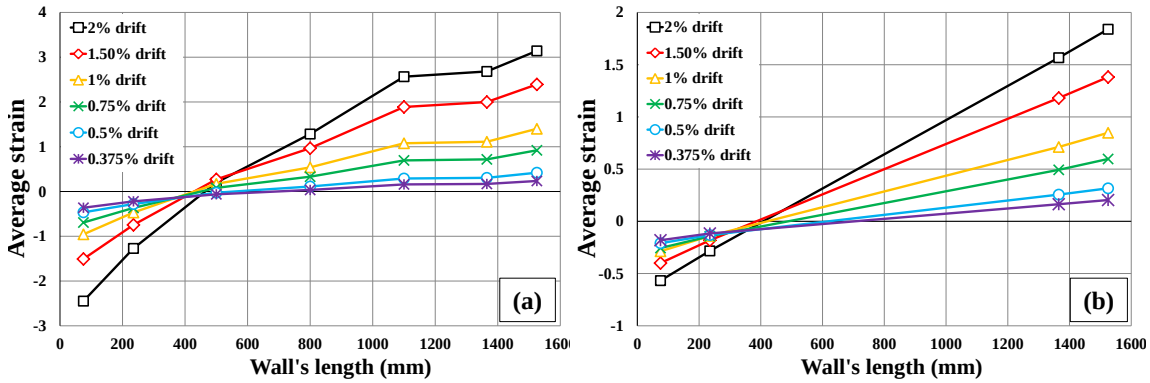

Figure 3-23 Strain profile of SP1-Skew based on an average strain measured for a length of (a) 250mm and (b) 1000mm above the base

As can be seen in Figure 2-25, in the case of SP1-Clover each of the three cycles of the clover leaf loading pattern affects the wall differently. Therefore, in Figure 3-24 strain profile of the specimen SP1-Clover at each cycle of 1.5% drift ratio was investigated (average strain was measured for a length of 1000mm above the base). Since the first cycle of the clover leaf loading pattern is basically a uni-directional one, therefore, in Figure 3-24, by comparing the strain profile of the first cycle with the second and third ones, the effects of bi-directional loading on the strain profile of the wall can be seen. Comparing the strain profile of the wall for the two bi-directional cycles of the clover leaf (second and third cycles) with the first cycle (the uni-directional one), it can be seen that the compressive strain values as well as the neutral axis depth were significantly increased due to bi-directional loading. It should be noted that for the first and third cycles the front LVDTs and for the second cycle the LVDTs in the backside of the wall were used to draw the strain profile (based on the side of the wall affected by the lateral load path). Figure 3-25 shows the strain profile of SP1-Clover at the third cycle of each drift level.

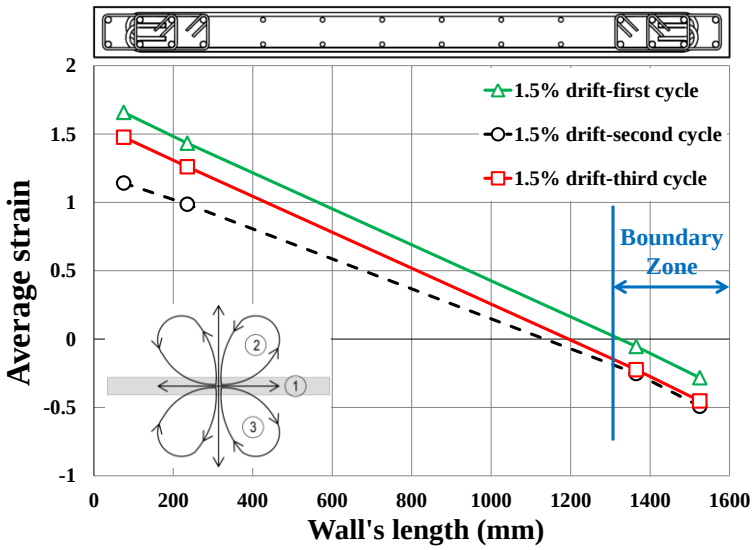

Figure 3-24 Strain profile of SP1-Clover for each cycle of 1.5% drift ratio

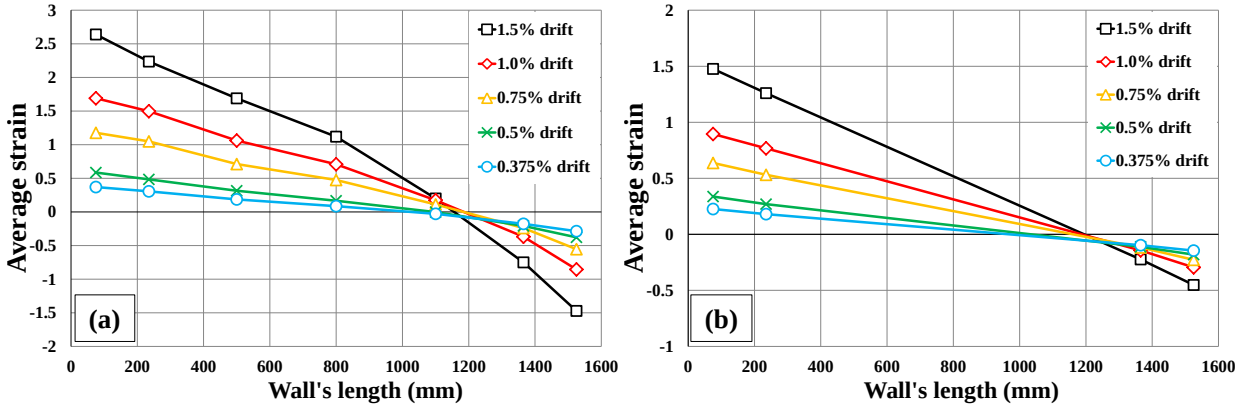

Figure 3-25 Strain profile of SP1-Clover based on an average strain measured for a length of (a) 250mm and (b) 1000mm above the base

Figure 3-26 shows the strain profile of the three specimens at the third cycle of 1.5% drift ratio. The reason that the average strain of each point along the wall was measured for a length of 250mm above the base was lack of instrumentation in the web for an average strain over a height of 1000mm which would affect the neutral axis depth calculation (see Figure 2-28b). At this drift level, neutral axis depth was 199 mm, 401 mm and 408 mm for SP1-Uni, SP1-Clover and SP1-Skew, respectively. It is worth noting that in Figure 3-26, the reason that the tensile strain of the specimen under skewed loading is less than the other two is that here the strain profile is drawn for a straight line while for a specimen under skew loading the maximum compressive and tensile strains do not occur on a straight line but along a skew direction (see Figure 3-17 and Figure 3-21).

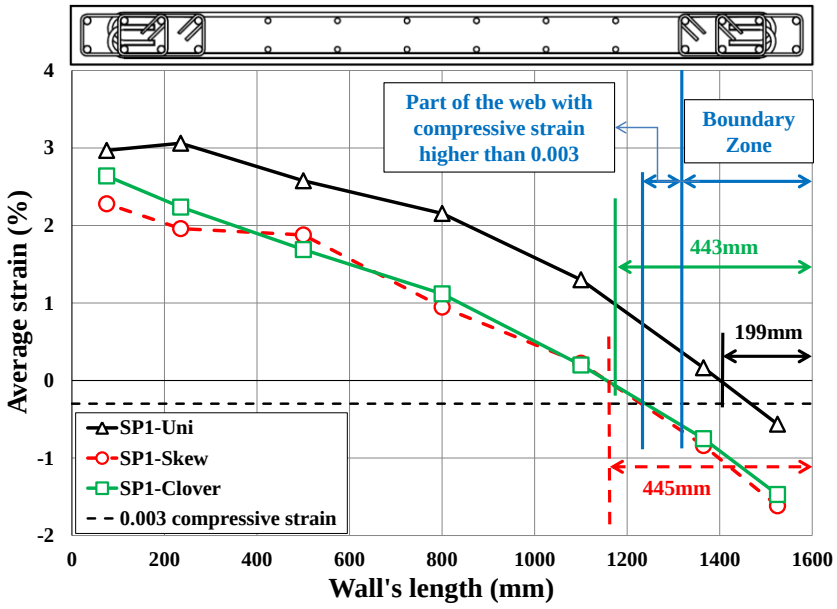

Figure 3-26 Strain profile along the wall's length of each specimen at the third cycle of 1.5% drift

It can be seen in Figure 3-26 that the neutral axis depth and therefore the compression zone increased substantially for the specimens under bi-directional loading. Therefore, although

the specimens were designed by Dashti et al. (2017b) for a ductile performance based on an in-plane lateral loading according to NZS3101 (2006), substantial bar buckling and concrete crushing was observed in the web when the wall was subjected to bi-directional loading especially in case of SP1-Skew (Figure 3-5 and Figure 3-7). At the third cycle of 1.5% drift, the maximum compressive strain in the web was 0.624% and 0.557% for SP1-Skew and SP1-Clover, respectively. While in case of SP1-Uni, the neural axis was within the boundary zone area. The maximum compressive strain in the web for SP1-Skew at the first cycle of 2% drift was 0.973% which explains the significant web crushing at that drift level shown in Figure 3-5 and Figure 3-7.

3.3.5. Crack pattern

A pure flexure cracking in both in-plane and out-of-plane directions was observed in the specimen SP1-Uni (see Figure 3-3 and Figure 3-27). However, as can be seen in Figure 3-7 and Figure 3-28, surprisingly some shear crack was observed in both in-plane and out-of-plane directions in the specimen SP1-Skew (perhaps torsional shear cracks in the case of out-of-plane ones). This type of crack differs from the observations in the previous studies on RC walls. Asymmetry in the damage due to the asymmetric bi-directional loading (e.g. skewed loading as shown in Figure 3-17 and Figure 3-21) could have helped with the development of shear cracks in the out-of-plane direction of the wall. The fact that there is no sign of out-of-plane shear cracks in SP1-Clover supports this hypothesis (Figure 3-29). The symmetric damage as a result of clover leaf loading pattern is a result of a full clover leaf loading on each side of the wall at each drift level as shown in Figure 3-17 and Figure 3-21. An increase in the angle of loading from 45 degree towards the out-of-plane direction and other parameters such as high axial load ratio can potentially lead to further development of such cracks. This can change the failure mode of the wall to an out-of-plane shear failure as it was observed in Wall D5-6 from Grand Chancellor Hotel after the 2011 Canterbury earthquake (Figure 1-4). It is worth noting that in-plane shear cracks were observed in both specimens subjected to bi-directional loading (SP1-Skew and SP1-Clover).

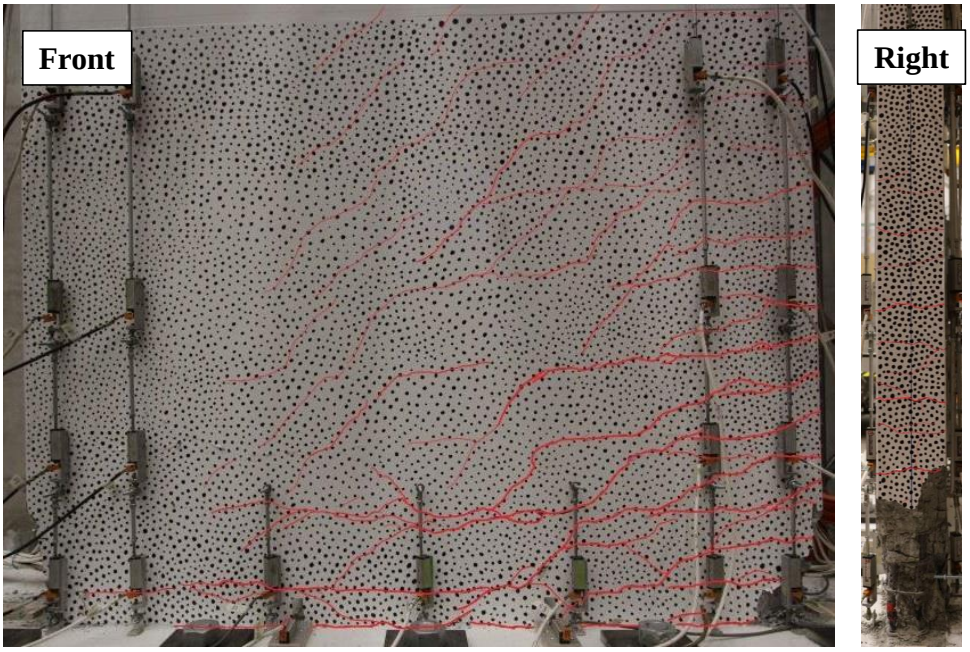

Figure 3-27 Crack pattern of the SP1-Uni at 2% drift level in the (a) in-plane and (b) out-of-plane directions

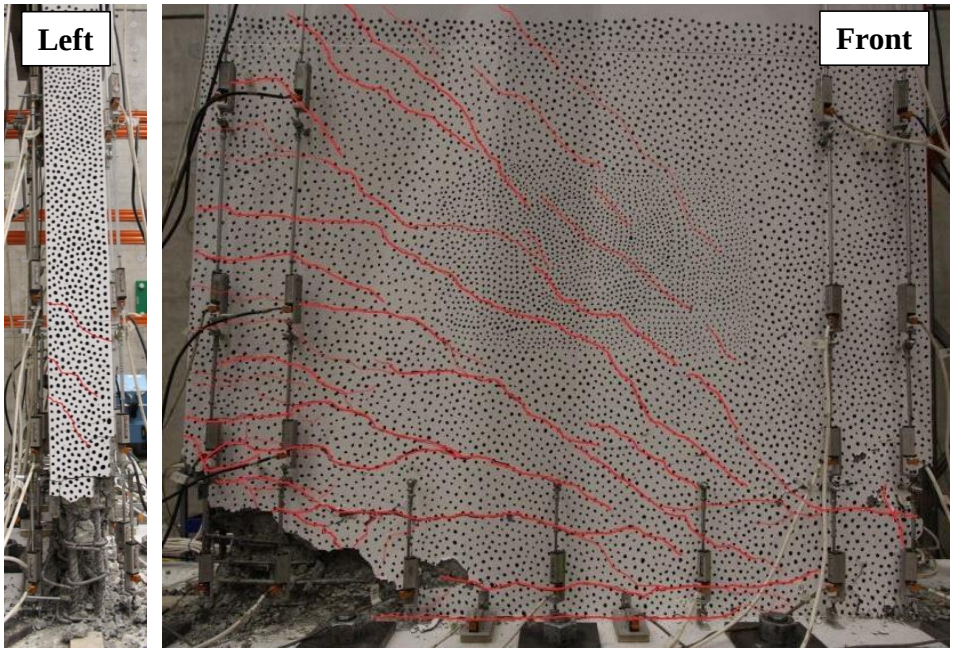

Figure 3-28 Crack pattern of the SP1-Skew at 2.5% drift level in the (a) in-plane and (b) out-of-plane directions

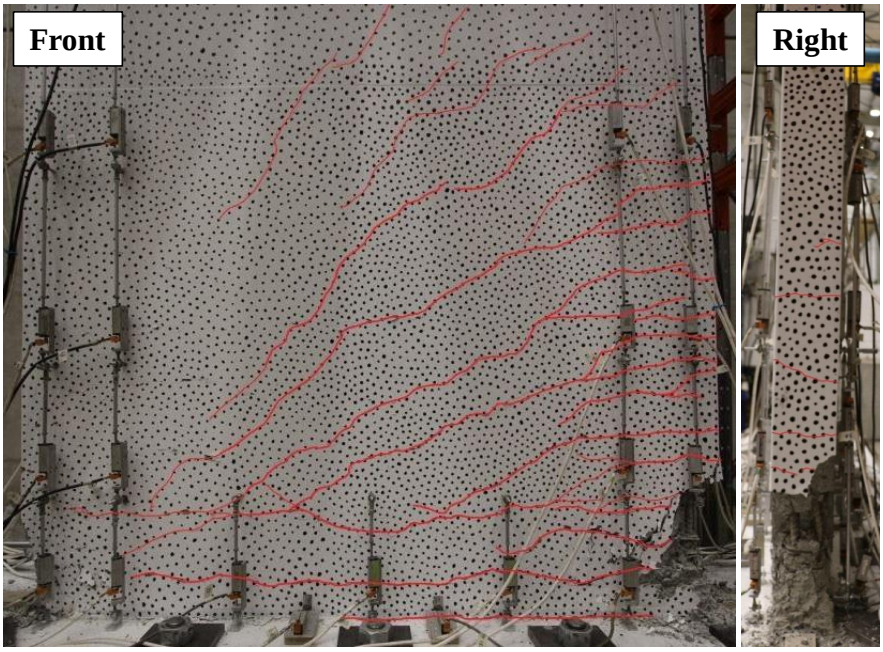

Figure 3-29 Crack pattern of the SP1-Clover at 2 % drift level in the (a) in-plane and (b) out-of-plane directions

3.3.6. Out-of-plane displacement evolution pattern

Figure 3-30 shows the evolution of out-of-plane displacement in regard to the in-plane drift ratio for SP1-Uni resulting from the draw wires (at the height of 275mm above the base).

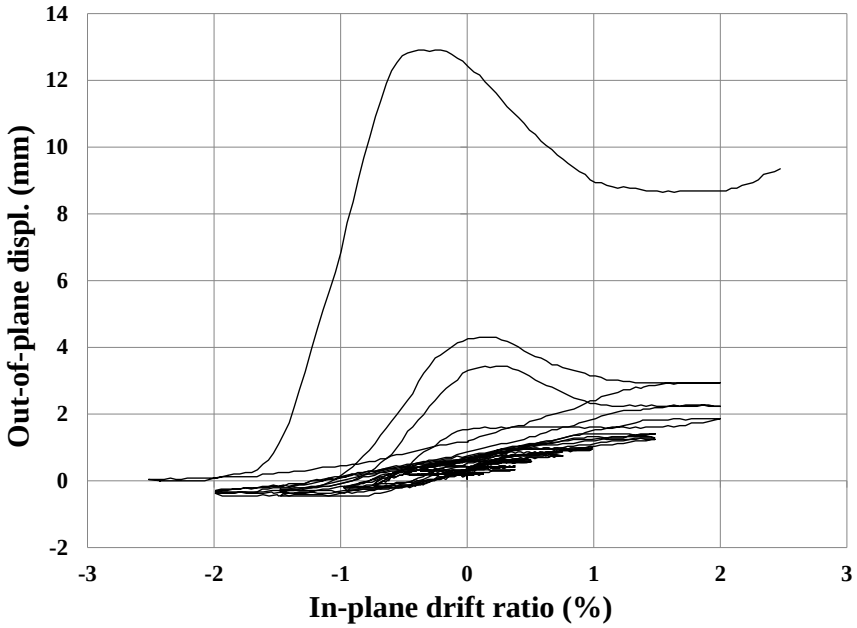

Figure 3-30 Evolution of out-of-plane displacement in regard to the in-plane drift ratio of SP1-Uni

Since some of the critical draw wires had to be removed due to concrete spalling in the case of specimens subjected to bi-directional loading and especially SP1-Clover, the results of the particle tracking was also used to capture the out-of-plane displacement of these specimens to the end of the test. Evolution of out-of-plane displacement in regard to the in-plane drift ratio

for SP1-Skew and Clover resulting from the draw wires and particle tracking are shown in Figure 3-31 and Figure 3-32, respectively.

As can be seen in Figure 3-31 and Figure 3-32, particle tracking technique was not only successful to capture the out-of-plane displacements before the draw wires removal but also to the end of the test. It is more obvious in the case of SP1-Clover since the specimen failed from its back face where the draw wires were attached.

In terms of developing more out-of-plane displacement, skew and in-plane uni-directional loadings were more effective than clover leaf, with skew loading slightly more effective than the other two. In regard to the pattern of the out-of-plane displacements, skew and in-plane uni-directional loadings develop a similar pattern while clover leaf develops a different pattern due to the complexity of its loading regimes (in-plane and out-of-plane loading were not always on the same direction).

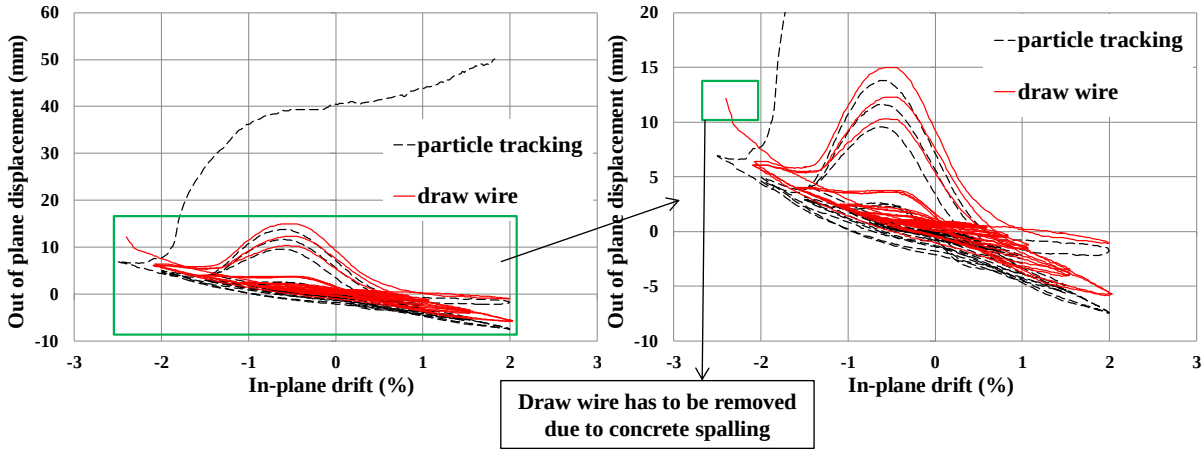

Figure 3-31 Evolution of out-of-plane displacement in regard to the in-plane drift ratio of SP1-Skew

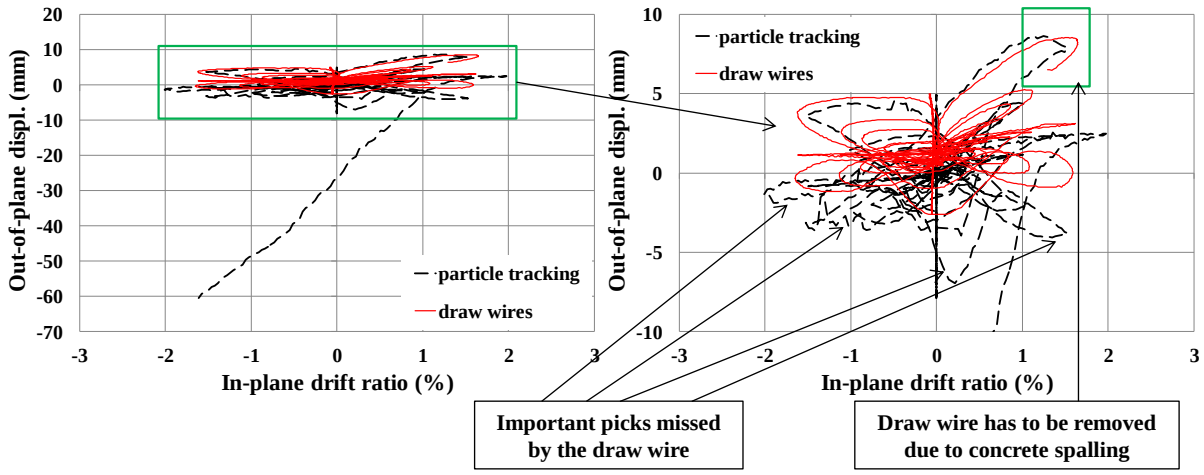

Figure 3-32 Evolution of out-of-plane displacement in regard to the in-plane drift ratio for SP1-Clover

3.3.7. Shear deformation

Figure 3-33 - Figure 3-35 show the base shear vs shear deformation of the three specimens. Shear deformation was calculated based on Equations 2-5 and 2-6. Table 3-5 shows the shear drift at the first cycle of each drift level when calculating using Equations 2-5 and 2-6 and the difference between the two methods. A difference between 20-25% was observed between the two methods for specimens under both uni- and bi-directional loadings. As can be seen in Figure 3-33 - Figure 3-35, the maximum shear deformation was increase when the wall was subjected to bi-directional loading, especially in the case of the wall under skewed loading. This increase in shear deformation of the specimen subjected to skew loading could have contributed to the development of shear cracks in the in-plane direction.

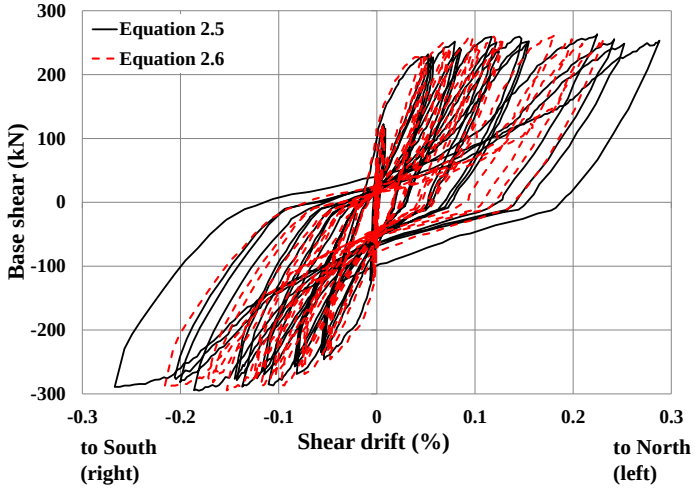

Figure 3-33 Shear deformation versus base shear of specimen SP1-Uni

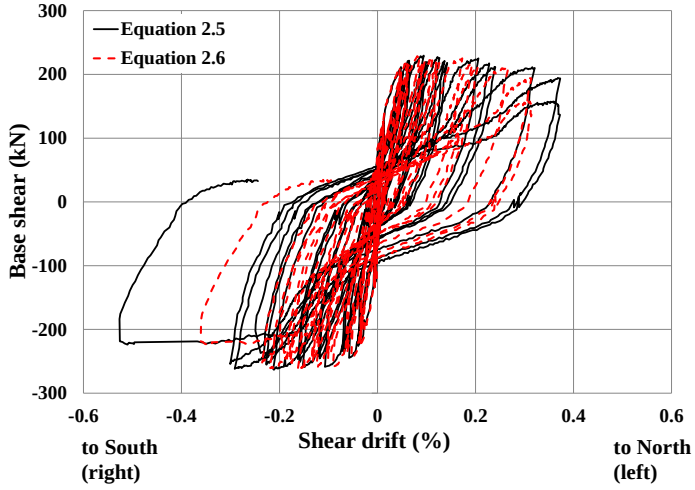

Figure 3-34 Shear deformation versus base shear of specimen SP1-Skew

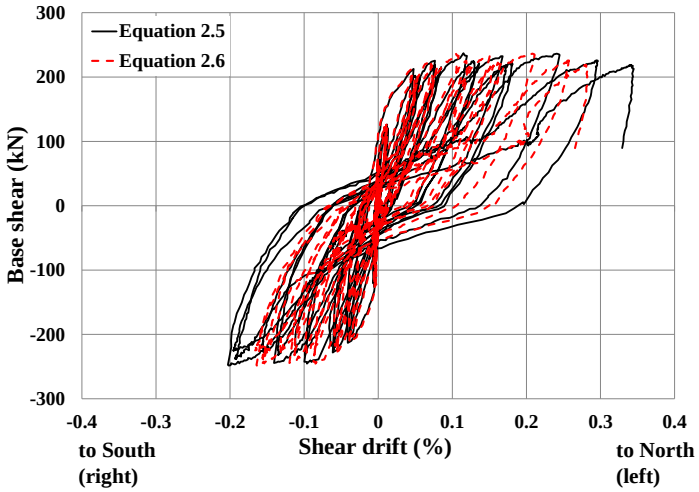

Figure 3-35 Shear deformation versus base shear of specimen SP1-Clover

Table 3-5 Shear deformation calculation using EQ. 2.5 and EQ. 2.6

Drift level	SP1-Uni			SP1-Skew			SP1-Clover		
	EQ. 2.5	EQ. 2.6	Difference	EQ. 2.5	EQ. 2.6	Difference	EQ. 2.5	EQ. 2.6	Difference
0.375%	-0.054	-0.047	14%	-0.036	-0.033	7%	-0.039	-0.036	8%
	0.052	0.045	16%	0.048	0.046	5%	0.052	0.050	4%
0.5%	-0.082	-0.074	11%	-0.058	-0.054	8%	-0.061	-0.057	8%
	0.079	0.069	16%	0.065	0.061	6%	0.077	0.072	7%
0.75%	-0.110	-0.098	12%	-0.107	-0.098	9%	-0.099	-0.087	14%
	0.117	0.098	20%	0.094	0.087	9%	0.130	0.120	8%
1%	-0.137	-0.119	16%	-0.153	-0.125	22%	-0.136	-0.114	19%
	0.145	0.119	22%	0.126	0.113	12%	0.182	0.165	10%
1.5%	-0.186	-0.153	22%	-0.213	-0.163	31%	-0.193	-0.157	23%
	0.224	0.180	24%	0.206	0.173	19%	0.296	0.257	15%
2%	-0.267	-0.216	23%	-0.291	-0.221	32%	-	-	-
	0.288	0.230	25%	0.321	0.267	20%	-	-	-

3.4. CONCLUSIONS

Seismic performance of three identical slender rectangular walls subjected to three different lateral loading patterns was investigated in this chapter. The main findings are categorized based on some of the key research questions regarding the effects of bi-directional loading on rectangular slender walls.

Effects of bi-directional loading on compressive and tensile strains of concrete

- Both compressive and tensile strains increased in the wall subjected to bi-directional loading.
- Substantial increase in neutral axis depth and the compression zone was observed in the case of specimens subjected to bi-directional loading compared to the same specimen under in-plane loading.

Effects of bi-directional loading on different failure modes

- Concrete cover spalling and bar buckling initiated earlier in walls subjected to bi-directional loading compared to the same wall under uni-directional loading due to the increase in steel and concrete compressive and tensile strains. Moreover, one of the longitudinal bars ruptured in the specimen subjected to bi-directional loading which was not observed in the case of the same of wall under uni-directional loading.
- Concrete crushing and bar buckling occurred in the web in walls subjected to bi-directional loading while it was not observed in the same wall under uni-directional loading even after lateral instability failure.
- Lateral instability failure occurred earlier when the wall was subjected to bi-directional loading compared to the same wall under uni-directional loading due to earlier concrete cover spalling/crushing and bar buckling/rupture in the wall which decreased the out-of-plane stiffness of the wall.

Effects of bi-directional loading on crack pattern

While specimen under uni-directional loading showed a pure flexure cracking in both in-plane and out-of-plane directions, surprisingly some shear cracks were observed in both in-plane and out-of-plane directions in the specimen subjected to skewed loading (perhaps torsional shear cracks in the case of out-of-plane ones). Asymmetry in the damage due to the asymmetric bi-directional loading could have helped with the development of shear cracks in the out-of-plane direction of the wall. The fact that there is no sign of out-of-plane shear cracks in case of the specimen subjected to clover leaf loading (since the damage on each side by the end of each clover leaf drift level is symmetry) also supports this hypothesis.

Effects of bi-directional loading on out-of-plane deformation pattern

- Skewed and in-plane uni-directional loadings developed a similar out-of-plane deformation pattern while clover leaf developed a different pattern due to its complex loading regimes.
- The wall subjected to skewed loading pattern had higher out-of-plane displacement compared to the other two loading regimes.
- Bi-directional loading was not able to considerably increase the out-of-plane buckling of the wall in terms of out-of-plane displacement.

Effects of bi-directional loading on shear deformation

Shear deformation was increased when the wall was subjected to bi-directional loading especially in the case of the specimen under skew loading. This significant increase in shear deformation could have contributed to the development of in-plane shear cracks in the specimens under bi-directional loading.

Effects of lateral load path on rectangular slender RC walls

One of the most important research objectives regarding the series of experiments presented in Chapters 2 and 3 was the effects of lateral load path on the seismic performance of rectangular slender walls. Three lateral loading patterns of in-plane uni-directional, skewed uni-directional with an angle of 45degree and clover leaf bi-directional were applied to three identical walls. The key differences between the two bi-directional loading patterns are discussed below.

- Maximum compressive and tensile strains were higher in the wall under skewed loading compared to the same wall subjected to clover leaf loading pattern.
- As a result of higher compressive and tensile strains in the wall subjected to skewed loading, one of the corner bars ruptured. This was not observed in the specimen under clover leaf loading pattern.
- Although skewed loading was affecting larger length of the wall, but it was not as effective as clover leaf in terms of decreasing the out-of-plane stiffness of the wall since the wall's damages were not in a symmetric shape. Therefore, lateral instability occurred earlier in the case of the specimen subjected to clover leaf bi-directional loading.
- As larger length of the wall was in compression when subjected to skewed loading compared to clover leaf loading pattern, therefore, concrete crushing and bar buckling occurred in the web of the specimen subjected to skew loading which was not observed in the wall under clover leaf loading. However, some concrete crushing and bar buckling were observed in the specimen subjected to clover leaf loading as well after lateral instability failure of the wall.
- Shear cracks formed in the in-plane direction of the wall in both cases of the walls under skewed and clover leaf loading patterns. However, in-plane shear cracks in the specimen subjected to skewed loading were more severe compared to the same wall under clover leaf loading. More importantly, some shear cracks were observed in the

out-of-plane direction of the specimen subjected to skewed loading which was not observed in the case of the specimen under clover leaf loading.

4. EXPERIMENTAL PROGRAMME FOR RC WALLS PRONE TO OUT-OF-PLANE SHEAR FAILURE SUBJECTED TO BI-DIRECTIONAL LOADING

4.1.INTRODUCTION

As was discussed in Chapter 1 and was shown in Figure 1-4, full out-of-plane shear failure was observed in a rectangular slender RC wall in the New Zealand 2011 February earthquake in a building in Christchurch city (Wall D5-6 from Grand Chancellor Hotel). However, until now, there is no experimental or numerical data to investigate this failure mode in details. This chapter intends to investigate some of the key research objectives regarding the effects of bi-directional loading on RC walls prone to out-of-plane shear failure based on experimental observations. These research objectives are:

1- Investigating the effects of bi-directional loading on RC walls susceptible to out-of-plane shear failure which was raised after the 2011 New Zealand earthquake.
2- Verifying the reliability of the current NZ design code (NZS3101:2006-A3 2017) for walls prone to out-of-plane shear failure.
3- Understanding the mechanics of out-of-plane shear failure and identifying the key parameters in the development of this failure mode
4- Validate the newly added maximum axial load ratio for RC structural walls in the NZ design code of practice, NZS3101:2006-A3 (2017).

Since at this stage of the study, there was no available method to identify walls prone to out-of-plane shear failure, the benchmark specimen was firstly designed based on the key parameters of Wall D5-6 from Grand Chancellor Hotel that failed in out-of-plane shear in the 2011 New Zealand earthquake (refer to Chapter 7 for further details about Wall D5-6). Then the failure mode of the wall (out-of-plane shear) was verified using finite element analysis. The specimen was scaled down due to the laboratory limitations. The benchmark wall was then re-designed for a limited ductile and ductile section detailing according to NZS3101:2006-A3 (2017). These walls were tested under a skewed loading pattern with an 85 degree angle with respect to the in-plane axis of the wall (the reasons are explained in

Section 4.6). Limited ductile and ductile section detailing levels refer to a ductility of 1.25-3 and at least 3, respectively.

The main difference between the second phase of experiments with the first three tests discussed in Chapter 2 and 3 was the axial load ratio which was increased significantly from $6.26\%A_g f_c'$ (438kN) to $30\%A_g f_c'$ (2304kN). In order to apply such amount of axial load to the wall, the two out-of-plane vertical actuators which had 400kN capacity (see Figure 2-18) were replaced by two 1000kN actuators. Therefore, the two out-of-plane steel loading beams from the first phase were replaced with two steel beams designed for the maximum capacity of the 1000kN actuators. Total axial load was applied to the specimen through the four vertical 1000kN actuators. These changes to the test setup were discussed in details in Section 4.5. Geometry of the specimens, material properties, test setup, instrumentation, and loading history were described in the following sections.

4.2. DESCRIPTION OF TEST UNITS

Specimens were 2:5 (40%) scale models of the first storey of a RC wall in a six-storey reference building with a total height of 21.43 m. Figure 4-1 shows the full scale wall, the scaled specimen and the loading pattern.

The benchmark specimen (SP2-ND) was designed based on NZS3101:2006-A3 (2017) for a nominal ductility. SP2-ND was expected to be vulnerable to out-of-plane shear failure based on numerical results using DIANA (refer to Chapter 6 for more information). The other two specimens namely, SP3-LD and SP4-D had the same geometry, axial load amount, total longitudinal and horizontal reinforcement ratios compared to SP2-ND. However, SP3-LD and SP4-D were designed for a limited ductile and ductile levels, respectively according to NZS3101:2006-A3 (2017).

A quick summary of the test matrix was given in Table 4-1. Summary of the main geometrical features and reinforcement details were listed in Table 4-2. Some of the notations used in Table 4-1 and Table 4-2 were shown in Figure 4-2 graphically. Cross-section and side-view of the reinforcement layout were shown in Figure 4-3-Figure 4-5. Details of the cap beam and foundation of the specimens were shown in Figure 4-6.

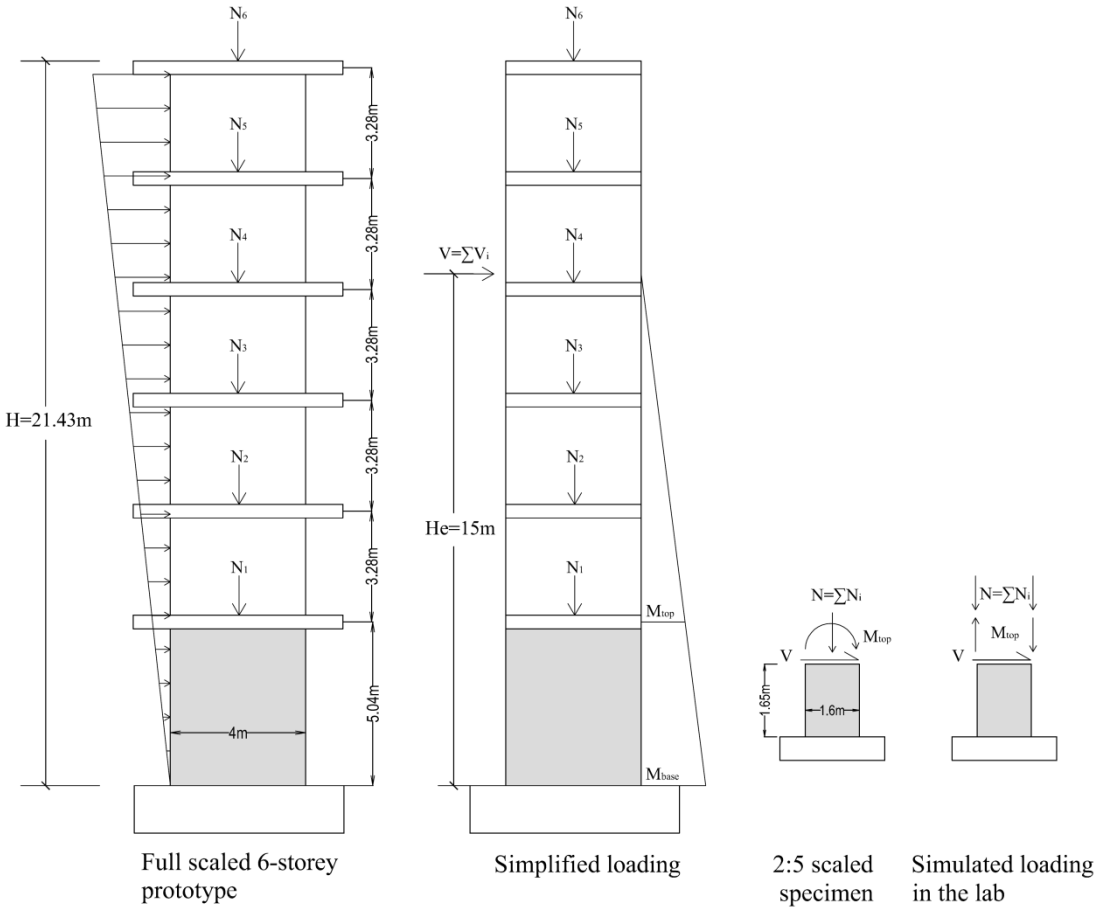

Figure 4-1 Specimen scaling and loading pattern

Table 4-1 Test matrix of the three RC walls specimens

Name	In-plane shear span ratio ($H_{e,inplane}/L_w$)	Out-of-plane shear span ratio (H_{out}/t)	Axial load ratio, $P/(A_g f'_c)$, using $f'_c = 30MPa$	Loading pattern	
				Type	Schematic view
SP2-ND	6000/1600 =3.75	2016/(160×2) =6.3	30%	Skew uni-directional	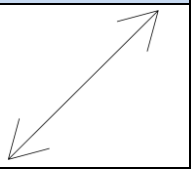
SP3-LD					
SP4-D					

Table 4-2 Details of the specimens

Specimen	SP2-ND	SP3-LD	SP4-D
Clear height, H_w (mm)	1650		
Length, L_w (mm)	1600		
Thickness, t (mm)	160		
Total longitudinal reinforcement ratio, $\rho_t = (A_{s,BZ} + A_{s,web})/(L_w \times t)$	0.92%		
Web longitudinal reinforcement ratio	0.885	1.13%	1.13%
Boundary zone (BZ) longitudinal reinforcement ratio	1.03%	0.879%	0.879%
BZ transverse reinforcement ratio, $\rho_{sx} = A_{vx}/(s \times t)$	0.295%	0.739%	1.05%
BZ transverse reinforcement ratio, $\rho_{sy} = A_{vy}/(s \times l_{BZ})$	0.248%	0.53%	0.75%
Web transverse reinforcement ratio, $\rho_{s(web)} = A_{v(web)}/(s \times l_{web})$	-	-	0.326%
Web shear reinforcement ratio, $\rho_v = A_{sv}/(s \times t)$	0.655%		

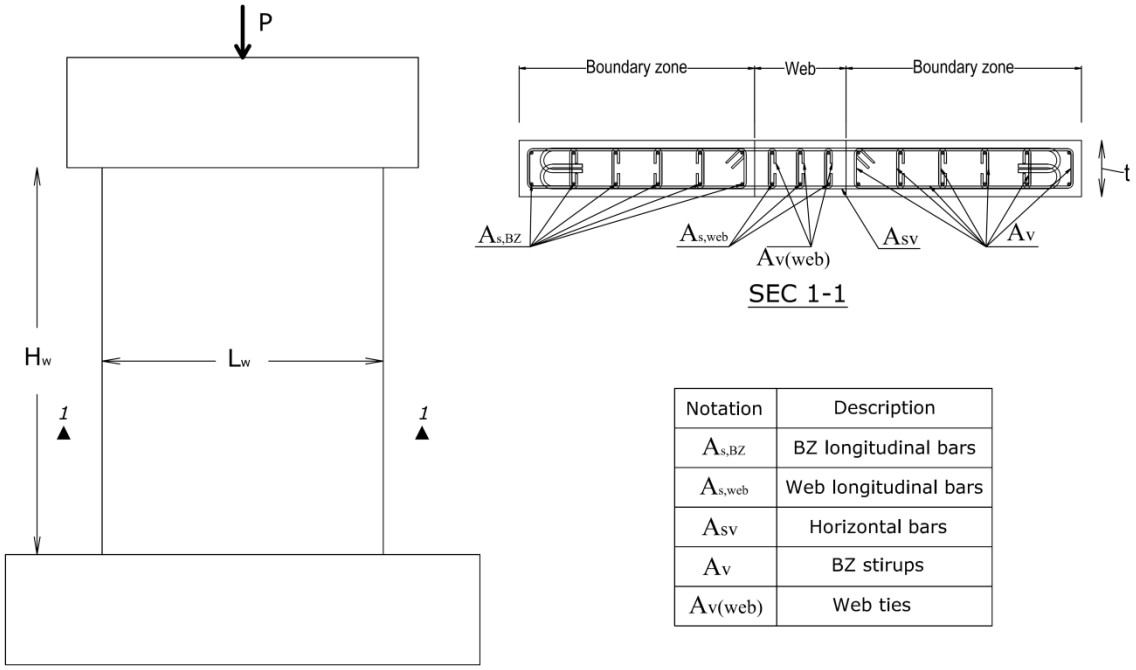

Notation	Description
$A_{s,BZ}$	BZ longitudinal bars
$A_{s,web}$	Web longitudinal bars
A_{sv}	Horizontal bars
A_v	BZ stirups
$A_{v(web)}$	Web ties

Figure 4-2 Notations used in Table 4-1 and Table 4-2

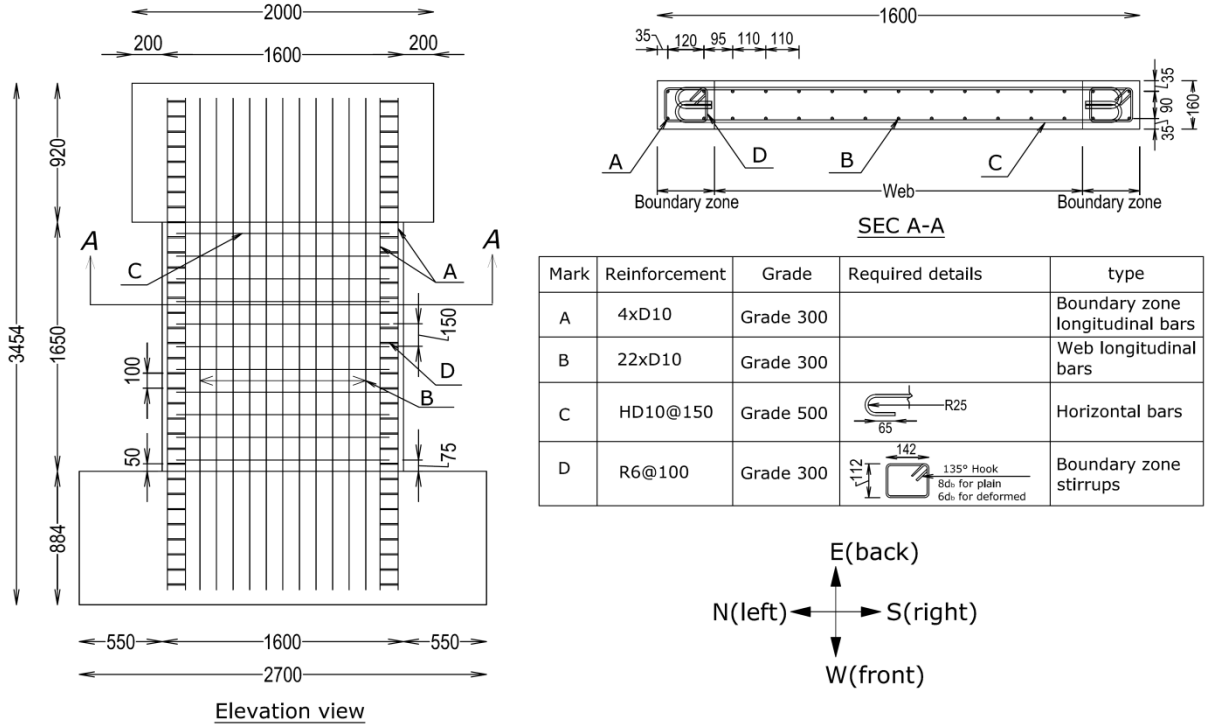

Mark	Reinforcement	Grade	Required details	type
A	4xD10	Grade 300		Boundary zone longitudinal bars
B	22xD10	Grade 300		Web longitudinal bars
C	HD10@150	Grade 500	R25, 65	Horizontal bars
D	R6@100	Grade 300	142, 112, 135° Hook, 8dₕ for plain, 6dₕ for deformed	Boundary zone stirrups

Figure 4-3 Details of the section and side view of the reinforcement layouts of the specimen SP2-ND

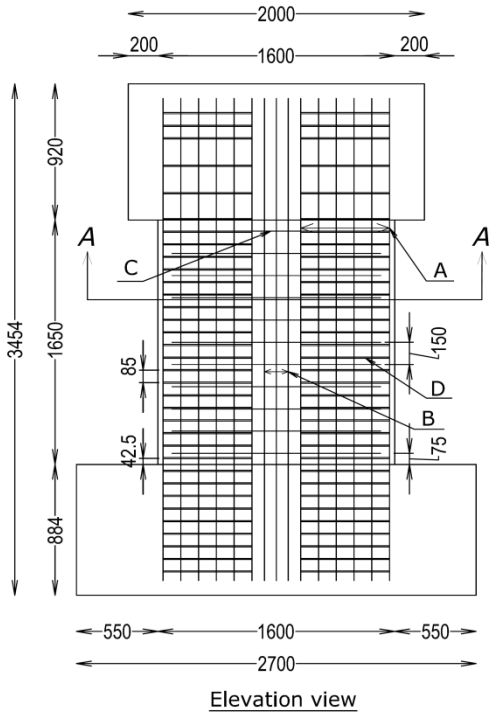

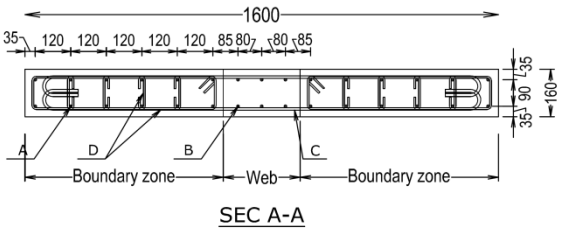

SEC A-A

Mark	Reinforcement	Grade	Required details	type
A	12xD10	Grade 300		Boundary zone longitudinal bars
B	6xD10	Grade 300		Web longitudinal bars
C	HD10@150	Grade 500	R25, 65	Horizontal bars
D	RH8@85	Grade 500	626, 116, 135° Hook, 8dₛ for plain, 6dₛ for deformed, 116	Boundary zone stirrups

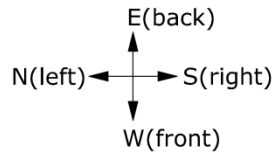

Figure 4-4 Details of the section and side view of the reinforcement layouts of the specimen SP3-LD

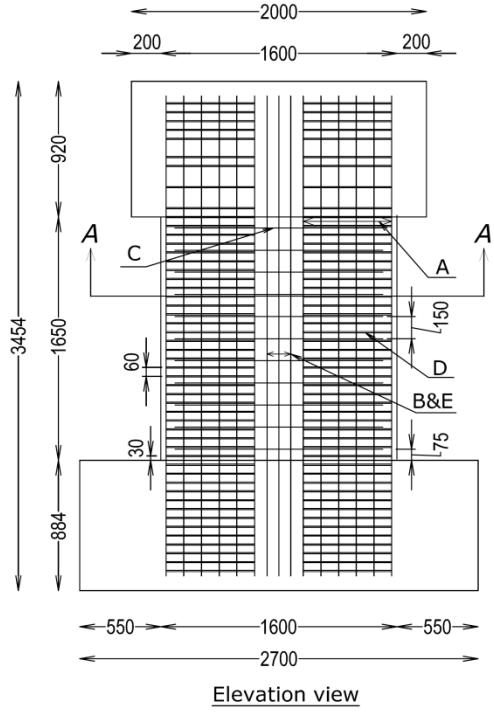

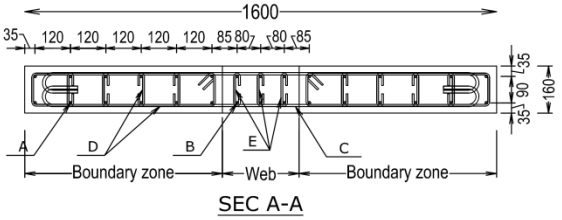

SEC A-A

Mark	Reinforcement	Grade	Required details	type
A	12xD10	Grade 300		Boundary zone longitudinal bars
B	6xD10	Grade 300		Web longitudinal bars
C	HD10@150	Grade 500	R25, 65	Horizontal bars
D	RH8@60	Grade 500	626, 116, 135° Hook, 8dₛ for plain, 6dₛ for deformed, 116	Boundary zone stirrups
E	RH6@100	Grade 500	116	Web stirrups

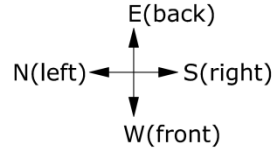

Figure 4-5 Details of the section and side view of the reinforcement layouts of the specimen SP4-D

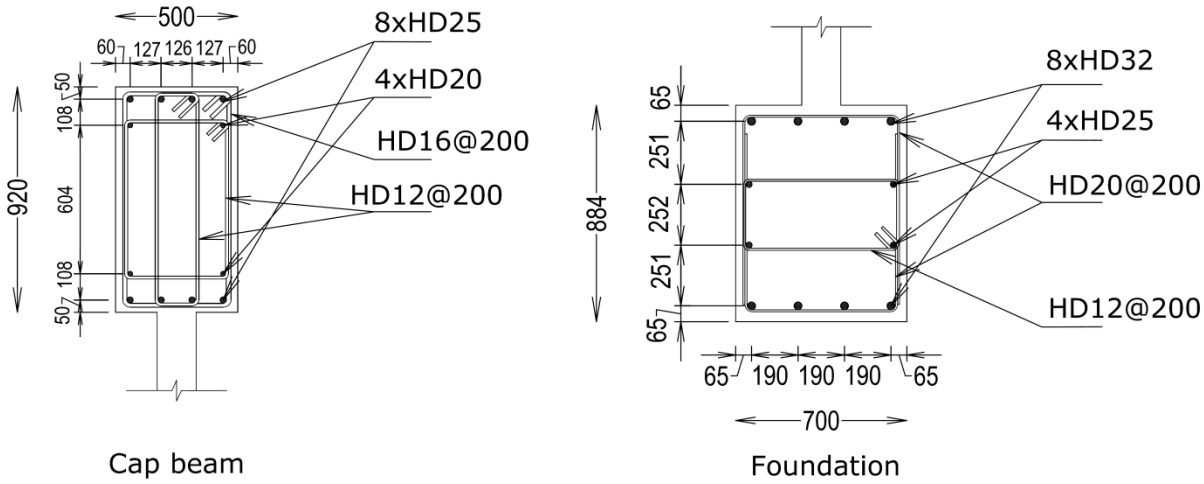

Figure 4-6 Details of the cap beam and foundation of the specimens

4.3.MATERIAL PROPERTIES

The target for concrete compressive strength to allow 30% axial load ratio, $P/A_g f_c'$, was 30MPa. The average concrete compressive strength of each specimen on the test day is shown in Table 4-3. The reason that the compressive strength of concrete is slightly less than the targeted one was due to the fact that it was critical not to get compressive strength higher than 30MPa to ensure at least 30% of axial load ratio for each wall as it was one of the important objectives of this series of experiments.

The steel reinforcing bars used for the specimens were NZ Grade 300 and Grade 500 as indicated in Figure 4-3-Figure 4-5. Table 4-4 shows the material properties of the steel reinforcement. Typical stress-strain curves of the steel rebars are shown in Figure 4-7.

Table 4-3 Average concrete compressive strength of each specimen on the day of testing

Specimen	Average concrete compressive strength (MPa)
SP2-ND	27.6
SP3-LD	24.5
SP4-D	24.2

Table 4-4 Material properties of the steel reinforcement

Bars	E_s (MPa)	f_y (MPa)	f_u (MPa)	ε_u
R6	200945	517	656	0.135
RH8	187080	534	687	0.122
D10	168460	273	420	0.21
HD10	204004	523	708	0.141

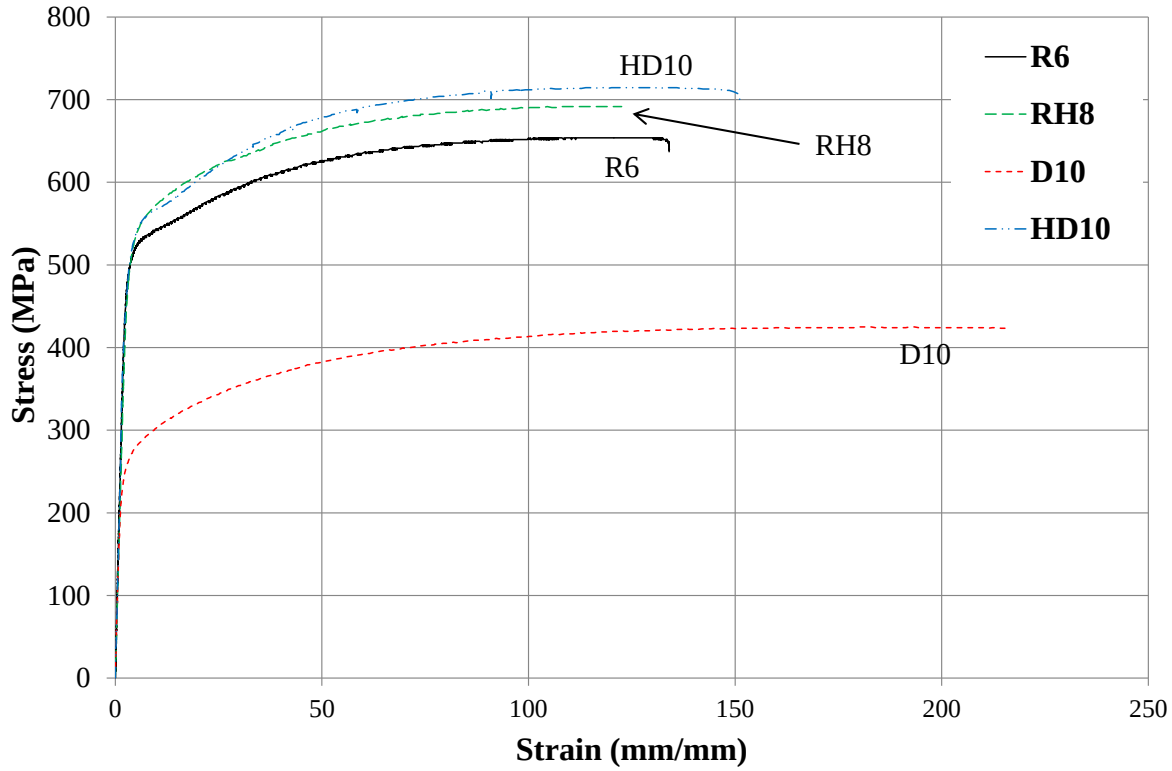

Figure 4-7 Typical monotonic behaviour of the rebars

4.4. SPECIMENS CONSTRUCTION

The specimens were constructed by Stahlton Engineered Concrete. Key construction steps include reinforcing cages, formwork and concrete casting are discussed below.

4.4.1. Reinforcing cages and Formwork

Steel reinforcing cages were assembled by Stahlton Engineered Concrete. The formwork was manufactured from plywood sheets. One of the main challenges here was placing 14 drossbachs in the foundation and 36 in the cap beam. The mould was oiled prior to casting to assist removal. Upon the placement of the reinforcing cage in the casting mould, plastic spacers were inserted to ensure a 20mm clear cover to the stirrups reinforcement and an approximately 35mm cover to the centroid of longitudinal reinforcement of the wall's boundary zone.

Figure 4-8 Steel reinforcing cage sitting in the mould

Figure 4-9 Formwork used for the specimens

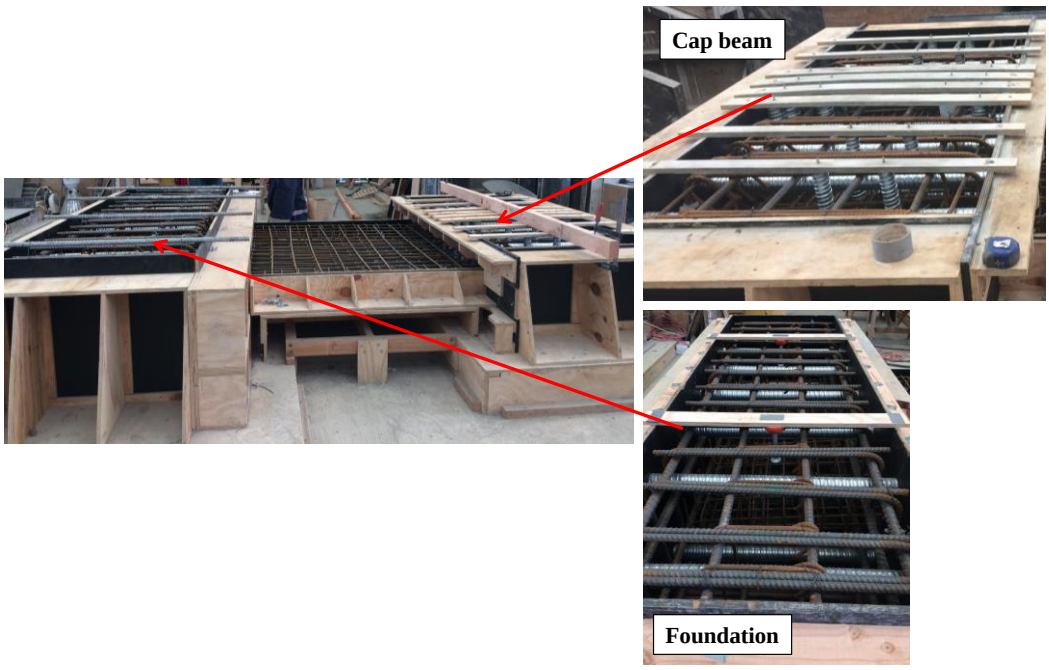

Figure 4-10 Drossbachs embedded in the cap beam and the foundation

4.4.2. Concrete casting

Specimens were casted horizontally in one single pour (Figure 4-11 and Figure 4-12). The maximum aggregate size was 13mm to allow for some concrete micro-structure scaling. For each specimen, some cylinders were prepared for the compressive strength (f'_c) test. Finally when the specimens were ready, they were transported carefully to the lab.

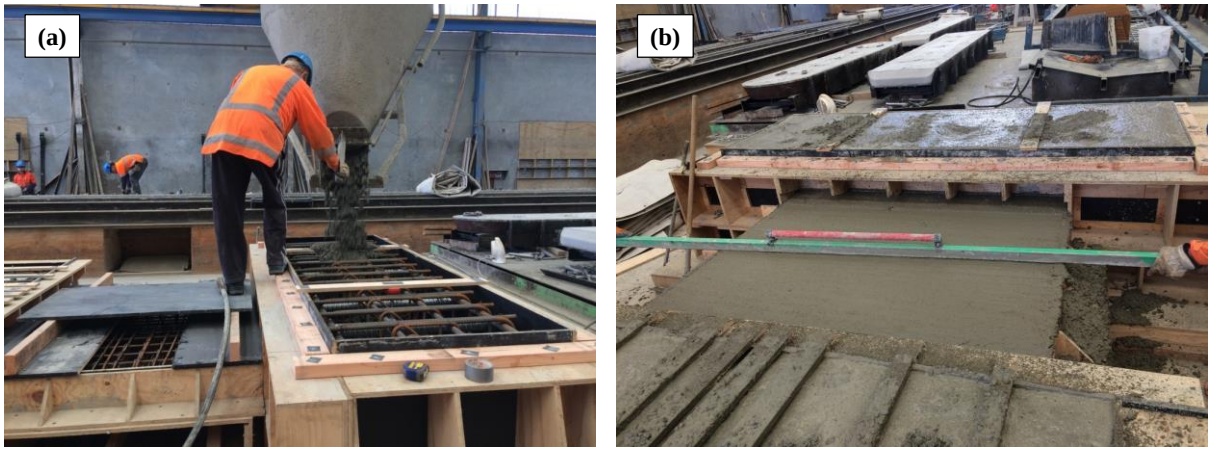

Figure 4-11 (a) Pouring the concrete and (b) Finishing work

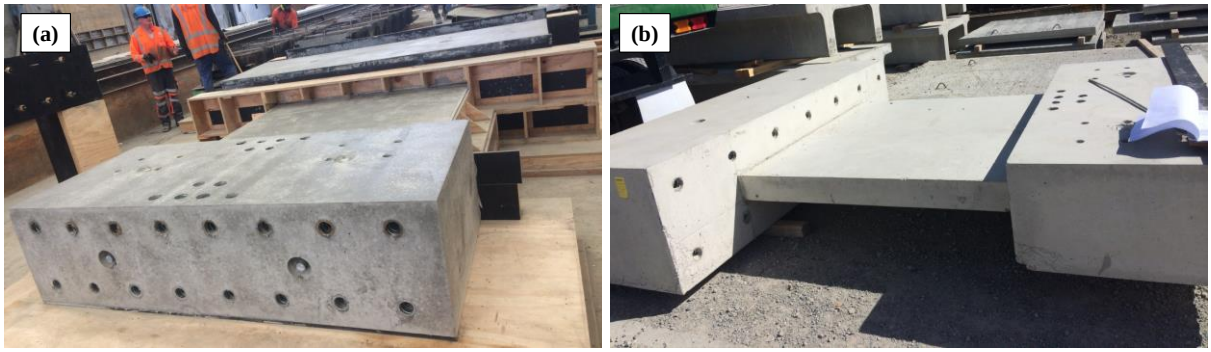

Figure 4-12 Specimen (a) before and (b) after its removal from the mould

4.5.TEST SETUP

A schematic view and a photo of the test setup used in this study to apply bi-directional loading are shown in Figure 4-13 and Figure 4-14, respectively. More details of the test setup are shown in Figure 4-15-Figure 4-17.

This complex test setup consists of an in-plane steel loading beam on top of the specimen and two out-of-plane steel loading beams attached to the specimen's cap beam. As was mentioned earlier these two beams in the out-of-plane differ from the ones used in the first phase of the experimental study. Details of these beams are shown in Figure 4-17. Seven hydraulic actuators were used to apply the gravity load and lateral in-plane and out-of-plane cyclic displacements. Out of these seven actuators, three 1000kN actuators were employed for applying the gravity (2 vertical jacks for half the axial load) and in-plane lateral displacement (identified as C in Figure 4-13). As shown before (Figure 4-1), only the bottom storey was tested and the effect of omitted higher stories were simulated by the two in-plane 1000kN vertical actuators as demonstrated in Figure 4-1. Therefore the vertical actuators applied part of the gravity load and bending moment corresponding to the chosen shear span ratio through the actuators' lever arm. The third horizontal 1000kN actuator applied the lateral in-plane displacement to the specimen. Out of the four hydraulic actuators left, two horizontal 400kN actuators apply the out-of-plane cyclic displacements (identified as D in Figure 4-13). The two out-of-plane vertical actuators had 1000kN capacity. They were used to apply the second half of the axial load and to create a double bending deformation in the wall (identified as C in Figure 4-13). The double bending deformation shape in the out-of-plane represents the rigidity of the slab compared to the wall's stiffness in the out-of-plane direction. It should be noted that the wall had a cantilever deformation shape in the in-plane direction. Equations 4-1 - 4-34-4 show how the actuators were controlled during the test.

$$T_{top} = \frac{(6000 - 2816)}{7544} C_1 \quad 4\text{-}1$$

$$C_2 + C_3 = \frac{Axial\ load}{2} \quad 4\text{-}2$$

$$C_4 + C_5 = \frac{Axial\ load}{2} \quad 4\text{-}3$$

$$\delta_{C4} = \delta_{C5} \quad 4\text{-}4$$

C_1, C_2, C_3, C_4, C_5 are shown in Figure 4-13. It is worth mentioning that in order to control and limit the foundation's movement, several jacking bolts were used. These jacking bolts were designed based on the base shear of the wall in each direction.

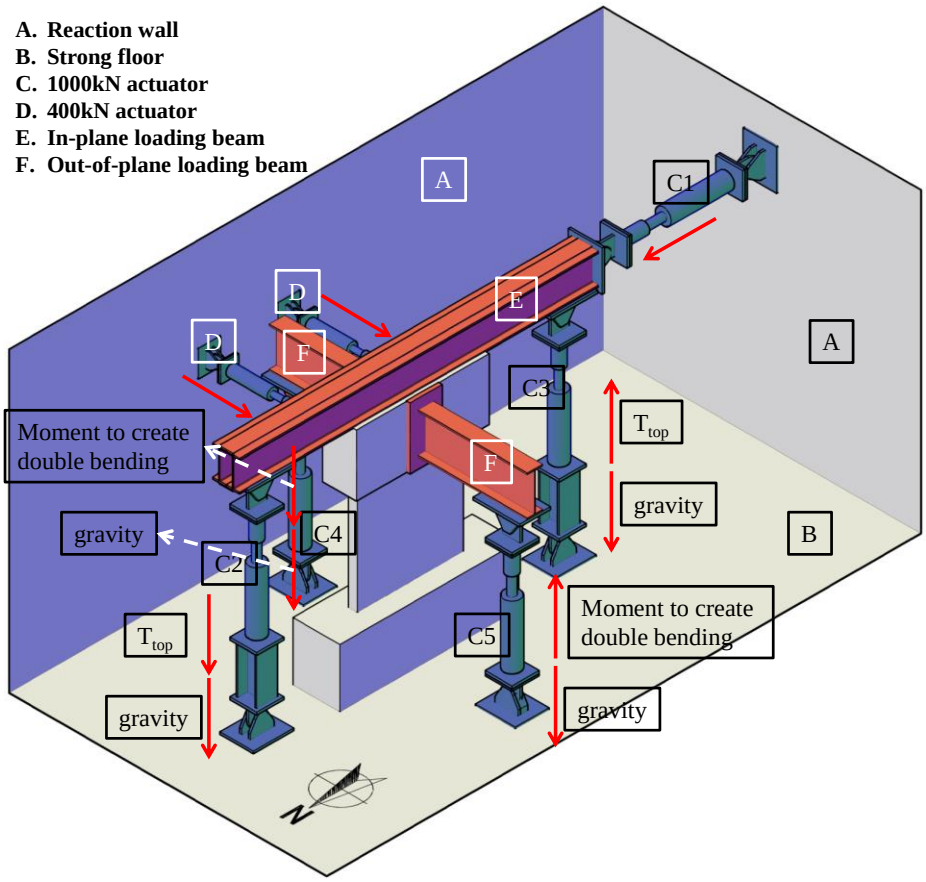

Figure 4-13 Schematic view of the test setup used for the experiments

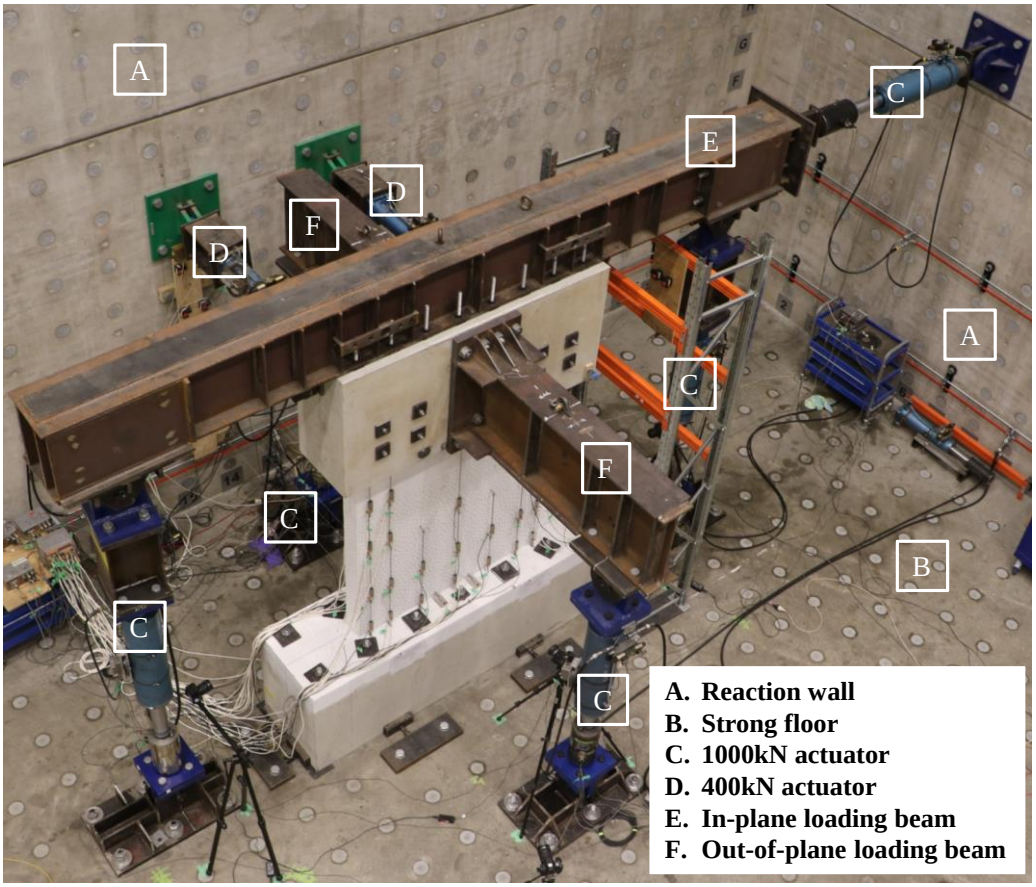

Figure 4-14 A photo of the test setup used for the experiments

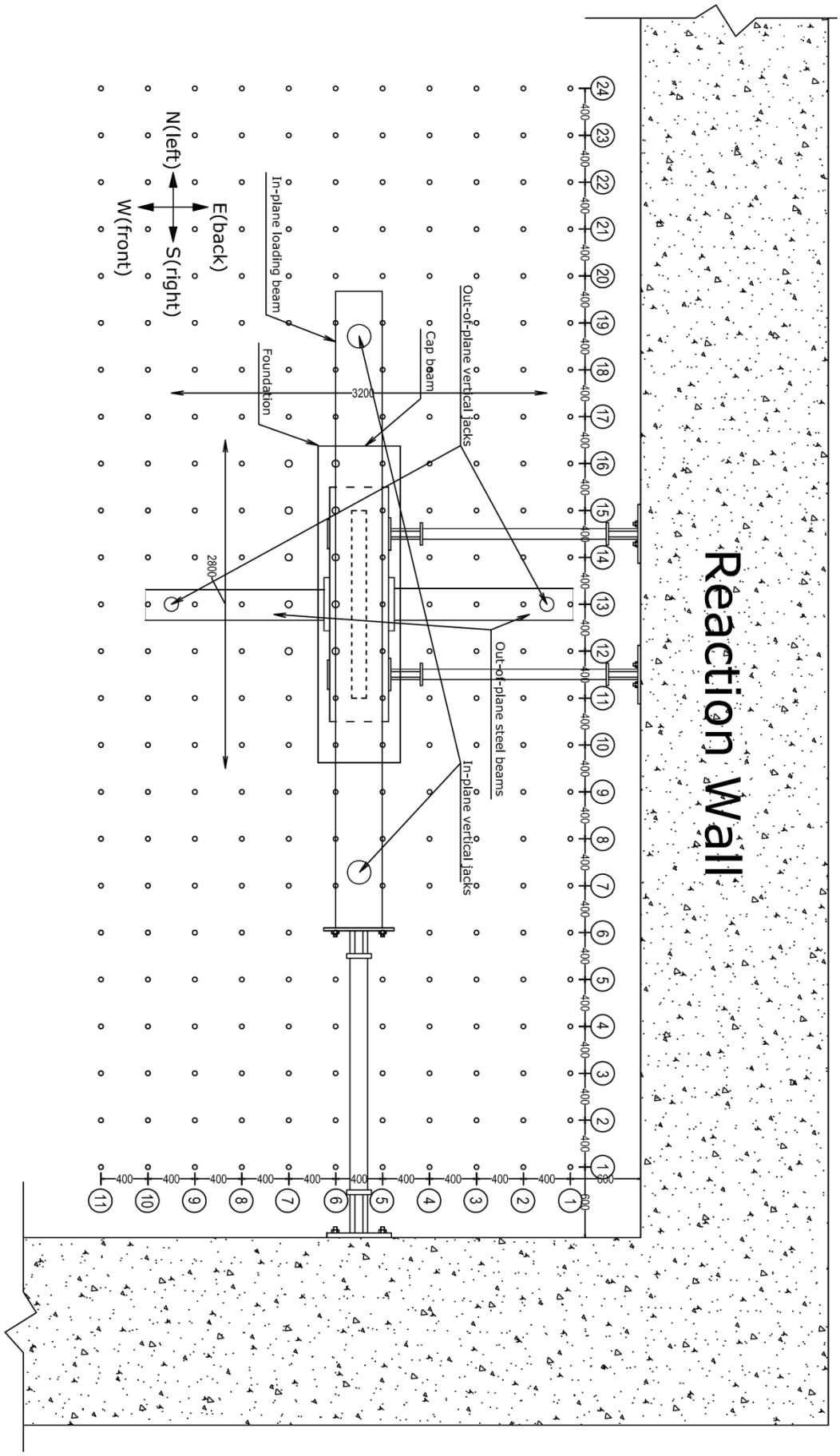

Figure 4-15 Schematic view of the test setup – plan view

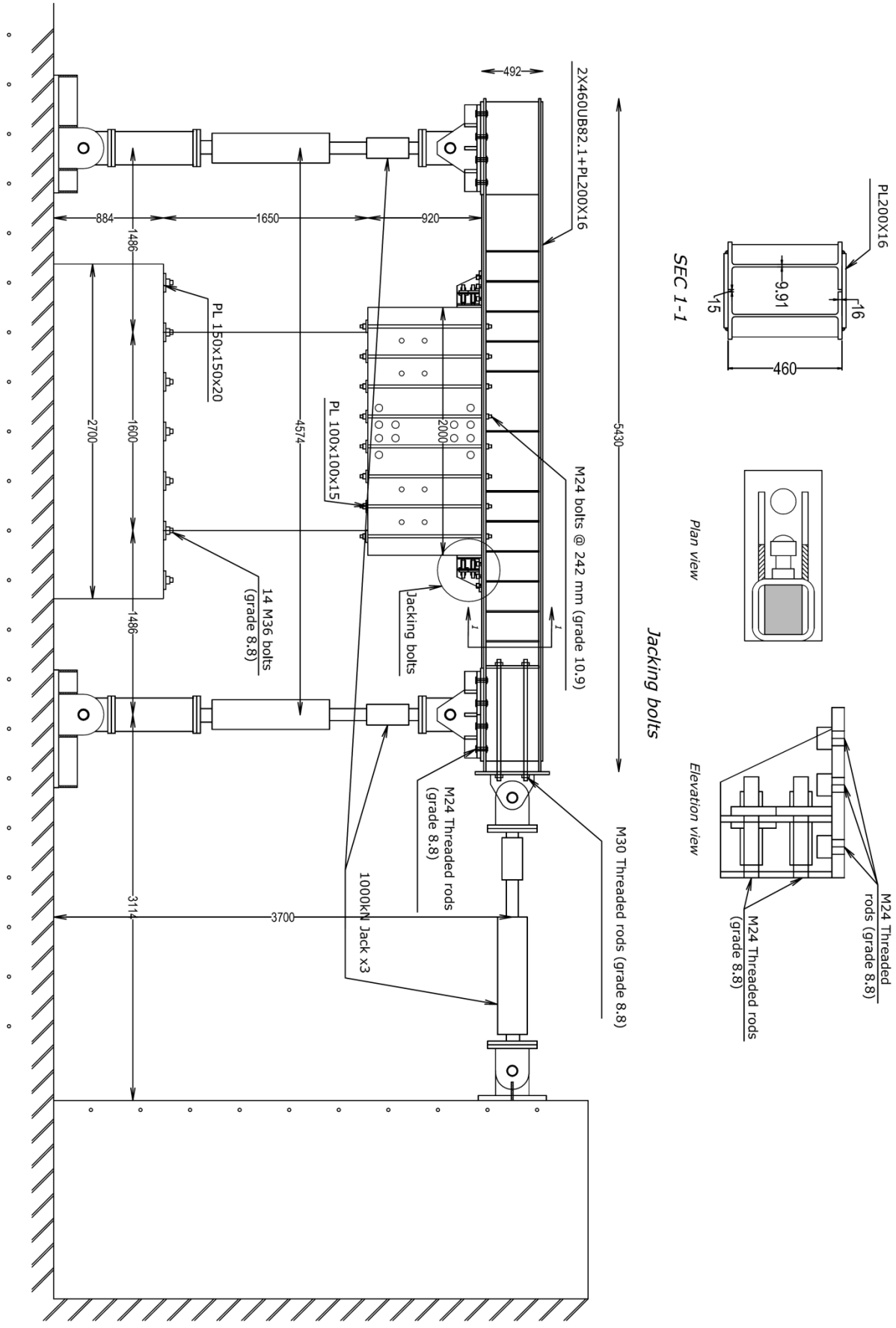

Figure 4-16 Schematic view of the test setup – Elevation (in-plane; front view)

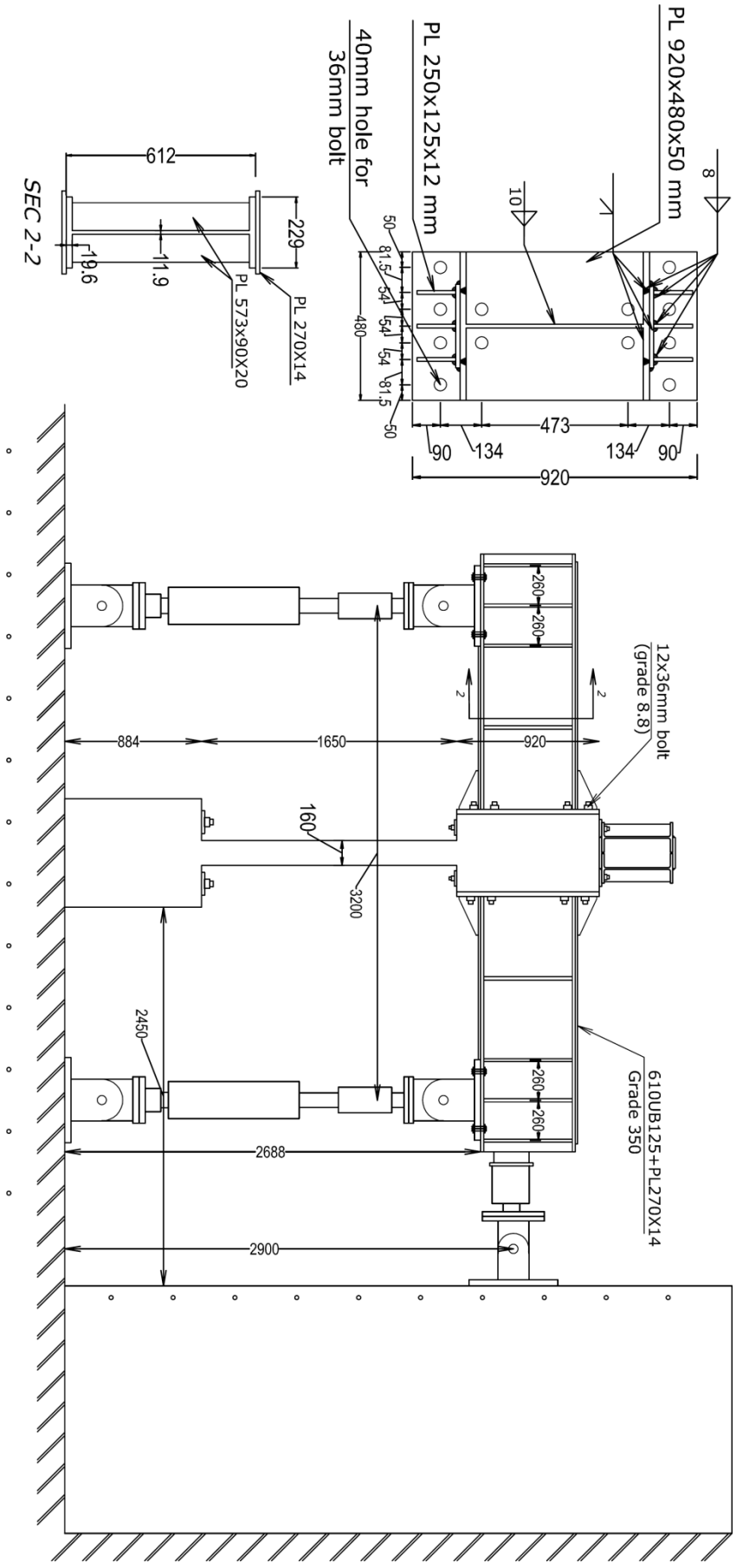

Figure 4-17 Schematic view of the test setup – Elevation (out-of-plane; right view)

4.6.LATERAL LOADING PROTOCOL

As a sign convention for the thesis, in-plane pull loading direction (right in Figure 4-3) refers to the negative top wall lateral displacement. In the out-of-plane also the pull loading direction (back in Figure 4-3) would be the negative out-of-plane displacement. These are also shown in Figure 4-18. It is worth noting, in-plane and out-of-plane cyclic displacements were applied at a height of 2016mm above the base.

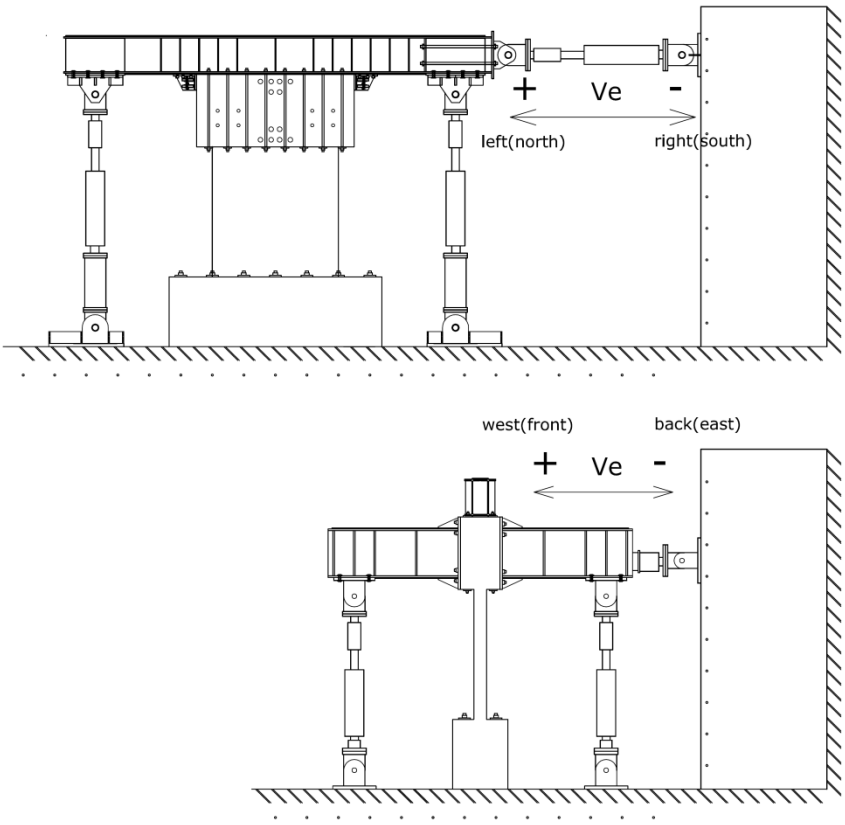

Figure 4-18 Definition of positive and negative directions of the (a) in-plane and (b) out-of-plane loadings

The loading protocol that was carefully chosen for the second phase of the experimental study was a skewed cyclic uni-directional with an 85 degree angle with respect to the in-plane axis as shown in Figure 4-19. The main reasons for choosing this loading pattern were:

1. Both skewed and clover leaf loading patterns were applied to identical rectangular walls and out-of-plane shear cracks were observed only in the case of the specimen under skewed loading (refer to Chapter 3 for more information).
2. Simulating an earthquake loading pattern similar to the one applied to Wall D5-6 from Grand Chancellor Hotel that failed in out-of-plane shear in the February 2011 Christchurch earthquake (refer to Chapter 7 for more information).
3. In a numerical parametric study conducted in Chapter 7, it was shown that increasing the loading angle of a skewed uni-directional pattern with respect to the in-plane axis

will increase the possibility of triggering an out-of-plane shear failure in the wall and 85 degree found to be the worst case scenario in triggering out-of-plane shear failure. The lateral loading protocol used in this experiment in both in-plane and out-of-plane directions consisted of three displacement-controlled cycles at increasing amplitudes. These amplitudes are presented in Figure 4-19a and Table 4-5.

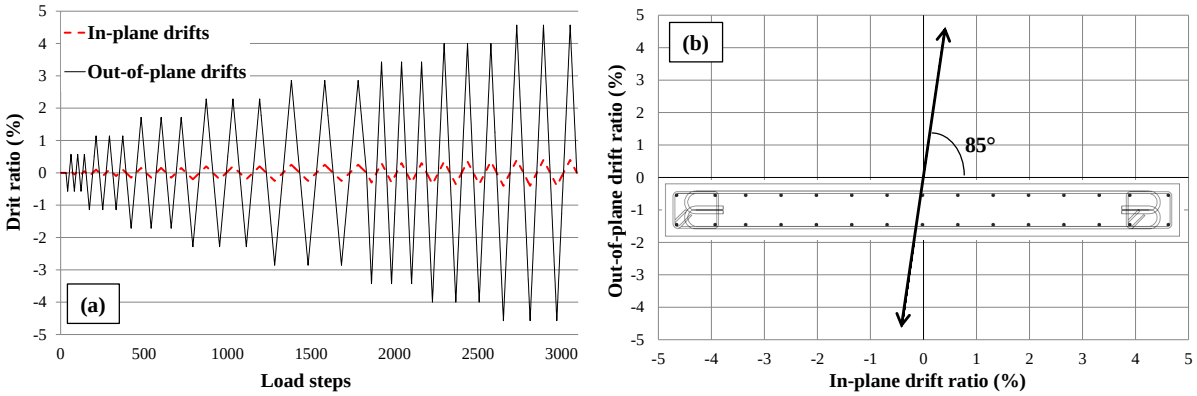

Figure 4-19 Loading protocol used for the experiment, (a) drift cycles and (b) skew's angle

Table 4-5 In-plane and out-of-plane drift ratios of each cycle

Cycle	1	2	3	4	5	6
In-plane drift ratio	0.05%	0.1%	0.15%	0.2%	0.25%	0.3%
Out-of-plane drift ratio	0.572%	1.143%	1.715%	2.286%	2.858%	3.429%

4.7.INSTRUMENTATION

All specimens were instrumented using both conventional instruments and modern particle tracking measurement system. In addition, crack widths were measured at the peak drifts and photos were taken at each displacement step. In order to make it easier when referring to each face of the specimen, as it is shown in Figure 4-3, Figure 4-13 and Figure 4-15, front face is the western, back face is eastern, right face is southern and left face is northern face of the specimen.

4.7.1. Measurements of loads

Applied loads and reactive forces were measured using load cells, which consisted of hollow cylinders machined from high strength steels and instrumented with two independent sets of full bridge circuits of 350Ω resistance strain gages. Five 1000kN capacity load cells were used to measure the horizontal in-plane lateral load and vertical axial forces, while two 400kN capacity load cells were used to measure the out-of-plane lateral load.

4.7.2. Measurements of displacements

Table 4-6 presents the description of each instrument and its specifications. It is worth noting that a draw wire (see Table 4-6) was used to measure the in-plane horizontal displacements. To measure the out-of-plane horizontal displacements, rotary potentiometers with a 5kΩ resistance was used (see Table 4-6).

Linear variable differential transducer (LVDT): 23 vertical LVDTs on the front and 22 on the back faces of the wall used to measure average axial strain of concrete on the front and back faces, respectively (Figure 4-20). Figure 4-21 shows the LVDTs on the front and back faces of the specimen. Three vertical LVDTs in the middle of the wall on the front side were used to calculate the elongation of the wall.

Table 4-6 Displacement instrument description and specifications

Instrument	Description	Stroke	Picture
LVDT	Used to measure the average compressive and tensile strains of concrete	±30 mm	
Spring LVDT	Used to measure the base movement of the wall's panel and the foundation	±30 mm	
Draw wire	Used to measure the in-plane and out-of-plane displacements	±150 mm	
Rotary pot	Used to measure the movement of the actuators	±150 mm	

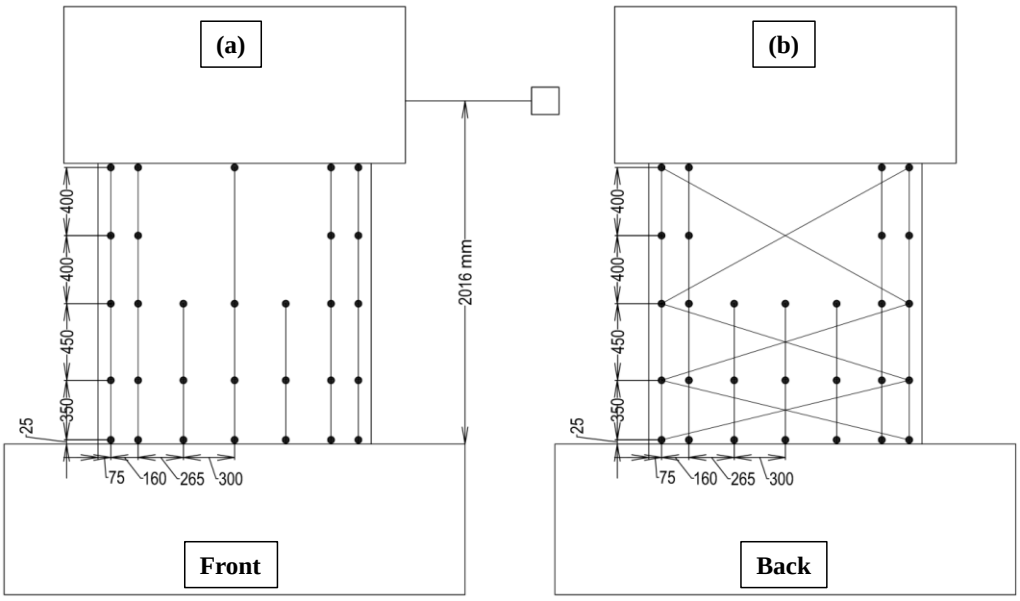

Figure 4-20 LVDTs on the (a) front and (b) back faces of the wall

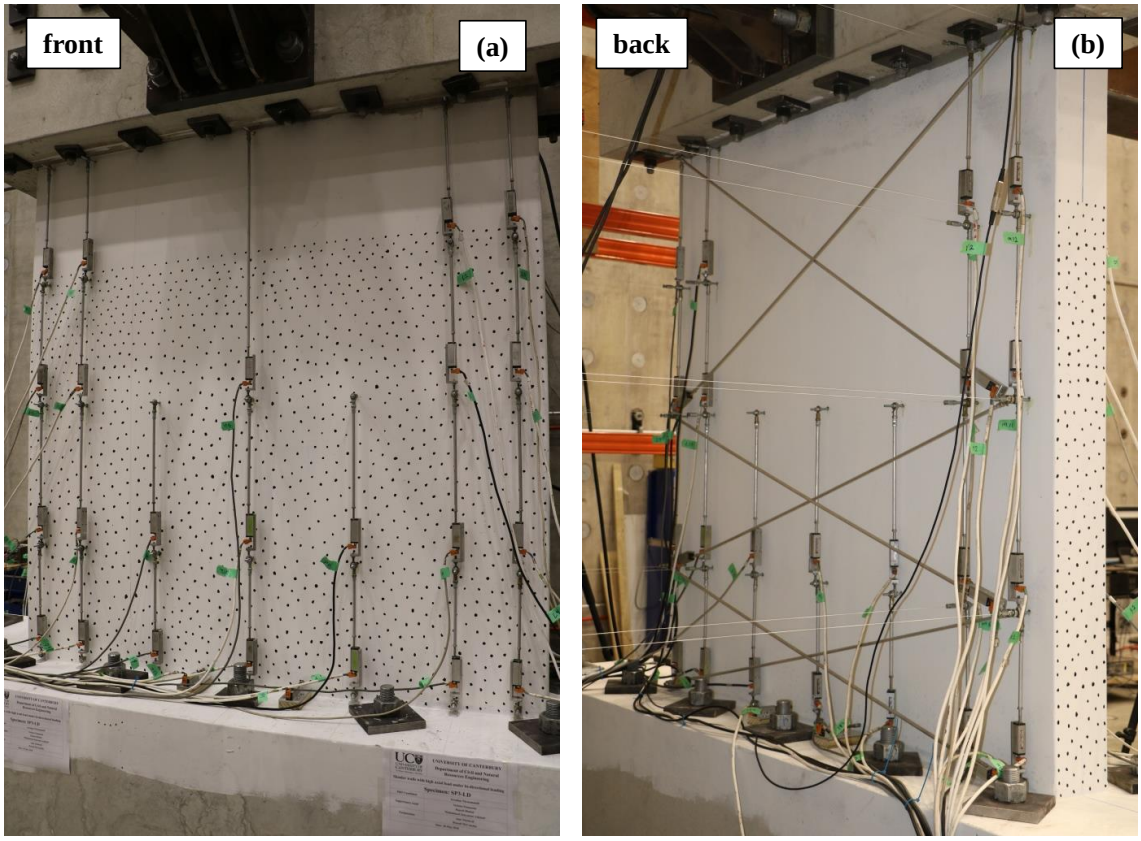

Figure 4-21 Photo of LVDTs on the (a) front and (b) back faces of the specimen

Spring LVDT: 4 spring LVDTs were used to measure the wall-to-foundation sliding in the out-of-plane direction. A typical photo of spring pots attached to the specimen is shown in Figure 4-22.

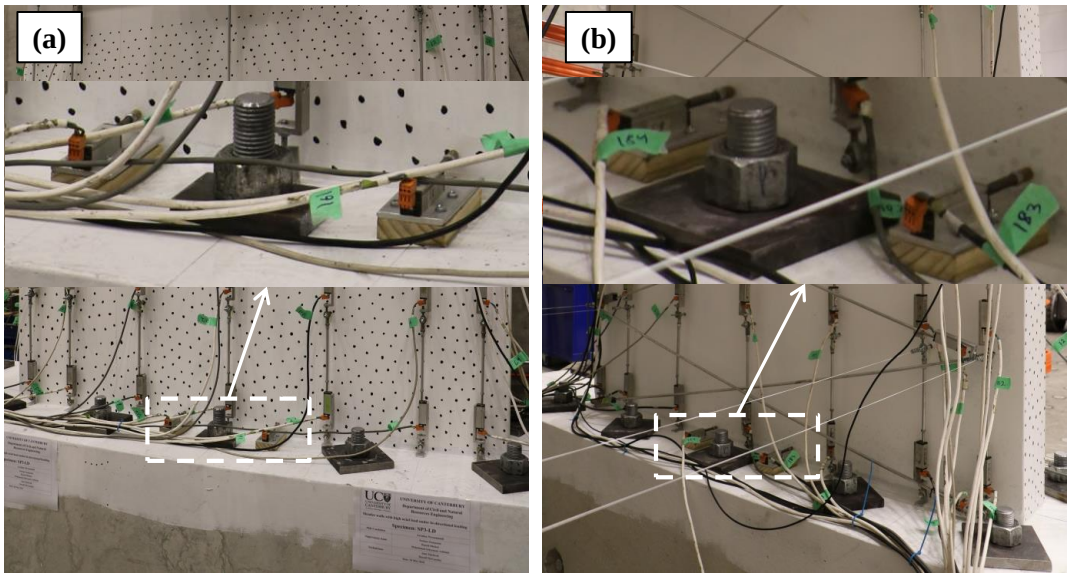

Figure 4-22 Spring pots, (a) front face and (b) back face

Draw wire: On the back face, 16 draw wires were used to measure out-of-plane deformations of the wall. Figure 4-23 shows typical draw wires attached to the back of the specimen. Two draw wires were also used to measure the in-plane deformations of the specimen (Figure 4-23). The positions of the draw wires are also shown in Figure 4-23.

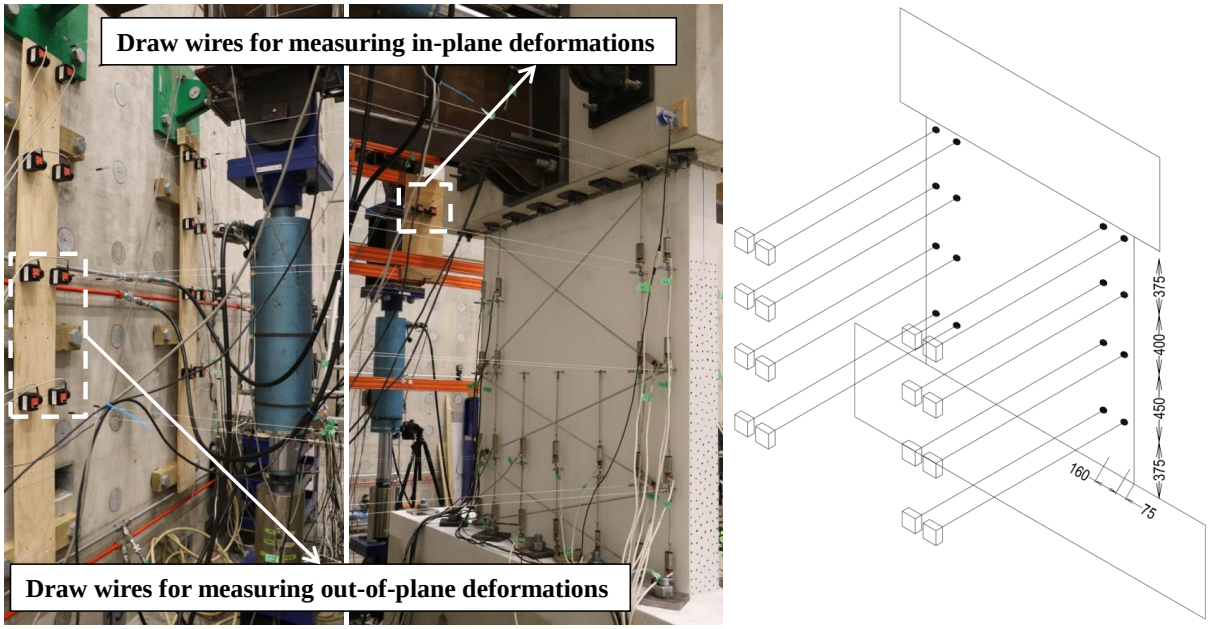

Figure 4-23 Draw wires used to measure the in-plane and out of plane displacements

5. TEST RESULTS OF RC WALLS PRONE TO OUT-OF-PLANE SHEAR FAILURE SUBJECTED TO BI-DIRECTIONAL LOADING

5.1. INTRODUCTION

In the first part of this chapter, experimental observations of the three specimens described in Chapter 4 were presented. In the second part, the experimental observations are discussed in more details. Failure mode, base shear vs drift ratio curves, average strain in concrete, strain profile along the height, 2D section strain profile, crack pattern and out-of-plane displacement pattern were investigated.

5.2. TEST OBSERVATIONS

Description of damage evolution and the final failure mechanism were provided in details for each specimen. In order to make it easier when referring to each side of the specimen, as it is shown in Figure 4-3, Figure 4-13 and Figure 4-15, front face is the western, back face is eastern, right face is southern and left face is northern face of the specimen.

5.2.1. SP2-ND

This was the benchmark specimen designed for a nominal ductility according to NZS3101:2006-A3 (2017). Based on numerical results and earthquake observations (Dunning Thornton 2011), the benchmark wall was expected to be prone to out-of-plane shear failure.

The first sign of cover concrete spalling was observed in the left side from the second cycle of 0.05% in-plane and 0.57% out-of-plane drift ratios. However, there was no sign of vertical splitting in the right side during this drift level. Horizontal tensile cracks on the front and back sides formed along the wall at a height of about 100mm above the base with a length of 1400 and 1100 mm, respectively. Maximum crack width by the end of 0.05% in-plane and 0.57% out-of-plane drift ratios was 0.2mm. There was no sign of residual cracks during this drift level.

Vertical splitting in concrete cover increased in the left side and initiated in the right side from the first cycle of 0.1% in-plane and 1.14% out-of-plane drift ratios and penetrated the boundary zone and web (Figure 5-1). Horizontal tensile cracks formed along the full length of the wall at a height of about 100mm on the front side with a maximum crack width of 0.8mm. On the back face, horizontal tensile cracks formed along the wall with a length of about 1400 mm with a maximum crack width of 0.8 mm. Maximum residual crack width was 0.25 mm during this drift level.

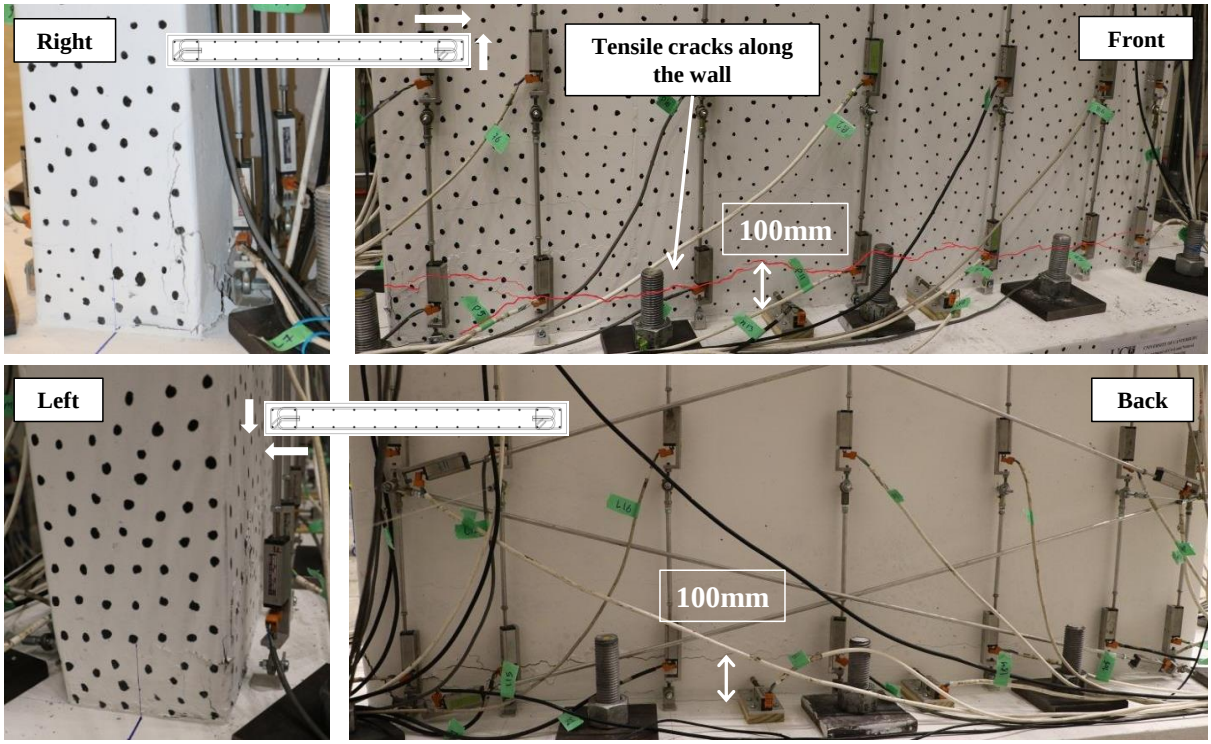

Figure 5-1 Specimen SP2-ND at 0.1% in-plane and 1.14% out-of-plane drift ratios

The first sign of out-of-plane diagonal compression cracks was observed from the first cycle of 0.15% in-plane and 1.72% out-of-plane drift ratios. As can be seen in Figure 5-2, these diagonal cracks were forming on each side when it was in compression. During this drift level, maximum crack width increased significantly to about 3mm. Maximum residual crack width was about 0.8-1mm by the end of 0.15% in-plane and 1.72% out-of-plane drift ratios. Diagonal compression cracks developed considerably by the end of 0.15% in-plane and 1.72% out-of-plane drift ratios (Figure 5-3).

The specimen failed suddenly and unexpectedly while applying the first cycle of 0.2% in-plane and 2.29% out-of-plane drift ratios half way through that cycle. Figure 5-4 shows the specimen in three different views just before and after the failure before removing the spalled concrete. The failure mode of the specimen SP2-ND after removing the spalled concrete can be seen in Figure 5-5.

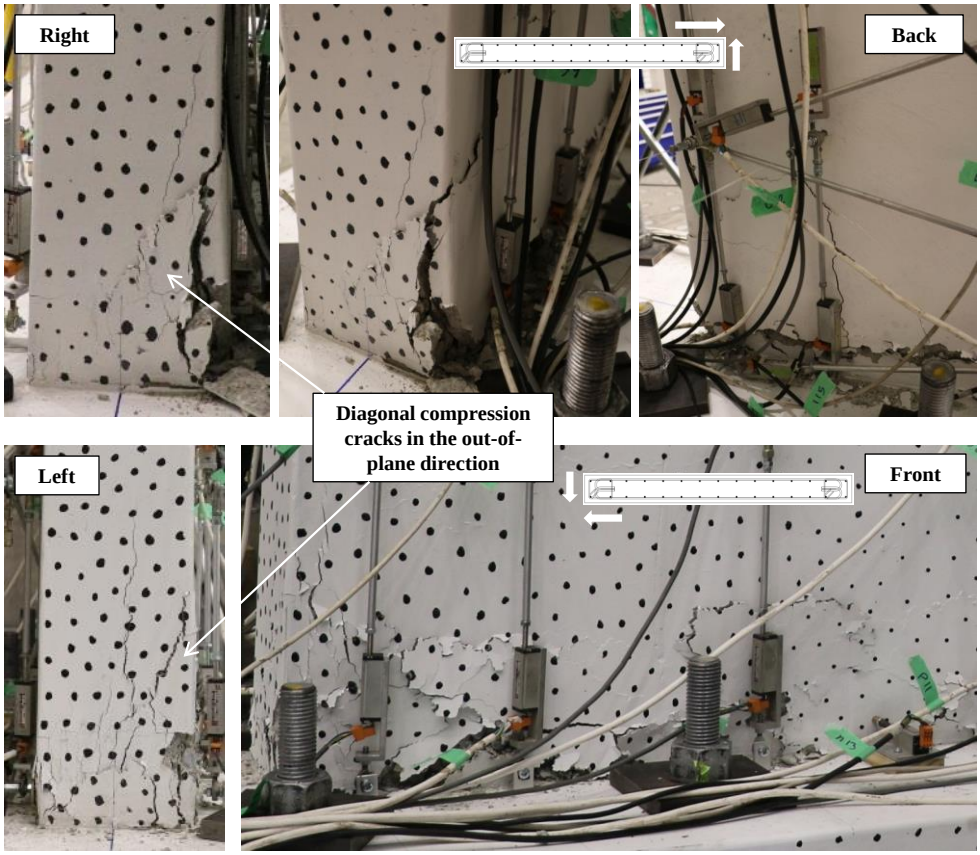

Figure 5-2 Specimen SP2-ND at 0.15% in-plane and 1.72% out-of-plane drift ratios

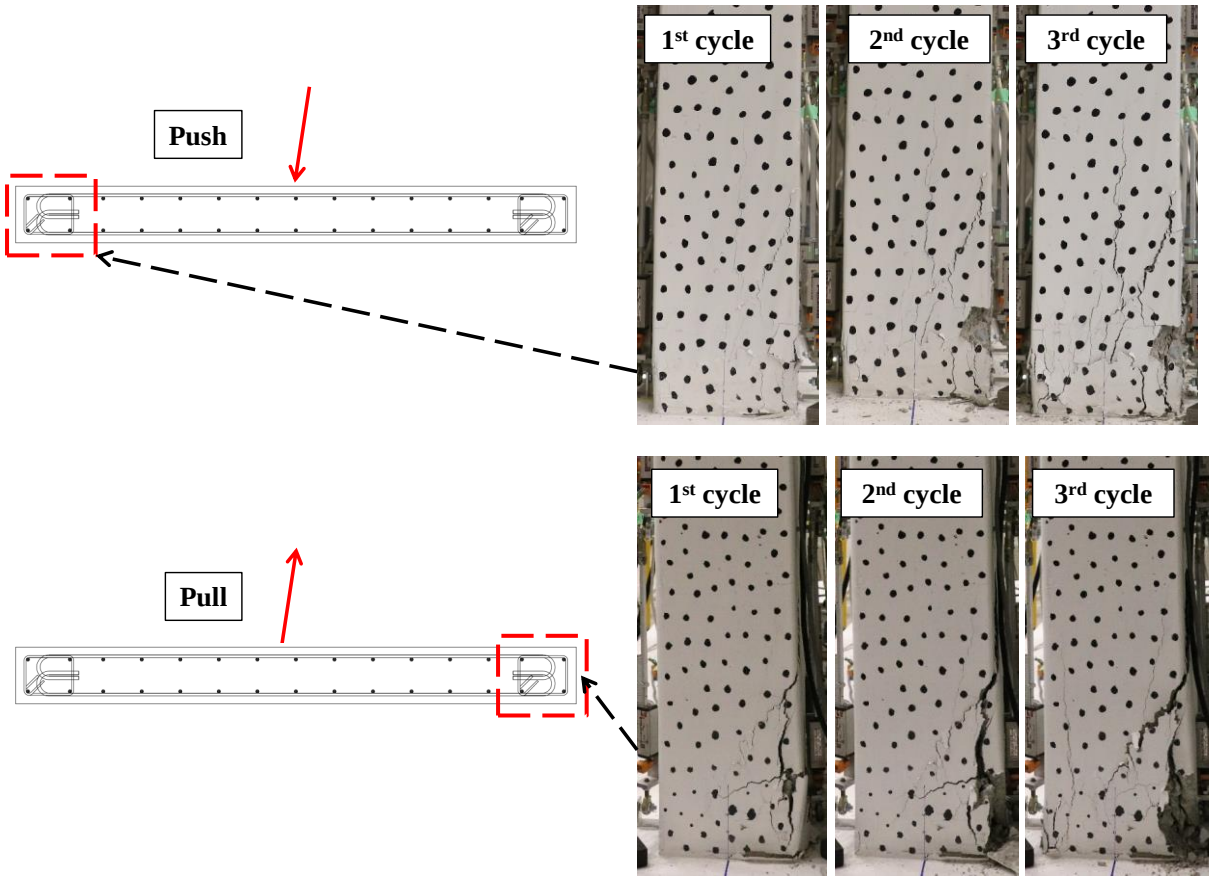

Figure 5-3 Diagonal compression cracks development during 0.15% in-plane and 1.72% out-of-plane drift ratios

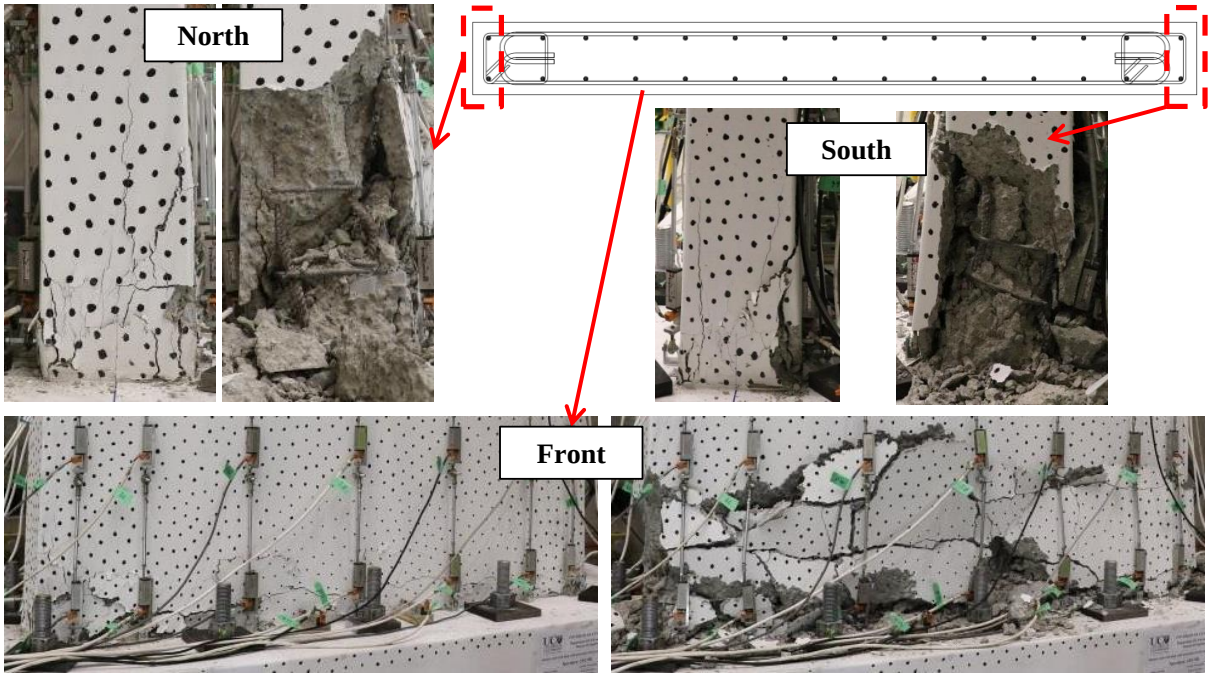

Figure 5-4 Specimen SP2-ND just before and after out-of-plane shear failure from three different faces

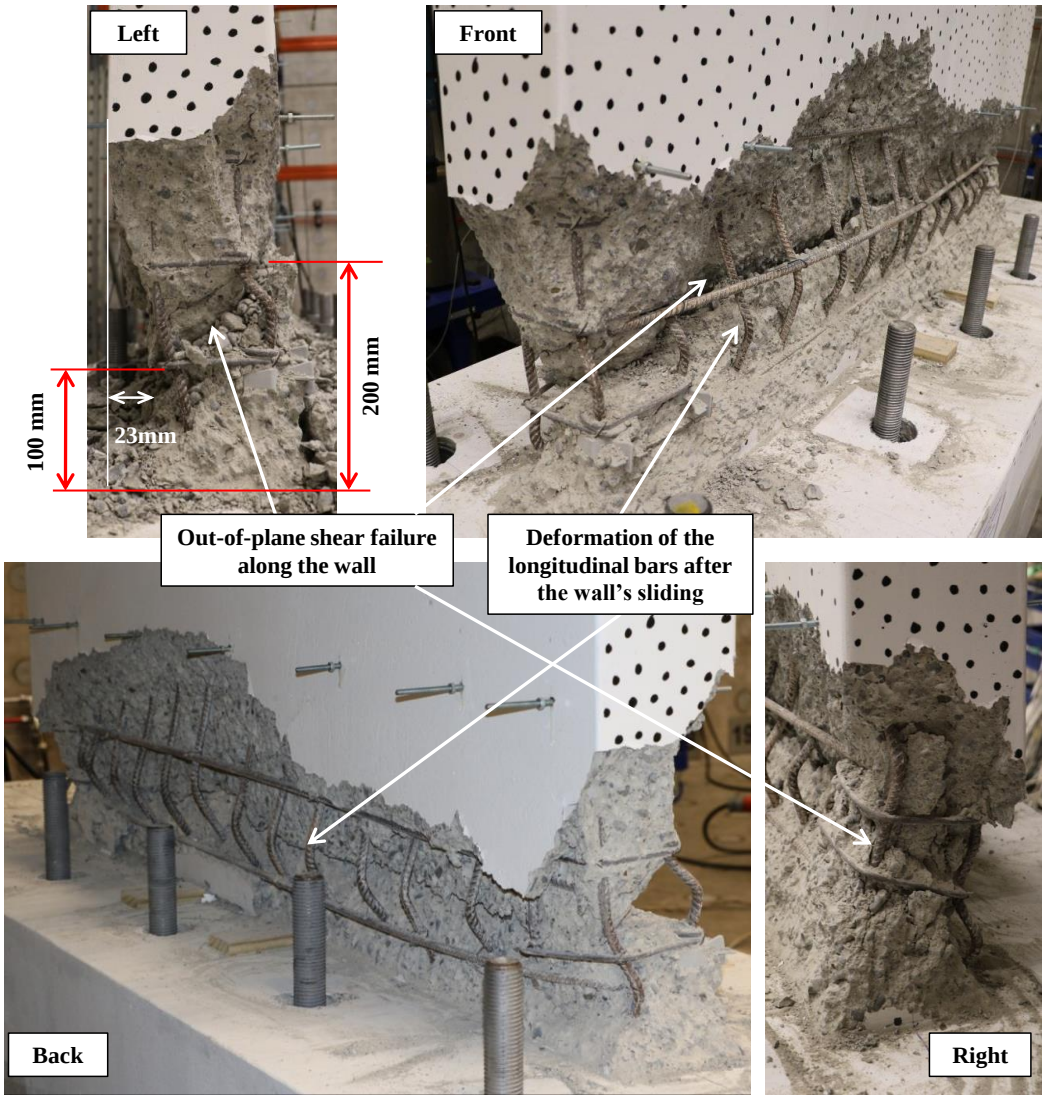

Figure 5-5 SP2-ND failure mode after removing the concrete spalling pieces

5.2.2. SP3-LD

Specimen SP3-LD had the same geometry, axial load ratio, total longitudinal and horizontal reinforcement ratios compared to SP2-ND. The only difference was that SP3-LD was designed for a limited ductility based on NZS3101:2006-A3 (2017) (see Figure 4-4).

There was no sign of vertical cracks which always appear before the onset of the cover concrete spalling on each side of the wall until the end of 0.05% in-plane and 0.57% out-of-plane drift ratios. On the front side, horizontal tensile cracks were observed during the second cycle of 0.05% in-plane drift at a height of about 80mm from the base with a length of 800-1400mm. Tensile cracks were observed on the back side during the third cycle of 0.05% at a height of about 85mm from the base. Maximum crack width by the end of 0.05% in-plane and 0.57% out-of-plane drift ratios was about 0.15 mm. There was no sign of residual cracks during this drift level. Vertical splitting initiated on both right and left sides (see Figure 5-6) from the first cycle of 0.1% in-plane and 1.14% out-of-plane drift ratios. On the front side, the main tensile cracks formed along the wall at a height of about 85mm above the base. Crack width was 0.9 mm on the front side. A maximum residual crack width of 0.3 mm was observed at the end of this drift level on the front side. Horizontal tensile cracks formed along the back of the wall with a maximum crack width of 1 mm during 0.1% in-plane and 1.14% out-of-plane drift ratios. A maximum residual crack width of 0.35 mm was observed at the end of this drift level on the back side of the wall.

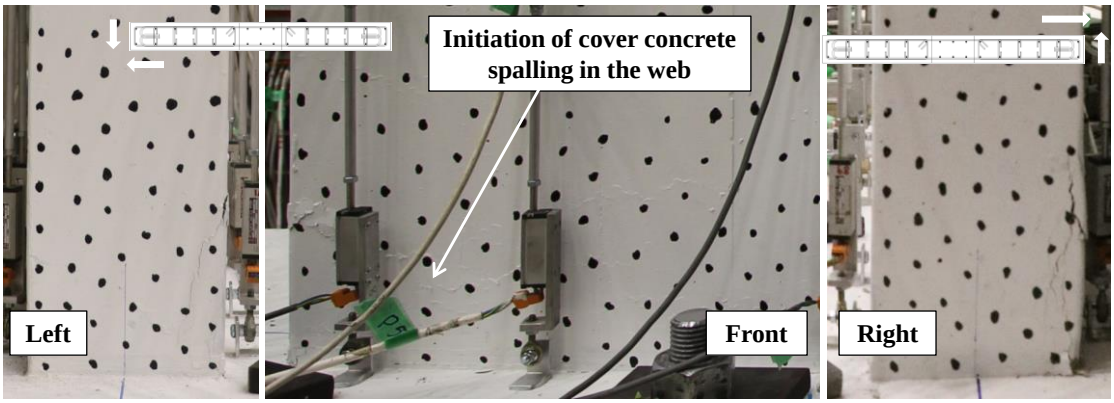

Figure 5-6 Specimen SP3-LD at 0.1% in-plane and 1.14% out-of-plane drift ratios

Concrete cover spalling occurred on both left and right sides of the wall and penetrated the boundary zone and the web during 0.15% in-plane and 1.72% out-of-plane drift ratios (see Figure 5-7). Maximum crack width of the horizontal tensile cracks on the front and back sides were 2 and 1.8 mm, respectively, during this drift level. Maximum residual crack width on both back and front sides were about 0.8 mm throughout 0.15% in-plane and 1.72% out-of-plane drift ratios.

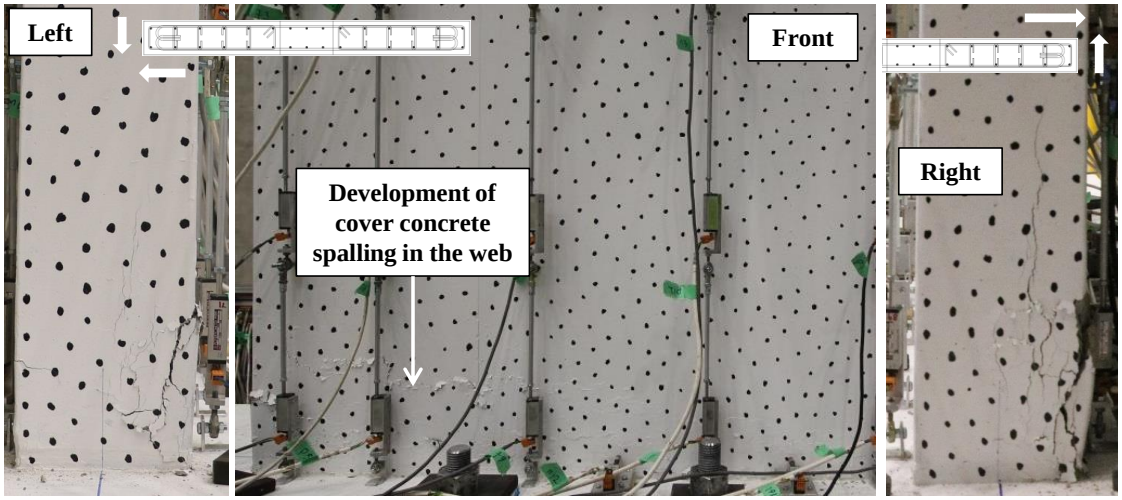

Figure 5-7 Specimen SP3-LD at 0.15% in-plane and 1.72% out-of-plane drift ratios

Concrete cover spalling developed on both left-front and right-back corners of the wall during 0.2% in-plane and 2.29% out-of-plane drift ratios. The first signs of out-of-plane diagonal compression cracks were observed on both left and right sides of the wall from the third cycle of 0.2% in-plane and 2.29% out-of-plane drift ratios (see Figure 5-8). Cover concrete spalling developed along the length of the wall in this drift ratio. Crack width of the horizontal tensile cracks on both back and front sides increased to 3 mm during this drift level. Residual cracks with a crack with of about 1 mm were observed on both sides (front and back) during 0.2% in-plane and 2.29% out-of-plane drift ratios.

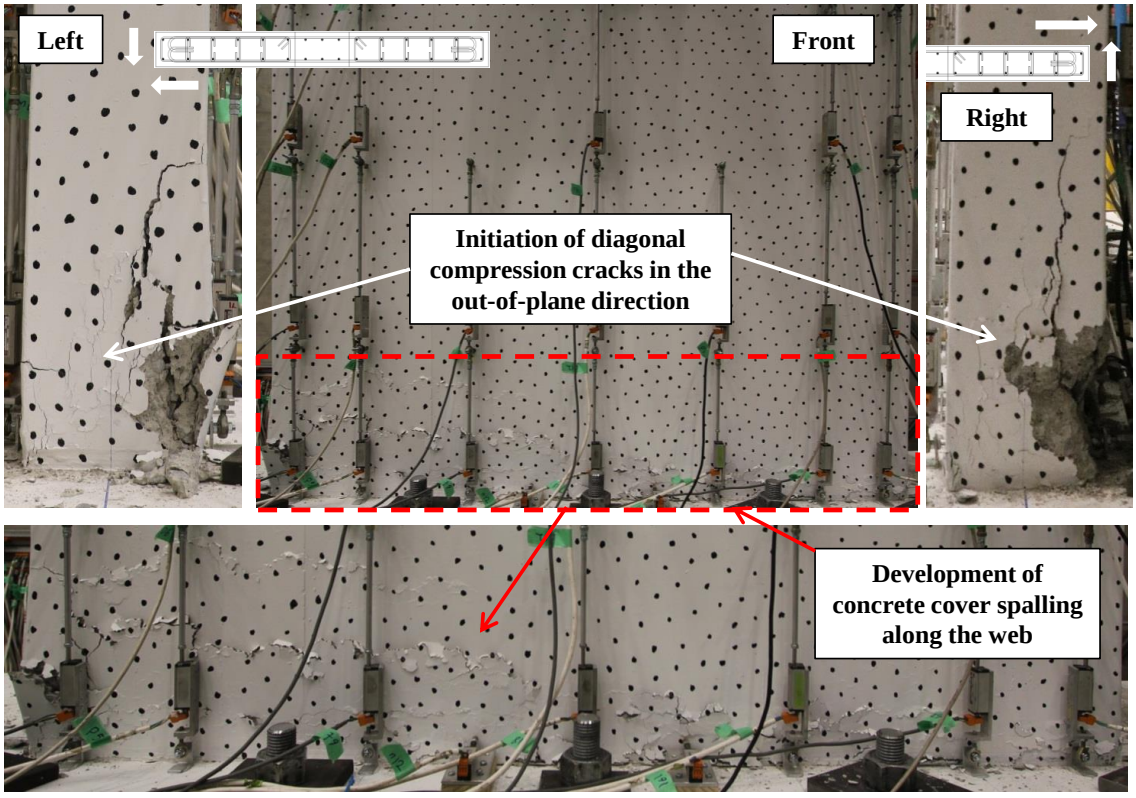

Figure 5-8 Specimen SP3-LD at 0.2% in-plane and 2.29% out-of-plane drift ratios

Concrete cover spalling and crushing increased during 0.25% in-plane and 2.86% out-of-plane drift ratios (see Figure 5-9). Out-of-plane diagonal compression cracks were more visible at this drift level not only at the base of the right and left sides, but also on top of the wall (see Figure 5-10). As can be seen in Figure 5-11, bar buckling was observed in the left-front corner longitudinal bar while loading the left side during 0.25% in-plane and 2.86% out-of-plane drift ratios.

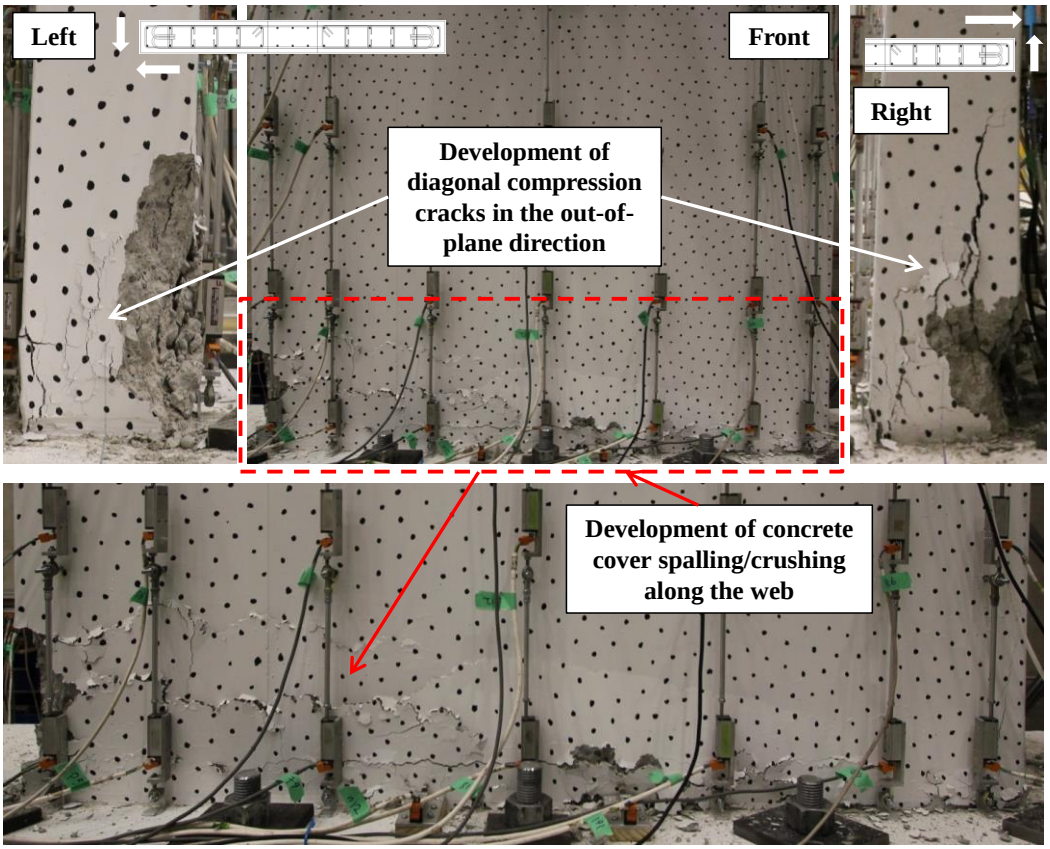

Figure 5-9 Specimen SP3-LD at 0.25% in-plane and 2.86% out-of-plane drift ratios

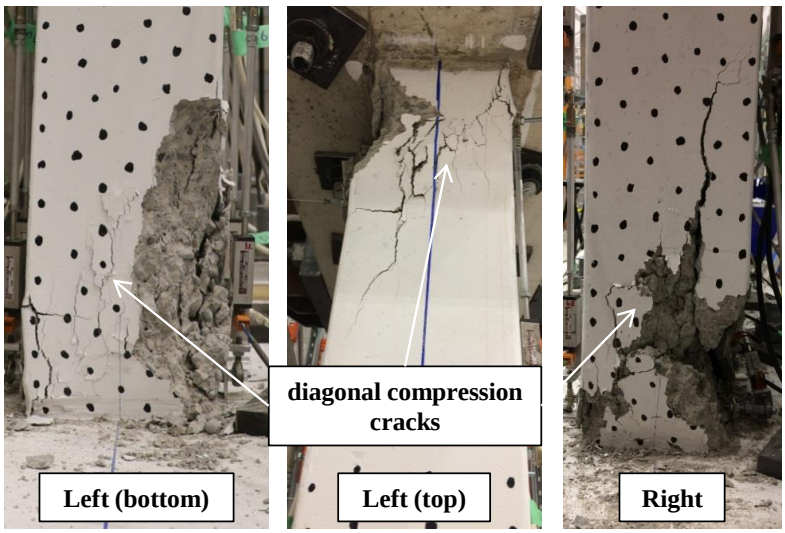

Figure 5-10 Diagonal compression cracks in SP3-LD at 0.25% in-plane and 2.86% out-of-plane drift ratios

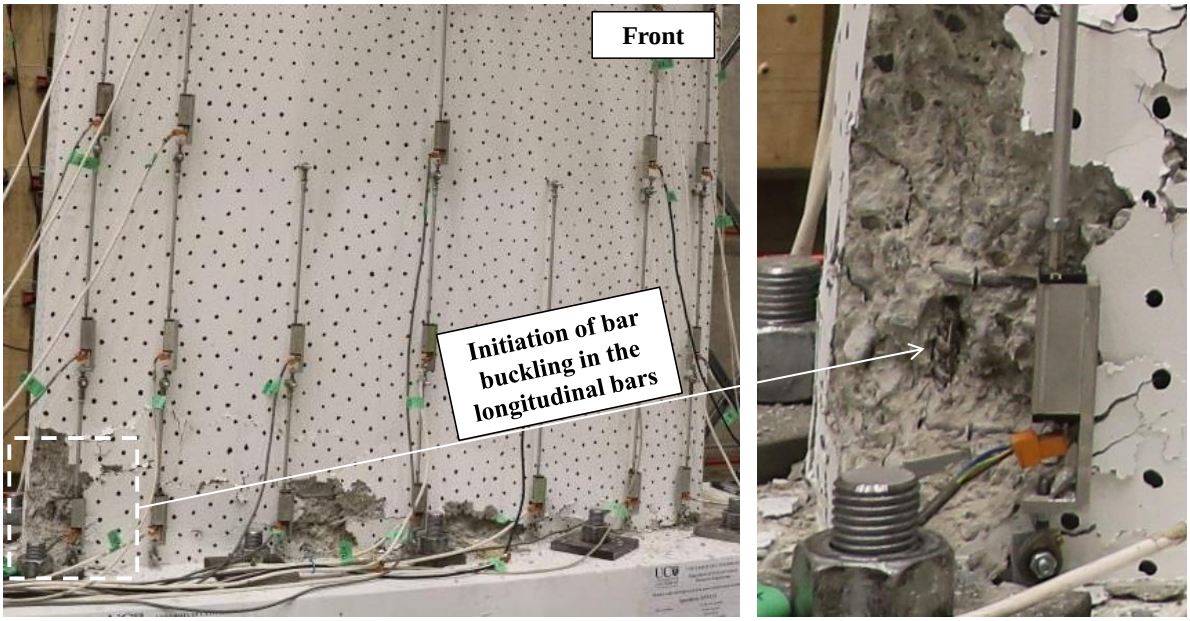

Figure 5-11 Initiation of bar buckling during 0.25% in-plane and 2.86% out-of-plane drift ratio

After one full cycle of 0.25% in-plane and 2.86% out-of-plane drift ratios, it was decided to stop applying further out-of-plane loading and apply a pure in-plane cyclic displacement. It should be noted that in-plane loading started when the wall was at zero in-plane and out-of-plane displacements. The main reasons were to investigate the in-plane strength and failure mode of a severely damaged wall in the out-of-plane when it is under pure in-plane loading which was not investigated before. The pure in-plane cyclic loading started with a 0.5% drift ratio. During unloading the first cycle of 0.5% drift ratio on the right side, significant concrete cover spalling happened to that side which led to an axial compression failure in SP3-LD. Figure 5-12 shows the evolution of cover concrete spalling in SP3-LD. Buckling of the longitudinal bars after the wall's failure is shown in Figure 5-13.

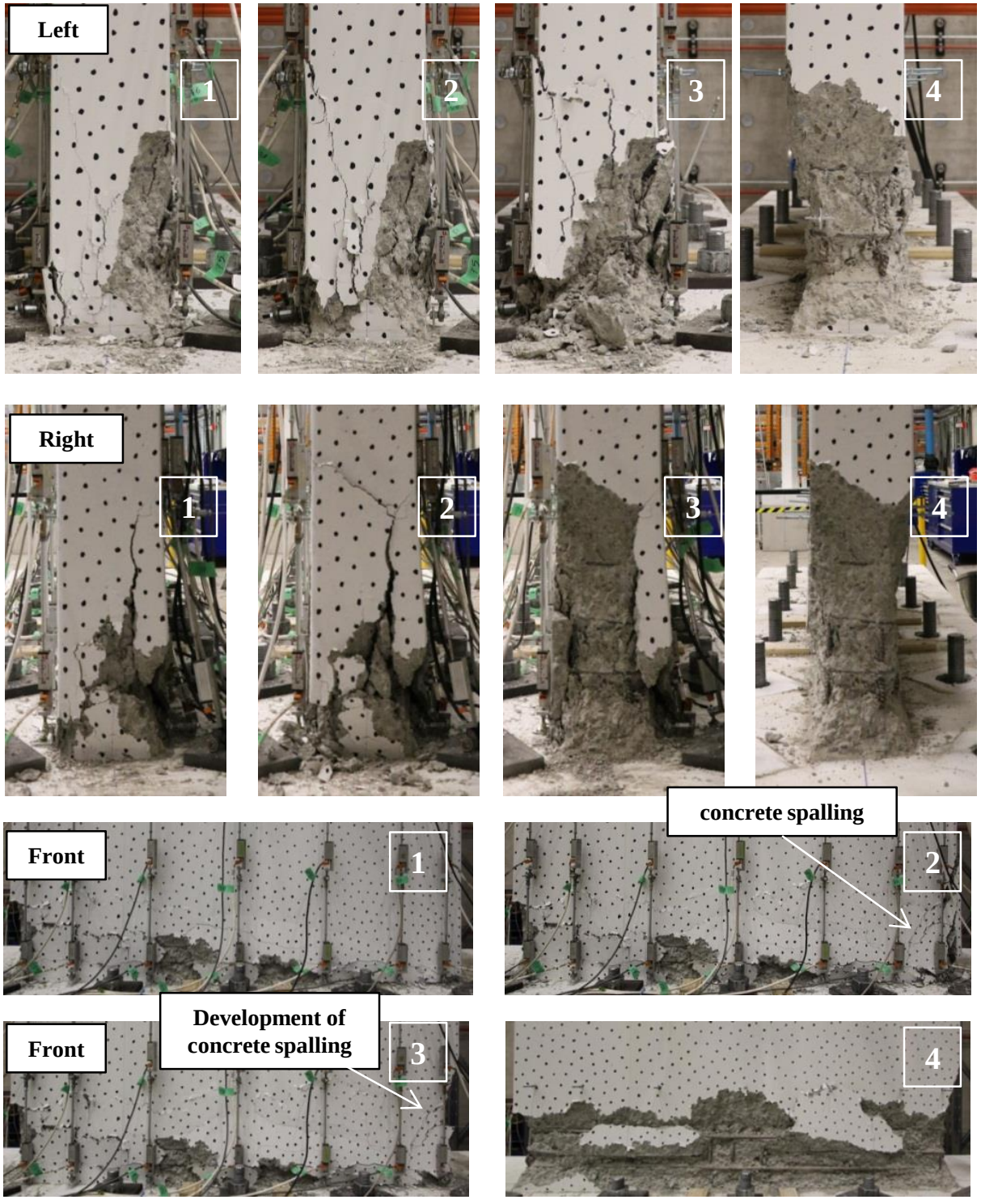

Figure 5-12 Evolution of axial compression failure in SP3-LD during 0.5% in-plane drift ratio

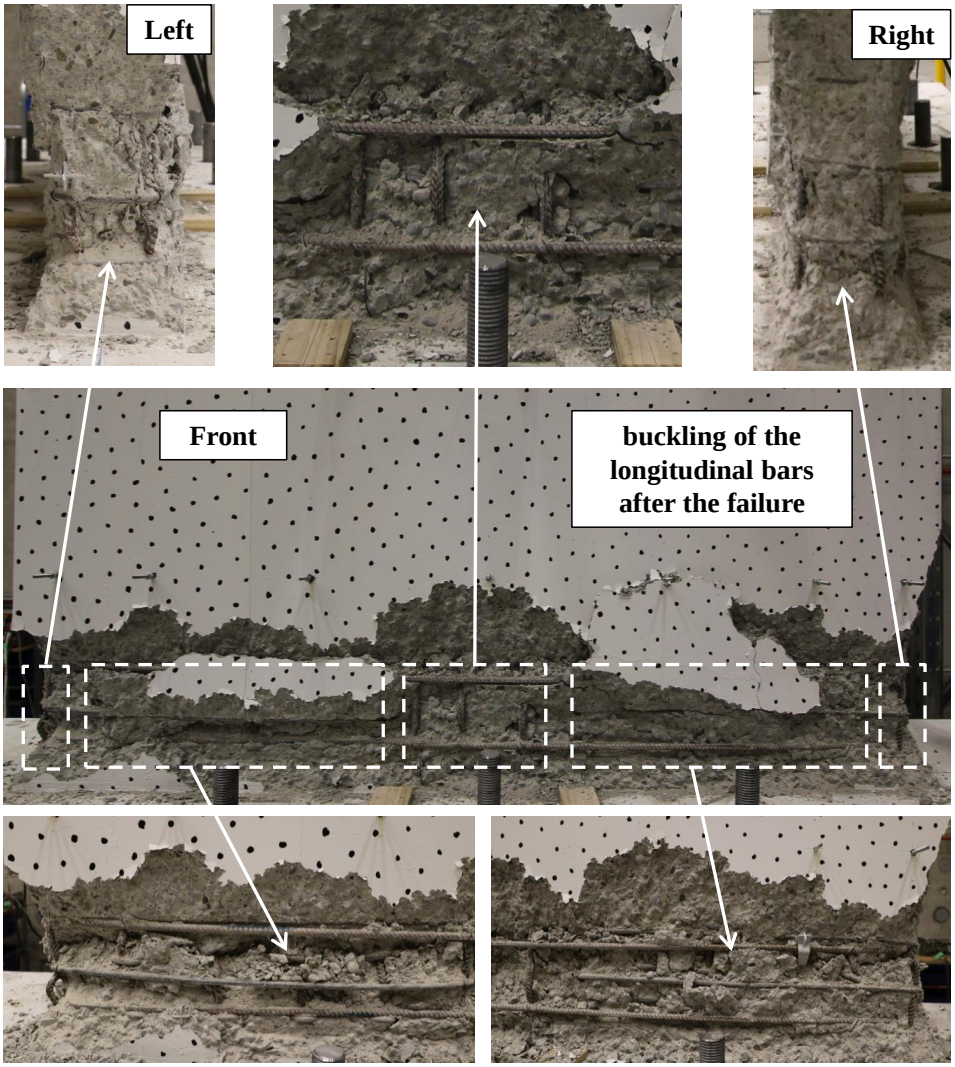

Figure 5-13 Buckling of the longitudinal bars after the wall's failure

5.2.3. SP4-D

Specimen SP4-D had the same geometry, axial load amount, total longitudinal and horizontal reinforcement ratios as SP2-ND and SP3-LD. The only difference was that SP4-D was designed for a ductile level based on NZS3101:2006-A3 (2017) (see Figure 4-5).

During 0.05% in-plane and 0.57% out-of-plane drift ratios, no sign of initiation of cover concrete spalling was observed in the specimen. Horizontal tensile cracks formed at a height of about 110 mm above the base on both back and front sides from the third cycle of 0.05% in-plane and 0.57% out-of-plane drift ratios. Maximum crack width of the tensile cracks on the front and back sides were 0.15 mm. There was no sign of residual cracks by the end of 0.05% in-plane and 0.57% out-of-plane drift ratios.

Cover concrete spalling initiated from the first cycle of 0.1% in-plane and 1.14% out-of-plane drift ratios on both right and left sides, penetrating the boundary zone and web (see Figure 5-14). On the front side, tensile cracks along the wall had a length of about 1400 mm

at an average height of 110 mm above the base with a maximum crack width of about 0.6 mm (see Figure 5-42). Horizontal tensile cracks on the back side formed along the full length of the wall at an average height of about 110 mm with a maximum crack width of 0.8 mm (see Figure 5-42). Residual cracks with a maximum crack width of about 0.1 mm and 0.2 mm were observed on the front and back sides, respectively.

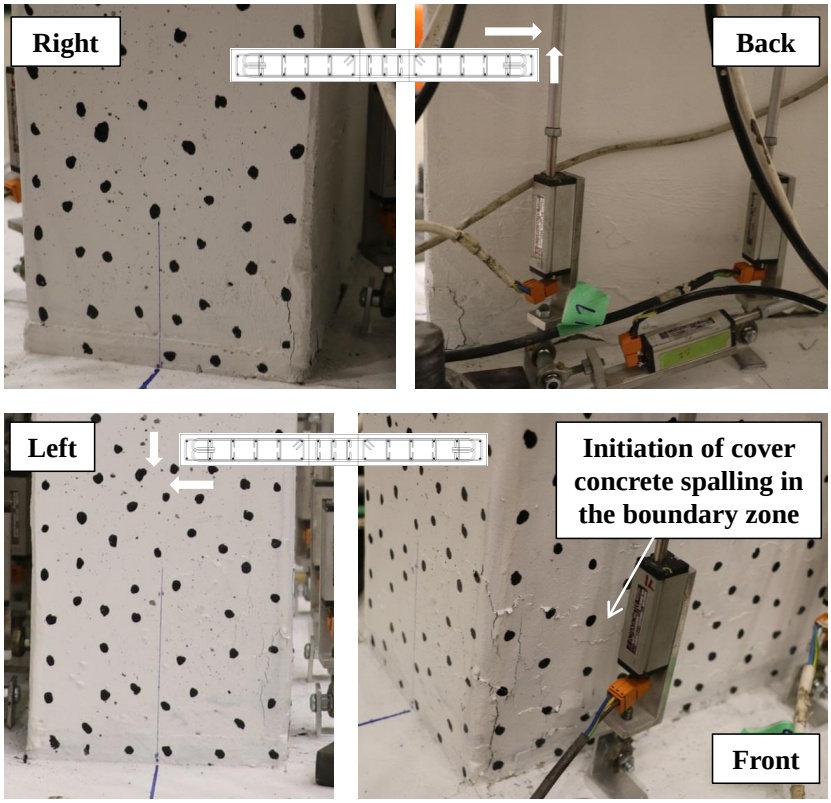

Figure 5-14 Specimen SP4-D at 0.1% in-plane and 1.14% out-of-plane drift ratios

Vertical splitting developed during 0.15% in-plane and 1.72% out-of-plane drift ratios on both right and left sides with some cover concrete spalling on the right-back corner (see Figure 5-15). As can be seen in Figure 5-15, cover concrete spalling which was initiated in the boundary zones, further developed along the wall on the front and back sides during 0.15% in-plane and 1.72% out-of-plane drift ratios. At this stage, tensile cracks formed along the full length of the wall on both front and back sides with a crack width of about 1 mm. Residual cracks were more visible at this stage with a crack width of about 0.4 and 0.5 on the front and back sides, respectively.

Concrete cover spalling increased on left-front and right-back sides during 0.2% in-plane and 2.26% out-of-plane drift ratios (see Figure 5-16). Cover concrete spalling also developed in the wall's web as is shown in Figure 5-16. Maximum crack widths of the tensile cracks were about 2.5 mm on the front and back sides. Residual cracks further developed up to maximum crack widths of about 0.8 mm and 0.6 mm on front and back sides, respectively.

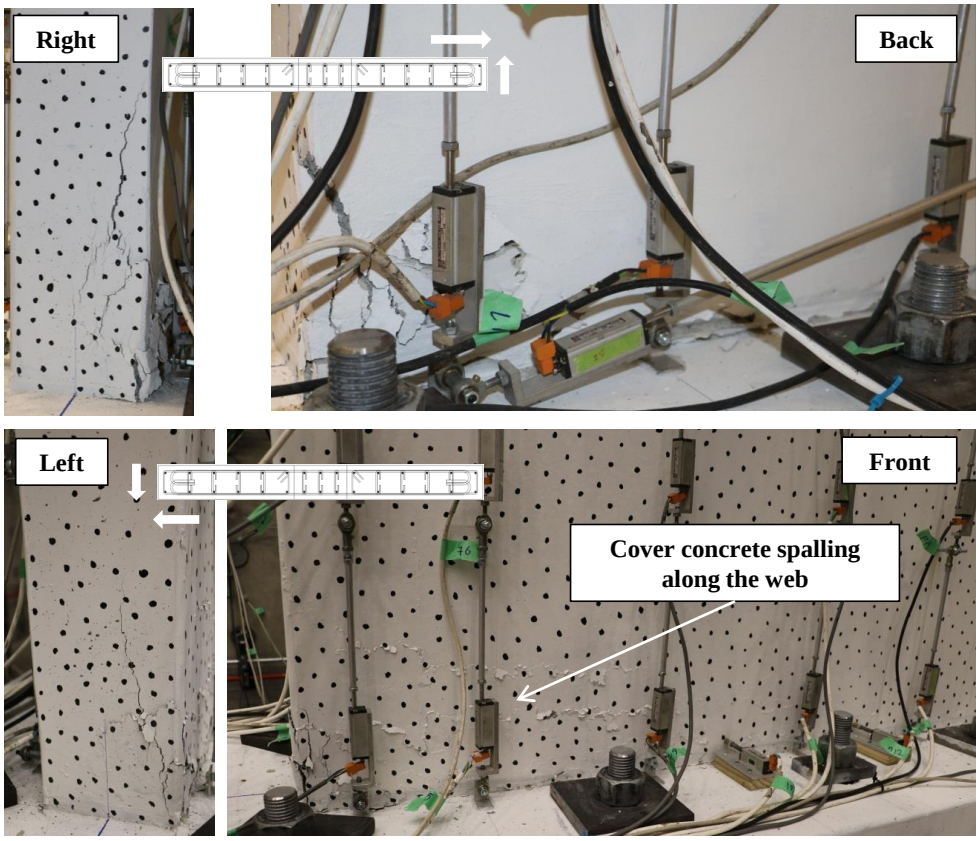

Figure 5-15 Specimen SP4-D at 0.15% in-plane and 1.72% out-of-plane drift ratios

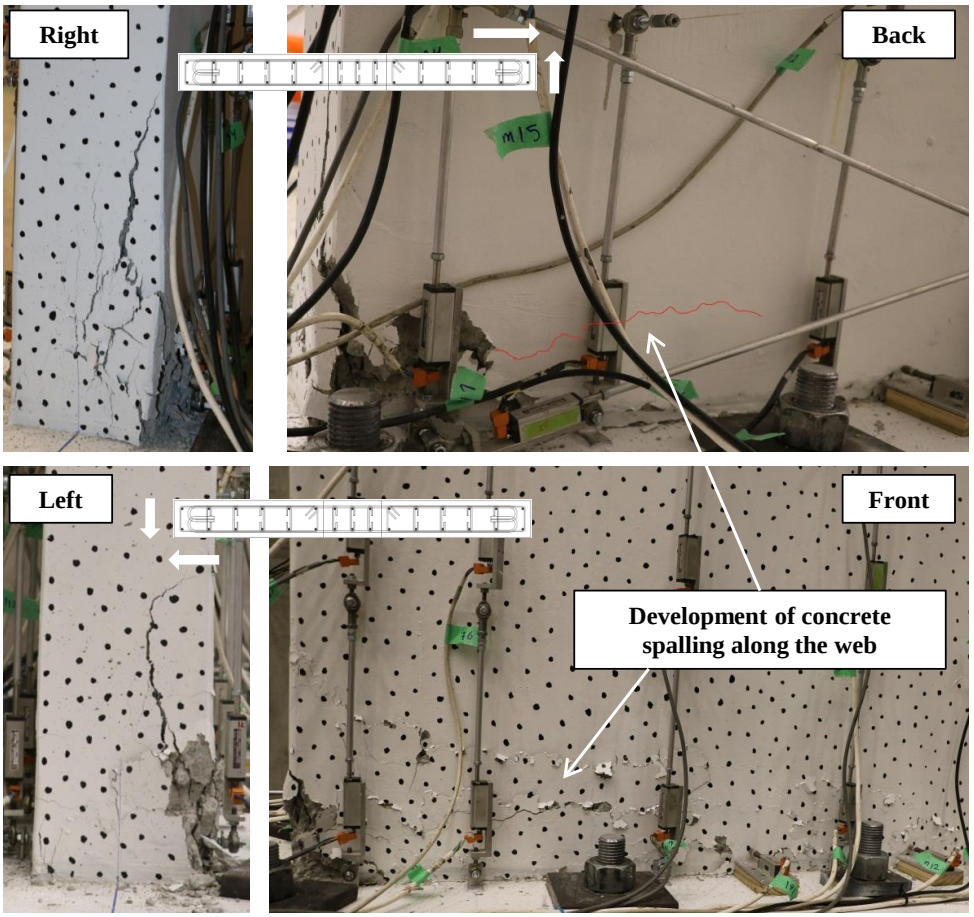

Figure 5-16 Specimen SP4-D at 0.2% in-plane and 2.26% out-of-plane drift ratios

Diagonal compression cracks in the out-of-plane direction were observed in the wall from the first cycle of 0.25% in-plane and 2.86% out-of-plane drift ratios. These diagonal cracks further developed by the end of this drift level (see Figure 5-17). At this stage, diagonal compression cracks formed not only at the bottom of each side, but also on top of the left and right sides as well (see Figure 5-17). Concrete cover spalling along the wall on the front and back sides also developed during this drift level. Maximum crack width of the tensile cracks increased to 3 mm during this drift level.

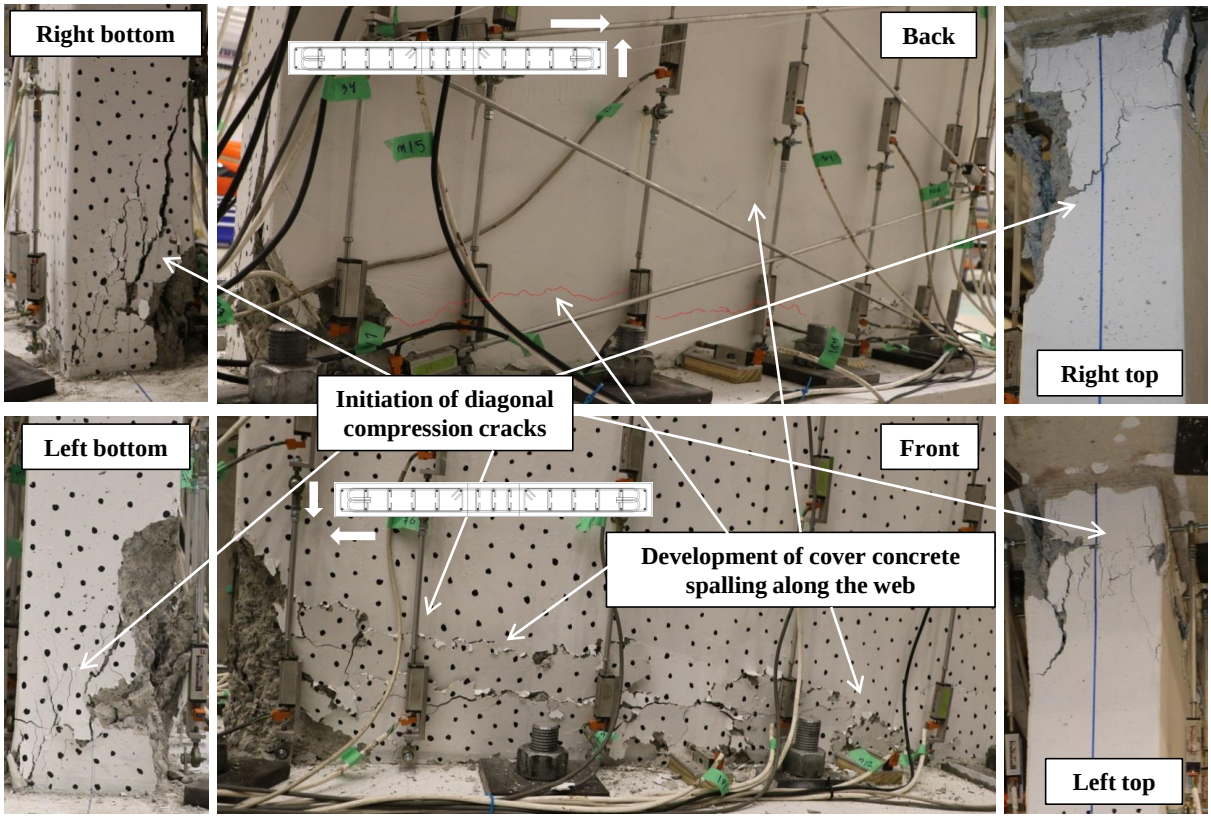

Figure 5-17 Specimen SP4-D at 0.25% in-plane and 2.86% out-of-plane drift ratios

Out-of-plane diagonal compression cracks developed during the first cycle of 0.3% in-plane and 3.43% out-of-plane drift ratios (Figure 5-18). However, during unloading this cycle substantial concrete cover spalling occurred along the wall in its back face (Figure 5-19) which led to considerable reduction in the wall's axial capacity. Consequently the wall failed in axial compression along with buckling in the longitudinal bars (Figure 5-19 and Figure 5-20). Another interesting observation with the specimen SP4-D was a skewed pattern in the longitudinal bar's buckling along the height of the wall which was revealed after removing the spalled concrete (see Figure 5-21).

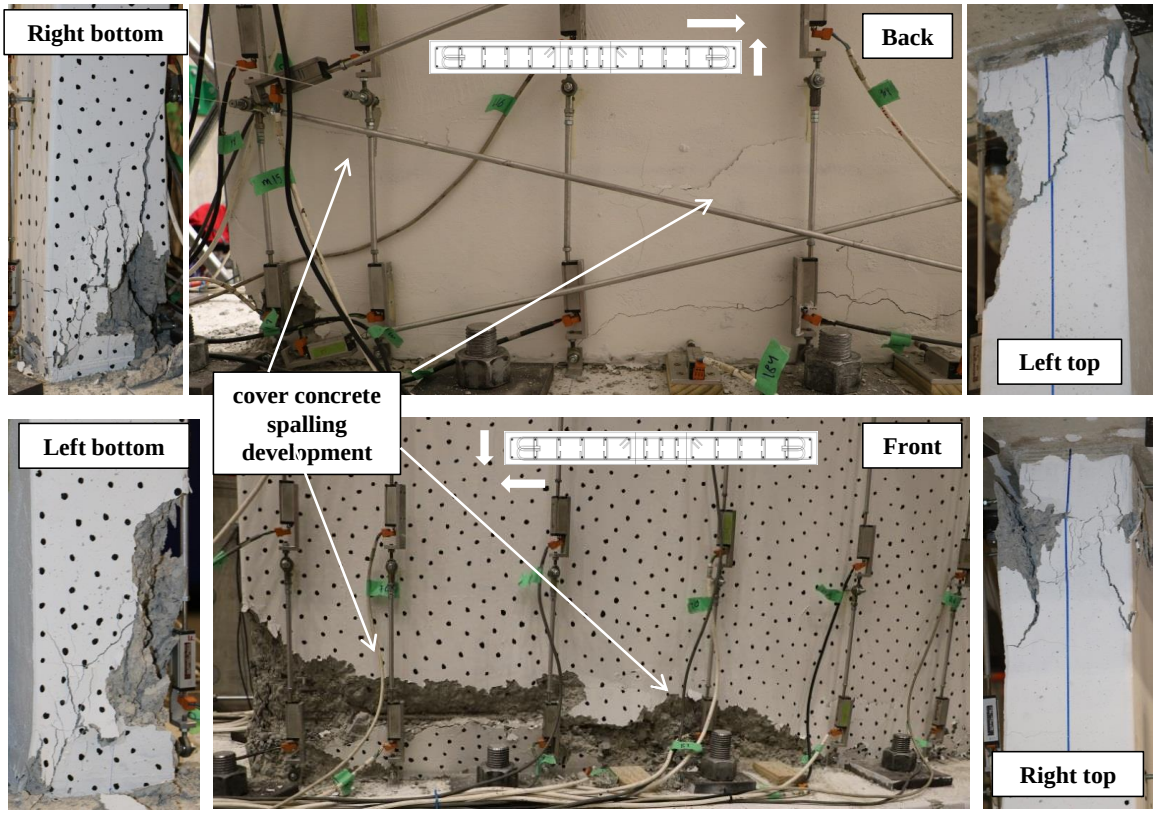

Figure 5-18 Specimen SP4-D during the first cycle of 0.3% in-plane and 3.43% out-of-plane drift ratios

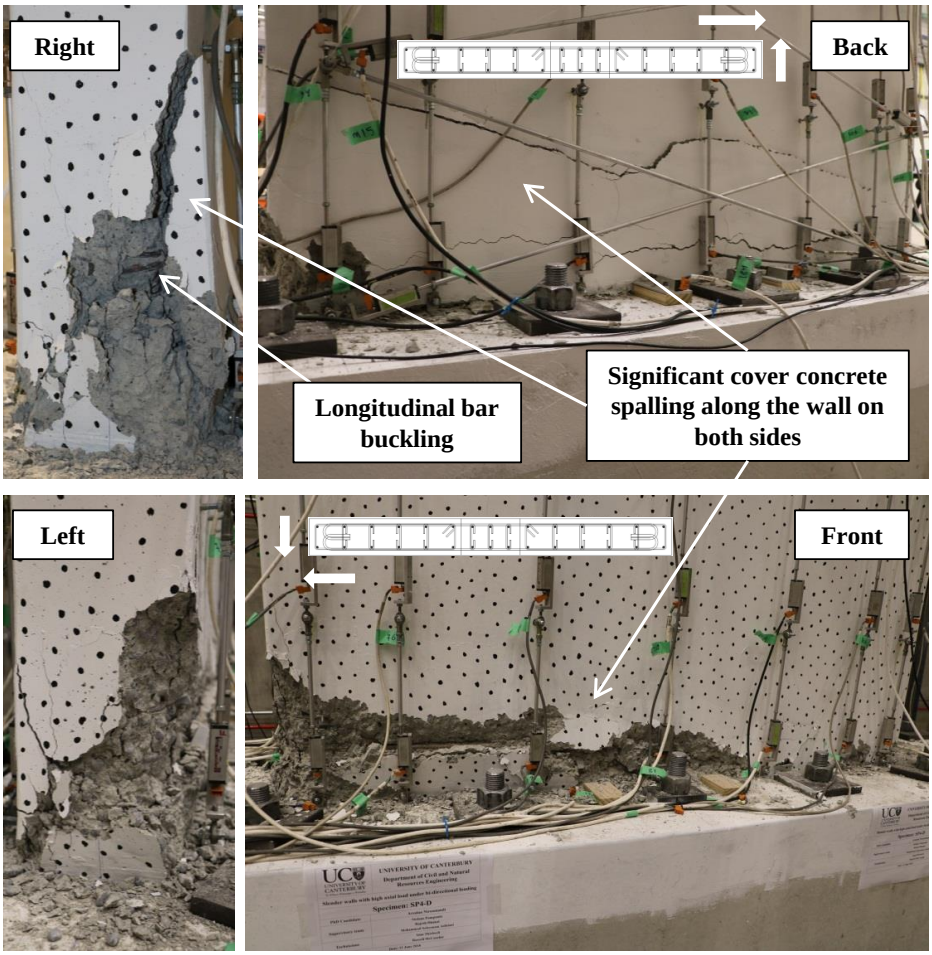

Figure 5-19 SP4-D during unloading the first cycle of 0.3% in-plane and 3.43% out-of-plane drift ratios

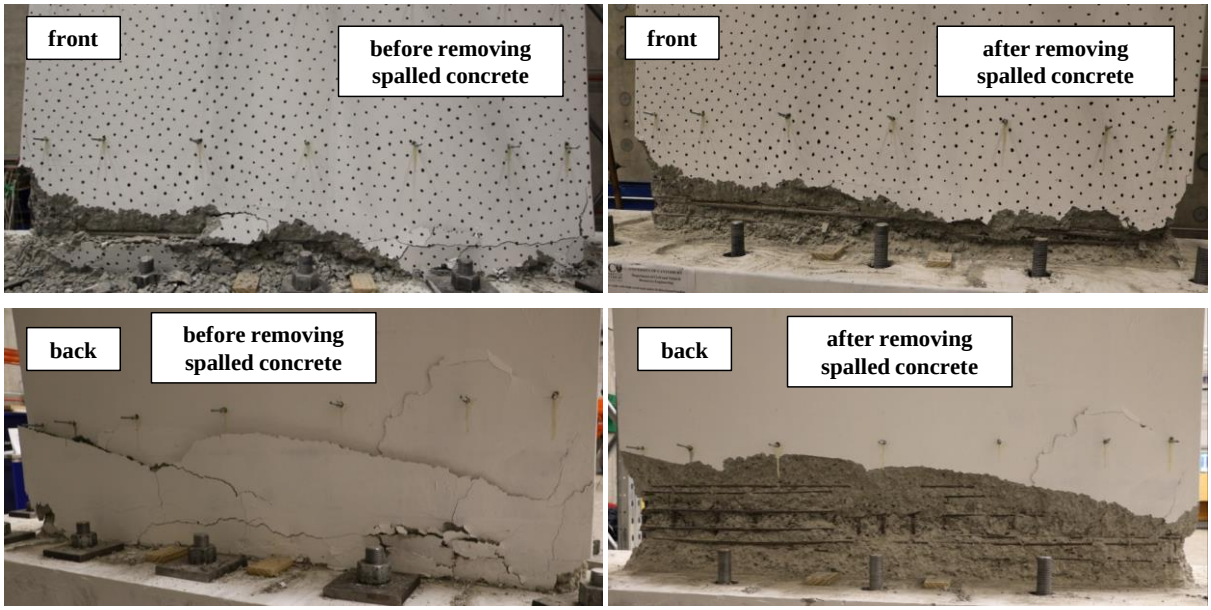

Figure 5-20 front and back faces of SP4-D before and after removing the spalled concrete

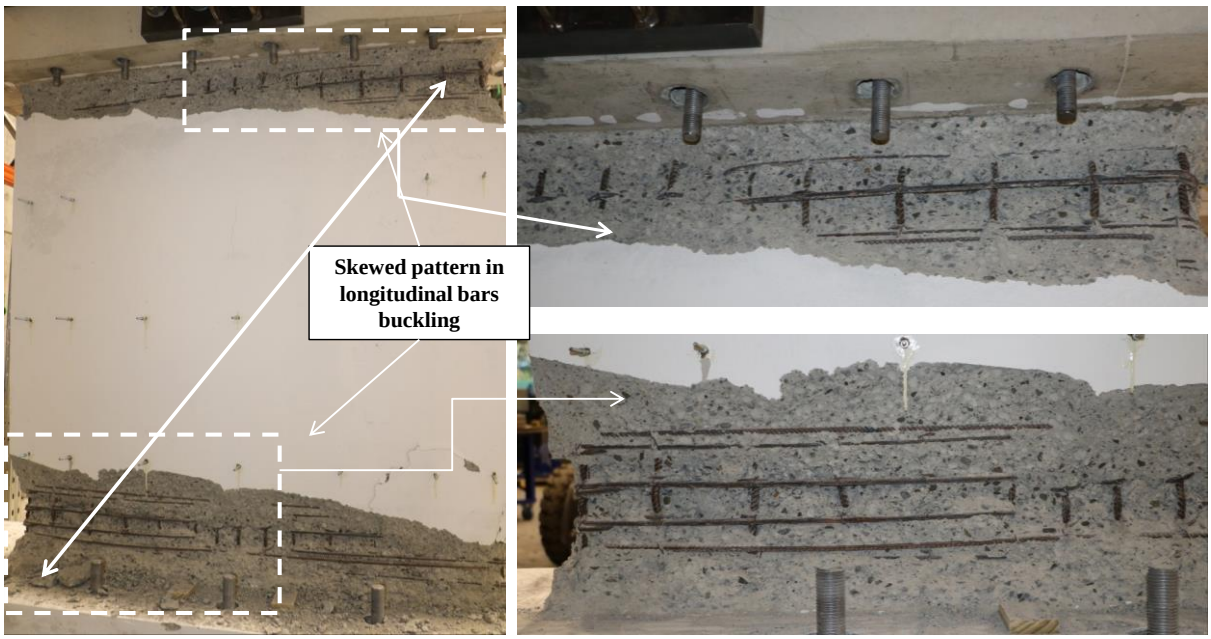

Figure 5-21 Longitudinal bar's buckling in the back face of the specimen SP4-D

5.3.DISCUSSION OF THE TEST RESULTS

5.3.1. Description of the failure mechanisms

In Section 5.2, the behaviour of each specimen during the experiment was presented in details. In this section failure mode of the specimens is discussed in more details. Table 5-1 shows a summary of the drift capacity and failure mode of the specimens. Table 5-2 shows the effects of section detailing ductility on different types of failure modes observed in the three specimens.

Table 5-1 Failure mode and drift capacity of the specimens at failure

Specimen	Drift capacity at failure		Failure mode
	In-plane	Out-of-plane	
SP2-ND	0.15%	1.72%	Out-of-plane shear
SP3-LD	0.25%	2.86%	Axial crushing
SP4-D	0.3%	3.43%	Axial crushing

Table 5-2 Effects of section detailing ductility on the failure mode

Specimen	initiation of out-of-plane diagonal compression cracks	initiation of bar buckling	Out-of-plane shear failure	Axial crushing
SP2-ND	First cycle of 0.15% in-plane 1.72% out-of-plane	-	0.15% in-plane 1.72% out-of-plane	-
SP3-LD	Third cycle of 0.2% in-plane 2.29% out-of-plane	0.25% in-plane 2.86% out-of-plane	-	0.5% in-plane (during pure in-plane loading)
SP4-D	First cycle of 0.25% in-plane 2.86% out-of-plane	after failure	-	0.3% in-plane 3.43% out-of-plane (during skew loading)

SP2-ND

Cover concrete spalling was initiated from the first cycle of 0.1% in-plane and 1.14% out-of-plane drift ratios as can be seen in Figure 5-1. Cover concrete spalling developed along the wall's length during 0.15% in-plane and 1.72% out-of-plane drift ratios (Figure 5-2). Out-of-plane diagonal compression cracks initiated from the first cycle of 0.15% in-plane and 1.72% out-of-plane drift ratios in both left and right sides of the wall and developed by the end of the third cycle of 0.15% in-plane and 1.72% out-of-plane drift ratios (Figure 5-2 and Figure 5-3). Consequently the specimen failed unexpectedly half way through the peak point of the first cycle of 0.2% in-plane and 2.29% out-of-plane drift ratios (Figure 5-4). Failure of the specimen involved a diagonal sliding of about 23mm transverse to the wall from its left side, penetrating the full length of the wall (Figure 5-5). As can also be seen in Figure 5-5, all the longitudinal bars along the wall moved down when the wall got shorten along its height after the out-of-plane shear failure. It is worth noting that, no pattern of out-of-plane buckling (global buckling) or longitudinal bar buckling were observed in the wall.

SP3-LD

Diagonal compression cracks initiated in the out-of-plane direction from the third cycle of 0.2% in-plane and 2.29% out-of-plane drift ratios (Figure 5-8) and developed during the first cycle of 0.25% in-plane and 2.86% out-of-plane drift ratios not only at the base but also at the top of the wall (Figure 5-9 and Figure 5-10). Significant cover concrete spalling also occurred

along the wall on the front and back sides (see Figure 5-9). Bar buckling was observed in the left-front corner longitudinal bar while loading the left side during 0.25% in-plane and 2.86% out-of-plane drift ratios (Figure 5-11). In order to investigate the in-plane strength capacity and failure mode of a wall which was undergone considerable out-of-plane displacements, out-of-plane loading was stopped at zero in-plane and out-of-plane displacements and only cyclic in-plane loading was applied to the wall. Specimen SP3-LD failed in an axial compression failure during the first cycle of 0.5% in-plane drift ratio (Figure 5-12). Cover concrete spalling along the wall was a product of high axial low ratio and the lateral loading pattern. After the axial compression failure of the wall, further buckling was observed in the longitudinal bars which can be seen in Figure 5-13. It can be seen in Figure 5-13, while the longitudinal bars of the web buckled due to lack of anti-buckling ties in the web, longitudinal bars performed better in the boundary zones due to the better confinement.

SP4-D

Diagonal compression cracks in the out-of-plane direction initiated from the first cycle of 0.25% in-plane and 2.86% out-of-plane drift ratios (Figure 5-17) and significantly developed during the first cycle of 0.3% in-plane and 3.43% out-of-plane drift ratios (Figure 5-18). During unloading the first cycle of 0.3% in-plane and 3.43% out-of-plane drift ratios, substantial concrete cover spalling occurred along the wall especially on the back side that led to significant reduction of axial capacity in the wall (Figure 5-19). Consequently the wall was not able to hold the axial load anymore and finally failed in axial compression. Similar to SP3-LD, although the wall didn't fail in out-of-plane shear, parameters such as high axial load ratio and the lateral loading pattern helped with the development of cover concrete spalling along the wall and axial crushing failure. It is worth noting that such axial crushing failure differs from the brittle axial crushing failure in walls with low confinement and high axial load ratio. Bar buckling was observed in the right-back corner longitudinal bar during unloading of 0.3% in-plane and 3.43% out-of-plane drift ratios (Figure 5-19). It was due to initiation of axial compression failure of the wall during this drift level. The other interesting observation was the skewed pattern of buckling in the longitudinal bars upon the axial compression failure as can be seen in Figure 5-21. This was mainly due to the torsion in the wall resulted from the lateral skewed loading pattern, diagonal compression cracks and axial crushing failure of the wall.

5.3.2. Base shear vs drift ratio of the specimens

Figure 5-22 and Figure 5-23 compare the base shear vs drift ratio of the three specimens in the in-plane and out-of-plane directions, respectively. Base shear vs drift ratio of each specimen in the in-plane and out-of-plane directions are shown in Figure 5-27-Figure 5-33. It is worth noting that there were some noises in the in-plane base shear vs drift ratio curve of the specimens which was smoothed using Microsoft Excel. The main source of these noises was small displacement steps of the loading in the in-plane direction (about 11times smaller than the out-of-plane displacement steps). These steps were smaller than the AD (Analog to digital) calibration factor of the actuators. Data smoothing was carried out using Microsoft Excel Data Analysis using the Exponential Smoothing with a damping factor of 0.6. It is worth noting that the in-plane and out-of-plane drift ratios were measured at the height of 2016 mm above the base.

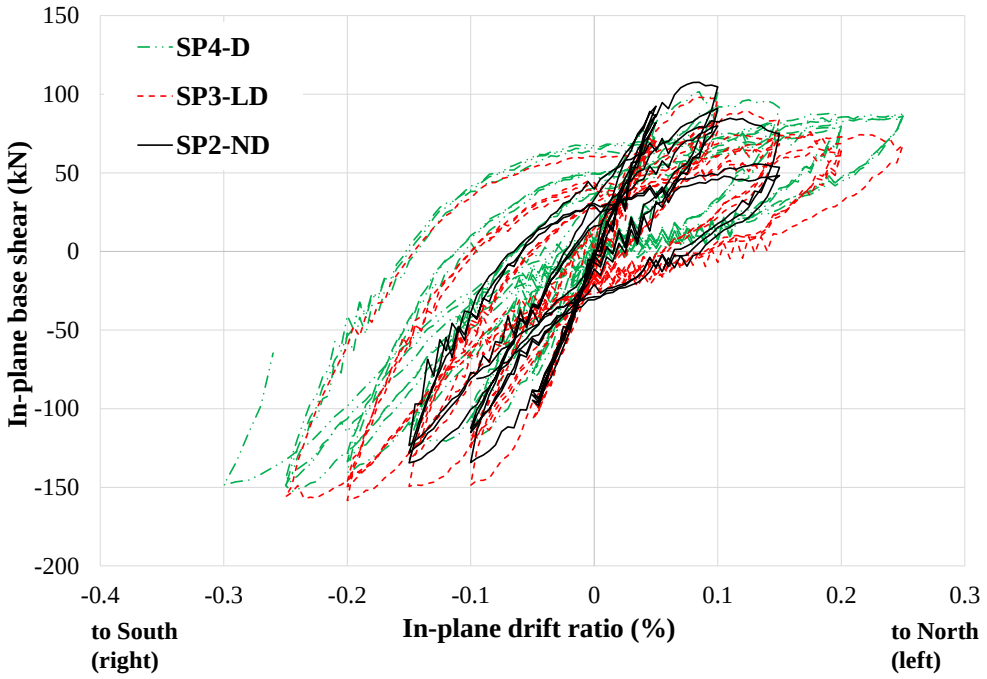

Figure 5-22 In-plane base shear - drift ratio of the specimens

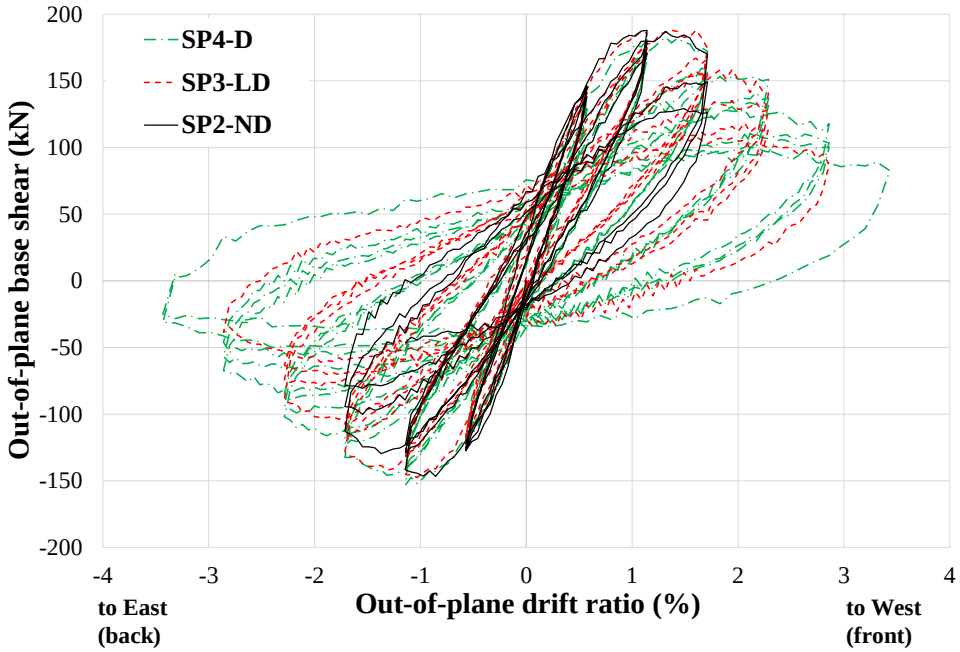

Figure 5-23 Out-of-plane base shear - drift ratio of the specimens

Asymmetric hysteresis curves can be seen in both Figure 5-22 and Figure 5-23 for all three specimens. Some of the potential reasons for such asymmetry in the hysteresis curves which most of them root in the complexity of the test setup and lateral loading pattern were investigated and explained below.

(1) Considering the robust system in the test setup as can be seen in Figure 5-24 and significant axial load ratio of the wall, movements in the foundation are unlikely. Nevertheless, these were measured and for instance the maximum movement of the foundation in the case of specimen SP1-Skew at 3% drift ratio was less than 0.6mm.

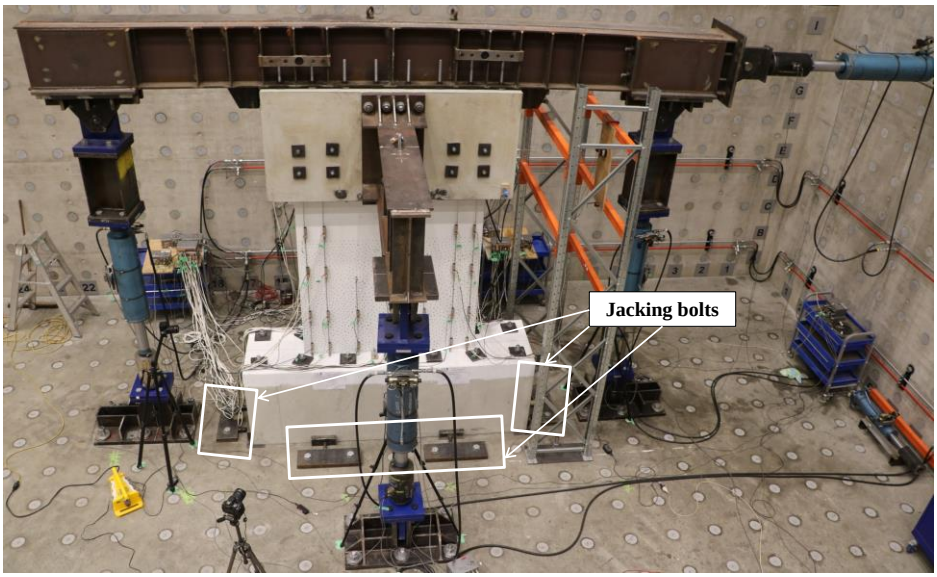

Figure 5-24 Jacking bolts used to control the foundations movement

(2) Although constructing the specimens involved considerable effort to avoid construction errors, some asymmetry were observed in the specimens after casting. For example, one of these construction errors that create asymmetry in the hysteresis curve of the specimen was cover concrete as shown in Figure 5-25.

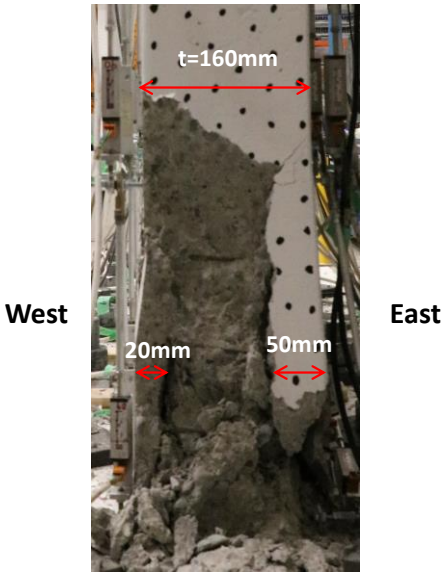

Figure 5-25 Construction error observed in one of the specimens (SP3-LD)

(3) Asymmetry in the test setup including the exact position of the actuators and specimen can potentially lead to asymmetry in the hysteresis curve of the specimens.

(4) Another cause of asymmetry in the in-plane hysteresis curves of the specimens relates to data reading of the horizontal actuator. Due to the lateral loading pattern applied to the wall, it was not possible to use a rotary pot for reading the in-plane displacements (controlling and logging of the horizontal actuator) as the string would have slipped during out-of-plane movements. Therefore, a draw wire should have been used (see Table 4-6). However, as the draw wire available in the lab were not capable of providing both controlling and logging, two draw wires had to be used to control the jack and logging the results. This is shown in Figure 5-26. It can be seen that considering the lateral loading pattern of the wall, such method of measuring displacement can lead to asymmetry in the applied displacement for the pulling and pushing cycles.

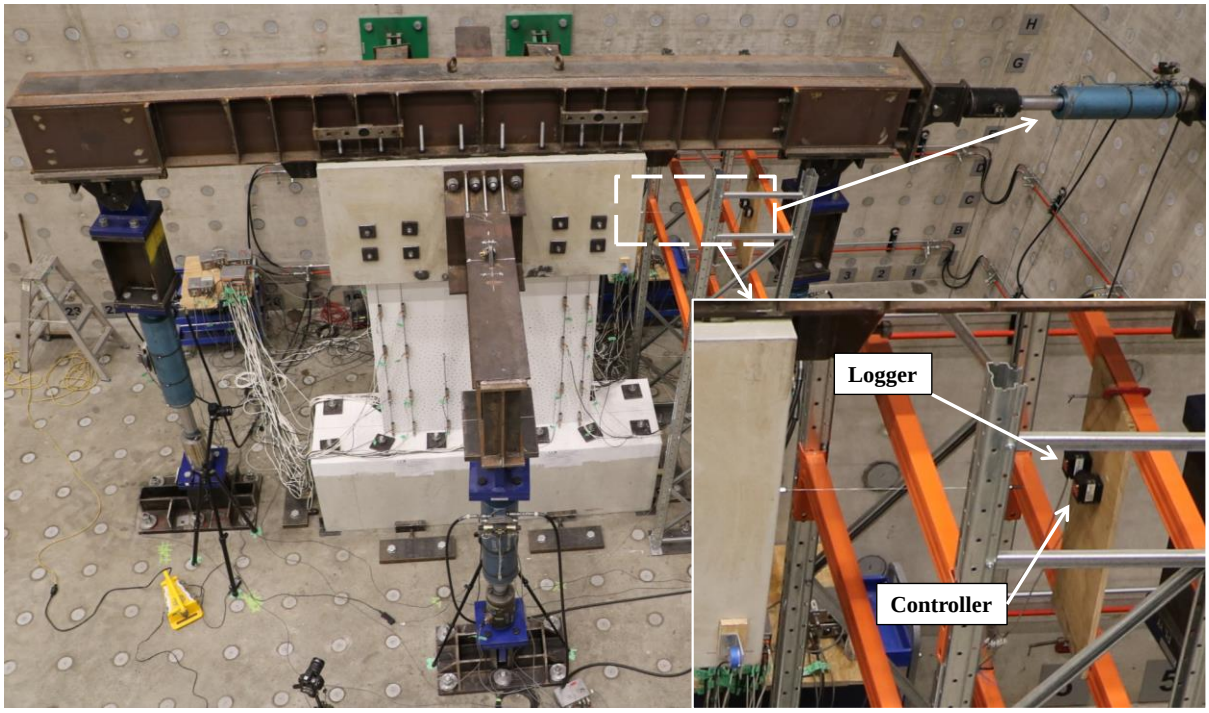

Figure 5-26 Draw wires used for controlling and logging the horizontal actuator

(5) Asymmetry in the lateral loading pattern (the exact loading angle in each direction) can lead to considerable asymmetry in the hysteresis curve. The fact that on the side that out-of-plane strength is lower, in-plane one is higher can suggest a compromise in the lateral loading angle. Considering the lateral loading pattern (skew loading with loading angle of 85 degree) applied to the specimens in the second phase, even 1-2 degree changes in the loading angle can lead to considerable increase or decrease in the attainable strength in each direction.

Based on all of these, the complexity of the test setup, lateral loading pattern (skew loading with 85 degree) and construction error observed were the key parameters led to the asymmetry observed in the hysteresis curves of the second phase specimens. Further investigations on walls tested under such loading pattern can help with understanding this issue.

SP2-ND

Figure 5-27 and Figure 5-28 show the base shear vs drift ratio curve of the specimen SP2-ND in the in-plane and out-of-plane directions, respectively. Initiation of concrete cover spalling, out-of-plane diagonal compression cracks and final failure point are shown in Figure 5-27 and Figure 5-28. Initiation of out-of-plane diagonal compression cracks was considered when these cracks formed transverse to the full thickness of the wall (see Figure 5-2). SP2-ND had

23% and 68% out-of-plane strength reductions from its left side at the onset of out-of-plane shear cracks and at final failure mode, respectively.

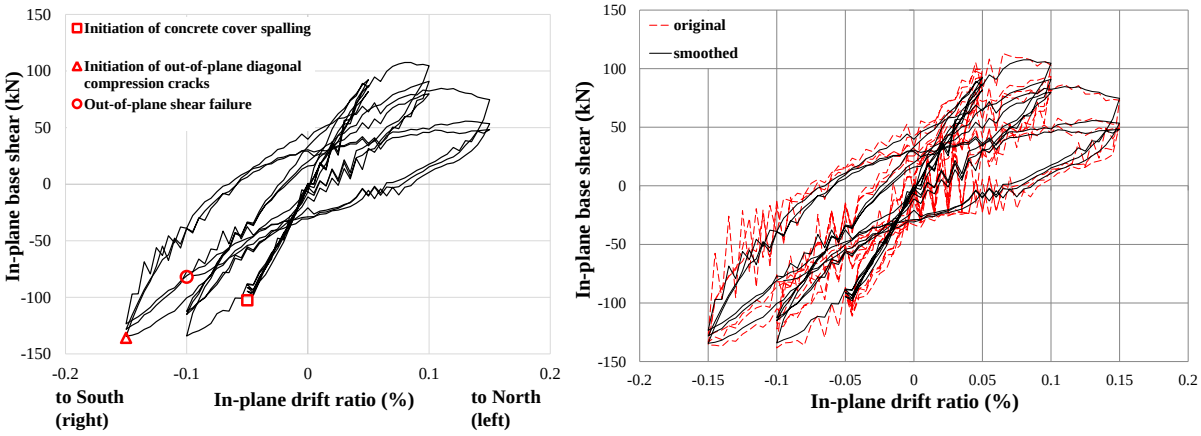

Figure 5-27 In-plane base shear - drift ratio of SP2-ND

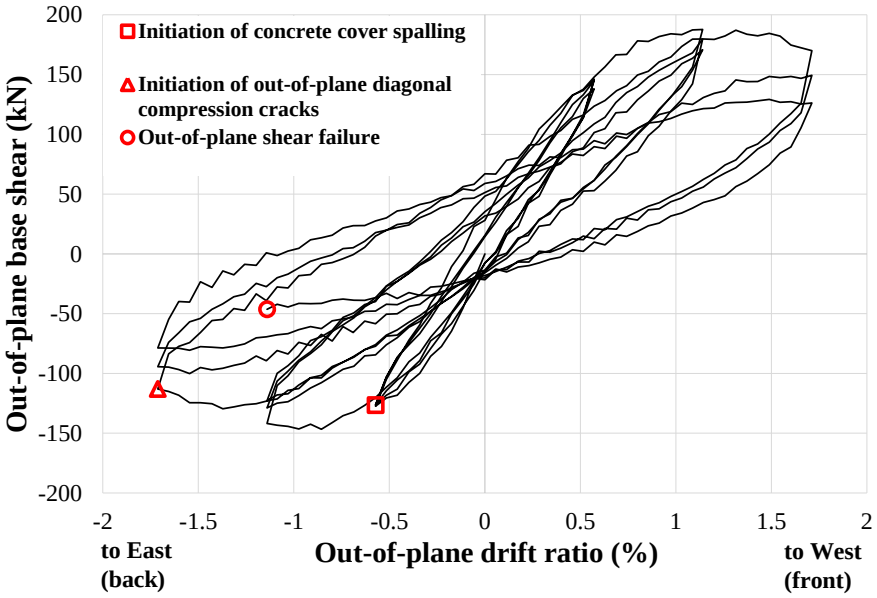

Figure 5-28 Out-of-plane base shear - drift ratio of SP2-ND

SP3-LD

Figure 5-29 and Figure 5-30 show the base shear vs drift ratio curves of the specimen SP3-LD in the in-plane and out-of-plane directions, respectively. Initiation of cover concrete spalling, out-of-plane diagonal compression cracks and longitudinal bar buckling are shown in Figure 5-29 and Figure 5-30. The specimen had 39% and 57% out-of-plane strength reduction from its left and right sides, respectively, when the out-of-plane diagonal compression cracks initiated. Figure 5-31 shows the in-plane base shear vs drift ratio of SP3-LD after continuing with in-plane loading only. The point that axial compression failure happened is shown in Figure 5-31. One of the interesting finding from applying in-plane loading to a wall which was undergone considerable out-of-plane drifts was that the in-plane

strength reduction due to lateral loading pattern didn't recover after applying in-plane loading only. While maximum attained in-plane strength under bi-directional loading in the experiment was less than 160kN, based on a section analysis carried out using SAP2000, a moment capacity of about 1487kN.m corresponding to a shear of 248kN was expected from specimen SP3-LD. This is equal to 36% reduction in the in-plane strength capacity of the wall which was not recovered even after removing the out-of-plane loading. Such reduction of strength due to bi-directional loading was not observed in previous studies on rectangular walls.

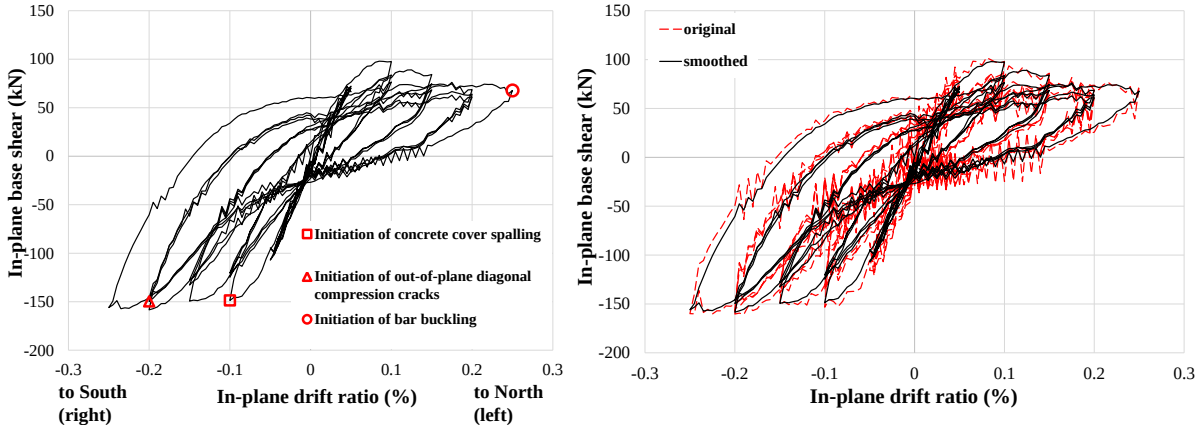

Figure 5-29 In-plane base shear - drift ratio of SP3-LD

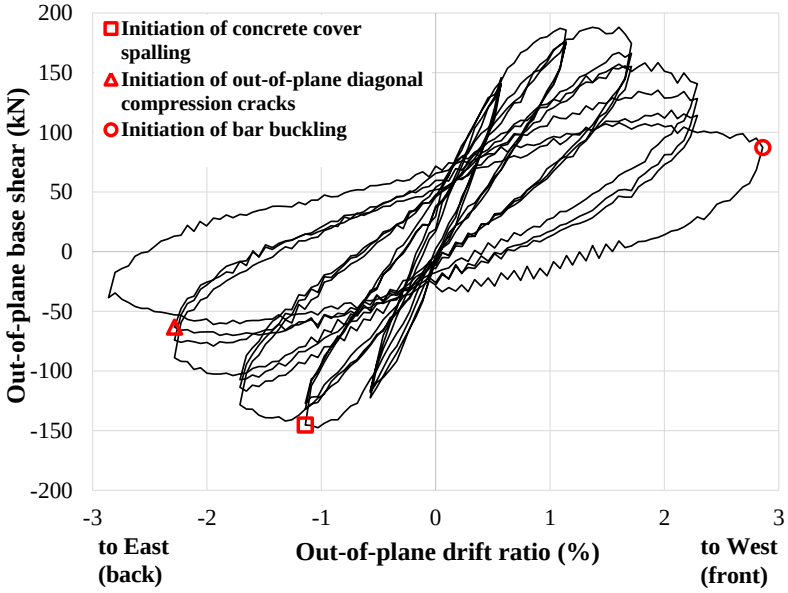

Figure 5-30 Out-of-plane base shear - drift ratio of SP3-LD

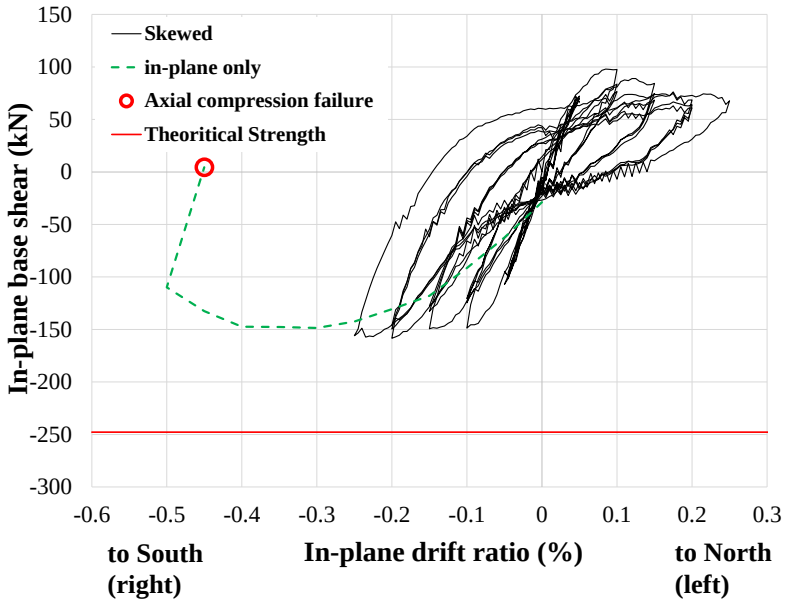

Figure 5-31 In-plane base shear - drift ratio of SP3-LD after applying in-plane loading only

SP4-D

Figure 5-32 and Figure 5-33 show the base shear vs drift ratio curve of the specimen SP4-D in the in-plane and out-of-plane directions, respectively. Initiation of cover concrete spalling, out-of-plane diagonal compression cracks and axial compression failure are shown in Figure 5-32 and Figure 5-33. Initiation of out-of-plane diagonal compression cracks was considered when these cracks formed transverse to the full thickness of the wall. The specimen had 36% and 56% out-of-plane strength reduction from its left and right sides, respectively, when the out-of-plane diagonal compression cracks initiated.

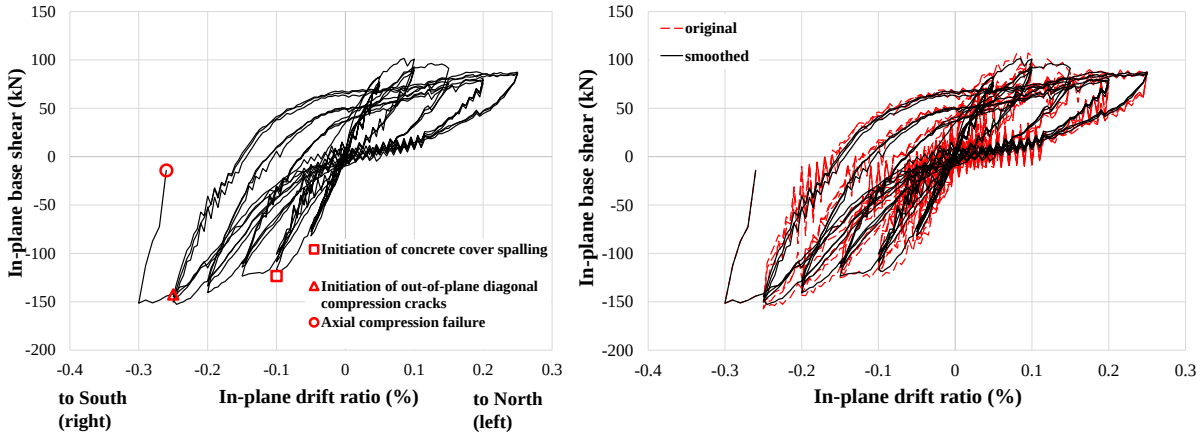

Figure 5-32 In-plane base shear - drift ratio of SP4-D

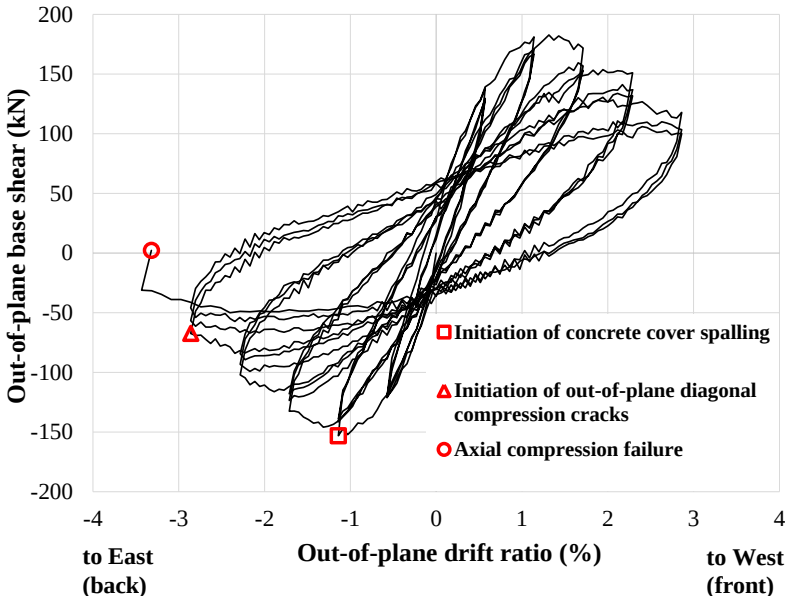

Figure 5-33 Out-of-plane base shear - drift ratio of SP4-D

5.3.3. Compressive and tensile strains in concrete

Maximum average compressive and tensile axial strains of the specimens at each drift level on the left and right sides of the wall are shown in Table 5-3. The average strains were measured for a length of 350mm above the base.

The same issue with measuring the strain in LVDTs discussed in Section 3.3.3 was truth for the second phase as well. Therefore, the strain measurement were modified for the three specimens accordingly by assuming a linear strain variation along the thickness.

It can be seen that both compressive and tensile strains followed similar trend in the three specimens with an increase in the maximum strains from the wall with lower section ductility towards the one with ductile detailing. As was expected, improvement in the section detailing ductility from the benchmark to the specimens with limited and ductile levels increased the maximum compressive strain capacity of the wall by 2.2 and 2.5 times, respectively. The other interesting finding was unlike most walls, tensile strain was lower than compressive strain due to high axial load ratio and lateral loading pattern applied to the wall.

Table 5-3 Maximum average compressive and tensile strains (strain measured for a length of 350mm above the base)

Specimen	Drift level	Maximum compressive strain		Maximum tensile strain	
		Left side	Right side	Left side	Right side
SP2-ND	0.05% in-plane 0.57% out-of-plane	-0.35%	-0.322%	0.076%	0.064%
	0.1% in-plane 1.14% out-of-plane	-0.660%	-0.679%	0.386%	0.279%
	0.15% in-plane 1.72% out-of-plane	-1.389%	-1.262%	0.539%	0.228%
SP3-LD	0.05% in-plane 0.57% out-of-plane	-0.28	-0.245	0.069	0.100
	0.1% in-plane 1.14% out-of-plane	-0.530	-0.595	0.333	0.358
	0.15% in-plane 1.72% out-of-plane	-0.858	-1.113	0.601	0.591
	0.2% in-plane 2.29% out-of-plane	-1.424	-1.879	0.691	0.727
	0.25% in-plane 2.86% out-of-plane	-1.933	-3.011	1.011	0.535
SP4-D	0.05% in-plane 0.57% out-of-plane	-0.35	-0.294	0.047	0.107
	0.1% in-plane 1.14% out-of-plane	-0.633	-0.610	0.307	0.390
	0.15% in-plane 1.72% out-of-plane	-0.966	-1.164	0.587	0.614
	0.2% in-plane 2.29% out-of-plane	-1.414	-1.769	0.823	0.755
	0.25% in-plane 2.86% out-of-plane	-2.067	-2.659	0.870	0.642
	0.3% in-plane 3.43% out-of-plane	-	-3.442	1.181	-

Average strain along the height

Figure 5-34-Figure 5-36 show the strain profile of the wall along the height for each specimen at the third cycle of each drift ratio. It should be noted that pull and push in Figure 5-34-Figure 5-36 indicate lateral loading to the right and left sides of the wall, respectively. Drift levels shown in Figure 5-34-Figure 5-36 were explained in Table 4-5. It can be seen in Figure 5-34-Figure 5-36 that concentration of strains was at the base and top of the wall due to the double bending deformation shape in the out-of-plane direction (the wall lateral movement was strongly towards out-of-plane direction). Both tensile and compressive strains were low in the mid height of the wall that explains the concentration of both tensile and compressive cracks at the base and top of the wall in all specimens (see Section 5.3.4).

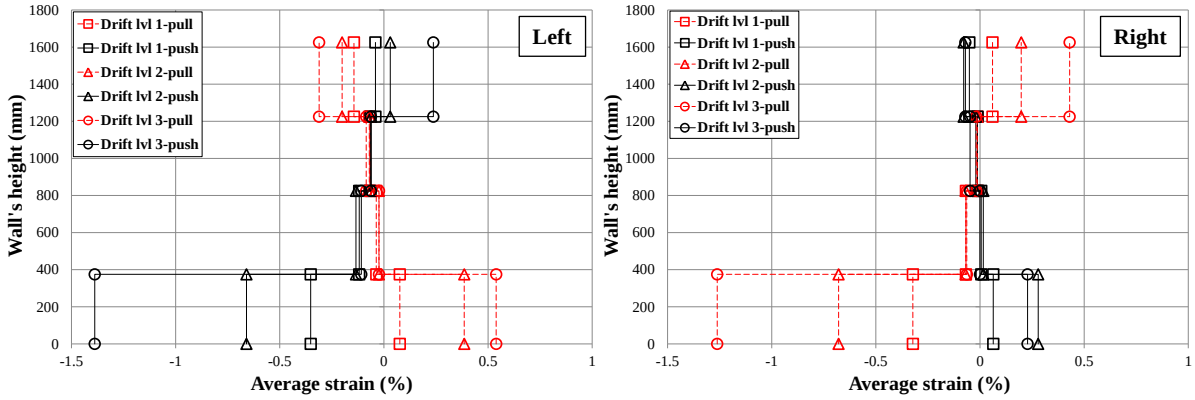

Figure 5-34 Strain profile along the height for specimen SP2-ND on its (a) left and (b) right sides

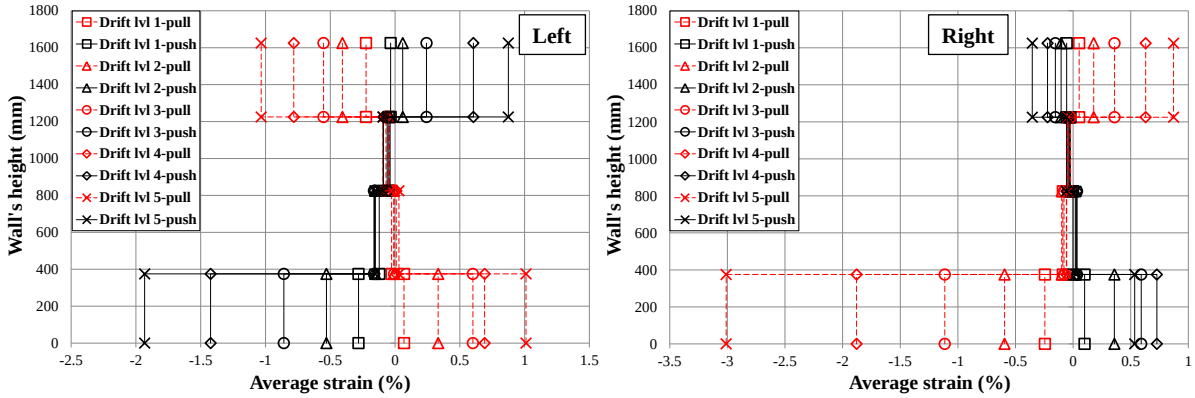

Figure 5-35 Strains along the height for specimen SP3-LD on its (a) left and (b) right sides

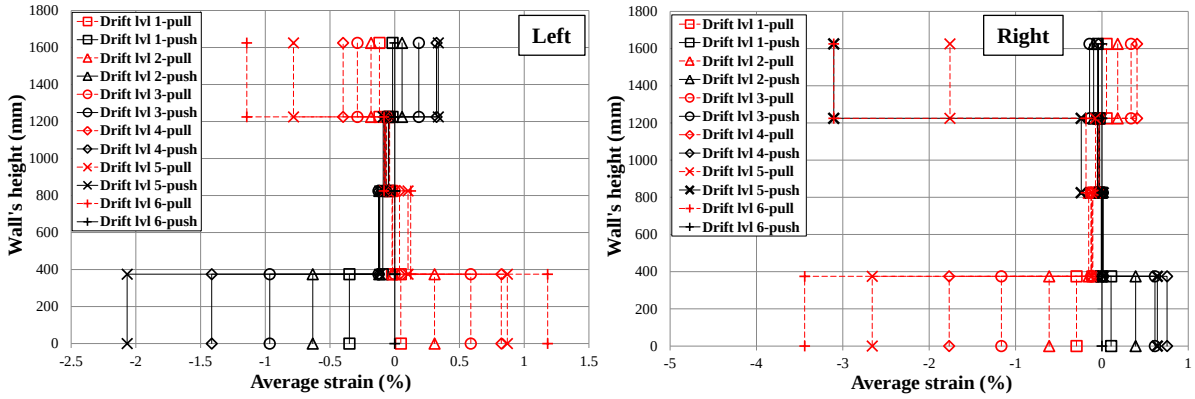

Figure 5-36 Strain profile along the height for specimen SP4-D on its (a) left and (b) right sides

Strain profile

Since the wall was subjected to a dominant skewed lateral loading pattern in the out-of-plane direction, the 2D strain profile of the wall from the section view was used for investigating the section strain profile of the wall. It is worth noting that the strain profile plane is also diagonal which needs a 3D strain profile to properly show that. Figure 5-37-Figure 5-39 show the parts in compression and tension at the peak of the last cycle of each drift level (the hatched part is in compression). These drift levels are explained in Table 4-5. The strain values of the corners are also shown in Figure 5-37-Figure 5-39. Pull and push in

Figure 5-37-Figure 5-39 indicate lateral loading to the right and left sides, respectively. It is worth noting that strain values used for the section strain profile was measured for a length of 350mm above the base (between 25mm-375mm above the base) as the failure mode of the wall in all three cases occurred at a height of less than 375mm above the base.

The 2D strain profile of specimen SP2-ND in Figure 5-37 shows the increase in the area in compression (when loading the left side) during the three cycle of the 0.15% in-plane and 1.72% out-of-plane drift ratios. The wall failed in out-of-plane shear failure when it was fully in compression just before the failure as is shown in Figure 5-37. Two of the key parameters that caused the majority of the wall to be in compression were the high axial load ratio of the wall and the lateral loading pattern (skewed loading with an 85 degree angle). The full length and thickness of the wall wouldn't be in compression if the wall had lower axial load ratio or was tested under a lateral loading pattern with lower loading angle with respect to the in-plane axis. However, in the case of specimens with limited ductile and ductile section detailing, transverse reinforcement were able to prevent the out-of-plane shear failure by increasing the out-of-plane shear capacity of the wall as well as the concrete compressive strain capacity that prevented the diagonal compression cracks to penetrate the core. Out-of-plane shear failure mechanism is discussed in Section 5.4 in more details.

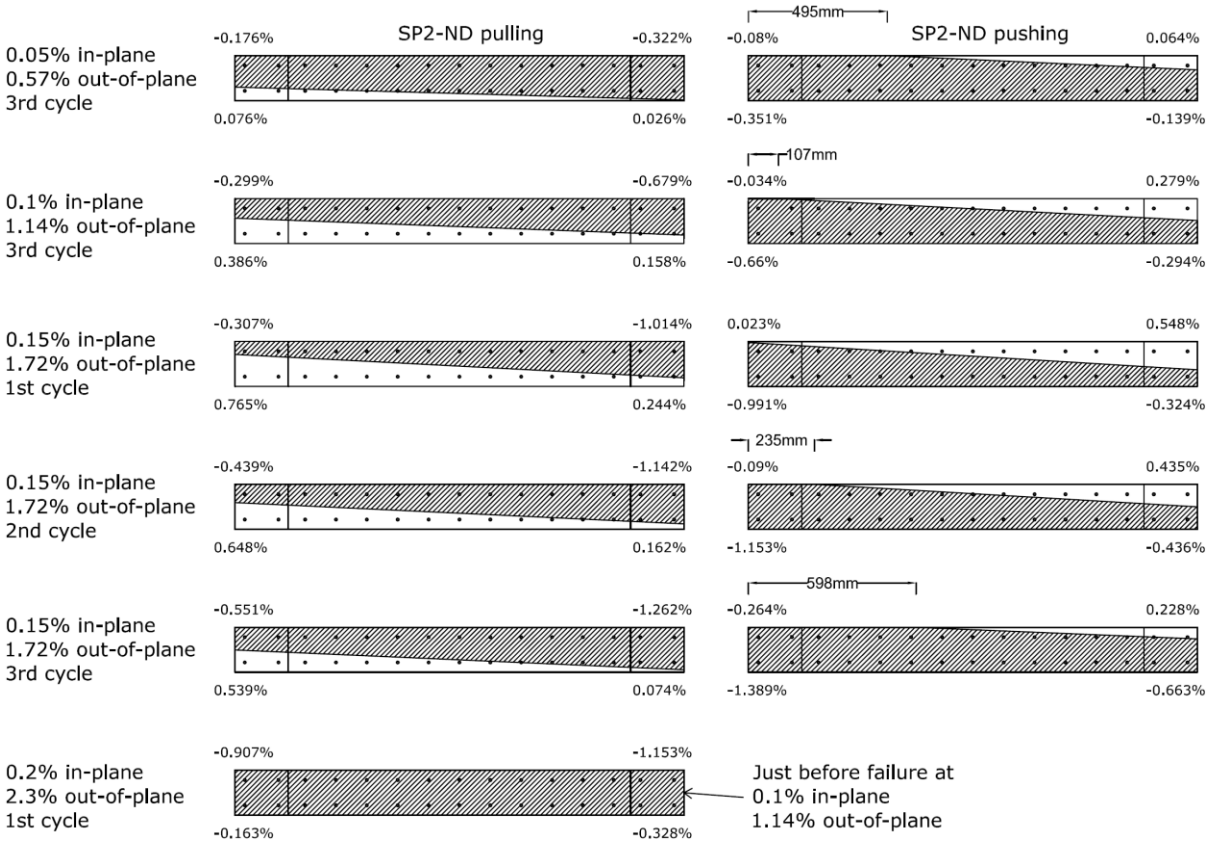

Figure 5-37 2D strain profile of the specimen SP2-ND at each drift level

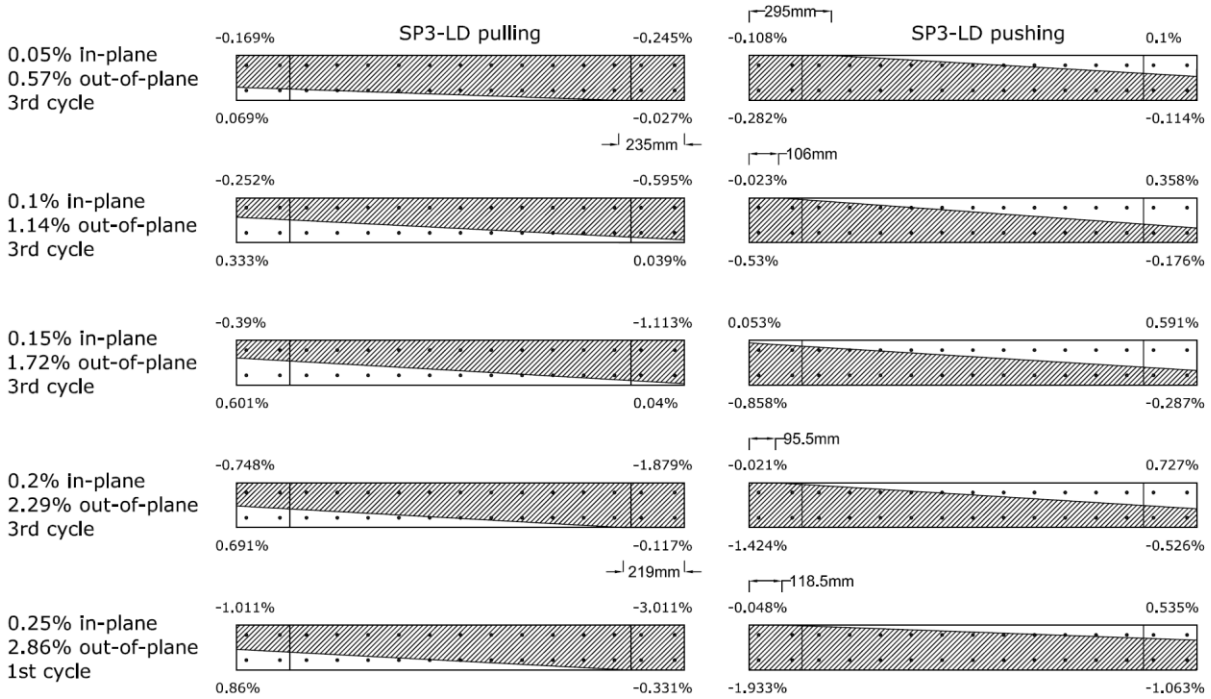

Figure 5-38 2D strain profile of the specimen SP3-LD for each drift level

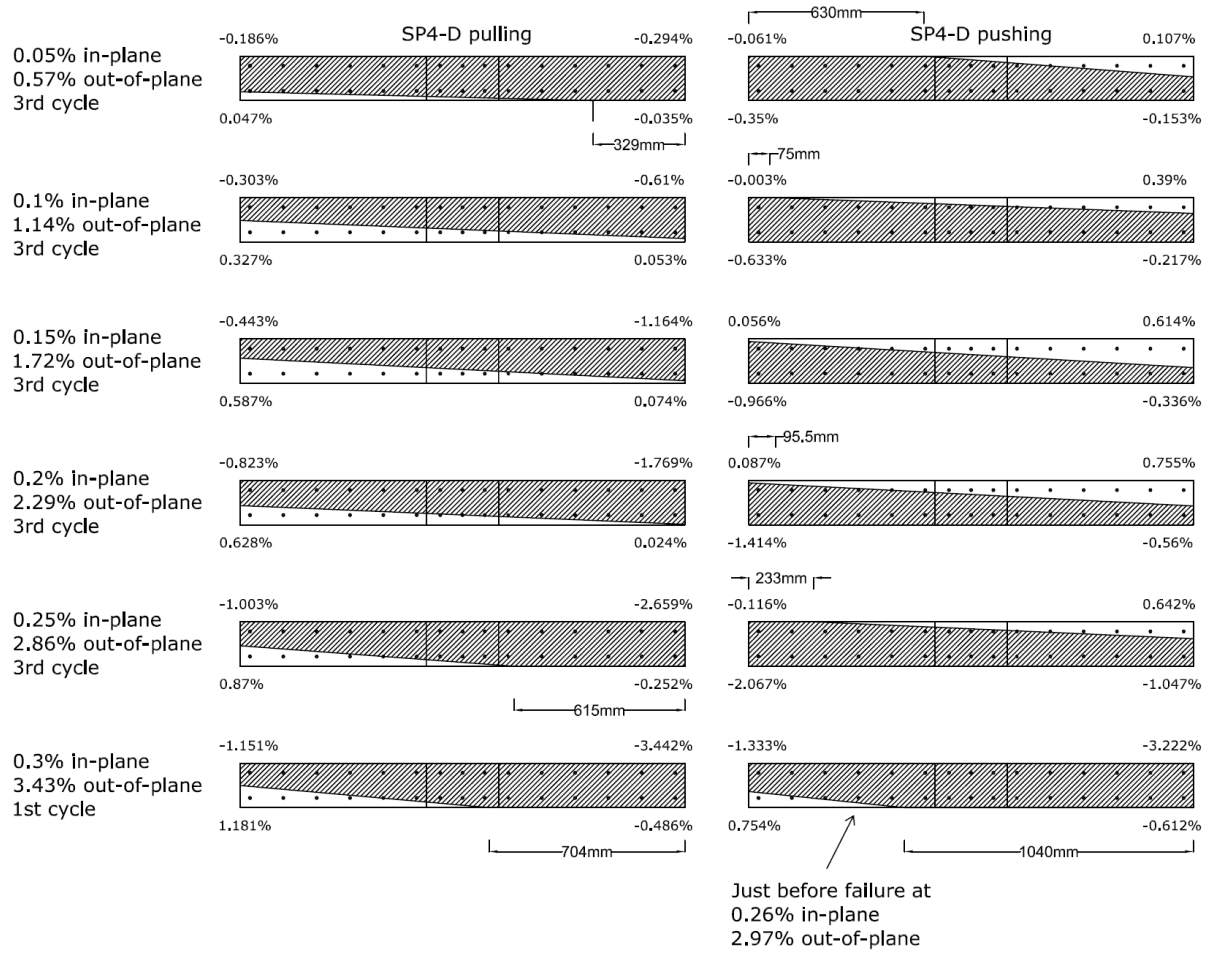

Figure 5-39 2D strain profile of the specimen SP4-D for each drift level

5.3.4. Crack pattern

Crack pattern of the left, front and right sides of the specimens SP2-ND, SP3-LD and SP4-D at the third cycle of each drift level are shown in Figure 5-40-Figure 5-42, respectively. As was also shown in Figure 5-34-Figure 5-36, concentration of cracks was mainly at the base and top of the wall ruled by the double bending deformation shape of the wall in the out-of-plane direction. This can be seen through Figure 5-40-Figure 5-42 as a main horizontal crack along the wall formed at a height of about 85-110 mm above the base in all cases. Evolution of shear cracks in the in-plane and out-of-plane directions can be also seen in Figure 5-40-Figure 5-42. It is worth pointing out that while in case of SP2-ND cracks were concentrated mainly at a height of about 100mm above the base (see Figure 5-40), in specimens SP3-LD and SP4-D, in-plane cracks also distributed above the main horizontal tensile crack. This was due to the transverse reinforcement that helped distributing the in-plane cracks along the height (see Figure 5-41 and Figure 5-42).

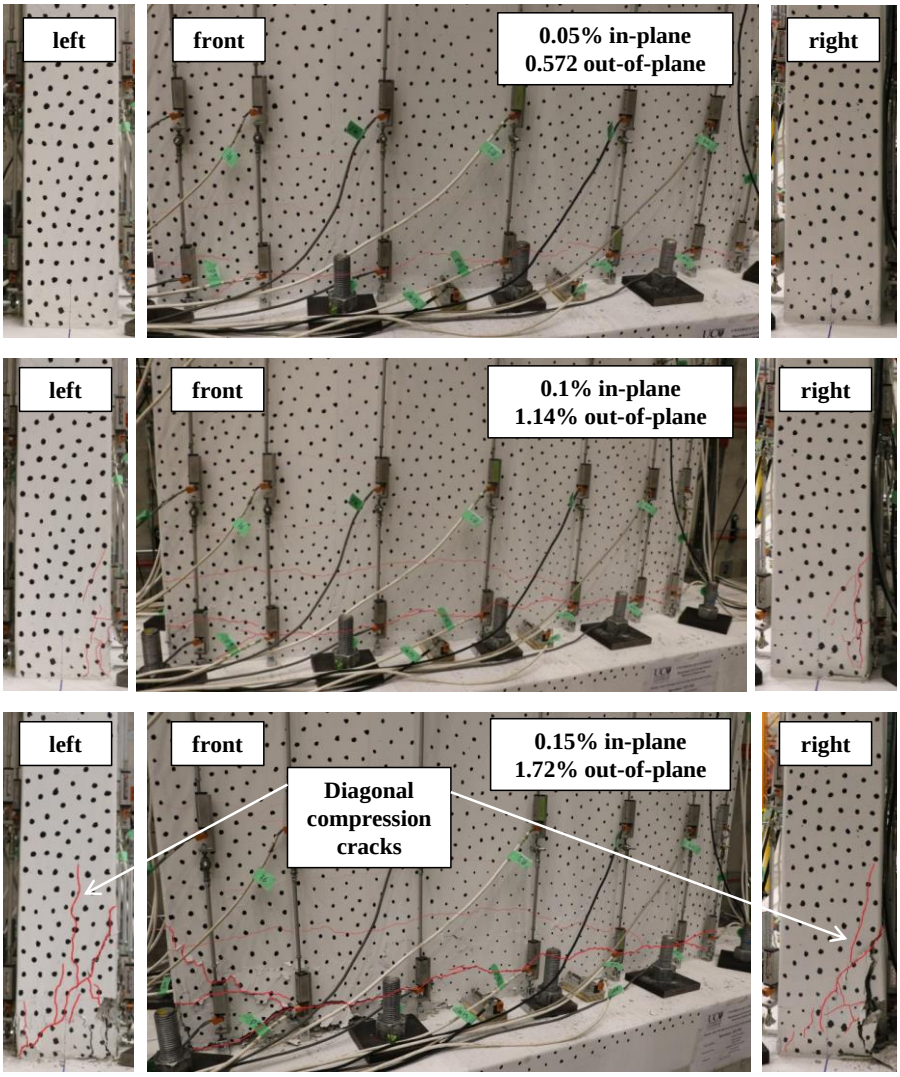

Figure 5-40 Crack patterns of SP2-ND at the third cycle of each different drifts

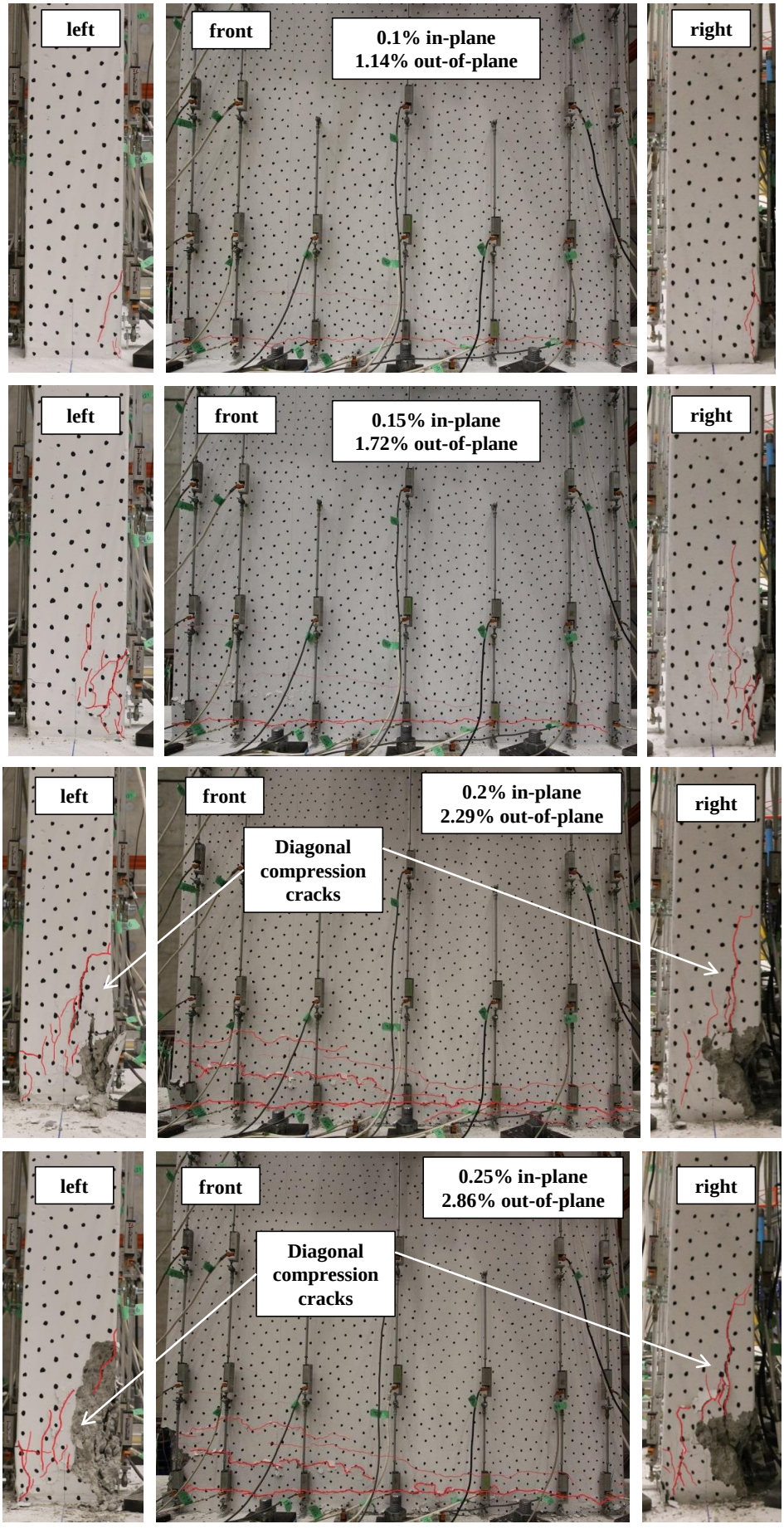

Figure 5-41 Crack patterns of SP3-LD at the third cycle of each different drifts

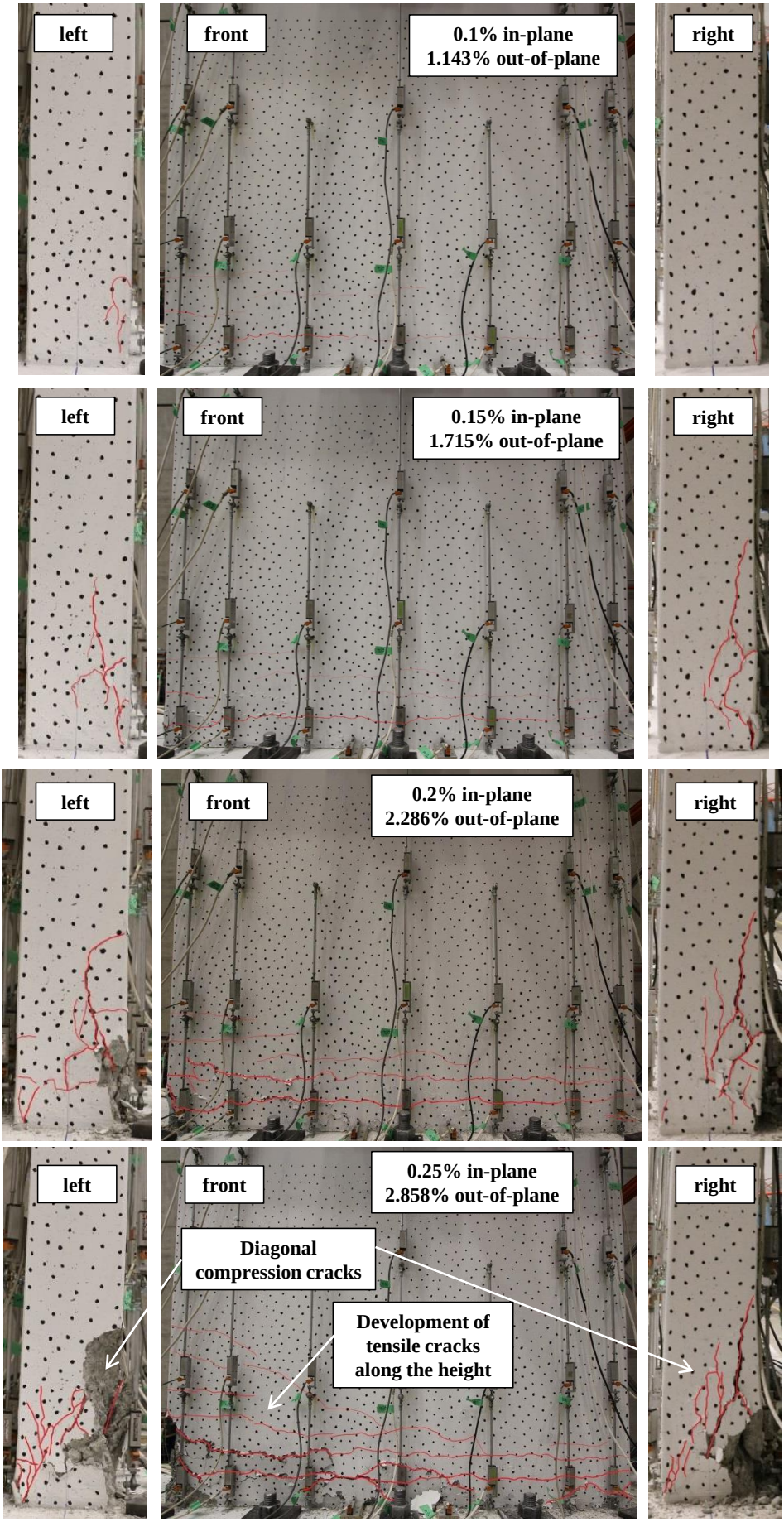

Figure 5-42 Crack patterns of SP4-D at the third cycle of each different drifts

5.3.5. Out-of-plane displacement pattern

Figure 5-43 shows the out-of-plane displacement pattern of the specimen SP2-ND just before and after out-of-plane shear failure. Figure 5-43 nicely shows how the wall slid by 23mm in the out-of-plane direction upon out-of-plane shear failure. Such out-of-plane sliding was not observed in the case of SP3-LD and SP4-D.

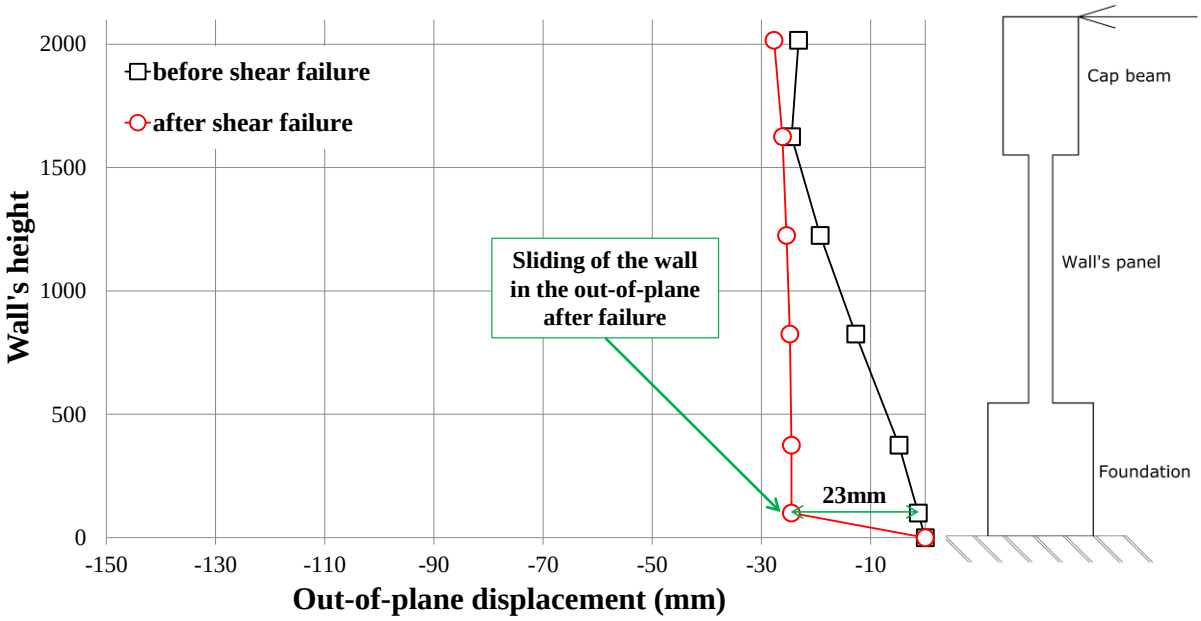

Figure 5-43 Out-of-plane displacement before and after shear failure in SP2-ND

5.4. OUT-OF-PLANE SHEAR FAILURE MECHANISM

In this section, out-of-plane shear failure mechanism is scrutinized and described based on the experimental observations, 2D strain profiles and a simple strut and tie model. Figure 5-44 shows the 2D strain profile and the strut and tie model of the specimen SP2-ND at the peak points of the first cycle of 0.15% in-plane and 1.72% out-of-plane drift ratios. Hatched area of the strain profile shows parts of the wall in compression. It can be seen that failure of the orthogonal strut showed in red in Figure 5-44, significantly increases the force in the diagonal strut and therefore initiation of out-of-plane diagonal compression cracks. The strut and tie model shows the direction of the diagonal cracks that expects to form under such lateral loading pattern which matches the experimental observations. It is worth noting that the strain profile plane is also diagonal which needs 3D strain profile to properly show that. Figure 5-45 shows the specimen at the peak points of the second cycle of 0.15% in-plane and 1.72% out-of-plane drift ratios. Looking at Figure 5-45, it can be seen that with the increase in the compressive strain along the wall, forces in the diagonal strut and consequently the out-of-plane diagonal compression cracks increased. It can also be seen during pushing (loading

the left-front corner), full thickness of the wall with a depth of 235mm was in compression which shows the penetration of the out-of-plane diagonal compression cracks along the length of the wall.

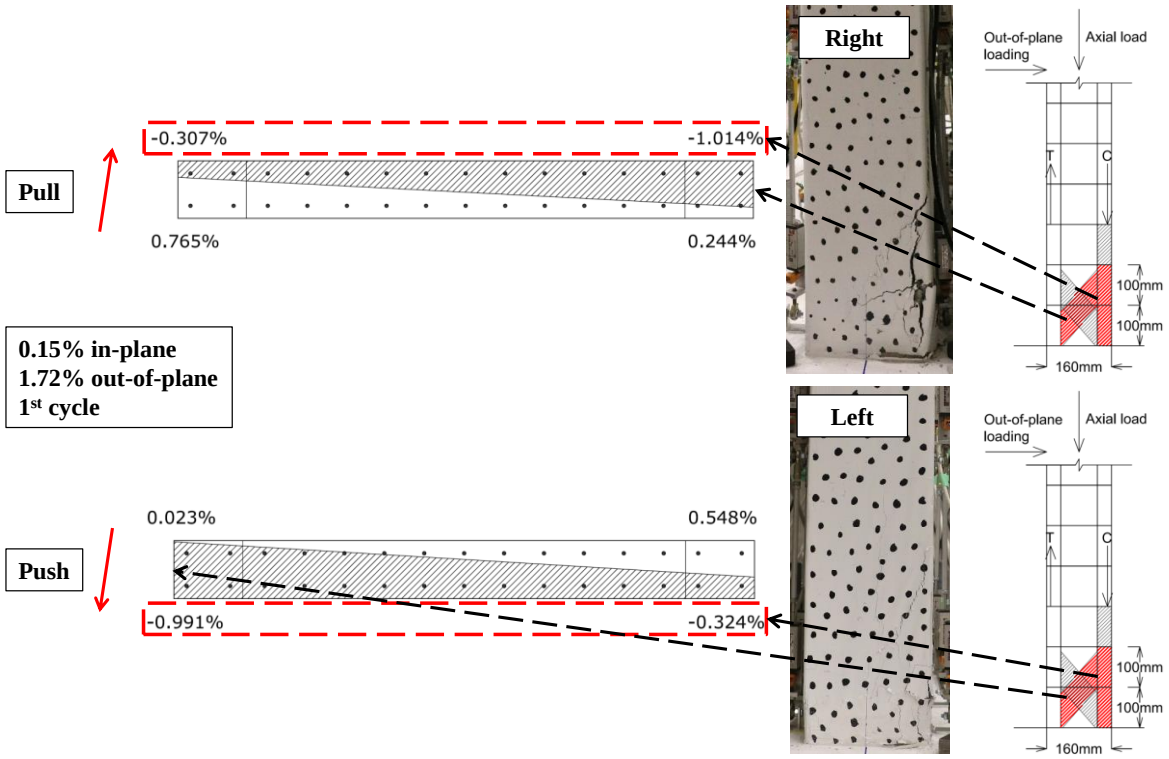

Figure 5-44 Strut and tie model of specimen SP2-ND at the first cycle of 0.15% in-plane and 1.72% out-of-plane drift ratios

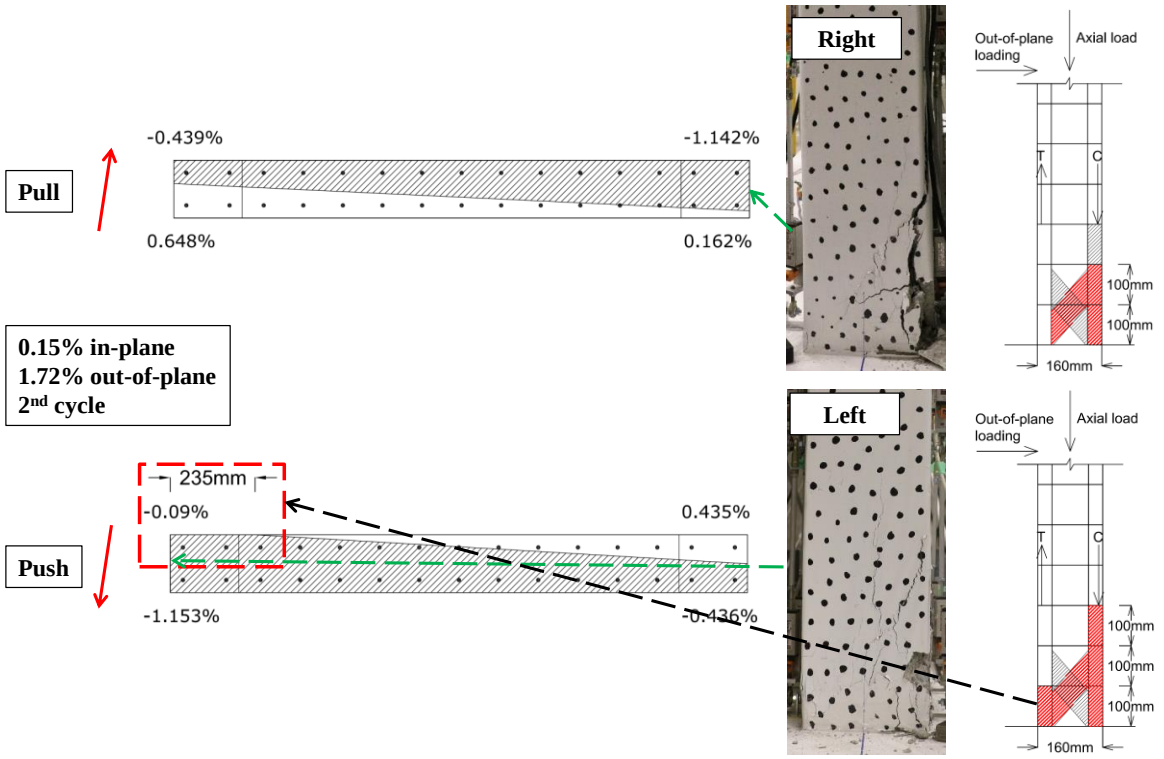

Figure 5-45 Strut and tie model of specimen SP2-ND at the second cycle of 0.15% in-plane and 1.72% out-of-plane drift ratios

During the peak points of the third cycle of 0.15% in-plane and 1.72% out-of-plane drift ratios (Figure 5-46), the penetration length of the diagonal compression cracks on the left side further increased to about 600mm (37.5% of the wall's length). During this drift cycle, full diagonal crack were visible along the thickness as the neutral axis depth in the out-of-plane was the full thickness of the wall.

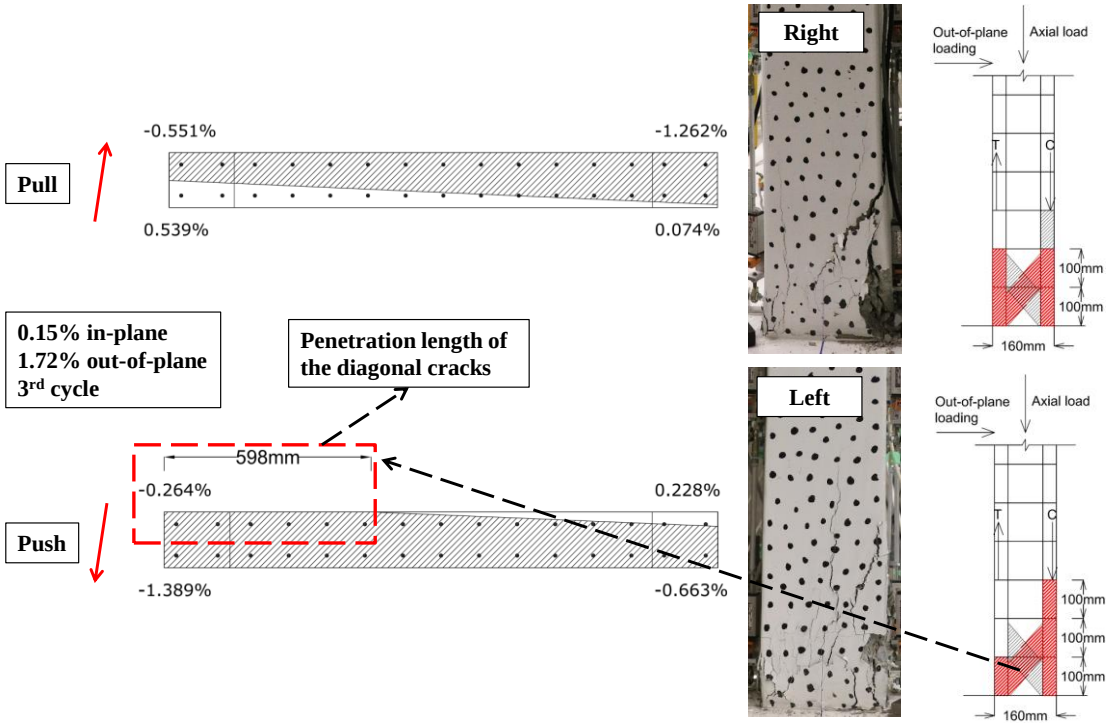

Figure 5-46 Strut and tie model of specimen SP2-ND at the third cycle of 0.15% in-plane and 1.72% out-of-plane drift ratios

Figure 5-47 shows the 2D strain profile of the wall just before failure during pulling (half way through the peak, loading the right-back corner). It can be seen that the whole wall was in compression and while the orthogonal struts on both sides (front and back) had failed and the diagonal struts were extensively cracked in compression, the out-of-plane shear applied to the right-back corner led to sliding of the wall to that direction. The name out-of-plane shear failure was chosen to reflect the shear force that led to the final failure of the wall. However, the final shear failure could have been the sliding to either back or front sides of the wall. In the case of SP2-ND since the penetration length of the diagonal cracks on the left side of the wall was considerably larger than the right side, the final failure mode was sliding to the back side of the wall (see Figure 5-46). Figure 5-47 shows the shear force that led to sliding and shear failure of the wall as a result of the out-of-plane and axial forces along the diagonal crack angle. What makes this failure mode interesting and complicated at the same time is the fact that the direction of the shear force that led to the final failure of the wall differs from the one that developed diagonal compression cracks along the wall. It is worth mentioning again,

one of the main reasons that the diagonal cracks were able to penetrate the entire length of the wall was bi-directional loading and its effects on the compression area.

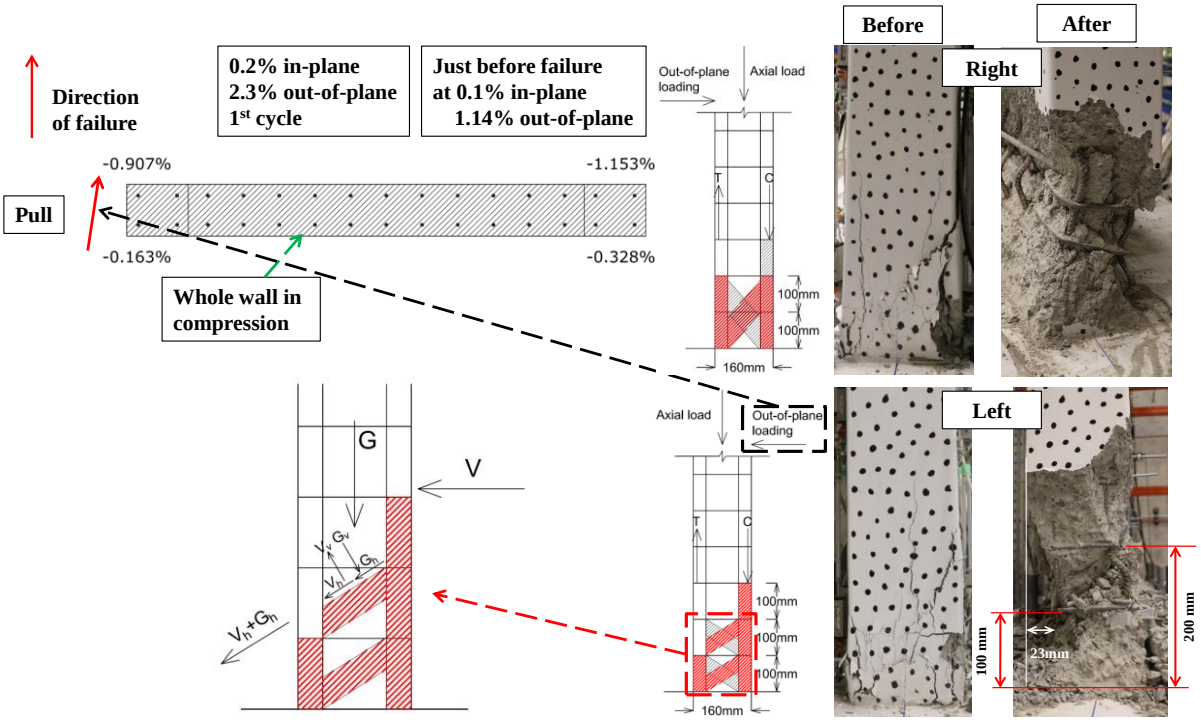

Figure 5-47 Strut and tie model of specimen SP2-ND just before failure

5.5. CONCLUSIONS

In an attempt to gain a better understanding on the seismic performance of walls prone to out-of-plane shear failure and the mechanics of this failure mode, a RC wall that was prone to out-of-plane shear failure based on numerical simulation was designed for a limited ductile and ductile section detailing according to NZS3101:2006-A3 (2017). These three walls were tested under high axial load ratio and bi-directional loading. The main conclusions of this series of experiments were categorized based on some of the key research questions regarding the effects of bi-directional loading on RC walls prone to out-of-plane shear failure. The key findings concerning each of these research questions were presented in the following sub-sections.

Out-of-plane shear failure mechanism

- Experimental results presented in this chapter showed that out-of-plane shear failure involves a diagonal sliding transverse to the wall, penetrating certain length of the wall. In case of a full out-of-plane shear failure it would be along the full length of the wall.

- Based on the observations of the 2011 New Zealand earthquake and experimental results, it was observed that out-of-plane shear failure shortens the wall along its height and create a total instability in the wall.
- As out-of-plane shear failure shortens the wall, during sliding, depends on the longitudinal reinforcement ratio it can lead to full rupture of the longitudinal bars along the wall.
- Based on the experimental investigations on the behaviour of the wall in the strain level, it was found that lateral loading pattern and axial load ratio are two of the key parameters that can cause out-of-plane shear failure by developing compression along the full length of the wall. When the full length of the wall is in compression it will lead to cover concrete spalling and therefore increases the diagonal force inside the concrete core. This will lead to initiation of diagonal compression cracks in the two corners of the wall. When the diagonal compression cracks develop and their penetration depth along the wall increases, a shear force in the opposite direction can lead to sliding of the wall and out-of-plane shear failure in case of insufficient out-of-plane shear capacity.
- Transverse reinforcement along the wall can prevent out-of-plane shear failure by increasing the out-of-plane shear and concrete compressive strain capacities of the wall.

Effects of section detailing ductility on walls prone to out-of-plane shear failure

One of the research objectives of this experimental study was to investigate whether increasing the section detailing ductility can prevent out-of-plane shear failure in RC walls prone to this failure mode or not. In another words, whether Wall D5-6 from Grand Chancellor Hotel would perform better in the 2011 New Zealand earthquake if it had better section detailing ductility or not. For this purpose, a wall prone to out-of-plane shear failure was designed for limited ductile and ductile section detailing according to NZS3101:2006-A3 (2017) and tested under bi-directional loading. The main findings regarding this research question are presented below.

- It was found that while the wall designed for nominal section detailing ductility failed in out-of-plane shear, designing the walls for limited ductile and ductile section detailing successfully prevented this unexpected and sudden failure mode. Significant contribution of transverse reinforcement in out-of-plane shear and concrete

compressive strain capacities helps the wall to resist sliding in the out-of-plane direction.

- Based on the experimental observations of the current study, out-of-plane diagonal compression cracks still form in walls prone to out-of-plane shear failure designed for limited or ductile section detailing when subjected to bi-directional loading. Although it's not likely that these walls fail in out-of-plane shear, but considerable cover concrete spalling will occur along the full length of the wall as a result of high axial load and bi-directional loading. Concrete spalling along the wall will reduce the axial capacity and consequently leads to an axial crushing failure in the wall. However, such axial crushing failure will occur after the wall undergo significant out-of-plane drift well beyond the drift ratio that a structure would be designed for.
- Anti-buckling ties in the web not only proved to be effective against buckling of the web's longitudinal bars but also help against out-of-plane shear failure in walls prone to this failure mode by increasing the out-of-plane shear and concrete compressive strain capacities of the wall.

Effects of axial load ratio on walls prone to out-of-plane shear failure

- Based on the investigations on the tensile and compressive strains of the specimens, it was found that in walls prone to out-of-plane shear failure, unlike most RC walls, tensile strain is lower than compressive strain. Axial load ratio is one of the key parameters in increasing the compressive to tensile strain ratio in the wall which found to be influential in the development of out-of-plane shear failure.
- 2D section strain profile of the specimen failed in out-of-plane shear showed that the full length of the wall needs to have compressive strain higher than the concrete crushing point. Axial load ratio had significant contribution in causing the full length of the wall to be in compression when combined with bi-directional loading.

Effects of longitudinal reinforcement ratio on walls prone to out-of-plane shear failure

Longitudinal reinforcement increase the out-of-plane shear capacity of the wall through their dowel action and can help decreasing the susceptibility of the wall to out-of-plane shear failure or at least delay such failure mode. Due to the limitations with the number of specimens in the current experimental study, effects of this parameter was not investigated properly as the amount of longitudinal reinforcement ratio was constant between the three specimens. However, comparing the performance of Wall D5-6 from Grand Chancellor Hotel

in the 2011 New Zealand earthquake (see Figure 1-4) with similar wall (specimen SP2-ND presented in this chapter) with higher longitudinal reinforcement ratio (almost by two times) tested in this experimental study showed that increasing the amount of longitudinal reinforcement ratio can prevent the full rupture of the longitudinal bars along the wall.

Effects of lateral load path on walls prone to out-of-plane shear failure

Experimental investigations presented in this chapter showed that the full length of the wall of the specimen failed in out-of-plane shear had compressive strain higher than concrete crushing point which is essential for a full out-of-plane shear failure to happen. Lateral loading pattern applied to the walls in this set of experiments (a skewed loading with an 85 degree angle with respect to the in-plane axis) found to be one of the key parameters that causes such high compressive strain along the wall. The full length of the wall wouldn't be in compression if the lateral loading pattern of the wall had lower loading angle with respect to the in-plane axis.

Crack pattern of walls prone to out-of-plane shear failure

In-plane and out-of-plane crack patterns of walls prone to out-of-plane shear failure with different section detailing ductility were investigated in details in Section 5.3.4. The key findings of this investigation are presented below.

- Concentration of cracks was mainly at the base and top of the wall ruled by the double bending deformation shape of the wall in the out-of-plane direction. A main horizontal crack along the wall formed at a height of about 85-110 mm above the base.
- In case of walls with higher section detailing ductility (limited or ductile levels), in-plane tensile cracks had a better distribution along the height compared to the wall with lower ductility in which cracks concentrated mostly above the base.

6. FINITE ELEMENT MODELLING OF RECTANGULAR SLENDER REINFORCED CONCRETE WALLS UNDER UNI- AND BI-DIRECTIONAL LOADINGS

6.1. INTRODUCTION

As was discussed in Chapter 1, so far only a few experimental studies investigated the effects of bi-directional loading on rectangular reinforced concrete (RC) walls. For the same reason, a limited number of numerical studies were conducted on this type of wall subjected to bi-directional loading in the past. The only numerical study that was found on rectangular RC walls subjected to bi-directional loading was conducted by Tatsuya (1996). They used fiber analysis for further investigations on their experimental study on rectangular RC walls under bi-directional loading. Therefore, in this thesis, a numerical model had to be developed and validated for the numerical part of the study on rectangular RC walls subjected to bi-directional loading. The Finite Element (FE) software, DIANA (DIANA 2015), was used to simulate rectangular slender RC walls subjected to uni- and bi-directional loadings. Some of the features that led to the selection of this software were the ability to model nonlinear behaviour of concrete (compressive and tensile behaviour), availability of material models to incorporate cyclic loading, variety of elements, capability of simulating different loading patterns include bi-directional loading and the ability to capture complex failure modes such as lateral instability and out-of-plane shear. DIANA was used before for numerical investigations on RC beam-column joints (Deaton 2013, Soleymani Ashtiani et al. 2014) and RC walls (Hube and Mosalam 2011, Dashti et al. 2014, Junemann et al. 2016a, Junemann et al. 2016b) and proved to be a powerful software for capturing the behaviour of RC structures. This chapter first presents the FE model in details and then discusses the comprehensive validation of the model by comparing with available experimental results. In order to validate the model, one of the specimens tested by Segura and Wallace (2017) and the six specimens tested in the current study (presented in Chapters 2, 3, 4 and 5) were chosen.

6.2.MATERIAL MODELS

6.2.1. Concrete: total strain rotating crack model

Total strain rotating crack model developed along the lines of the Modified Compression Field Theory developed by Vecchio et al. (1986) was used to simulate concrete behaviour. This model follows a smeared crack approach for the fracture energy (Litton 1975). In the smeared crack concept, a cracked solid is assumed to be a continuum. The procedure is attractive not only because it preserves the topology of the original finite element mesh, but also because it does not impose restrictions with respect to the orientation of the crack planes, i.e. the axes of orthotropy (Rots and Blaauwendraad 1989).

Compressive behaviour: The model proposed by Mander et al. (1988) was used to define confined and unconfined concrete (Figure 6-1a). The modulus of elasticity of concrete was estimated using Equation 6-1 proposed by Priestley et al. (2007).

$$E_c(MPa) = 5000\sqrt{f_c'(MPa)} \qquad 6\text{-}1$$

Where in Equation 6-1, $f_c^{'}$ is the compressive strength of concrete.

The ultimate compressive strain of concrete, ε_{cu}, was calculated using Equation 6-2 proposed by Priestley et al. (1996) which is a conservative estimate of the method proposed by Mander et al. (1988).

$$\varepsilon_{cu} = 0.004 + 1.4\rho_s f_{yh}\varepsilon_{su}/f_{cc}' \qquad 6\text{-}2$$

Where in Equation 6-2, ρ_s is the volumetric ratio of confining steel ($\rho_s=\rho_x+\rho_y$), $\rho_x=A_{vx}/(d_c\times s)$, $\rho_y=A_{vy}/(b_c\times s)$, b_c and d_c are the core dimensions to centrelines of perimeter hoop in x and y directions, f_{yh} is the yield stress of transverse reinforcement, ε_{su} is the ultimate strain of transverse reinforcement (assumed 6% in this study, proposed by Kowalsky (2000) and NZSEE (2017)) and $f_{cc}^{'}$ is the maximum confined concrete stress.

Tensile behaviour: One of the other inputs required for the total strain rotating crack model is the concrete response under uniaxial tensile loading. Here the tensile behaviour of concrete was defined following the model proposed by Belarbi and Hsu (1994) (Figure 6-1b). Mathematical expression of this model is presented in Equations 6-3 and 6-4.

$$\sigma_r = E_c\varepsilon_r \quad for \quad \varepsilon_r \le \varepsilon_{cr} \qquad 6\text{-}3$$

$$\sigma_r = f_{cr}\left(\frac{\varepsilon_{cr}}{\varepsilon_r}\right)^{0.4} \quad for \quad \varepsilon_r > \varepsilon_{cr} \qquad 6\text{-}4$$

In Equation 6-4, tensile strength of concrete, f_{cr}, was calculated based on Equation 6-5 proposed by Belarbi and Hsu (1994).

$$f_r(MPa) = 0.31\sqrt{f_c'(MPa)} \qquad 6\text{-}5$$

Figure 6-2 shows the monotonic and cyclic curves adopted in the FE model for concrete compressive and tensile behaviour. As can be seen, the cyclic response does not account for the residual strain and the unloading/reloading loops always pass through the origin with secant stiffness. Although this reduces the accuracy of the FEA in predicting cyclic response of concrete, the model is capable of capturing the overall response of the member (Hube and Mosalam 2011, Deaton 2013, Soleymani Ashtiani 2013, Dashti et al. 2014, Soleymani Ashtiani et al. 2014, Junemann et al. 2016a, Junemann et al. 2016b).

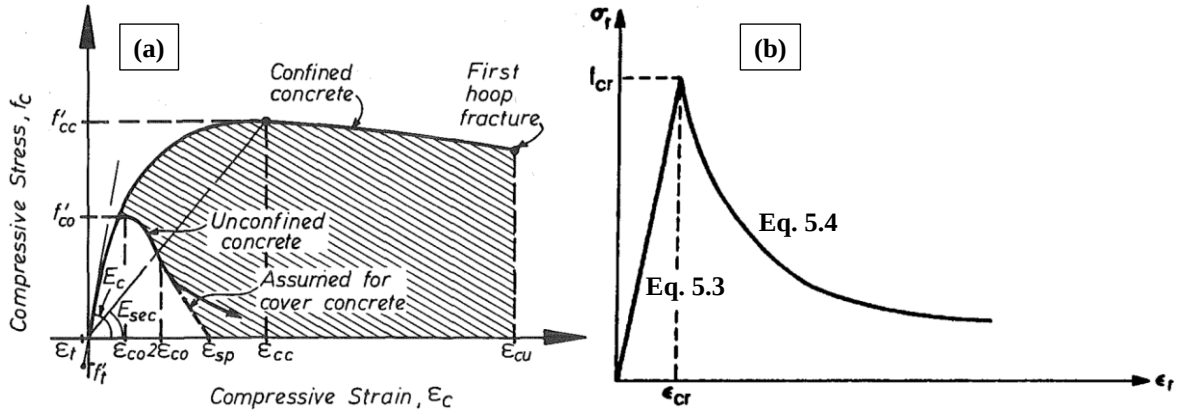

Figure 6-1 Constitutive models of concrete (a) compressive (Mander et al. 1988) and (b) tensile (Belarbi and Hsu 1994)

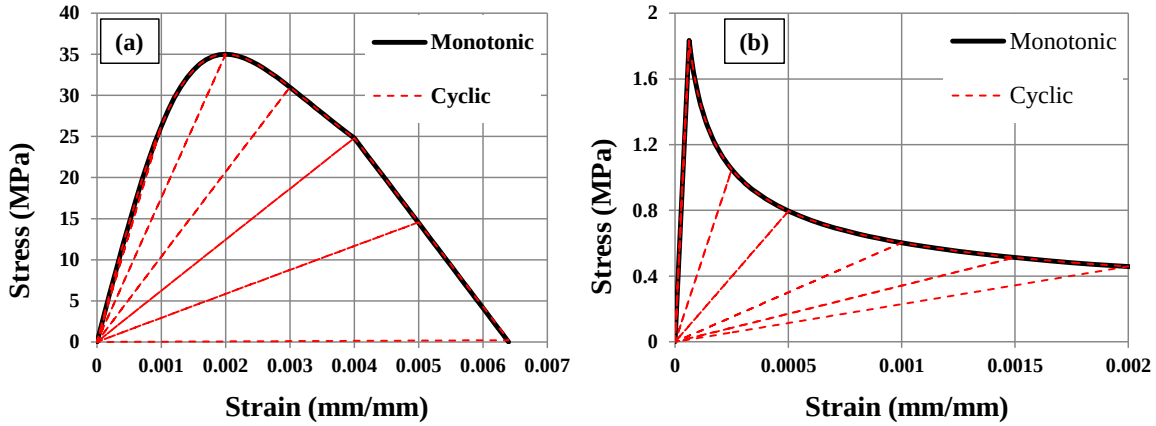

Figure 6-2 Monotonic and cyclic curves adopted in the model for concrete in (a) compression and (b) tension

6.2.2. Steel reinforcement: Menegotto-Pinto model

The Menegotto-Pinto model (Menegotto and Pinto 1973), which has a bilinear backbone curve and considers Bauschinger effect, was used to model the steel behaviour (Figure 6-3a). As pointed out by Filippou et al. (1983), isotropic hardening can significantly affect the

cyclic behaviour of reinforcing bars in RC members. It can have a substantial effect on strain development in bars during crack closure. The stress shift to the yield asymptote proposed by Filippou et al. (1983) (Figure 6-3b) improves the Menegotto-Pinto model in strain prediction of reinforcing bars. It is worth noting that these modifications are implemented in the Menegotto-Pinto model in DIANA software (DIANA 2015). Due to the limitation of Menegotto-Pinto constitutive model, here bar buckling was not considered in the analysis.

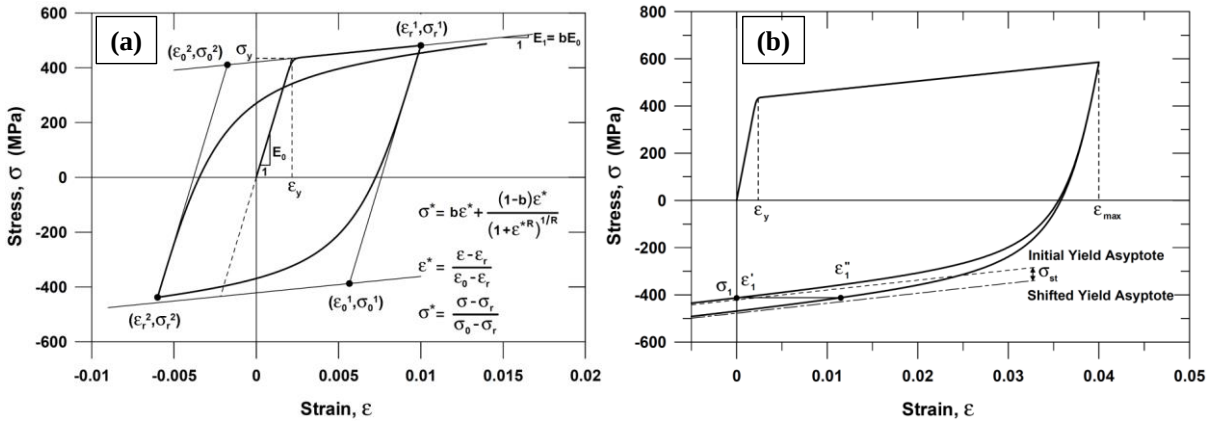

Figure 6-3 Steel reinforcement model (a) Constitutive model (Menegotto and Pinto 1973, Orakcal et al. 2006) and (b) Stress shift due to isotropic strain hardening (Filippou et al. 1983, Orakcal et al. 2006)

The other important parameter considered in the FE model was the effect of so called "reinforcing bars stiffening". As was pointed out by Belarbi and Hsu (1994), the stress-strain curve of a steel bar embedded in concrete does not show the long plateau after yielding; this is usually observed in a bare bar tensile test (Figure 6-4).

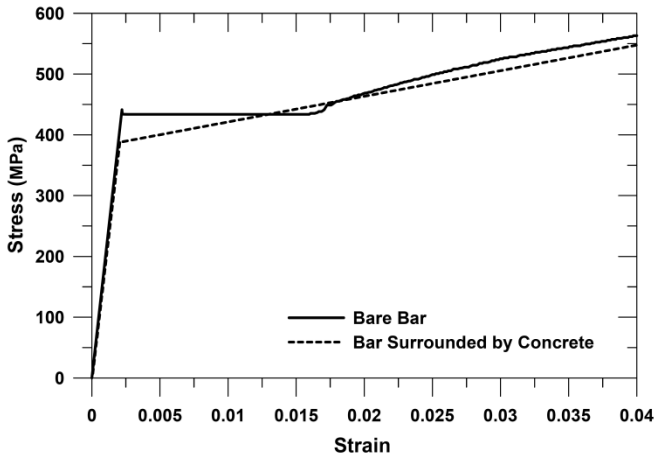

Figure 6-4 Effect of tension stiffening on reinforcing bars (Belarbi and Hsu 1994, Orakcal et al. 2006)

One of the differences found by Belarbi and Hsu (1994) was that the yield stress, f_y, of the steel bar embedded in concrete was lower than the same bar tested alone. Belarbi and Hsu (1994) also found that the strain-hardening slope (plastic modulus) of the steel bar embedded in concrete differs from the plastic modulus of a bare bar.

Based on evaluation and characterization of experimental data from the RC panels, Belarbi and Hsu (1994) proposed a bilinear constitutive model for steel bars embedded in concrete (Figure 6-5).

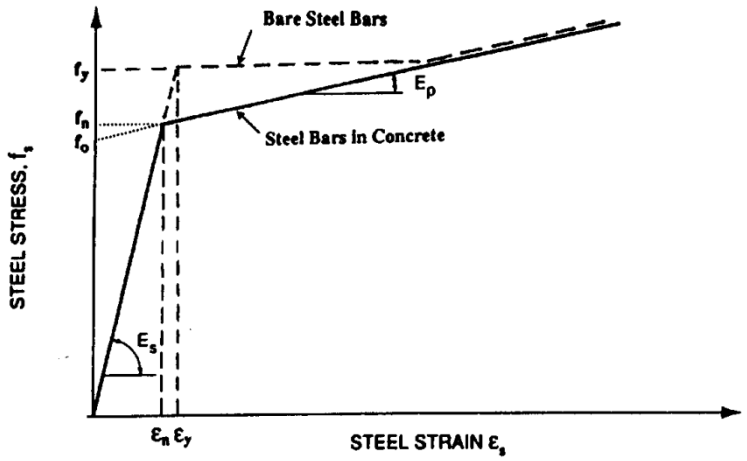

Figure 6-5 Stress-strain curve for reinforcing bars embedded in concrete (Belarbi and Hsu 1994)

The stress at the intersection of the two lines, f_n, and the plastic slope, E_p, are given by Equations 6-6 and 6-7.

$$f_n = (0.93 - 2B) f_y \qquad 6\text{-}6$$

$$E_p = (0.8b + 0.25B) E_s \qquad 6\text{-}7$$

Where the parameter B is defined as:

$$B = \frac{1}{\rho}\left(\frac{f_{cr}}{f_y}\right)^{1.5} \qquad 6\text{-}8$$

In the equations above, f_y and E_s are the yield stress and modulus of elasticity of the bare bars, b is the strain-hardening ratio (E_p/E_s), ρ is the cross-sectional area ratio of the longitudinal steel bars in the RC element, and f_{cr} is the concrete cracking stress, obtained according to the relation in Equation 6-5.

6.3.ELEMENTS

6.3.1. Solid vs shell elements

DIANA provides a wide selection of different elements. Solid and shell elements are the two possible options to simulate RC walls. Depending on the geometry of the wall, boundary conditions and the possible failure modes, shell or solid elements can be used to simulate RC walls. However, if a more detailed investigation is required, solid elements should be used (Figure 6-6).

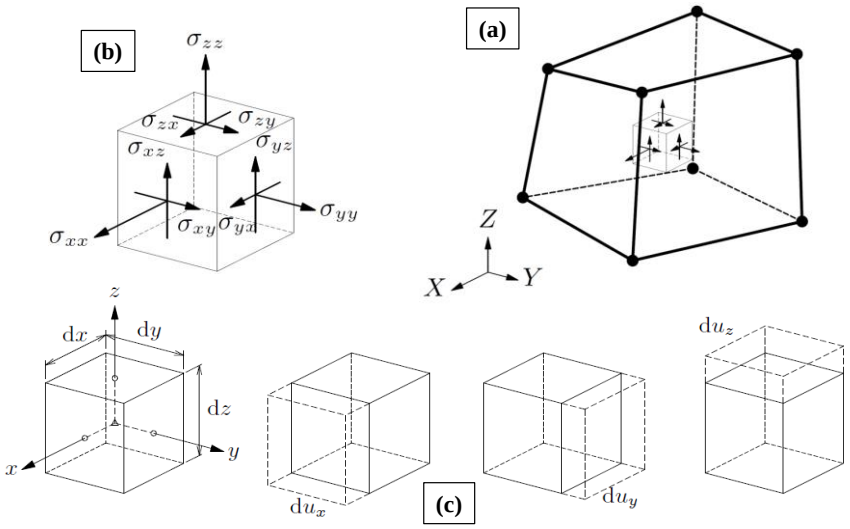

Figure 6-6 Solid elements (a) characteristics, (b) Cauchy stresses and (c) deformation (DIANA 2015)

There are several benefits that can be obtained when using solid elements compared to shell ones. The main advantages of solid elements over other available shell elements such as curved shell in regard to the current study are discussed below:

1. In curved shell elements, the in-plane strains ε_{xx}, ε_{yy} and γ_{xy} vary linearly in the thickness direction while solid elements do not have such limitation (DIANA 2015).
2. Transverse shear strains γ_{xz} and γ_{yz} are forced to be constant in the thickness direction in curved shell elements, while the actual transverse shearing stresses and strains vary parabolically over the thickness (DIANA 2015).
3. Due to the limitations of shell elements with calculating stress and strain along the thickness, it was found that capturing the seismic performance of RC walls prone to out-of-plane shear failure subjected to bi-directional loading is not possible when using curved shell elements (see Section 6.5.5 for further details).

6.3.2. Solid elements

Brick 8 nodes (HX24L) and 20 nodes (CHX60) elements are the two options available in DIANA for solid elements that could be used for concrete material (Figure 6-7). Depends on the case, each of these elements could be used.

For a rectangular 8nodes brick element, DIANA approximates the following strain and stress distribution over the element volume. The strain ε_{xx} and stress σ_{xx} are constant in x direction and vary linearly in y and z direction. The strain ε_{yy} and stress σ_{yy} are constant in y direction and vary linearly in x and z direction. The strain ε_{zz} and stress σ_{zz} are constant in z direction and vary linearly in x and y direction. By default DIANA applies a 2×2×2 integration scheme for 8nodes elements.

However, for a rectangular 20nodes brick element, the strain ε_{xx} and stress σ_{xx} vary linearly in x direction and quadratically in y and z direction. The strain ε_{yy} and stress σ_{yy} vary linearly in y direction and quadratically in x and z direction. The strain ε_{zz} and stress σ_{zz} vary linearly in z direction and quadratically in x and y direction. By default DIANA applies a 3×3×3 integration scheme for 20nodes elements.

Here the default values were used for both of these elements as was recommended by DIANA (2015). Examples of different integration schemes are shown in Figure 6-8. In Section 6.5.1, the capability of these two elements in simulating RC walls under bi-directional loading is evaluated.

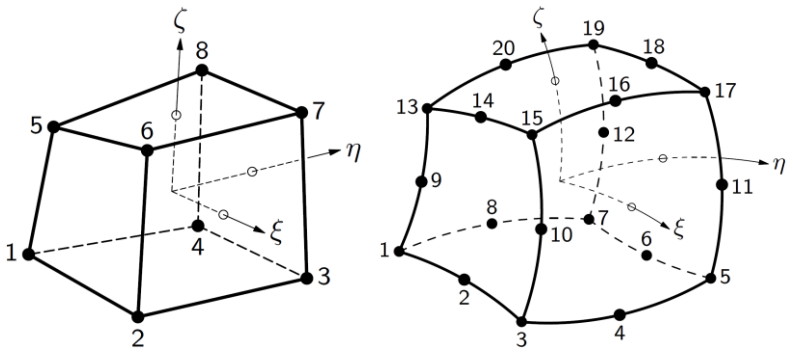

Figure 6-7 Solid elements in DIANA, brick 8 nodes (HX24L) and 20 nodes (CHX60) (DIANA 2015)

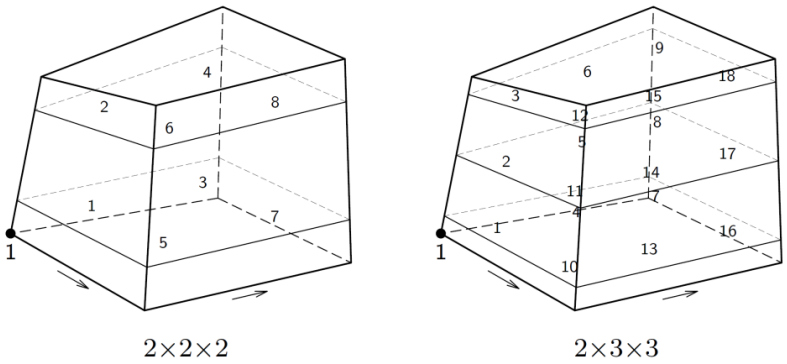

Figure 6-8 Integration schemes examples (DIANA 2015)

6.3.3. Truss elements

Longitudinal, horizontal and boundary zone (BZ) transverse reinforcement were modelled using truss elements (Figure 6-9). In DIANA, reinforcing steel bars can be modelled using embedded reinforcement, discrete reinforcement and bond-slip reinforcement. The common way to consider bond-slip response in the FE analysis is to use embedded reinforcement and couple them with the bond-slip option. However, if a more detailed bond-slip analysis is required, discrete reinforcement elements can be employed and connected to concrete using interface elements (such as bond-slip).

In the current study, perfect bond between the reinforcement and the surrounding concrete was considered. The main reason was the limitation of the current version of DIANA (2015) in coupling the bond-slip for embedded reinforcement with the Menegotto-Pinto model (1973). Therefore, if bond-slip has to be considered, the Menegotto-Pinto model should be replaced with the von Mises Plasticity or other available models for the reinforcement. However, the latter option was found to be less effective in predicting the cyclic response of steel bars and overestimates the energy dissipation in each cycle. It is worth noting that although using other types of elements for modelling steel reinforcement (e.g. solid elements) would help with modelling bar buckling and rupture to a certain level, it would not allow using Menegotto-Pinto model in the current version of DIANA.

Figure 6-10 shows a typical view of solid and truss elements in DIANA.

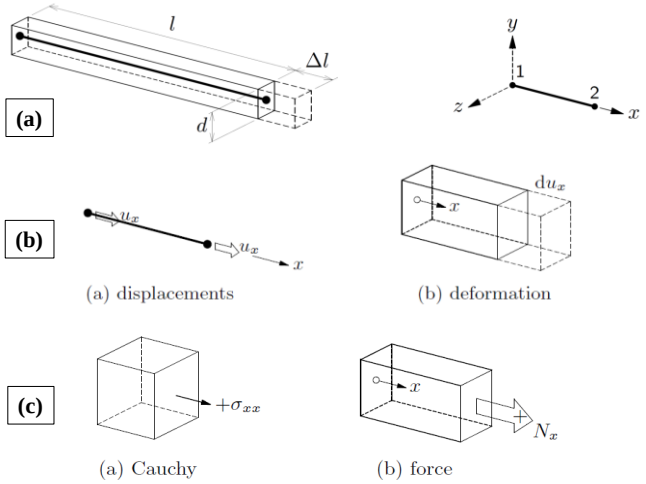

Figure 6-9 Truss elements (a) characteristics, (b) deformation and (c) stress (DIANA 2015)

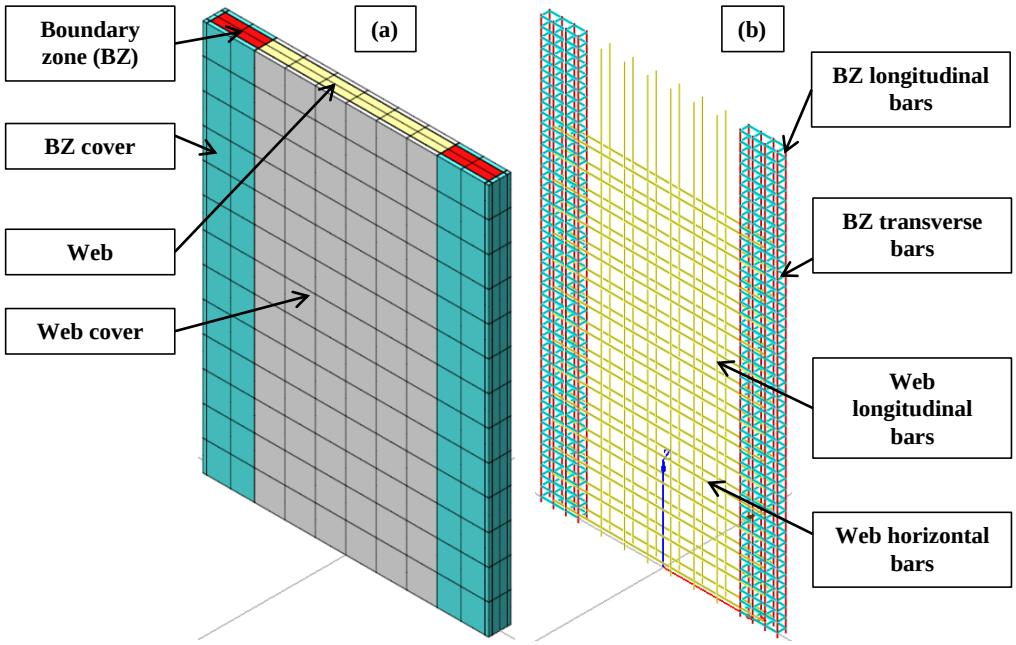

Figure 6-10 Typical view of the elements in DIANA (a) solid and (b) truss

6.4. GEOMETRIC NONLINEARITY

When nonlinear displacement-strain relation is involved in the structure, it is essential to consider geometric nonlinearity in the analysis. Diana offers two types of geometrically nonlinear analysis: a Total Lagrange and an Updated Lagrange description (Bathe 2006, Crisfield et al. 2012). In this study, Total Lagrange is used to consider both small and large geometrical nonlinearities. In a Total Lagrange description, strain and stress measures are defined with reference to the undeformed geometry. It should be noted that p-delta effect is also included in the geometric nonlinearity.

6.5. VERIFICATION OF THE FE MODEL

In order to validate the FE model presented in Section 6.2 and 6.3, seven walls namely WP1 (Segura and Wallace 2017), SP1-Uni, SP1-Skew and SP1-Clover (presented in Chapters 2 and 3) and SP2-ND, SP3-LD and SP4-D (presented in Chapters 4 and 5) were chosen. Table 6-1 shows the matrix of the walls used for the FE model validation. In-plane shear span ratio, axial load ratio, lateral loading pattern and the failure mode observed in the lab are shown in Table 6-1.

Table 6-1 Matrix of the RC wall specimens used for validation of the FE model

Number	Name	In-plane Shear span ratio (H_e/L_w)	Axial load ratio, $P/(A_g f'_c)$	Loading pattern		Failure mode observed in the lab
				Type	Schematic view	
1	SP1-Skew	3.75	6.26%	Skewed uni-directional	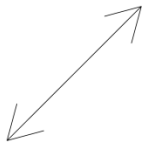	Concrete crushing, bar buckling, web crushing, lateral instability
2	SP1-Uni			In-plane uni-directional	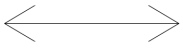	Concrete crushing, bar buckling, lateral instability
3	SP1-Clover			Clover leaf	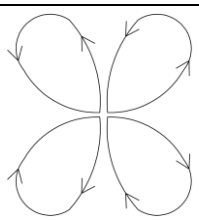	Concrete crushing, bar buckling, lateral instability
4	WP1(Segura and Wallace 2017)	3.744	9.63%	In-plane uni-directional		Concrete crushing, bar buckling
5	SP2-ND	3.75	30%	Skewed uni-directional	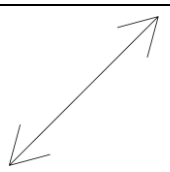	Out-of-plane shear
6	SP3-LD					Axial crushing
7	SP4-D					Axial crushing

For each case, details of each specimen including the geometry, material properties and the loading patterns are presented first and then the FE results are compared with the experimental ones. A comparison between the numerical vs experimental results was carried out with reference to the base shear vs drift ratio curve, the failure mode, crack patterns, strain profile and the out-of-plane displacement evolution.

6.5.1. SP1-Skew

Table 6-2 and Figure 6-11 summarize the basic characteristics of the specimen SP1-Skew. Table 6-3 and Table 6-4 show the material properties of the specimen. Figure 6-12 shows the loading pattern of specimen SP1-Skew. For more information, refer to Chapter 2.

Table 6-2 Details of the specimens SP1-Uni, SP1-Skew and SP1-Clover

Specimen	SP1-Uni, SP1-Skew & SP1-Clover
Clear height, H_w (mm)	2200
Length, L_w (mm)	1600
Thickness, t (mm)	125
Total longitudinal reinforcement ratio, $\rho_t = (A_{s,BZ} + A_{s,web})/(L_w \times t)$	1.95%
Web longitudinal reinforcement ratio	0.55%
Boundary zone (BZ) longitudinal reinforcement ratio	4.15%
BZ transverse reinforcement ratio, $\rho_{sx} = A_{vx}/(s \times t)$	0.75%
BZ transverse reinforcement ratio, $\rho_{sy} = A_{vy}/(s \times l_{BZ})$	0.61%
Web shear reinforcement ratio, $\rho_v = A_{sv}/(s \times t)$	0.84%

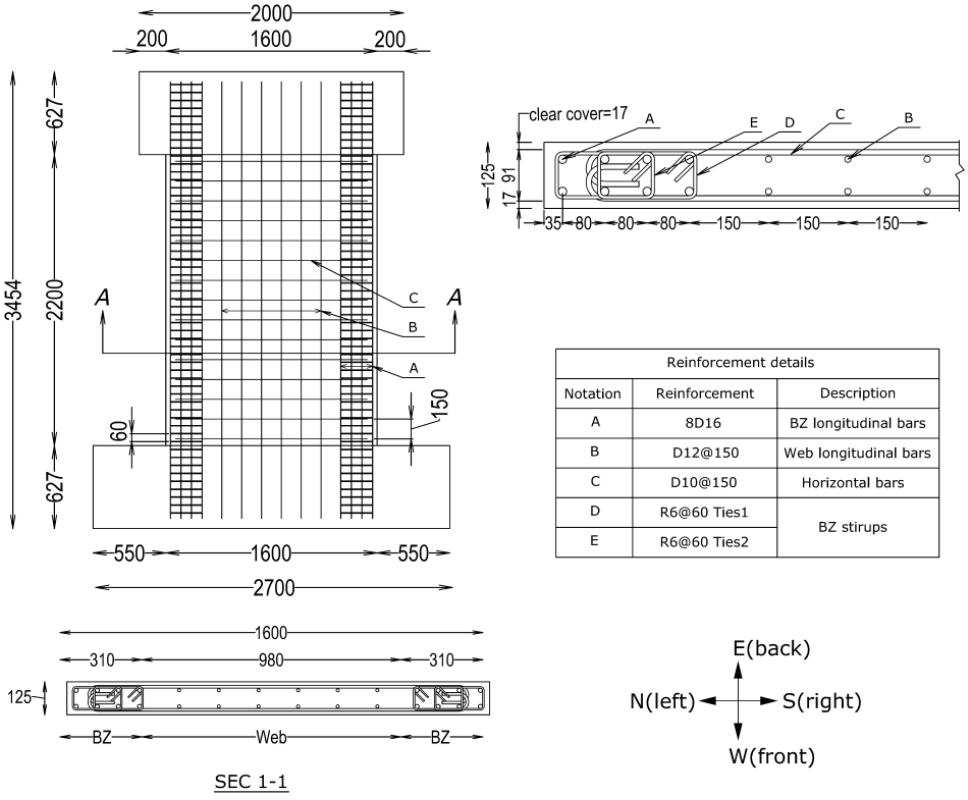

Figure 6-11 Details of the reinforcement layouts of SP1-Uni, SP1-Skew and SP1-Clover

Table 6-3 Steel reinforcing bar properties of SP1-Uni, SP1-Skew and SP1-Clover

Specimen	Bar size	Bar Diameter (mm)	E_s (MPa)	f_y (MPa)	f_u (MPa)	ε_u
SP1-Uni, SP1-Skew and SP1-Clover	R6	6	200918	548	681	0.152
	D10	10	180822	278	385	0.193
	D12	12	171387	334	420	0.13
	D16	16	185210	362	445	0.15

Table 6-4 Concrete cylinder test result for SP1-Skew

Specimen	Average concrete compressive strength (MPa)
SP1-Skew	50.4

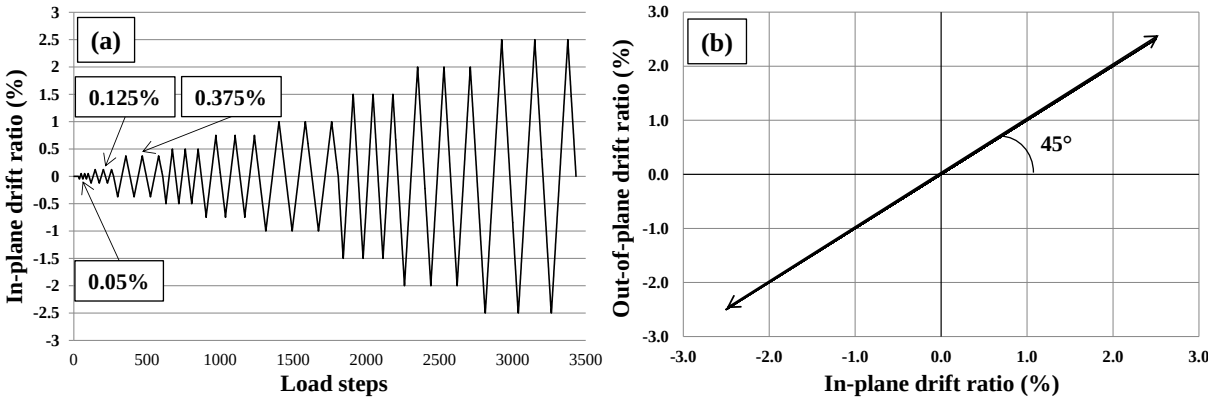

Figure 6-12 Loading pattern of SP1-Skew (a) Loading protocols and (b) Angle of loading

Finite element model and boundary conditions of the specimen are shown in Figure 6-13. It should be noted that since the cap beam's out-of-plane rotation was restrained in specimens SP1-Skew, SP1-Uni and SP1-Clover, the nodes at the midpoints of the cap beam were tied together as shown in Figure 6-13 to restrain the rotation of the cap beam in the out-of-plane direction. These nodes were tied to each other for translations in the Z direction (along the height). It should be noted that SP1-Skew had a double bending deformation shape in the out-of-plane direction and a cantilever deformation shape in the in-plane direction.

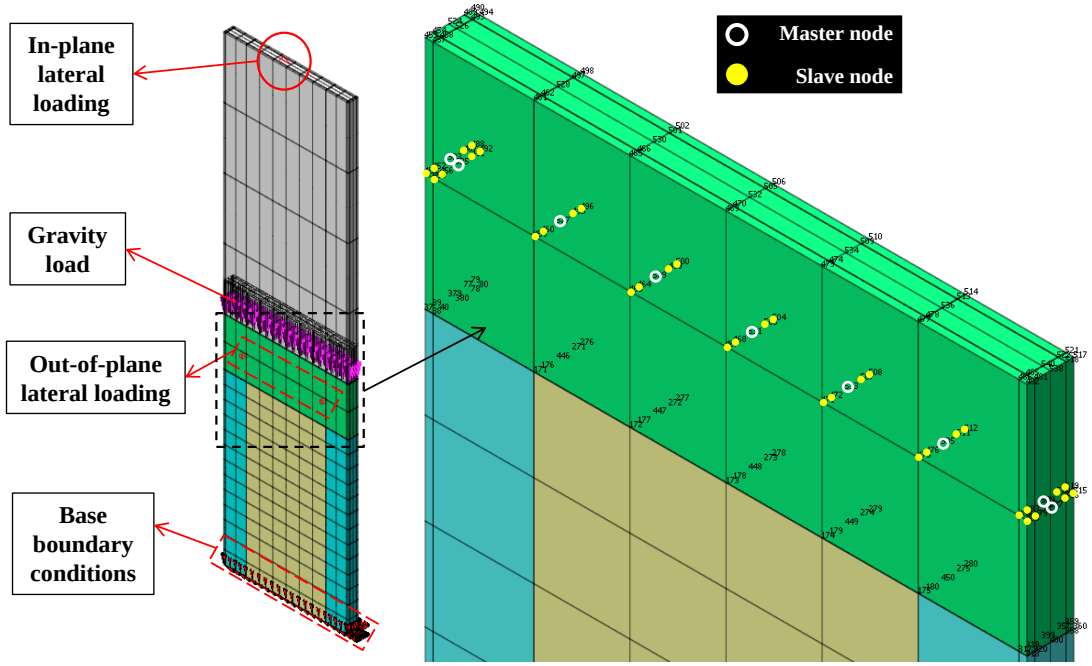

Figure 6-13 Finite element model and boundary conditions of SP1-Skew and SP1-Clover

Brick 8nodes vs 20nodes elements

As was discussed in Section 6.3.2, there are two possible options when using solid brick elements in DIANA. These options are 8nodes and 20nodes elements (Figure 6-7). Capability of these two elements was investigated for specimen SP1-Skew (see Table 6-1). The main reasons for choosing this specimen were:

1. Both in-plane and out-of-plane loadings were involved which allows the behaviour of the wall in both directions to be investigated.
2. The loading pattern was relatively simple compared to clover leaf loading pattern and can be applied monotonically as well.

In order to compare the two types of elements, first, a mesh sensitivity analysis was performed. Geometric nonlinearity was considered in all analysis. Five different mesh configurations described in Table 6-5 and shown graphically in Figure 6-14 were chosen for these analyses. Figure 6-15 and Figure 6-16 show the base shear vs drift ratio curve of the wall when using 8 nodes and 20 nodes elements, respectively.

Table 6-5 Details of each mesh size

Mesh type	Mesh size (mm)				Number of nonlinear elements
	Boundary zone	Web	Along the height	Along the thickness	
a	268.0	511	550	41.5	96
b	268.0	255.5	244.4	41.5	288
c	134.0	170.3	169.2	41.5	624
d	89.3	127.8	129.4	41.5	1088
e	89.3	102.2	100.0	20.8	2376

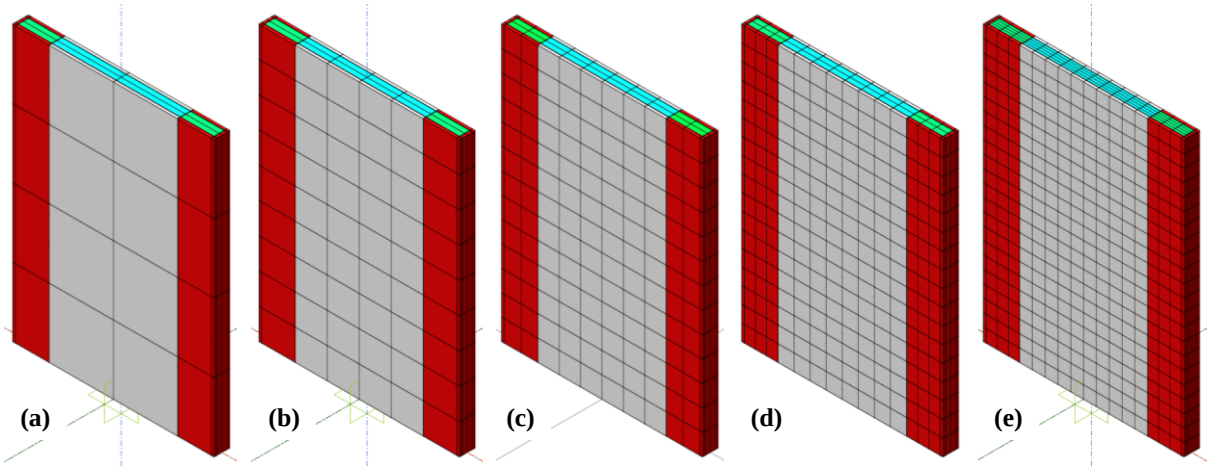

Figure 6-14 Mesh configurations used for the mesh sensitivity analysis

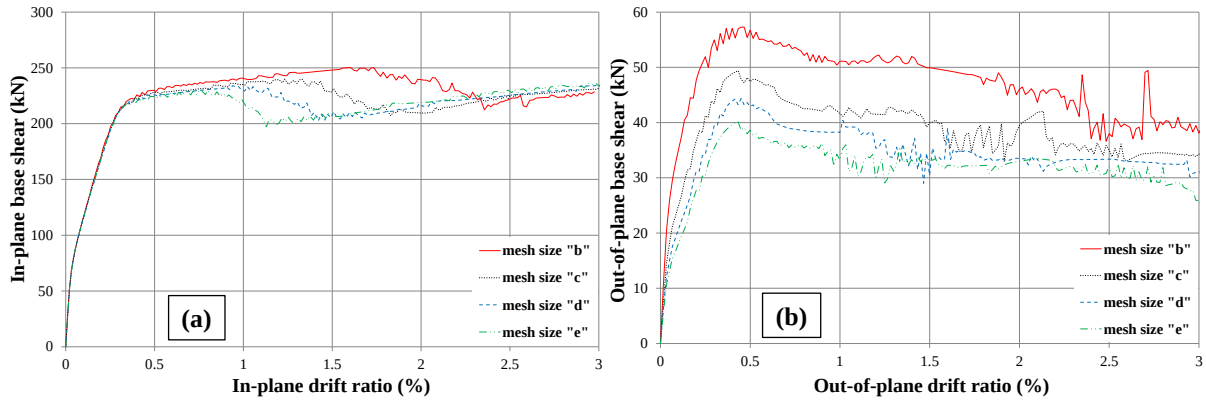

Figure 6-15 Force – drift curves of the wall using 8nodes elements with different mesh configurations in the (a) in-plane and (b) out-of-plane directions

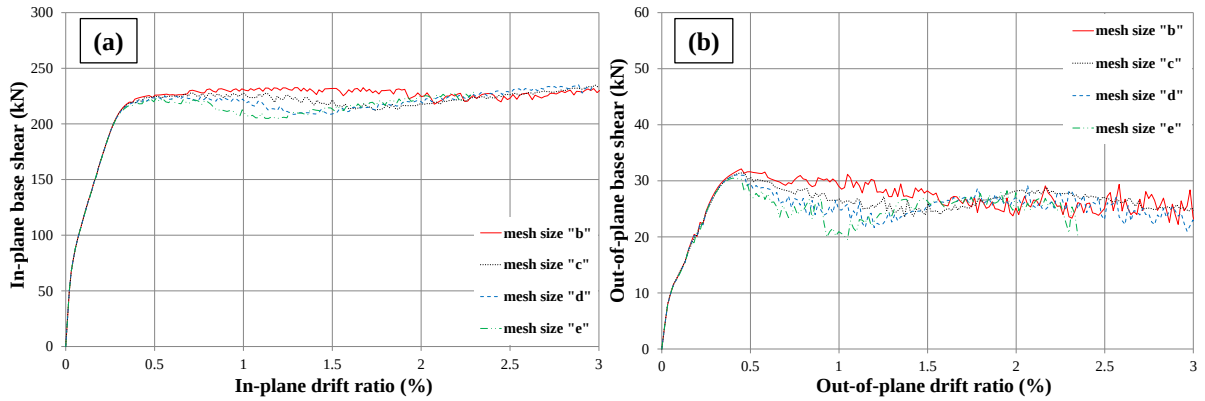

Figure 6-16 Force – drift curves of the wall using 20nodes elements with different mesh configurations in the (a) in-plane and (b) out-of-plane directions

Looking at Figure 6-15 and Figure 6-16, it can be concluded that:

1. In terms of the behaviour of the wall in the in-plane direction (looking at stiffness and strength capacity), both 8nodes and 20nodes elements show relatively similar results (Figure 6-15a and Figure 6-16a). However, 20nodes elements are less sensitive to the mesh size and show less discrepancy with the changes in the number of elements (Figure 6-16a).

2. In terms of the behaviour of the wall in the out-of-plane direction (looking at stiffness and strength capacity), it can be seen when using 8nodes elements the stiffness and strength capacity are decreasing with the decrease in the mesh size (Figure 6-15b). While, when using 20nodes elements, the stiffness is not dependant on the mesh size (Figure 6-16b).

In order to have a better comparison between the two types of brick elements, here the force-drift relation of the wall in the in-plane and out-of-plane directions with and without considering geometric nonlinearity for a moderate mesh size (mesh configuration "c" in Figure 6-14) are investigated (Figure 6-17).

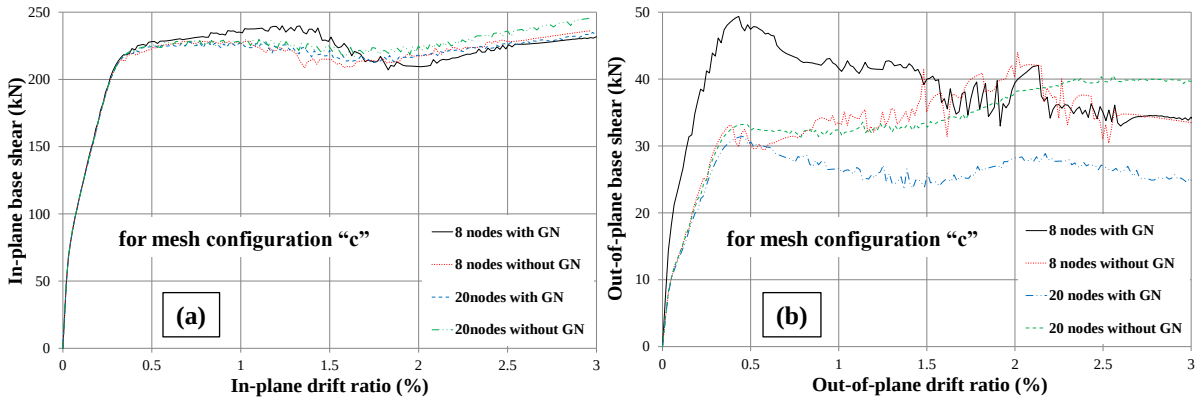

Figure 6-17 Force-drift curves of the wall using different element types with and without considering geometric nonlinearity for mesh configuration "c" in the (a) in-plane) and (b) out-of-plane directions

Based on Figure 6-17, it can be concluded that:

1. Looking at Figure 6-17a, not much discrepancy can be seen in the behaviour of the wall in the in-plane direction in terms of stiffness and strength capacity when using 8nodes and 20nodes elements whether geometric nonlinearity is considered or not in the analysis.
2. Looking at Figure 6-17b, significant increase in the out-of-plane stiffness and strength capacity of the wall can be seen when 8nodes elements were used and geometric nonlinearity was considered compared to the case when geometric nonlinearity was not considered or when 20nodes elements were used.

As was shown in Figure 6-15b, by decreasing the mesh size, the stiffness is also decreasing. Figure 6-18 compares the two element types when having a fine mesh (mesh configuration "e" in Figure 6-15 and Figure 6-16).

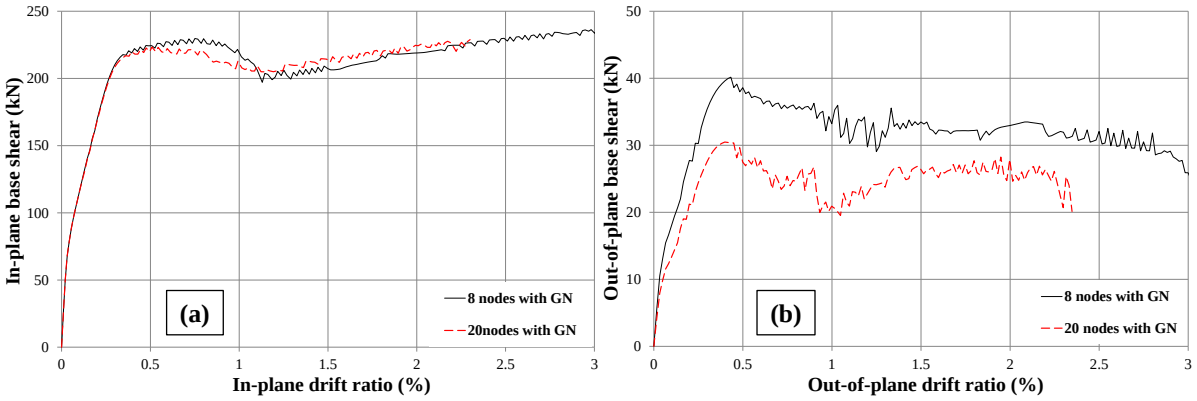

Figure 6-18 Force-drift curves of the wall using different element types for a fine mesh in the (a) in-plane and (b) out-of-plane directions

It can be seen in Figure 6-18b that there's still significant difference in the stiffness and strength capacity of the wall in the out-of-plane direction when using 8nodes elements compared with 20nodes elements.

Conclusions on 8nodes vs 20nodes solid elements

Based on the study on 8nodes and 20nodes solid elements, the following conclusions can be derived.

1. If the loading pattern of the wall only involves in-plane loading, both 8nodes and 20nodes elements show similar results. However, 20nodes elements might be less sensitive to mesh size.
2. If the loading pattern involves both in-plane and out-of-plane loadings, but the failure mode is still happening in the in-plane direction (cases such as specimens SP1-Skew and SP1-Clover presented in Chapter 3), the behaviour of the wall in the in-plane direction in terms of stiffness, strength capacity, drift capacity and failure mode could be acceptable and the error in the out-of-plane stiffness and strength capacity can be neglected. However, it should not be recommended.
3. If the loading pattern involves both in-plane and out-of-plane loadings and the failure mode is affected by the out-of-plane behaviour of the wall (such as specimen SP2-ND presented in Chapter 5), using 8nodes elements would lead to different stiffness, strength capacity and failure mode compared to the actual behaviour of the wall.

Mesh sensitivity analysis

Based on the investigations on 8nodes and 20nodes solid elements, 20nodes elements were used to simulate concrete in RC walls subjected to uni- and bi-directional loadings. One of the important parameters that can change the force-drift curve or even the failure mode of a

wall is the mesh size. Therefore, a mesh sensitivity analysis was performed for each wall to find the most stable and efficient mesh size for the wall. The five mesh configurations shown in Table 6-5 and Figure 6-14 were chosen for the mesh sensitivity analysis. Monotonic force-drift curves of the wall for each mesh configuration are shown in Figure 6-19 and Figure 6-20 for the in-plane and out-of-plane directions, respectively.

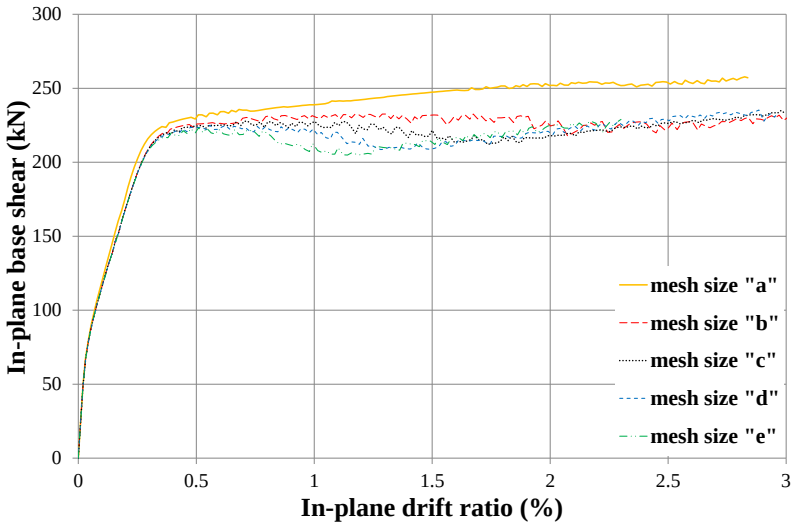

Figure 6-19 Mesh sensitivity analysis of specimen SP1-Skew for the in-plane direction

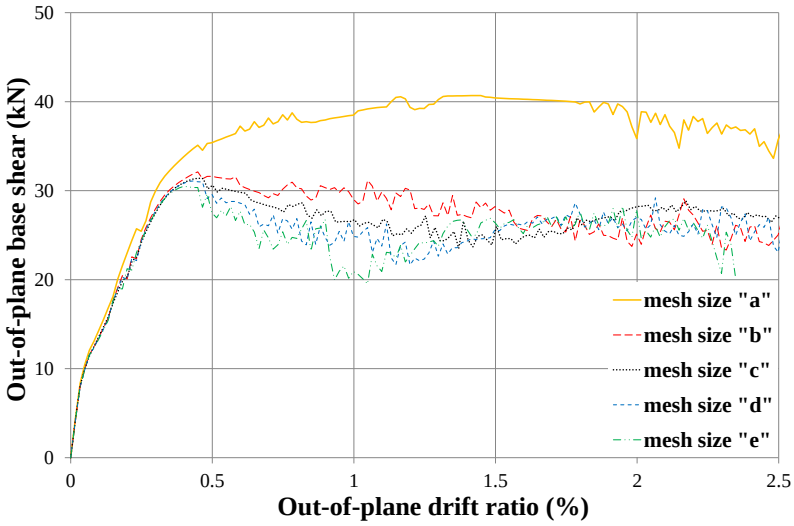

Figure 6-20 Mesh sensitivity analysis of specimen SP1-Skew for the out-of-plane direction

It can be seen that except mesh configuration “a”, other mesh configurations have limited discrepancy and making similar results. Considering the accuracy and also efficiency of each mesh size based on the amount of time and data space required, mesh configurations “b” and “c” were found to be suitable.

In a more detailed investigation, it was found that coarser mesh configurations such as the one in Figure 6-14b could be more accurate when investigating the wall at strain level. Figure 6-21 shows the strain profile of the specimen SP1-Skew when using mesh

configurations “b” and “c”, respectively. Therefore, mesh configuration “b” was chosen for this specimen. It is worth noting that similar trend was observed for other cases as well. Strain profile was drawn for a length of about 1000mm above the base in both the experimental and numerical cases.

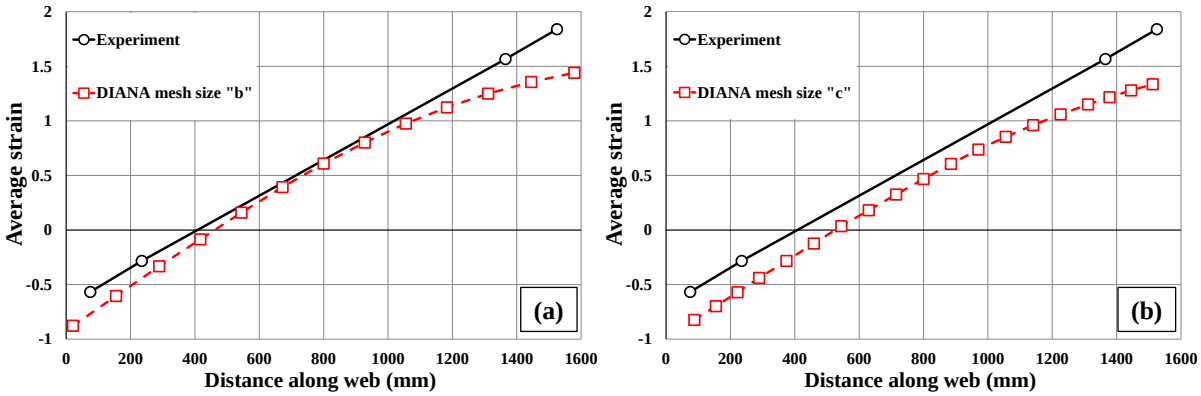

Figure 6-21 Strain profile of the specimen SP1-Skew for (a) mesh configuration “b” and (b) mesh configuration “c”

Base shear vs drift ratio

In-plane and out-of-plane base shear vs drift ratio curves of SP1-Skew obtained from DIANA are shown and compared with the experimental results in Figure 6-22. It can be seen that force-drift ratio curves of the specimen were captured by the FE analysis reasonably well. However, as was explained in section 6.2.2, the FE model was not capable of simulating the reduction of strength due to bar buckling. This explains the difference in the strength values between the FE results and the experiment shown in Figure 6-22a after the second cycle of 1.5% drift where the bar buckling initiated in the experiment.

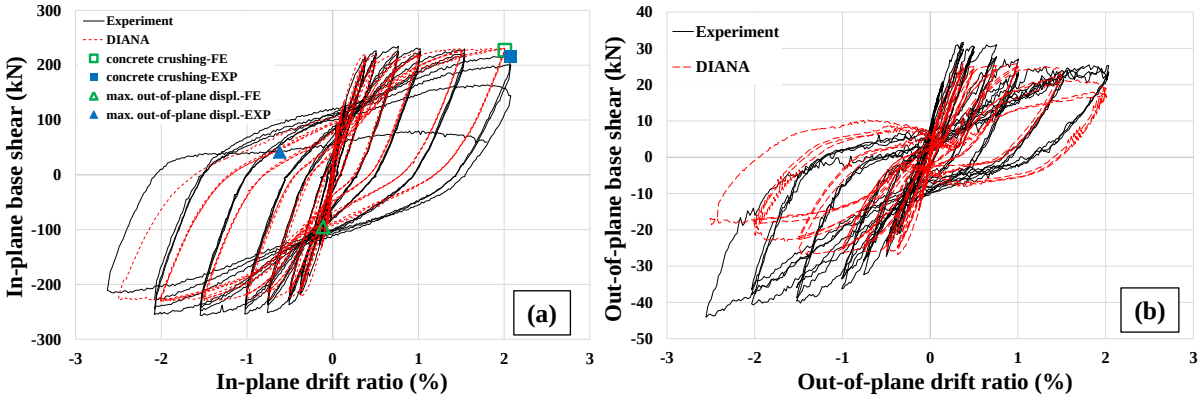

Figure 6-22 Base shear vs drift ratio curves of SP1-Skew, experiment vs FE (a) in-plane (b) out-of-plane

Failure mode

Figure 6-23 compares the failure mode captured by DIANA and the experiment (see Figure 6-22 for the point of failure). Axial strain and stress contours were used to interpret

the failure mode of the specimen. The failure mode of the wall in the experiment was concrete crushing from the left side (Figure 6-23c). Drop of stress in the left hand side of the wall in Figure 6-23b shows concrete crushing resulted from exceeding the ultimate strain of concrete. However, bar buckling was also observed in the experiment which was not considered in the FE model and consequently was not captured. It is worth noting that local out-of-plane buckling was observed in the specimen as well which will be discussed in details in the out-of-plane displacement evolution section.

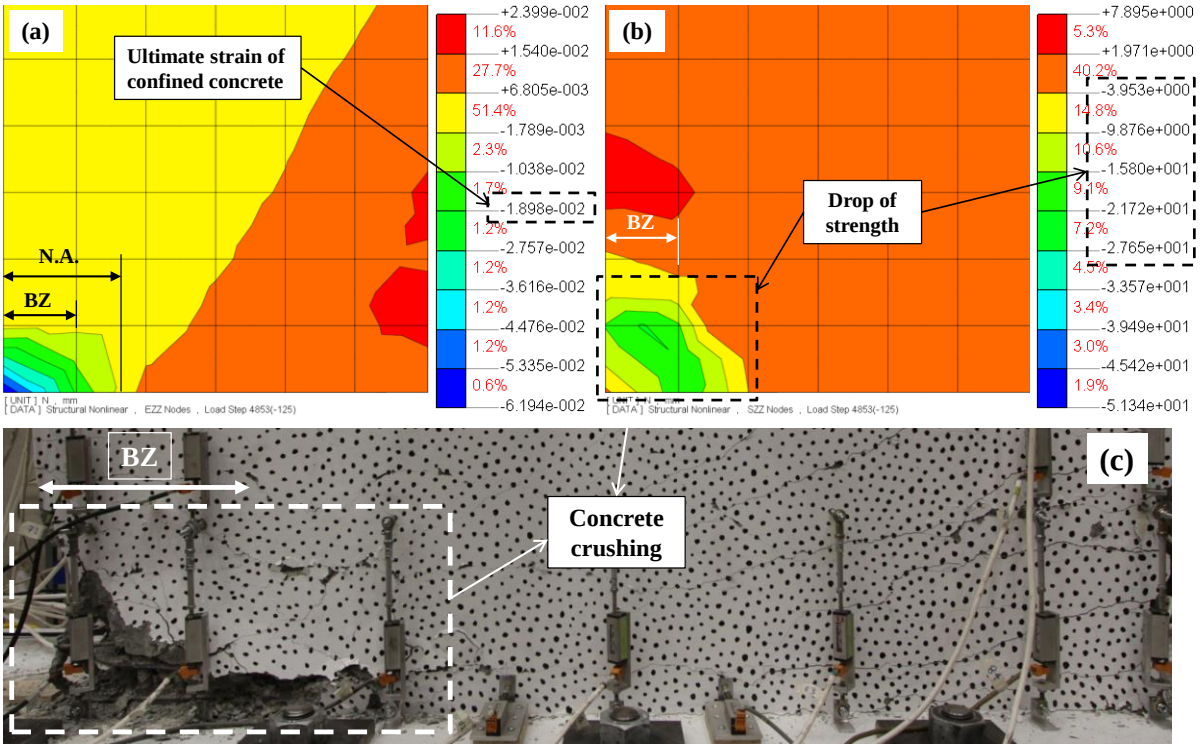

Figure 6-23 Specimen SP1-Skew at failure (a) axial strain, (b) axial stress and (c) experiment

Crack pattern

Figure 6-24 shows the crack pattern and von Mises strain contours of specimen SP1-Skew at the third cycle of 2% drift ratio. Von Mises strain contours can be beneficial as it reflects the overall strain pattern of the wall especially when subjected to bi-directional loading that affects the wall in different directions simultaneously and strain in one direction might not be able to represent the behaviour of the wall. Von Mises strain is the corresponding equivalent strain at the onset of plastic yielding and beyond (Equation 6-9). ε_{xx}, ε_{yy} and ε_{zz} are the strains in each direction and e_{xx}, e_{yy} and e_{zz} are the deviatoric strains determined using Equations 6-10-6-12. γ_{ij} is the engineering strain which is defined by Equation 6-13. For more information, refer to DIANA user's manual (DIANA 2015).

$$\varepsilon_{eq} = \frac{2}{3}\sqrt{\frac{3\left(e^{2}_{xx} + e^{2}_{yy} + e^{2}_{zz}\right)}{2} + \frac{3\left(\gamma^{2}_{xy} + \gamma^{2}_{yz} + \gamma^{2}_{zx}\right)}{4}} \quad 6\text{-}9$$

$$e_{xx} = \frac{2}{3}\varepsilon_{xx} - \frac{1}{3}\varepsilon_{yy} - \frac{1}{3}\varepsilon_{zz} \quad 6\text{-}10$$

$$e_{yy} = -\frac{1}{3}\varepsilon_{xx} + \frac{2}{3}\varepsilon_{yy} - \frac{1}{3}\varepsilon_{zz} \quad 6\text{-}11$$

$$e_{zz} = -\frac{1}{3}\varepsilon_{xx} - \frac{1}{3}\varepsilon_{yy} + \frac{2}{3}\varepsilon_{zz} \quad 6\text{-}12$$

$$\gamma_{ij} = 2 \times \varepsilon_{ij} \quad 6\text{-}13$$

It can be seen that the FE model was able to capture not only the tensile cracks (both horizontal along the base and the inclined ones above the base) but also concrete crushing of the wall as well. It should be noted that cracks shown in Figure 6-24a are filtered to remove the minor cracks with strains smaller than 6.4×10^{-3}.

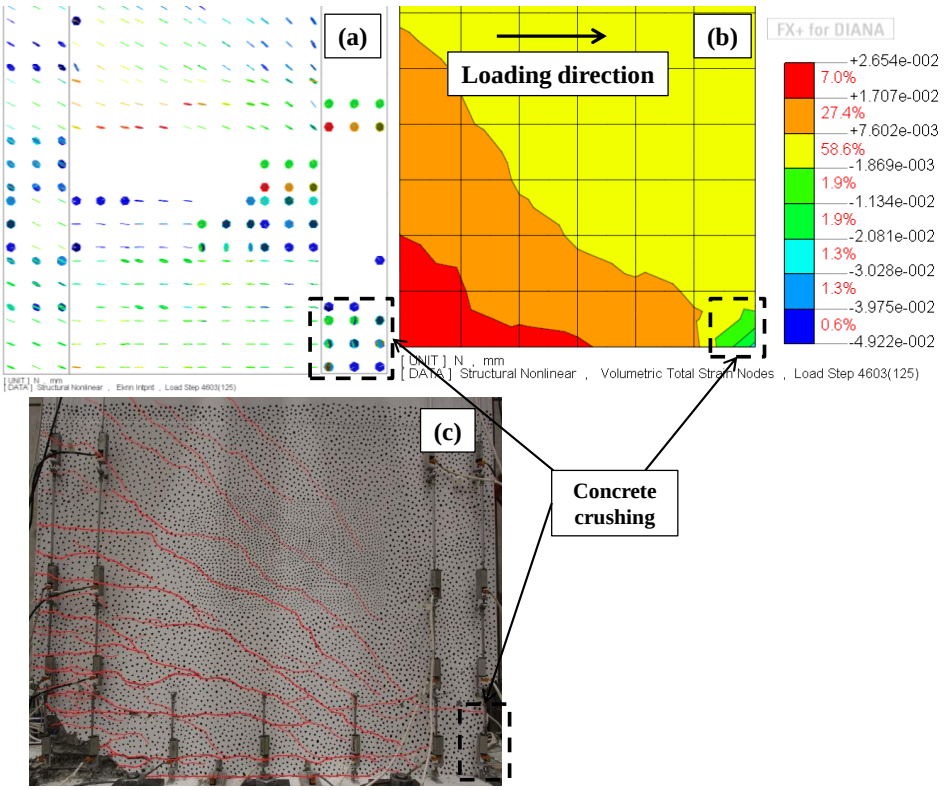

Figure 6-24 Crack pattern of SP1-Skew at 2% drift, (a) resulted from FE, (b) von Mises strain contours and (c) experiment

Strain profile

Figure 6-25 shows the strain profile of the specimen SP1-Skew at the peak of the first cycle of 0.75%, 1%, 1.5% and 2% drift ratios (loading in the positive direction, to the left). It is worth noting that these strain values along the length of the wall are average strain measured for a length of 1000mm above the base which was assumed as the plastic hinge length of the

wall (to represent a global behaviour of the wall in the strain level). As can be seen, the model captured the compressive strains and the neutral axis depth as well as the trend of the strain profile nicely. However, it lost its accuracy in regard to the tensile strains at higher drift ratios (1.5% and 2%). The main reason is due to the deficiency of the FE model in capturing the residual strain of concrete (discussed in section 6.2.1) which led to less elongation in the wall. As a result, the FE model predicts less tensile strain in the specimen.

In a numerical study by Dashti et al. (2017a) using DIANA, facing the same issue, they have concluded this was due to the assumption of full bond between the concrete and steel reinforcing bars. Same assumption was considered here which can further affect the strains similarly at higher drift ratios that the bond is deteriorated.

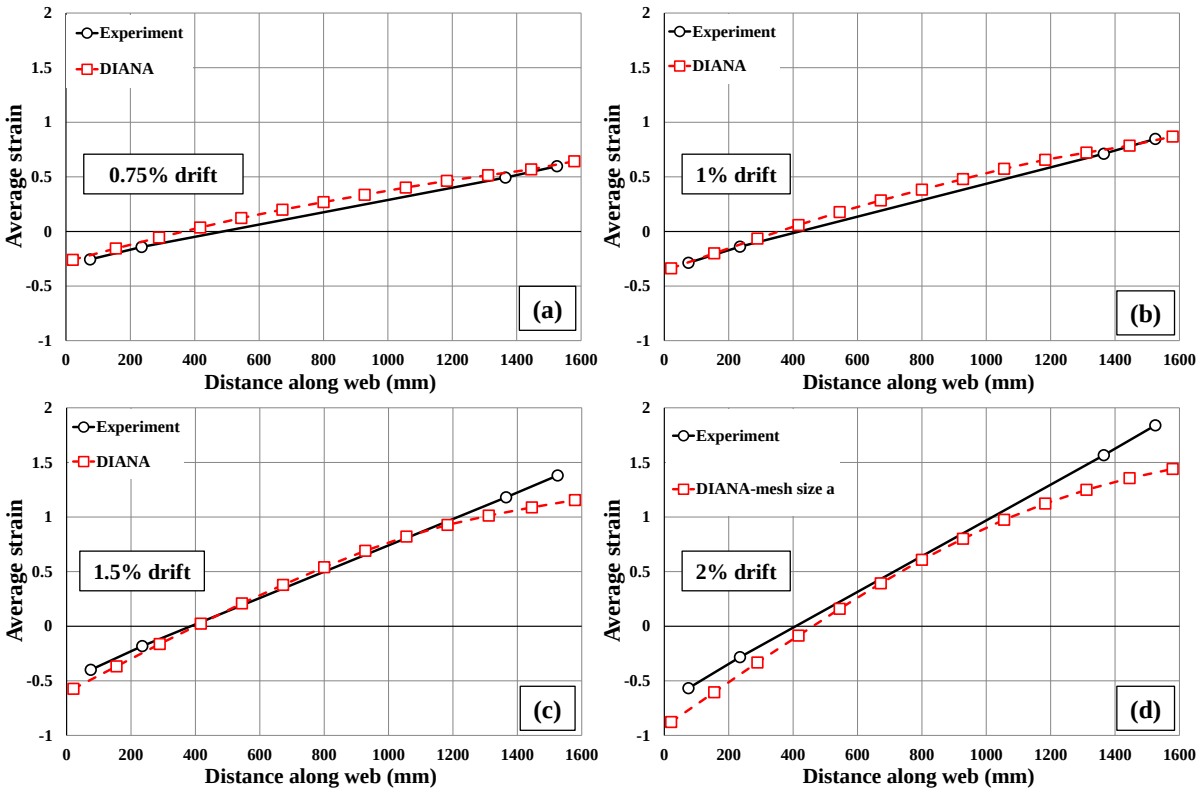

Figure 6-25 Strain profile of SP1-Skew at the first cycle of (a) 0.75% drift, (b) 1%, (c) 1.5% drift and (d) 2% drift, experiment vs FE

Out-of-plane displacement evolution

SP1-Skew showed some out-of-plane buckling on its left side which was also captured in the FE analysis (Figure 6-26). As was shown in Figure 6-22 and can be seen in Figure 6-26, the specimen buckled from its left face in the experiment while in the FE analysis, the specimen buckled from its right face. This is due to the fact that the direction and side of maximum out-of-plane buckling or instability is a random phenomenon. Figure 6-27 shows the evolution of out-of-plane displacement vs in-plane drift of the specimen obtained from the FE analysis

and the experiment. One of the important parameters in developing out-of-plane buckling/instability is the tensile strain of concrete (Paulay and Priestley 1993). As was discussed earlier and shown in Figure 6-25, the model cannot fully predict the tensile strain of the specimen at higher drift levels in which out-of-plane buckling is higher. This deficiency affects the accuracy of the model in calculating the out-of-plane buckling, hence capturing the out-of-plane instability. Other parameters such as random asymmetry in the construction of the specimen can further affect the comparison between the FE results and the experimental ones in regards to predicting the out-of-plane buckling of the wall. Although the model was successful in capturing the out-of-plane buckling, it was not able to capture the local lateral instability in the wall that occurred during the 2.5% drift cycle. It is worth noting that, the local lateral instability failure occurred following significant concrete crushing and bar buckling and was not the main failure mode of the specimen.

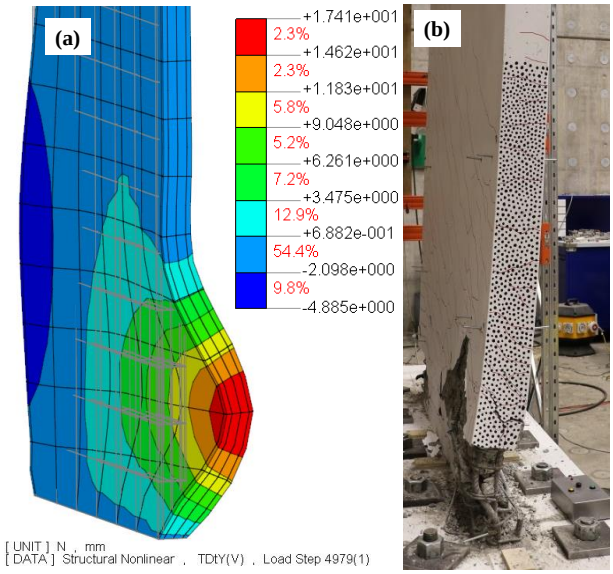

Figure 6-26 Out-of-plane deformation of specimen SP1-Skew (a) FE and (b) Experiment

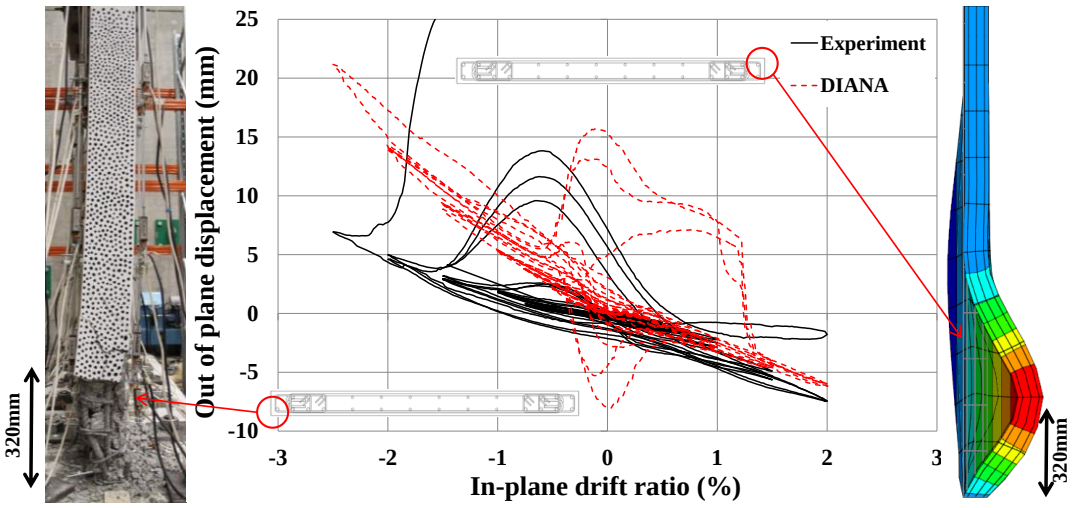

Figure 6-27 Out-of-plane displacement evolution of specimen SP1-Skew, experiments vs FE

6.5.2. SP1-Uni

Table 6-2 and Figure 6-11 summarize the basic characteristics of the specimen. Table 6-3 and Table 6-6 show the material properties of the specimen. Figure 6-28a shows the loading pattern of SP1-Uni. For more information, refer to Chapter 3. The FE model and the boundary conditions of specimen SP1-Uni are also shown in Figure 6-28b.

Table 6-6 Concrete cylinder test result for specimen SP1-Uni

Specimen	Average concrete compressive strength (MPa)
SP1-Uni	47.3

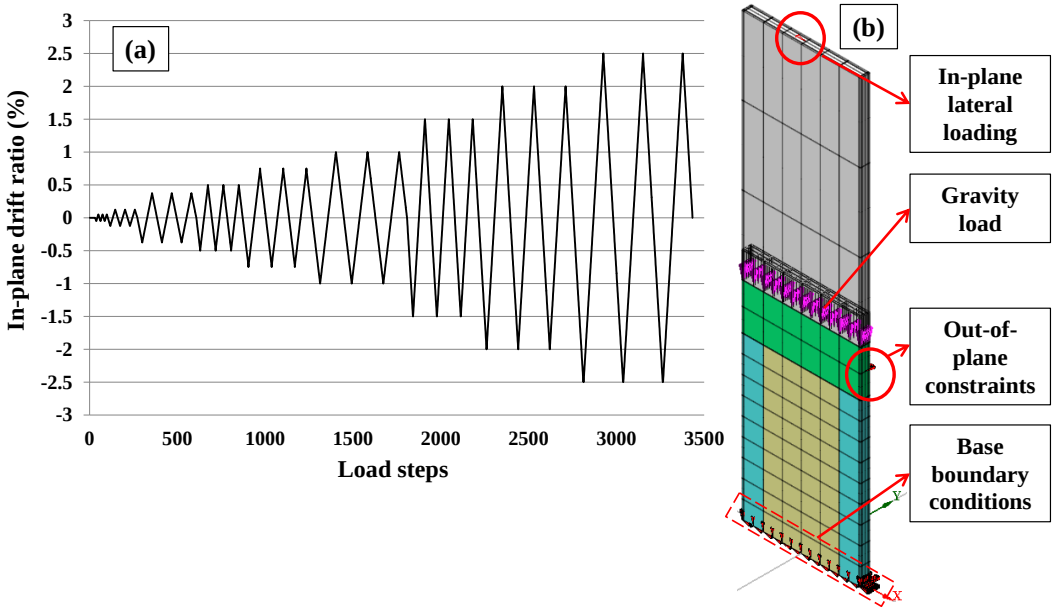

Figure 6-28 (a) Loading protocol and (b) Finite element model and boundary conditions of specimen SP1-Uni

Base shear vs drift ratio

In-plane base shear vs drift ratio curve resulted from DIANA is shown and compared to the experimental results in Figure 6-29. The points where concrete crushing and maximum out-of-plane displacement occurred are also shown in Figure 6-29. It can be seen that the FE model was able to capture the capacity curve of the specimen SP1-Uni properly. Some of the reduction of strength due to bar bucking was not captured in the simulation due to the FE model limitation as was discussed before.

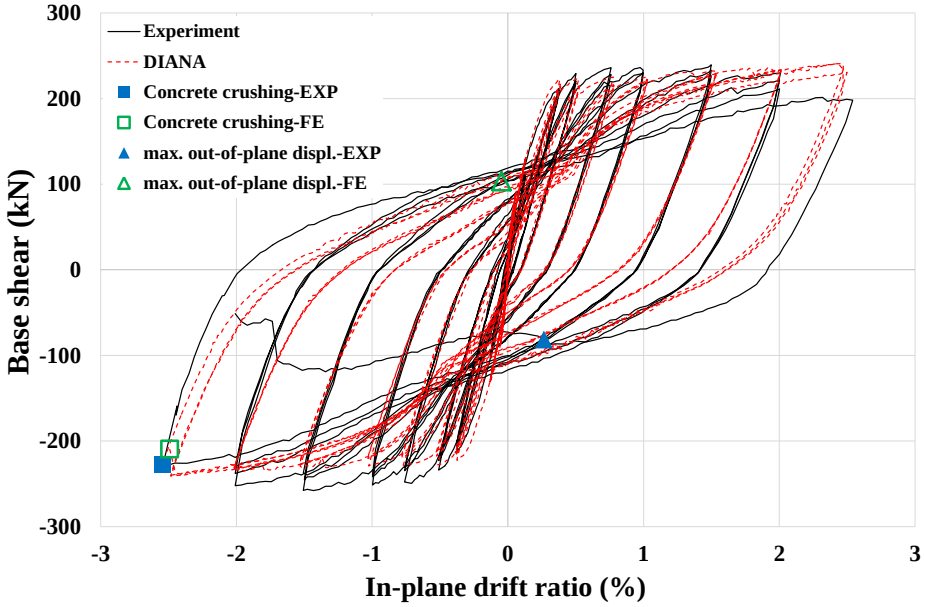

Figure 6-29 Base Shear vs drift ratio of specimen SP1-Uni, experiment vs FE

Failure mode

Figure 6-30 compares the failure mode captured by DIANA and the experiment (see Figure 6-29 for the point of failure). Axial strain and stress contours of the specimen resulted from FE were used to interpret the failure mode. In Figure 6-30b, it can be seen at this drift level, axial strain is above the ultimate strain of concrete (shown in Figure 6-30a) and consequently axial stress dropped. This crushing of concrete captured in the analysis matched the experimental observations as can be seen in Figure 6-30. As was explained earlier, bar buckling was also observed in the experiment which could not be captured in the FE model (bar buckling was not considered in the model). It is worth noting that local out-of-plane buckling was observed in the specimen as well which will be discussed in details in the out-of-plane displacement evolution section.

Crack pattern

Figure 6-31 shows the crack pattern of SP1-Uni at the third cycle of 2% drift ratio. It can be seen in Figure 6-31a&b that using crack pattern and von Mises strain contours, flexural tensile cracks as well as concrete crushing were captured by the FE model which matched the experimental observations as well.

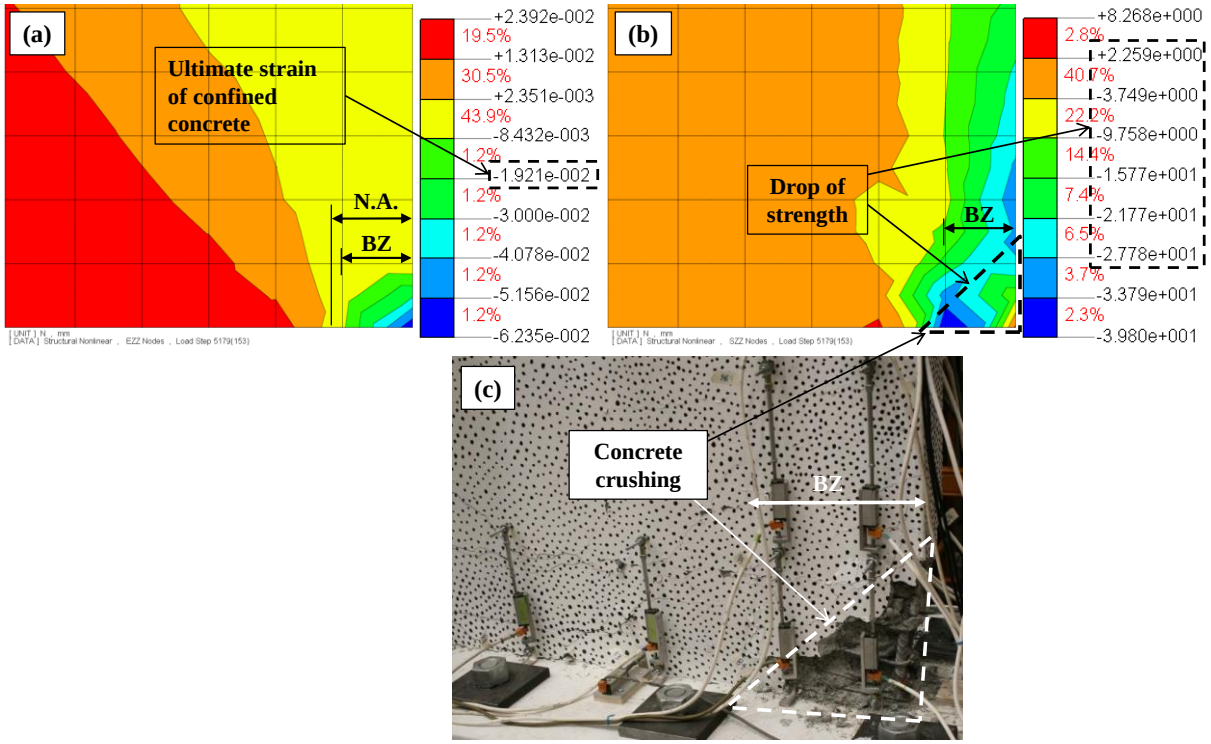

Figure 6-30 Specimen SP1-Uni at failure (a) axial strain, (b) axial stress and (c) experiment

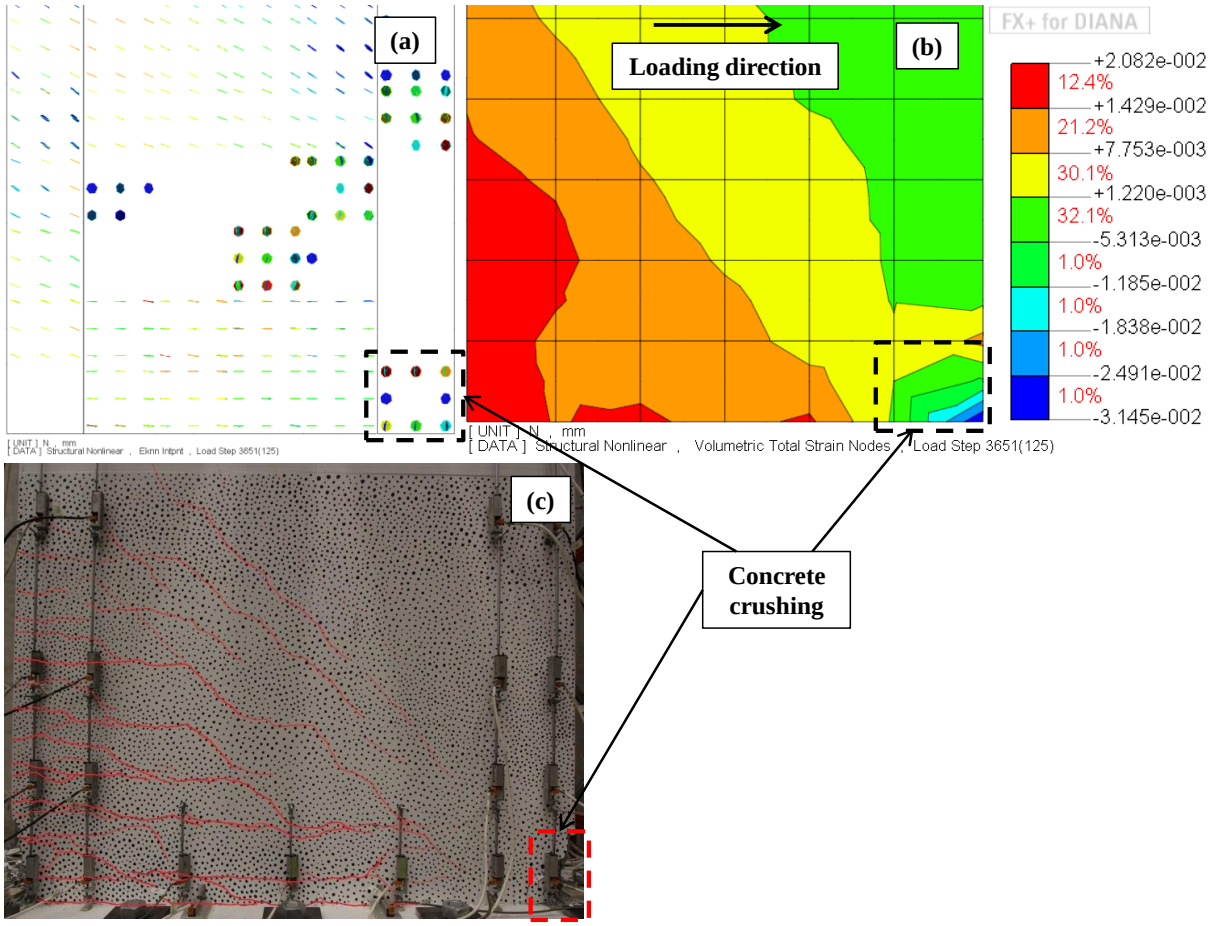

Figure 6-31 Crack pattern of SP1-Uni at 2% drift (negative), (a) resulted from FE, (b) von Mises strain contours and (c) experiment

Strain profile

Figure 6-32 shows the strain profile of the specimen SP1-Uni in the first cycle of 0.75%, 1 %, 1.5% and 2% drift ratios (loading in negative direction, to the right). It is worth noting that these strain values along the wall are average strain measured for a length of 1000mm above the base assumed as the plastic hinge length. As can be seen in Figure 6-32 the FE model nicely captured the compressive strains and the neutral axis depth as well as the trend of the strain profile. However, it is less accurate when calculating the tensile strains at higher drift ratios as discussed before.

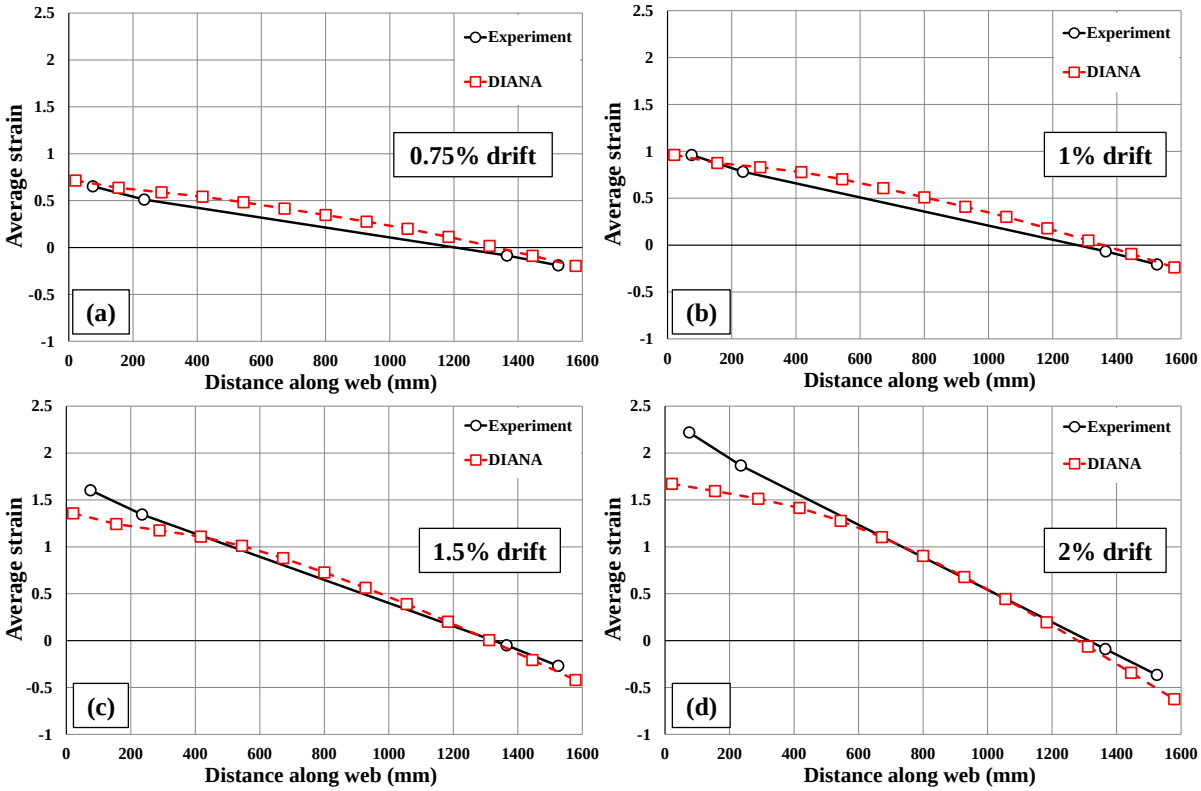

Figure 6-32 Strain profile of SP1-Uni, experiment vs FE at (a) 0.75% drift, (b) 1 % drift, (c) 1.5% drift and (d) 2% drift

Out-of-plane displacement evolution

As can be seen in Figure 6-33b, the specimen had out-of-plane buckling in its right side in the experiment. This was also captured by the FE analysis (Figure 6-33a). Figure 6-34 shows the evolution of the out-of-plane displacement at different in-plane drift ratios of the specimen obtained from FE analysis and the experiment. As can be seen in Figure 6-29 and Figure 6-34, the specimen buckled from its right face in the experiment while in the FE analysis, the specimen buckled from its left face. The local lateral instability observed in the experiment (Figure 6-33b) was not observed in the FE analysis due to the deficiency of the FE model with considering the residual capacity of concrete and perfect bond assumption

between concrete and steel reinforcement as was discussed before. It should be noted that the local lateral instability failure that occurred at the end of the test was following severe concrete crushing and bar buckling and was not the main failure mode of the wall.

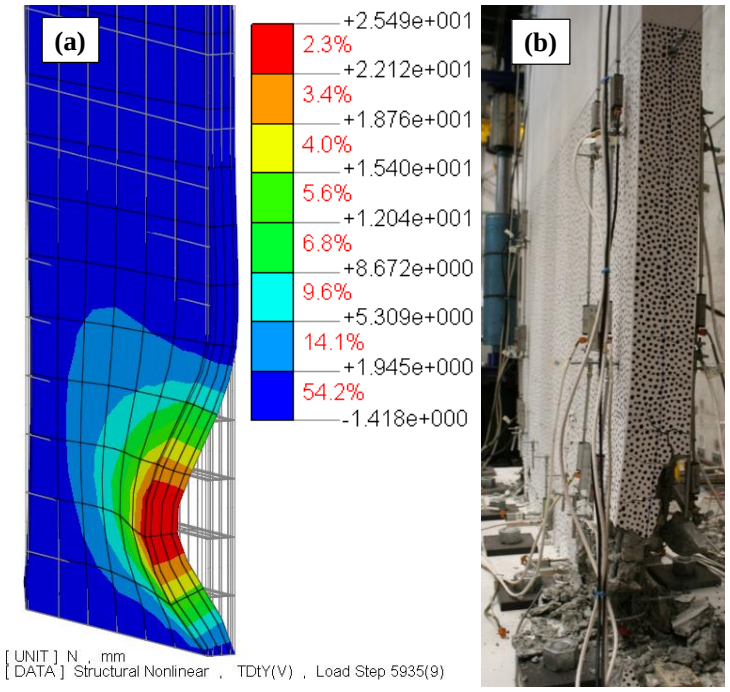

Figure 6-33 Out-of-plane deformation of SP1-Uni (a) FE and (b) Experiment

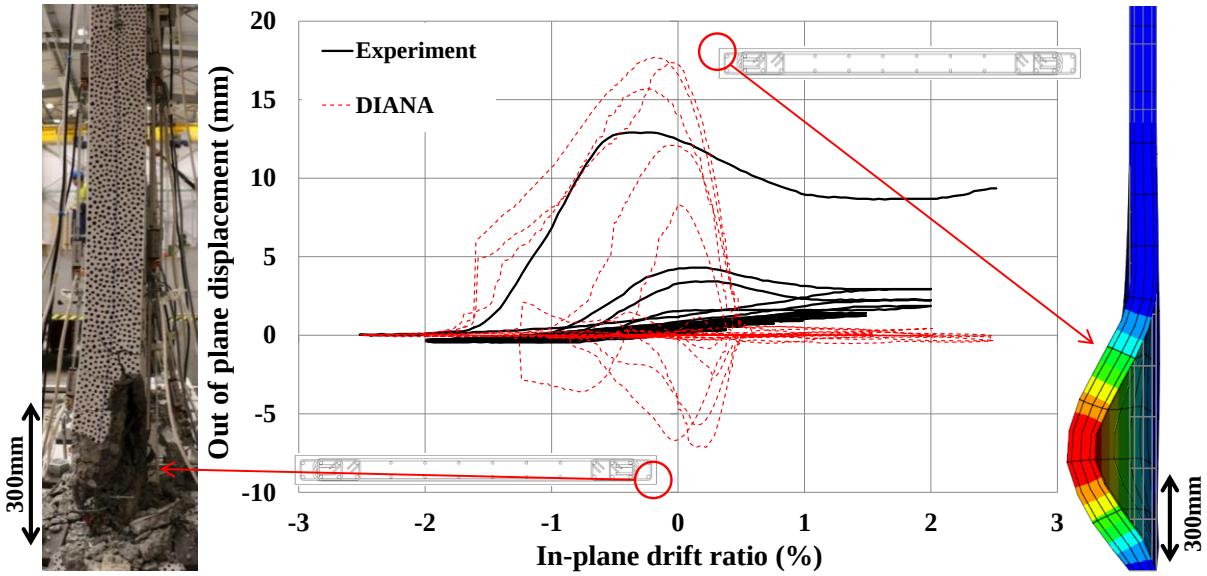

Figure 6-34 Out-of-plane displacement evolution of SP1-Uni, experiments vs FE

6.5.3. SP1-Clover

Table 6-2 and Figure 6-11 summarize the basic characteristics of the specimen. Table 6-3 and Table 6-7 show the material properties of the specimen. Figure 6-35 shows the loading protocol of specimen SP1-Clover. For more information, refer to Chapter 3.

Since the only difference between SP1-Clover and SP1-Skew was the loading protocol, therefore the finite element model and the boundary conditions of the specimen was identical to the one used for SP1-Skew (see Figure 6-13).

Table 6-7 Concrete cylinder test result for specimen SP1-Clover

Specimen	Average concrete compressive strength (MPa)
SP1-Clover	52.7

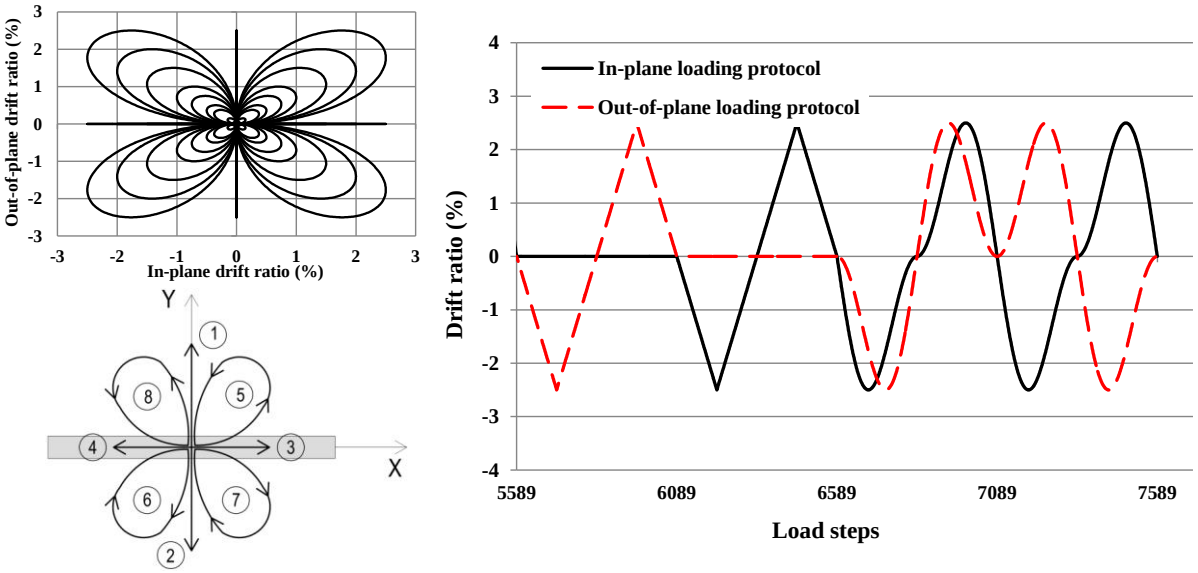

Figure 6-35 Loading protocol of specimen SP1-Clover

Base shear vs drift ratio

The in-plane and out-of-plane base shear vs drift ratio curves obtained from DIANA are shown in Figure 6-36 and compared with the experimental results. Points of failure and maximum out-of-plane displacement are also shown in Figure 6-36. As can be seen, the numerical result and experimental measurement of the base shear vs top drift ratio curves matched properly.

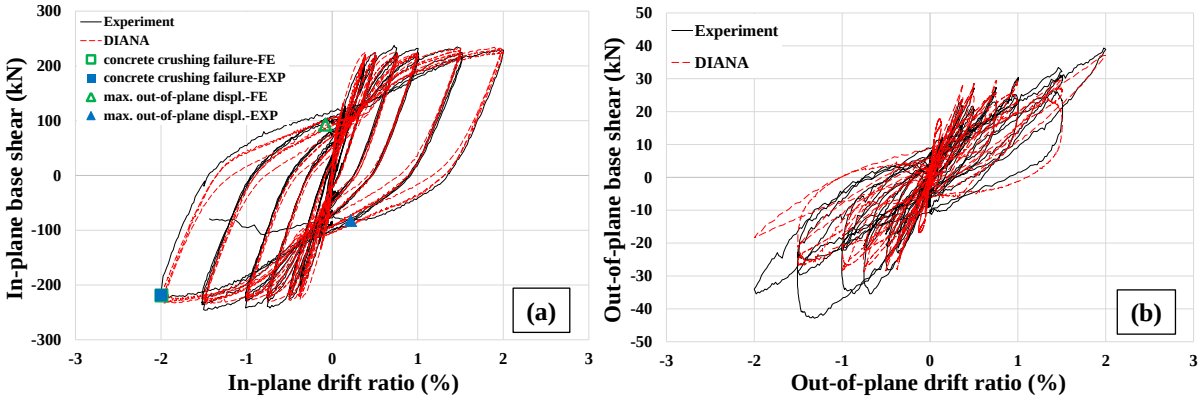

Figure 6-36 Base shear vs drift ratio curves of SP1-Clover, experiment vs FE (a) in-plane (b) out-of-plane

Failure mode

Figure 6-37 compares the failure mode captured by DIANA and the experiment (see Figure 6-36 for the point of failure). The wall failed in concrete crushing from its right side in the experiment (Figure 6-37c). As can be seen in Figure 6-37a and b, concrete stress dropped after the compressive strain reached its ultimate value which implies crushing of concrete in those elements. The failure occurred at the first cycle of 2% drift which was the in-plane uni-directional cycle (see Figure 6-35). Bar buckling was also observed in the experiment which was not captured in the FE analysis as buckling of steel reinforcement was not considered in the model. Local out-of-plane buckling was observed in the test as well which will be discussed in details in the out-of-plane displacement evolution section.

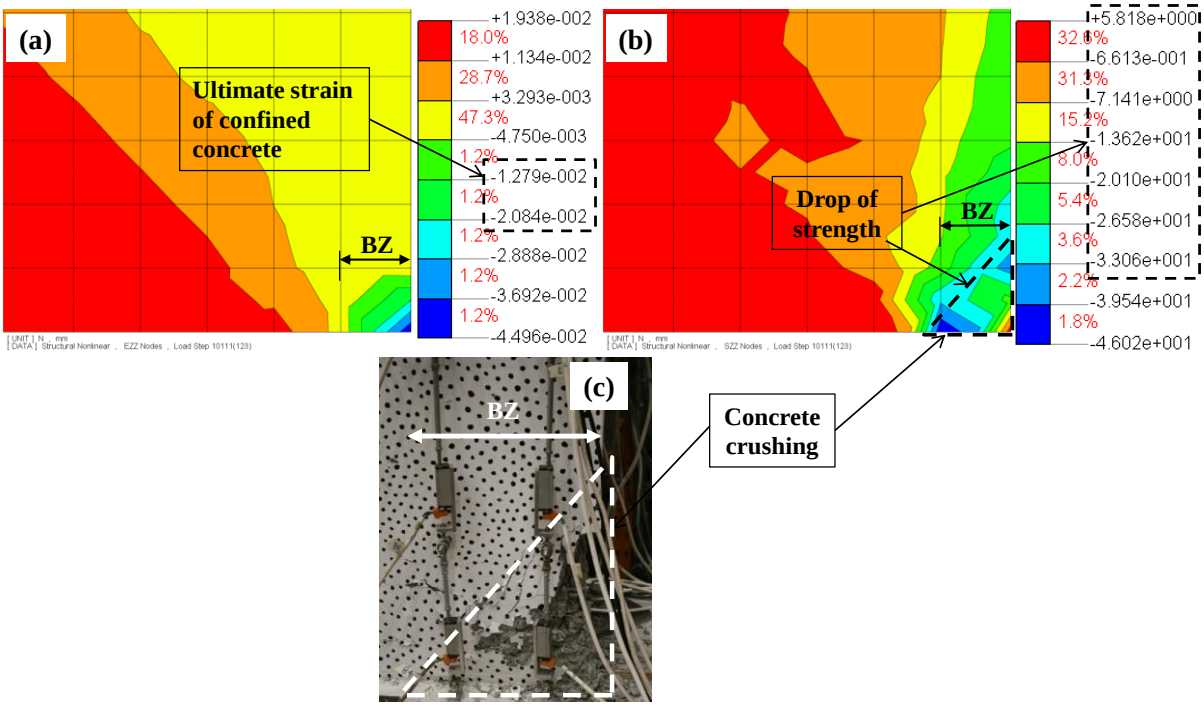

Figure 6-37 Specimen SP1-Clover at failure (a) axial strain, (b) axial stress and (c) experiment

Crack pattern

Figure 6-38 shows the crack pattern of SP1-Clover at the first cycle of 2% drift ratio. It can be seen that both horizontal cracks along the base and the inclined ones above the base were captured in the FE analysis. Crushing of concrete was also captured using both crack pattern and von Mises strain contours as shown in Figure 6-38a&b.

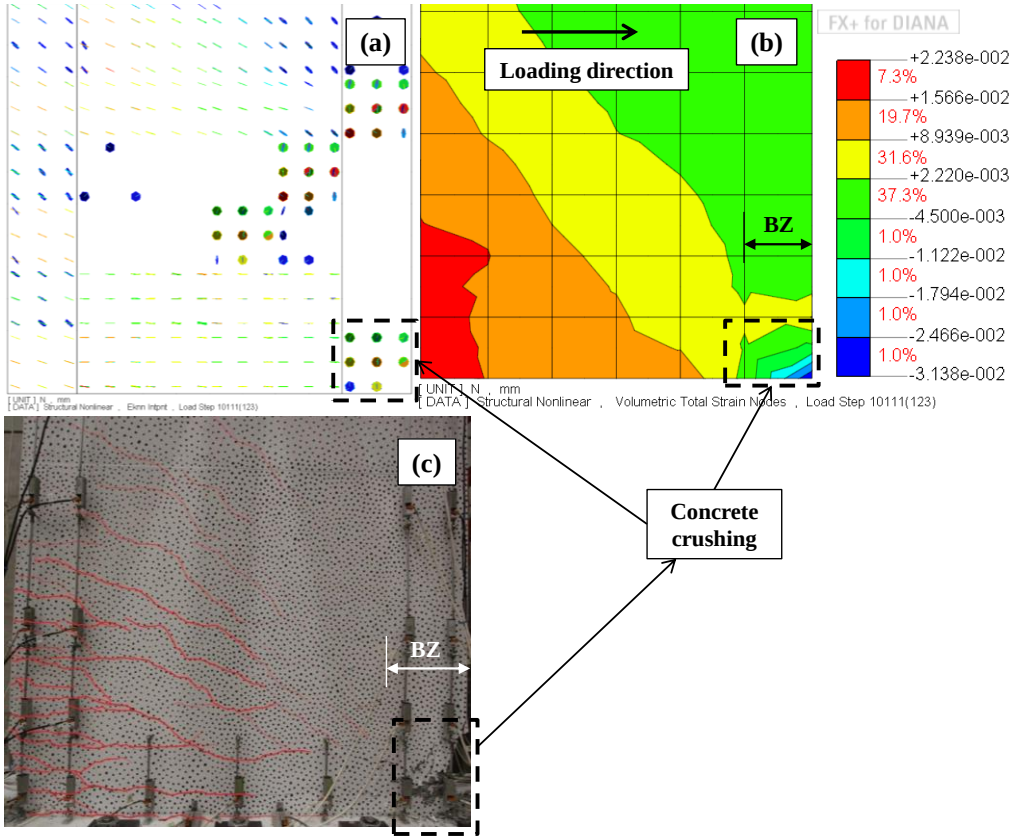

Figure 6-38 Crack pattern of SP1-Clover at 2% drift (negative), (a) resulted from FE, (b) von Mises strain contours and (c) experiment

Strain profile

Figure 6-39 shows the strain profile of the specimen SP1-Clover at the peak of the third cycle of 0.5%, 0.75%, 1% and 1.5% drift ratios (loading in the negative direction, to the right). These strain values along the length of the wall are average strains measured for a length of 1000mm above the base which was assumed as the plastic hinge length of the wall. As can be seen, similar to other cases, the FE model nicely captured the compressive strains and the neutral axis depth as well as the trend of the strain profile, but it does not accurately capture the tensile strains at higher drift ratios. The main reasons for that were discussed earlier for specimen SP1-Skew.

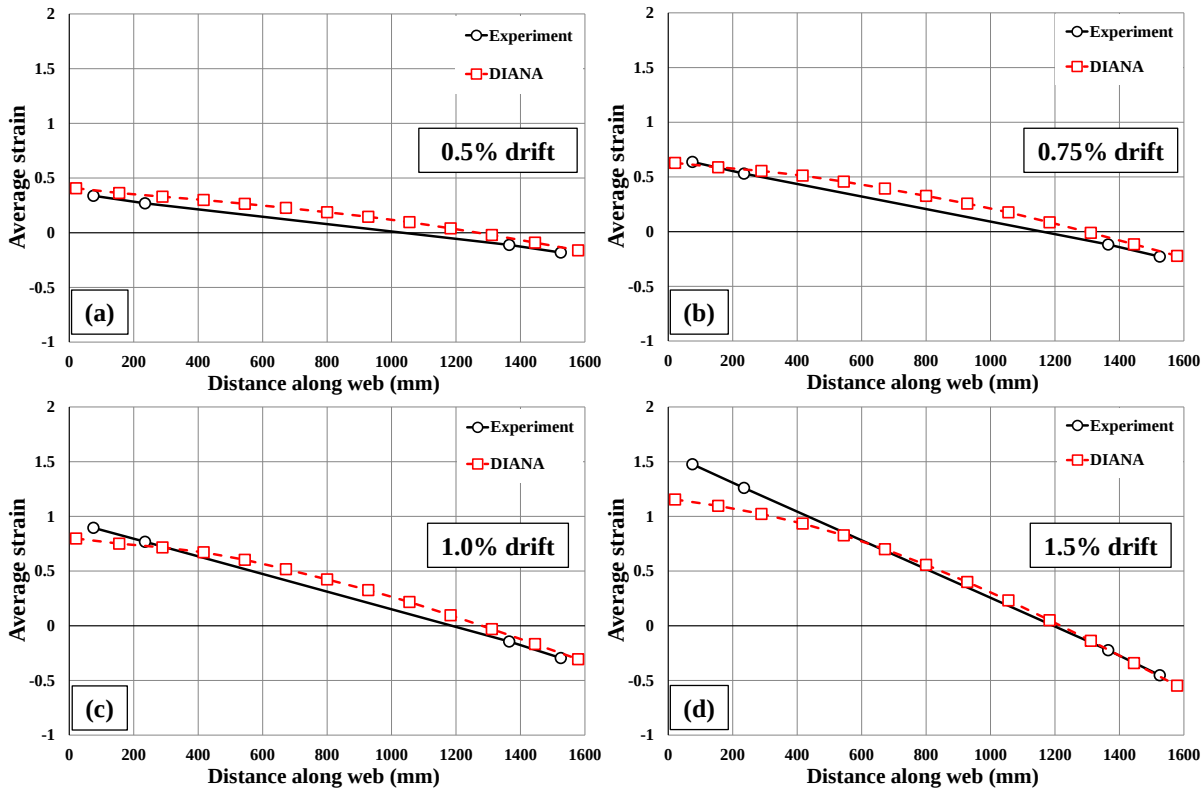

Figure 6-39 Strain profile of SP1-Clover, experiment vs FE (a) 0.5% drift, (b) 0.75% drift, (c) 1% drift and (d) 1.5% drift

Out-of-plane displacement evolution

As can be seen in Figure 6-40b, the specimen had out-of-plane buckling in its right side. This was also captured in the FE analysis (Figure 6-40a). Figure 6-41 shows the evolution of out-of-plane displacement vs in-plane drift obtained from the FE analysis and the experiment. At 2% drift, local lateral instability happened in the right side of the specimen which was not captured in the analysis. The reasons were explained earlier when describing the out-of-plane displacement evolution of SP1-Skew.

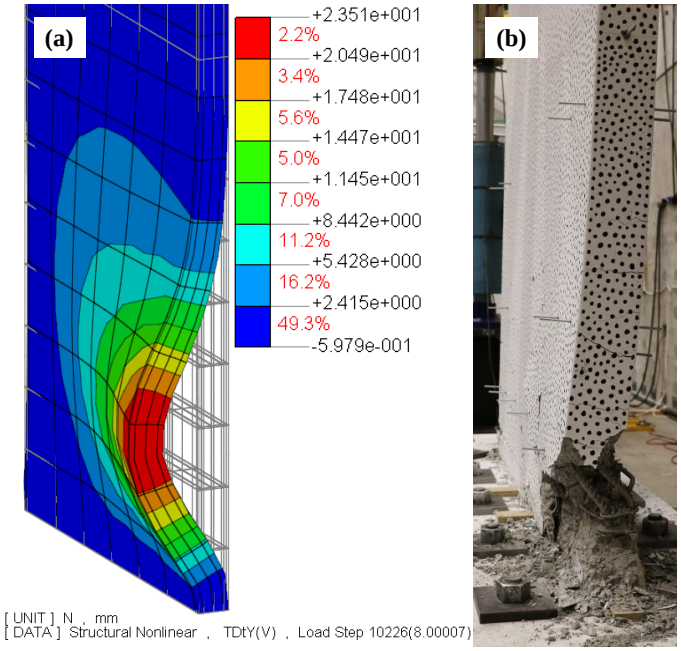

Figure 6-40 Out-of-plane deformation of specimen SP1-Clover (a) FE and (b) Experiment

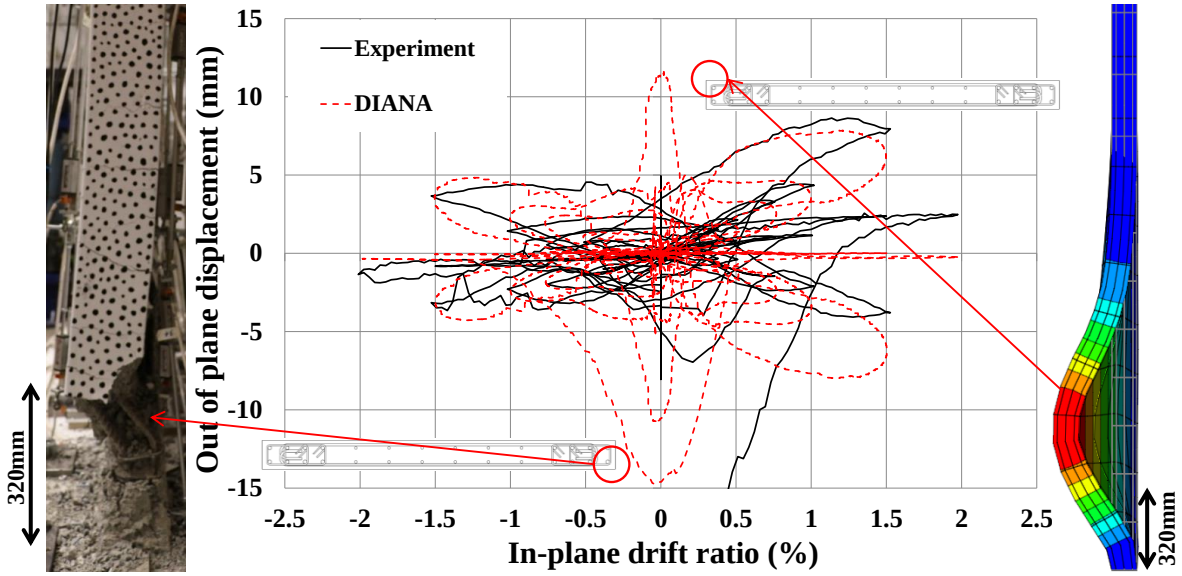

Figure 6-41 Out-of-plane displacement evolution of specimen SP1-Clover, experiments vs FE

6.5.4. WP1 (Segura and Wallace 2017)

Table 6-8 and Figure 6-42 summarize the basic characteristics of the specimen WP1 tested by Segura and Wallace (2017). Material properties of the specimen are presented in Table 6-9 and Table 6-10. Figure 6-43 shows the test setup used for the specimen WP1. Loading protocol, the FE model and the boundary conditions of the specimen WP1 are shown in Figure 6-44. More information can be found in Segura and Wallace (2017).

Table 6-8 Details of the specimen WP1 (Segura and Wallace 2017)

Clear height, H_w (mm)	2133.6
Length, L_w (mm)	2286
Thickness, t (mm)	152.4
Total longitudinal reinforcement ratio, $\rho_t = (A_{s,BZ} + A_{s,web}) / (L_w \times t)$	1.29%
Web longitudinal reinforcement ratio	0.475%
Boundary zone (BZ) longitudinal reinforcement ratio	3.1%
BZ transverse reinforcement ratio, $\rho_{sx} = A_{vx} / (s \times t)$	0.834%
BZ transverse reinforcement ratio, $\rho_{sy} = A_{vy} / (s \times l_{BZ})$	0.715%
Web shear reinforcement ratio, $\rho_v = A_{sv} / (s \times t)$	0.46%

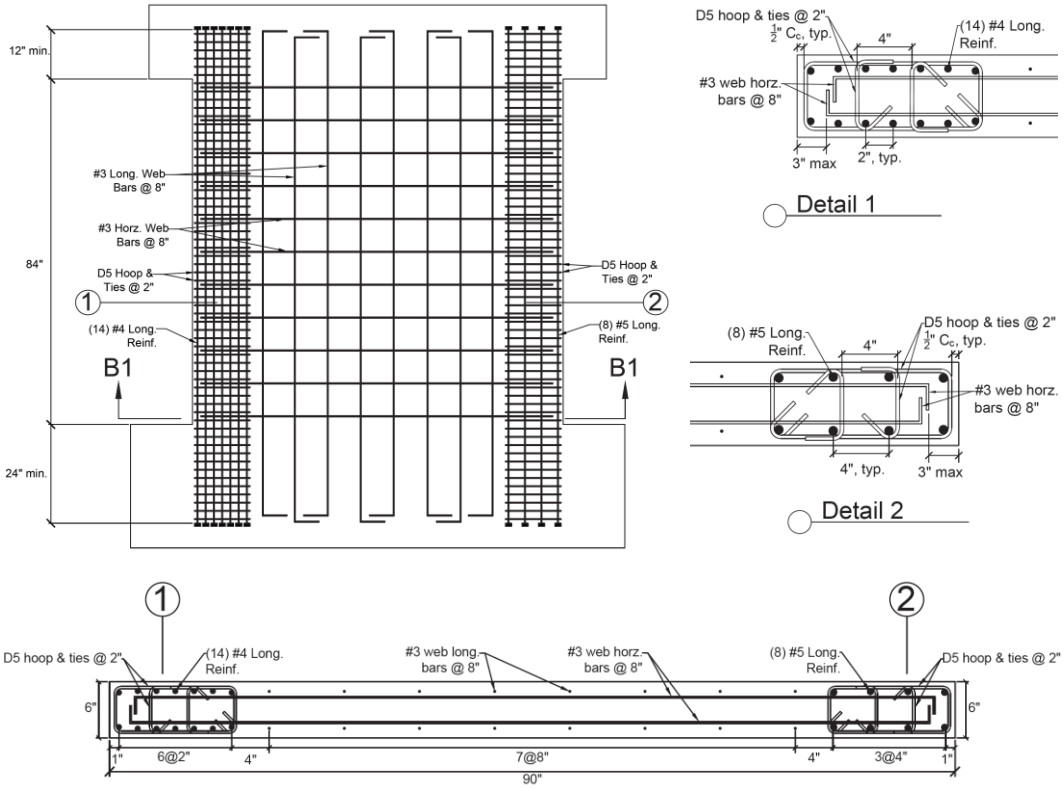

Figure 6-42 Details of the reinforcement layouts of specimen WP1 (Segura and Wallace 2017)

Table 6-9 Steel reinforcing bar properties for specimen WP1 (Segura and Wallace 2017)

Specimen	Bar size	Bar Diameter (mm)	f_y (MPa)	f_u (MPa)	ε_u
WP1	D5	6.41	343	406	0.15
	#3	9.53	493	714	0.15
	#4	12.7	459	694	0.17
	#5	15.88	461	686	0.16

Table 6-10 Concrete cylinder test results for specimen WP1 (Segura and Wallace 2017)

Specimen	Average concrete compressive strength (MPa)
WP1	35.8

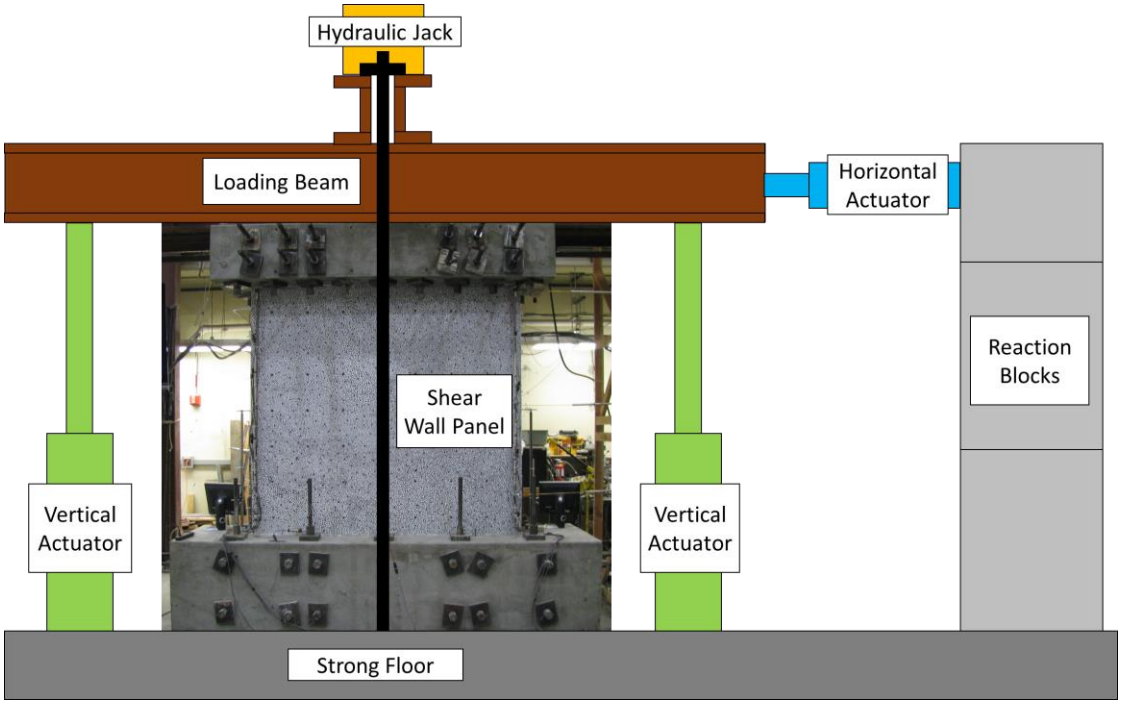

Figure 6-43 Test setup used for specimen WP1 (Segura and Wallace 2017)

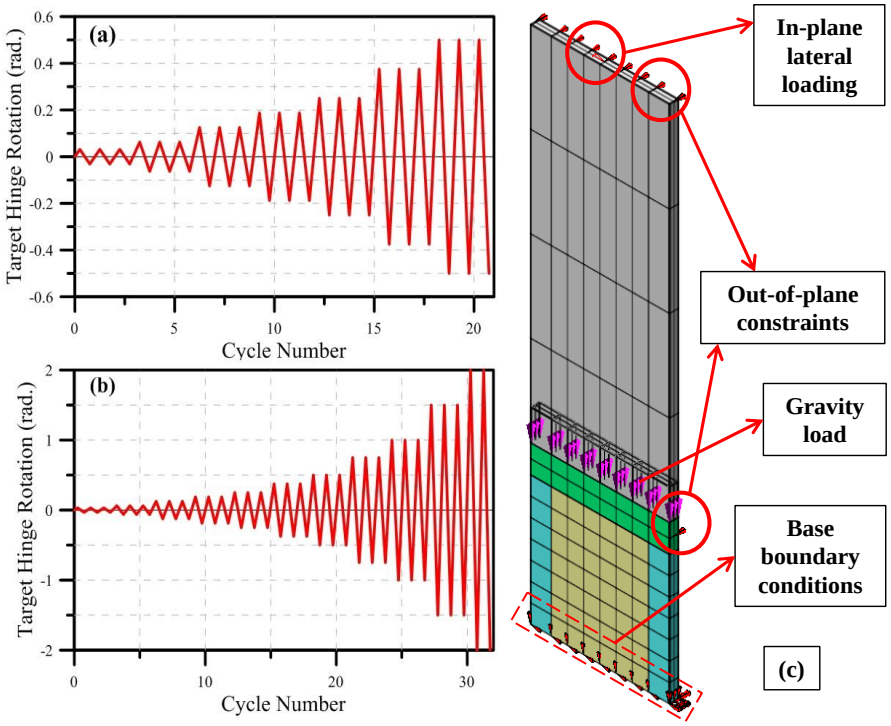

Figure 6-44 (a & b)Loading protocol of WP1 up to 0.5% and 2% drifts, respectively (Segura and Wallace 2017) and (c) Finite element model and boundary conditions of specimen WP1

Base shear vs drift ratio

The base shear vs drift ratio curve of the specimen WP1 obtained from DIANA is compared with the experimental results in Figure 6-45. As can be seen in Figure 6-45, the numerical results are in reasonably good agreement with the experimental ones.

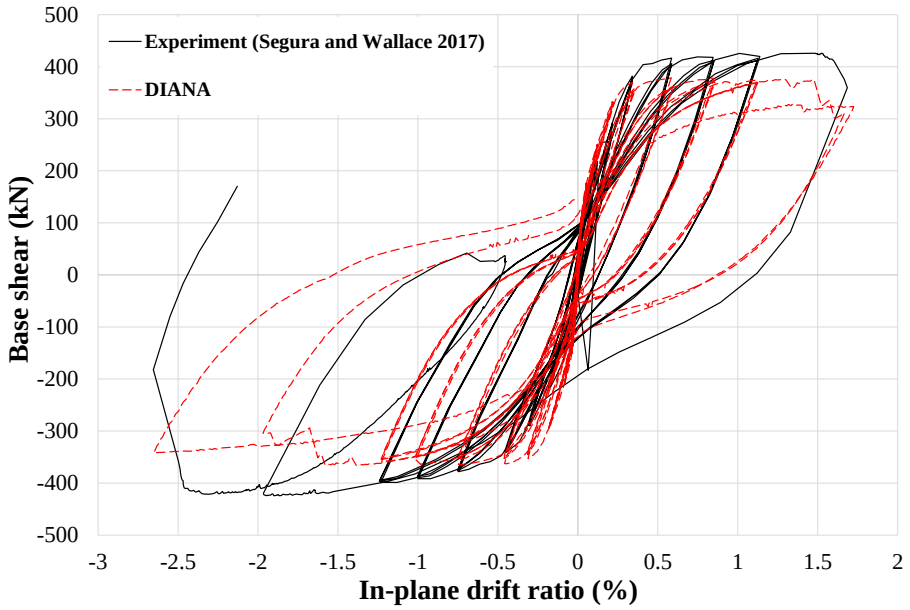

Figure 6-45 Base Shear vs drift ratio of specimen WP1, experiment vs FE

Failure mode

Figure 6-46 compares the failure mode captured by DIANA and the experiment. As can be seen in Figure 6-46, the wall failed in concrete crushing from its right-hand side in the experiment and the FE model was able to capture the failure mode of the specimen. Drop of strength shown in Figure 6-46b is due to compressive axial strain of concrete reaching its ultimate limit (see Figure 6-46a).

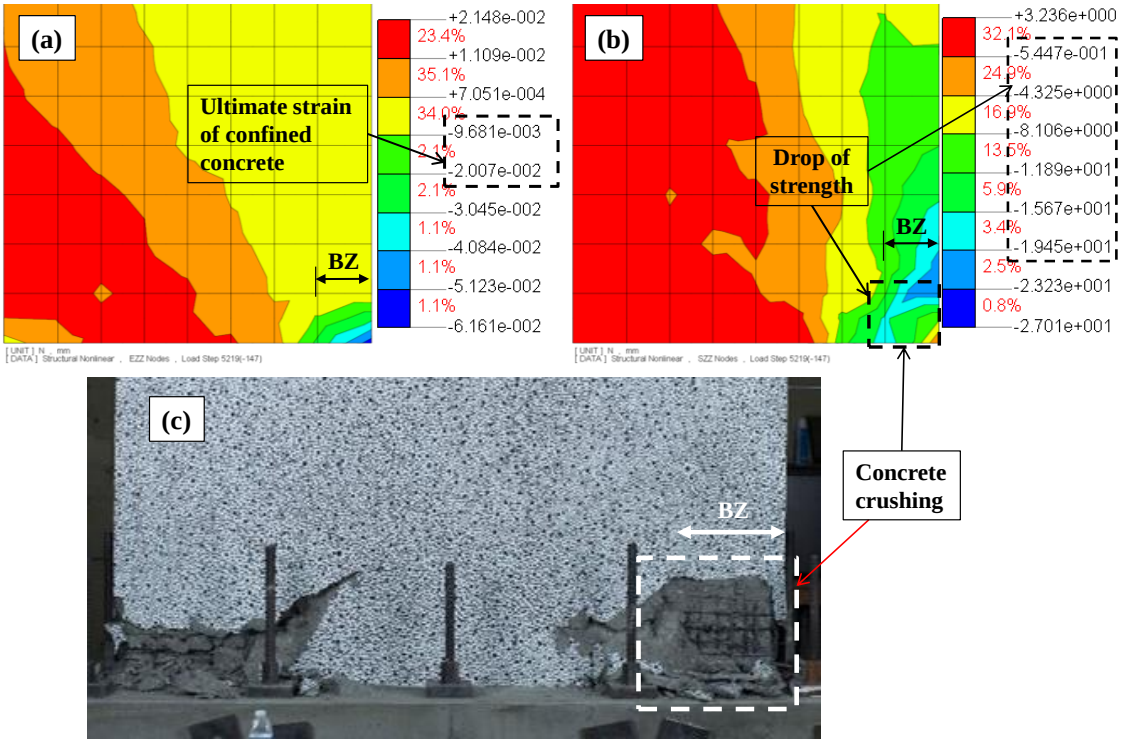

Figure 6-46 Failure mode of WP1 (a & b) axial strain and stress and (c) experiment (Segura and Wallace 2017)

Crack pattern

Figure 6-47 shows the crack pattern of the specimen WP1 at about 1.7% drift in the positive direction (to the right). As can be seen, the FE model was able to capture the crack pattern (both horizontal and inclined cracks) and crushing (using both crack pattern and von Mises strain contours) of the specimen. It should be noted that the cracks captured by the FE analysis were filtered to remove the minor cracks with a strain smaller than 6.4×10^{-3} (Figure 6-47a).

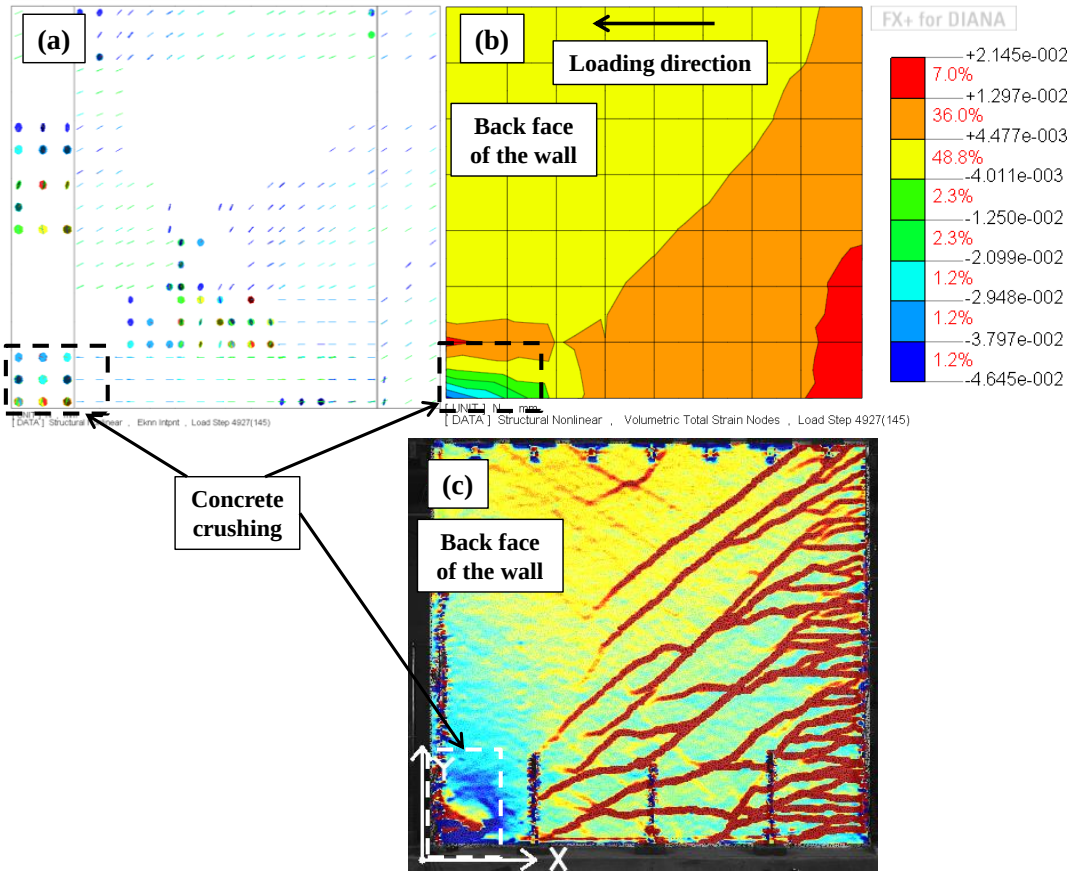

Figure 6-47 Crack pattern of WP1 (a) resulted from FE, (b) von Mises strain contours and (c) experiment (Segura and Wallace 2017)

Strain profile

Figure 6-48 shows the strain profile of the specimen WP1 at different drift levels (loading in the positive direction, to the right). It is worth noting that these strain values along the wall are average strains measured for a length of 1118mm above the base equal to half the length of the wall assumed as the plastic hinge length. It can be seen that the model captured the compressive strains and the neutral axis depth as well as the trend of the strain profile nicely. However, it loses its accuracy in regard to the tensile strains at higher drift ratios. The reasons were discussed in details for specimen SP1-Skew (Section 6.5.1).

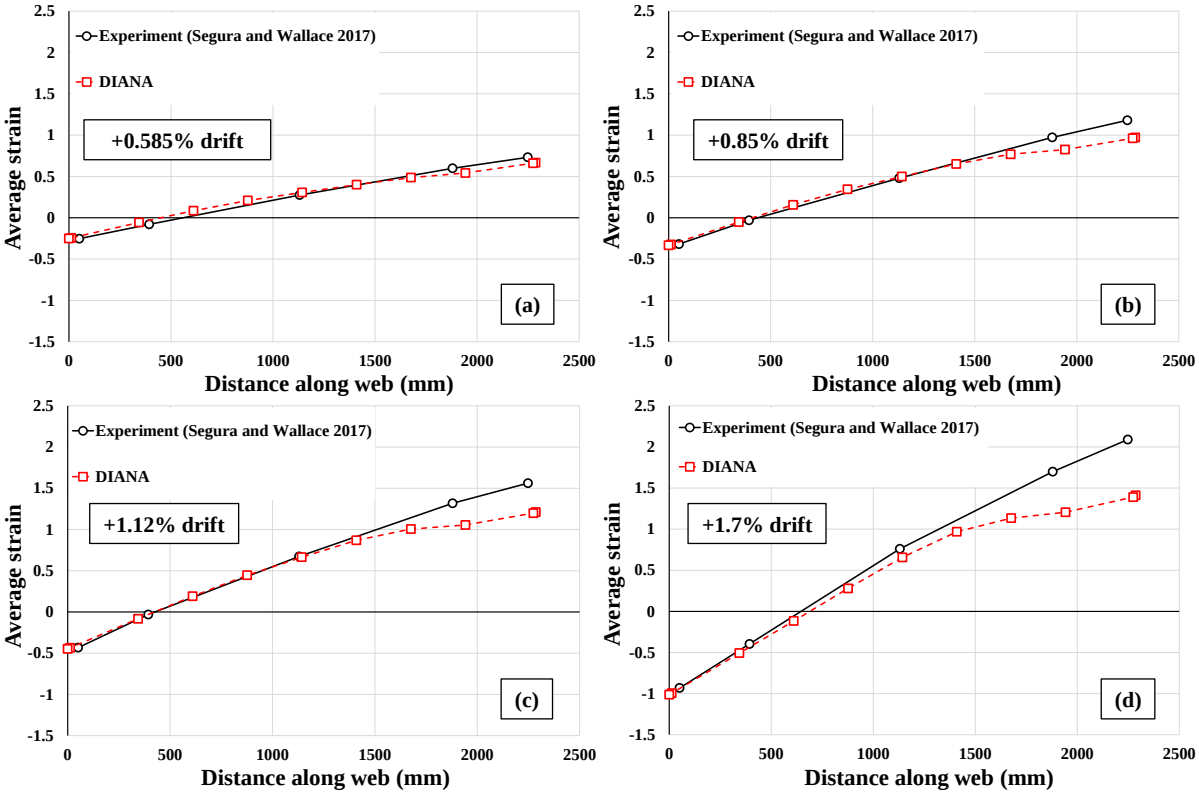

Figure 6-48 Strain profile of WP1, FE vs experiment (Segura and Wallace 2017) at (a) 0.585% drift, (b) 0.85% drift, (c) 1.12% drift and (d) 1.7% drift

Out-of-plane displacement evolution

As can be seen in Figure 6-49b, the specimen had some out-of-plane buckling in its left side in the experiment. The model was able to capture this out-of-plane buckling as well (Figure 6-49a). Figure 6-50 shows the evolution of out-of-plane displacement at different in-plane drift ratios obtained from FE analysis. Unfortunately since the out-of-plane displacement evolution was not reported in the experiment, here only the FE results are presented. It is worth noting that as was reported by Segura and Wallace (2017), concrete crushing and bar buckling were the main failure modes of the wall and the local lateral instability failure shown in Figure 6-49b was a secondary failure mode.

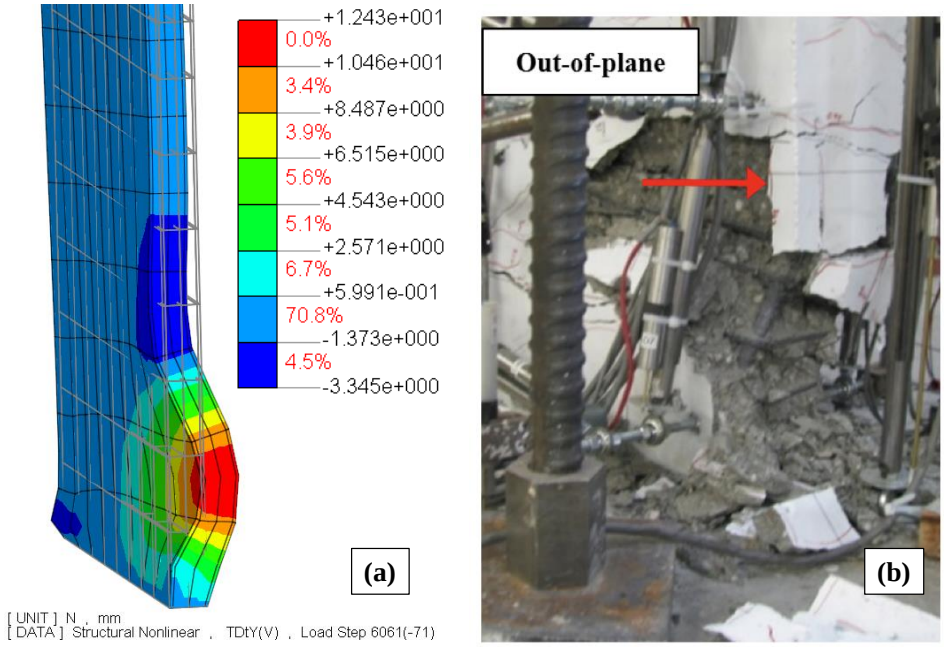

Figure 6-49 Out-of-plane deformation of WP1 (a) FE and (b) Experiment (Segura and Wallace 2017)

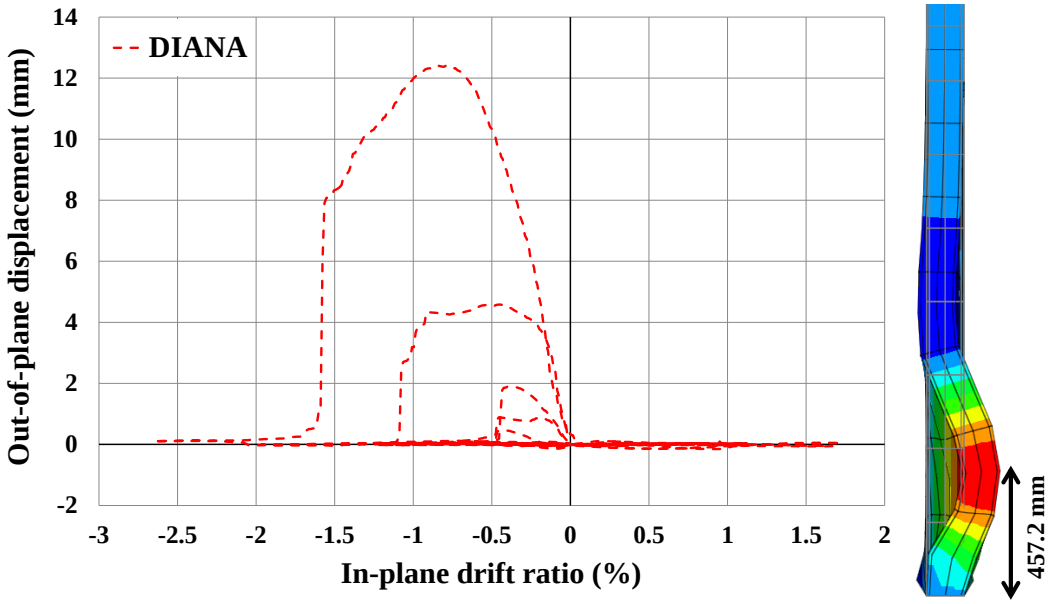

Figure 6-50 Out-of-plane displacement evolution of WP1 resulted from FE

6.5.5. SP2-ND

Table 6-11 and Figure 6-51 summarize the basic characteristics of the specimen SP2-ND. Table 6-12 and Table 6-13 show the material properties of the wall. Figure 6-52 shows the loading pattern applied to SP2-ND which was applied to SP3-LD and SP4-D as well. For more information, refer to Chapters 4 and 5.

Table 6-11 Details of the specimens SP2-ND, SP3-LD and SP4-D

Specimen	SP2-ND	SP3-LD	SP4-D
Clear height, H_w (mm)	1650		
Length, L_w (mm)	1600		
Thickness, t (mm)	160		
Total longitudinal reinforcement ratio, $\rho_t = (A_{s,BZ} + A_{s,web}) / (L_w \times t)$	0.92%		
Web longitudinal reinforcement ratio	0.885	1.13%	1.13%
Boundary zone (BZ) longitudinal reinforcement ratio	1.03%	0.879%	0.879%
BZ transverse reinforcement ratio, $\rho_{sx} = A_{vx} / (s \times t)$	0.295%	0.739%	1.05%
BZ transverse reinforcement ratio, $\rho_{sy} = A_{vy} / (s \times l_{BZ})$	0.248%	0.53%	0.75%
Web transverse reinforcement ratio, $\rho_{s(web)} = A_{v(web)} / (s \times l_{web})$	-	-	0.326%
Web shear reinforcement ratio, $\rho_v = A_{sv} / (s \times t)$	0.655%		

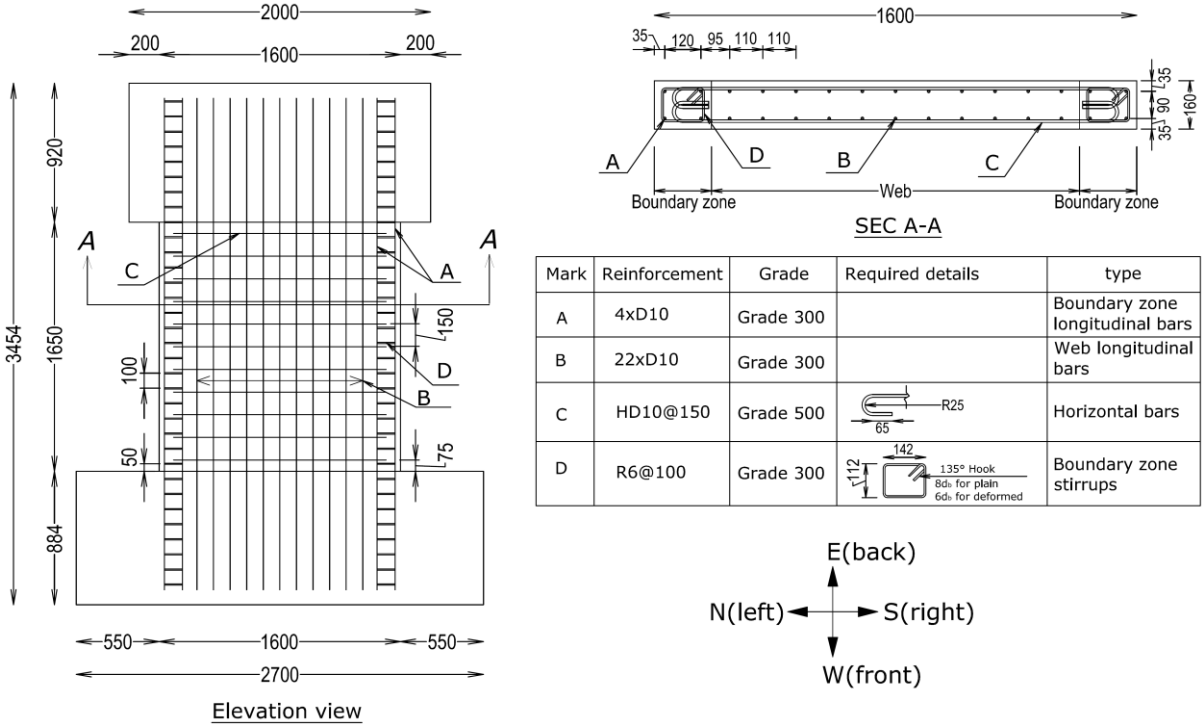

Mark	Reinforcement	Grade	Required details	type
A	4xD10	Grade 300		Boundary zone longitudinal bars
B	22xD10	Grade 300		Web longitudinal bars
C	HD10@150	Grade 500	R25, 65	Horizontal bars
D	R6@100	Grade 300	142, 112, 135° Hook, 8d_b for plain, 6d_b for deformed	Boundary zone stirrups

Figure 6-51 Details of the reinforcement layouts of SP2-ND

Table 6-12 Steel reinforcing bar properties of SP2-ND, SP3-LD and SP4-D

Specimen	Bar size	Bar Diameter (mm)	E_s (MPa)	f_y (MPa)	f_u (MPa)	ε_u
SP2-ND, SP3-LD and SP4-D	R6	6	200945	517	656	0.135
	RH8	8	187080	534	687	0.122
	D10	10	168460	273	420	0.21
	HD10	10	204004	523	708	0.141

Table 6-13 Concrete cylinder test result for SP2-ND

Specimen	Average concrete compressive strength (MPa)
SP2-ND	27.6

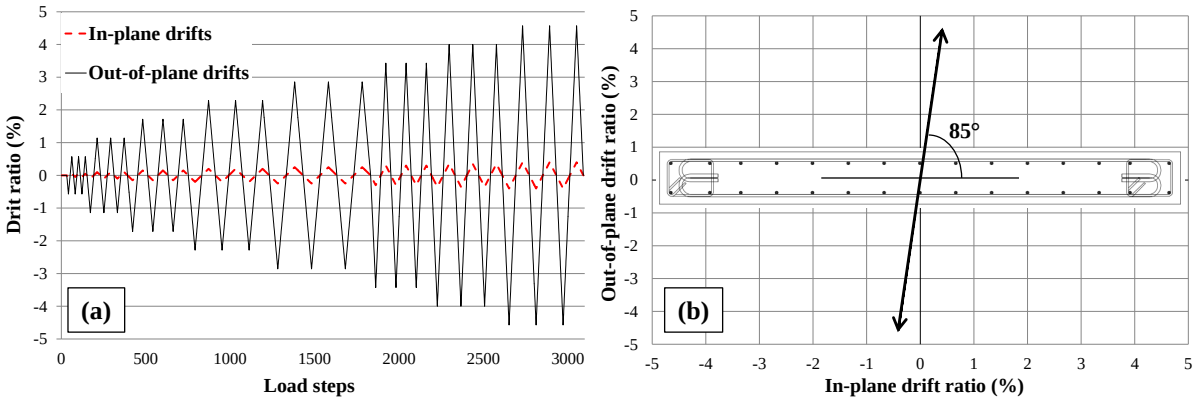

Figure 6-52 Lateral loading pattern of SP2-ND, SP3-LD and SP4-D (a) Loading protocols and (b) Angle of loading

Curved shell vs solid 20 nodes elements

Limitations of curved shell elements compared to solid 20nodes elements especially regarding simulating out-of-plane shear failure were discussed briefly in Section 6.3.1. As the failure mode of the specimen SP2-ND tested in the lab was out-of-plane shear (refer to Chapter 5 for more details), the capability of curved shell and solid elements in simulating this type of failure was investigated in this section.

One of the parameters that can affect the behaviour of the wall when using curved shell elements is the number of integration points. The effect of this parameter on the force-drift curve of SP2-ND was investigated in Figure 6-54. The only difference between these integration point schemes is the number of integration points in the out-of-plane direction (3, 5 and 7 points). Based on the force-drift curve of the wall shown in Figure 6-54, integration point schemes with 7 integration points in the out-of-plane direction were used to investigate the failure mode of the wall using crack pattern (Figure 6-55). Figure 6-56 shows the crack pattern of specimen SP2-ND using 20nodes solid elements. It can be seen in Figure 6-55 and Figure 6-56 that while 20nodes solid elements were able to capture out-of-plane shear cracks

and consequently out-of-plane shear failure, curved shell elements were capturing a horizontal/flexural crack pattern which is different than what was observed in the laboratory. Hence, when using curved shell elements, it was not possible to capture the out-of-plane shear failure and the strength drop due to out-of-plane shear cracks (Figure 6-54b).

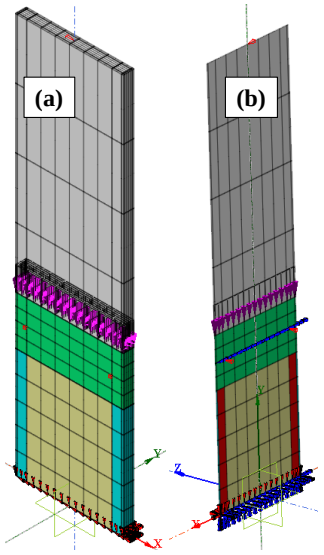

Figure 6-53 The FE model of the wall SP2-ND using (a) solid and (b) shell elements

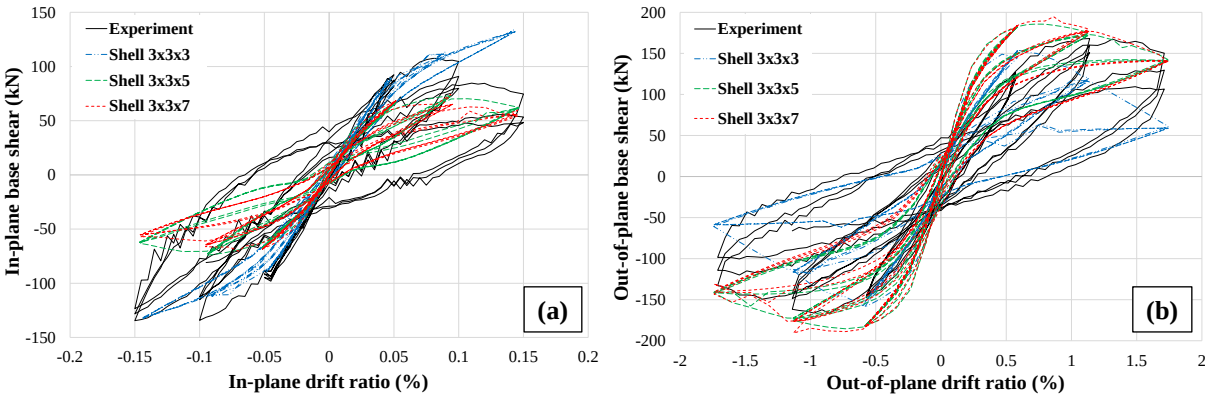

Figure 6-54 Effect of number of integration points on force-drift ratio of the wall in the (a) in-plane and (b) out-of-plane directions

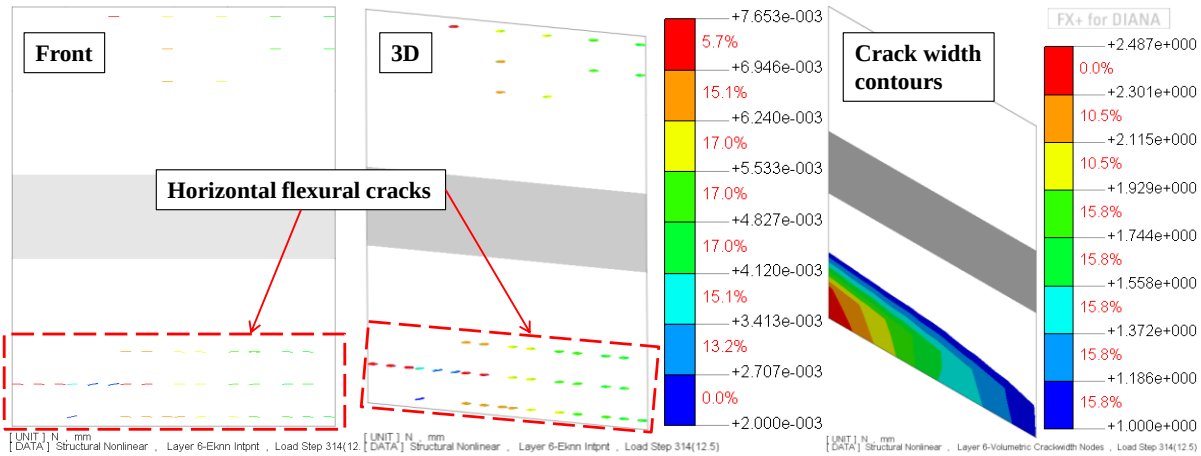

Figure 6-55 Crack pattern of SP2-ND using curved shell elements with 3x3x7 integration points

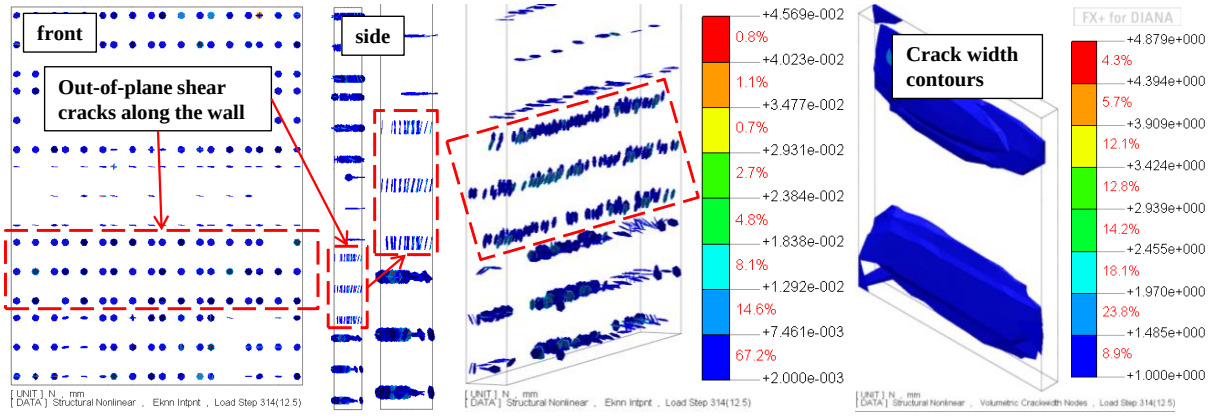

Figure 6-56 Crack pattern of the wall SP2-ND using 20nodes solid elements

Base shear vs drift ratio of SP2-ND

Figure 6-57 compares the FE results with the experiment of the base shear vs drift ratio of specimen SP2-ND in the in-plane and out-of-plane directions. It can be seen that considering the complicated lateral loading pattern and the final failure mode of the wall, the FE model was able to capture the overall behaviour of the wall in terms of strength and drift capacities reasonably well. However, it was not so accurate in capturing the stiffness of the wall. One of the reasons for having different stiffness in the FE analysis for SP2-ND could be the sensitivity of the wall's stiffness to the lateral loading angle of the wall (skewed loading with 85degree with respect to the in-plane axis, see Figure 6-52) which was not easy to capture exactly as the experiment in the FE analysis for each loading step. It is worth noting that the FE model was able to properly capture the stiffness of the wall in the case of SP1-Skew which was a skew loading with 45 degree (see Section 6.5.1). As was explained in Section 6.5.1 in details and can be seen in Figure 6-57 as well, the in-plane base shear vs drift ratio curve of SP2-ND was quite sensitive to the small displacement steps applied in the test which was problematic when comparing to FE results.

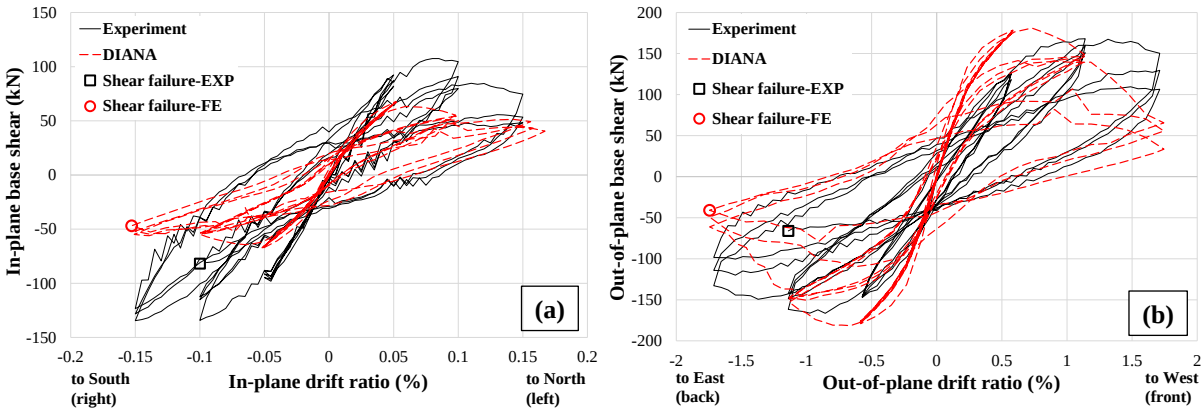

Figure 6-57 Base shear-drift ratio of SP2-ND in the (a) in-plane and (b) out-of-plane directions

Failure mode of SP2-ND captured in the FE analysis

Failure mode of SP2-ND observed in the laboratory was a shear failure in the out-of-plane direction. Figure 6-58 shows the crack pattern of SP2-ND at failure point captured in the FE analysis. Minor cracks were filtered to show the crack pattern more clearly. Failure mode captured in DIANA was compared with the experimental observations in Figure 6-59. It can be seen that the FE model was able to capture the complex failure mode of SP2-ND properly. It is worth noting, in DIANA, out-of-plane shear failure was considered when the out-of-plane shear (diagonal) cracks form along the full length and thickness of the wall. This was based on the experimental observations and the limitation of the FE model in capturing bar rupture and buckling after the instability of the wall. It is worth noting that these cracks are inclined along the thickness of the wall similar to an in-plane shear failure in which the cracks are inclined along the length.

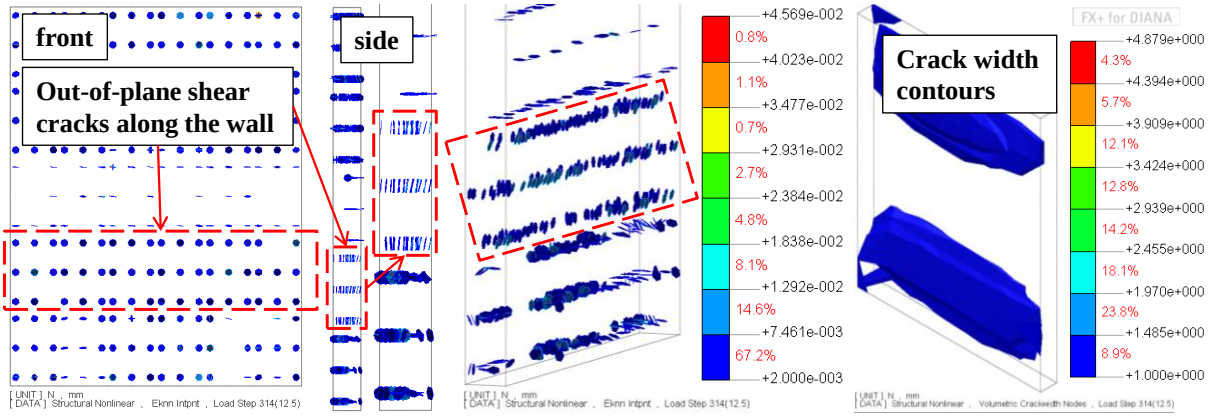

Figure 6-58 Crack pattern of SP2-ND captured in DIANA

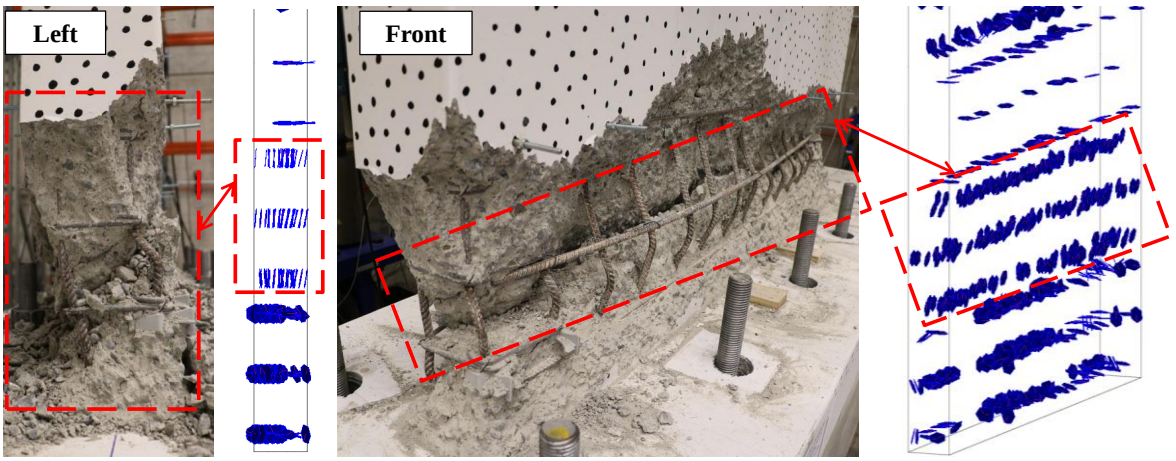

Figure 6-59 Failure mode of the wall captured in FE compared with experimental observations

Von Mises strain and stress contours were also used to investigate the failure mode of the wall captured in the FE analysis (Figure 6-60 and Figure 6-62). The reason that von Mises strain was used here was the complexity of the crack pattern for this specific failure mode

which includes cracks/strain along different planes. Therefore, one type of strain wouldn't be able to show the full crack pattern of the wall. Von Mises strain contours of the wall is shown at the first cycle of 0.15% in-plane and 1.71% out-of-plane drift ratios and compared with the experiment in Figure 6-60. It can be seen that the strain contours representing the crack pattern of the wall match the experimental observations (equations related to von Mises strain was presented in Section 6.5.1).

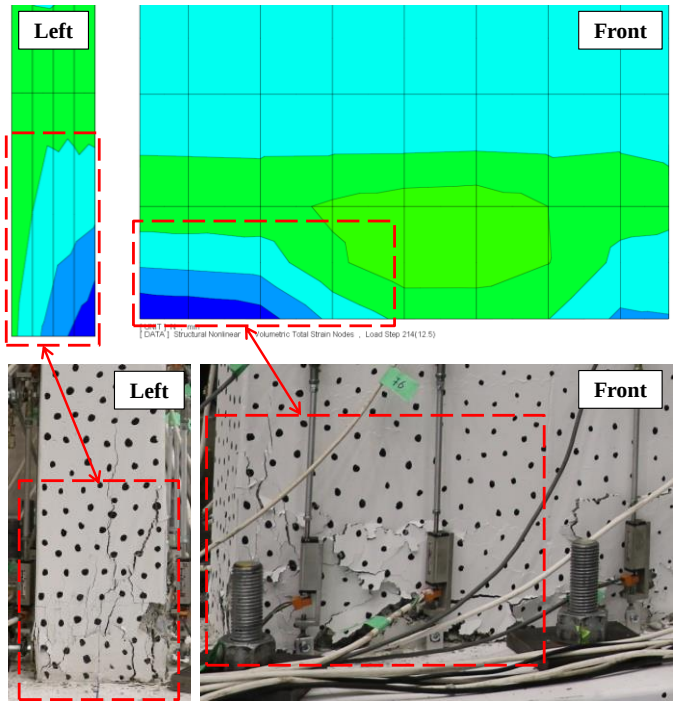

Figure 6-60 Von Mises strain contours of SP2-ND compared with experiment

Von Mises strain and stress contours of specimen SP2-ND are shown in Figure 6-62. Small strains were filtered in the Von Mises strain contours to show the von Mises strain pattern more clearly. Concentration of von Mises strain in Figure 6-62 at the same area that out-of-plane shear failure occurred further proved the capability of the model in capturing this failure mode. It was shown in Chapter 5 that the length of the wall in compression is the key in the development of out-of-plane shear failure. As walls prone to out-of-plane shear failure usually don't have proper confinement in the boundary zones and the web, therefore a compressive strain of 0.003 was assumed as the point that concrete starts to crush (see Figure 6-61). Axial strain contours of the wall shown in Figure 6-62 were filtered to show only the parts with compressive strains higher than 0.003. Looking at the axial strain contours of the wall shown in Figure 6-62, it can be seen that the full length of the wall is vulnerable to out-of-plane shear failure. Von Mises stress contours of the wall shown in Figure 6-62 were filtered to show only compressive von Mises stress higher than the minimum compressive stress defined in the FE model for concrete of the web (20% of maximum unconfined

compressive strength as shown in Figure 6-61). The axial strain and von Mises stress patterns shown in Figure 6-62 will be used for future reference to help identifying out-of-plane shear failure in RC walls investigated in Chapter 7 and Chapter 8. As can be seen in Figure 6-59, in the experiment after the wall got shorten along its height, it moved all the longitudinal bars along the wall down with it. However, this was not captured in the FE analysis as buckling and rupture of the longitudinal bars was not considered in the model. In the experiment out-of-plane shear failure led to sliding of the wall in the transverse direction which can be seen in Figure 6-59 (left side view). Such sliding of the wall was not captured by the FE model. This can be mainly due to the limitation of the FE model in capturing buckling and rupture of the longitudinal and transverse reinforcement and hence did not allow the sliding of the wall in its out-of-plane direction.

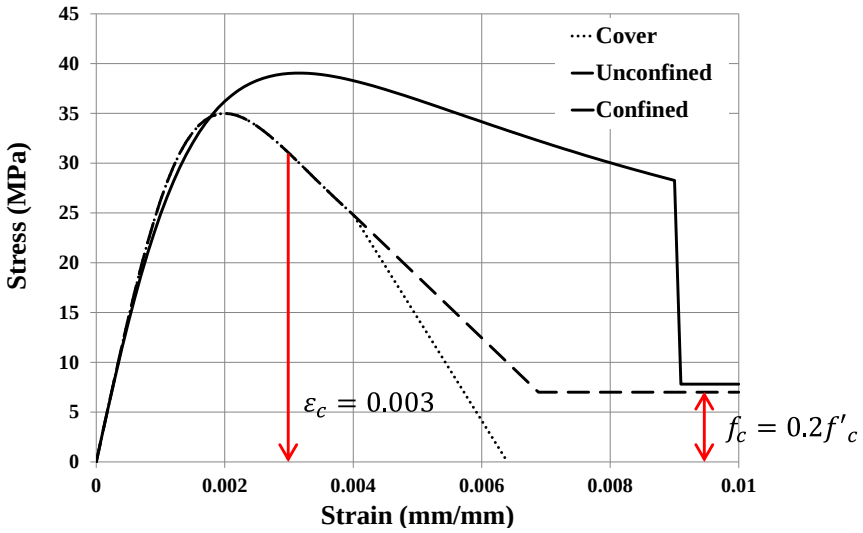

Figure 6-61 Strain and stress limitation used for filtering the axial strain and stress contours

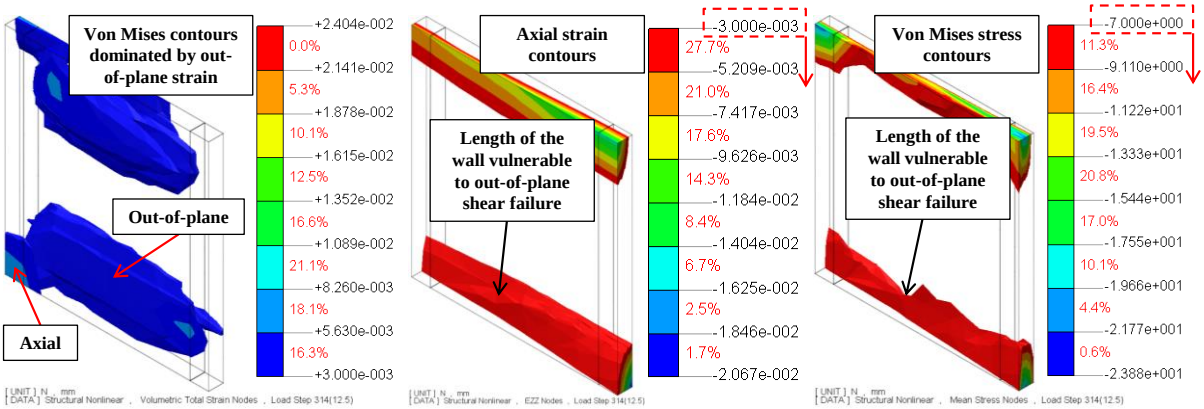

Figure 6-62 Von Mises and axial strain and von Mises stress contours of SP2-ND

6.5.6. SP3-LD

Table 6-11 and Figure 6-63 summarize the basic characteristics of the specimen SP3-LD. Table 6-12 and Table 6-14 show the material properties of the specimen. Figure 6-52 shows the loading pattern applied to the specimen SP3-LD. For more information, refer to Chapters 4 and 5.

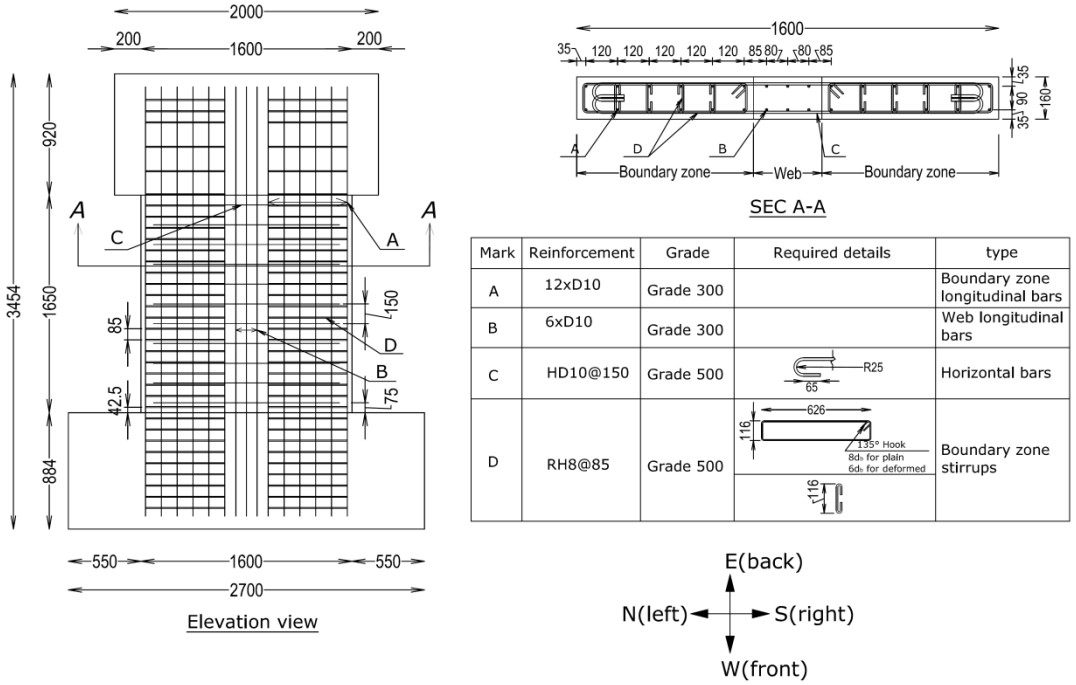

Mark	Reinforcement	Grade	Required details	type
A	12xD10	Grade 300		Boundary zone longitudinal bars
B	6xD10	Grade 300		Web longitudinal bars
C	HD10@150	Grade 500	R25, 65	Horizontal bars
D	RH8@85	Grade 500	626, 116, 135° Hook, 8d_b for plain, 6d_b for deformed, 116	Boundary zone stirrups

Figure 6-63 Details of the reinforcement layouts of SP3-LD

Table 6-14 Concrete cylinder test result for SP3-LD

Specimen	Average concrete compressive strength (MPa)
SP3-LD	24.5

Base shear vs drift ratio of SP3-LD

Figure 6-64 shows the base shear vs drift ratio of SP3-LD in the in-plane and out-of-plane directions, comparing the FE results with the experiment. It can be seen that the FE model was able to capture the overall behaviour of the wall reasonably well especially in the out-of-plane direction which was the main direction of the lateral loading. One of the key reasons that the force-drift curve of specimen SP3-LD resulted from DIANA has less energy absorption than the one observed in the experiment is the deficiency of the concrete model in considering the residual behaviour of concrete (see Section 6.2.1).

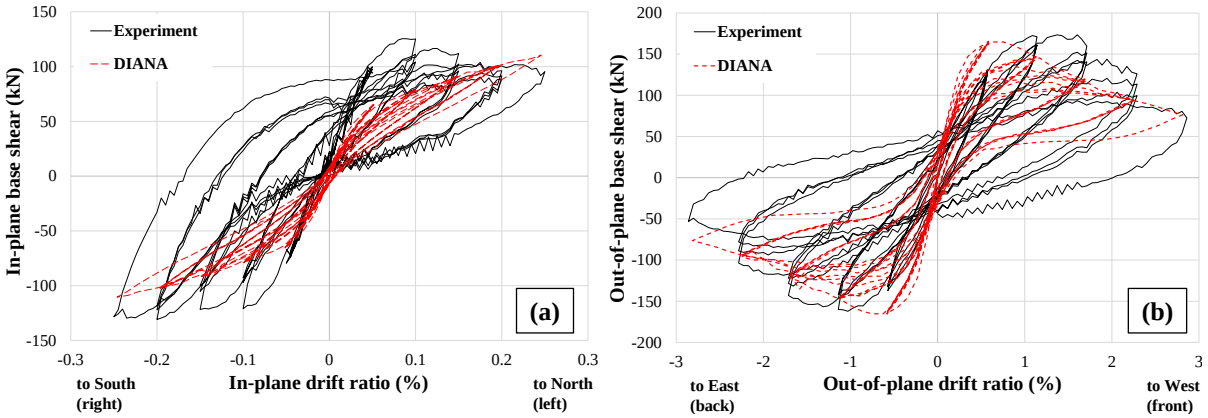

Figure 6-64 Base shear-drift ratio of SP3-LD in the (a) in-plane and (b) out-of-plane directions

Failure mode of SP3-LD captured in DIANA

Figure 6-65 shows the crack pattern of SP3-LD at 0.25% in-plane and 2.86% out-of-plane drift ratios resulted from FE analysis. Out-of-plane shear cracks can be seen in both sides of the wall in Figure 6-65. These out-of-plane shear cracks matched the experimental observations shown in Figure 6-65.

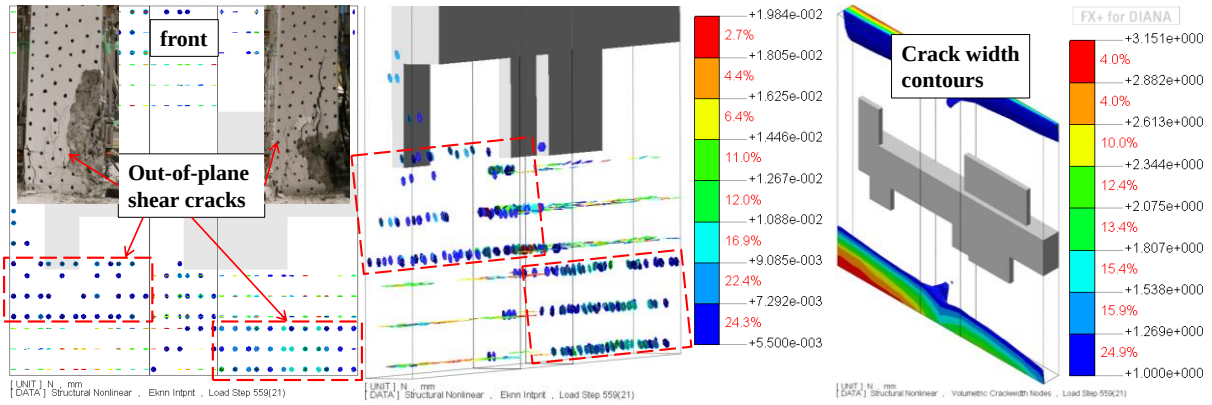

Figure 6-65 Crack pattern of SP3-LD

Von Mises strain contours of the wall is shown in Figure 6-66 at 0.25% in-plane and 2.86% out-of-plane drift ratios and were compared with the experiment. It can be seen that von Mises strain contours matched the crack pattern of the wall observed in the experiment.

Von Mises strain and stress and axial strain contours of SP3-LD are shown in Figure 6-67. It can be seen that unlike SP2-ND, for the case of SP3-LD, axial strains dominated the von Mises strain contours due to the contribution of transverse reinforcement. Von Mises stress contours of the specimen SP3-LD shows a distribution of stress along the height of the wall also affected by axial stress which differs from the case of SP2-ND in which the von Mises stress formed along the length of the wall (see Figure 6-62). Axial strain contours of the wall in Figure 6-67 also show that the length of the part with compressive strain higher than 0.003 is also decreased compared to specimen SP2-ND (see Figure 6-62). Moreover, the concrete

compressive strain capacity is also increased due to the confinement resulted from the transverse reinforcement in the boundary elements. Both von Mises strain and stress contours of specimen SP3-LD indicate the domination of axial strain and stress which matches with the axial crushing failure of the specimen observed in the experiment.

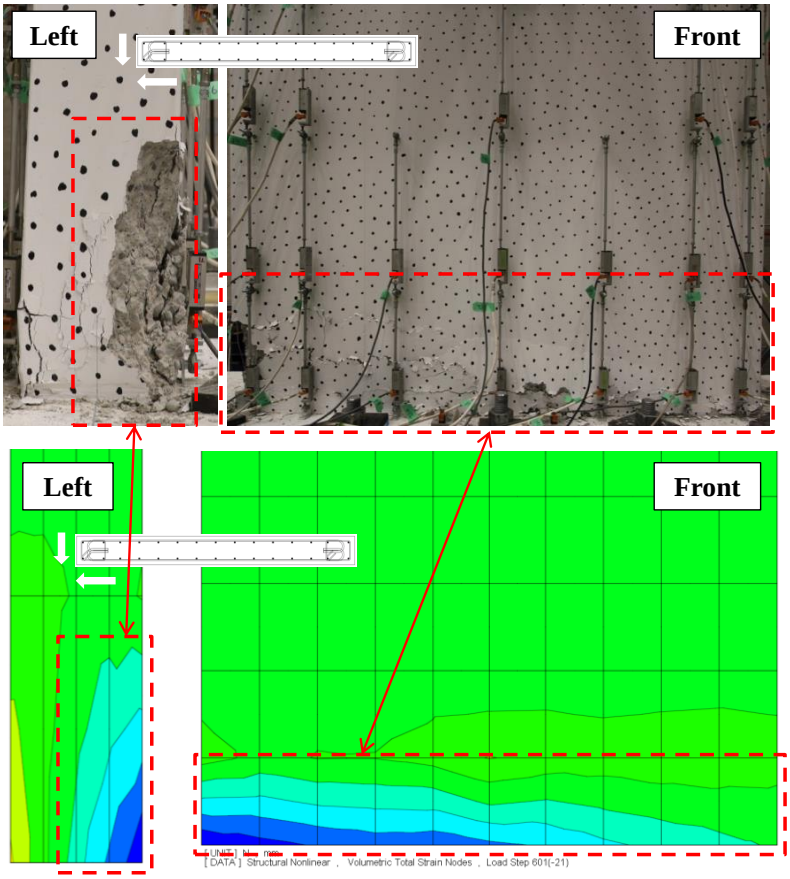

Figure 6-66 von Mises strain contours of SP3-LD compared with crack pattern observed in the lab

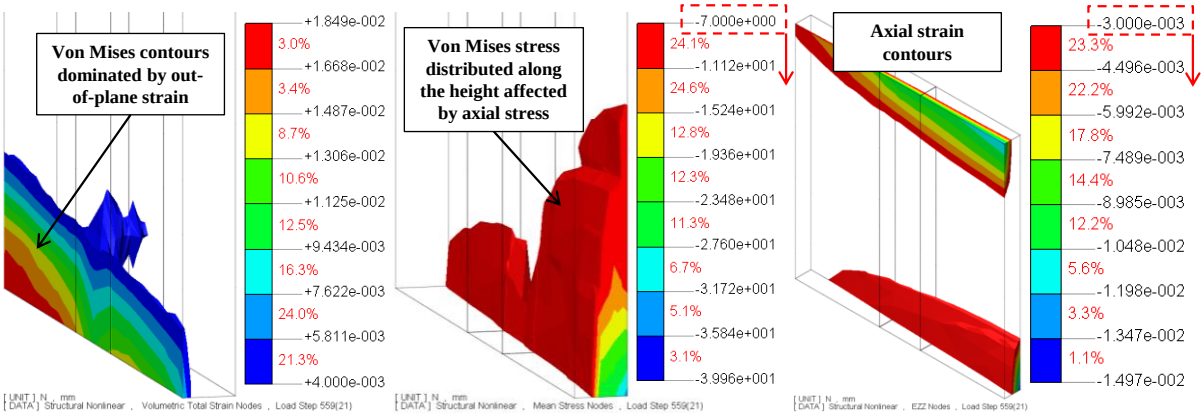

Figure 6-67 Von Mises strain and stress and axial strain contours of SP3-LD

6.5.7. SP4-D

Table 6-11 and Figure 6-68 summarize the basic characteristics of the specimen SP4-D. Table 6-12 and Table 6-15 show the material properties of the specimen. Figure 6-52 shows the loading pattern applied to the specimen SP4-D. For more information, refer to Chapters 4 and 5.

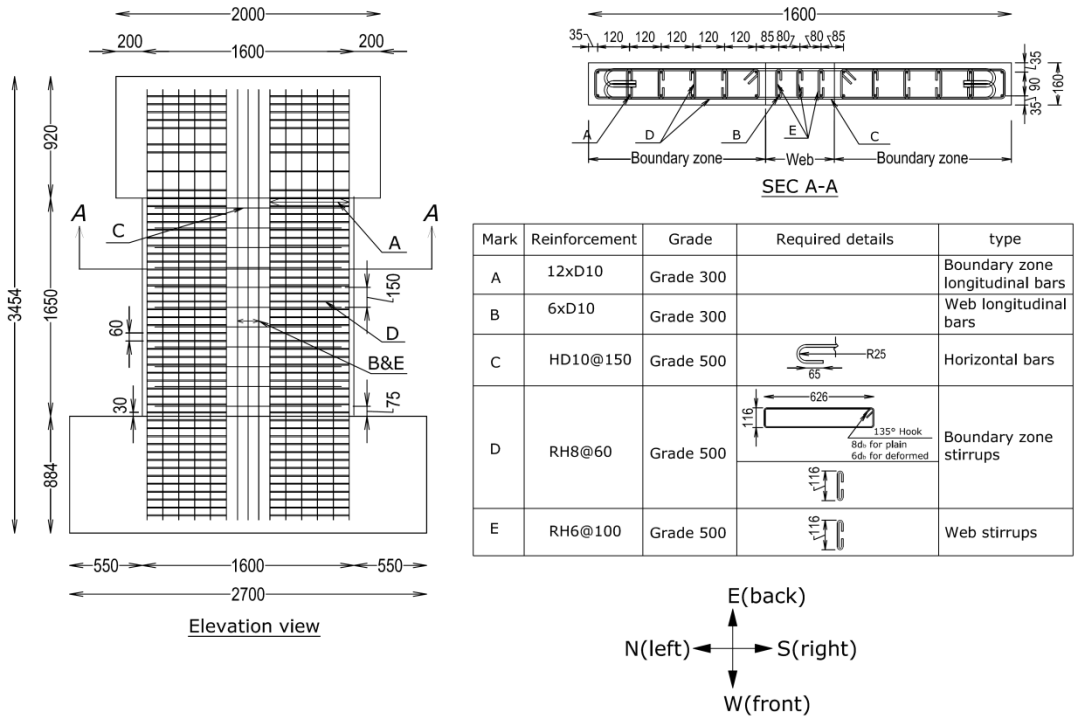

Mark	Reinforcement	Grade	Required details	type
A	12xD10	Grade 300		Boundary zone longitudinal bars
B	6xD10	Grade 300		Web longitudinal bars
C	HD10@150	Grade 500	R25, 65	Horizontal bars
D	RH8@60	Grade 500	626, 116, 135° Hook, 8d_b for plain, 6d_b for deformed, 116, C	Boundary zone stirrups
E	RH6@100	Grade 500	116, C	Web stirrups

Figure 6-68 Details of the reinforcement layouts of SP4-D

Table 6-15. Concrete cylinder test result for SP4-D

Specimen	Average concrete compressive strength (MPa)
SP4-D	24.2

Base shear vs drift ratio of SP4-D

Figure 6-69 shows the base shear vs drift ratio of SP4-D in the in-plane and out-of-plane directions, comparing the FE results with the experiment. It can be seen that the FE model was able to capture the overall behaviour of the wall reasonably well in terms of strength and drift capacities especially in the out-of-plane direction which was the main direction of the lateral loading. For the same reason discussed for the case of specimen SP3-LD, force-drift curves of specimen SP4-D resulted from DIANA had less energy absorption compared to the experimental results.

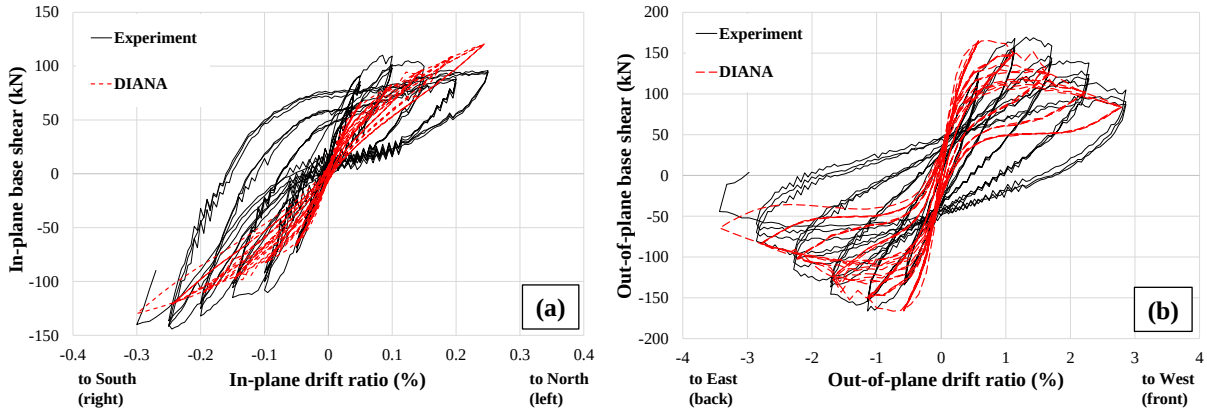

Figure 6-69 Base shear-drift ratio of SP4-D in the (a) in-plane and (b) out-of-plane directions

Failure mode of SP4-D captured in DIANA

Figure 6-70 shows the crack pattern of SP4-D at 0.3% in-plane and 3.43% out-of-plane drift ratios resulted from FE analysis. Some out-of-plane shear cracks can be seen on each sides of the wall in Figure 6-70. These out-of-plane shear cracks were observed in the experiment as well as can be seen in Figure 6-70.

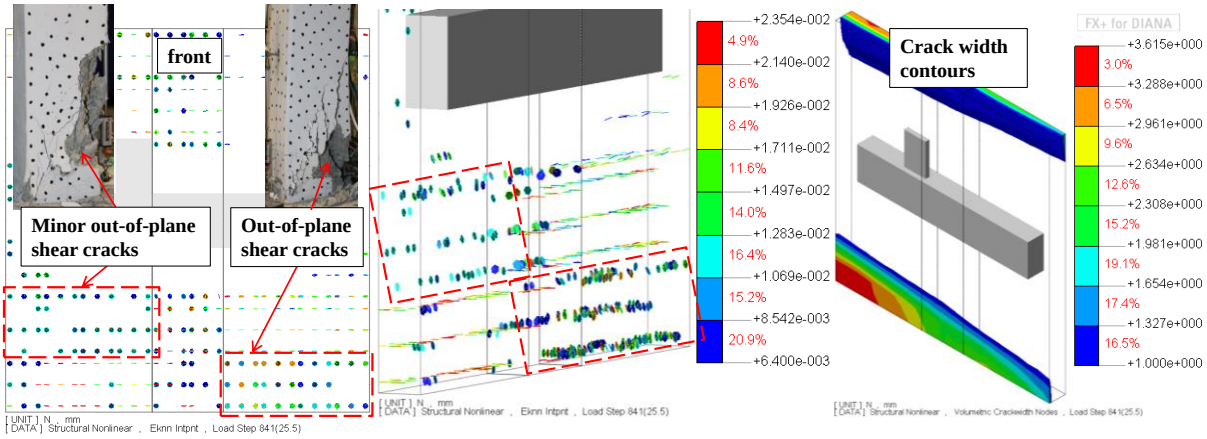

Figure 6-70 Crack pattern of SP4-D in DIANA

Von Mises strain contours of the wall is shown at 0.3% in-plane and 3.43% out-of-plane drift ratios and compared with the experiment in Figure 6-71. It can be seen that the von Mises strain contours representing the crack pattern of the wall matched the experimental observations.

Figure 6-72 shows the cover concrete spalling observed in the experiment from its back side which led to reduction of axial capacity of the wall. It can be seen in Figure 6-72 that the FE results match the experimental observation regarding the cover concrete spalling along the wall as well.

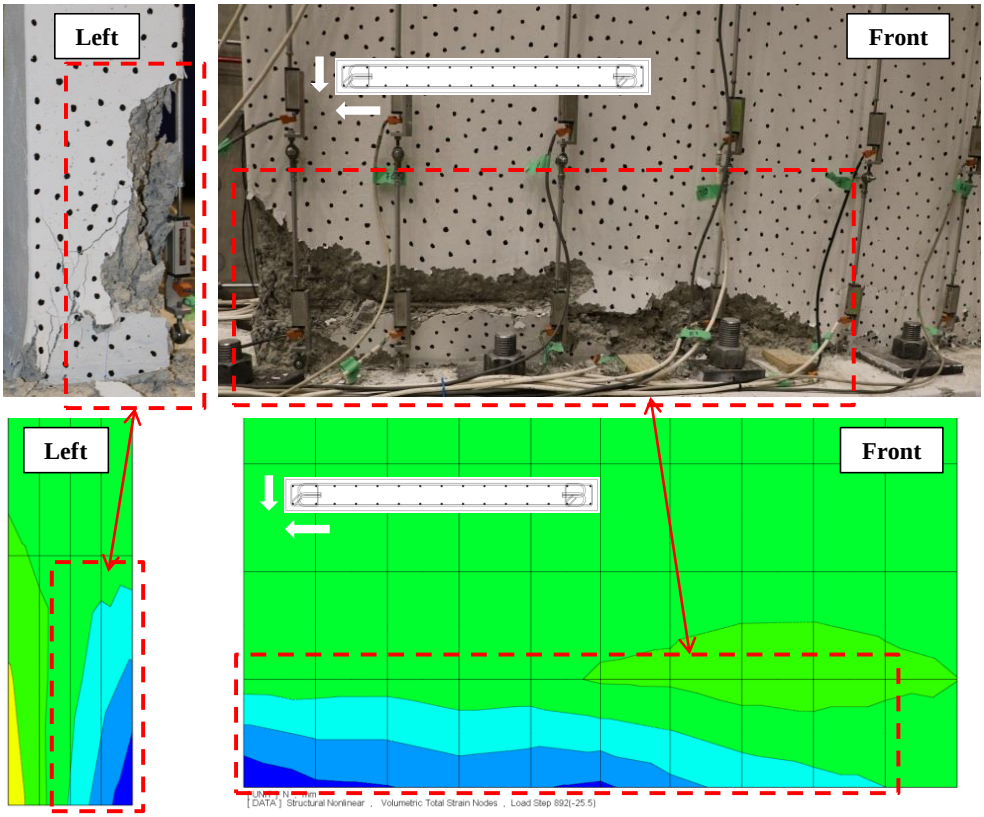

Figure 6-71 von Mises strain contours of SP4-D compared with the experiment

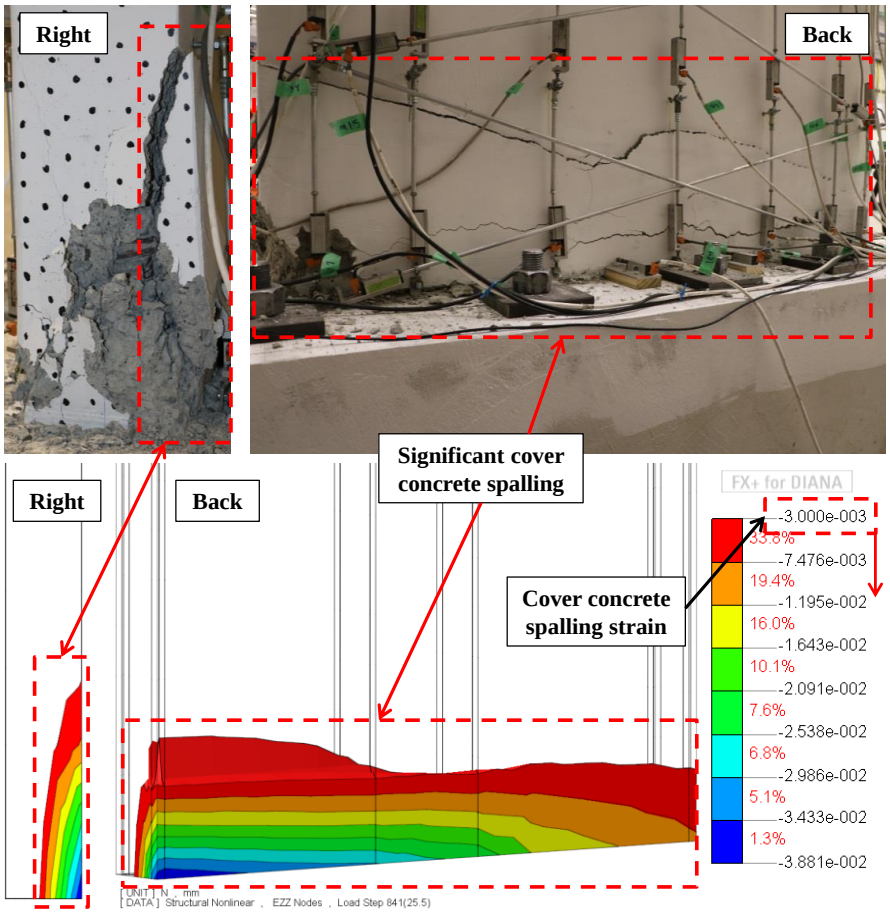

Figure 6-72 Axial compressive strain contours of SP4-D at 0.3%in-plane and 3.43% out-of-plane drift ratios

Von Mises strain and stress contours of SP4-D are shown in Figure 6-73. It can be seen that both von Mises strain and stress contours of the wall are dominated by axial strain and stress and differ from what was observed in Figure 6-62 for SP2-ND which failed in out-of-plane shear. Domination of axial strain and stress in the von Mises contours also match the experimental observations regarding axial crushing failure.

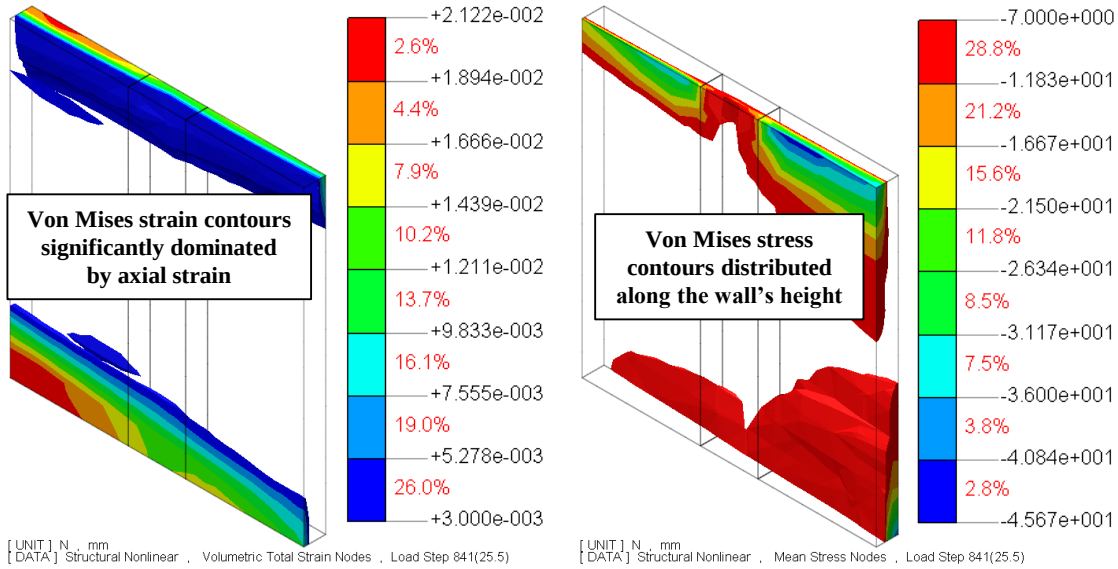

Figure 6-73 Von Mises strain and stress contours of SP4-D

6.6. CONCLUSIONS

In this chapter, firstly the finite element model used to capture the seismic performance of rectangular slender walls subjected to uni- and bi-directional loadings was presented in details. Then the FE model was validated extensively against experimental results of seven RC walls tested under uni- and bi-directional loadings (four different types of bi-directional loading patterns). The FE model was able to capture complex failure modes such as out-of-plane shear. Solid and truss elements were used to simulate concrete and steel reinforcement bars, respectively. A smeared crack approach was used to model concrete. Mander/Belarbi and Menegetto-Pinto models were used to capture the behaviour of concrete and steel reinforcement, respectively. Fully bond between the concrete and steel reinforcement were assumed in the model. Reinforcing bar stiffening was also considered in the FE model of the steel reinforcement. However, bar buckling was not considered in the FE model. It was shown that the FE model and the analysis approach can be utilized to simulate rectangular slender RC walls subjected to uni- and bi-directional loadings. The key findings of this chapter are summarised below.

- It was shown that the FE model can capture the force-drift curve of RC walls properly.
- The FE model was able to simulate different failure modes of RC walls under uni- and bi-directional loadings include concrete crushing and out-of-plane shear failures.
- Although out-of-plane instability was not captured by the FE model for the specimens used for validation, the model was able to capture the out-of-plane buckling properly. It should be noted that lateral instability failure was not the main failure mode of any of the specimens used for validation of the FE model.
- Crack pattern of the walls captured in the FE analysis matched the experimental observations. The FE model was able to capture crushing of concrete and flexural and shear cracks in the in-plane and out-of-plane directions.
- Compressive strains and neutral axis depth as well as the trend of the strain profile of the wall were captured closely by the FE model. However, the FE model did not have the same accuracy with the tensile strains at high drift ratios.
- It was found that when simulating RC walls subjected to bi-directional loading and the failure mode is affected by the out-of-plane behaviour of the wall, using 8nodes elements would lead to different stiffness, strength capacity and failure mode compared to the actual behaviour of the wall.
- Due to the limitations of shell elements with calculating stress and strain along the thickness, it was found that capturing the seismic performance of RC walls prone to out-of-plane shear failure subjected to bi-directional loading is not possible when using curved shell elements.

7. FINITE ELEMENT SIMULATION OF A CASE STUDY RC WALL – WALL D5-6 FROM GRAND CHANCELLOR HOTEL, CHRISTCHURCH, NEW ZEALAND

7.1.INTRODUCTION

In the short but violent Lyttelton aftershock of 22 February 2011, the Christchurch Grand Chancellor Hotel (GCH) building suffered major structural damage. The extent of damage suffered by the building was significantly increased by the collapse of a key supporting shear wall which failed in a brittle manner (Wall D5-6). The building survived the 4 September 2010 earthquake and the 26 December 2010 aftershock events without apparent significant structural damage and was fully in use when the February event occurred. During the approximate 12 seconds of intense shaking that occurred at 12.51pm on 22 February 2011, the building suffered a major structural failure with the brittle rupture of Wall D5-6 in the south-east corner of the building. This shear wall had supported vertically approximately one-eighth of building's mass and was also expected to carry a portion of lateral earthquake loads. As a result of the wall failure, the south-east corner of the building dropped by approximately 800mm and deflected horizontally approximately 1300mm at the top of the building (Dunning Thornton 2011).

The main objective of this chapter is to investigate the key parameters caused the out-of-plane shear failure of Wall D5-6 using FE analysis. For this purpose, firstly the characteristics of the wall was presented, then directionality of the September 2010 and February 2011 earthquakes were discussed and finally using the FE model described in Chapter 6, seismic performance of the wall subjected to various lateral loading patterns was investigated. Effect of the wall's out-of-plane boundary condition was investigated in this chapter as well.

7.1.1. Description of the building and Wall D5-6

The 22-storey GCH building was constructed in two phases. The lower 7 (or 14 half-height car park) storey structure, which comprises RC shear walls and cast-in-place flat slabs and columns, was constructed first in 1970s. The upper 15 full-height storey structure, which comprises of perimeter moment frames with a precast floor system, was added subsequently (Kam et al. 2011). The tower was constructed between 1985 and 1988 according to the NZS4203:1984 loading standard and NZS3101:1982 concrete design standard (Elwood 2013). Figure 7-1 shows the plan and an elevation view of the building. Figure 7-2 and Table 7-2 show the details and the characteristics of Wall D5-6. Material properties of the wall are shown in Table 7-1. For further details refer to studies conducted by Dunning Thornton Consultants Ltd (2011), Kam et al. (2011), Elwood et al. (2012) and Elwood (2013).

As can be seen in Figure 7-1, while the building had good amount of structural walls in the north-south direction (in-plane to Wall D5-6) which would properly control the drift of the structure in that direction, along the east-west direction of the building (out-of-plane of Wall D5-6), there are significantly less amount of structural walls. This would allow Wall D5-6 to undergo significant out-of-plane drift in case of an earthquake along the east-west direction of the building.

Looking at the key characteristics of Wall D5-6 in Figure 7-2 and Table 7-2, it can be seen that the wall had about 25% axial load ratio which is quite high for structural walls in general. Moreover, for a wall with such amount of axial load ratio, it does not have boundary elements with sufficient length and proper section detailing ductility. The other important characteristic of Wall D5-6 is the longitudinal reinforcement ratio that is 0.45%. This is slightly above the minimum allowed by NZS3101:2006-A3 (2017).

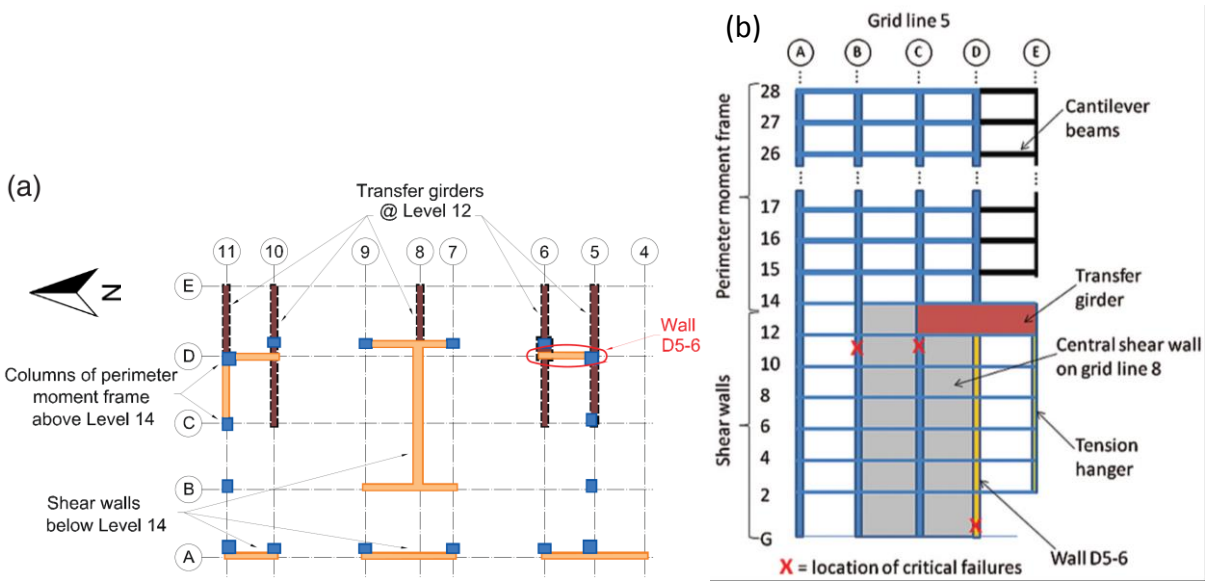

Figure 7-1 GCH structural layout sketch (a) plan and (b) elevation along grid line 5 (Elwood 2013)

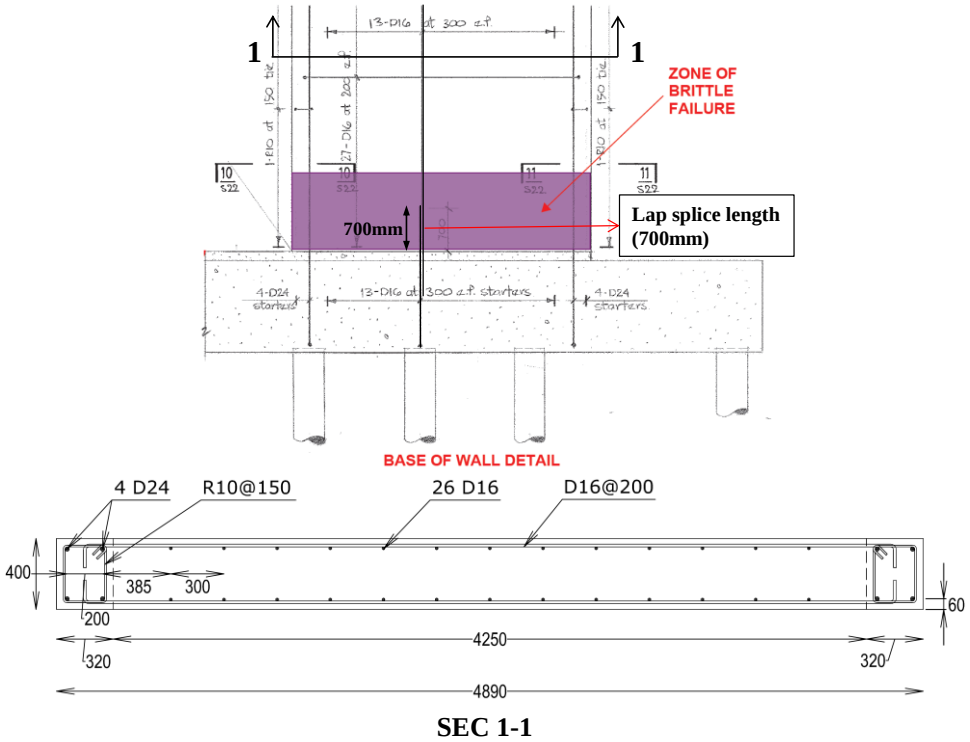

Figure 7-2 Details of the wall D 5-6 (Dunning Thornton 2011)

Table 7-1 Concrete and steel reinforcing bar properties (Dunning Thornton 2011)

Steel reinforcement		Concrete
f_y (MPa)	f_u (MPa)	f'_c (MPa)
300	450	35

Table 7-2 Characteristics of the wall D 5-6 (Dunning Thornton 2011)

Clear height, H_w (mm)	5100
Length, L_w (mm)	4890
Thickness, t (mm)	400
In-plane shear span, H_e (mm) [1]	16875
In-plane shear span ratio (H_e/L_w)	3.45
Out-of-pane shear span, H_{out} (mm) [2]	2675
Out-of-plane shear span ratio (H_{out}/t)	6.69
Axial load ratio, $P/(A_g f'_c)$, using $f'_c = 35\ MPa$	24.8%
Total longitudinal reinforcement ratio, $\rho_t = (A_{s,BZ} + A_{s,web})/(L_w \times t)$	0.452%
Boundary zone transverse reinforcement ratio, $\rho_{sx} = A_{vx}/(s \times t)$	0.262%
Boundary zone transverse reinforcement ratio, $\rho_{sy} = A_{vy}/(s \times l_{BZ})$	0.429%
Web shear reinforcement ratio, $\rho_v = A_{sv}/(s \times t)$	0.503%

1. In-plane shear span of the wall is equal to the in-plane effective height of the building

2. Out-of-plane shear span of the wall was considered half the length of the first storey height to the slab centre, assuming a double bending deformation shape in the out-of-plane direction

7.1.2. Failure description of wall D5-6

Significant structural irregularities influenced the behaviour of GCH building in the 22 February 2011 earthquake. Most notably the east side of the building (bay D-E) was cantilevered over an adjacent service lane (Figure 7-1). As indicated in Figure 7-1, the eastern bay of the lower 14 floors was cantilevered using several very deep transfer girders between levels 12 and 14. The southernmost transfer girders were supported on a critical shear wall denoted as D5-6 in Figure 7-1. Wall D5-6 supports a disproportionately large tributary gravity load from all floors as a result of the cantilever system. The wall D5-6 failed between ground and first floor displaced downward along a diagonal failure plane through the thickness of the wall (Figure 7-3).

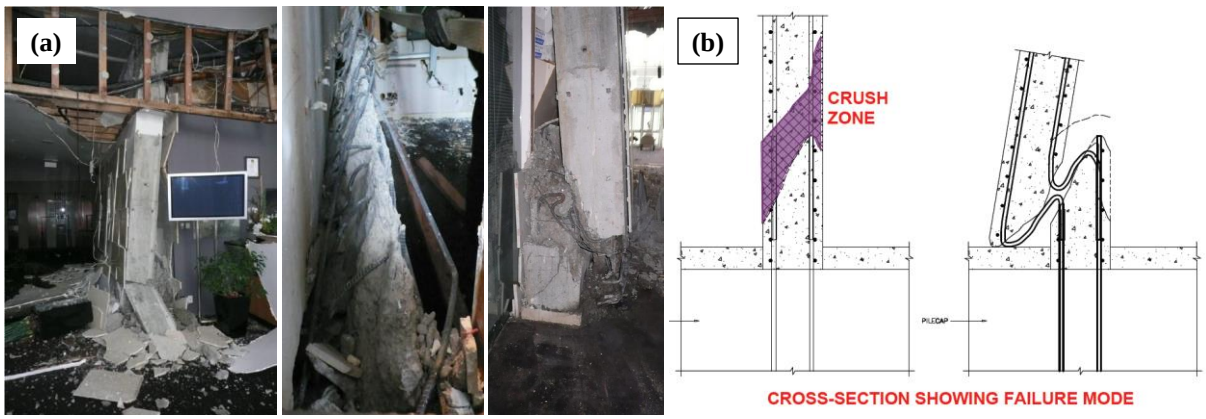

Figure 7-3 Wall D5-6 (a) Failure and (b) Cross section view of the failure mode (Dunning Thornton 2011)

The failure plane, extending the full length of the wall, appeared to initiate at the top of the lap splice in the web vertical reinforcement located 700mm above the ground floor. Wall D5-6 was supporting high axial loads from several sources. First, the wall supported a disproportionately high tributary area since it acted as a prop for the cantilevered bay on the east side of the building. Secondly, the corner column of the upper tower perimeter moment frame would have imparted high axial loads to the wall due to overturning moments, particularly with any bi-directional movement to the south-east. Thirdly, vertical excitation of the cantilever structure could have exacerbated the axial load on the wall (Kam et al. 2011). Out-of-plane drift of the wall during the earthquake excitation further contributed to the failure observed in Figure 7-3.

7.1.3. Liquefaction and Foundation Issues

Visual observation and ground floor survey level data suggests that neither liquefaction nor foundation failure have had significant effects on the performance of the Grand Chancellor structure. There have been no significant surface signs of liquefaction in the vicinity and geotechnical advice is that the area has not been subject to slumping or localized displacement. There are also no signs of significant local level changes around the building (Dunning Thornton 2011).

7.2. DIRECTIONALLY OF THE CANTERBURY'S SEPTEMBER 2010 AND FEBRUARY 2011 EARTHQUAKES

It is known that ground motion intensity is not uniform in all orientations. In some cases ground motions can be polarized and intensity in one orientation can be significantly stronger than the other orientations (Campbell and Bozorgnia 2008, Huang et al. 2008). This phenomenon is often referred as "directionality" of ground motion. One of the important parameters that led to the failure of some of the buildings in the February 2011 Christchurch earthquake (e.g. GCH) was the directionality of the earthquake. While Wall D5-6 from Grand Chancellor Hotel building did not have any apparent damage in the 4 September 2010 earthquake with 7.1 Magnitude, it failed miserably in the 22 February 2011 earthquake with 6.2 Magnitude. Hence, in this section directionality of these two earthquakes and the way they shook Wall D5-6 were investigated. For this purpose, displacement response for Single Degree Of Freedom (SDOF) systems with 5% damping for the initial periods of the building in each direction under the recorded ground accelerations from the 4 September 2010 and 22 February 2011 earthquakes at nearby strong motion stations were used. Initial periods of 2.4

and 2.8 seconds were used to represent the strong axis of the building (i.e., the north-south direction, and y axis in plots), and the weak axis of the building (i.e., east-west direction, and x axis in plots), respectively. It should be noted that the 2.8 and 2.4 seconds periods were reported by Dunning Thornton (2011) as the initial periods of the building in the weak and strong axis, respectively. The displacement responses of the two SDOF systems were plotted against each other to illustrate the directionality in the displacement response to these ground motions. Locations of the four strong motion stations around Christchurch central business district that recorded the two September and February earthquakes are shown in Figure 7-4 along with the building's location. Figure 7-5 and Figure 7-6 show displacement responses for SDOF systems under the recorded ground accelerations from the 4 September 2010 and 22 February 2011 earthquakes at nearby strong motion stations shown in Figure 7-4. Direction of the wall in regards to each earthquake is also shown in Figure 7-5 and Figure 7-6. Figure 7-5 and Figure 7-6 clearly illustrates north-south directionality in the response to the 4 September 2010 earthquake with most of the large displacement cycles oriented in this direction. On the contrary, the displacement response is more strongly directed to the east-west under the 22 February 2011 earthquake likely with an angle (skew). This information significantly helped both numerical and experimental phases of this study. Principal direction of these earthquakes was also reported by Kam et al. (2011).

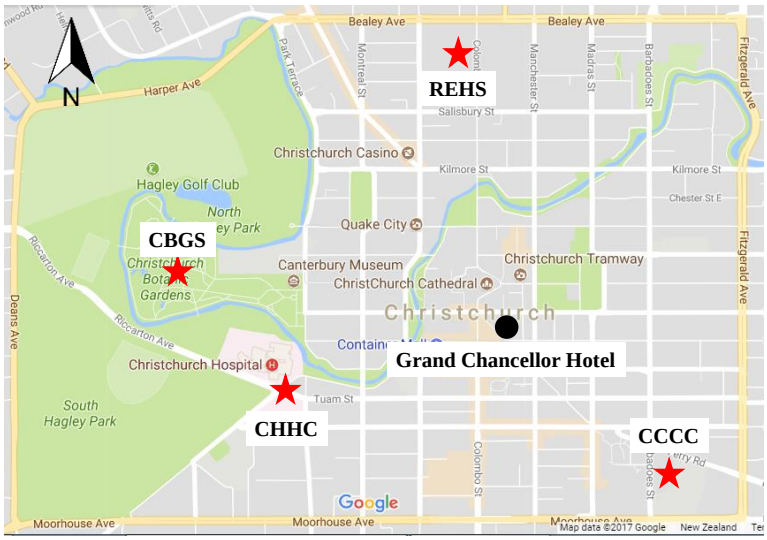

Figure 7-4 Locations of the 4 strong motion stations and Grand Chancellor Hotel

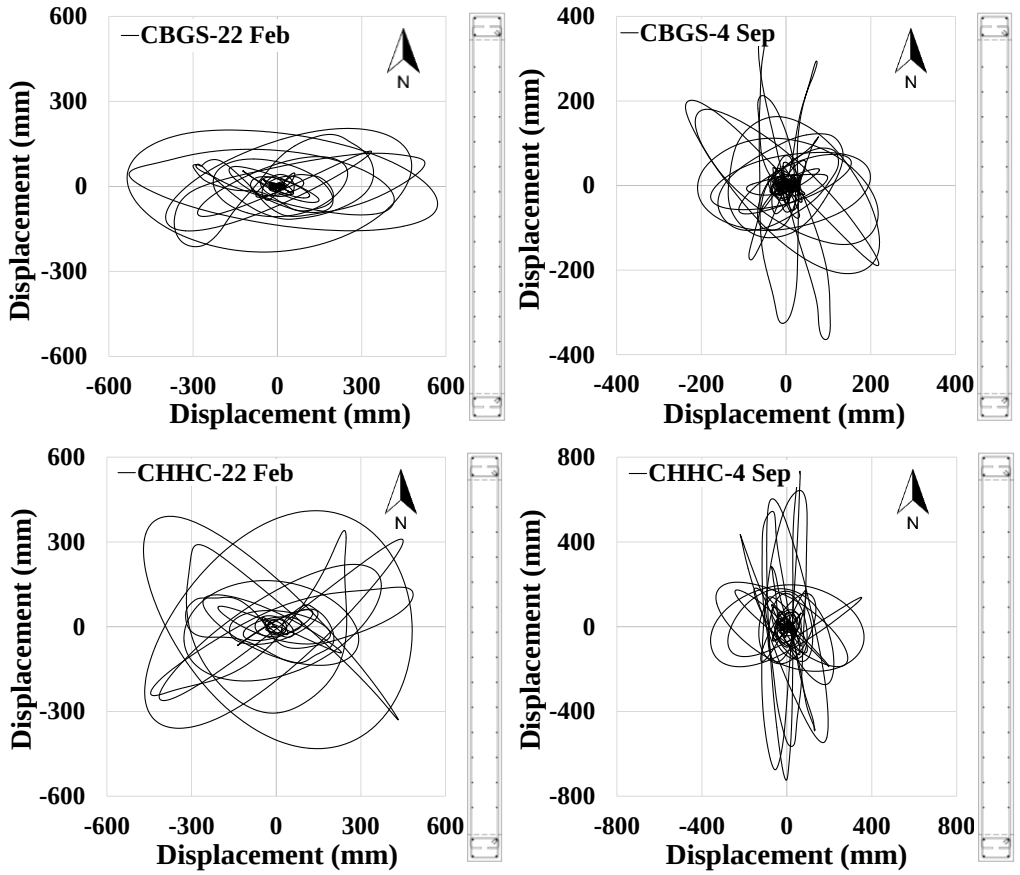

Figure 7-5 Directionality of the 4 September and 22 February earthquakes at CBGS and CHHC stations

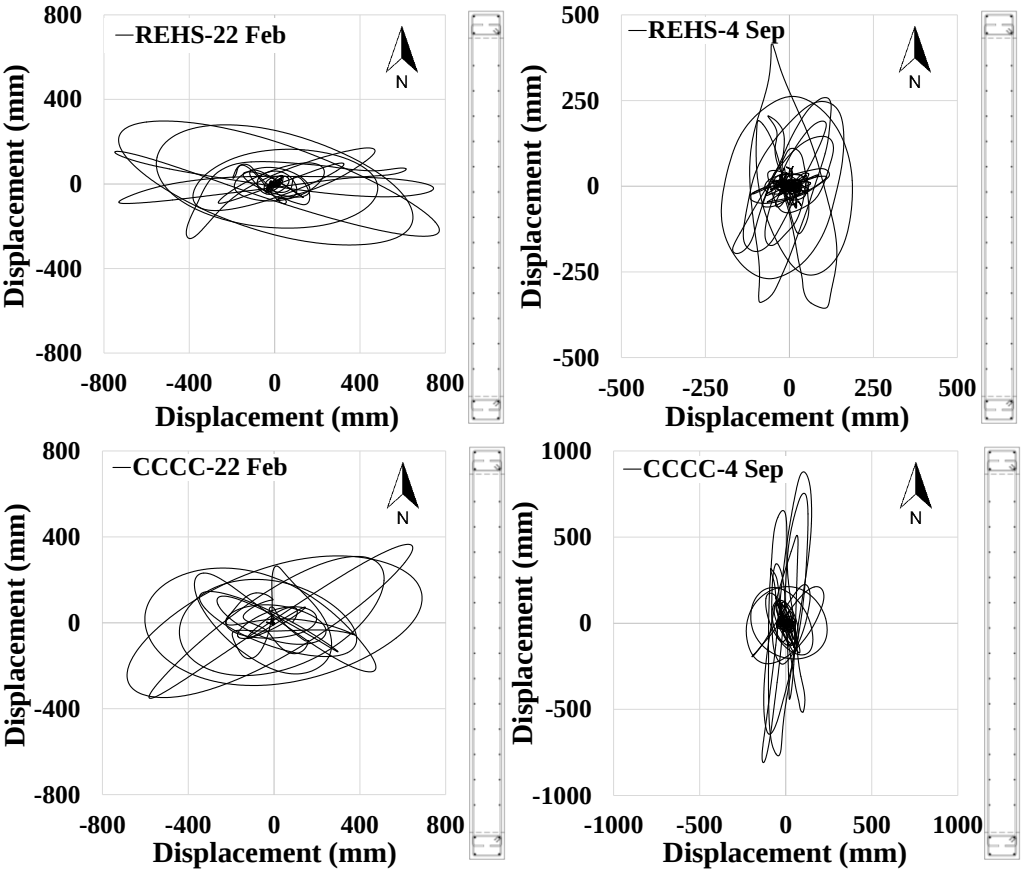

Figure 7-6 Directionality of the 4 September and 22 February earthquakes at REHS and CCCC stations

7.3.SECTION ANALYSIS OF WALL D5-6

Before starting the FE simulation, a section analysis is performed using SAP2000 (2015). The effects of confinement due to transverse reinforcement in the boundary zone and concrete tensile strength are considered in the analysis. It is worth noting that maximum tensile strain of steel reinforcement was limited to 6% (as proposed by Kowalsky (2000) and NZSEE guideline (2017)). Confined and unconfined stress-strain of concrete was assumed based on Mander et al. (1988) model as shown in Figure 7-7. Moment-curvature diagram of the wall for four different levels of axial load ratio (5%, 15%, 25% and 35%) in the in-plane and out-of-plane directions are shown in Figure 7-8 and Figure 7-9, respectively. Moment and shear capacity of the wall with different axial load ratios are shown in Table 7-3. As was described in Table 7-2, the in-plane shear span of the wall was considered as the effective height of the wall (16875 mm) and the out-of-plane shear span of the wall was considered half of the first storey height (2675 mm) assuming a double bending deformation shape in the out-of-plane direction. It can be seen in Figure 7-8 the out-of-plane moment capacity of the wall and consequently its corresponding shear are increased by 2.43 times in the out-of-plane direction, when the axial load is increased from 5% to 25% (25% was the axial load ratio of the wall reported by Dunning Thornton (2011) as original design axial load of the wall). This means a significant increase of shear demand to the wall in the out-of-plane direction.

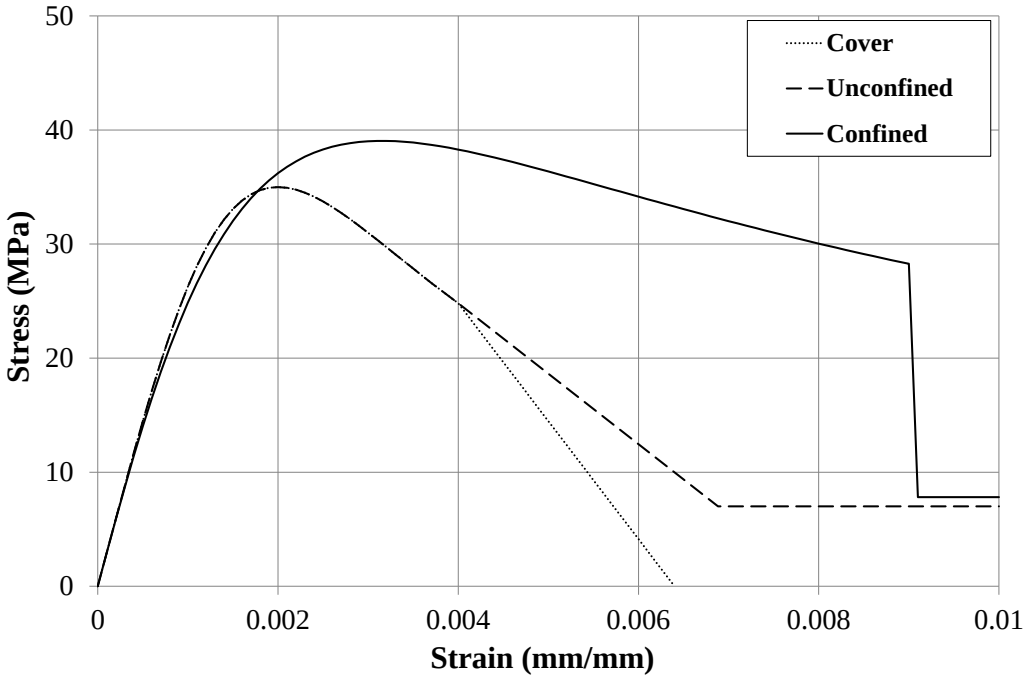

Figure 7-7 Concrete compressive behaviour of Wall D5-6 (Mander et al. 1988)

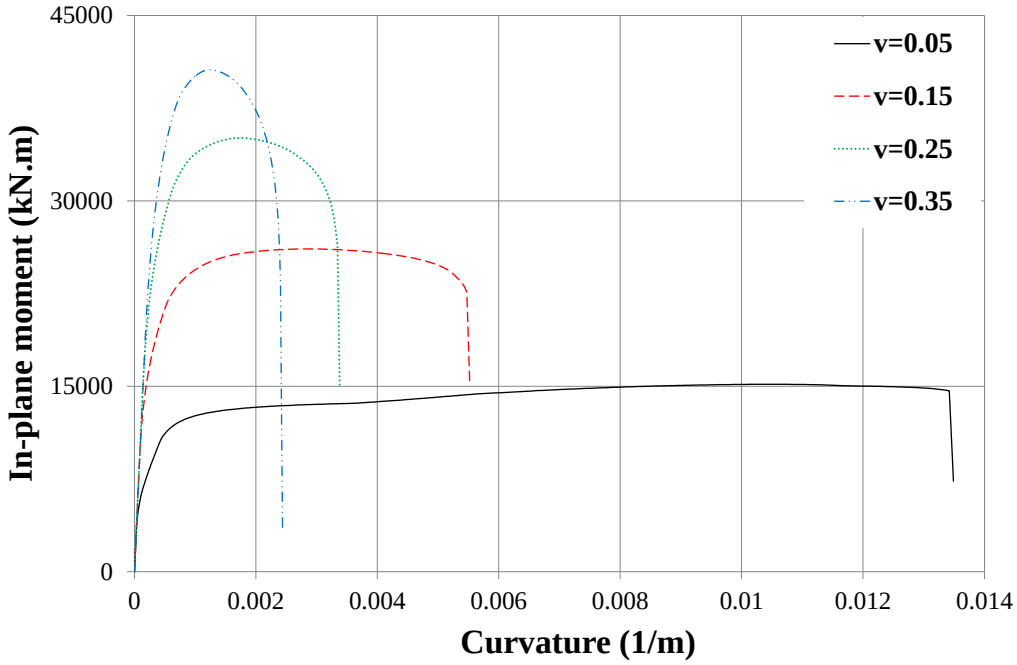

Figure 7-8 In-plane moment-curvature diagram of Wall D 5-6 for different axial load ratios

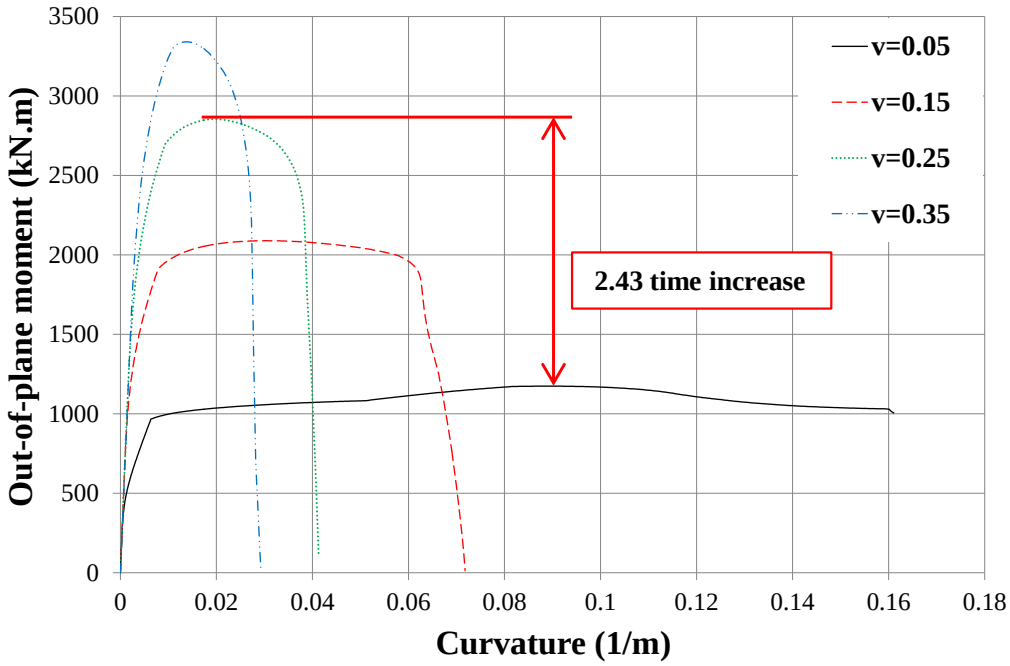

Figure 7-9 Out-of-plane moment-curvature diagram of Wall D 5-6 for different axial load ratios

Table 7-3 Moment capacity and coresponding shear of Wall D5-6 under different axial load levels

Axial load ratio, $P/(A_g f'_c)$, ν	In-plane moment capacity (kN.m)	Out-of-plane moment capacity (kN.m)	Corresponding in-plane shear (kN)	Corresponding out-of-plane shear (kN)	
				Cantilever	Double bending
5%	15160	1173.7	898.4	219.4	438.8
15%	26117	2088.8	1547.7	390.4	780.8
25%	35076	2854.1	2078.6	533.5	1066.9
35%	40593	3339.9	2405.5	624.3	1248.6

7.4.FE ANALYSIS OF WALL D5-6

Characteristics of Wall D5-6 and the earthquake loading pattern of the two September 2010 and February 2011 earthquakes were discussed in Sections 7.1.1 and 7.2, respectively. The next step would be to numerically simulate Wall D5-6 using finite element analysis. The FE model presented in Chapter 6 was used to simulate Wall D5-6 subjected to different lateral loading patterns include in-plane uni-directional, out-of-plane uni-directional and skewed uni-directional loadings. Effect of boundary condition of the wall in the out-of-plane direction on the base shear-drift ratio and failure mode was investigated here as well. Since this chapter was dedicated to the simulation of Wall D5-6, other parameters such as axial load ratio, section aspect ratio, longitudinal reinforcement ratio and section detailing ductility level were not discussed here. However, the effects of these parameters on the seismic performance of RC walls were investigated comprehensively in Chapter 8. For further information regarding the material models, elements and the analysis procedure refer to Chapter 6.

7.4.1. Wall D5-6 under in-plane uni-directional loading

Figure 7-10 and Figure 7-11 show the FE model of Wall D5-6 in DIANA. As was shown in Figure 7-2, the wall had 700mm lap splices coming from the base which was simulated in the model as well as can be seen in Figure 7-11. However, here slippage of these lap splices was not considered in the model. The reasons were discussed in Section 6.3.3.

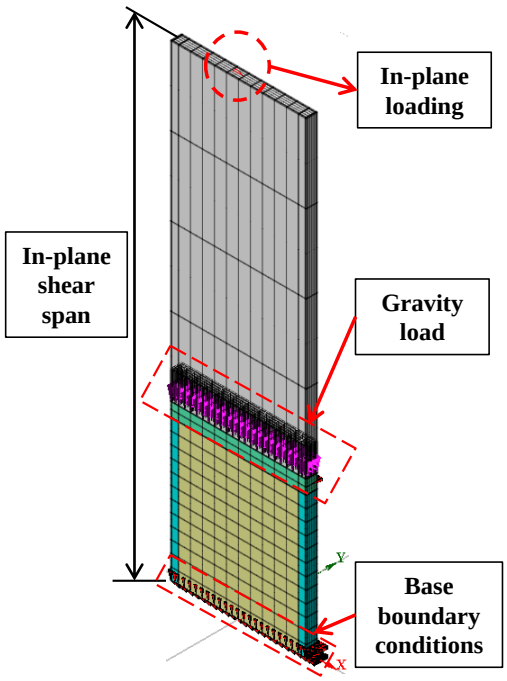

Figure 7-10 The FE model of Wall D5-6 when under in-plane loading only

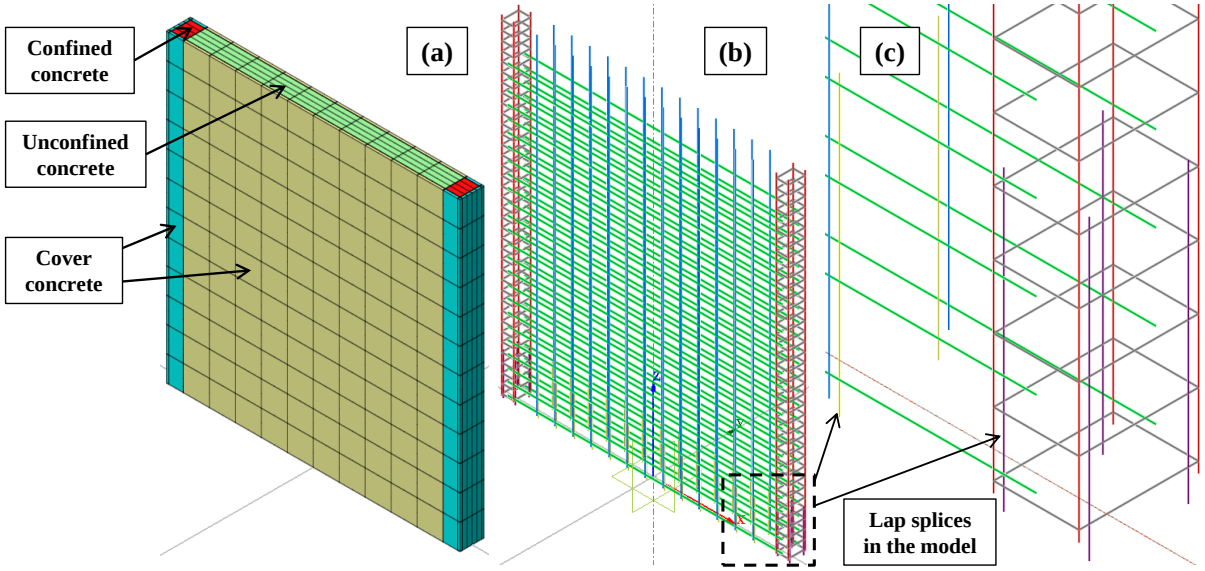

Figure 7-11 Elements in DIANA (a) solid, (b) truss and (c) lap splices

Mesh sensitivity analysis

A mesh sensitivity analysis was performed on the wall to find the mesh configuration that provides the most stable and efficient results. Table 7-4 and Figure 7-12 show the details of the mesh configurations used for the mesh sensitivity analysis. Figure 7-13 shows the monotonic base shear vs drift ratio of Wall D5-6 for the mesh configurations shown in Figure 7-12. Based on the mesh sensitivity analysis results, mesh configuration "c" was chosen.

Table 7-4 details of the mesh cofigurations used for the mesh sensitivity analysis

Mesh type	Mesh size (mm)				Number of nonlinear elements
	Boundary zone	Web	Along the height	Along the thickness	
a	244	721.0	728.6	81	420
b	244	432.6	425.0	81	1008
c	244	360.5	364.3	81	1344
d	244	309.0	300.0	81	1836

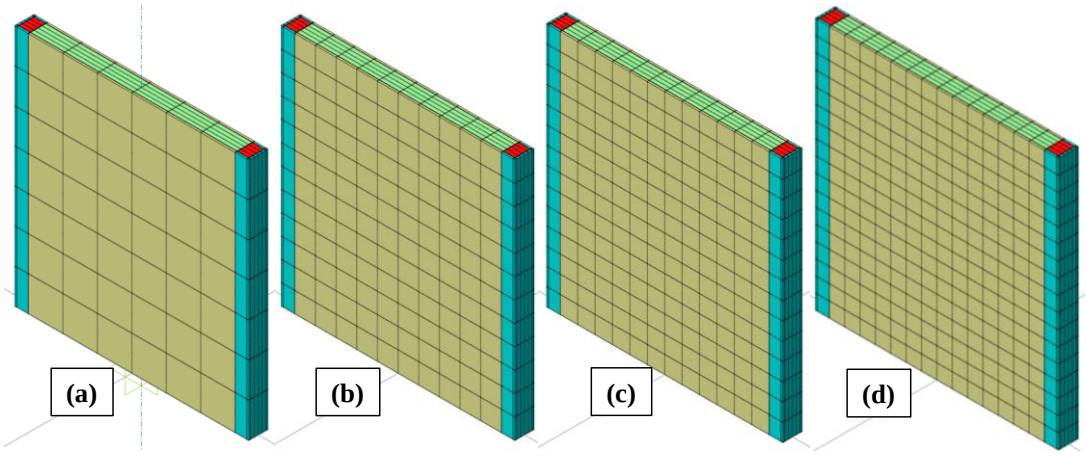

Figure 7-12 mesh configurations used for the mesh sensitivity analysis

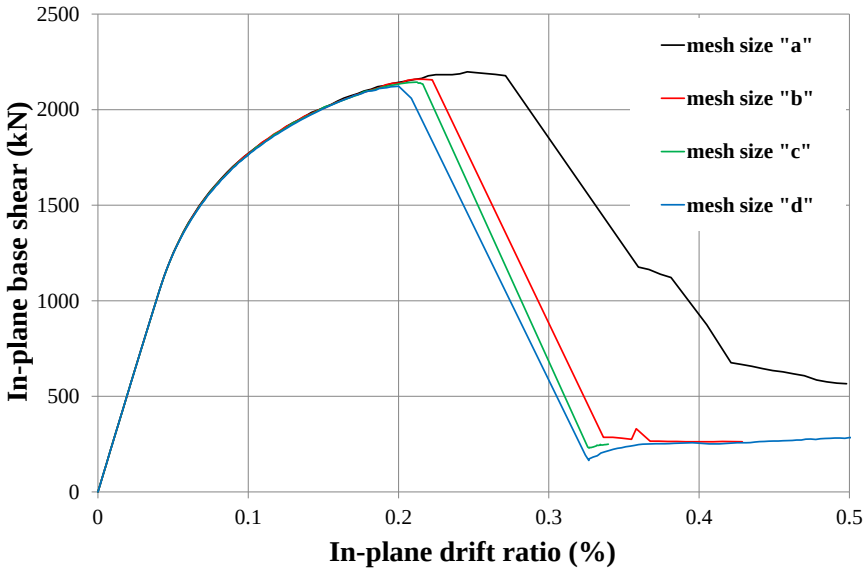

Figure 7-13 force-drift ratio of wall D5-6 under in-plane loading for different mesh configurations

Base shear vs drift ratio and failure mode of the wall

Figure 7-14 shows the base shear vs drift ratio as well as the failure point of the Wall D5-6 under cyclic in-plane loading. Significant drop of strength resulted from axial crushing failure can be seen in Figure 7-14.

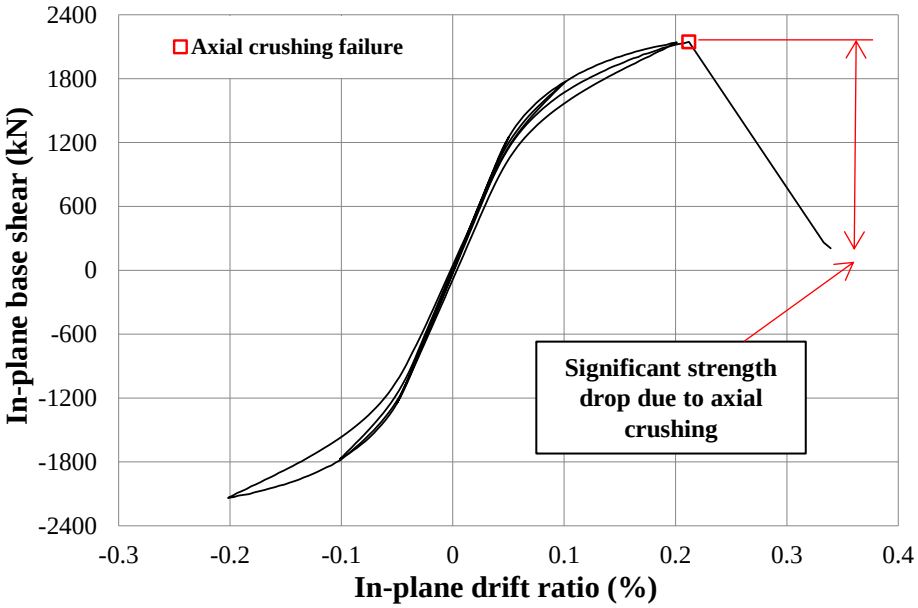

Figure 7-14 Base shear-drift ratio of wall D5-6 under in-plane uni-directional loading

Figure 7-15 and Figure 7-16 show the axial strain and stress contours of the wall under in-plane loading before and after failure, respectively. Significant increase of compressive axial strain and drop of compressive axial stress in Figure 7-15 and Figure 7-16 were due to the axial crushing of the wall resulted from high axial load and lack of confinement. This reduction of compressive stress shown in Figure 7-16 led to the significant drop of strength in

the wall as was shown in Figure 7-14. Figure 7-17 shows a flexural crack pattern in the wall just before the axial crushing failure. It can be seen that there's no sign of out-of-plane shear cracks in the wall. Figure 7-18 shows the axial strain contours of Wall D5-6 just before and after axial crushing failure. The axial strain contours were filtered to first only show parts of the wall in compression and secondly parts of the wall with compressive strain higher than 0.003 which is when an unconfined concrete starts to crush. It can be seen that axial crushing failure affected more than half the length of the wall but not the full length. Figure 7-19 shows the von Mises stress contours of Wall D5-6 just before axial crushing failure and at the failure point. The patterns shown in Figure 7-18 and Figure 7-19 will be compared later on when investigating Wall D5-6 under out-of-plane and skewed loadings.

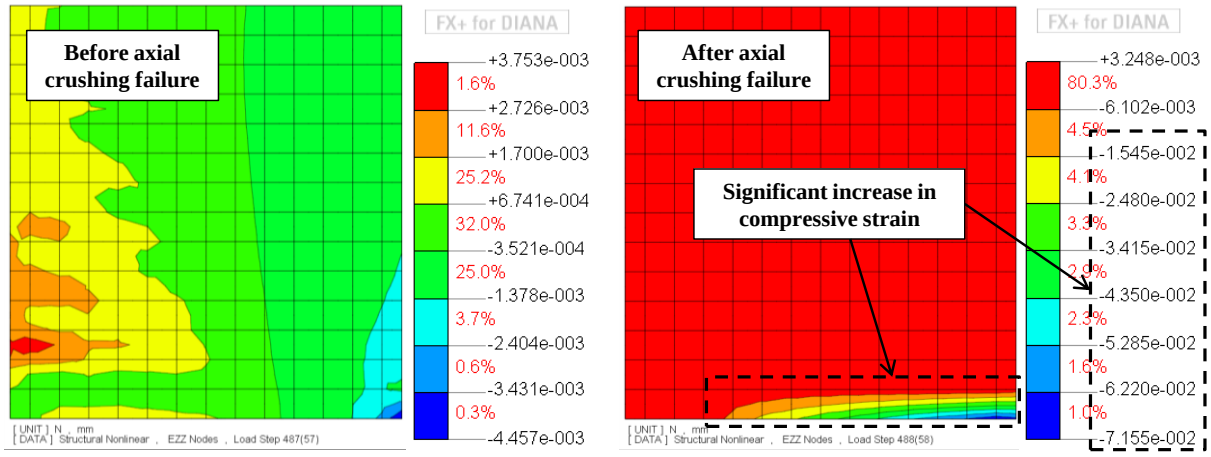

Figure 7-15 Axial strain contours of wall D5-6 under in-plane uni-directional loading before and after failure

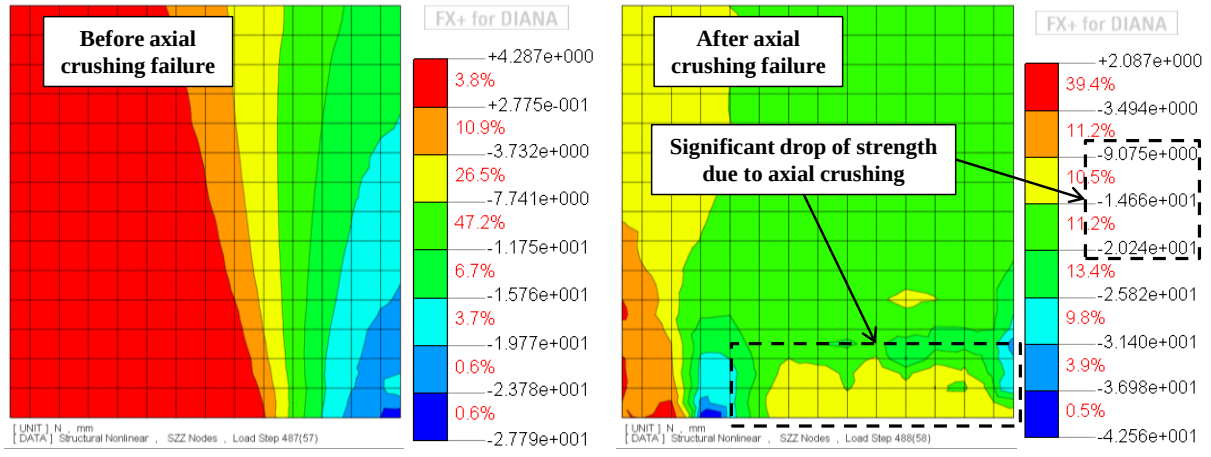

Figure 7-16 Axial stress contours of wall D5-6 under in-plane uni-directional loading before and after failure

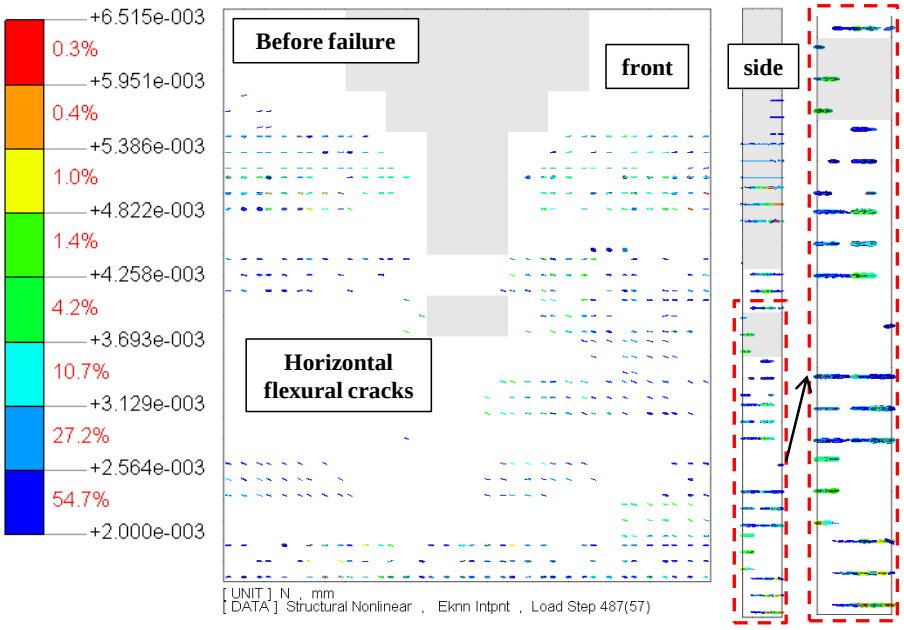

Figure 7-17 Crack pattern of wall D5-6 under in-plane uni-directional loading just before failure

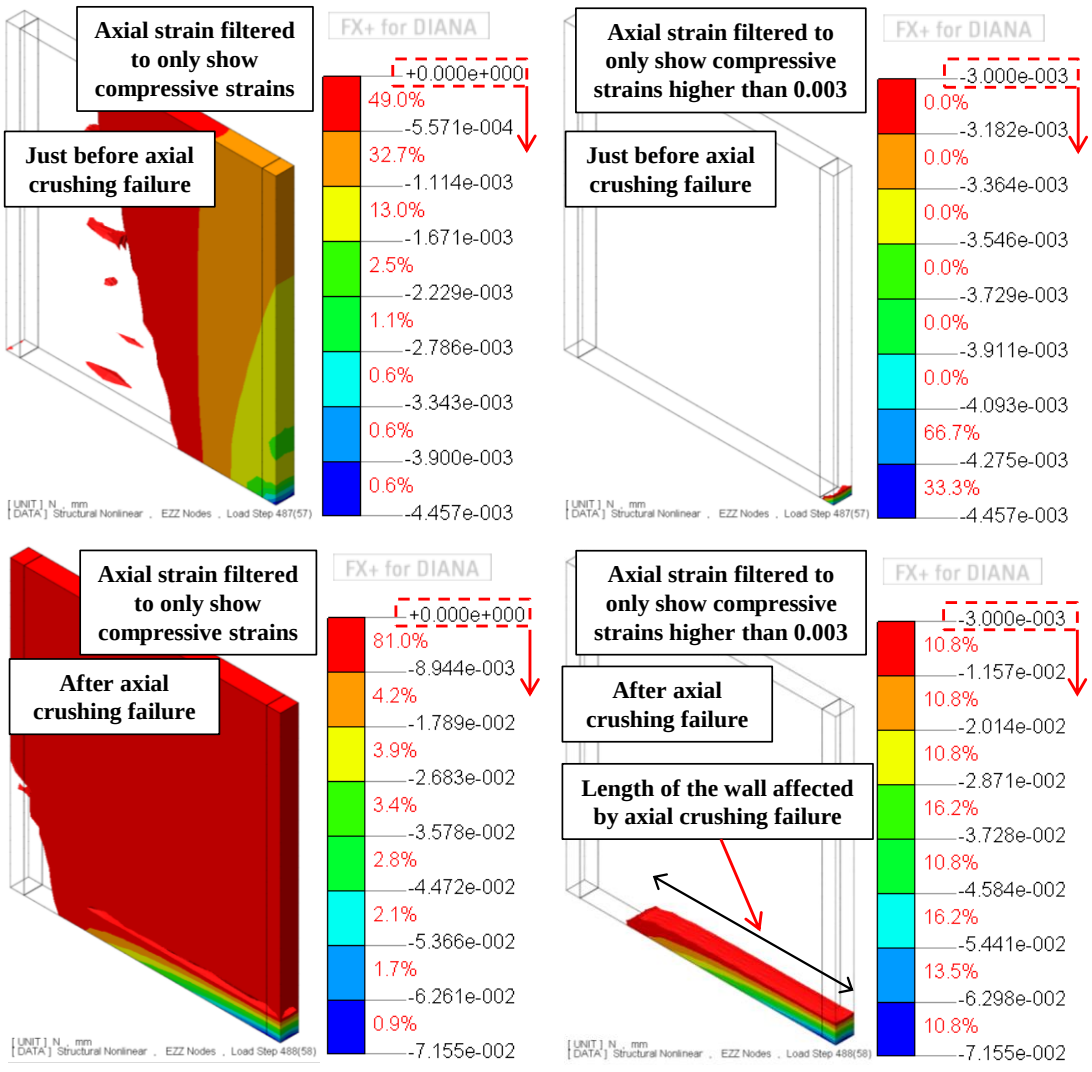

Figure 7-18 Axial strain contours of Wall D5-6 under in-plane uni-directional loading just before and after axial crushing failure

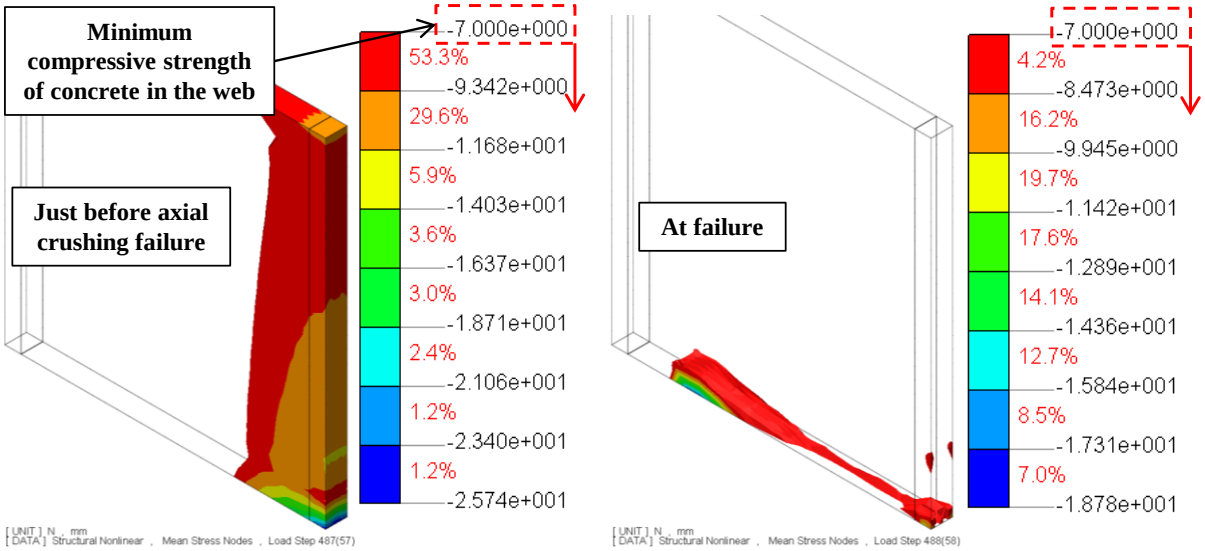

Figure 7-19 Von Mises stress contours of Wall D5-6 under in-plane uni-directional loading just before and after axial crushing failure

7.4.2. Wall D5-6 under out-of-plane uni-directional loading

Figure 7-20 shows the FE model of the wall under out-of-plane uni-directional loading. The only difference in the FE model is the changes in the boundary conditions of the wall. Considering the slab rigidity and the wall's out-of-plane stiffness, the deformation shape of the wall in the out-of-plane direction was assumed to be double curvature.

Mesh sensitivity analysis

A mesh sensitivity analysis was performed on the wall to find the mesh configuration that provides the most stable and efficient results. Table 7-4 and Figure 7-12 show the details of the mesh configurations used for the mesh sensitivity analysis. Figure 7-21 shows the monotonic base shear vs drift ratio of Wall D5-6 for the mesh configurations shown in Figure 7-12. Based on the mesh sensitivity analysis results, mesh configuration "c" was chosen.

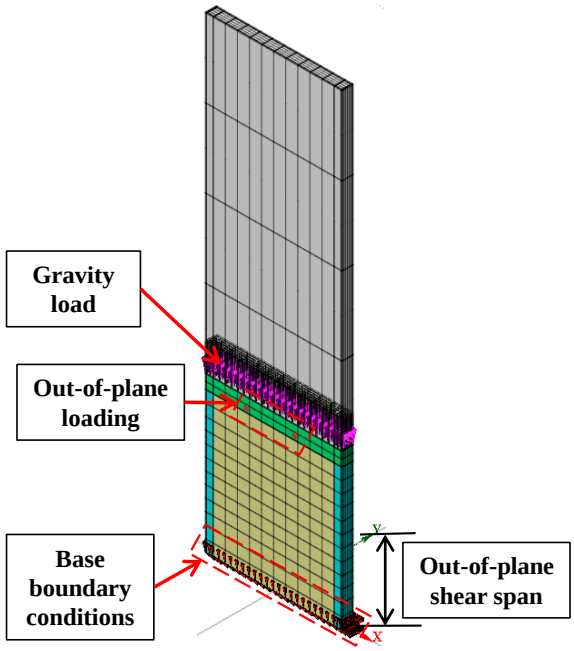

Figure 7-20 The FE model of the wall in DIANA under out-of-plane uni-directional loading only

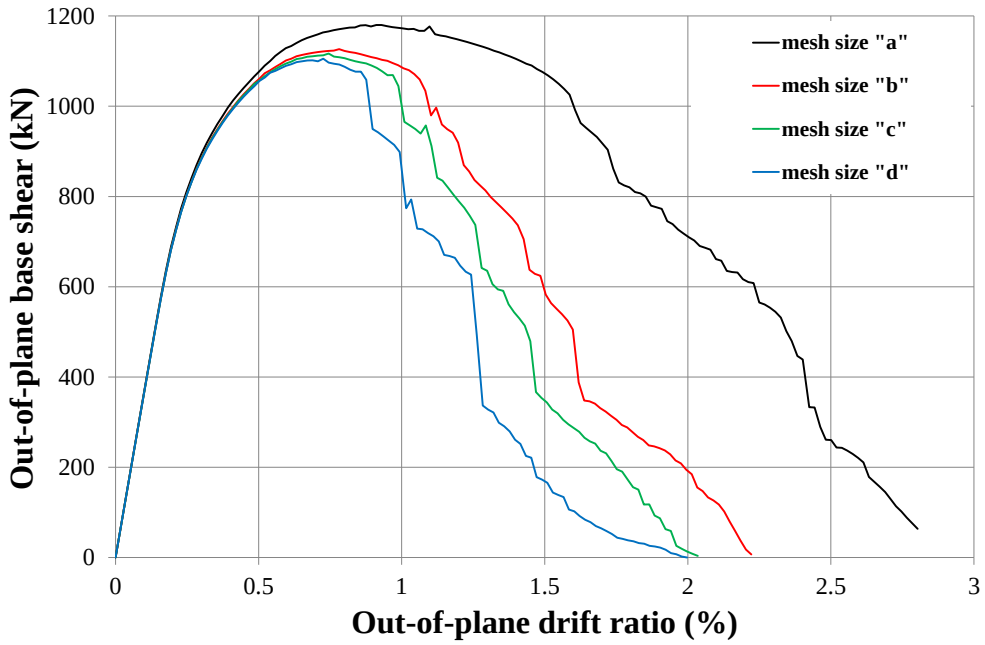

Figure 7-21 force-drift ratio of wall D5-6 under out-of-plane loading for different mesh configurations

Base shear vs drift ratio and failure mode of the wall

Figure 7-22 shows the base shear vs drift ratio as well as the failure point of the wall under cyclic out-of-plane loading. Significant out-of-plane strength reduction of the wall shown in Figure 7-22 was due to initiation and development of out-of-plane shear cracks in the wall. The wall failed in out-of-plane shear at 1.45% out-of-plane drift ratio. Out-of-plane shear failure was defined as the point that out-of-plane shear cracks form along the full length and thickness of the wall.

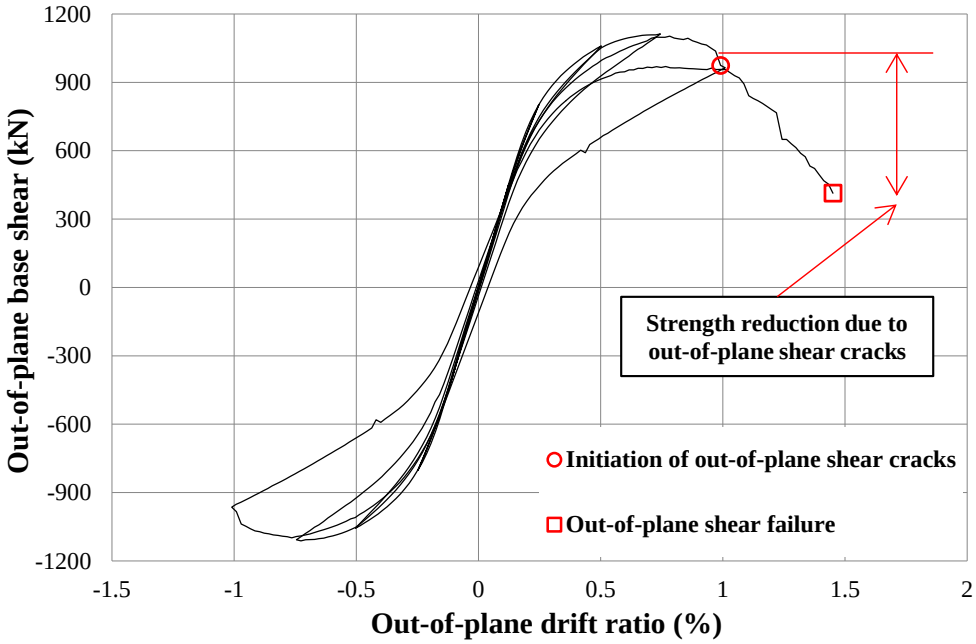

Figure 7-22 Base shear-drift ratio curve of Wall D5-6 under out-of-plane uni-directional loading

Figure 7-23 shows the crack pattern of Wall D5-6 before initiation of out-of-plane shear cracks and at the failure point. It can be seen in Figure 7-23 that the horizontal flexural cracks at the base turned into out-of-plane shear cracks initiated in the two left and right sides of the wall and developed along the wall's length and thickness until the wall's failure (similar to the experimental observations of specimen SP2-ND presented in Chapter 5). In Figure 7-23, minor cracks were filtered to show the crack pattern more clearly. Figure 7-24 compares the crack pattern resulted from FE analysis with the earthquake observations. It can be seen in Figure 7-24 that the crack pattern captured in FE analysis matches the earthquake observations.

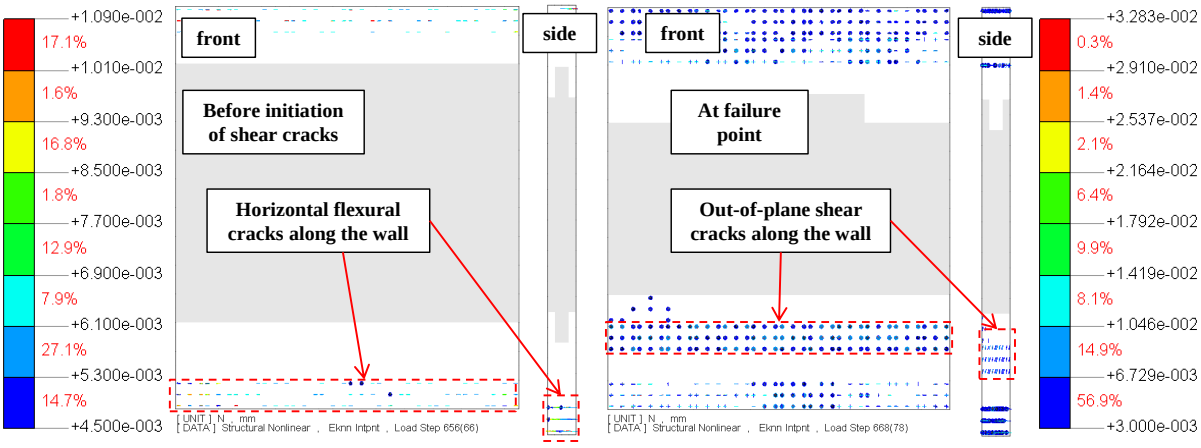

Figure 7-23 Crack pattern of wall D5-6 under out-of-plane uni-directional loading before initiation of out-of-plane shear cracks and at failure point

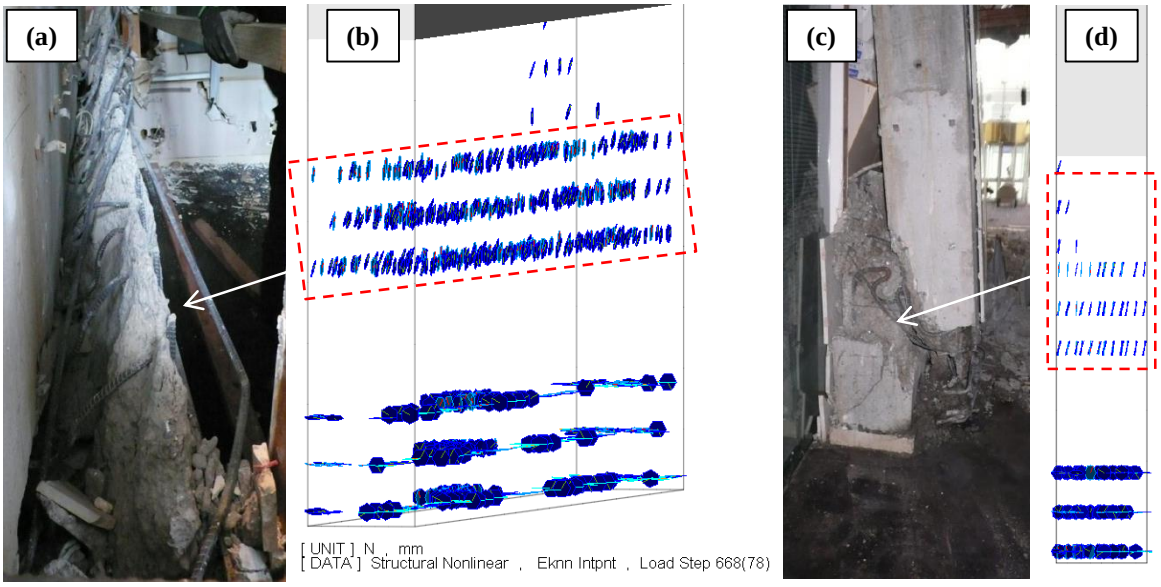

Figure 7-24 Crack pattern of wall D5-6 under out-of-plane uni-directional loading (a & c) February 2011 earthquake (Dunning Thornton 2011), (b & d) 3D and side view of the cracks in DIANA

Von Mises strain contours (refer to Section 6.5.1 for the basic of von Mises strain) of the wall before initiation of out-of-plane shear cracks and at the point of failure were shown in Figure 7-25. The strain contours were filtered to show only the parts with higher strain values. It can be seen in Figure 7-25, while the von Mises strain contours of Wall D5-6 were dominated by axial strain before initiation of out-of-plane shear cracks, at the failure point von Mises strain contours were strongly dominated by out-of-plane shear strain (which contributes to the development of out-of-plane shear cracks). Figure 7-26 shows the axial strain contours of Wall D5-6 at the failure point. In Figure 7-26, axial strain contours is filtered to only show parts of the wall under compression and parts of the wall with compressive strain higher than 0.003. It can be seen that under out-of-plane lateral loading, the full length of the wall had compressive strain higher than 0.003 which shows the vulnerability of the wall to out-of-plane shear failure. Comparing axial strain contours of Wall D5-6 in Figure 7-18 and Figure 7-26, it can be seen that the full length of the wall was vulnerable to out-of-plane shear when the wall was subjected to out-of-plane loading while only part of the wall had compressive strain higher than 0.003 when it was subjected to in-plane loading only.

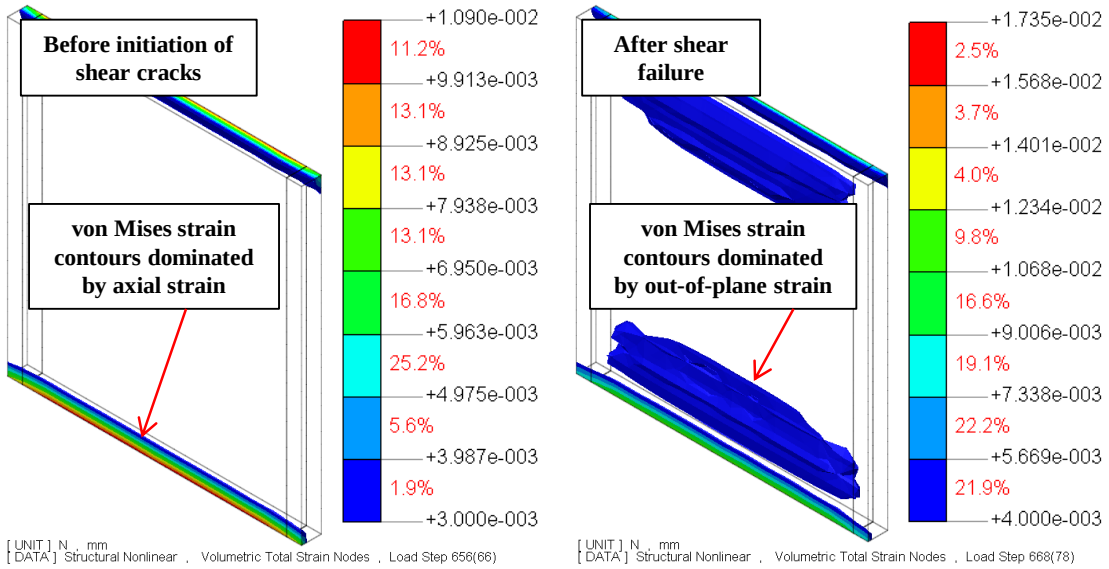

Figure 7-25 Von Mises strain contours of wall D5-6 before initiation of out-of-plane shear cracks and at the failure point

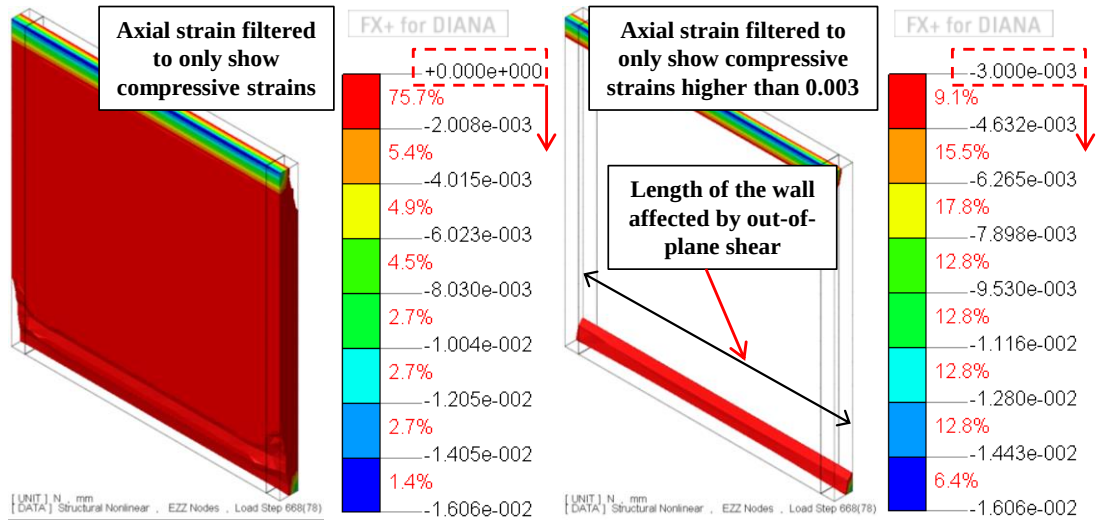

Figure 7-26 Axial strain contours of the wall D5-6 under out-of-plane uni-directional loading showing the length of the wall vulnerable by out-of-plane shear

7.4.3. Wall D5-6 under skewed loading

In section 7.2 it was shown that directionality of the 2011 February earthquake was towards the east-west of Grand Chancellor Hotel building and was in the out-of-plane direction of Wall D5-6. In this section, in order to understand the effects of earthquake loading angle on the base shear-drift ratio and failure mode of RC walls, Wall D5-6 was investigated under skewed loading with different angles. Based on the results of several analyses, a typical 45° angle and three most critical angles in terms of developing out-of-plane shear cracks, 75°, 80° and 85° with respect to the in-plane axis as shown in Figure 7-27 were chosen.

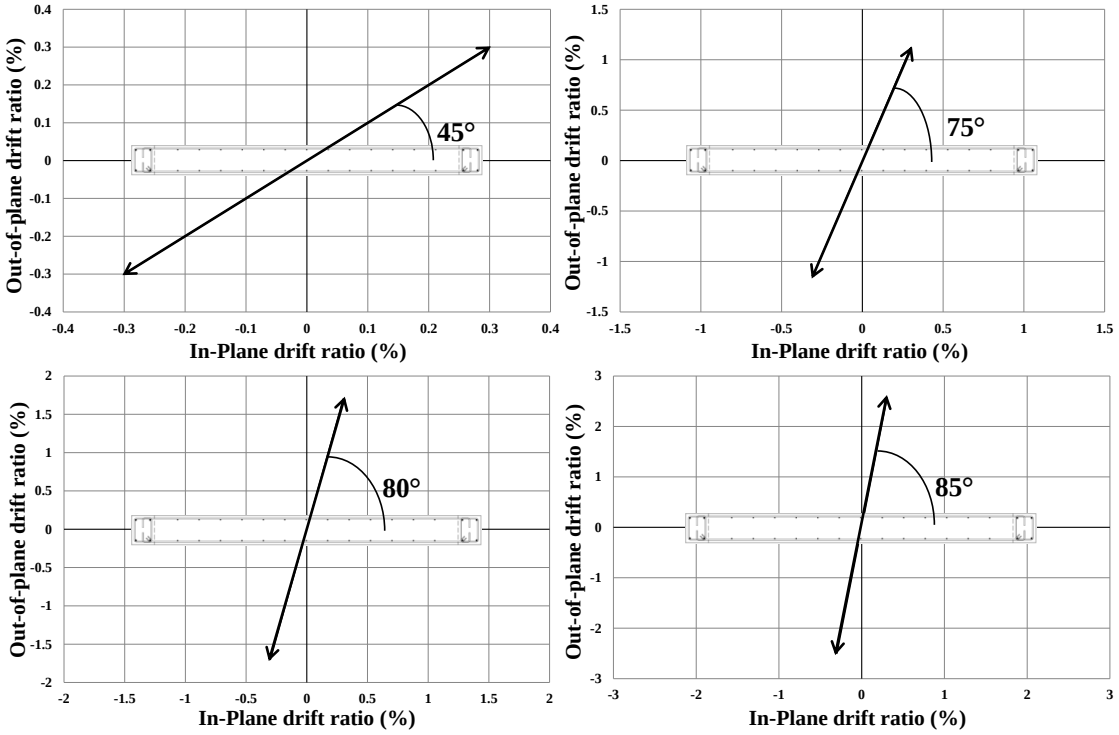

Figure 7-27 Skewed loading pattern with different loading angles

Base shear vs drift ratio of Wall D5-6 under lateral skewed loading with different angles in the in-plane and out-of-plane directions were shown in Figure 7-28 and Figure 7-29, respectively. Table 7-5 show the maximum attained in-plane strength of the wall under different skewed loading angle. Reduction of in-plane strength of the wall subjected to different loading angels is compared to the case when the wall was under in-plane uni-directional loading only in Table 7-5 as well. It can be seen that increasing the angle of loading to 85° with respect to the in-plane axis can decrease the maximum attainable in-plane strength capacity of the wall by 61%. Based on the numerical results, it can be concluded that a pre-existing displacement in the out-of-plane direction reduces the maximum attainable strength in rectangular walls. It is important to note that in order to apply the skewed loading pattern for each loading angles, the in-plane displacement amplitude was kept constant and the corresponding out-of-plane displacement was calculated based on the loading angle. Base shear vs drift ratio as well as the failure mode of the wall under skewed loading with different loading angles were discussed in more details in the following sub-sections.

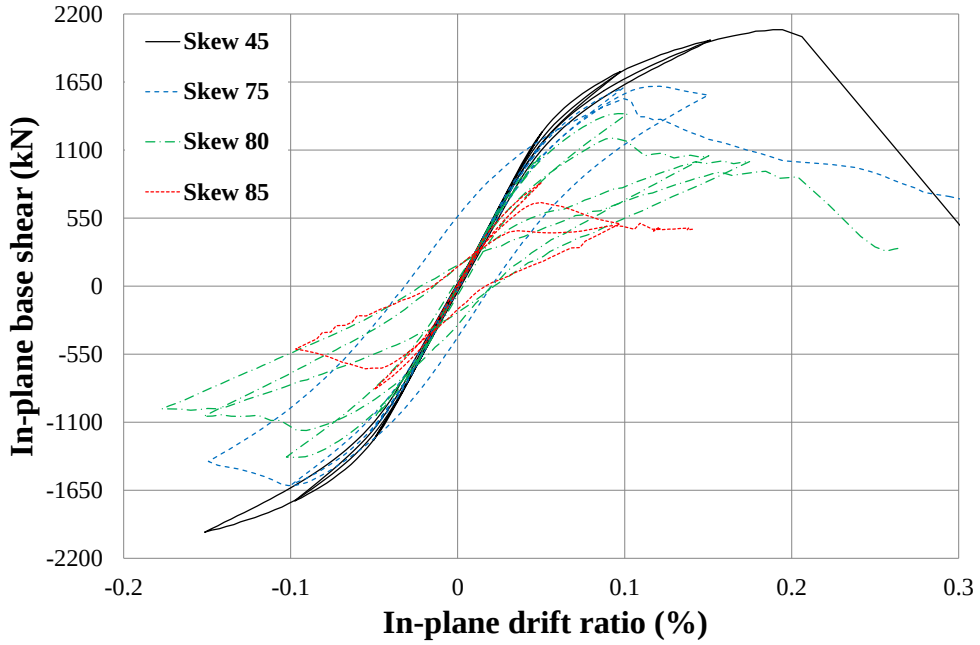

Figure 7-28 In-plane base shear-drift ratio of wall D5-6 under skew loading with different angles

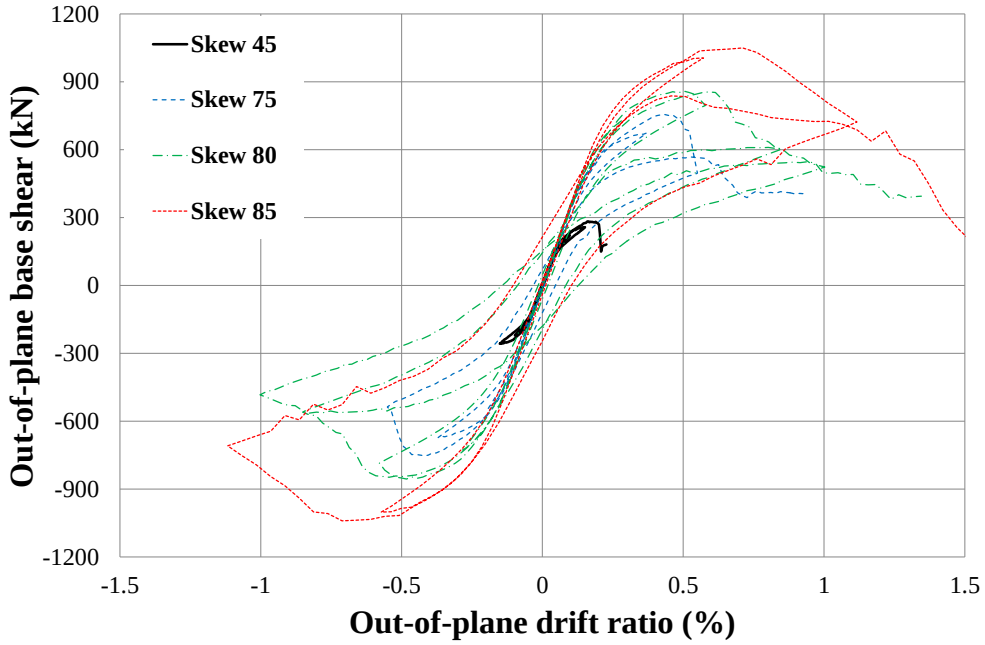

Figure 7-29 Out-of-plane base shear-drift ratio of wall D5-6 under skew loading with different angles

Table 7-5 Effect of loading angle on attainable in-plane strength capacity of Wall D5-6

Angle	In-plane strength (kN)	Reduction compared to in-plane only
0°	2146	-
45°	2074	3.3 %
75°	1604	25.2 %
80°	1395	35.0 %
85°	836	61.0 %

Wall D5-6 under skewed loading with a 45 degree angle

Figure 7-30 shows the in-plane and out-of-plane base shear-drift ratio curves of Wall D5-6 subjected to skewed uni-directional loading with a 45 degree angle. Significant drop of in-plane strength in Figure 7-30a indicates an axial crushing failure in the wall.

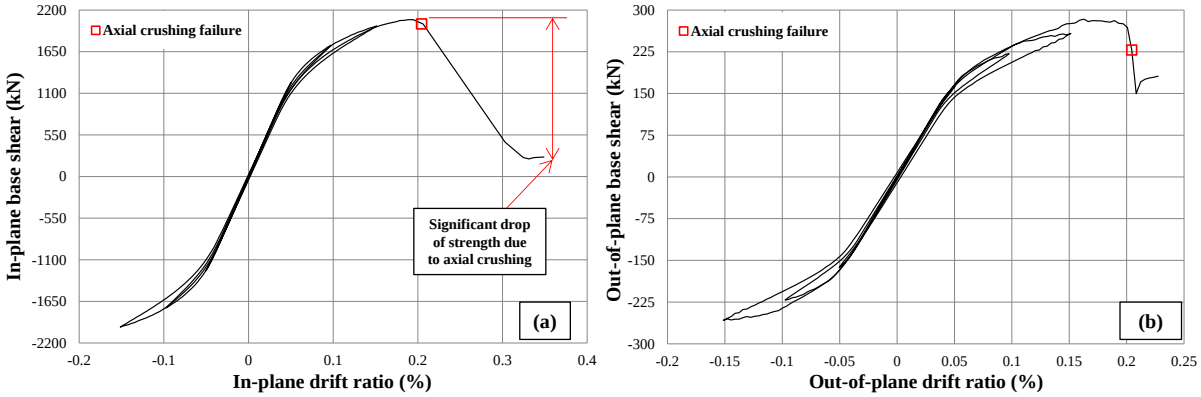

Figure 7-30 Base shear-drift ratio curves of Wall D5-6 under skew loading with an 45 degree angle in the (a) in-plane and (b) out-of-plane directions

Failure mode of the wall is described in more details using axial strain and stress contours, cracks pattern and von Mises strain and stress contours in Figure 7-31-Figure 7-35. Axial strain and stress contours of the wall in Figure 7-31 and Figure 7-32 show similar behaviour to the case when the wall was subjected to in-plane lateral loading only (see Figure 7-15 and Figure 7-16). It can be seen that axial compressive strain of the wall increased at the failure point which led to significant drop of compressive stress of concrete and consequently in-plane strength drop in the wall. Crack pattern of the wall in Figure 7-33 shows no out-of-plane shear cracks before the axial crushing failure.

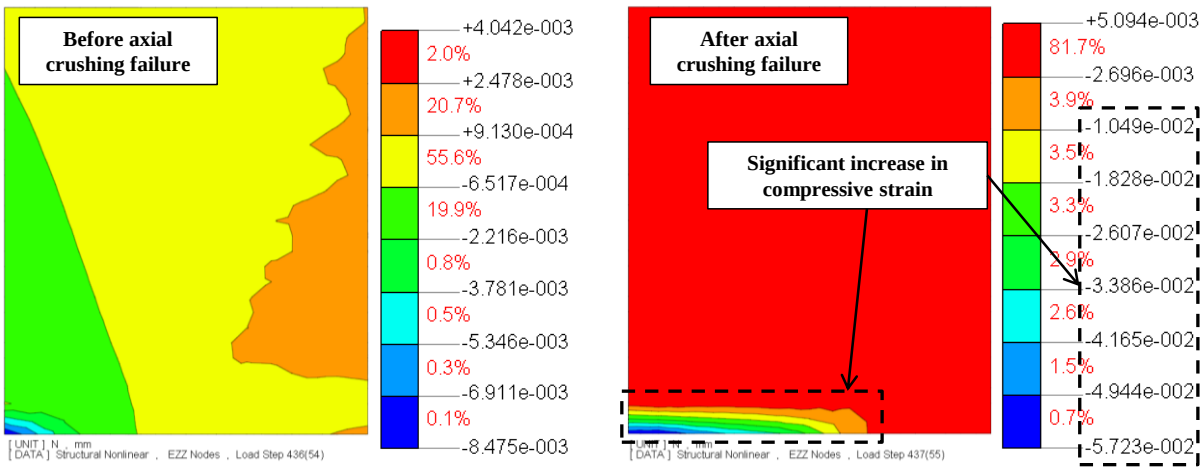

Figure 7-31 Axial strain contours of Wall D5-6 under skew loading with a 45 degree angle before and after failure

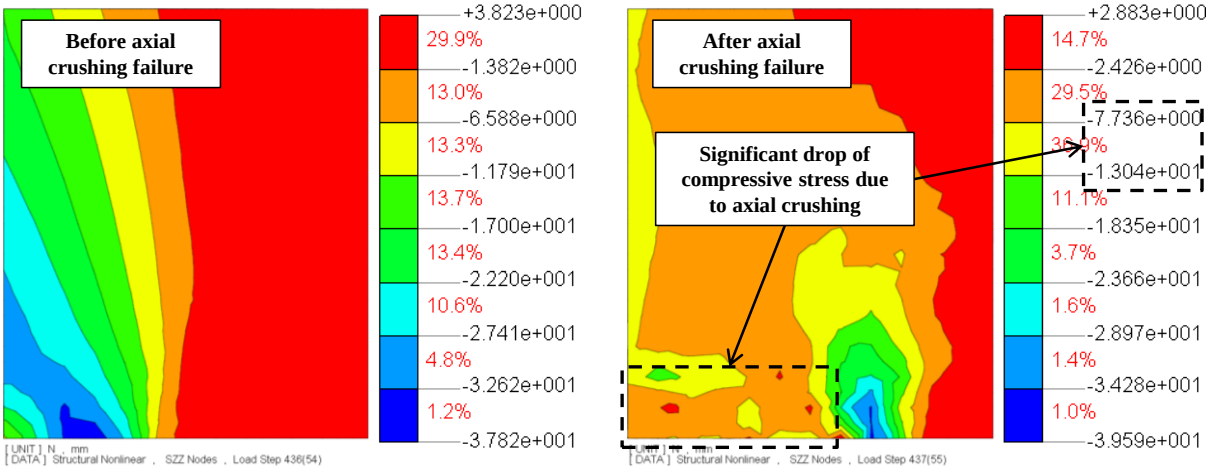

Figure 7-32 Axial stress contours of Wall D5-6 under skew loading with a 45 degree angle before and after failure

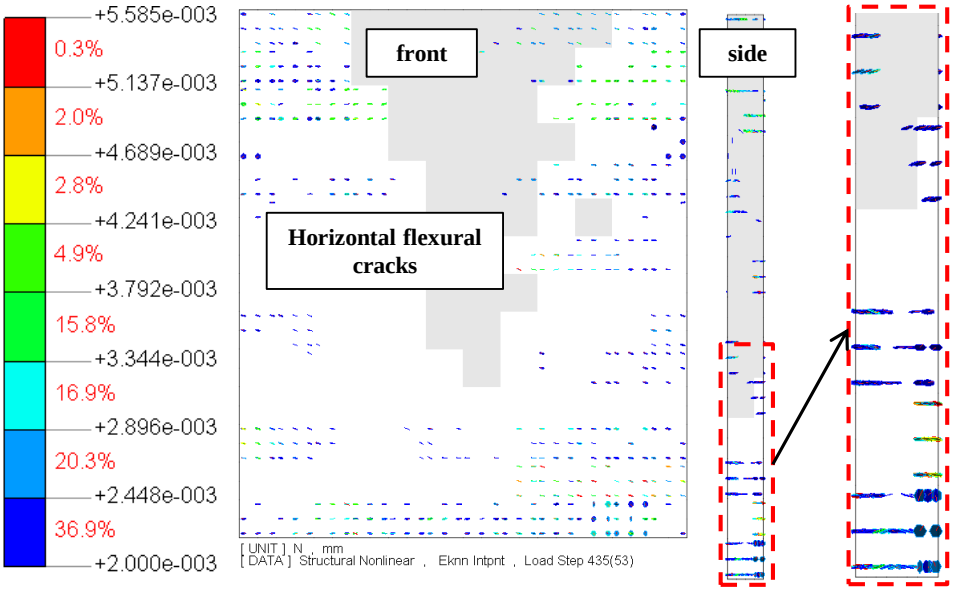

Figure 7-33 Crack pattern of Wall D5-6 under skew loading with a 45 degree angle before the failure

Von Mises strain and stress contours of the wall were shown in Figure 7-34. These contours show the domination of axial strain and stress in the wall under skewed loading with a 45 degree angle. Figure 7-35 shows the axial strain contours of the wall just before and after the wall's failure. Axial strain contours in Figure 7-35 were filtered to show only the parts of the wall under compression and parts with compressive strains higher than 0.003. It can be seen in Figure 7-35 that axial crushing failure of the wall affected about half the length of the wall.

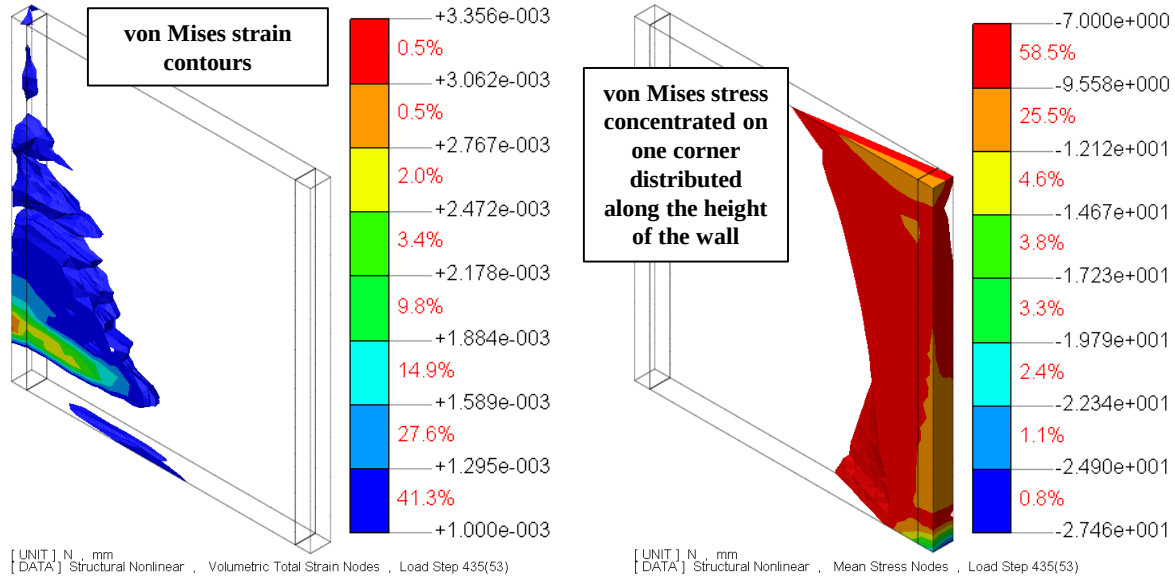

Figure 7-34 Von Mises strain and stress contours of Wall D5-6 under skew loading with a 45 degree angle before the failure

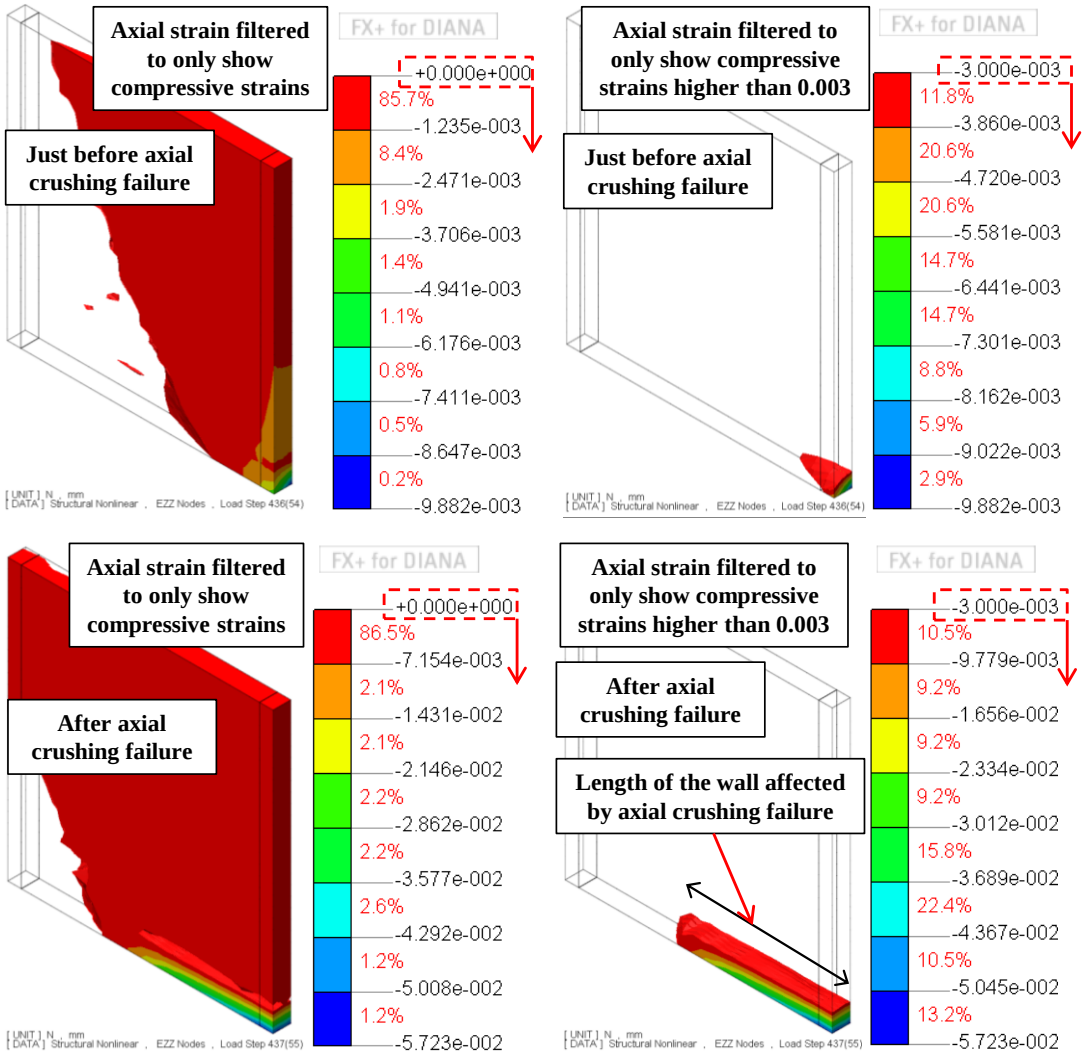

Figure 7-35 Axial strain contours of Wall D5-6 under skewed loading with a 45 degree angle before and after failure

Wall D5-6 under skewed loading with a 75 degree angle

Figure 7-36 shows the in-plane and out-of-plane base shear-drift ratio curves of Wall D5-6 under skewed uni-directional loading with a 75 degree angle. Initiation of out-of-plane shear cracks and the final failure point were also shown in Figure 7-36. These key points are described in more details using crack pattern in Figure 7-37 and Figure 7-38, axial stress contours in Figure 7-39, von Mises strain and stress contours in Figure 7-40 and axial strain contours in Figure 7-41. Although some out-of-plane shear cracks formed in the wall which initiated at 0.14% in-plane and 0.54% out-of-plane drift ratios (see Figure 7-37 and Figure 7-38), these cracks didn't form along the full length of the wall. Significant drop of in-plane strength shown in Figure 7-36a and axial compressive stress in concrete shown in Figure 7-39 indicate an axial crushing failure in the wall at 0.2% in-plane and 0.73% out-of-plane drift ratios.

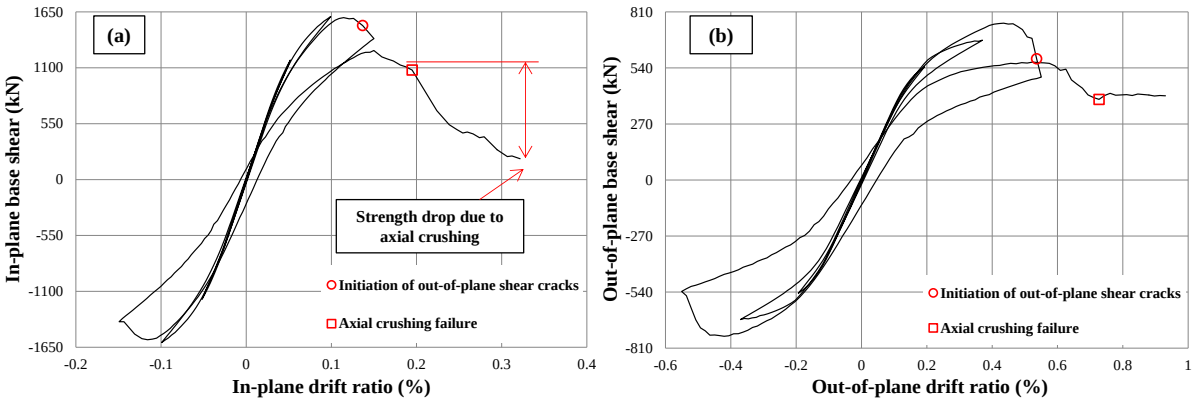

Figure 7-36 Base shear-drift ratio curves of Wall D5-6 under skew loading with an 75 degree angle in the (a) in-plane and (b) out-of-plane directions

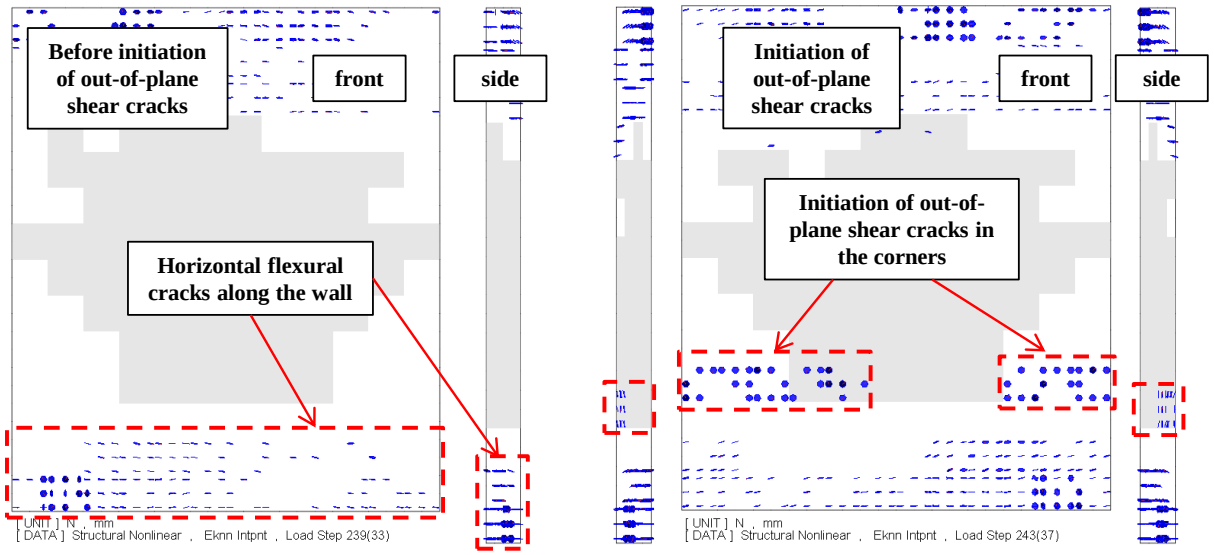

Figure 7-37 Crack pattern of wall D5-6 under skew loading with a 75 degree angle before and after initiation of out-of-plane shear shear cracks

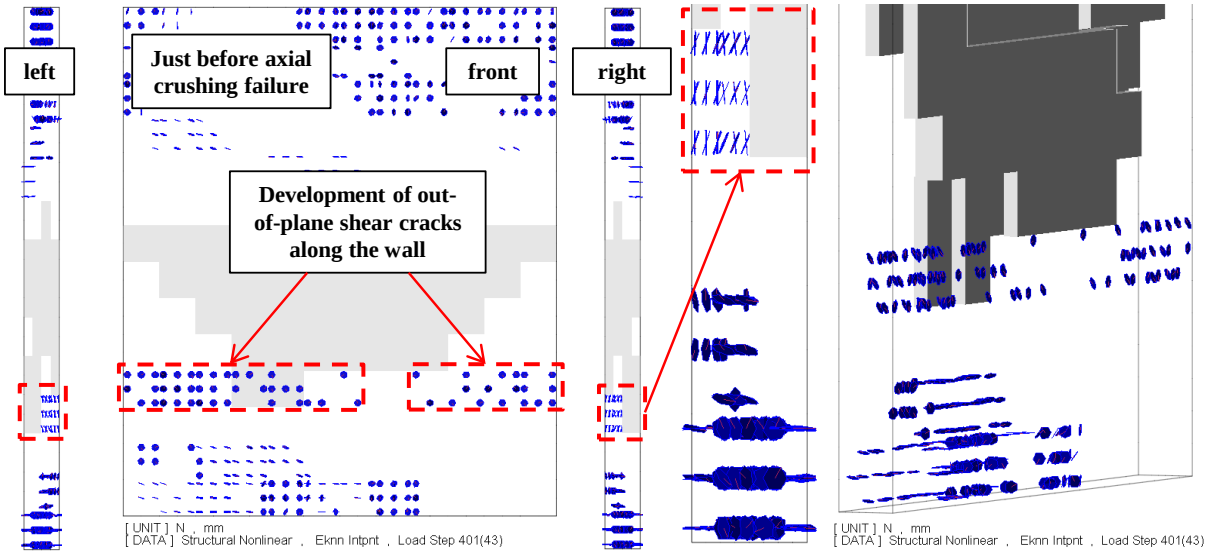

Figure 7-38 Crack pattern of wall D5-6 under skew loading with a 75 degree angle before axial crushing failure

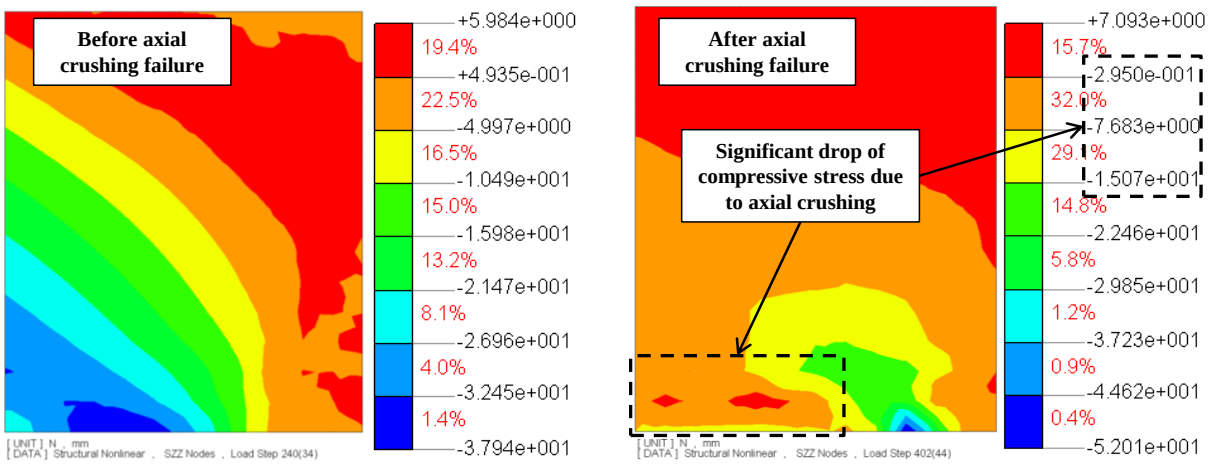

Figure 7-39 Axial stress contours of wall D5-6 under skew loading with a 75 degree angle before and after axial crushing failure

Figure 7-40 shows the von Mises strain and stress contours of the wall. It can be seen that although von Mises strain was shifted above the base affected by out-of-plane strains, von Mises stress contours were still concentrated on one side of the wall and distributed along the height which is different than the case of an out-of-plane shear failure (see Figure 6-62). Figure 7-41 shows the axial strain contours of the wall filtered in a way to show the parts of the wall in compression and the parts with compressive strain higher than 0.003. It can be seen in Figure 7-41 that more than half of the wall was vulnerable to out-of-plane shear failure due to the changes in the angle of loading. However, before out-of-plane shear cracks develop along the full length and thickness of the wall, it failed in axial crushing.

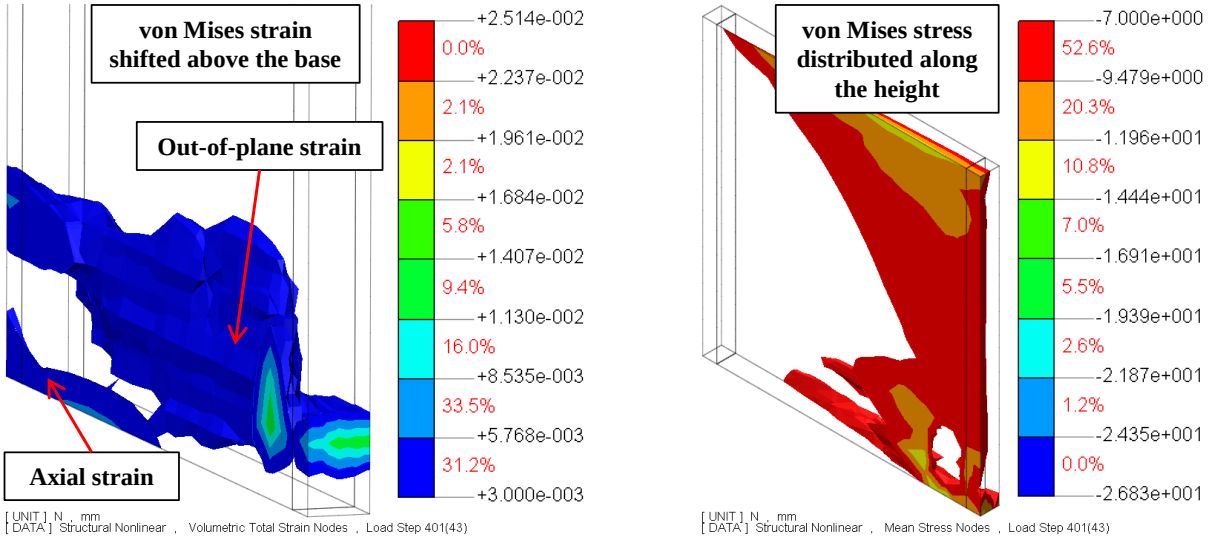

Figure 7-40 Von Mises strain and stress contours of Wall D5-6 under skew loading with a 75 degree angle before failure

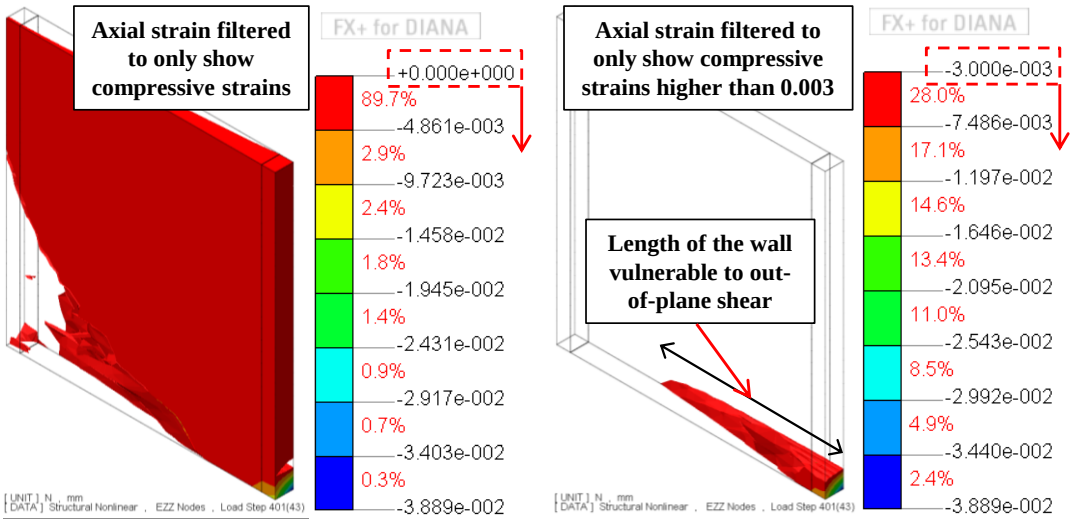

Figure 7-41 Axial strain contours of the wall D5-6 under skewed loading with a 75 degree angle showing the length of the wall vulnerable to out-of-plane shear

Wall D5-6 under skewed loading with an 80 degree angle

Figure 7-42 shows the in-plane and out-of-plane base shear-drift ratio curves of Wall D5-6 under skewed uni-directional loading with an 80 degree angle. Initiation of out-of-plane shear cracks and the final failure point were also shown in Figure 7-42. These key points were described in more details using crack pattern in Figure 7-43 and Figure 7-44, axial stress contours in Figure 7-45, von Mises stress and axial strain contours in Figure 7-46. Although out-of-plane shear cracks formed in the wall, initiated at 0.1% in-plane and 0.66% out-of-plane drift ratios and increased up to the failure point, before these cracks develop along the full length of the wall, it failed in axial crushing at 0.22% in-plane and 1.25% out-of-plane drift ratios. Significant drop of in-plane strength as can be seen in Figure 7-42a indicates an

axial crushing failure in the wall. This drop of in-plane strength was due to the significant reduction of compressive stress in concrete as is shown in Figure 7-45.

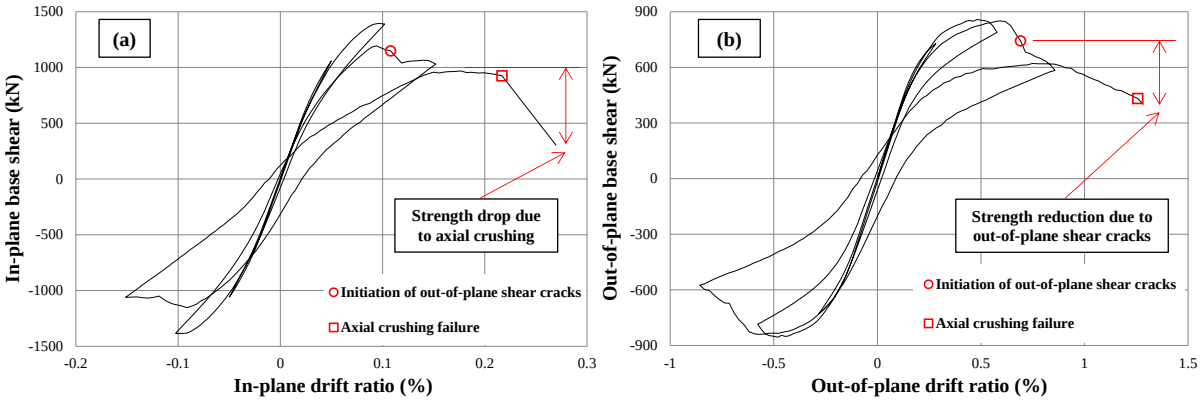

Figure 7-42 Base shear-drift ratio curves of Wall D5-6 under skew loading with an 80 degree angle in the (a) in-plane and (b) out-of-plane directions

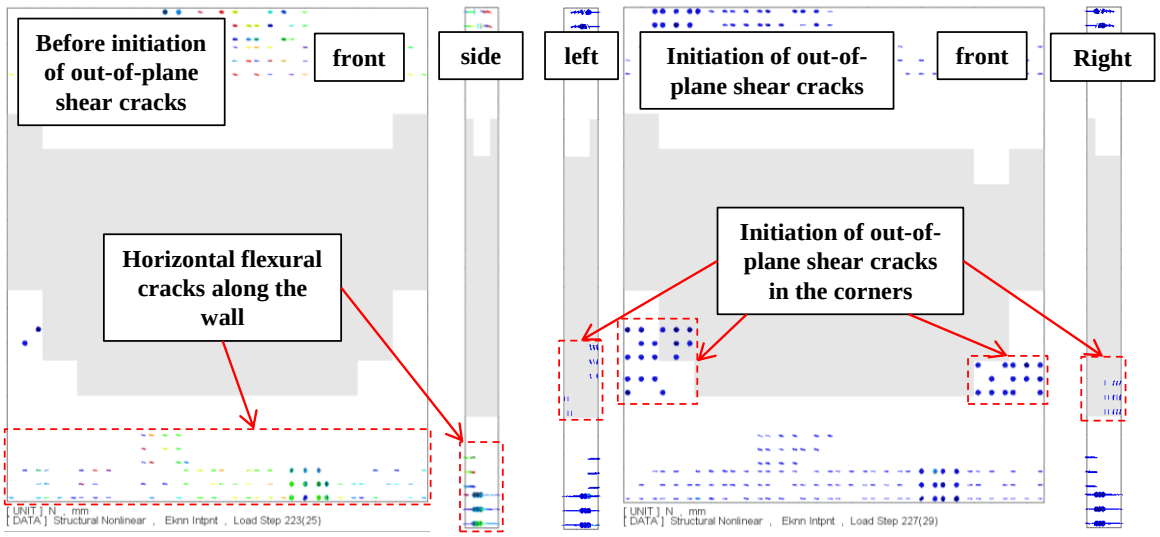

Figure 7-43 Crack pattern of Wall D5-6 under skew loading with an 80 degree angle before and after initiation of out-of-plane shear cracks

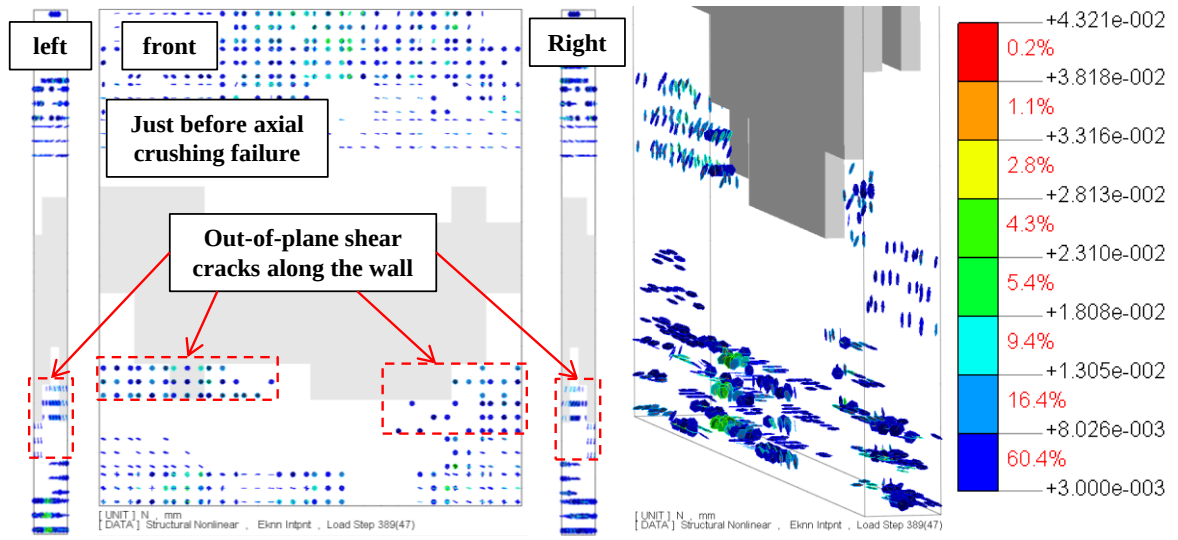

Figure 7-44 Crack pattern of Wall D5-6 under skew loading with an 80 degree angle just before axial crushing failure

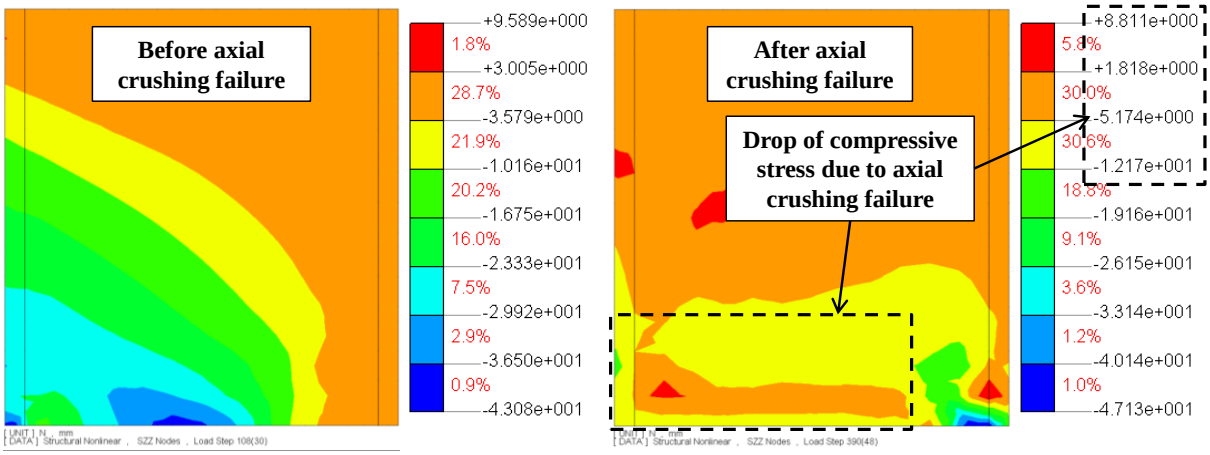

Figure 7-45 Axial stress contours of Wall D5-6 under skew loading with an 80 degree angle before and after failure

Von Mises stress contours of the wall just before the failure shown in Figure 7-46 is still strongly affected by axial stress which is different than the case when out-of-plane shear failure happens. Axial strain contours shown in Figure 7-46 was filtered to only show parts of the wall with compressive strains higher than 0.003. It can be seen that increasing the angle of loading further increased the length of the wall vulnerable to out-of-plane shear failure compared to the case under skewed loading with a 75 degree angle. However, it was not enough to completely cover the full length of the wall and hence out-of-plane shear failure didn't occur.

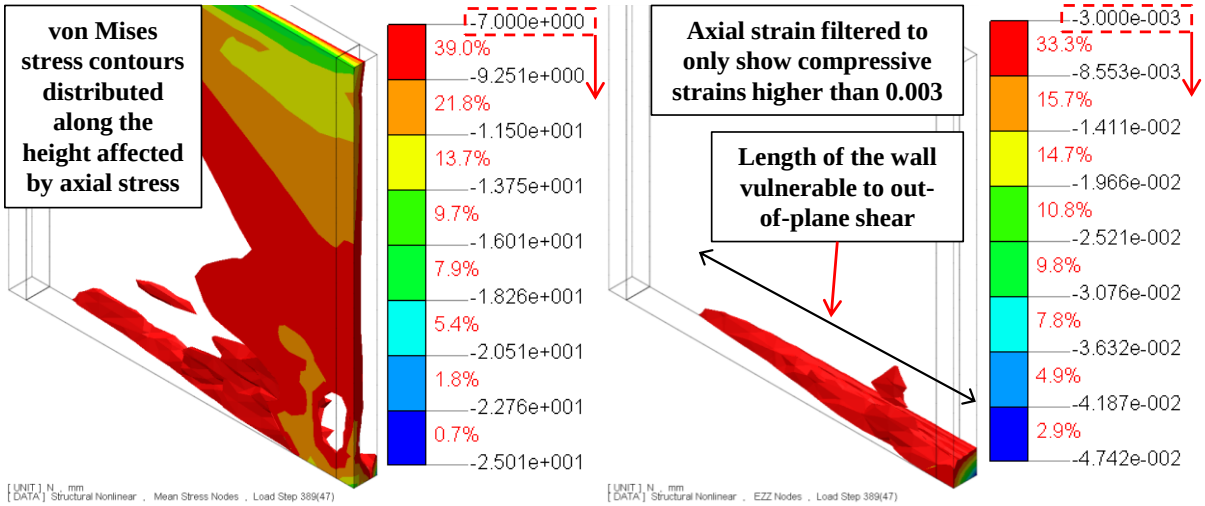

Figure 7-46 Von Mises strain and stress contours of Wall D5-6 under skew loading with an 80 degree angle just before failure

Wall D5-6 under skewed loading with an 85 degree angle

Figure 7-47 shows the in-plane and out-of-plane base shear-drift ratio curves of Wall D5-6 subjected to skewed uni-directional loading with an 85 degree angle. The key points that show the behaviour of the wall during the analysis were shown in Figure 7-47. These key points were described in more details using crack pattern in Figure 7-48, von Mises strain and stress contours in Figure 7-49 and axial strain contours in Figure 7-50. It can be seen in Figure 7-48 that out-of-plane shear cracks formed along the full length and thickness of Wall D5-6 under skewed loading with an 85 degree angle with respect to the in-plane axis and the wall failed in out-of-plane shear failure at 0.12% in-plane and 1.37% out-of-plane drift ratios.

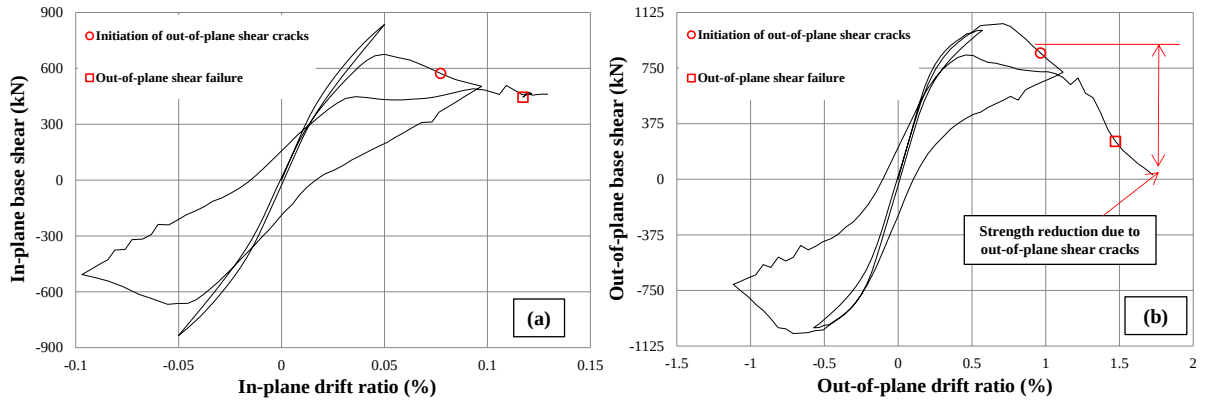

Figure 7-47 Base shear-drift ratio curves of Wall D5-6 under skew loading with an 85 degree angle in the (a) in-plane and (b) out-of-plane directions

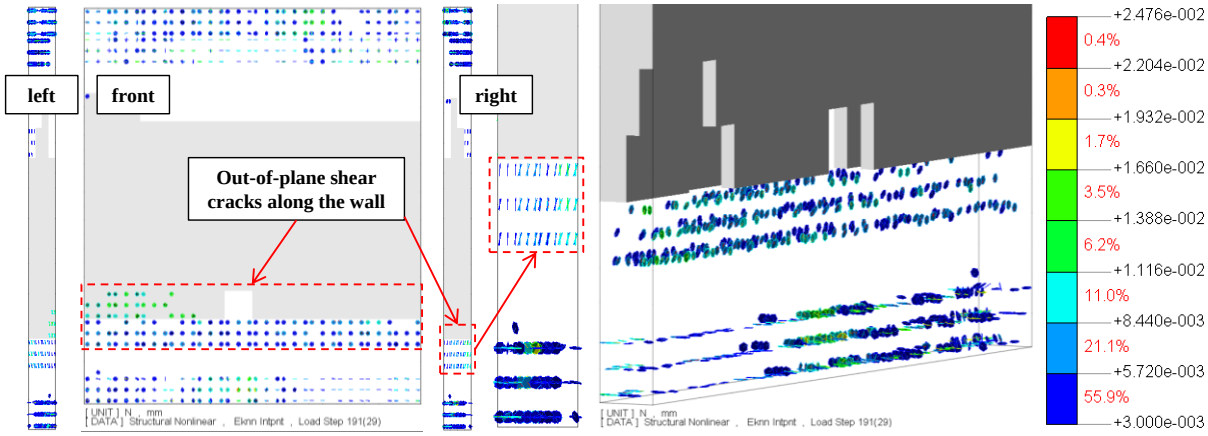

Figure 7-48 Crack pattern of wall D5-6 under skewed uni-directional loading with an 85 degree angle at failure point

Von Mises strain contours of the wall presented in Figure 7-49 shows the domination of out-of-plane strains which contribute to the development of out-of-plane shear cracks. Von Mises stress contours of the wall in Figure 7-49 shows the length of the wall vulnerable to out-of-plane shear failure which is equal to the length of the wall. Moreover, axial strain contours of the wall at failure point showed in Figure 7-50 also confirms that the full length of the wall is vulnerable to out-of-plane shear failure (as the full length of the wall had compressive strain higher than the concrete crushing point). Crack pattern, von Mises strain and stress and axial strain contours of Wall D5-6 subjected to skewed loading with an 85 degree are similar to the numerical results captured for specimen SP2-ND presented in Section 6.5.5 that failed in out-of-plane shear in the lab. It can be concluded that when the wall was vulnerable to out-of-plane shear failure along its full length, lack of sufficient out-of-plane shear capacity led to the failure of the wall.

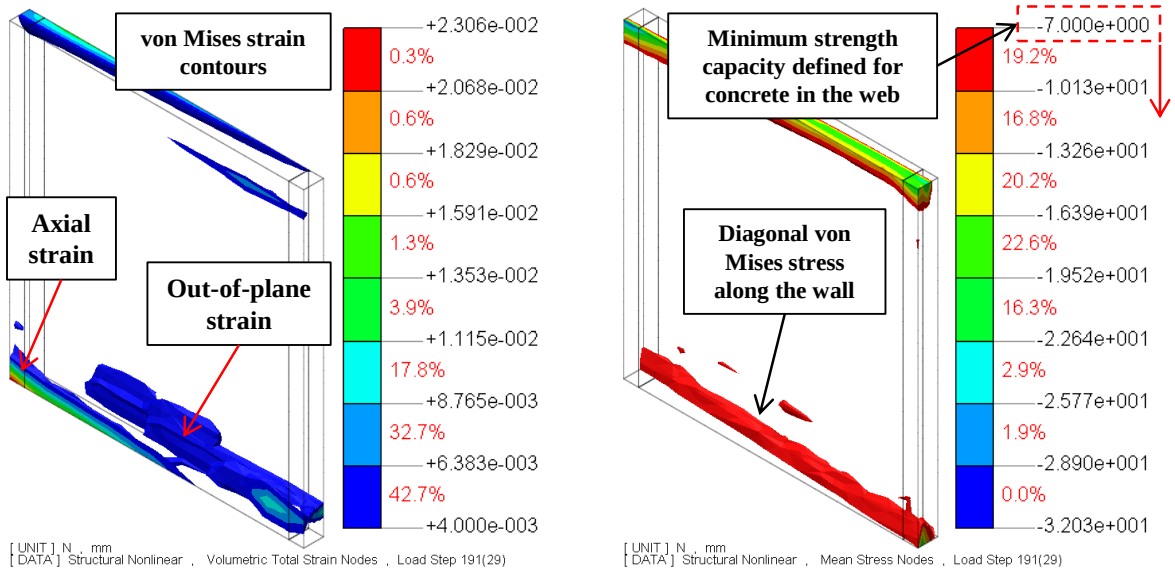

Figure 7-49 Von Mises stress and strain contours of Wall D5-6 under skewed uni-directional loading with an 85 degree angle at failure point

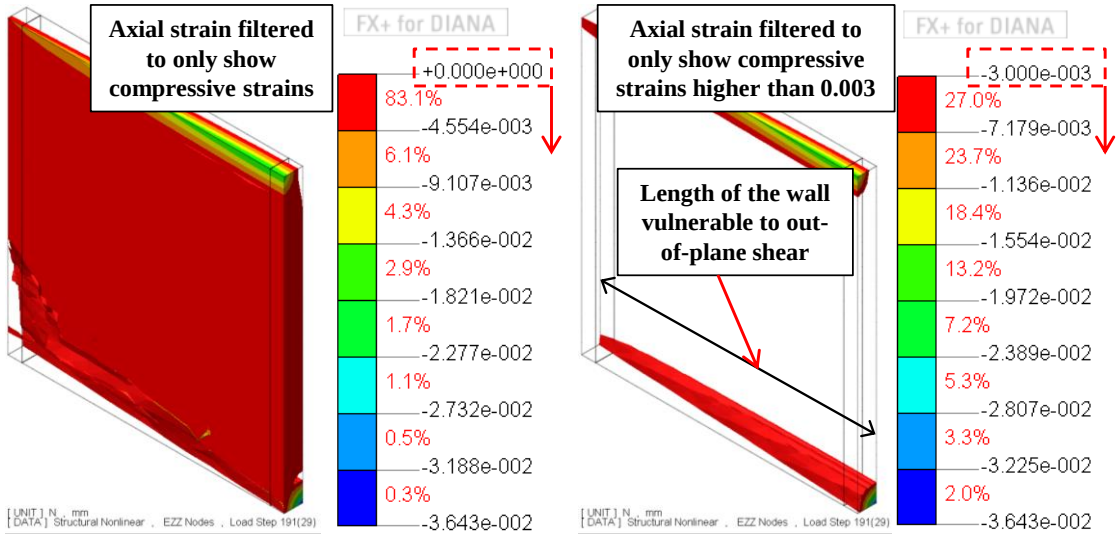

Figure 7-50 Axial strain contours of the wall D5-6 under skewed loading with an 85 degree angle showing the length of the wall vulnerable to out-of-plane shear failure

Conclusion

Wall D5-6 was investigated numerically when subjected to different lateral loading pattern with different loading angel (pure in-plane, 45°, 75°, 80°, 85° and pure out-of-plane). It was found that skew loading with 85° with respect to the in-plane axis is the worst case scenario in triggering out-of-plane shear failure. Comparing skew loading with 85° angle with the earthquake loading pattern applied to Wall D5-6 in the February 2011 earthquake shows similarity between the two loading pattern. It is worth mentioning that the numerical investigation was carried out first and then later on compared with the displacement response of Wall D5-6 in the February earthquake. It can also be seen in Figure 7-26 and Figure 7-50 that when the wall is subjected to a pure out-of-plane loading, although the full length of the wall is in compression, the full thickness wouldn't be in compression even under extreme axial load. On the other hand looking at Figure 7-50, it can be seen that not only the full length of the wall would be in compression under skewed loading with 85°, the full thickness would be in compression as well which is essential for a full out-of-plane shear failure as was discussed in Section 5.4.

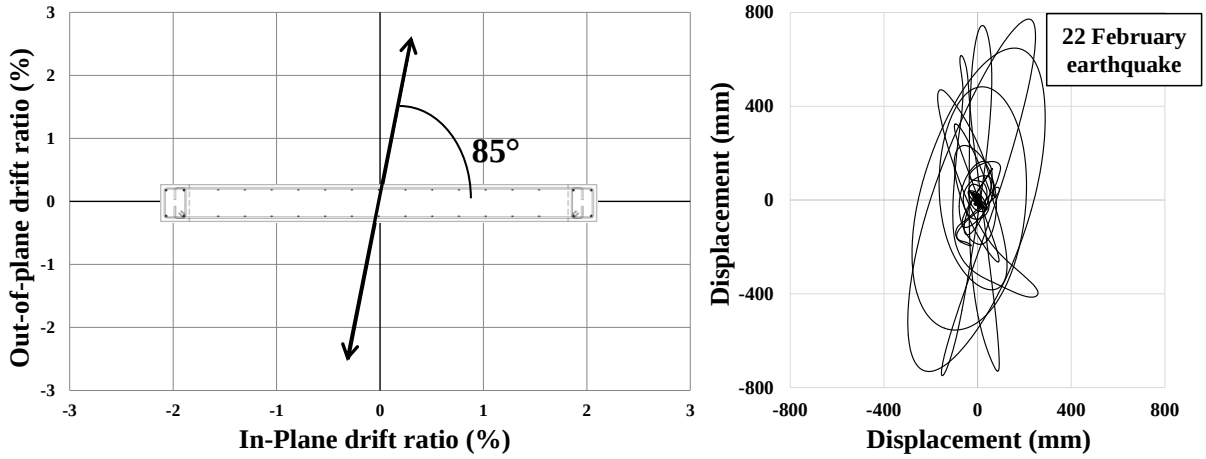

Figure 7-51 Comparing skew loading with 85° with the displacement response of Wall D5-6 in the 2011 earthquake

7.4.4. Effect of out-of-plane boundary condition

The other parameter that can affect the development of out-of-plane shear cracks is the boundary condition of the wall in the out-of-plane direction as it significantly affects the out-of-plane shear demand of the wall (see Table 7-3). In the previous sections a double bending deformation shape was assumed for Wall D5-6 in the out-of-plane direction based on the slab rigidity and wall's out-of-plane stiffness. Here for the sake of comparison, the same wall is analysed assuming a cantilever deformation shape in the out-of-plane direction. Skewed uni-directional loading with an 85 degree angle with respect to the in-plane axis was chosen as the lateral load path for this comparison (see Figure 7-27). Figure 7-52 and Figure 7-53 compares the base shear vs drift ratio curves of the wall in the in-plane and out-of-plane directions, respectively, when the out-of-plane boundary condition is cantilever or double bending. It can be seen that the double bending deformation shape not only increased the out-of-plane shear demand of the wall but also decreased the attained in-plane strength of the wall.

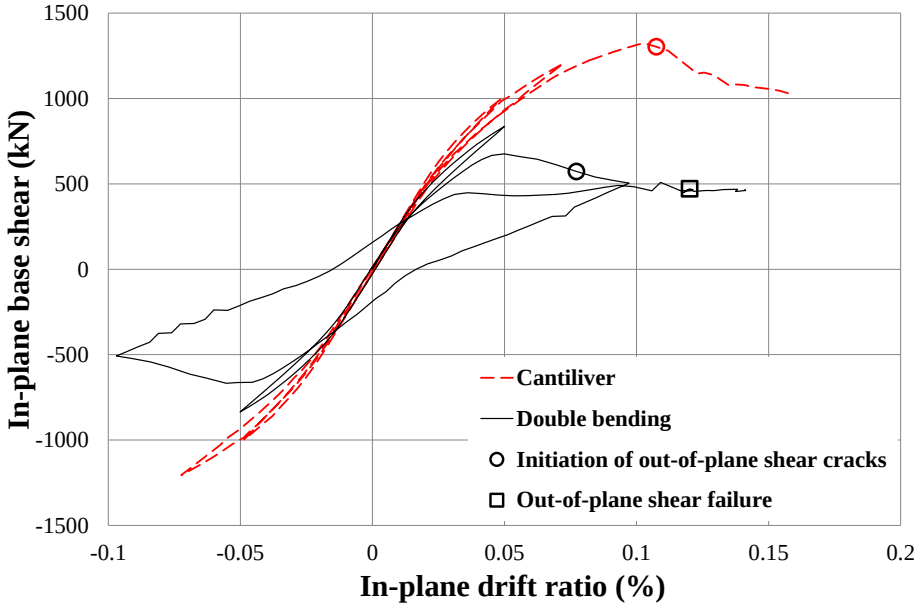

Figure 7-52 In-plane base shear vs drift ratio of Wall D5-6 with different out-of-plane boundary conditions

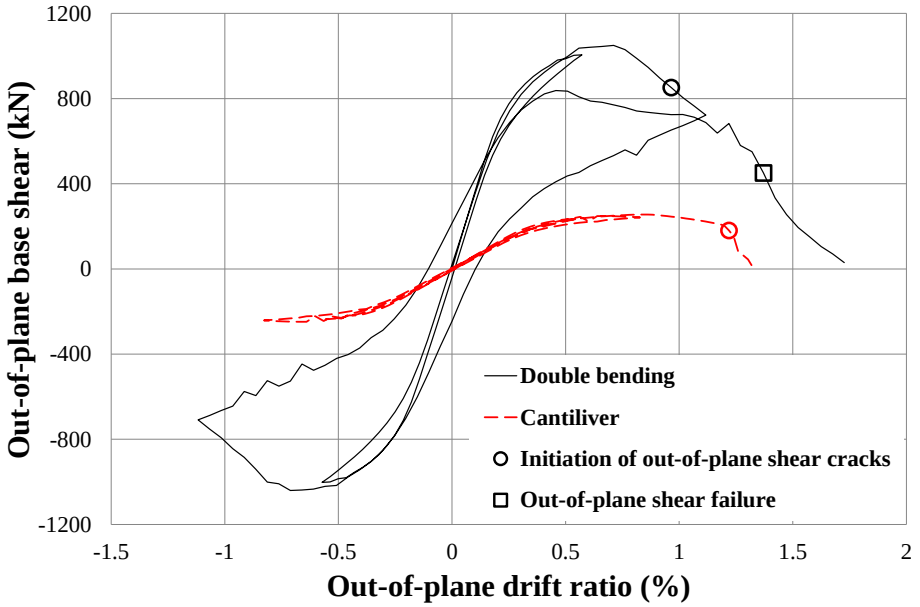

Figure 7-53 Out-of-plane base shear vs drift ratio of Wall D5-6 with different out-of-plane boundary conditions

Figure 7-54-Figure 7-57 show the failure mode of the wall with different boundary conditions in the out-of-plane direction. It can be seen in Figure 7-54 that out-of-plane shear cracks decreased in the wall for the case of a cantilever deformation shape in the out-of-plane direction. In Figure 7-55, it can be seen that the von Mises strain contours of the wall with a cantilever deformation shape was dominated by axial strains which differs from when out-of-plane shear failure happens. The diagonal von Mises stress pattern that formed along the wall with double bending deformation in the out-of-plane which is one of the indications of out-of-plane shear failure didn't form in the wall with cantilever deformation shape as can be

seen in Figure 7-56. Figure 7-57 shows parts of the wall with compressive axial strain higher than 0.003. It can be seen in Figure 7-57 that while the full length of the wall with double bending deformation shape in the out-of-plane was vulnerable to out-of-plane shear, in the wall with cantilever deformation, only less than half the wall was susceptible to out-of-plane shear failure.

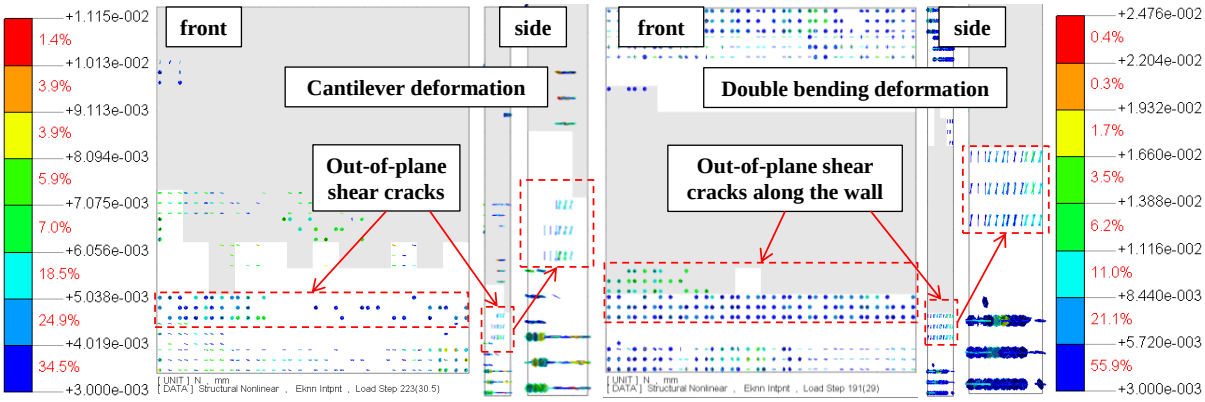

Figure 7-54 Crack pattern of Wall D5-6 under skew loading with cantilever or double bending deformation shape in the out-of-plane direction

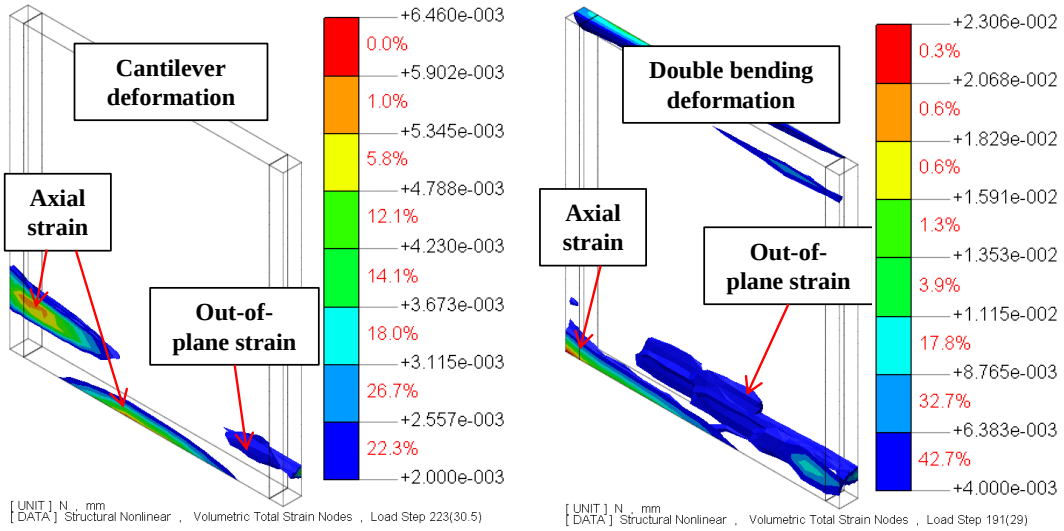

Figure 7-55 Von Mises strain contours of Wall D5-6 under skew loading with cantilever or double bending deformation shape in the out-of-plane direction

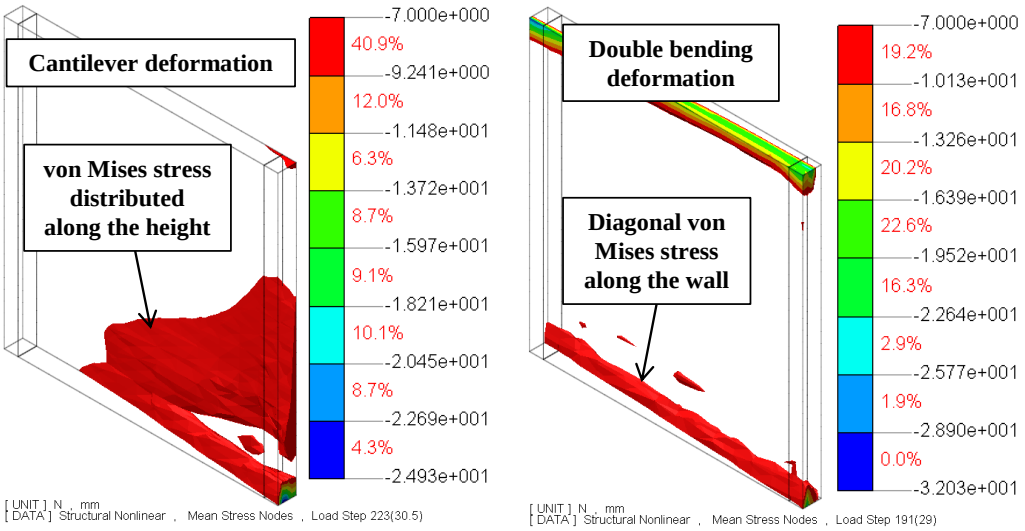

Figure 7-56 Von Mises stress contours of Wall D5-6 under skew loading with cantilever or double bending deformation shape in the out-of-plane direction

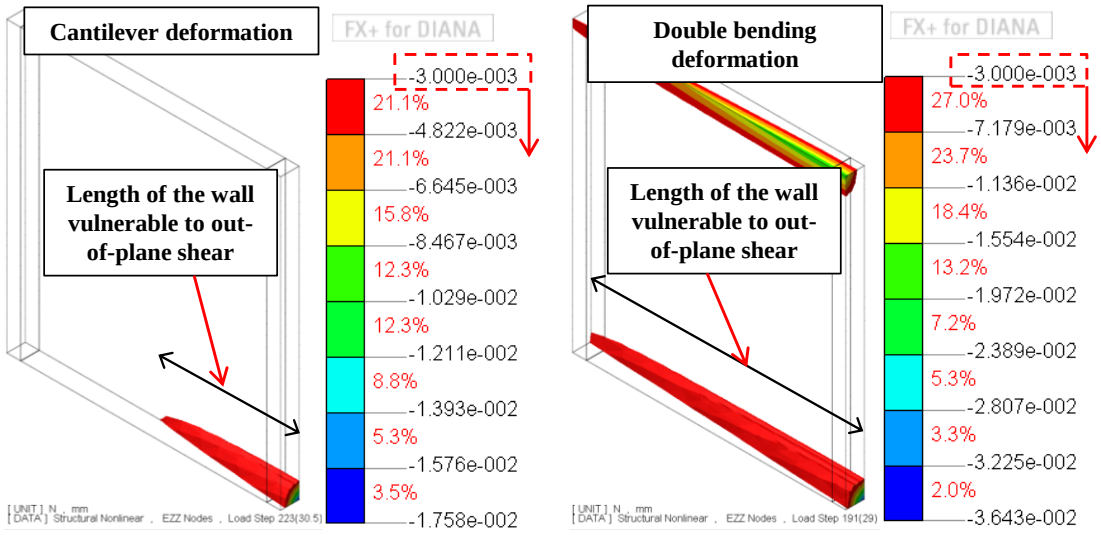

Figure 7-57 Axial strain contours of Wall D5-6 with cantilever or double bending deformation shape in the out-of-plane direction

7.5. CONCLUSIONS

This chapter presented a comprehensive numerical investigations on a case study wall namely Wall D5-6 from Grand Chancellor Hotel in Christchurch, New Zealand that failed in out-of-plane shear in the February 2011 earthquake. The main aspect that was investigated by means of these analysis concern the key parameters caused the failure mode observed in Wall D5-6 using FE analysis. The key findings of this numerical study for each research question are summarised below.

Directionality of the September 2010 and February 2011 New Zealand Earthquakes

Displacement responses for SDOF systems for the initial periods of the building in each direction under the recorded ground accelerations from the 4 September 2010 and 22 February 2011 earthquakes at nearby strong motion stations were plotted against each other. It was found that lateral load path was one of the key parameters in developing the out-of-plane shear failure in the Wall D5-6 in the February 2011 earthquake as the wall had no apparent damage from the September 2010 earthquake which was along its in-plane direction and failed in shear in the February 2011 earthquake that was towards its out-of-plane direction.

Effects of lateral load path on walls prone to out-of-plane shear failure

Numerical investigations were performed on the seismic performance of Wall D5-6 subjected to different lateral load path include in-plane uni-directional, out-of-plane uni-directional and skewed loading with different loading angles. The key findings are presented below.

- Numerical results showed that an axial crushing failure under in-plane uni-directional loading would turn into an out-of-plane shear failure when subjected to out-of-plane uni-directional loading.
- It was found that increasing the loading angle of a skewed uni-directional pattern with respect to the in-plane axis will increase the possibility of triggering an out-of-plane shear failure in the wall as a larger length of the wall would be vulnerable to out-of-plane shear failure.
- The numerical study showed that while Wall D5-6 was vulnerable to out-of-plane shear failure due to high axial load ratio, large thickness, low longitudinal reinforcement ratio and lack of sufficient transverse reinforcement, 2011 February earthquake which was a skewed loading towards the out-of-plane direction of the wall caused a shear failure in that direction.
- Based on the numerical results, it can be concluded that a pre-existing displacement in the out-of-plane direction reduces the maximum attainable strength in rectangular walls.

Effects of out-of-plane boundary conditions on walls prone to out-of-plane shear failure

FE results showed that a wall with a double bending deformation shape in its out-of-plane direction would develop more out-of-plane shear cracks and a larger length of the wall would be susceptible to out-of-plane shear failure compared to the same wall with a cantilever deformation shape in its out-of-plane direction.

8. NUMERICAL PARAMETRIC STUDY ON RECTANGULAR SLENDER RC WALLS SUBJECTED TO BI-DIRECTIONAL LOADING

8.1 INTRODUCTION

In Chapter 7, it was shown that parameters such as lateral loading pattern and out-of-plane boundary condition can change the failure mode of a rectangular RC wall from a flexural failure to an out-of-plane shear. In this chapter, while focusing on walls prone to out-of-plane shear failure the effects of other key parameters on the seismic behaviour of rectangular slender walls are investigated.

8.2 KEY PARAMETERS IN DEVELOPING OUT-OF-PLANE SHEAR FAILURE IN RC WALLS

Based on the earthquake observations (2011 New Zealand), experimental results presented in Chapter 5 and the numerical study of Chapter 7, axial load ratio, section aspect ratio, section detailing ductility and longitudinal reinforcement ratio along with lateral load path which was investigated in Chapter 7 found to be the key parameters in developing out-of-plane shear failure in rectangular RC walls. Effects of each of these parameters on the seismic performance of walls prone to out-of-plane shear failure were investigated in a comprehensive numerical study using FE analysis. Table 8-1 shows the basic characteristics of the walls used for the numerical parametric study. It is worth noting that in all cases in-plane and out-of-plane shear span ratios and horizontal reinforcement ratio were kept constant. Longitudinal reinforcement ratio was also constant for all cases except when investigating the effects of this parameter itself. Based on the numerical study conducted in Chapter 7, each wall was investigated only under cyclic skewed uni-directional loading pattern with 85 degree angle with respect to the in-plane axis described in Figure 8-1 and Table 8-2. This lateral loading pattern found to be the worst case in triggering out-of-plane shear failure as was discussed in Section 7.4.3.

Table 8-1 Characteristics of the walls used for the numerical parametric study

Parameters	Axial load ratio [1]	Section aspect ratio [2]	Section detailing ductility	In-plane shear span ratio [3]	Out-of-plane shear span ratio [4]	Longitudinal reinforcement ratio [5]	Horizontal reinforcement ratio [6]
Axial load ratio [1]	5%	12.2	Nominal Ductile	3.45	6.69	0.45%	0.503%
	10%						
	15%						
	20%						
	25%						
	30%						
Section aspect ratio [2]	15%	7.5	Nominal Ductile	3.45	5.04	0.45%	0.503%
		9.78					
		12.22					
		16.3					
Section detailing ductility	15%	7.5	Nominal Ductile	3.45	5.04	0.45%	0.503%
	15%-25%		Limited Ductile				
	15%-25%		Ductile				
Longitudinal reinforcement ratio [5]	20%	12.2	Nominal Ductile	3.45	6.69	0.45%	0.503%
						0.75%	
						1.5%	

[1] $P/(A_g f_c')$, using $f_c' = 35MPa$.
[2] L_w/t
[3] H_e/L_w, In-plane shear span of the wall is equal to the in-plane effective height of the building
[4] H_{out}/t, Out-of-plane shear span of the wall was considered half the length of the first storey height to the slab centre, assuming a double bending deformation shape in the out-of-plane direction
[5] $\rho_t = (A_{s,BZ} + A_{s,web})/(L_w \times t)$
[6] $\rho_v = A_{sv}/(s \times t)$

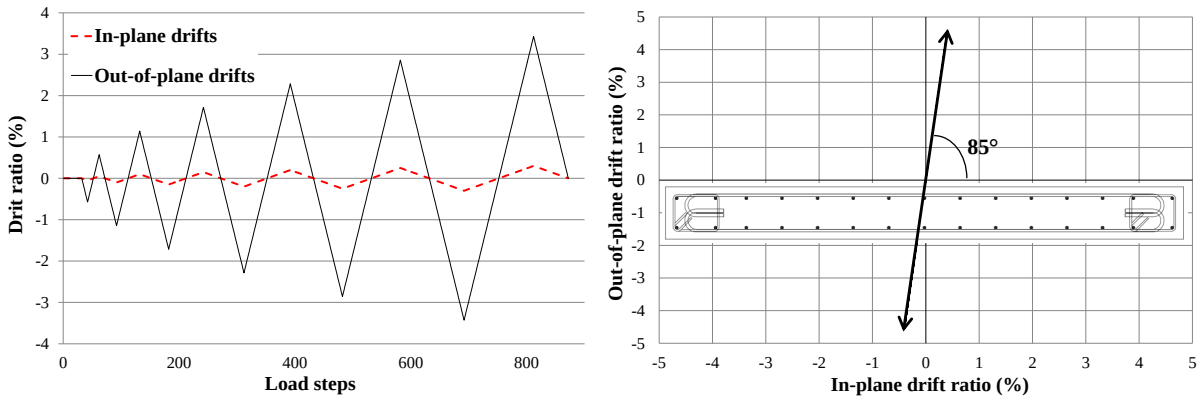

Figure 8-1 Lateral loading pattern used for the parametric study

Table 8-2 In-plane and out-of-plane drift ratios of each lateral loading pattern cycle

Cycle	1	2	3	4	5	6
In-plane drift ratio	0.05%	0.1%	0.15%	0.2%	0.25%	0.3%
Out-of-plane drift ratio	0.572%	1.143%	1.715%	2.286%	2.858%	3.429%

8.3 NUMERICAL PARAMETRIC STUDY RESULTS

The FE model described in Chapter 6 was used for the numerical parametric study of rectangular slender walls under bi-directional loading. Details and the key characteristics of the walls were presented first and then behaviour of the walls were discussed based on the base shear vs drift ratio curve, crack pattern, von Mises stress, axial, out-of-plane and von Mises strains contours.

8.3.1 Axial load ratio, $P/(A_g f'_c)$

Axial load ratio was one of the key parameters contributed to the failure of Wall D5-6 from Grand Chancellor Hotel in the 2011 New Zealand earthquake. Experimental study presented in Chapter 5 further proved the importance of axial load ratio in the development of out-of-plane shear failure. However, due to the limitations with the number of specimens, it was not possible to investigate the effects of this parameter on walls prone to out-of-plane shear failure properly in Chapter 5. Therefore, in this section the effects of this parameter on walls prone to out-of-plane shear failure were investigated in more details. For this purpose, six different axial load ratios of 5%, 10%, 15%, 20%, 25% and 30% were chosen. Table 8-3 shows the key characteristics of the walls used for this parametric study. Figure 8-2 shows the section details of the wall. Material properties of concrete were shown in Figure 8-3.

Table 8-3 Characteristics of walls used for parametric study on axial load ratio

Parameters	Axial load ratio, $P/(A_g f'_c)$					
	5%	10%	15%	20%	25%	30%
Out-of-plane shear span, H_{out} (mm)	2675					
Thickness, t (mm)	400					
Out-of-plane shear span ratio, H_{out}/t	6.69					
In-plane effective height, H_e (mm)	16875					
Length, L_w (mm)	4890					
In-plane shear span ratio, H_e/L_w	3.45					
Section aspect ratio, L_w/t	12.2					
Section detailing ductility	Nominal Ductility					
Longitudinal reinforcement ratio (%) $\rho_t = (A_{s,BZ} + A_{s,web})/(L_w \times t)$	0.45					
Horizontal reinforcement ratio (%) $\rho_v = A_{sv}/(s \times t)$	0.5					
Compressive strength of concrete (MPa)	35					
Yield strength of reinforcement (MPa)	300					

* Out-of-plane shear span is half the first floor height

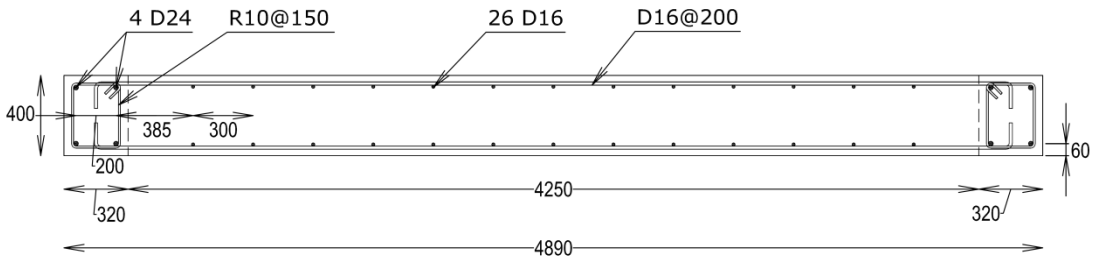

Figure 8-2 Details of the wall used for the parametric study on axial load ratio

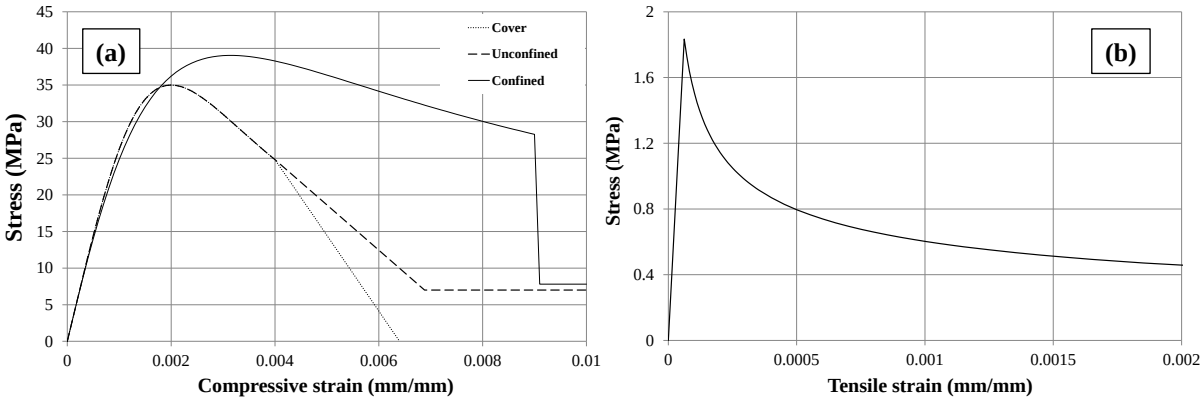

Figure 8-3 Material properties of concrete (a) compressive (Mander et al. 1988) and (b) tensile (Belarbi and Hsu 1994) behaviours

Axial load ratio: 5%

Figure 8-4 shows the base shear-drift ratio curve of the wall with 5% axial load ratio subjected to bi-directional loading. The wall showed a ductile behaviour under skewed loading with 85 degree considering no confinement in the wall. Axial, out-of-plane and von Mises strain contours of the wall were shown in Figure 8-5. In Figure 8-5, strain contours were filtered to show only tensile strains higher than 0.004 to be able to see the pattern of each strain contours more clearly. As can be seen in Figure 8-5, von Mises strain contours of the wall with 5% axial load ratio was dominated by axial strains and only a small part of the wall was affected by out-of-plane strain (Equations behind von Mises strain are provided in Section 6.5.1). Figure 8-6 shows the axial strain and von Mises stress contours of the wall, filtered in a way to show parts of the wall vulnerable to out-of-plane shear failure. As was discussed in Section 6.5.5, filtering the axial strain contours to compressive strain higher than 0.003 (when concrete starts to crush) and von Mises stress contours to compressive stress higher than 7 MPa (minimum compressive strength of concrete in the web, see Figure 8-3), would show part of the wall vulnerable to out-of-plane shear failure. As can be seen in Figure 8-6 for the wall with 5% axial load ratio, only a small part of the wall was vulnerable to out-of-plane shear failure. Figure 8-7 shows the crack pattern of the wall at 0.3% in-plane and 3.429% out-of-plane drift ratios. Although there were some out-of-plane shear cracks in

the two corners of the wall, the cracks were not formed along the full length and thickness of the wall.

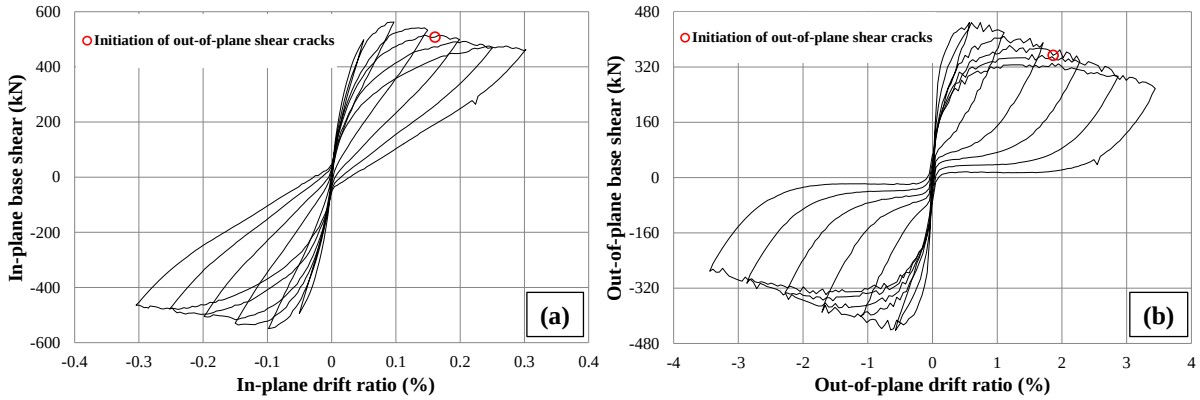

Figure 8-4 Base shear-drift ratio of the wall with 5% axial load ratio in the (a) in-plane and (b) out-of-plane directions

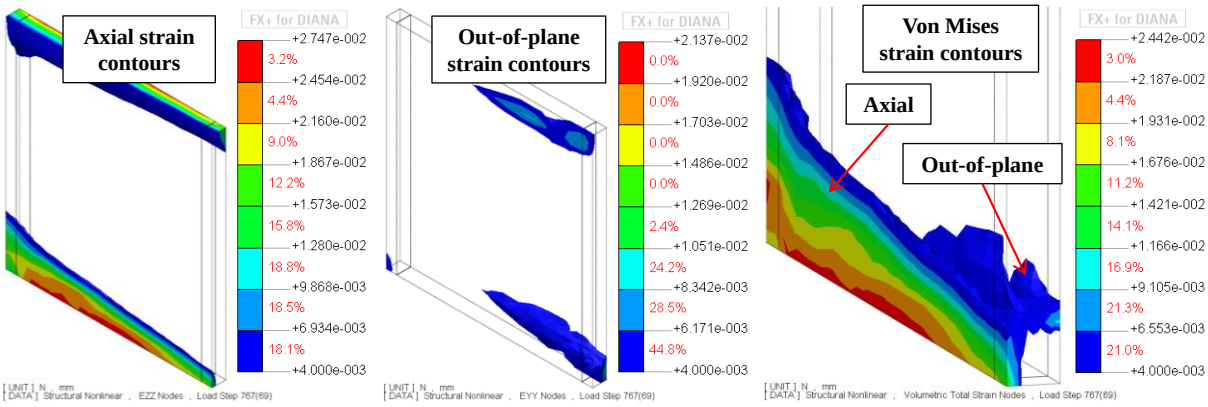

Figure 8-5 Axial, out-of-plane and von Mises strain contours of the wall with 5% axial load ratio

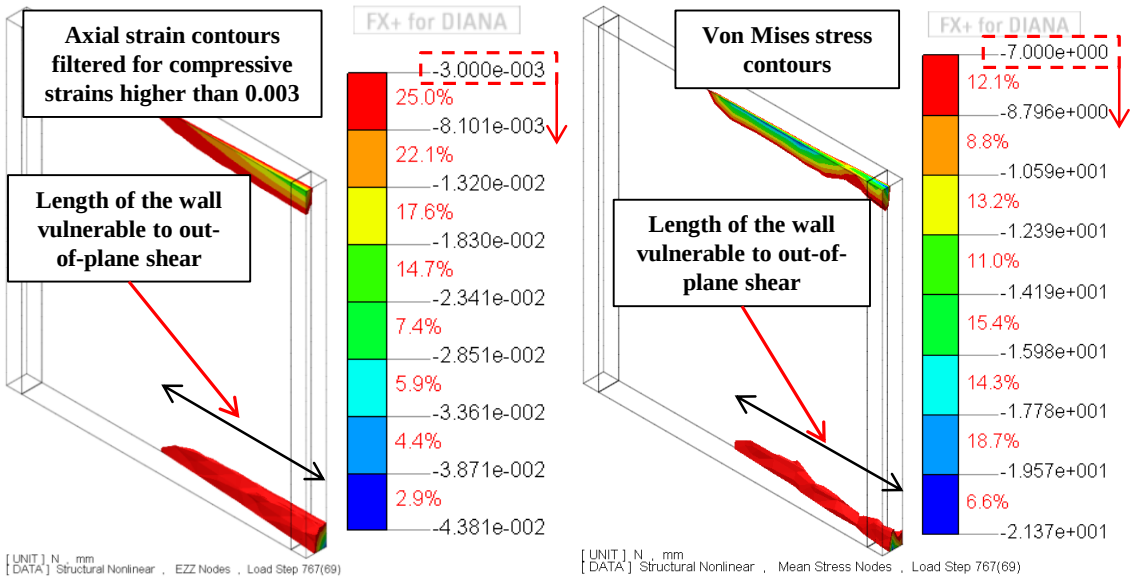

Figure 8-6 Axial strain and von Mises stress contours of the wall with 5% axial load ratio

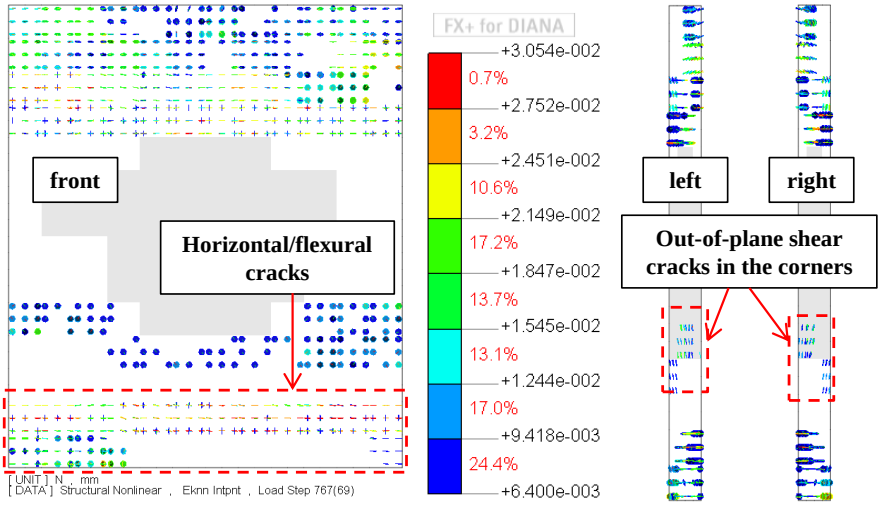

Figure 8-7 Crack pattern of the wall with 5% axial load ratio

Axial load ratio: 10%

Figure 8-8 shows the base shear-drift ratio curve of the wall with 10% axial load ratio subjected to bi-directional loading. The wall showed a ductile behaviour in its in-plane direction. However, in the out-of-plane direction, the wall showed a less ductile behaviour by losing strength capacity compared to the one with 5% axial load ratio.

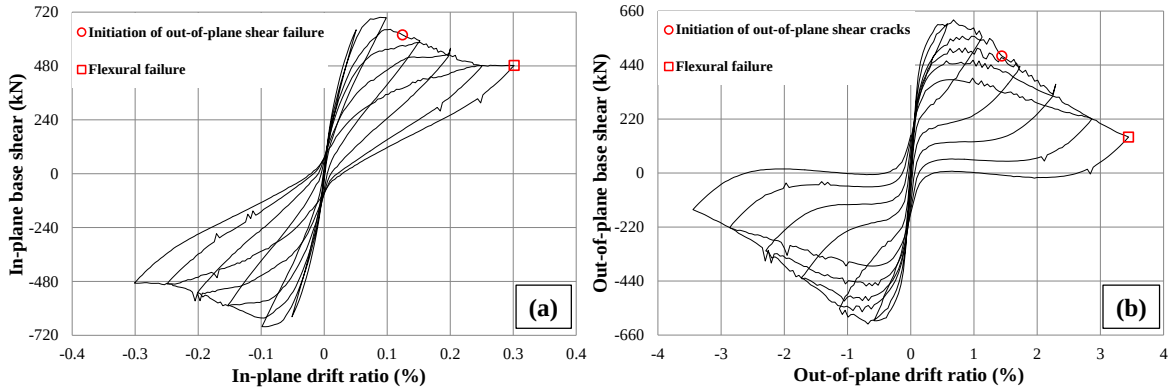

Figure 8-8 Base shear-drift ratio of the wall with 10% axial load ratio in the (a) in-plane and (b) out-of-plane directions

Axial, out-of-plane and von Mises strain contours of the wall were shown in Figure 8-9. As can be seen in Figure 8-9, the von Mises strain contours of the wall with 10% axial load ratio was still dominated by axial strains. Looking at the axial strain and von Mises stress contours in Figure 8-10, it can be seen that the length of the wall vulnerable to out-of-plane shear was increased in the wall with 10% axial load ratio compared to the one with 5%. Figure 8-11 shows the crack pattern of the wall at 0.3% in-plane and 3.429% out-of-plane drift ratios. Similar to the wall with 5% axial load ratio, some out-of-plane shear cracks formed in the two corners of the wall. However, these cracks were not formed along the full length and thickness of the wall. Comparing Figure 8-7 and Figure 8-11, it can be seen that out-of-plane

shear cracks were increased in the wall with 10% axial load ratio. However, the ultimate failure mode of the wall was a flexural failure with some concrete crushing at the base.

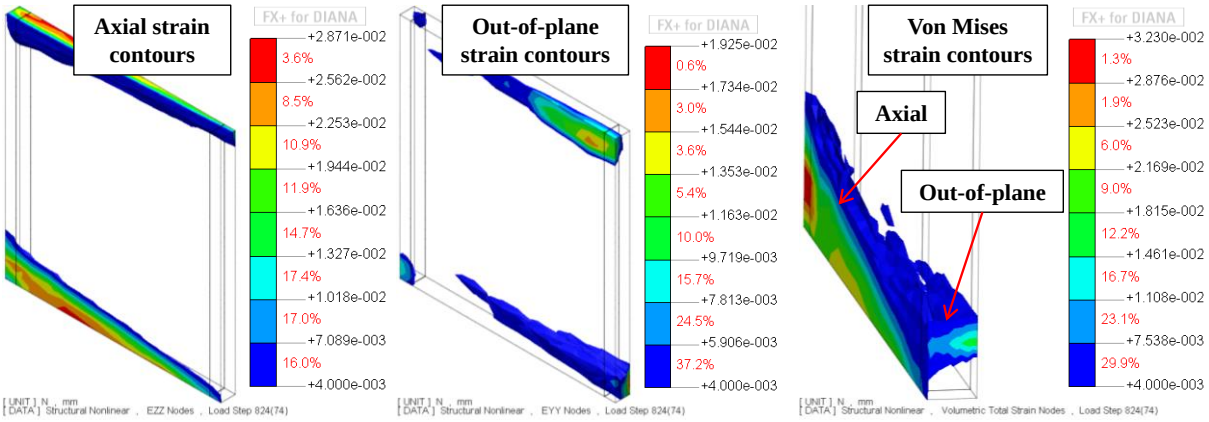

Figure 8-9 Axial, out-of-plane and von Mises strain contours of the wall with 10% axial load ratio

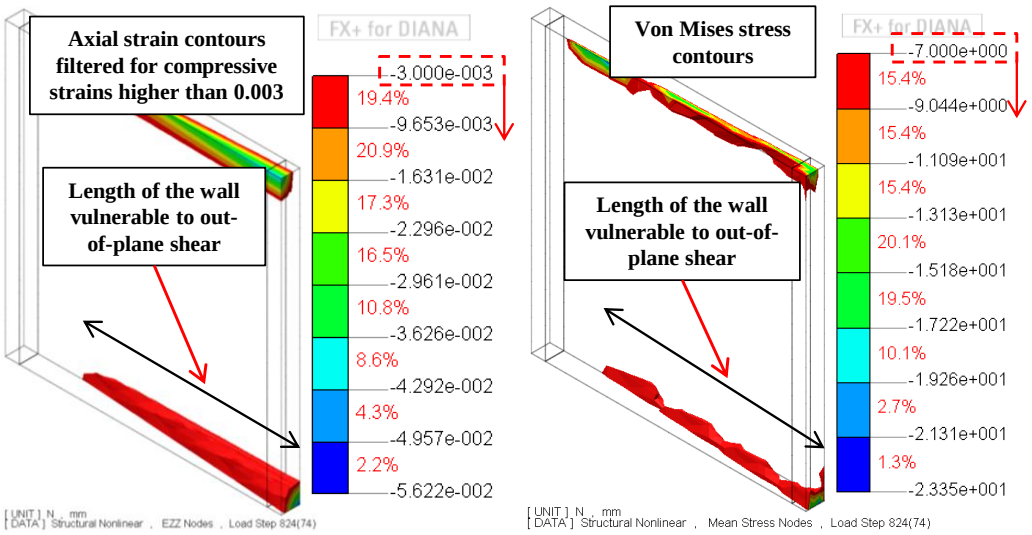

Figure 8-10 Axial strain and von Mises stress contours of the wall with 10% axial load ratio

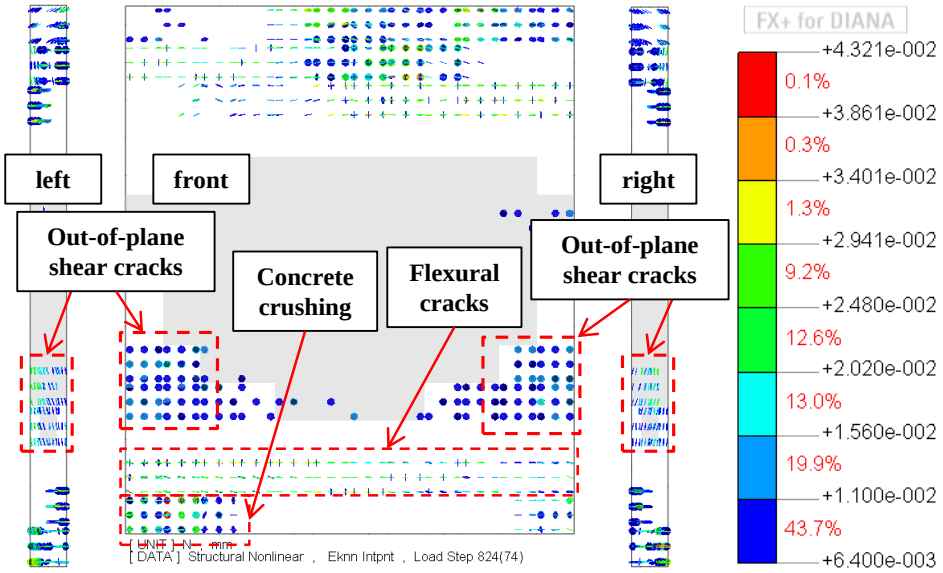

Figure 8-11 Crack pattern of the wall with 10% axial load ratio

Axial load ratio: 15%

Figure 8-12 shows the base shear-drift ratio curve of the wall with 15% axial load ratio subjected to bi-directional loading. While the wall showed a more stable behaviour in its in-plane direction, it lost significant out-of-plane strength capacity and failed at 0.21% in-plane and 2.35% out-of-plane drift ratios.

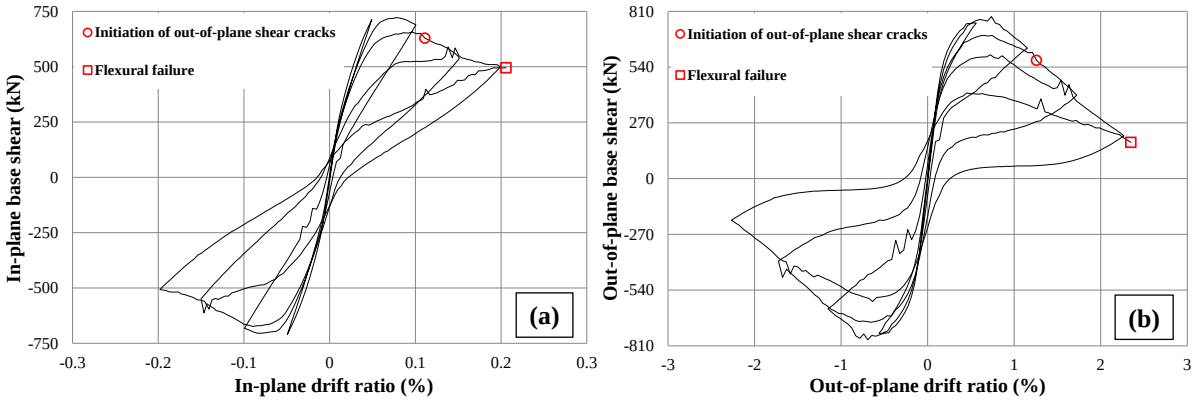

Figure 8-12 Base shear-drift ratio of the wall with 15% axial load ratio in the (a) in-plane and (b) out-of-plane directions

Axial, out-of-plane and von Mises strain contours of the wall were shown in Figure 8-13. It can be seen that von Mises strain contours of the wall with 15% axial load ratio was still slightly dominated by axial strains. Looking at the axial strain and von Mises stress contours in Figure 8-14, it can be seen that the length of the wall vulnerable to out-of-plane shear failure was increased in the wall with 15% axial load ratio compared to the ones with 5% and 10%. Figure 8-15 shows the crack pattern of the wall. Although out-of-plane shear cracks formed in the wall, the cracks were not formed along the full length and thickness of the wall. The ultimate failure mode of the wall was a flexural failure along with concrete crushing and out-of-plane shear cracks as can be seen in Figure 8-15.

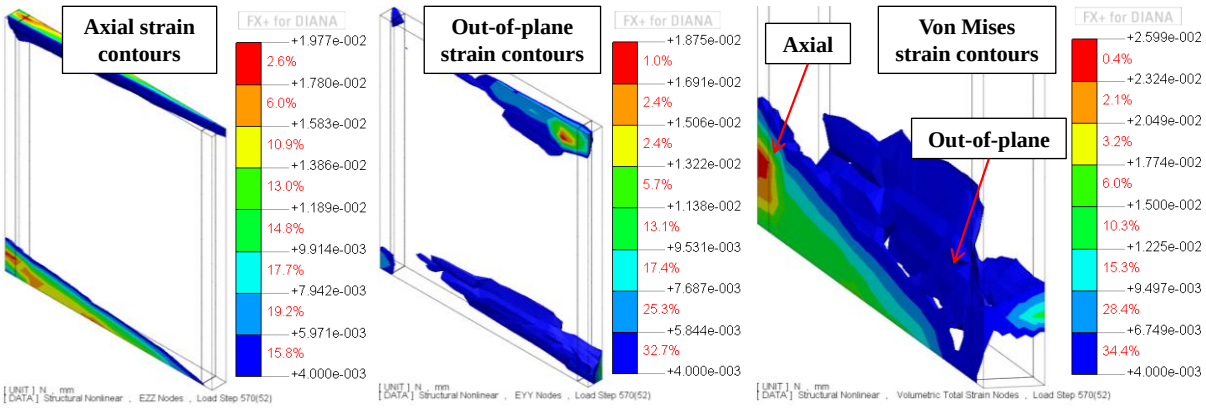

Figure 8-13 Axial, out-of-plane and von Mises strain contours of the wall with 15% axial load ratio

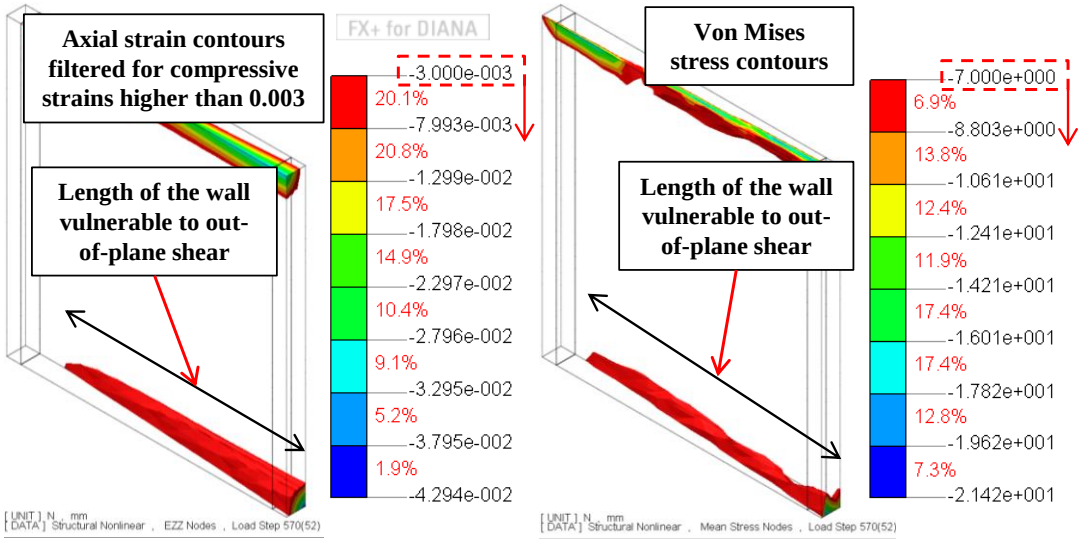

Figure 8-14 Axial strain and von Mises stress contours of the wall with 15% axial load ratio

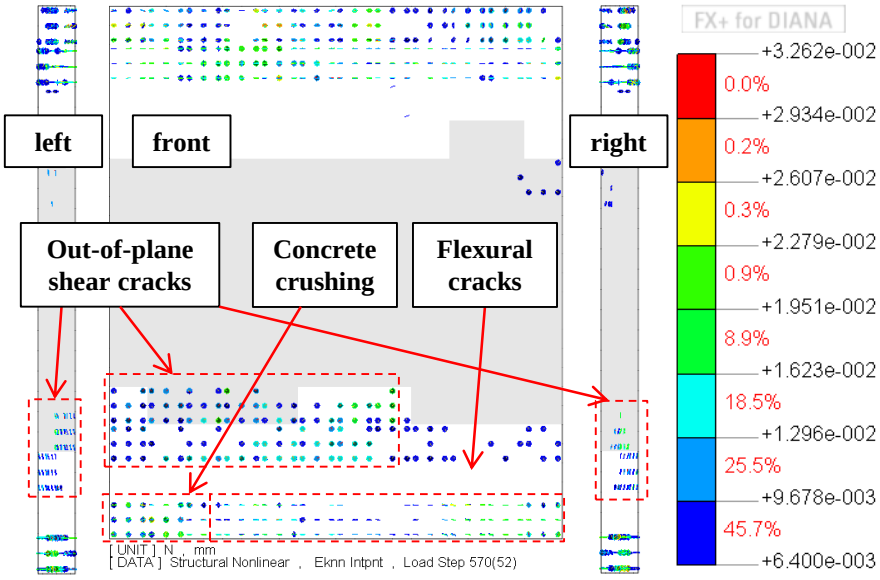

Figure 8-15 Crack pattern of the wall with 15% axial load ratio

Axial load ratio: 20%

Figure 8-16 shows the base shear-drift ratio curve of the wall with 20% axial load ratio subjected to bi-directional loading. The wall showed brittle behaviour especially in the out-of-plane direction and failed at 0.16% in-plane and 1.83% out-of-plane drift ratios. Axial, out-of-plane and von Mises strain contours of the wall were shown in Figure 8-17. It can be seen that the von Mises strain contours of the wall with 20% axial load ratio was dominated by out-of-plane strains. Development of this type of strain contributes to the development of out-of-plane shear cracks. Axial strain and von Mises stress contours of the wall were shown in Figure 8-18. Looking at the axial strain and von Mises stress contours in Figure 8-18, it can be seen that the length of the part vulnerable to out-of-plane shear failure is almost equal to the length of the wall and in a diagonal form. This was similar to the axial strain and von

Mises stress contours of specimen SP2-ND that failed in out-of-plane shear in the lab (discussed in Section 6.5.5). Figure 8-19 shows the crack pattern of the wall at 0.16% in-plane and 1.83% out-of-plane drift ratios. Significant out-of-plane shear cracks were formed along the full length and thickness of the wall which indicates a shear failure in that direction.

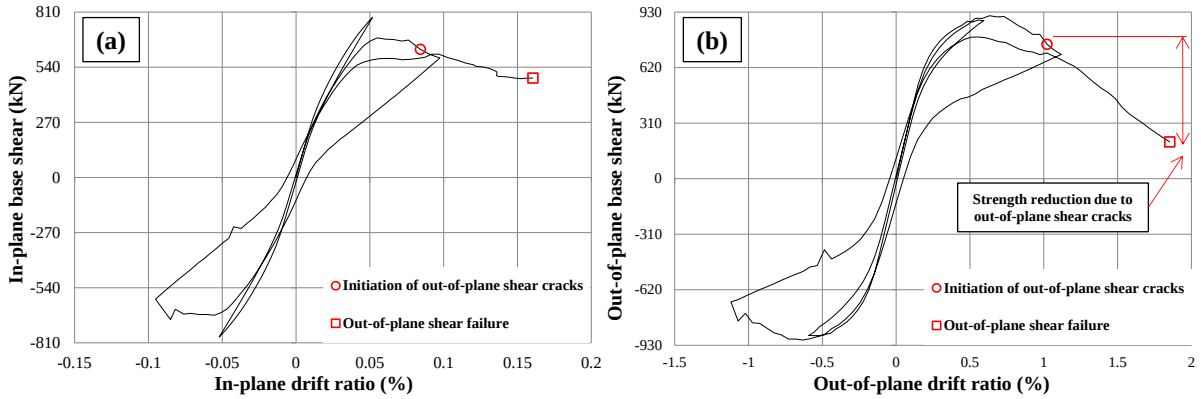

Figure 8-16 Base shear-drift ratio of the wall with 20% axial load ratio in the (a) in-plane and (b) out-of-plane directions

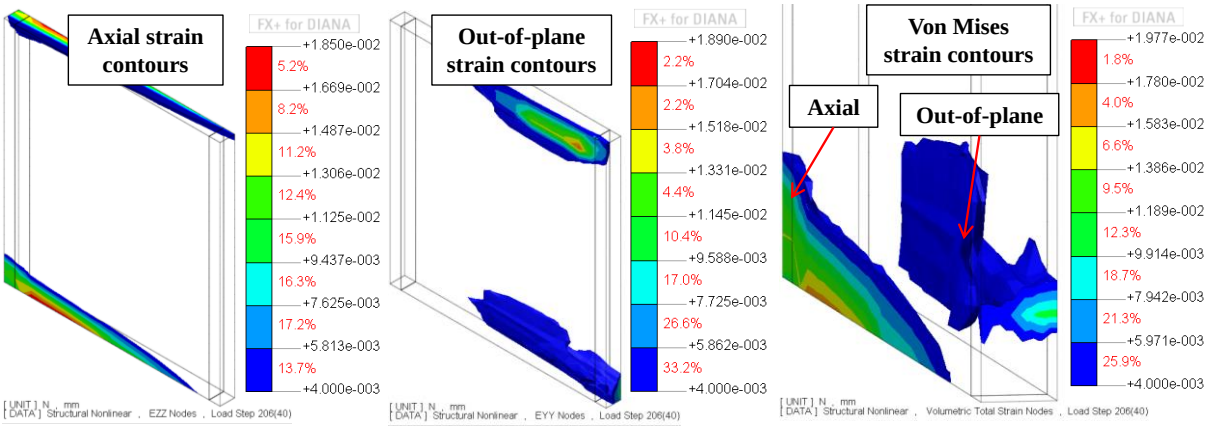

Figure 8-17 Axial, out-of-plane and von Mises strain contours of the wall with 20% axial load ratio

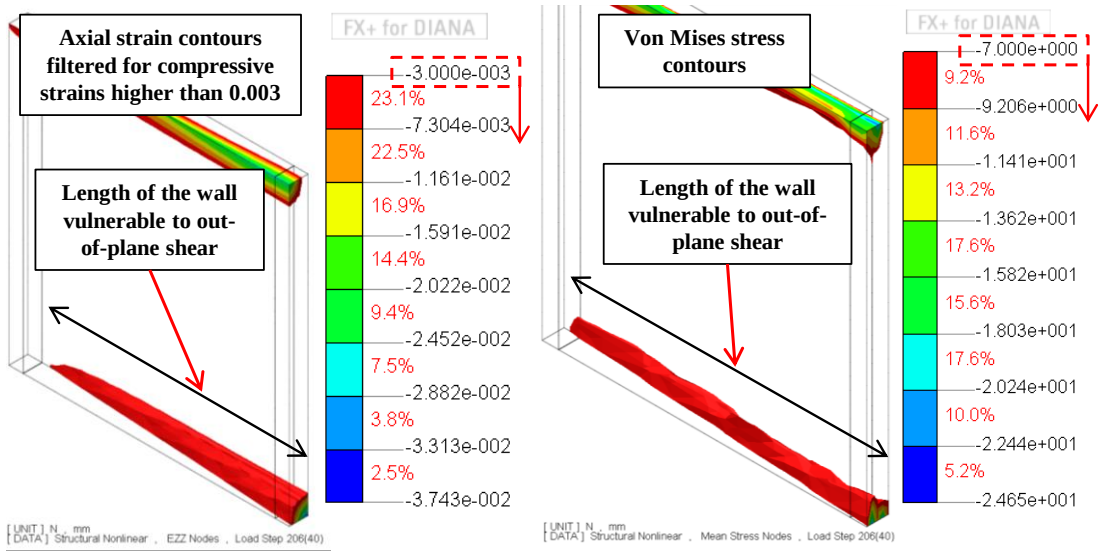

Figure 8-18 Axial strain and von Mises stress contours of the wall with 20% axial load ratio

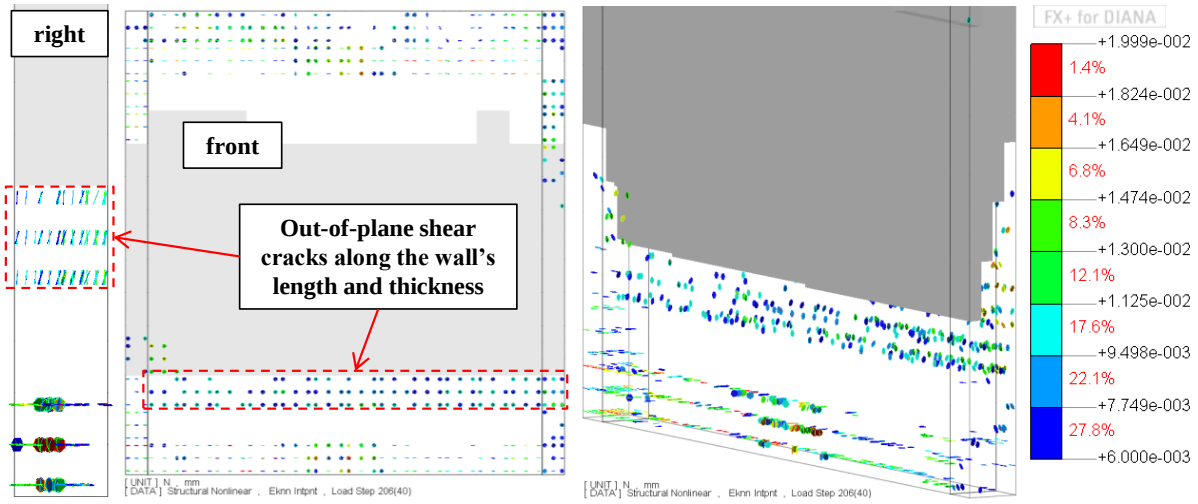

Figure 8-19 Crack pattern of the wall with 20% axial load ratio

Axial load ratio: 25%

Figure 8-20 shows the base shear-drift ratio curve of the wall with 25% axial load ratio subjected to bi-directional loading. The wall showed brittle behaviour in both in-plane and out-of-plane directions and failed in 0.133% in-plane and 1.52% out-of-plane drift ratios.

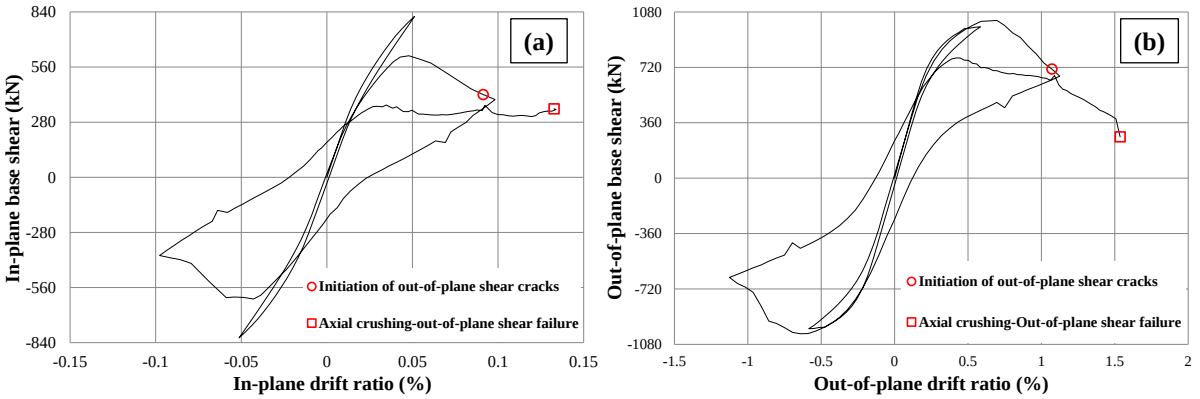

Figure 8-20 Base shear-drift ratio of the wall with 25% axial load ratio in the (a) in-plane and (b) out-of-plane directions

Axial, out-of-plane and von Mises strain contours of the wall were shown in Figure 8-21. It can be seen in Figure 8-21, the von Mises strain contours of the wall with 25% axial load ratio was dominated by out-of-plane strains. Axial strain and von Mises stress contours of the wall were shown in Figure 8-22. Although axial strain contours of the wall show that the full length of the wall was vulnerable to out-of-plane shear, but looking at the von Mises stress contours, it can be seen that the pattern of the von Mises stress contours differ from the one shown in Figure 6-62 for specimen SP2-ND that failed in out-of-plane shear in the laboratory.

Figure 8-23 shows the crack pattern of the wall at 0.133% in-plane and 1.52% out-of-plane drift ratios. Out-of-plane shear cracks was initiated and developed up to the failure point.

However, these cracks didn't form along the full length and thickness of the wall. Based on the significant reduction of in-plane strength capacity shown in Figure 8-20a (about 58%), von Mises stress contours pattern and crack pattern of the wall, an axial crushing failure along with significant out-of-plane shear cracks is most likely the failure mode for this wall.

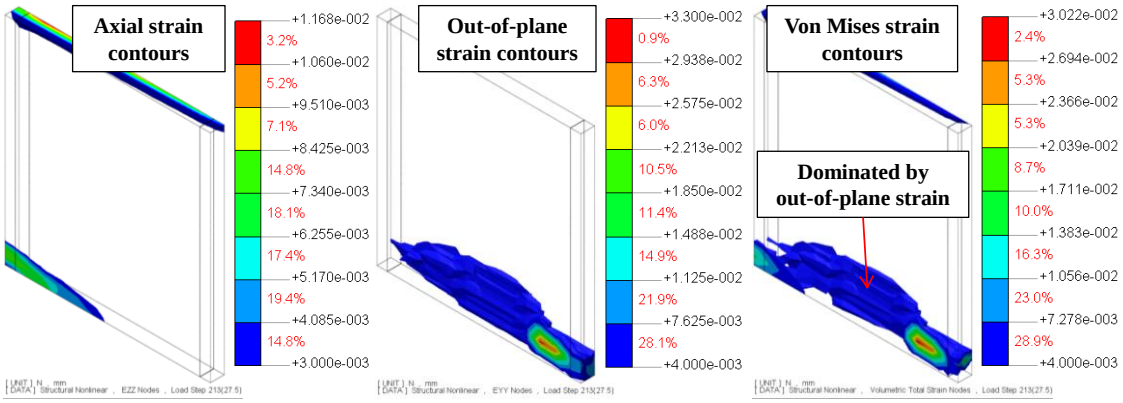

Figure 8-21 Axial, out-of-plane and von Mises strain contours of the wall with 25% axial load ratio

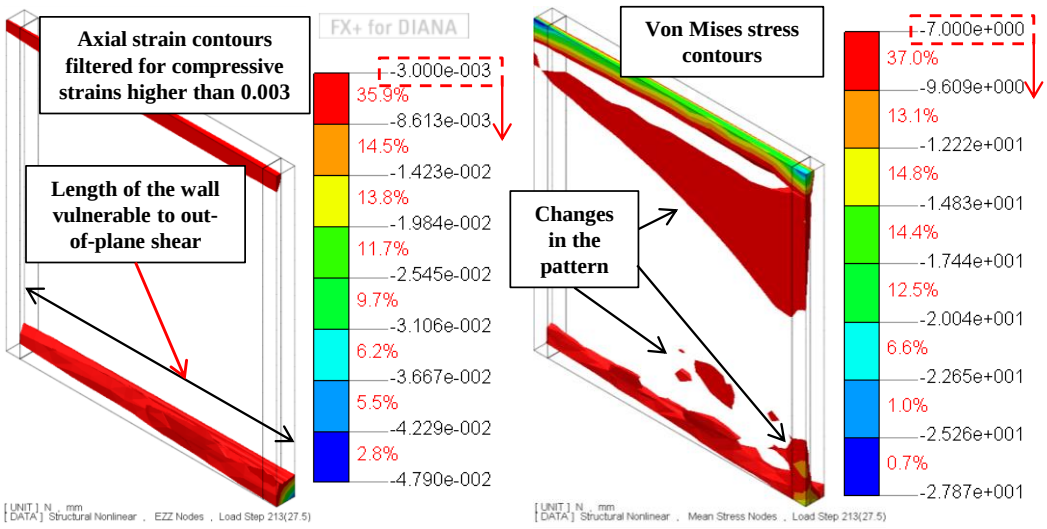

Figure 8-22 Axial strain and von Mises stress contours of the wall with 25% axial load ratio

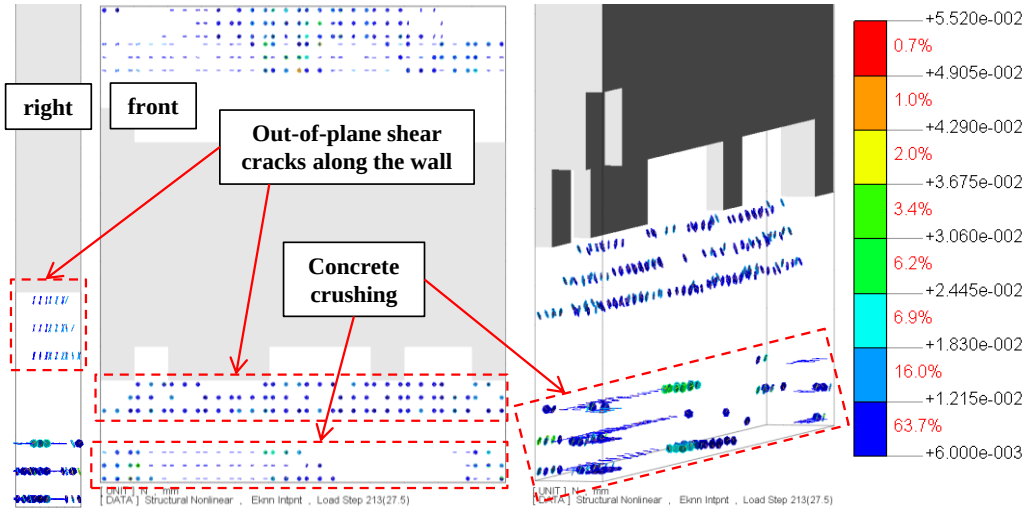

Figure 8-23 Crack pattern of the wall with 25% axial load ratio

Axial load ratio: 30%

Figure 8-24 shows the base shear-drift ratio curve of the wall with 30% axial load ratio subjected to bi-directional loading. The wall showed an extremely brittle behaviour in both in-plane and out-of-plane directions and failed in 0.075% in-plane and 0.857% out-of-plane drift ratios. Axial, out-of-plane and von Mises strain contours of the wall were shown in Figure 8-25. It can be seen that the von Mises strain contours of the wall with 30% axial load ratio was dominated by the out-of-plane strains due to high axial load ratio of the wall. Axial strain and von Mises stress contours of the wall were shown in Figure 8-26. Looking at the axial strain in Figure 8-26, it can be seen that length of the wall vulnerable to out-of-plane shear was decreased compared to the case with 20% or 25% axial load ratios. Moreover, pattern of the von Mises stress contours differs from the one shown in Figure 6-62 for specimen SP2-ND that failed in out-of-plane shear in the laboratory. Figure 8-27 shows the crack pattern of the wall just before and after the failure point. It can be seen that while there was no sign of out-of-plane shear cracks before the failure, some out-of-plane shear cracks showed up at the failure point. Based on the significant reduction of in-plane strength capacity (about 62%), axial strain (reduction in the vulnerable length), von Mises stress contours (changes in the pattern) and crack pattern of the wall (no sign of out-of-plane shear cracks until final failure), it can be concluded that axial crushing is the failure mode of the wall.

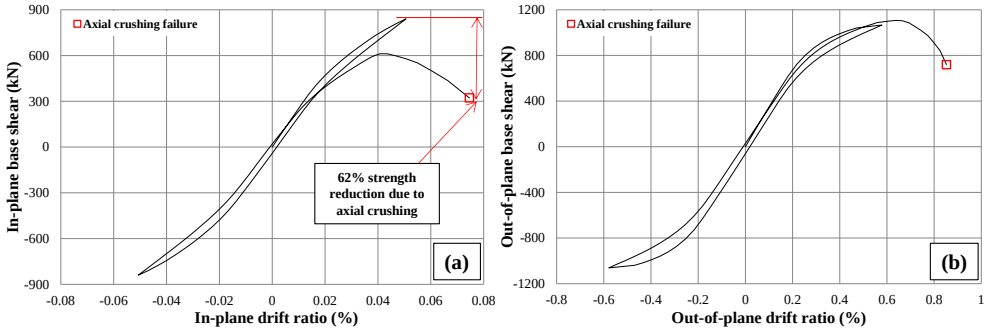

Figure 8-24 Base shear-drift ratio of the wall with 30% axial load ratio in the (a) in-plane and (b) out-of-plane directions

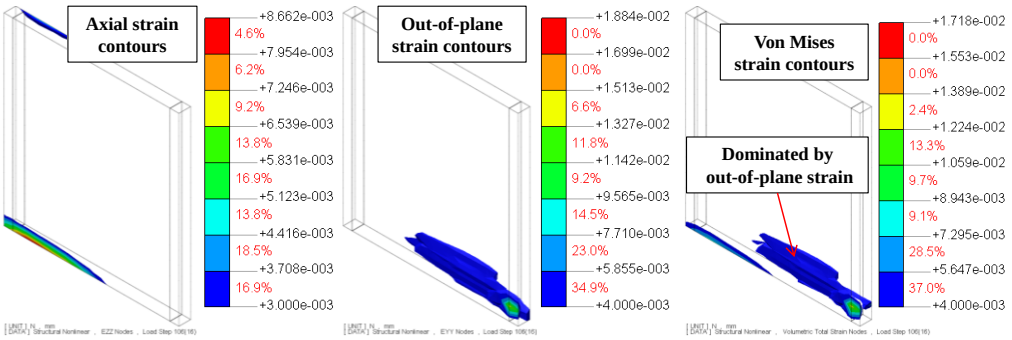

Figure 8-25 Axial, out-of-plane and von Mises strain contours of the wall with 30% axial load ratio

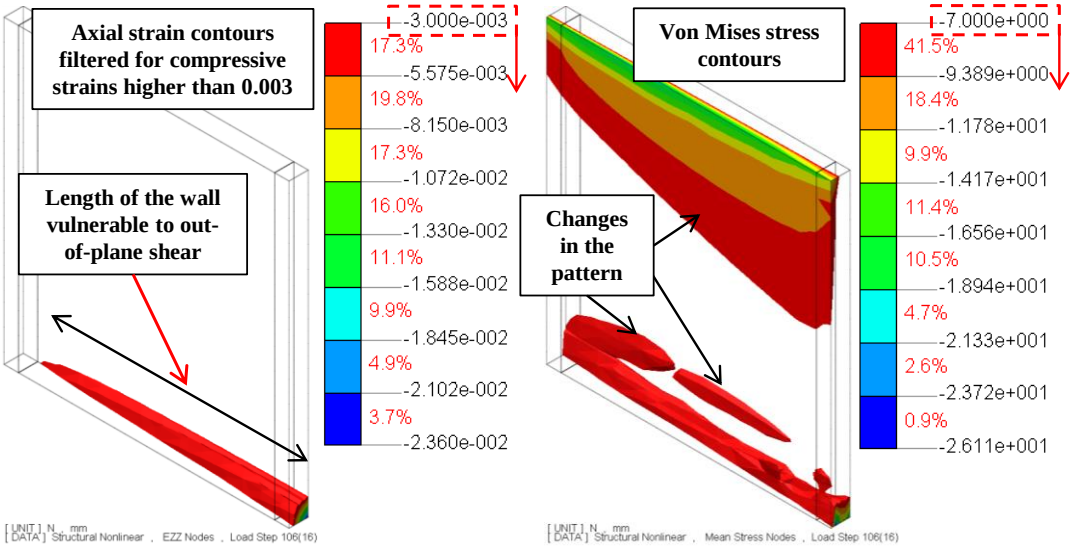

Figure 8-26 Axial strain and von Mises stress contours of the wall with 30% axial load ratio

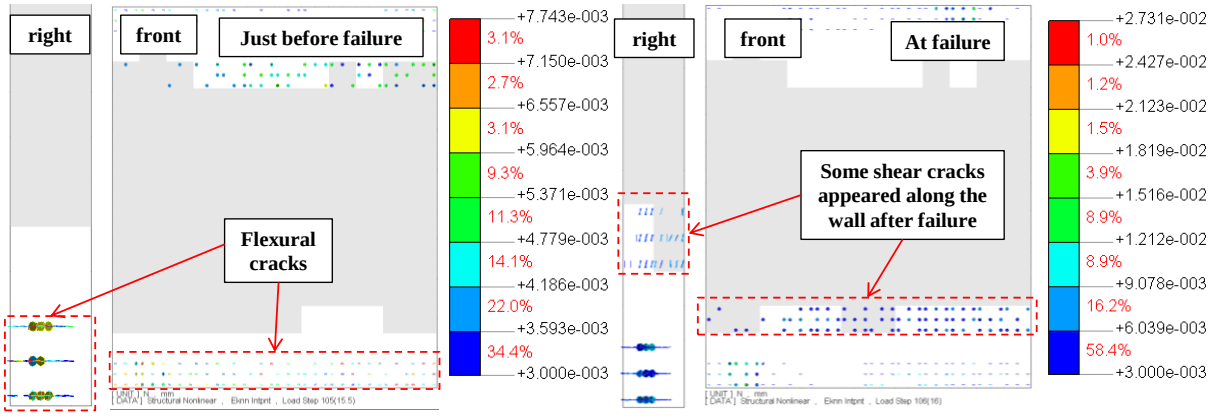

Figure 8-27 Crack pattern of the wall with 30% axial load ratio just before and after failure

Conclusions

Looking at the axial strain and von Mises stress contours of walls with different axial load ratio shown in Figure 8-6, Figure 8-10, Figure 8-14, Figure 8-18, Figure 8-22 and Figure 8-26, it was found that higher axial load ratio increases the length of the part vulnerable to out-of-plane shear failure and therefore increases the susceptibility of the wall to this type of failure. Moreover, higher axial load ratio changes the von Mises strain patterns of the wall towards the domination of out-of-plane strain which helps with the development of out-of-plane shear cracks. In terms of failure mode, it was found that a flexural failure under low axial load ratio would turn into an out-of-plane shear failure by the increase in axial load ratio. However, further increase of axial load ratio would change the failure mode to an axial crushing failure. Table 8-4 shows the drift capacity and the failure mode of the wall under each axial load ratio. As was expected, increasing the axial load ratio decreased the drift capacity of the wall.

Table 8-4 Drift capacity and failure mode of the wall with different axial load ratio

Axial load ratio	Drift ratio at failure point		Failure mode
	In-plane drift (%)	Out-of-plane drift (%)	
5%	0.3	3.429	Flexural
10%	0.3	3.429	Flexural + concrete crushing
15%	0.21	2.35	Flexural + concrete crushing
20%	0.16	1.83	Out-of-plane shear
25%	0.133	1.52	Axial crushing + out-of-plane shear
30%	0.075	0.857	Axial crushing

8.3.2 Section aspect ratio, (L_w/t)

The other key parameter that contributes to the development of out-of-plane shear cracks is the section aspect ratio of the wall. Four different section aspect ratios of 7.5, 9.8, 12.2 and 16.3 were chosen to investigate the effects of this parameter on the behaviour of walls prone to out-of-plane shear failure. Table 8-5 shows the section of these walls. Details of each wall used for this parametric study was shown in

Table 8-6. Material properties of concrete were shown in Figure 8-3. It is worth noting that all the walls investigated in this section had 15% axial load ratio. Effects of section aspect ratio on the seismic performance of walls prone to out-of-plane shear failure are discussed in more details in the following sub-sections.

Table 8-5 Walls used for the parametric study on section aspect ratio

Section aspect ratio	Section
7.5	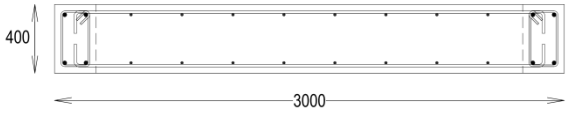
9.78	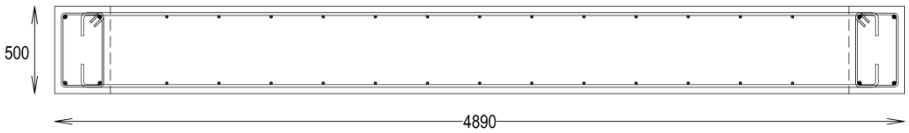
12.2	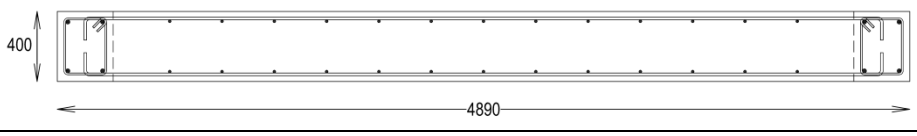
16.3	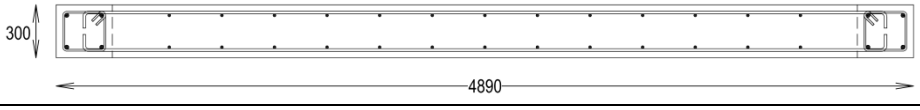

Table 8-6 Characteristics of the walls used for the parametric study on section aspect ratio

Parameters	Section aspect ratio, L_w/t			
	7.5	9.8	12.2	16.3
Length, L_w (mm)	3000	4890		
Thickness, t (mm)	400	500	400	300
Out-of-plane shear span, H_{out} (mm)	2015	2520	2015	1512
Out-of-plane shear span ratio, H_{out}/t	5.04			
In-plane effective height, H_e (mm)	10353	16875		
In-plane shear span ratio, H_e/L_w	3.45			
Axial load ratio, $P/(A_g f_c')$ (%)	15			
Section detailing ductility	Nominal Ductility			
Longitudinal reinforcement ratio (%) $\rho_t = (A_{s,BZ} + A_{s,web})/(L_w \times t)$	0.45			
Horizontal reinforcement ratio (%) $\rho_v = A_{sv}/(s \times t)$	0.5			
Compressive strength of concrete (MPa)	35			
Yield strength of reinforcement (MPa)	300			

* Out-of-plane shear span is half the first floor height

Section aspect ratio of 7.5

Figure 8-28 shows the base shear-drift ratio curve of the wall with section aspect ratio of 7.5 subjected to bi-directional loading. The wall showed brittle behaviour in both in-plane and out-of-plane directions and failed at 0.18% in-plane and 2.06% out-of-plane drift ratios. Von Mises strain and stress contours of the wall were shown in Figure 8-29. Von Mises strain contours of the wall shown in Figure 8-29 were dominated by out-of-plane shear strains. Looking at von Mises stress contours in Figure 8-29, it can be seen that length of the part vulnerable to out-of-plane shear failure is equal to the length of the wall.

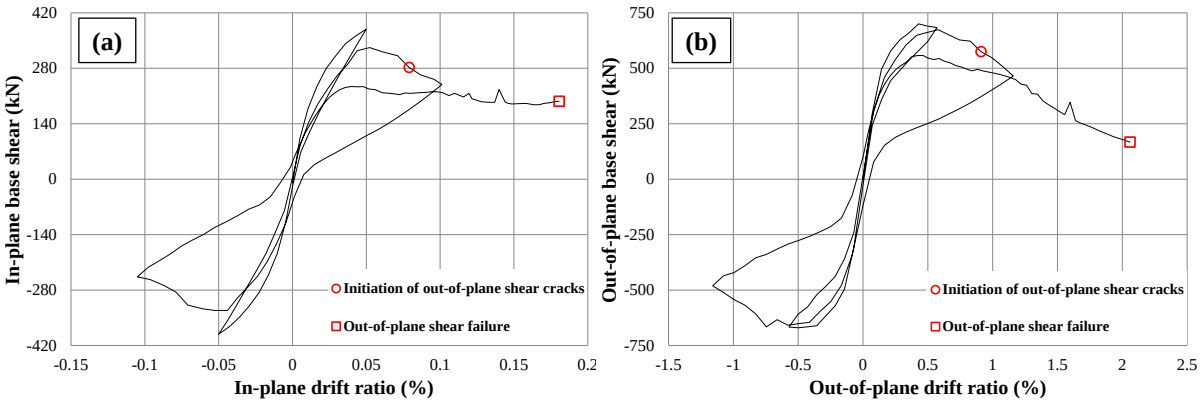

Figure 8-28 Base shear-drift ratio of the wall with section aspect ratio of 7.5 in the (a) in-plane and (b) out-of-plane directions

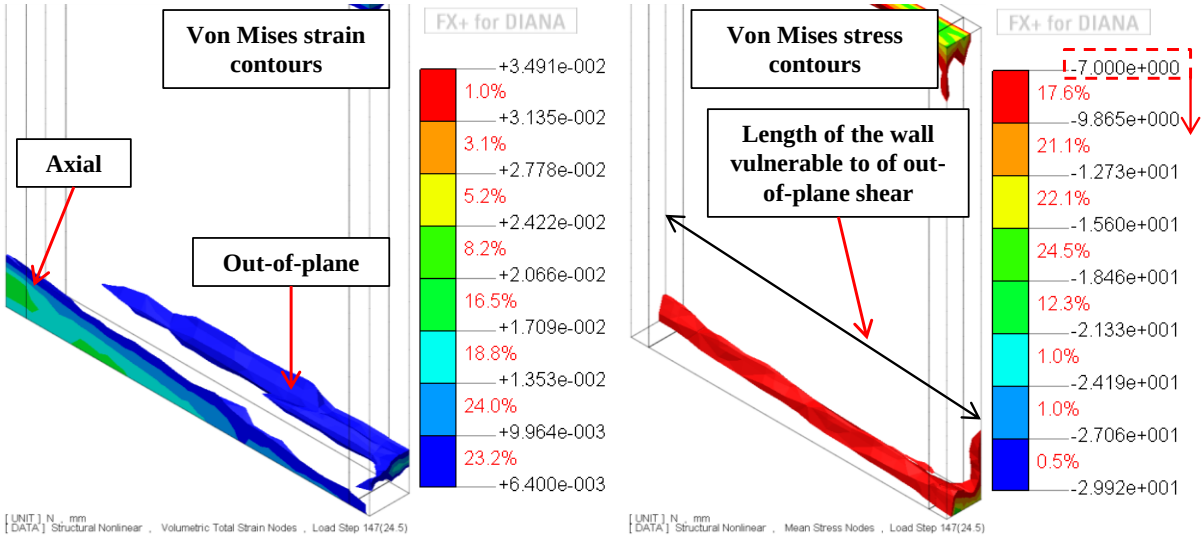

Figure 8-29 Von Mises strain and stress contours of the wall with section aspect ratio of 7.5

Axial strain contours of the wall in Figure 8-30 also show that length of the part with compressive strain higher than 0.003 (when concrete starts to crush) is equal to the wall's length. The other key parameter that can be calculated from Figure 8-30 is the compressive to tensile strains ratio of the wall which is $5.25/2.21 = 2.37$ for the wall with a section aspect ratio of 7.5. This ratio shows the domination of compressive strain compared to tensile ones that was found to be one of the key parameters in the development of out-of-plane shear failure as was discussed in Section 5.3.3. Figure 8-31 shows the crack pattern of the wall at 0.18% in-plane and 2.06% out-of-plane drift ratios. It can be seen that the out-of-plane shear cracks formed along the full length and thickness of the wall suggesting an out-of-plane shear failure in the wall.

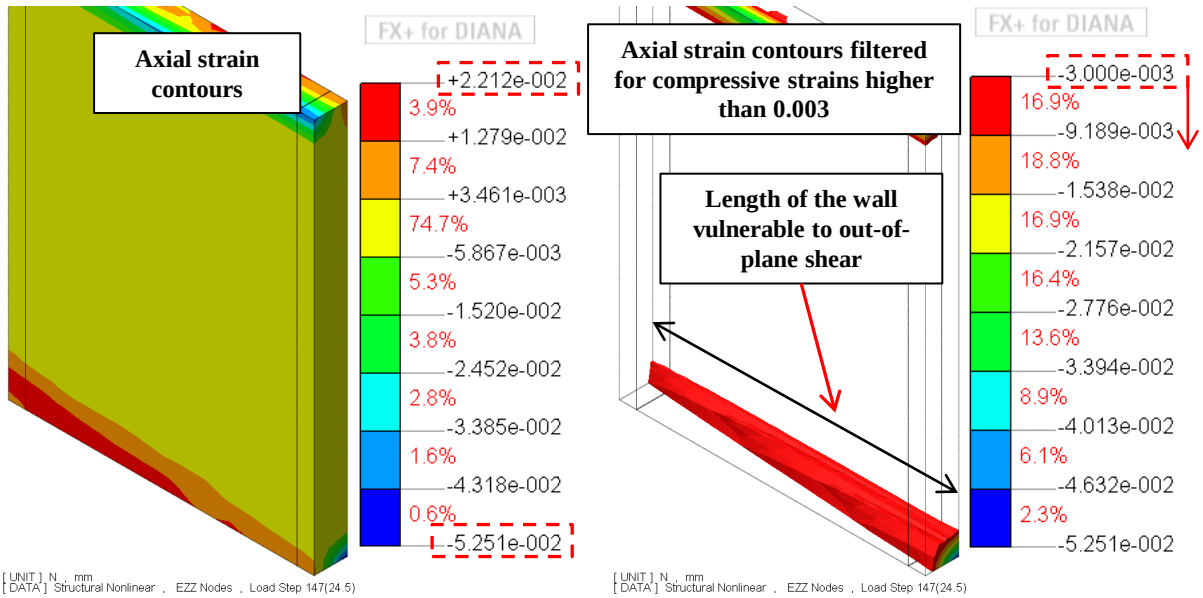

Figure 8-30 Axial strain contours of the wall with section aspect ratio of 7.5

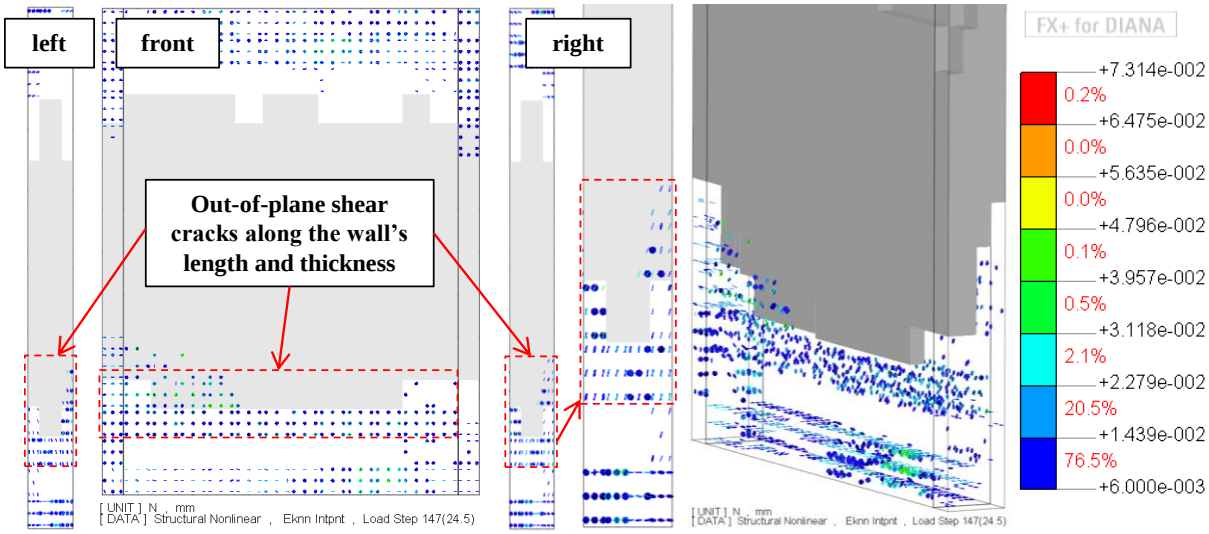

Figure 8-31 Crack pattern of the wall with section aspect ratio of 7.5

Section aspect ratio of 9.8

Figure 8-32 shows the base shear-drift ratio curve of the wall with section aspect ratio of 9.8 subjected to bi-directional loading. The wall showed brittle behaviour in both in-plane and out-of-plane directions and failed at 0.237% in-plane and 2.71% out-of-plane drift ratios. Von Mises strain and stress contours of the wall were shown in Figure 8-33. As can be seen in Figure 8-33, the von Mises strain contours of the wall was slightly dominated by out-of-plane strains. Von Mises stress contours of the wall shows that the length of the part vulnerable to out-of-plane shear failure is equal to the length of the wall.

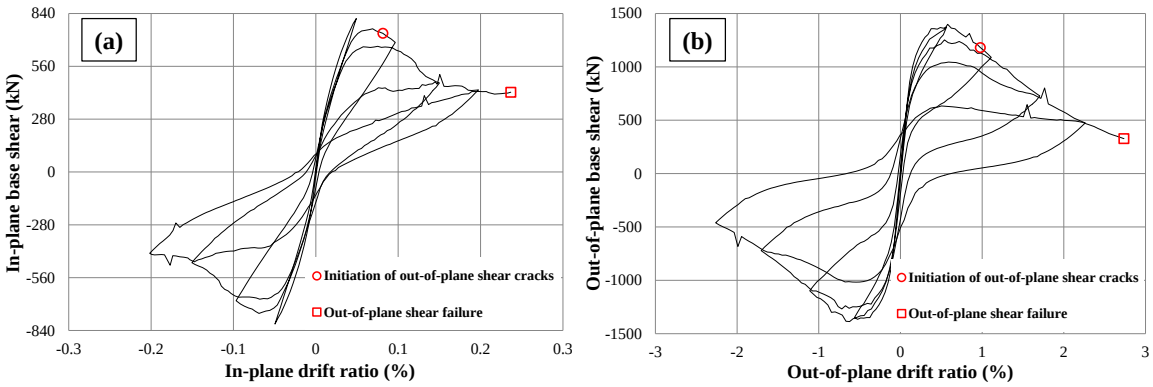

Figure 8-32 Base shear-drift ratio of the wall with section aspect ratio of 9.8 in the (a) in-plane and (b) out-of-plane directions

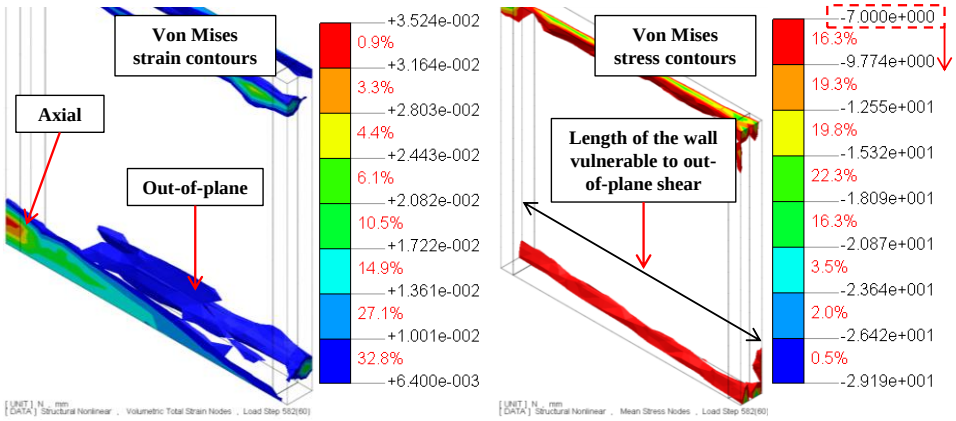

Figure 8-33 Von Mises strain and stress contours of the wall with section aspect ratio of 9.8

Axial strain contours of the wall in Figure 8-34 also show that the full length of the wall is vulnerable to out-of-plane shear failure. Compressive to tensile strains ratio of the wall was $6.042/2.775 = 2.18$ for the wall with a section aspect ratio of 9.8. Figure 8-35 shows the crack pattern of the wall at 0.237% in-plane and 2.71% out-of-plane drift ratios. Significant out-of-plane shear cracks along the full length and thickness of the wall indicate an out-of-plane shear failure in the wall.

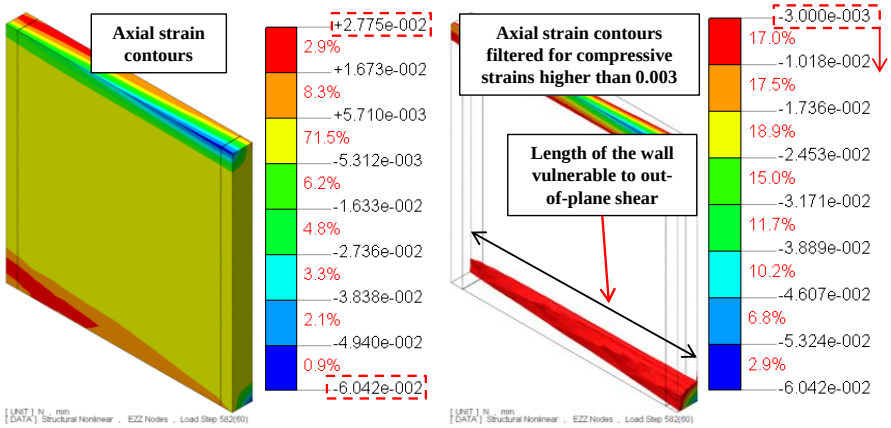

Figure 8-34 Axial strain contours of the wall with section aspect ratio of 9.8

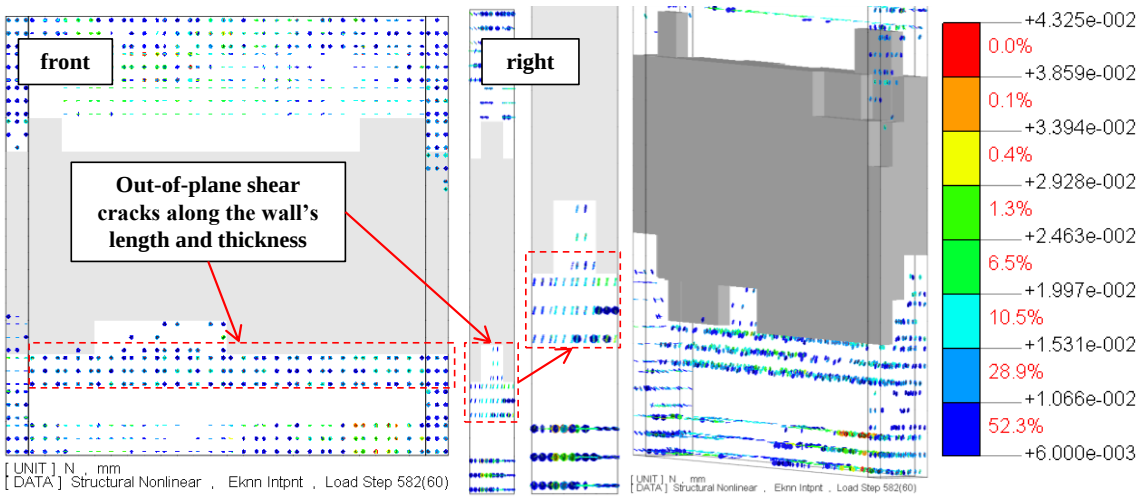

Figure 8-35 Crack pattern of the wall with section aspect ratio of 9.8

Section aspect ratio of 12.2

Figure 8-36 shows the base shear-drift ratio curve of the wall with a section aspect ratio of 12.2 subjected to bi-directional loading. The wall showed a brittle behaviour in both in-plane and out-of-plane directions (more brittle in the out-of-plane) and failed at 0.221% in-plane and 2.53% out-of-plane drift ratios. Von Mises strain and stress contours of the wall were shown in Figure 8-37. Von Mises strain contours of the wall with section aspect ratio of 12.2 was slightly dominated by axial strain. Looking at the von Mises stress contours in Figure 8-37, it can be seen that part of the wall vulnerable to out-of-plane shear failure doesn't cover the full length of the wall.

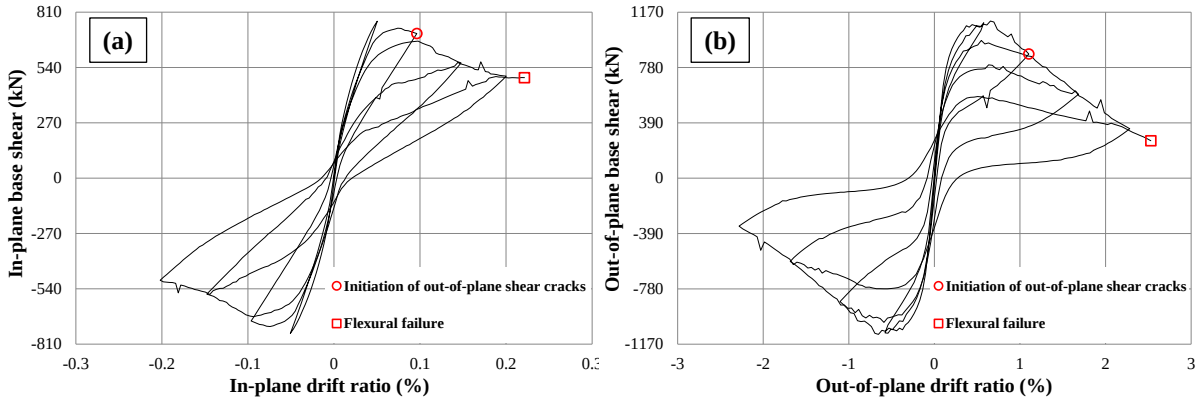

Figure 8-36 Base shear-drift ratio of the wall with section aspect ratio of 12.2 in the (a) in-plane and (b) out-of-plane directions

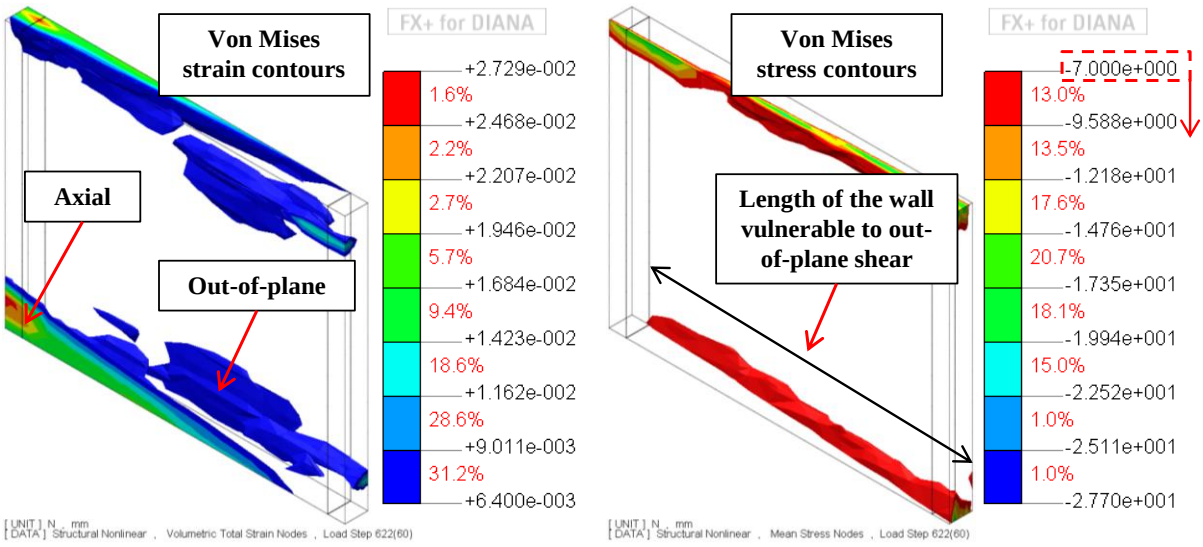

Figure 8-37 Von Mises strain and stress contours of the wall with section aspect ratio of 12.2

Axial strain contours of the wall in Figure 8-38 confirms the von Mises stress results regarding the length of the wall vulnerable to out-of-plane shear failure. Compressive to tensile strains ratio of the wall was $4.53/2.41 = 1.88$ for the wall with a section aspect ratio of 12.2. Figure 8-39 shows the crack pattern of the wall. Although out-of-plane shear cracks

formed in certain length of the wall as shown in Figure 8-39, these cracks didn't continue along the full length and thickness of the wall. The final failure of the wall is a flexural failure along with concrete crushing and out-of-plane shear cracks.

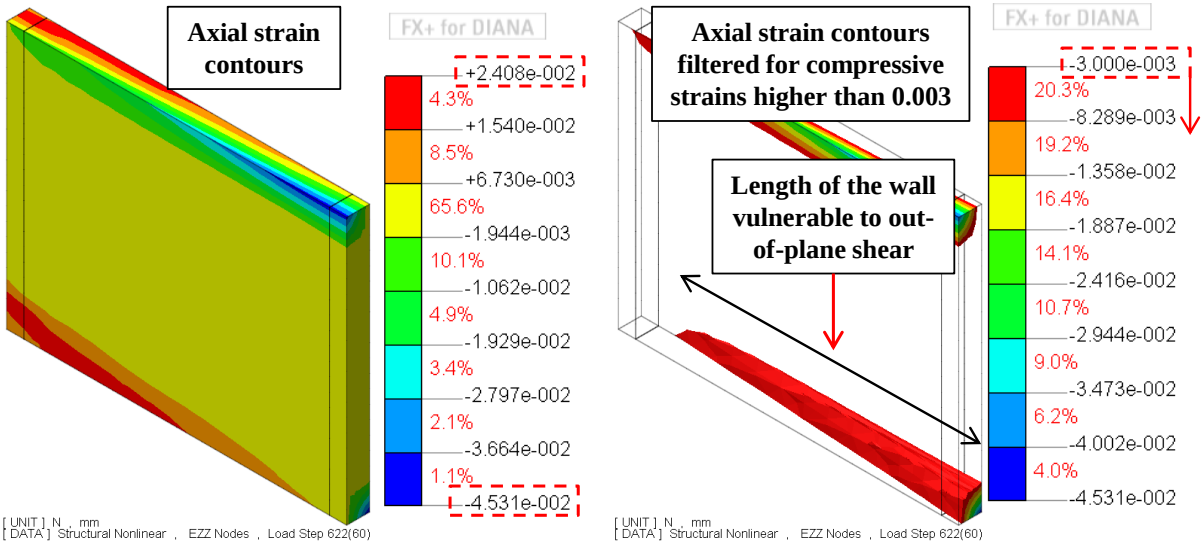

Figure 8-38 Axial strain contours of the wall with section aspect ratio of 12.2

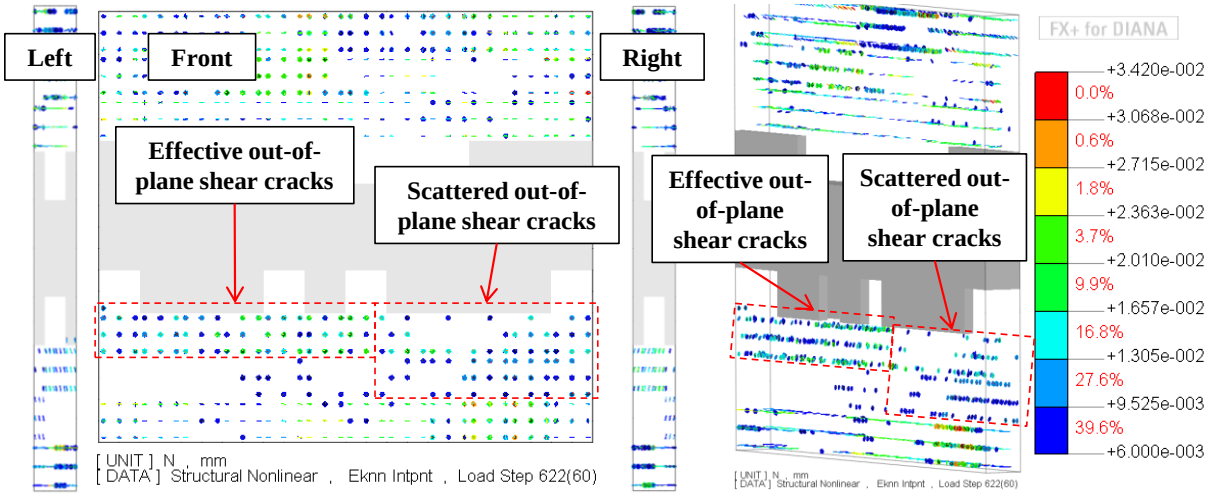

Figure 8-39 Crack pattern of the wall with section aspect ratio of 12.2

Section aspect ratio of 16.3

Figure 8-40 shows the base shear-drift ratio curve of the wall with section aspect ratio of 16.3 subjected to bi-directional loading. The wall showed a stable behaviour in the in-plane but a brittle one in the out-of-plane direction and failed at 0.217% in-plane and 2.48% out-of-plane drift ratios. Von Mises strain and stress contours of the wall were shown in Figure 8-41. Looking at the von Mises stress contours in Figure 8-41, it can be seen that part of the wall vulnerable to out-of-plane shear failure was further decreased compared to the wall with a section aspect ratio of 12.2. Axial strain contours of the wall shown in Figure 8-42 confirm the reduction of the length of the part vulnerable to out-of-plane shear failure. Compressive to

tensile strains ratio of the wall was $4.28/2.41 = 1.78$ for the wall with a section aspect ratio of 16.3. Figure 8-43 shows the crack pattern of the wall. Some scattered out-of-plane shear cracks can be seen along the wall in Figure 8-43. However, out-of-plane shear cracks didn't form along the full length and thickness of the wall and the wall failed in flexure along with concrete crushing at 0.217% in-plane and 2.48% out-of-plane drift ratios.

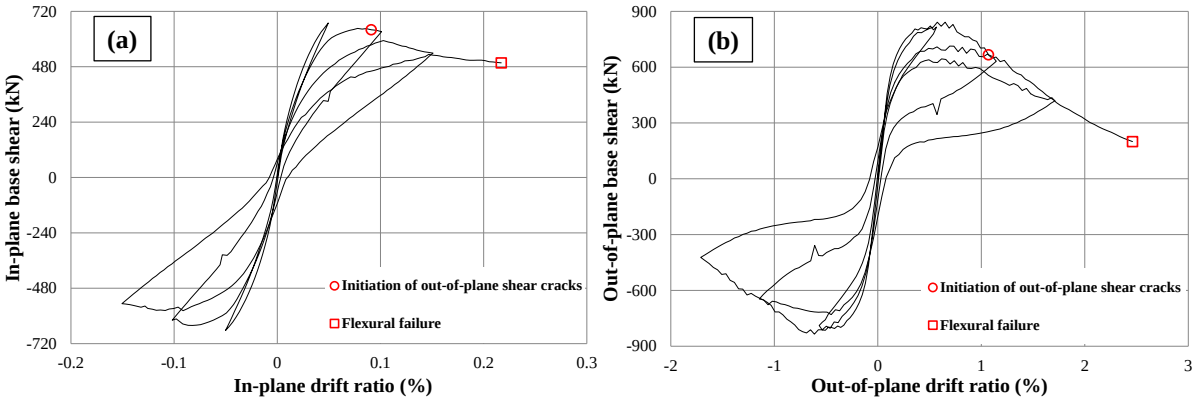

Figure 8-40 Base shear-drift ratio of the wall with section aspect ratio of 16.3 in the (a) in-plane and (b) out-of-plane directions

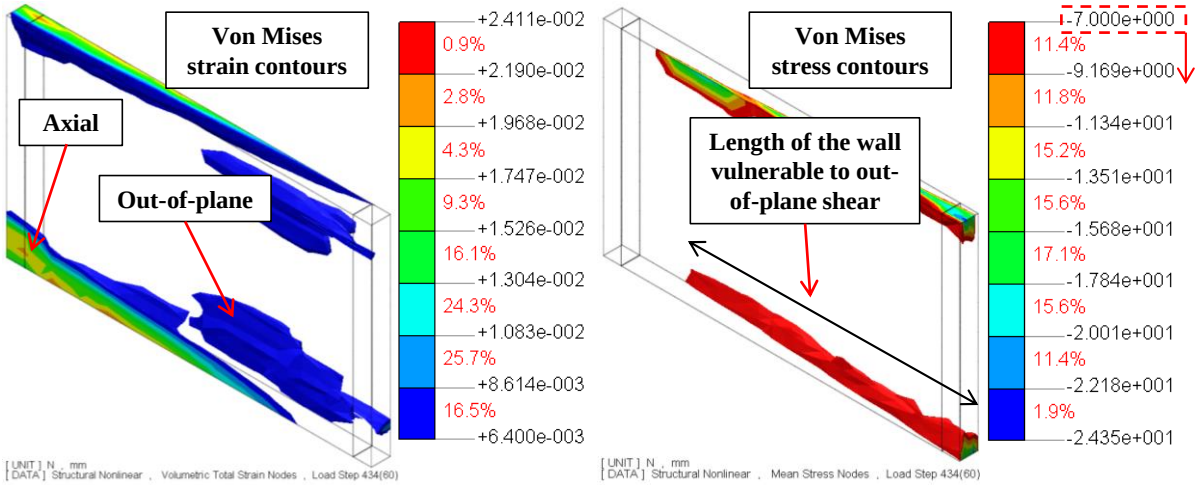

Figure 8-41 Von Mises strain and stress contours of the wall with section aspect ratio of 16.3

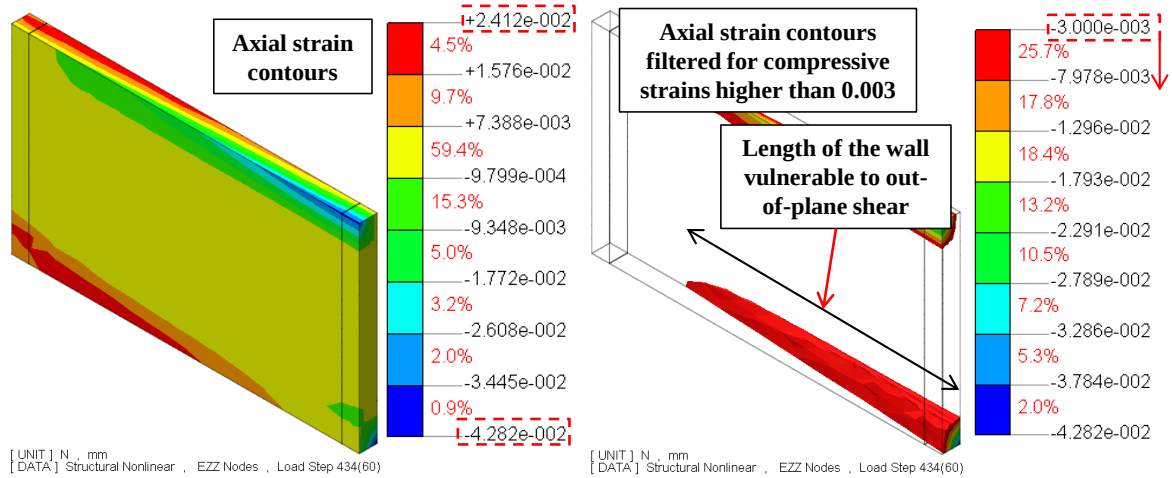

Figure 8-42 Axial strain contours of the wall with section aspect ratio of 16.3

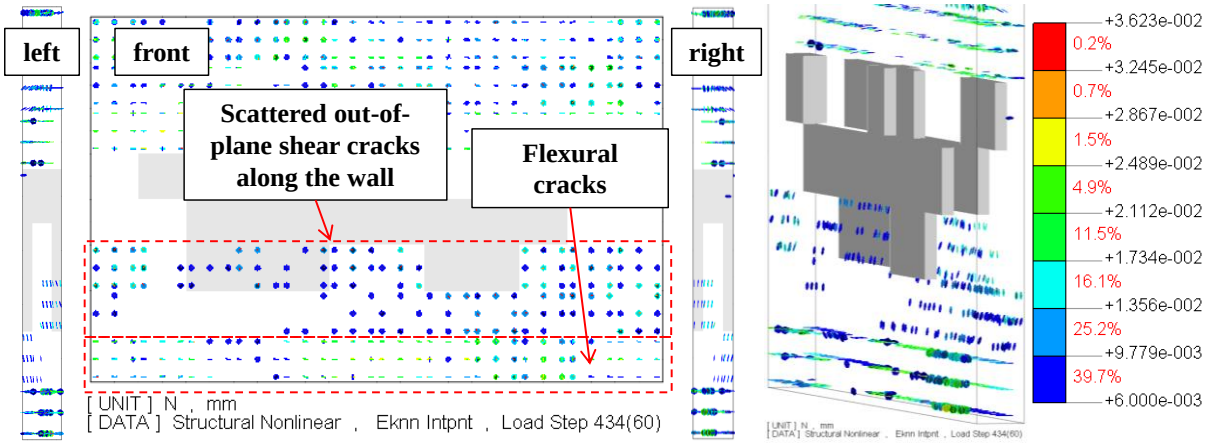

Figure 8-43 Crack pattern of the wall with section aspect ratio of 16.3

Conclusions

Based on the axial strain and von Mises stress contours, it was found that lower section aspect ratio increases the length of the part vulnerable to out-of-plane shear failure and consequently increases the susceptibility of the wall to this failure mode. Table 8-7 shows the maximum compressive and tensile strains and maximum von Mises compressive stress in the wall for each section aspect ratio. It can be seen that the compressive to tensile strains ratio of the wall increased with a decrease in the section aspect ratio of the wall. As was shown in Section 5.3.3, higher compressive to tensile strains ratio would increase the susceptibility of the wall to out-of-plane shear failure. Maximum compressive von Mises stress in the wall which helps with the development of out-of-plane shear cracks increased by 19% when the section aspect ratio of the wall was decreased from 16.3 to 7.5. Moreover, lower section aspect ratio changes an axially dominated von Mises strain contours in the wall towards the domination of out-of-plane ones. Development of out-of-plane strain increases the out-of-plane shear cracks in the wall.

Table 8-7 Effects of section aspect ratio on compressive and tensile strains and compressive von Mises stress

Section aspect ratio	Maximum compressive strain (%)	Maximum tensile strain (%)	Compressive to tensile strains ratio	Maximum compressive von Mises stress	Increase in the compressive von Mises stress (%)
7.5	-5.251	2.212	2.37	-29.92	18.6
9.8	-6.042	2.775	2.18	-29.19	16.6
12.2	-4.531	2.408	1.88	-27.7	12.1
16.3	-4.282	2.412	1.78	-24.35	-

8.3.3 Section detailing ductility

It was shown in Chapter 5 that the behaviour of a wall that was designed for a nominal ductility (specimen SP2-ND) was changed completely when the section detailing ductility

was upgraded to limited ductile or ductile levels according to NZS3101:2006-A3 (2017). Here this was investigated numerically in more details. Three different ductility levels of nominal, limited and ductile based on NZS3101:2006-A3 (2017) were chosen for this investigation. A wall with nominal section ductility that fails in out-of-plane shear was chosen as the benchmark. Here the walls designed for limited ductile and ductile levels for 15% axial load ratio were also investigated under a higher axial load ratio of 25% (assuming an increase in the axial load ratio during the earthquake). Section details of each wall were shown in Table 8-8. Characteristics of these walls were shown in Table 8-9. Material properties of concrete used for the FE analyses were shown in Figure 8-3, Figure 8-44 and Figure 8-45 for the walls designed for nominal, limited and ductile levels, respectively.

Table 8-8 walls used for the parametric study on section detailing ductility

Section ductility	Section
Nominal ductile	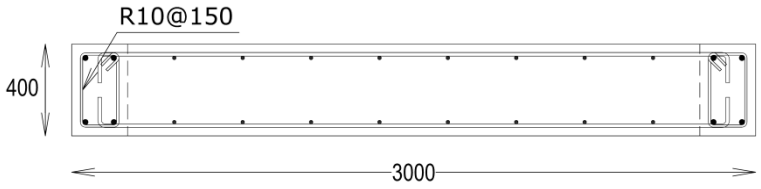
Limited ductile	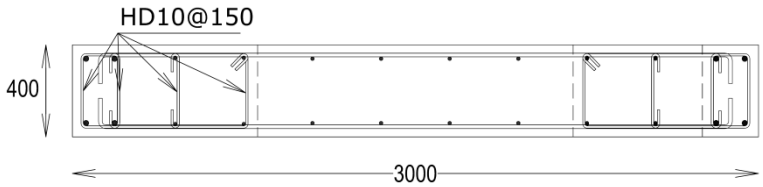
Ductile	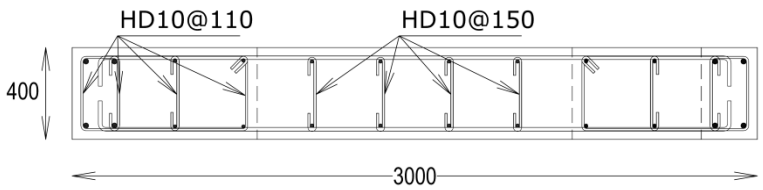

Table 8-9 Characteristics of walls used for parametric study on section detailing ductility

Parameters	Section detailing ductility		
	Nominal Ductile	Limited Ductile	Ductile
Out-of-plane shear span, H_{out} (mm)	2015		
Thickness, t (mm)	400		
Out-of-plane shear span ratio, H_{out}/t	5.04		
In-plane effective height, H_e (mm)	10353		
Length, L_w (mm)	3000		
In-plane shear span ratio, H_e/L_w	3.45		
Section aspect ratio, L_w/t	7.5		
Axial load ratio, $P/(A_g f_c')$ (%)	15%	15%-25%	15%-25%
Longitudinal reinforcement ratio (%) $\rho_t = (A_{s,BZ} + A_{s,web}) / (L_w \times t)$	0.45		
Horizontal reinforcement ratio (%) $\rho_v = A_{sv} / (s \times t)$	0.5		
Compressive strength of concrete (MPa)	35		
Yield strength of longitudinal and horizontal reinforcement (MPa)	300		
Yield strength of transverse reinforcement (MPa)	300	500	

* Out-of-plane shear span is half the first floor height

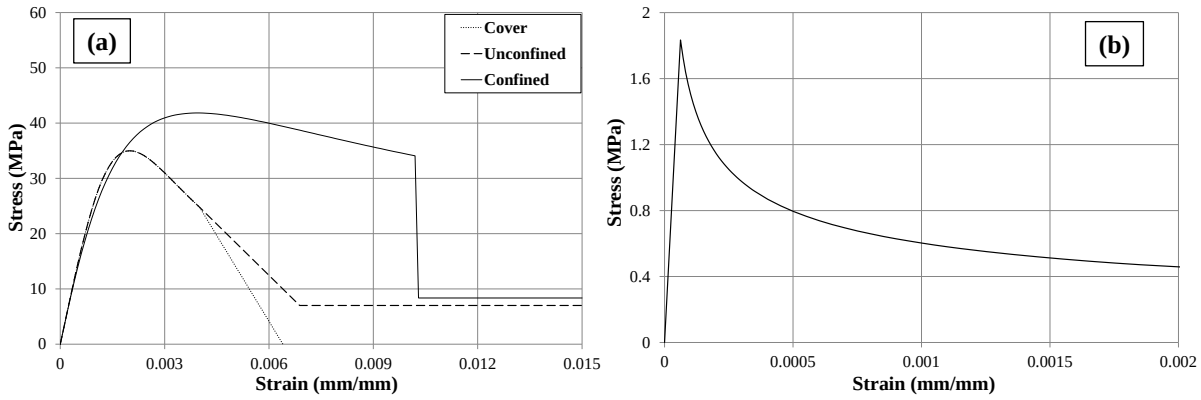

Figure 8-44 Material properties of concrete for the wall with limited ductility (a) compressive (Mander et al. 1988) and (b) tensile (Belarbi and Hsu 1994) behaviours

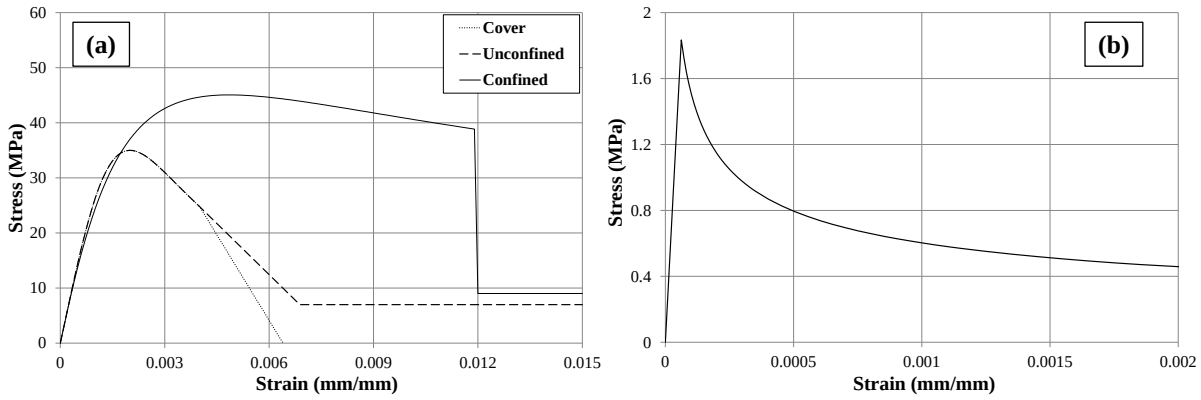

Figure 8-45 Material properties of concrete for the wall with ductile design (a) compressive (Mander et al. 1988) and (b) tensile (Belarbi and Hsu 1994) behaviours

Nominal section detailing with 15% axial load ratio

Figure 8-46 shows the base shear-drift ratio curve of the wall with nominal section detailing ductility subjected to bi-directional loading. The wall showed brittle behaviour in both in-plane and out-of-plane directions and failed at 0.18% in-plane and 2.06% out-of-plane drift ratios. Von Mises strain and stress and axial strain contours of the wall were shown in Figure 8-47. As can be seen in Figure 8-47, von Mises strain contours of the wall were dominated by out-of-plane strains. Looking at the axial strain and von Mises stress contours in Figure 8-47, it can be seen that the length of the part vulnerable to out-of-plane shear failure is equal to the length of the wall. Figure 8-48 shows out-of-plane shear cracks along the full length and thickness of the wall. It can be seen that while the wall was vulnerable to out-of-plane shear failure, lack of sufficient out-of-plane shear strength led to out-of-plane shear failure of the wall.

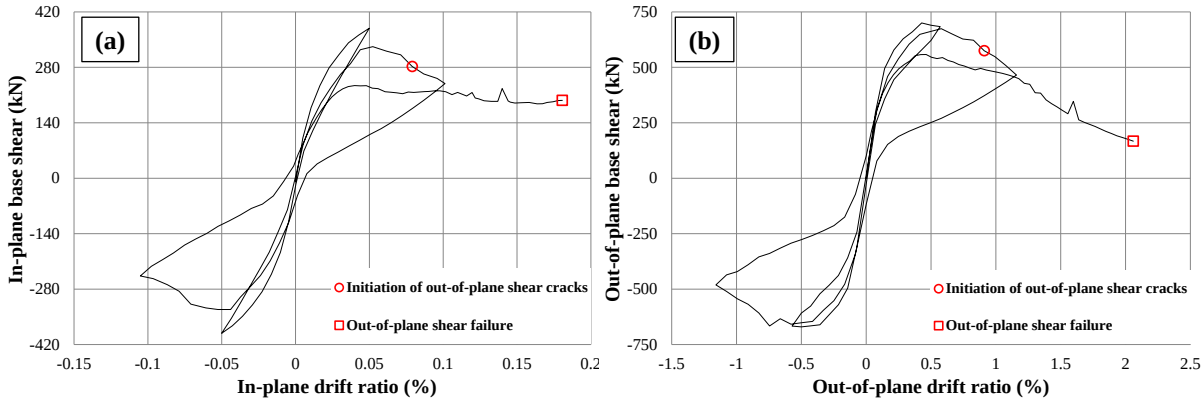

Figure 8-46 Base shear-drift ratio of the wall with nominal section ductility in the (a) in-plane and (b) out-of-plane directions

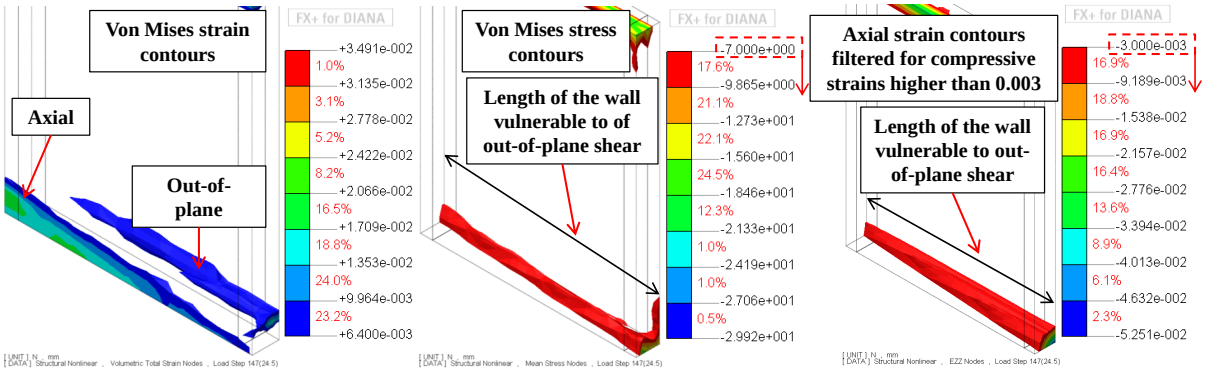

Figure 8-47 Axial strain, von Mises strain and stress contours of the wall with nominal section ductility

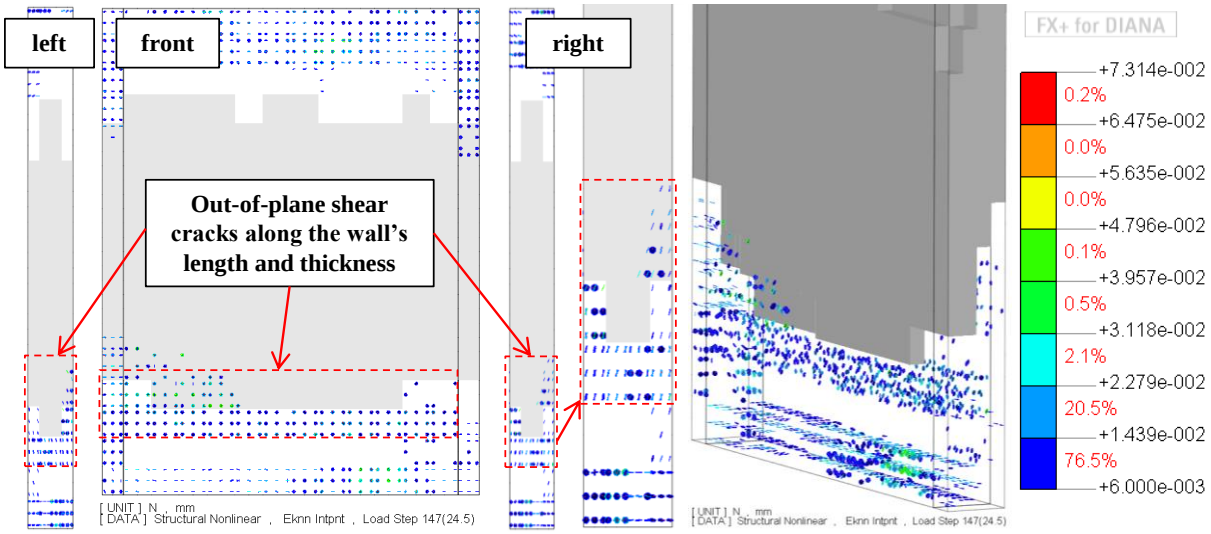

Figure 8-48 Crack pattern of the wall with nominal section ductility

Limited ductile section detailing with 15% axial load ratio

Figure 8-49 shows the base shear-drift ratio curve of the wall with 15% axial load ratio designed for limited section ductility subjected to bi-directional loading. The wall showed a stable behaviour in both in-plane and out-of-plane directions in terms of drift capacity. However, it showed a less ductile behaviour in the out-of-plane direction due to out-of-plane strength loss.

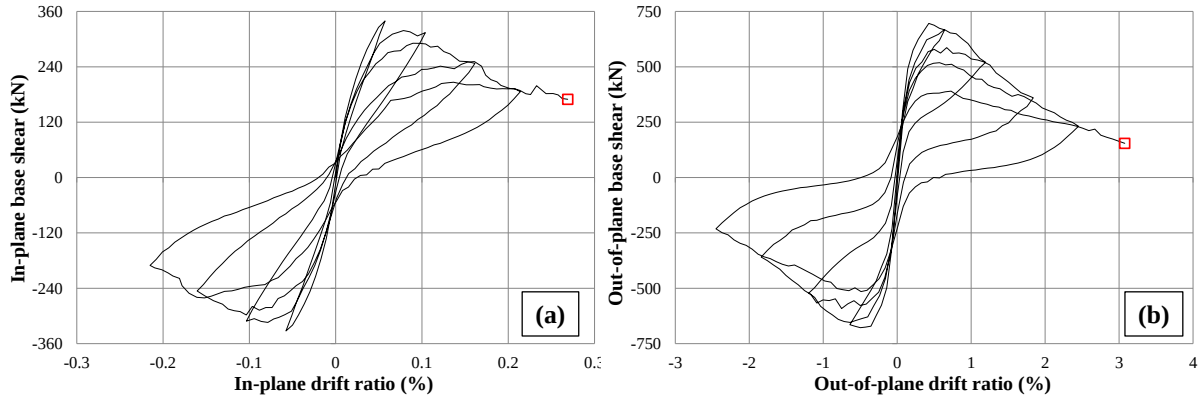

Figure 8-49 Base shear-drift ratio of the wall with limited section ductility under 15% axial load ratio in the (a) in-plane and (b) out-of-plane directions

Axial strain, von Mises strain and stress contours of the wall are shown in Figure 8-50. Looking at the axial strain and von Mises stress contours, it can be seen that length of the part vulnerable to out-of-plane shear failure is equal to the length of the wall. However, as can be seen in Figure 8-50, although the wall was still prone to out-of-plane shear failure, the von Mises strain contours was not dominated by out-of-plane strain due to the increase in the transverse reinforcement in the wall. Figure 8-51 shows the crack pattern of the wall. It can be seen that some out-of-plane shear cracks formed, but they didn't develop through the full

length and thickness of the wall. The wall failed in web crushing at 0.27% in-plane and 3.07% out-of-plane drift ratios due to bi-directional loading.

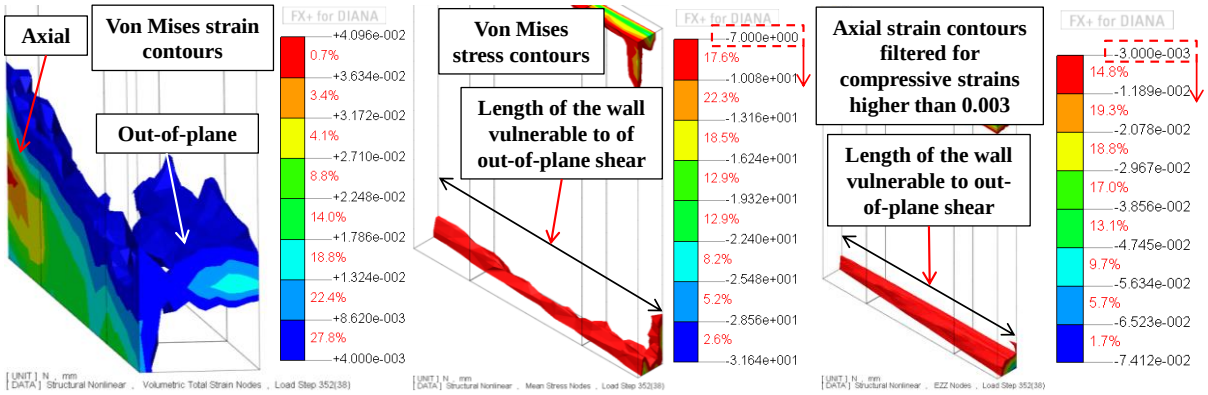

Figure 8-50 Axial strain, von Mises strain and stress contours of the wall with limited section ductility under 15% axial load ratio

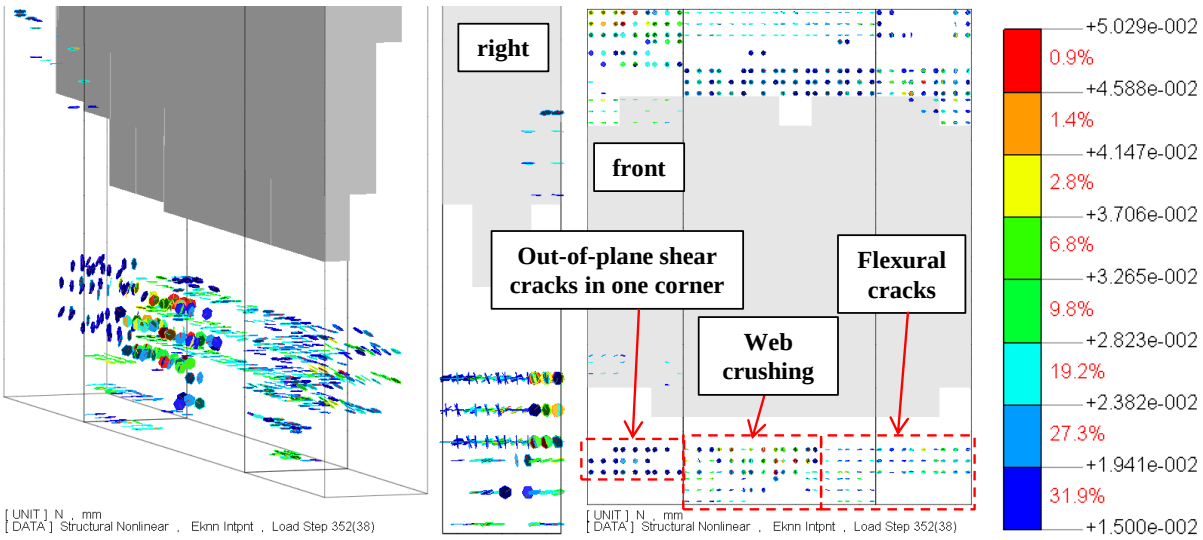

Figure 8-51 Crack pattern of the wall with limited section ductility under 15% axial load ratio

Limited ductile section detailing with 25% axial load ratio

Figure 8-52 shows the base shear-drift ratio curve of the wall that was designed for limited section ductility for 15% axial load ratio subjected to 25% axial load ratio and bi-directional loading. The wall showed brittle behaviour in both in-plane and out-of-plane directions and failed at 0.124% in-plane and 1.42% out-of-plane drift ratios. Von Mises strain and stress and axial strain contours of the wall are shown in Figure 8-53. Looking at the axial strain and von Mises stress contours in Figure 8-53, it can be seen that the full length of the wall is vulnerable to out-of-plane shear failure. Von Mises strain contours were also slightly dominated by out-of-plane strains due to high axial load ratio. Figure 8-54 shows the crack pattern of the wall. It can be seen that although the wall was designed only for 15% axial load ratio, only some out-of-plane shear cracks formed in the wall. The wall failed at 0.124% in-

plane and 1.42% out-of-plane drift ratios in concrete crushing mostly in the web due to lack of transverse reinforcement when subjected to high axial load ratio and bi-directional loading.

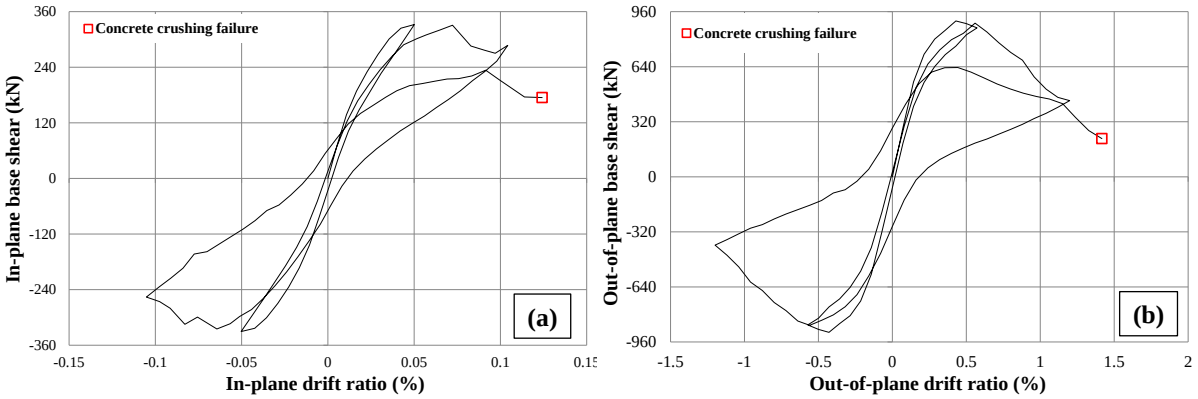

Figure 8-52 Base shear-drift ratio of the wall with limited section ductility under 25% axial load ratio in the (a) in-plane and (b) out-of-plane directions

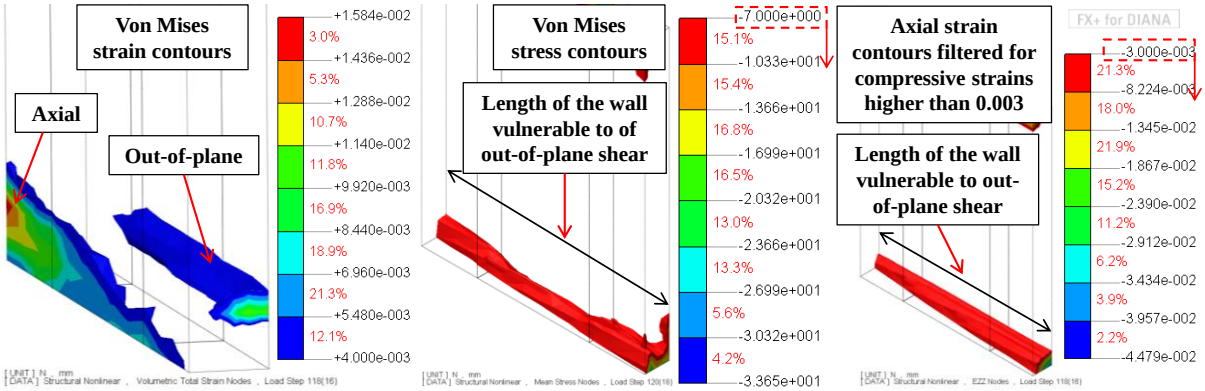

Figure 8-53 Von Mises strain and stress contours of the wall with limited section ductility under 25% axial load ratio

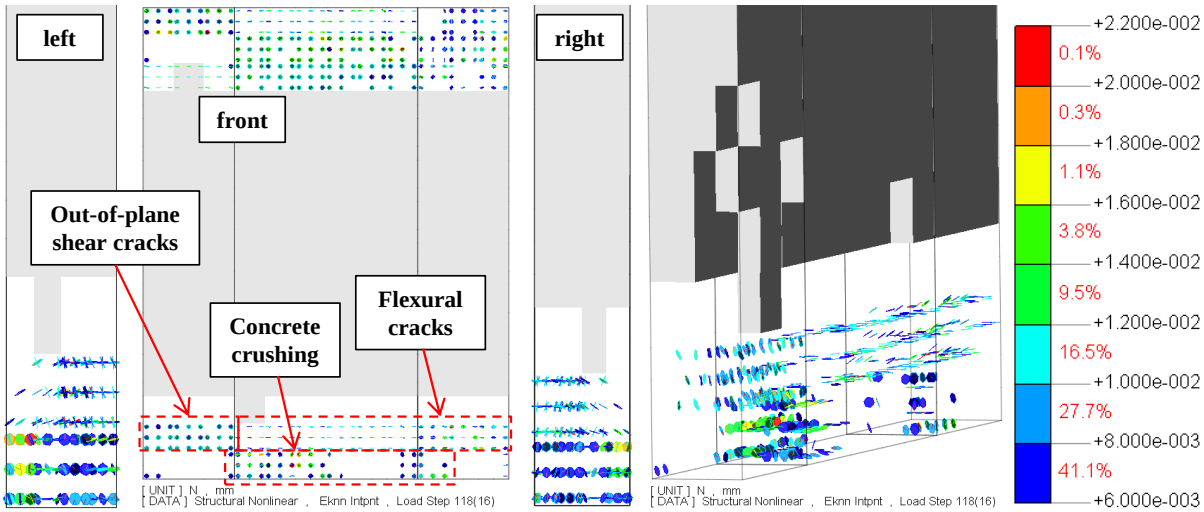

Figure 8-54 Crack pattern of the wall with limited section ductility under 25% axial load ratio

Ductile section detailing with 15% axial load ratio

Figure 8-55 shows the base shear-drift ratio curve of the wall with 15% axial load ratio designed for ductile section detailing subjected to bi-directional loading loading. The wall showed stable behaviour in both in-plane and out-of-plane directions in terms of drift capacity. However, it showed less ductile behaviour in the out-of-plane direction due to strength capacity loss. Von Mises strain and stress and axial strain contours of the wall are shown in Figure 8-56. Looking at the axial strain and von Mises stress contours, it can be seen that the full length of the wall is vulnerable to out-of-plane shear failure. However, von Mises strain contours of the wall was dominated by axial strain due to sufficient transverse reinforcement along the wall.

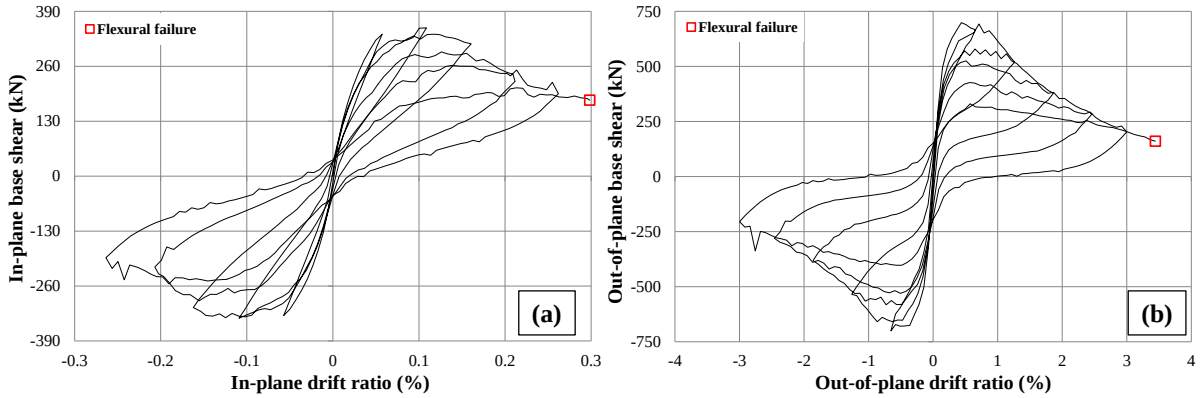

Figure 8-55 Base shear-drift ratio of the wall designed for ductile level under 15% axial load ratio in the (a) in-plane and (b) out-of-plane directions

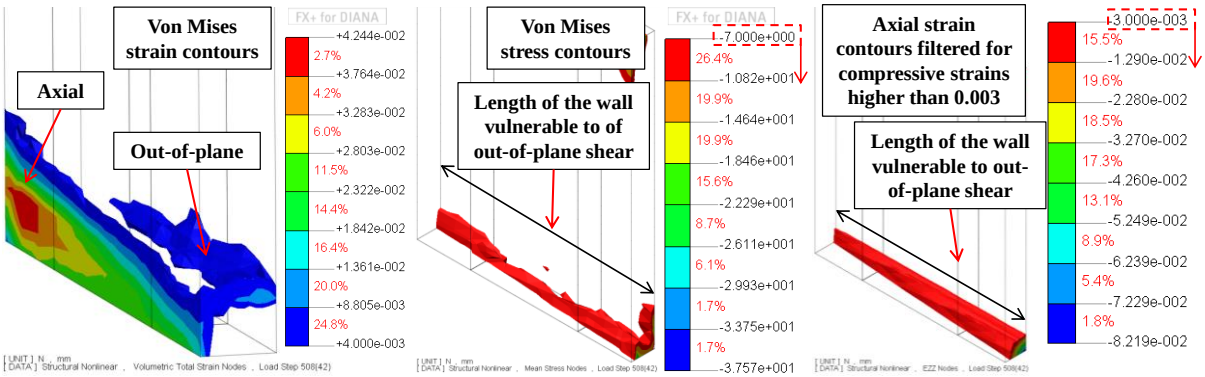

Figure 8-56 Von Mises strain and stress contours of the wall designed for ductile level under 15% axial load ratio

Figure 8-57 shows the crack pattern of the wall. It can be seen that the wall performed better especially in the web compared to the case with limited ductility due to the additional transverse reinforcement in the web. It can be seen that some out-of-plane shear cracks formed in the wall. However, out-of-plane shear cracks didn't develop and the wall failed in flexure at 0.299% in-plane and 3.42% out-of-plane drift ratios.

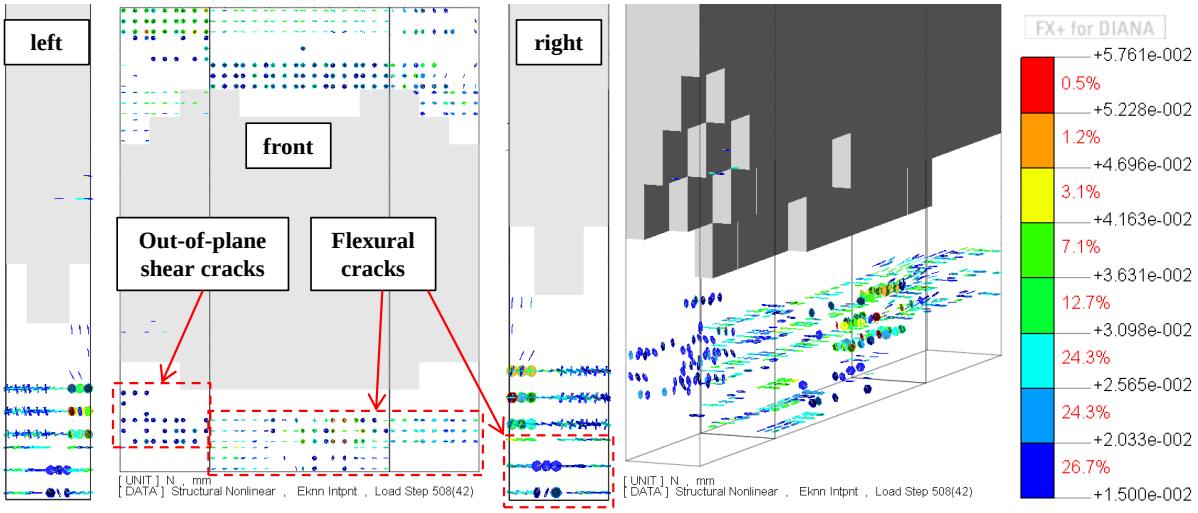

Figure 8-57 Crack pattern of the wall designed for ductile level under 15% axial load ratio

Ductile section detailing with 25% axial load ratio

Figure 8-58 shows the base shear-drift ratio curve of the wall designed for 15% axial load ratio for a ductile section detailing subjected to 25% axial load ratio and bi-directional loading. The wall showed a brittle behaviour in both in-plane and out-of-plane directions and failed at 0.147% in-plane and 1.68% out-of-plane drift ratios. Axial strain, von Mises strain and stress contours of the wall are shown in Figure 8-59. Looking at the axial strain and von Mises stress contours, it can be seen that the full length of the wall was vulnerable to out-of-plane shear failure. However, it can be seen that von Mises strain contours were slightly dominated by axial strains due to the transverse reinforcement of the wall. Figure 8-60 shows the crack pattern of the wall. Some out-of-plane shear cracks can be seen in the wall. However, shear cracks didn't propagate through the wall's length. High axial load ratio and bi-directional loading subjected to the wall led to a brittle flexural failure at 0.147% in-plane and 1.68% out-of-plane drift ratios along with concrete crushing at the base.

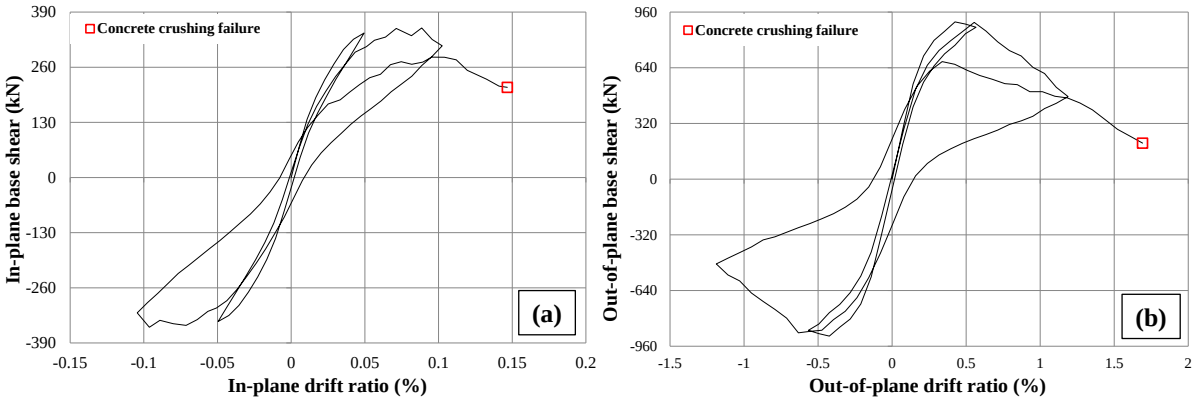

Figure 8-58 Base shear-drift ratio of the wall designed for ductile level under 25% axial load ratio in the (a) in-plane and (b) out-of-plane directions

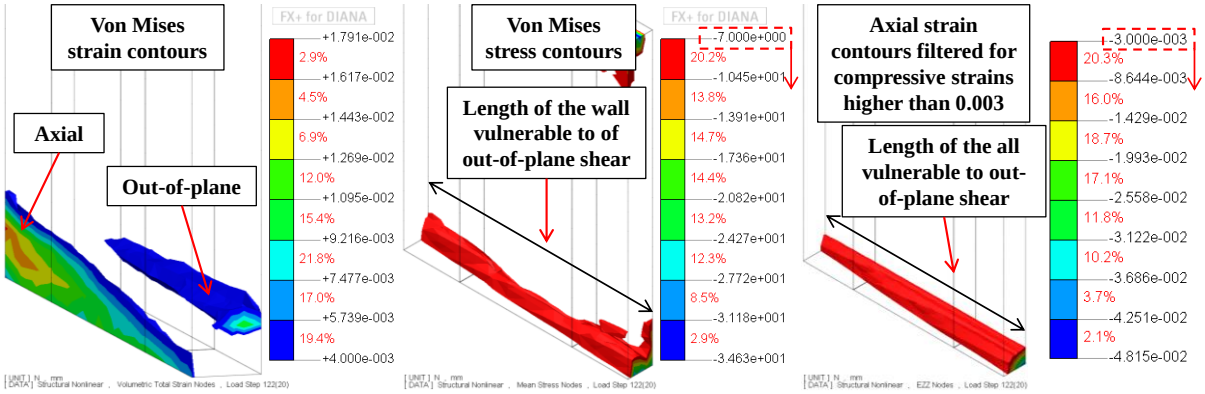

Figure 8-59 Von Mises strain and stress contours of the wall designed for ductile level under 25% axial load ratio

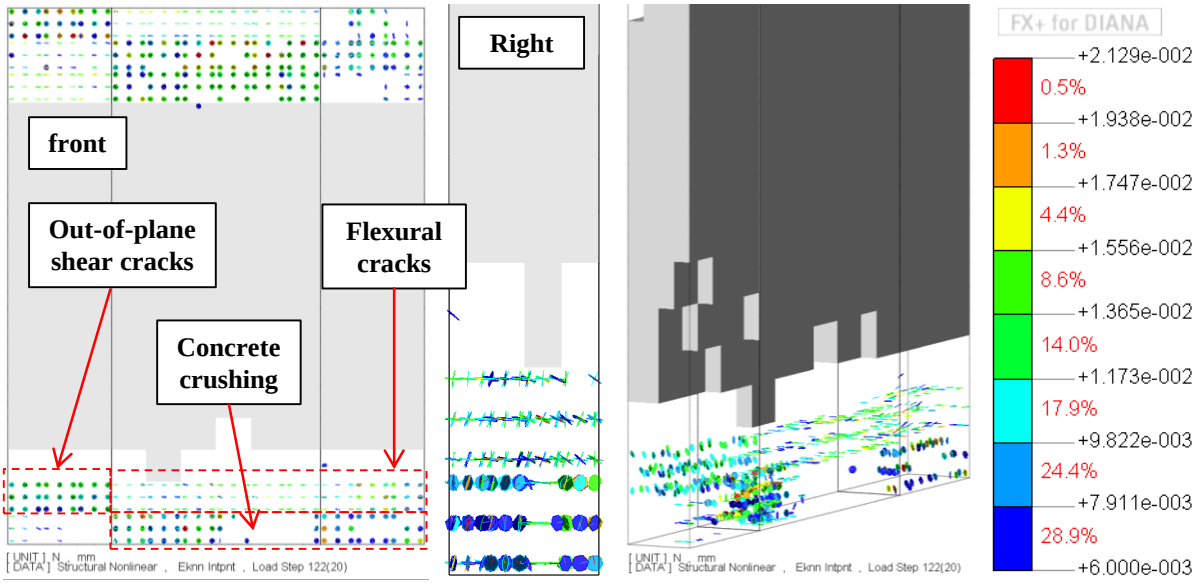

Figure 8-60 Crack pattern of the wall designed for ductile level under 25% axial load ratio

Conclusions

Numerical study of this section confirmed the experimental findings of Chapter 5 that increasing section detailing ductility can prevent out-of-plane shear failure in walls prone to this failure mode. Higher section detailing ductility increases the amount of transverse reinforcement in the wall and therefore increases the out-of-plane shear capacity of the wall as well as compressive strength of concrete due to confinement. Transverse reinforcement throughout the wall's length were able to prevent the development of out-of-plane strain and consequently out-of-plane cracks. Walls designed for limited ductility had web crushing under the initial axial load ratio that the wall was designed for due to bi-directional loading. Moreover, it was shown that designing the walls for limited ductile or ductile levels for a lower axial load ratio can still prevent out-of-plane shear failure under higher axial load ratios during the earthquake.

8.3.4 Longitudinal reinforcement ratio, $\rho_t = (A_{s,BZ} + A_{s,web})/(L_w \times t)$

As longitudinal reinforcement contribute to both vertical and out-of-plane shear (through dowel action) capacities of the wall, they can be influential in walls prone to out-of-plane shear failure. Moreover, comparing Wall D5-6 from Grand Chancellor Hotel (Figure 7-3) with specimen SP2-ND discussed in Chapter 5, it was observed that increasing the longitudinal reinforcement ratio from 0.45% to 0.92% prevented the full rupture of the longitudinal reinforcement along the wall. Due to the limitations with the number of specimens, it was not possible to investigate the effects of this parameter in the experimental phase of the study. Therefore, the effects of this parameter on walls prone to out-of-plane shear failure were investigated numerically. As was discussed in Chapter 6, the FE model has limitations in simulating bar buckling and bar fracture and it is not possible to see the full effects of this parameter on the behaviour of RC walls in this numerical study. However, general effects of this parameter on walls prone to out-of-plane shear failure can still be investigated. Three different longitudinal reinforcement ratios of 0.45%, 0.75% and 1.5% were chosen for the investigation of this parameter. Section details of the wall are shown in Figure 8-61. Material properties of concrete were shown in Figure 8-3. Other characteristics of the walls were shown in Table 8-10.

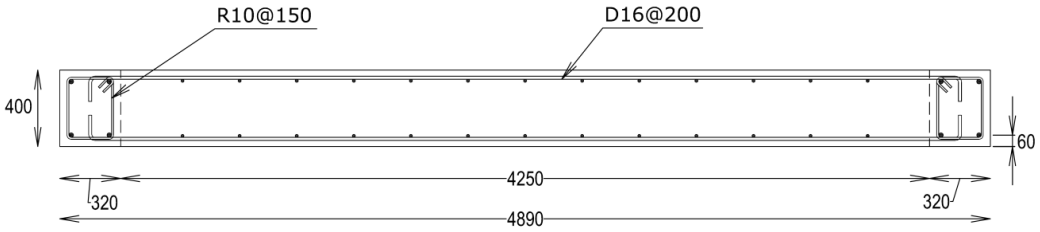

Figure 8-61 Details of the wall used for the parametric study on longitudinal reinforcement ratio

Table 8-10 Characteristics of walls used for parametric study on longitudinal reinforcement ratio

Parameters	Longitudinal reinforcement ratio (%)		
	0.45	0.75	1.5
Out-of-plane shear span, H_{out} (mm)	2675		
Thickness, t (mm)	400		
Section detailing ductility	Nominal ductile		
In-plane effective height, H_e (mm)	16875		
Length, L_w (mm)	4890		
In-plane shear span ratio, H_e/L_w	3.45		
Section aspect ratio, L_w/t	12.2		
Axial load ratio, $P/(A_g f_c')$ (%)	20		
Out-of-plane shear span ratio, H_{out}/t	6.69		
Horizontal reinforcement ratio (%) $\rho_v = A_{sv}/(s \times t)$	0.5		
Compressive strength of concrete (MPa)	35		
Yield strength of reinforcement (MPa)	300		

* Out-of-plane shear span is half the first floor height

Longitudinal reinforcement ratio of 0.45%

Figure 8-62 shows the base shear-drift ratio curve of the wall with a longitudinal reinforcement ratio of 0.45% subjected to bi-directional loading. While the wall showed a less brittle behaviour in the in-plane, it had a brittle one in the out-of-plane direction and failed at 0.16% in-plane and 1.83% out-of-plane drift ratios. Von Mises strain and stress and axial strain contours of the wall were shown in Figure 8-63. It can be seen that von Mises strain contours of the wall were dominated by out-of-plane strains. Looking at the axial strain and von Mises stress contours in Figure 8-63, it can be seen that the length of the part vulnerable to out-of-plane shear was almost equal to the length of the wall and in a diagonal form. This was similar to the axial strain and von Mises stress contours of specimen SP2-ND which failed in out-of-plane shear in the lab (discussed in Section 6.5.5). Figure 8-64 shows the crack pattern of the wall at 0.16% in-plane and 1.83% out-of-plane drift ratios. Significant out-of-plane shear cracks were formed along the full length and thickness of the wall which indicates a shear failure in that direction.

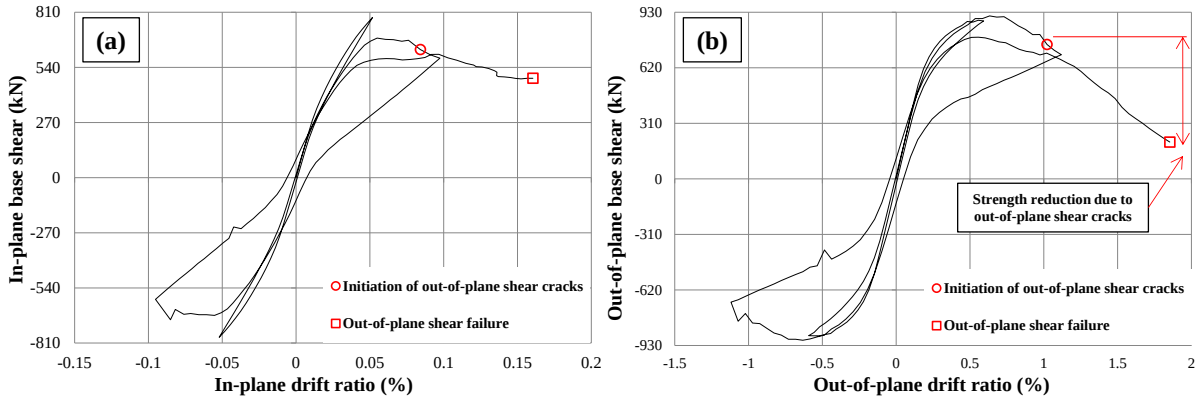

Figure 8-62 Base shear-drift ratio of the wall with longitudinal reinforcement ratio of 0.45% in the (a) in-plane and (b) out-of-plane directions

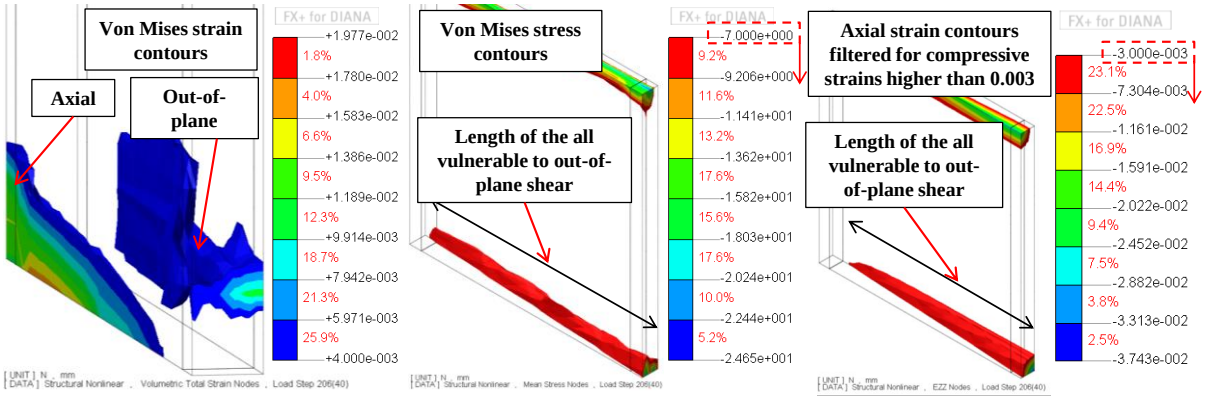

Figure 8-63 Von Mises strain and stress and axial strain contours of the wall with longitudinal reinforcement ratio of 0.45%

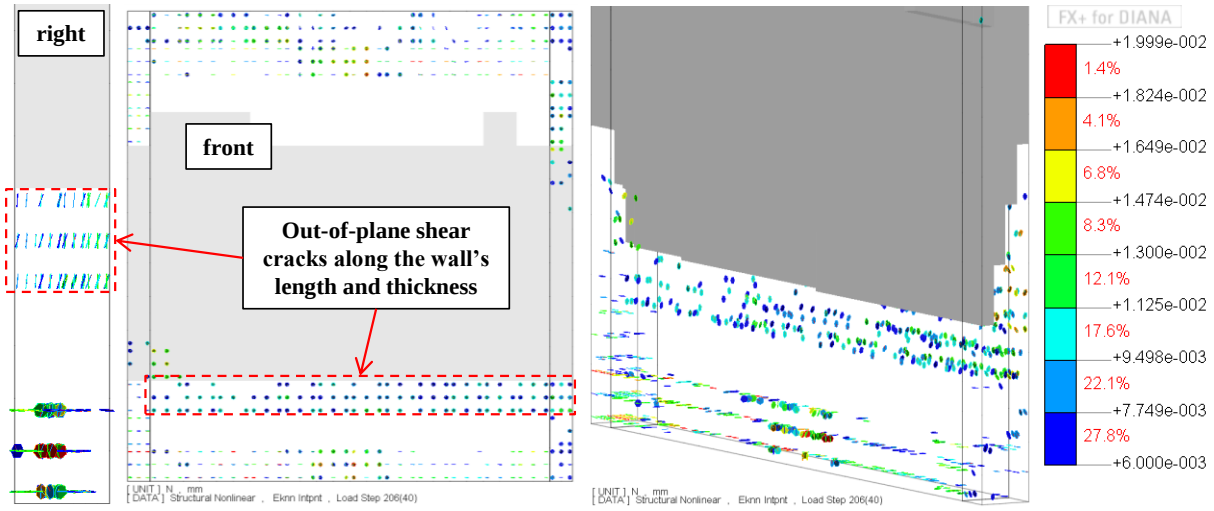

Figure 8-64 Crack pattern of the wall with longitudinal reinforcement ratio of 0.45%

Longitudinal reinforcement ratio of 0.75%

Figure 8-65 shows the base shear-drift ratio curve of the wall with 0.75% longitudinal reinforcement ratio subjected to bi-directional loading. The wall showed a less brittle behaviour in the in-plane direction, but a brittle one in the out-of-plane direction and failed at 0.166% in-plane and 1.9% out-of-plane drift ratios. Von Mises strain and stress contours of the wall were shown in Figure 8-66. Von Mises strain contours of the wall with longitudinal reinforcement ratio of 0.75% were slightly dominated by axial strains. Looking at the axial strain and von Mises stress contours in Figure 8-66, it can be seen that length of the part vulnerable to out-of-plane shear is almost equal to the wall's length. Figure 8-67 shows the crack pattern of the wall. Considerable out-of-plane shear cracks formed in the wall which indicates a likely out-of-plane shear failure. However, out-of-plane shear cracks decreased compare to the case with less longitudinal reinforcement ratio.

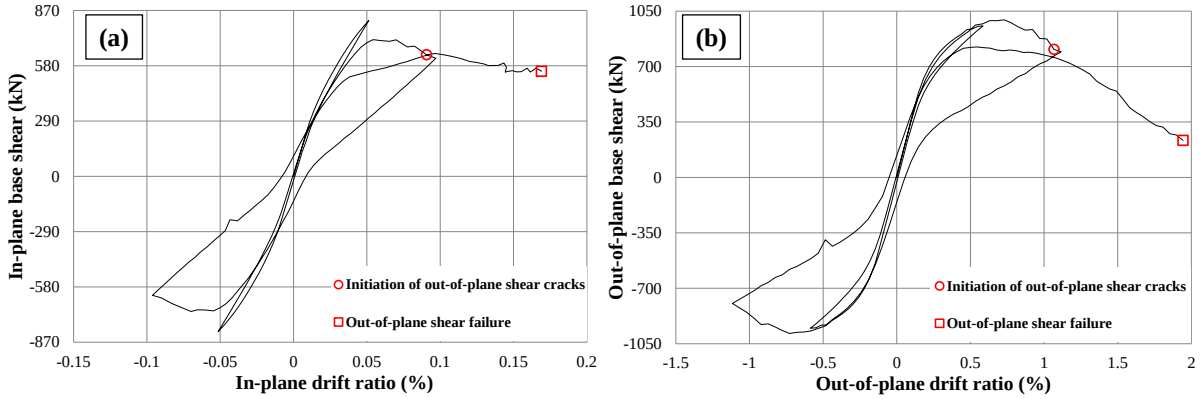

Figure 8-65 Base shear-drift ratio of the wall with longitudinal reinforcement ratio of 0.75% in the (a) in-plane and (b) out-of-plane directions

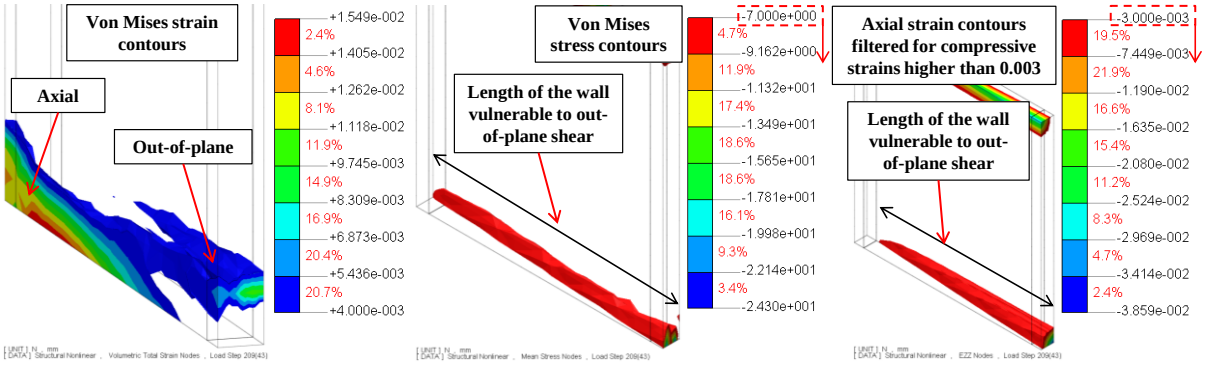

Figure 8-66 Von Mises strain and stress contours of the wall with longitudinal reinforcement ratio of 0.75%

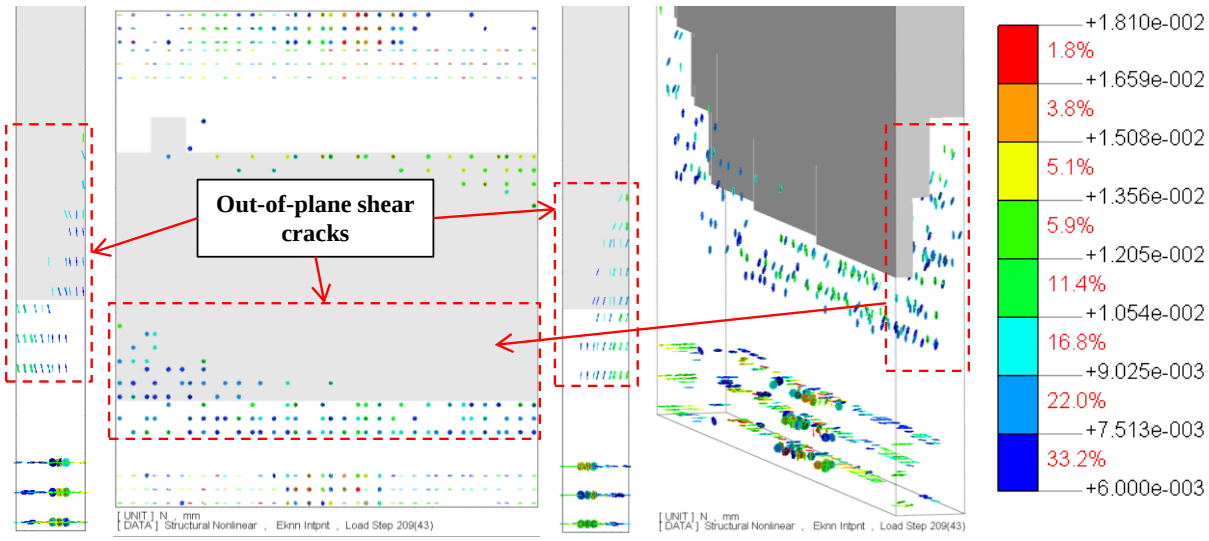

Figure 8-67 Crack pattern of the wall with longitudinal reinforcement ratio of 0.75%

Longitudinal reinforcement ratio of 1.5%

Figure 8-68 shows the base shear-drift ratio curve of the wall with 1.5% longitudinal reinforcement ratio subjected to bi-directional loading. The wall showed a relatively stable behaviour in the in-plane but a brittle one in the out-of-plane direction and failed at 0.234% in-plane and 2.68% out-of-plane drift ratios. Von Mises strain and stress and axial strain contours of the wall were shown in Figure 8-69. Von Mises strain contours of the wall with 1.5% longitudinal reinforcement ratio shows the domination of out-of-plane strains. Looking at the axial strain and von Mises stress contours in Figure 8-69, it can be seen that part of the wall vulnerable to out-of-plane shear had a length equal to the length of the wall. Figure 8-70 shows the crack pattern of the wall at 0.234% in-plane and 2.68% out-of-plane drift ratios. The wall performed quite well up to 0.2% in-plane and 2.28% out-of-plane drift ratios despite having some minor out-of-plane shear cracks. However, when pushing towards 0.25% in-plane and 2.86% out-of-plane drift ratios, as can be seen in Figure 8-70, out-of-plane shear

cracks formed along the wall's length and thickness that indicate a strong possibility of out-of-plane shear failure in the wall.

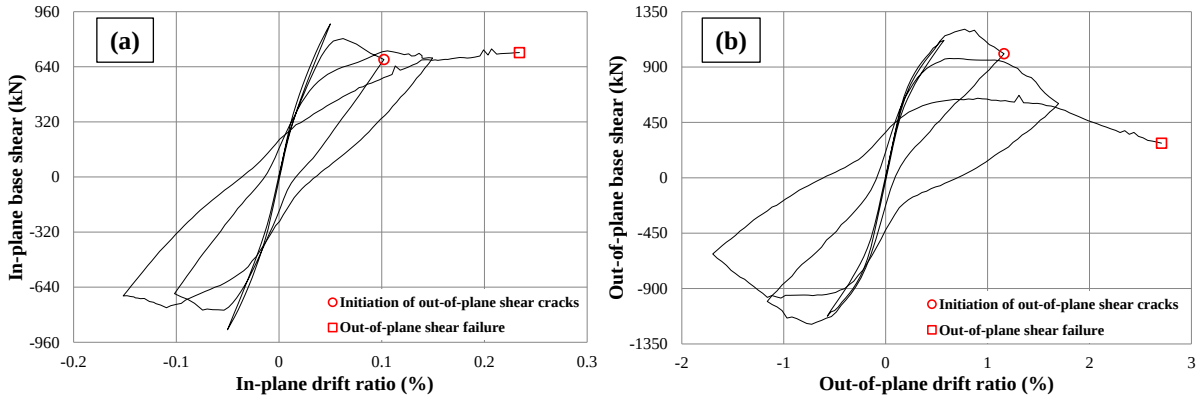

Figure 8-68 Base shear-drift ratio of the wall with longitudinal reinforcement ratio of 1.5% in the (a) in-plane and (b) out-of-plane directions

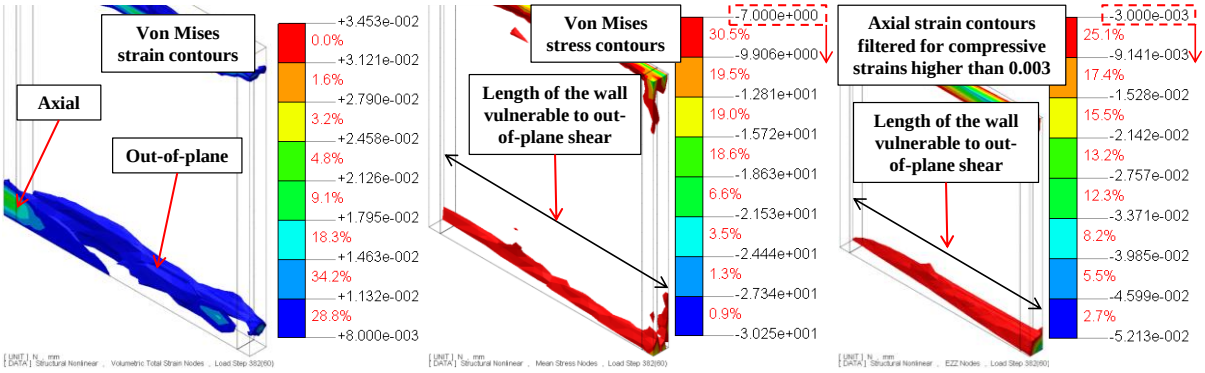

Figure 8-69 Von Mises strain and stress contours of the wall with longitudinal reinforcement ratio of 1.5%

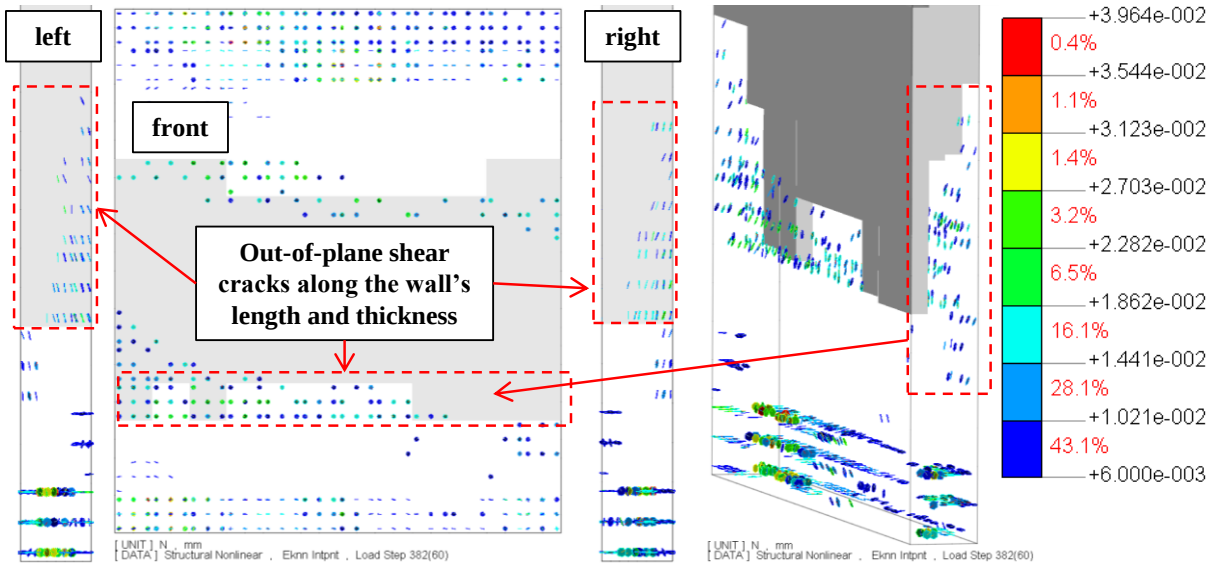

Figure 8-70 Crack pattern of the wall with 1.5% longitudinal reinforcement ratio

Conclusions

Considering the limitations of the FE model with bar buckling and bar fracture, it can be concluded that increasing the longitudinal reinforcement ratio can delay the out-of-plane shear failure. However, it's not likely that it can prevent this failure mode. Drift capacities of the wall in the in-plane and out-of-plane directions for each longitudinal reinforcement ratio are shown in Table 8-11. It is worth mentioning that out-of-plane shear cracks captured for walls with higher longitudinal reinforcement ratio decreased compared to the ones captured for walls with lower longitudinal reinforcement ratio. However, considerable out-of-plane shear cracks were captured in all cases.

Table 8-11 Drift capacity of the walls with different longitudinal reinforcement ratio

Longitudinal reinforcement ratio	In-plane drift capacity at failure (%)	Out-of-plane drift capacity at failure (%)
0.45%	0.16%	1.83%
0.75%	0.166%	1.9%
1.5%	0.234%	2.68%

8.4 PARAMETRIC STUDY MATRIX

In the previous sections, the effects of key parameters on the seismic performance of RC walls prone to out-of-plane shear failure were investigated and each parameter was scrutinized in details. Based on these numerical results, it was found that the two important parameters causing vulnerability in walls against out-of-plane shear failure are section aspect ratio and axial load ratio. Therefore, a matrix of walls with a combination of these two parameters was formed. A skewed lateral loading pattern with an 85 degree angle with respect to the in-plane axis of the wall that found to be the worst case load path in terms of triggering the out-of-plane shear failure was used for these analyses (see Section 7.4.3). Key parameters of the walls used for the parametric study matrix were shown in Table 8-12.

Table 8-12 Characteristics of the walls used for the parametric study matrix

Parameters	Section aspect ratio, L_w/t				
	7.5	9.78	12.2	14	16.2
Length, L_w (mm)	3000	4890			
Thickness, t (mm)	400	500	400	350	300
Out-of-plane shear span*, H_{out} (mm)	2015	2520	2015	1763	1512
Out-of-plane shear span ratio, H_{out}/t	5.04				
In-plane shear span ratio, H_e/L_w	3.45				
Section detailing ductility	Nominal Ductility				
Axial load ratio, $P/(A_g f_c')$ (%)	10%, 15%, 20% and 25%				
Longitudinal reinforcement ratio (%) $\rho_t = (A_{s,BZ} + A_{s,web}) / (L_w \times t)$	0.45				
Horizontal reinforcement ratio (%) $\rho_v = A_{sv} / (s \times t)$	0.5				
Compressive strength of concrete (MPa)	35				
Yield strength of reinforcement (MPa)	300				

* Out-of-plane shear span is half the first floor height

Table 8-13 and Table 8-14 show the summary of the numerical results for each cell of the matrix. In-plane and out-of-plane drift-ratio curves of each wall and the final failure mode were shown in Table 8-13 and Table 8-14. Although longitudinal reinforcement ratio can be influential in the development of out-of-plane shear failure, due to the limitations of the FE model with capturing bar buckling, bar rupture and dowel action, it was unconservative to develop a set of curves for walls with higher longitudinal reinforcement ratios based on the current FE model. As was mentioned in Section 8.3.4, based on the numerical results, higher longitudinal reinforcement ratio can only delay out-of-plane shear failure, but it's not likely that it can prevent this failure mode. This is consistent with the comparison of Wall D5-6 and specimen SP2-ND results. The matrix shown in Table 8-13 and Table 8-14 was developed only for walls with nominal section detailing ductility. It was due to the fact that it is not likely for walls designed for limited or ductile levels according to NZS3101:2006-A3 (2017) to fail in out-of-plane shear. This is based on the experimental and numerical studies conducted in this study and presented in Chapter 4 & 5 and Section 8.3.3.

Table 8-13 Parametric study matrix of walls prone to out-of-plane shear failure-Part I

Name	Section details	Section aspect ratio	Axial load ratio (%)			
			10%		15%	
ND-7.5		7.5	Failure mode: Flexural		Failure mode: Out-of-plane shear	
			In-plane curve	Out-of-plane curve	In-plane curve	Out-of-plane curve
			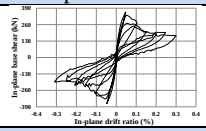	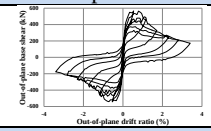	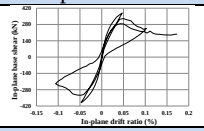	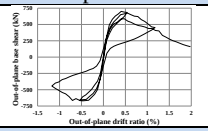
ND-9.8	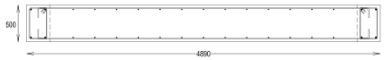	9.8	Failure mode: Flexural		Failure mode: Out-of-plane shear	
			In-plane curve	Out-of-plane curve	In-plane curve	Out-of-plane curve
			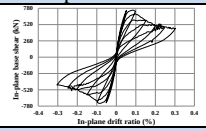	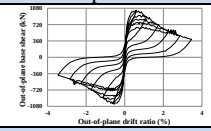	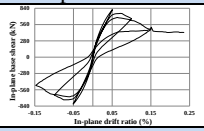	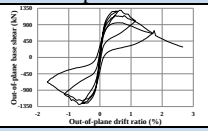
ND-12.2	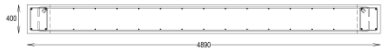	12.2	Failure mode: Flexural		Failure mode: Flexural	
			In-plane curve	Out-of-plane curve	In-plane curve	Out-of-plane curve
			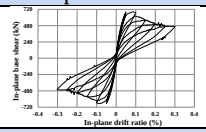	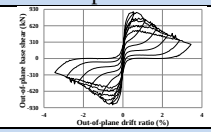	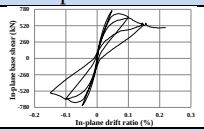	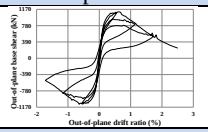
ND-14		14	Failure mode: Flexural		Failure mode: Flexural	
			In-plane curve	Out-of-plane curve	In-plane curve	Out-of-plane curve
			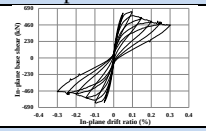	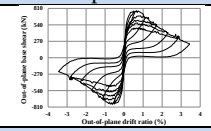	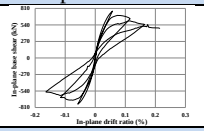	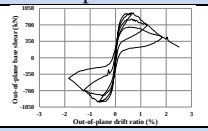
ND-16.3	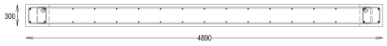	16.3	Failure mode: Flexural		Failure mode: Flexural	
			In-plane curve	Out-of-plane curve	In-plane curve	Out-of-plane curve
			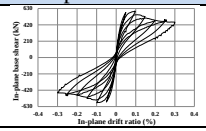	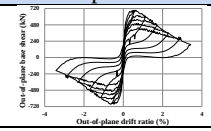	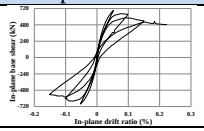	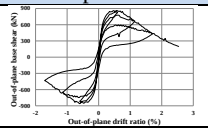

Table 8-14 Parametric study matrix of walls prone to out-of-plane shear failure-Part II

Name	Section details	Section aspect ratio	Axial load ratio (%)			
			20%		25%	
ND-7.5		7.5	Failure mode: Out-of-plane shear		Failure mode: Out-of-plane shear	
			In-plane curve	Out-of-plane curve	In-plane curve	Out-of-plane curve
			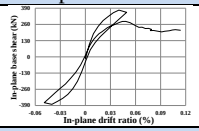	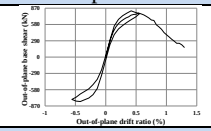	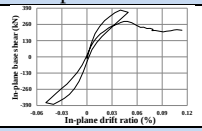	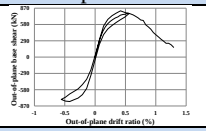
ND-9.8	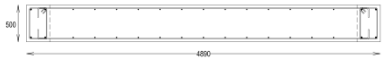	9.8	Failure mode: Out-of-plane shear		Failure mode: Out-of-plane shear	
			In-plane curve	Out-of-plane curve	In-plane curve	Out-of-plane curve
			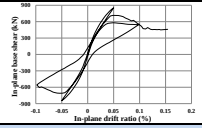	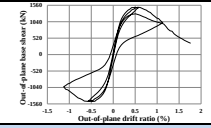	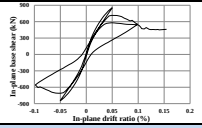	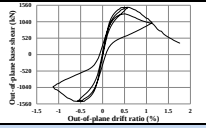
ND-12.2	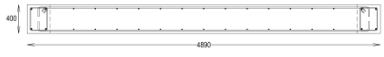	12.2	Failure mode: Out-of-plane shear		Failure mode: Axial crushing/Out-of-plane shear	
			In-plane curve	Out-of-plane curve	In-plane curve	Out-of-plane curve
			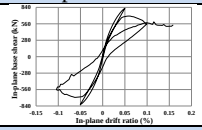	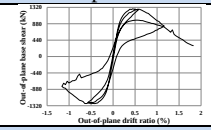	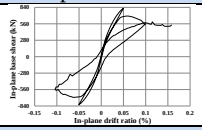	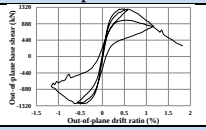
ND-14		14	Failure mode: Out-of-plane shear		Failure mode: Axial crushing	
			In-plane curve	Out-of-plane curve	In-plane curve	Out-of-plane curve
			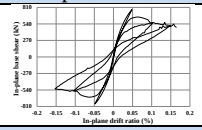	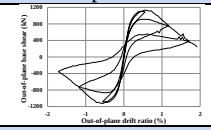	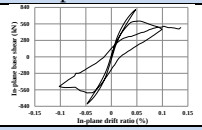	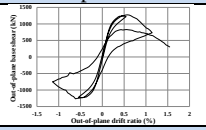
ND-16.3	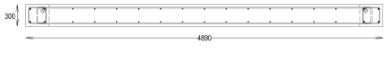	16.3	Failure mode: Out-of-plane shear		Failure mode: Axial crushing	
			In-plane curve	Out-of-plane curve	In-plane curve	Out-of-plane curve
			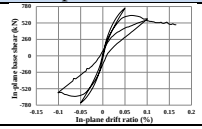	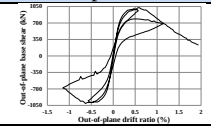	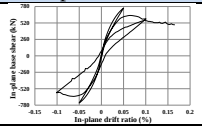	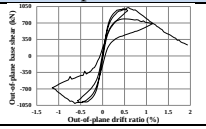

8.5 PROPOSED METHOD FOR IDENTIFYING WALLS PRONE TO OUT-OF-PLANE SHEAR FAILURE

One of the key objectives of this thesis was to find a method for identifying RC walls prone to out-of-plane shear failure. For this purpose, based on the numerical results presented in Table 8-13 and Table 8-14, failure modes captured for walls with different section aspect ratio and axial load ratio were categorized in three groups of flexural, out-of-plane shear and axial crushing failures and plotted in Figure 8-71. Based on these three categories of failure modes, an upper and lower bound limit curves were developed for the possibility of out-of-plane shear failure in rectangular RC walls as is shown in Figure 8-71. Figure 8-72 shows the equations of the two curves shown in Figure 8-71. These curves can be used for engineering purposes when designing/assessing RC walls to avoid out-of-plane shear failure. To use the method shown in Figure 8-72, engineers only need to have the wall's section aspect ratio and axial load ratio to find whether the wall is prone to out-of-plane shear failure or not. For the lower bound limit shown in in Figure 8-72, the proposed method does not specify the type of flexural failure such as bar buckling, out-of-plane instability and etc. Other methods should be used to capture these types of failure in the wall. In order to show how to use the method shown in Figure 8-72, two examples were provided.

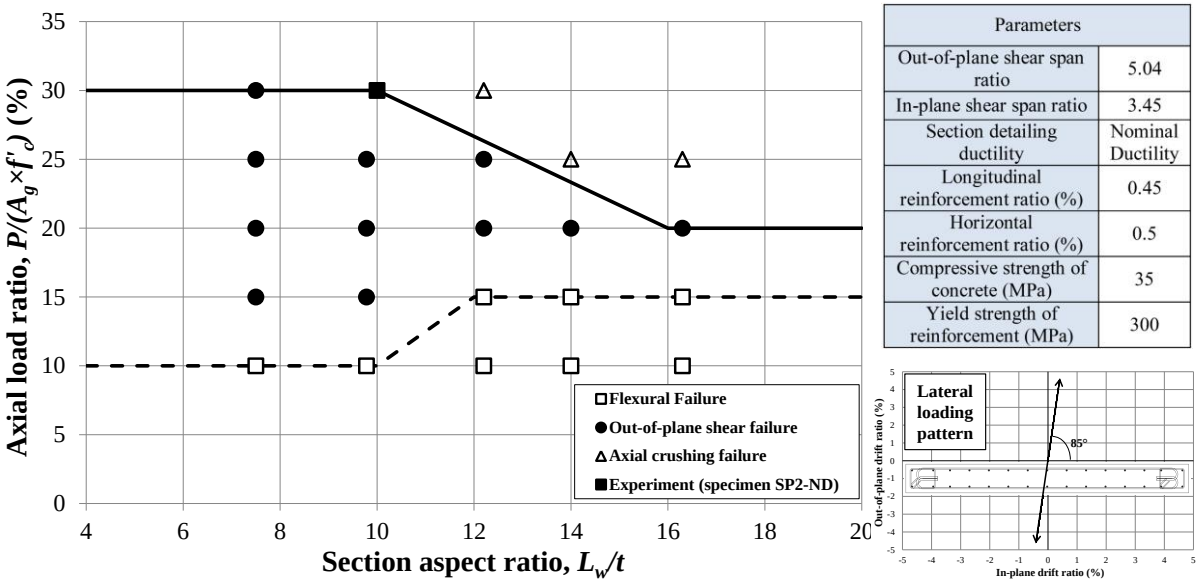

Figure 8-71 Upper and lower bounds of out-of-plane shear failure in rectangular slender RC walls

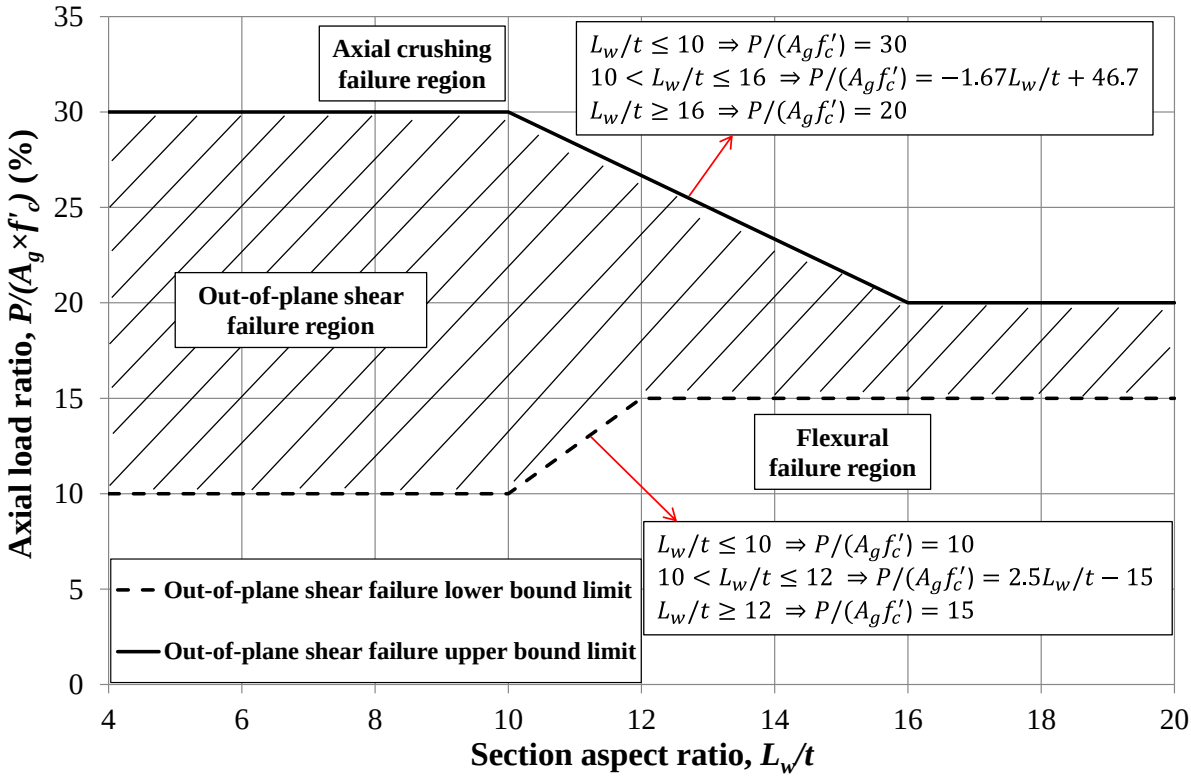

Figure 8-72 Equations of the upper and lower bound curves of out-of-plane shear failure in rectangular slender RC walls

8.6 EXAMPLES

Details of the walls used as examples were shown in Table 8-15 and Table 8-16. In order to capture the failure mode of each wall, firstly, possible failure mode of these walls was evaluated using the method shown in Figure 8-72 and then compared with the ones captured in FE analysis.

Table 8-15 Sections details of the walls used for the examples

Section name	Details
Wall-Ex1	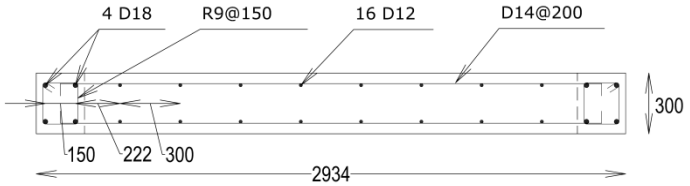
Wall-Ex2	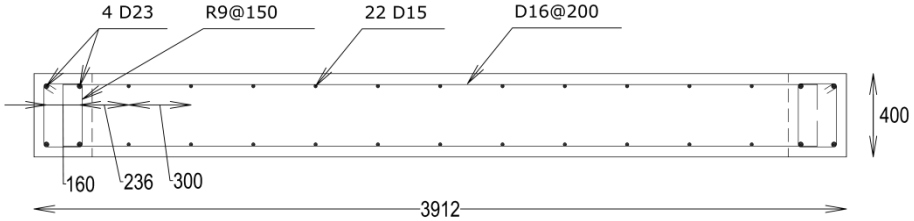

Table 8-16 Characteristics of walls used as examples for checking the proposed method

Parameters	Wall-Ex1	Wall-Ex2
Out-of-plane shear span, H_{out} (mm)	1605	2675
Thickness, t (mm)	300	400
Out-of-plane shear span ratio, H_{out}/t	5.35	6.69
Section detailing ductility	Nominal ductile	
In-plane effective height, H_e (mm)	10125	13500
Length, L_w (mm)	2934	3912
In-plane shear span ratio, H_e/L_w	3.45	
Section aspect ratio, L_w/t	9.78	
Axial load ratio, $P/(A_g f_c')$ (%)	20	15
Longitudinal reinforcement ratio (%) $\rho_t = (A_{s,BZ} + A_{s,web})/(L_w \times t)$	0.45	
Horizontal reinforcement ratio (%) $\rho_v = A_{sv}/(s \times t)$	0.5	
Compressive strength of concrete (MPa)	35	
Yield strength of reinforcement (MPa)	300	

* Out-of-plane shear span is half the first floor height

8.6.1 Example 1

As can be seen in Figure 8-73, based on the method shown in Figure 8-72, the possible failure mode of Wall-Ex1 is an out-of-plane shear failure.

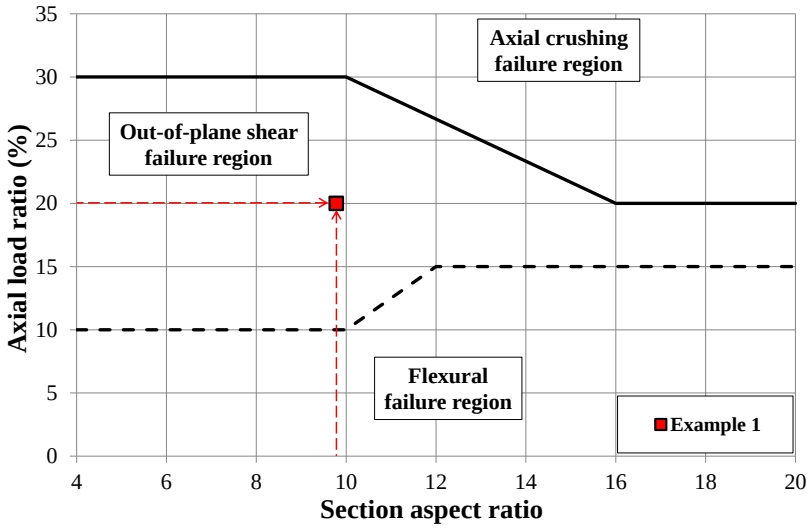

Figure 8-73 Predicted failure mode for Wall-Ex1 using the proposed method

Figure 8-74 shows the base shear-drift ratio curve of Wall-Ex1 subjected to skewed loading captured in DIANA. The wall showed brittle behaviour in both in-plane and out-of-plane directions and failed at 0.135% in-plane and 1.54% out-of-plane drift ratios. Von Mises strain and stress and axial strain contours of the wall were shown in Figure 8-75. It can be seen that von Mises strain contours of Wall-Ex1 was slightly dominated by the out-of-plane strains.

Looking at the von Mises stress and axial strain contours in Figure 8-75, it can be seen that the length of the part vulnerable to out-of-plane shear was equal to the length of the wall. Figure 8-76 shows the crack pattern of the wall. Significant out-of-plane shear cracks were formed along the full length and thickness of the wall that indicates a shear failure in that direction.

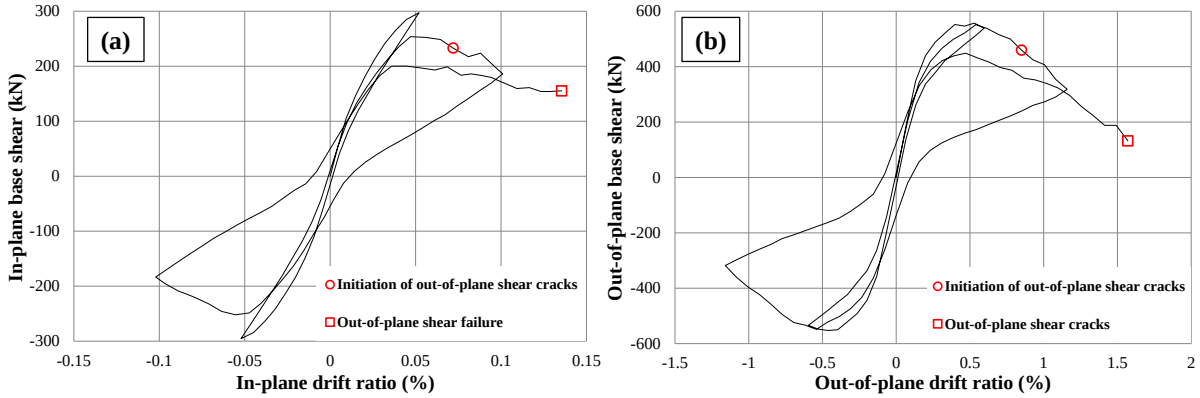

Figure 8-74 Base shear-drift ratio of the wall-Ex1 in the (a) in-plane and (b) out-of-plane directions

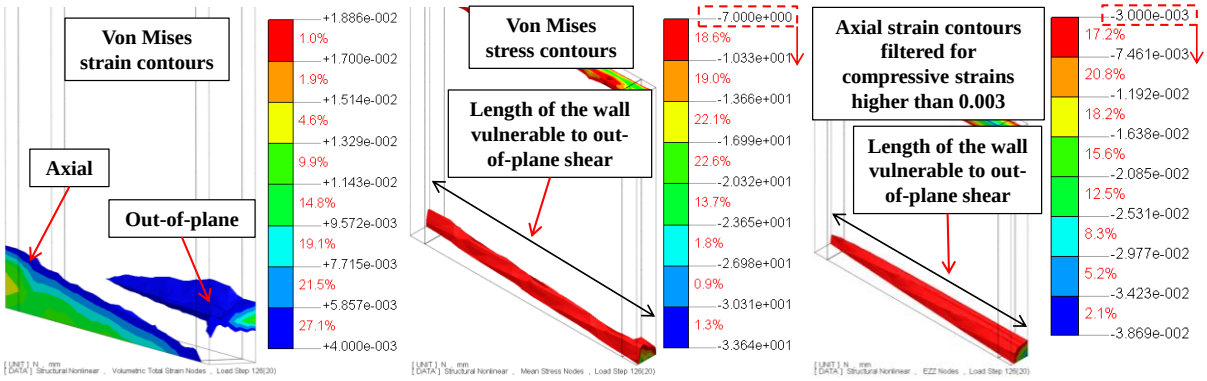

Figure 8-75 Von Mises strain and stress contours of Wall-Ex1 subjected to skewed loading

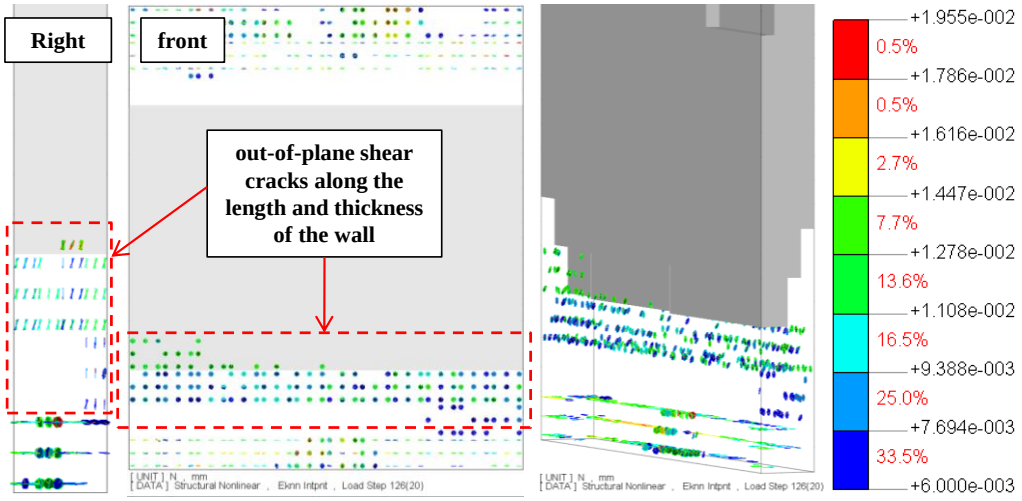

Figure 8-76 Crack pattern of Wall-Ex1 subjected to skewed loading

8.6.2 Example 2

As can be seen in Figure 8-77, based on the method shown in Figure 8-72, the possible failure mode of Wall-Ex2 is an out-of-plane shear failure.

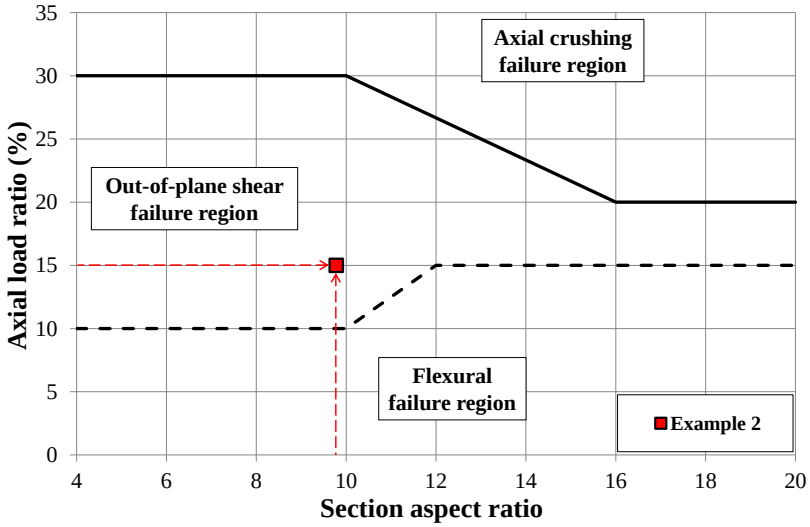

Figure 8-77 Predicted failure mode for Wall-Ex2 using the proposed method

Figure 8-78 shows the base shear-drift ratio curve of Wall-Ex2 subjected to skewed loading captured in DIANA. The wall showed brittle behaviour in both in-plane and out-of-plane directions and failed at 0.189% in-plane and 2.16% out-of-plane drift ratios.

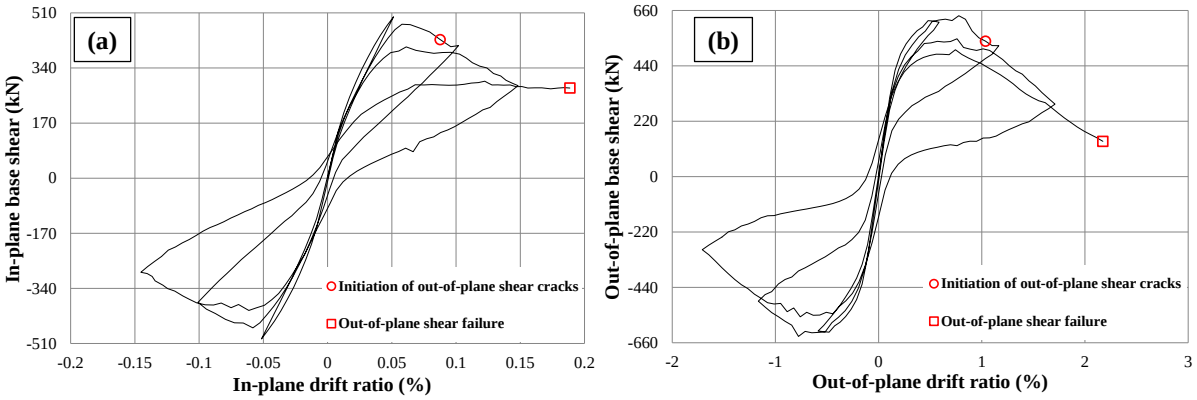

Figure 8-78 Base shear-drift ratio of wall-Ex2 in the (a) in-plane and (b) out-of-plane directions

Von Mises strain and stress and axial strain contours of the wall are shown in Figure 8-79. As can be seen in Figure 8-79, the von Mises strain contours of Wall-Ex2 was slightly dominated by out-of-plane strains. Looking at the von Mises stress and axial strain contours in Figure 8-79, it can be seen that the length of the part vulnerable to out-of-plane shear was equal to the length of the wall. Figure 8-80 shows the crack pattern of the wall. Significant out-of-plane shear cracks were formed along the full length and thickness of the wall which indicates a strong possibility of a shear failure in that direction.

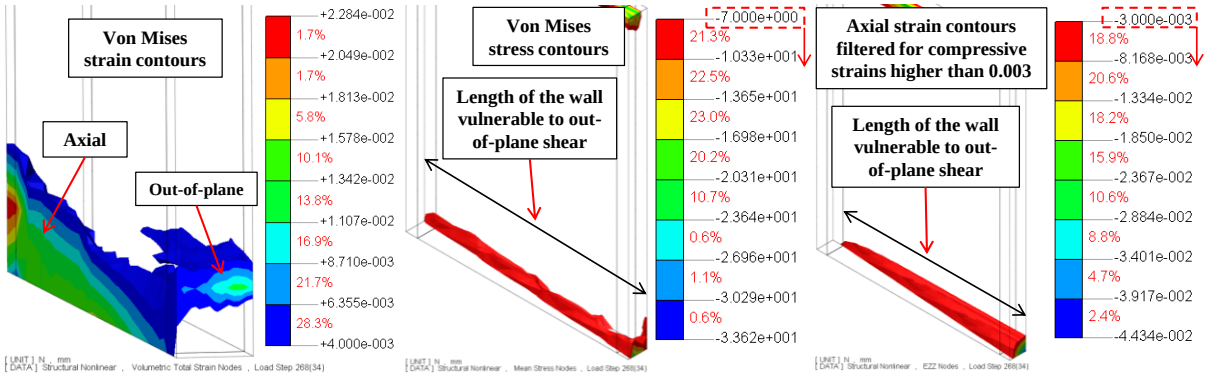

Figure 8-79 Von Mises strain and stress contours of Wall-Ex2

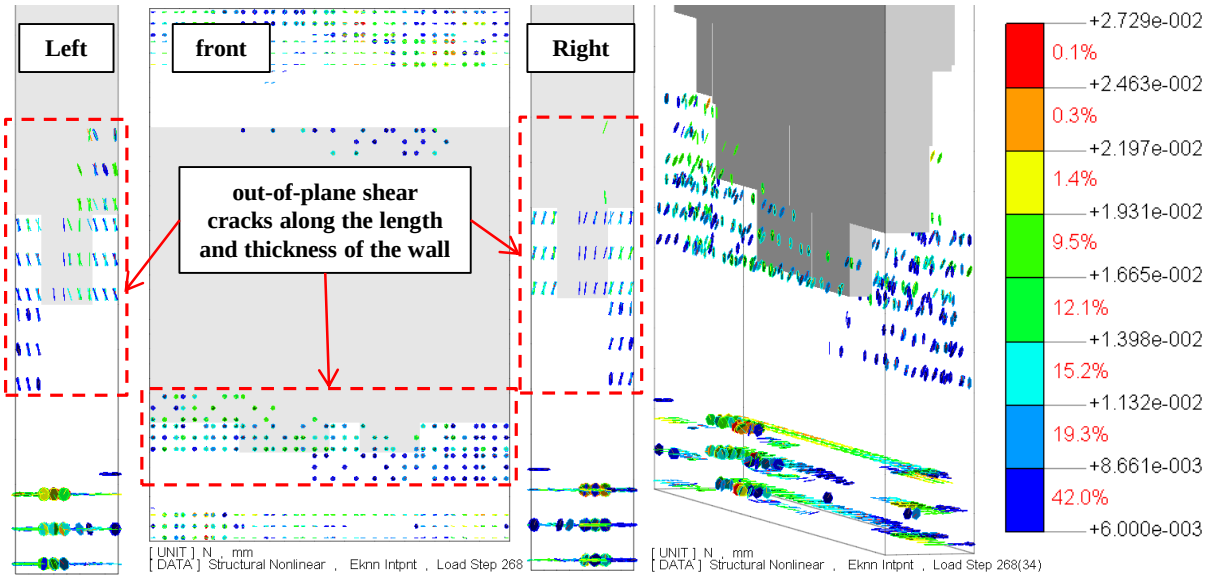

Figure 8-80 Crack pattern of Wall-Ex2

8.7 CONCLUSIONS

A comprehensive numerical parametric study was conducted based on the FE model presented in Chapter 6 which was extensively validated against different lateral loading patterns and complex failure modes. In this chapter, firstly key parameters in developing out-of-plane shear failure were investigated in details and then based on these investigations a matrix of walls was formed which was used to develop a method that can be used for the design and assessment of RC walls. The main findings of this chapter regarding the key parameters in developing out-of-plane shear failure in RC walls are presented in the following sub-sections.

Effects of axial load ratio on walls prone to out-of-plane shear failure

Axial load ratio was one of the key parameters that led to the out-of-plane shear failure of Wall D5-6 in the 2011 New Zealand earthquake. This was further confirmed with the out-of-plane shear failure of specimen SP2-ND in the experimental study of the current study. Due

to the limitations with the number of specimens, it was not possible to see the effects of various axial load ratios on walls prone to out-of-plane shear failure. Therefore, this parameter was numerically investigated in this chapter. The key findings are presented below.

- It was found that higher axial load ratio increases the susceptibility of the wall to out-of-plane shear failure by increasing the length of the part vulnerable to out-of-plane shear (parts with axial compressive strain higher than 0.003).
- Higher axial load ratio changes the von Mises strain pattern of the wall towards the domination of out-of-plane strain which helps with the development of out-of-plane shear cracks.
- In terms of failure mode, it was found that a flexural failure under low axial load ratio would turn into out-of-plane shear failure by the increase in axial load ratio. However, further increase in the axial load ratio would change the failure mode to an axial crushing failure.
- As was expected with the increase in axial load ratio, drift capacity of the wall decreases.

Effects of section aspect ratio on walls prone to out-of-plane shear failure

- It was found that lower section aspect ratio increases the length of the part vulnerable to out-of-plane shear failure which increases the susceptibility of the wall to out-of-plane shear failure.
- It was shown in Section 5.3.3 that higher compressive to tensile strains ratio would increase the susceptibility of the wall to out-of-plane shear failure. Numerical results showed that compressive to tensile strain ratio of the wall would increase with a decrease in the section aspect ratio of the wall.
- Maximum compressive von Mises stress in the wall which can help with the development of out-of-plane shear failure increases with a decrease in the section aspect ratio of the wall.
- Lower section aspect ratio changes an axially dominated von Mises strain contours in the wall towards the domination of out-of-plane strains which helps with the development of out-of-plane shear cracks.

Effects of section detailing ductility on walls prone to out-of-plane shear failure

As was shown in Chapter 5, the level of section detailing ductility is a key parameter in the development of out-of-plane shear failure. Here the effects of this parameter were investigated numerically and some complementary analyses were performed. Key findings are presented below.

- Numerical results confirmed the experimental findings of Chapter 5 that increasing the section detailing ductility would prevent the out-of-plane shear failure. Higher section detailing ductility increases the amount of transverse reinforcement in the wall and hence increases the out-of-plane shear capacity of the wall as well as concrete compressive strain capacity due to confinement.
- Transverse reinforcement throughout the wall's length are able to help against the development of out-of-plane strains which help reducing out-of-plane shear cracks in the wall.
- Walls designed for limited ductility had web crushing under the initial axial load ratio that the wall was designed for due to bi-directional loading.
- It was shown that designing the walls for limited or ductile levels for a lower axial load ratio can still prevent out-of-plane shear failure under higher axial load ratios during the earthquake.

Effects of longitudinal reinforcement ratio on walls prone to out-of-plane shear failure

Due to the limitations with the number of specimens, it was not possible to investigate the effects of longitudinal reinforcement ratio on walls prone to out-of-plane shear failure. Therefore, the effects of this parameter were investigated numerically here. The key findings are presented below.

- Based on the numerical results, it can be concluded that increasing the longitudinal reinforcement ratio can delay the out-of-plane shear failure. However, it is not likely that it can prevent this failure mode.
- Out-of-plane shear cracks captured for walls with higher longitudinal reinforcement ratio were less and more spread out compared to the one with lower longitudinal reinforcement ratio. However, considerable out-of-plane shear cracks were captured in all cases.

Simplified method for identifying walls prone to out-of-plane shear failure

Based on the two most influential parameters in causing vulnerability in RC walls against out-of-plane shear failure (section aspect ratio and axial load ratio) a matrix of walls was formed from which the lower and upper bound limits of the possibility of out-of-plane shear failure was established. Using these lower and upper bound limits, a method was proposed that can be used to identify walls prone to out-of-plane shear failure for both assessment and design purposes.

9. CONCLUSIONS AND RECOMMENDATIONS FOR FUTURE RESEARCH

9.1. INTRODUCTION

Following the two earthquakes in Chile in 2010 and New Zealand in 2011, some unexpected failure modes were observed in RC structural walls that haven't been seen in the previous earthquakes. Two of the failure modes that got the attention of researchers were lateral instability and out-of-plane shear failures of slender RC walls. Following these new observations, several researchers started working on different aspects of these failure modes. One of the important research questions regarding these new observations was the effects of bi-directional loading on rectangular RC structural walls that were so far ignored/neglected in the current design/assessment procedures.

In this thesis, as one of the first steps to enlighten this research question, the effects of bi-directional loading on the seismic behaviour of rectangular slender RC walls were investigated based on experimental and FEM numerical studies. The main conclusions and contributions of this study are described in this chapter together with recommendations for future research.

9.2. CONCLUSIONS AND CONTRIBUTIONS

This dissertation began by outlining the key research objectives that it intended to investigate. These objectives were thoroughly investigated and described in different chapters of this dissertation. In the following sub-sections, the key findings of this thesis will be summarised and restated with the intention of addressing the research objectives outlined in Section 1.5.

9.2.1. Key parameters influencing the seismic performance of rectangular RC walls subjected to bi-directional loading

As was discussed in Chapter 1, key parameters affecting the seismic performance of rectangular slender RC walls when subjected to bi-directional loading were not investigated in the previous studies. It was found that in the case of rectangular RC walls, the most critical failure mode that can be triggered only when the wall is subjected to bi-directional loading is

out-of-plane shear. The key parameters were identified based on earthquake observations (2011 New Zealand), experimental study presented in Chapter 5 and numerical study presented in Chapter 7. Experimental study included three specimens. The benchmark specimen was a wall prone to out-of-plane shear failure (based on numerical results). Then this benchmark wall was designed for a limited and ductile section detailing ductility according to NZS3101:2006-A3 (2017). The three specimens were tested under bi-directional loading. The numerical phase of the study presented in Chapter 7 and Chapter 8 investigated the identified key parameters in a comprehensive parametric study. The main conclusions regarding these studies are presented below.

Axial load ratio, $P/(A_g \times f'_c)$

- Based on the experimental investigations on the strain level (presented in Chapter 5), it was found that in walls prone to out-of-plane shear failure, unlike most RC walls, tensile strain is lower than compressive strain. Axial load ratio is one of the key parameters that increase the compressive to tensile strain ratio in the wall which is critical in the development of out-of-plane shear failure.
- Based on the investigations on the 2D section strain profile of the walls (presented in Chapter 5), it was found that out-of-plane shear failure occurs when the axial compressive strain along the full length of the wall reaches the crushing point (i.e. 0.003 for unconfined concrete). Axial load ratio is one of the key parameters in increasing the length of the part in compression.
- Based on the numerical study on walls with different axial load ratio discussed in Chapter 8, it was found that higher axial load ratio increases the susceptibility of the wall to out-of-plane shear failure by increasing the length of the part vulnerable to out-of-plane shear (parts with axial compressive strain higher than 0.003).
- Numerical results of Chapter 8 showed that higher axial load ratio changes the von Mises strain patterns of the wall towards the domination of out-of-plane strain which helps with the development of out-of-plane diagonal compression cracks.
- Based on the numerical parametric study results presented in Chapter 8 on walls with axial load ratio of 5% to 30%, it was found that in terms of failure mode, a flexural failure under low axial load ratio would turn into out-of-plane shear failure by the increase in axial load ratio. However, further increase in the axial load ratio would change the failure mode to an axial crushing failure.

Section aspect ratio, L_w/t

- Experimental results presented in Chapter 5 showed that higher maximum compressive to tensile strains ratio in the wall would increase the susceptibility of the wall to out-of-plane shear failure. Numerical results presented in Chapter 8 showed that compressive to tensile strain ratio would increase with a decrease in the section aspect ratio of the wall.
- Based on the numerical parametric study results presented in Chapter 8 on walls with section aspect ratio of 7.5 to 16, it was found that lower section aspect ratio increases the length of the part vulnerable to out-of-plane shear failure (parts with high compressive strain) which increases the susceptibility of walls to out-of-plane shear failure.
- Based on the numerical results presented in Chapter 8, it was found that maximum compressive von Mises stress in the wall which can help with the development of out-of-plane shear failure increases with a decrease in the section aspect ratio of the wall.
- Numerical parametric study results presented in Chapter 8 showed that lower section aspect ratio changes an axially dominated von Mises strain contours in the wall towards the domination of out-of-plane ones which helps with the development of out-of-plane shear cracks.

Section detailing ductility

- Based on both numerical (presented in Chapter 8) and experimental (presented in Chapter 5) results, it was found that while a wall prone to out-of-plane shear failure designed for nominal section ductility fails in out-of-plane shear, designing the walls for limited ductile and ductile section detailing can successfully prevent the out-of-plane shear failure. Significant contribution of transverse reinforcement in the out-of-plane shear capacity as well as concrete compressive strain capacity due to confinement allows the wall to resist sliding in the out-of-plane direction.
- Based on the experimental observations presented in Chapter 5, out-of-plane diagonal compression cracks still occur in walls prone to out-of-plane shear failure designed for limited or ductile section detailing when subjected to bi-directional loading. Although it is not likely for these walls to fail in out-of-plane shear, but the full length of the wall would have significant compressive strain due to section aspect ratio of the wall when subjected to high axial load ratio and bi-directional loading. Such high compressive strain in concrete would lead to cover concrete spalling along the full

length of the wall that will significantly decrease the axial capacity and consequently leads to an axial crushing failure in the wall. However, this axial crushing failure is likely to occur after the wall undergo significant out-of-plane drift ratio well beyond the drift ratio that a structure would be designed for.

- Experimental results presented in Chapter 5 showed that anti-buckling ties in the web are not only effective against buckling of the web's longitudinal bars but also help against the development of out-of-plane shear failure in the wall by increasing the out-of-plane shear capacity and concrete compressive strain capacity due to confinement.
- Based on the numerical results presented in Chapter 8 it was found that designing the walls for limited or ductile levels can still prevent out-of-plane shear failure even under higher axial load ratios during the earthquake.

Longitudinal reinforcement ratio, $\boldsymbol{\rho_t = (A_{s,BZ} + A_{s,web})/(L_w \times t)}$

- Comparing the performance of Wall D5-6 from Grand Chancellor Hotel in the 2011 New Zealand earthquake with similar wall with higher longitudinal reinforcement ratio tested in this study (specimen SP2-ND presented in Chapter 5) showed that increasing the amount of longitudinal reinforcement ratio in walls prone to out-of-plane shear failure can prevent the full rupture of the longitudinal bars along the wall.
- Based on the numerical parameter study results presented in Chapter 8 and comparing the behaviour of Wall D5-6 with a wall with similar characteristics but with higher longitudinal reinforcement ratio (specimen SP2-ND presented in Chapter 5), it was found that increasing the longitudinal reinforcement ratio in walls prone to out-of-plane shear failure can decrease and spread out the out-of-plane shear cracks (by increasing the out-of-plane shear capacity of the wall through their dowel action) and delay this failure mode. However, it is not likely that it can prevent the out-of-plane shear failure.

Lateral loading pattern

- Numerical parametric study presented in Chapter 7 on walls prone to out-of-plane shear failure subjected to various lateral loading patterns showed that an axial crushing failure under in-plane uni-directional loading would turn into an out-of-plane shear failure when subjected to out-of-plane uni-directional loading.
- Based on the numerical parametric study presented in Chapter 7, it was found that by increasing the loading angle of a skewed uni-directional pattern with respect to the in-

plane axis, the possibility of wall's failure in shear in the out-of-plane direction would increase as a larger length of the wall would be under high compressive axial strain which makes the wall vulnerable to out-of-plane shear failure.

- Based on the numerical study presented in Chapter 7, it can be concluded that a pre-existing displacement in the out-of-plane direction reduces the maximum attainable strength in rectangular walls.

9.2.2. Failure modes in rectangular slender walls affected or triggered by bi-directional loading

The effects of bi-directional loading on several failure modes such as lateral instability, concrete crushing, out-of-plane shear, longitudinal bar buckling and bar rupture were investigated experimentally as presented in Chapter 3 and Chapter 5 for rectangular slender RC walls. Moreover, both numerical (presented in Chapter 7 and Chapter 8) and experimental (presented in Chapter 3 and Chapter 5) approaches were used to investigate whether bi-directional loading can trigger modes of failure that would not be trigger by cyclic uni-directional loading or not. Some of the key conclusions are presented below.

- As was shown in Chapter 3, concrete cover spalling, crushing and bar buckling initiate earlier in walls subjected to bi-directional loading compared to the same wall under cyclic in-plane loading due to the increase in steel and concrete compressive and tensile strains.
- Experimental study presented in Chapter 3 showed that significant increase in compressive and tensile strains due to bi-directional loading increase the possibility of bar rupture in longitudinal reinforcement.
- Experimental observations presented in Chapter 3 showed that significant concrete crushing and bar buckling can occur in the web of walls subjected to bi-directional loading which wouldn't occur in the same wall under cyclic in-plane loading.
- As was shown in Chapter 3, lateral instability failure can occur earlier when the wall is subjected to bi-directional loading compared to the same wall under cyclic in-plane loading due to earlier concrete cover spalling/crushing and bar buckling/rupture in the wall which decreases the out-of-plane stiffness of the wall.
- Based on both experimental results presented in Chapter 5 and numerical studies of Chapter 7 it was found that out-of-plane shear failure can only be triggered when the wall is subjected to bi-directional loading. It is due to the fact that out-of-plane shear failure only occurs when the full length of the wall has compressive strain beyond

concrete crushing point. Such situation cannot happen even under severe high axial load ratio as a certain length of the wall would be in tension when the wall is subjected to cyclic in-plane loading.

- Based on the experimental observations of Chapter 5, out-of-plane shear cracks still occur in walls prone to out-of-plane shear failure designed for a ductile section detailing when subjected to bi-directional loading. Although, such wall is not likely to fail in out-of-plane shear due to sufficient out-of-plane shear strength, cover concrete spalling will occur along the full length of the wall that will lead to significant reduction of axial capacity and consequently an axial crushing failure. Such wall is expected to perform properly even under severe axial load and in-plane loading
- Walls prone to out-of-plane shear failure with low longitudinal reinforcement ratio complies with NZS3101:2006-A3 (2017) are prone to a type of failure that includes rupture of the longitudinal bars along the full length of the wall as was observed in the 2011 Christchurch earthquake. Such failure mode would only trigger when the wall is subjected to bi-directional loading. Increasing the longitudinal reinforcement ratio can change the bar rupture along the wall to bar buckling which is a less unstable failure mode.

9.2.3. Effects of lateral load path on rectangular slender RC walls

One of the most important research objectives of this thesis was investigating the effects of lateral load path on the seismic performance of rectangular slender walls. In the first set of experiments presented in Chapter 3, three lateral loading patterns of in-plane uni-directional, skewed uni-directional with a 45degree angle and clover leaf bi-directional were applied to three identical walls. In the second set of experiments presented in Chapter 5, the effects of a skewed uni-directional loading pattern with an angle of 85degree with respect to the in-plane axis was investigated on rectangular RC walls. Moreover, in Chapter 7, the effects of lateral loading angle on the seismic performance of walls prone to out-of-plane shear failure were investigated numerically. The key findings are presented below.

Skewed loading with 45 degree vs clover leaf loading pattern

- Based on the experimental study presented in Chapter 3 and comparing skewed loading with 45 degree with clover leaf, it was found that maximum compressive and tensile strains were higher in the wall under skewed loading compared to the same wall subjected to clover leaf loading pattern. One of the consequences of higher

compressive and tensile strains in the wall subjected to skewed loading was bar rupture which did not occur in the same wall under clover leaf loading pattern.

- Comparing skewed loading with 45 degree with clover leaf (based on the experimental results of Chapter 3), it was observed that although skewed loading was affecting a larger length of the wall, it was not as effective as clover leaf in terms of decreasing the out-of-plane stiffness of the wall since the damages in the wall were not in a symmetric shape when the wall was subjected to skewed loading. Therefore, as a result, lateral instability failure occurred earlier in the case of the specimen subjected to clover leaf bi-directional loading.
- As larger length of the wall was affected by skewed loading compared to clover leaf loading, therefore, concrete crushing and bar buckling occurred in the web of the specimen subjected to skew loading which was not observed in the wall under clover leaf loading pattern until the final failure of the specimen due to lateral instability.
- Experimental observations of Chapter 3 showed that shear cracks formed in the in-plane direction of the wall in both cases of skewed (with 45 degree) and clover leaf loading patterns which didn't occur in the case of the same wall under in-plane loading. However, in-plane shear cracks in the specimen subjected to skewed loading were more severe compared to the same wall under clover leaf loading pattern. More importantly, some shear cracks were observed in the out-of-plane direction of the specimen subjected to skewed loading which was not observed in the case of the specimen under clover leaf loading.

Effects of Skewed loading with 85 degree with respect to in-plane axis on walls prone to out-of-plane shear failure

- Based on the experimental results presented in Chapter 5, it was found that under a skewed loading with 85 degree, the full length of the wall would have compressive strain beyond the concrete crushing point (0.003 for an unconfined concrete) that allows an out-of-plane shear failure along the full length of the wall in the absence of sufficient confinement/out-of-plane shear capacity. The possibility of such cracks along the full length of the wall would decrease when subjected to a lateral load path with loading angle smaller than 85 degree with respect to the in-plane axis.
- Experimental observations of Chapter 5 showed that cover concrete spalling occurs along the full length of the walls subjected to skewed loading with an 85 degree angle as the full length of the wall would be in compression. Such cover concrete spalling

along the wall would lead to significant reduction of axial capacity in the case of walls with higher section detailing ductility.

Effects of various lateral load path on walls prone to out-of-plane shear failure (Based on numerical results)

- Based on the numerical parametric study on walls prone to out-of-plane shear failure presented in Chapter 7, it was found that by increasing the loading angle of a skewed uni-directional pattern with respect to the in-plane axis, the possibility of out-of-plane shear failure would increase as a larger length of the wall would be under high compressive axial strain which makes the wall vulnerable to out-of-plane shear failure.
- Numerical parametric study results presented in Chapter 7 showed that increasing the lateral loading angle with respect to the in-plane axis changes an axially dominated von Mises strain contours in the wall towards the domination of out-of-plane ones which helps with the development of out-of-plane shear cracks.
- Based on the numerical results presented in Chapter 7, it can be concluded that a pre-existing displacement in the out-of-plane direction reduces the maximum attainable in-plane strength in rectangular walls.

9.2.4. Effects of bi-directional loading pattern on walls prone to lateral instability failure

One of the failure modes observed in the 2010 Chile and 2011 New Zealand earthquakes was lateral instability failure. Following these observations, several researchers started working on different aspects of this failure mode. One of the research questions was whether bi-directional loading contributed to the development of this failure mode or not. As was presented in Chapter 3, three identical walls prone to lateral instability failure were tested under various lateral loading patterns. One of the research objectives of this set of experiments was to investigate the effects of bi-directional loading on the development of lateral instability failure. The key findings of this experimental study are presented below.

- Experimental observations on identical walls subjected to different lateral loading patterns presented in Chapter 3 showed that bi-directional loading is not able to considerably increase the out-of-plane buckling of walls prone to lateral instability failure. Between the two bi-directional loading patterns, skewed loading pattern was

able to develop larger out-of-plane displacements/buckling compared to clover leaf loading.

- Experimental observations presented in Chapter 3 showed that lateral instability failure occurs earlier when the wall is subjected to bi-directional loading compared to the same wall under cyclic in-plane loading due to earlier concrete cover spalling/crushing and bar buckling/rupture in the wall which decrease the out-of-plane stiffness of the wall.
- Comparing walls subjected to skewed loading and clover leaf (based on the experimental results shown in Chapter 3), it was observed that although skewed loading was affecting a larger length of the wall, it was not as effective as clover leaf in terms of decreasing the out-of-plane stiffness of the wall since the damages in the wall were not in a symmetric shape when the wall was subjected to skewed loading. Therefore, as a result, lateral instability failure occurred earlier in the case of the wall subjected to clover leaf bi-directional loading.

9.2.5. Verifying the newly added limitations to NZS3101:2006-A3 (2017) on maximum axial load ratio for RC walls

NZS3101: 2006–A3 (2017) limits the maximum axial load ratio of walls to $0.3\phi f_c' A_g$ or $0.4\phi f_c' A_g$ depends on whether earthquake is considered or not. However, it does not distinguish between walls designed for nominal ductile, limited ductile or ductile levels. On the other hand, February 2011 New Zealand earthquake revealed the vulnerability of nominal ductile walls with high axial load ratio. Therefore, in this thesis this limitation on the maximum axial load ratio was investigated both experimentally (in Chapter 5) and numerically (in Chapter 8). As was presented in Chapter 5, three rectangular slender walls with different section detailing ductility according to NZS3101: 2006–A3 (2017) were investigated under high axial load and bi-directional loading to validate the maximum allowable axial load ratio in the code. Moreover, in Chapter 8, walls with various section aspect ratio and axial load ratio were investigated under bi-directional loading and the maximum axial load ratio that allows a flexural failure in the wall was obtained.

- The experimental results presented in Chapter 5 and numerical findings of Chapter 8 confirm the vulnerability of nominally ductile walls with high axial load ratio when subjected to bi-directional loading as was observed in the 2011 New Zealand earthquake. It was found that walls with nominal section ductility and high axial load

ratio are vulnerable to out-of-plane shear failure when subjected to bi-directional loading.

- Based on a comprehensive numerical parametric study presented in Chapter 8, a pattern for the minimum axial load ratio that can trigger out-of-plane shear failure in rectangular slender walls with nominal ductility was proposed. Based on this pattern maximum allowable axial load ratio for each wall (depends on the section aspect ratio of the wall) can be calculated.
- Based on the experimental investigations on the behaviour of the wall in the strain level, it was found that lateral loading pattern and axial load ratio are two of the key parameters that can cause out-of-plane shear failure by developing compression along the full length of the wall. When the full length of the wall is in compression it will lead to cover concrete spalling and therefore increase the diagonal force inside the concrete core. This will lead to initiation of diagonal compression cracks along the wall. When the diagonal compression cracks develop and their penetration depth along the wall increases, a shear force in the opposite direction can lead to sliding of the wall and out-of-plane shear failure in case of insufficient out-of-plane shear capacity.

9.2.6. The mechanics of out-of-plane shear failure

When this study was began, out-of-plane shear failure was only observed in an earthquake (2011 New Zealand earthquake) and there were no available experimental or numerical data to investigate this failure mode in details. In this study, three rectangular slender RC walls prone to out-of-plane shear failure designed for different section detailing ductility according to NZS3101: 2006–A3 (2017) were tested under bi-directional loading (presented in Chapter 5). Moreover, key parameters in developing out-of-plane shear failure were identified and investigated in a comprehensive numerical parametric study using finite element analysis (presented in Chapter 7 and Chapter 8). The key findings regarding this research question are presented below.

- Experimental observations presented in Chapter 5 showed that out-of-plane shear failure involves a diagonal sliding transverse to the wall, penetrating certain length of the wall. In case of a full out-of-plane shear failure it would be along the full length of the wall.

- Based on the observations of the 2011 New Zealand earthquake and experimental results presented in Chapter 5, it was observed that out-of-plane shear failure shortens the wall along its height and create a total instability in the wall.
- As out-of-plane shear failure shortens the wall, during sliding, depends on the longitudinal reinforcement ratio it could lead to full rupture of the longitudinal bars along the wall.
- Based on the experimental (presented in Chapter 5) and numerical (presented in Chapter 8) investigations on the behaviour of the wall in the strain level, it was found that section aspect ratio and axial load ratio are the key parameters that can cause out-of-plane shear failure by developing compression along the full length of the wall. When the full length of the wall is in compression it will lead to cover concrete spalling and therefore increase the diagonal force inside the concrete core. This will lead to initiation of diagonal compression cracks in the two corners of the wall. When the diagonal compression cracks develop and their penetration depth along the wall increases, a shear force in the opposite direction can lead to sliding of the wall and out-of-plane shear failure in case of insufficient out-of-plane shear capacity. Parameters such as transverse and longitudinal reinforcement ratios can prevent or delay the out-of-plane shear failure by increasing the out-of-plane shear capacity of the wall.
- Based on both numerical (presented in Chapter 7) and experimental (presented in Chapter 5) results, it was found that out-of-plane shear failure would only trigger when the earthquake loading pattern has directionality towards the wall's out-of-plane direction (similar to the 2011 February earthquake in New Zealand). Under such earthquake loading the full length and thickness of the wall would have high compressive strains which lead to diagonal compression cracks and allow the out-of-plane shear failure to occur along the wall's length in the absence of sufficient out-of-plane sear capacity.

9.2.7. Identifying RC walls prone to out-of-plane shear failure

Following the breakthrough in identifying the key parameters in developing out-of-plane shear failure based on the experimental results presented in Chapter 5 and numerical parametric study conducted in Chapter 7 and Chapter 8, a method to identify walls prone to out-of-plane shear failure that can be used in practice by engineers was proposed. The method was developed based on the two most influential parameters on the seismic

performance of walls prone to out-of-plane shear failure, section aspect ratio and axial load ratio. As was presented in Chapter 8, a matrix of walls from the combination of these two parameters was formed from which the lower and upper bound limits of the possibility of out-of-plane shear failure in rectangular slender RC walls was established. Using these lower and upper bound limits, an analytical method was proposed in Chapter 8 that can be used to identify walls prone to out-of-plane shear failure for both assessment and design purposes.

9.2.8. Reliability of current design code of practice for severe axial and lateral loadings

In the past few years, significant changes were made to the New Zealand design code of practice (NZS3101) for structural walls that still need to be validated under severe axial and lateral loadings. Three rectangular walls designed based on NZS3101:2006-A3 (2017) for different section detailing ductility of nominal, limited and ductile levels were tested under high axial load ratio and bi-directional loading (presented in Chapter 5). Moreover, walls designed for a medium axial load ratio were numerically investigated under higher axial load ratio and bi-directional loading to find out whether the changes in the axial load level during the earthquake can change the failure mode of the wall or not (whether the increase in the axial load can trigger out-of-plane shear failure or not). The key findings are presented below.

- Based on the experimental results presented in Chapter 5 and the numerical investigations of Chapter 8, it was found that walls designed for limited ductile and ductile levels perform reasonably well when subjected to high axial load and bi-directional loading, while the walls designed for nominal ductility are likely to fail in out-of-plane shear.
- Experimental observations presented in Chapter 5 showed that out-of-plane diagonal compression cracks still occur in limited ductile or ductile walls with high axial load ratio subjected to bi-directional loading. Although, such wall is not likely to fail in out-of-plane shear, but significant cover concrete spalling will occur along the wall. Such cover concrete spalling along the full length of the wall significantly reduces the axial capacity of the wall and help with the development of an axial crushing failure. It is worth noting that such axial crushing failure mode differs from the case of walls with lack of proper confinement and occur at a high drift ratio.
- Based on the experimental results presented in Chapter 5 and the numerical study presented in Chapter 8, it was found that anti-buckling ties in the web can help against buckling of the web's longitudinal bars and preventing/delaying out-of-plane shear failure by increasing the out-of-plane shear capacity of the wall. Therefore, the

findings of the current study confirm the effectiveness of anti-buckling ties in the web which is compulsory by NZS3101:2006-A3 (2017) for ductile walls.

- Based on the numerical investigations presented in Chapter 8, it was shown that designing the walls prone to out-of-plane shear failure for limited or ductile levels can still prevent out-of-plane shear failure under higher axial load ratios during the earthquake.

9.2.9. Recommendations/guidelines to improve current practice for both the design of new walls and the assessment of existing ones

Based on the experimental and numerical findings of this thesis, following recommendations are provided for New Zealand design code of practice (NZS3101) and assessment guideline (NZSEE).

- Based on the comprehensive numerical parametric study presented in Chapter 8, a method was proposed that can be used for identifying walls prone to out-of-plane shear failure for both assessment and design purposes. Using this method, engineers only need to have their section aspect ratio and axial load ratio to be able to assess whether out-of-plane shear failure is going to be an issue or not.
- Based on the numerical parametric study results presented in Chapter 8, a pattern for maximum axial load ratio of RC walls (with nominal section detailing ductility) is proposed. A constant maximum axial load ratio of 10% can be suggested for rectangular walls with nominal detailing ductility. To apply more than 10% axial load ratio, the full pattern should be used which is based on the section aspect ratio of the wall. Axial load ratio of walls with nominal section detailing should not be higher than 15% regardless of the section aspect ratio, unless proving that the failure mode of the wall is other than out-of-plane shear.
- Based on the experimental results presented in Chapter 5 as well as the numerical study presented in Chapter 8, walls that are identified as prone to out-of-plane shear failure (using the method proposed in this study) should be designed for limited or ductile section detailing, unless proving that the failure mode of the wall is other than out-of-plane shear.
- Based on the experimental results presented in Chapter 5 as well as the earthquake observations (Wall D5-6 in the February 2011 earthquake), the minimum longitudinal reinforcement ratio of walls prone to out-of-plane shear failure should be increased to avoid rupture of the longitudinal reinforcement in case of an out-of-plane shear

failure. This will prevent failure modes such as what was observed in Wall D5-6 in the Grand Chancellor Hotel.

- Based on experimental results presented in Chapter 3, concrete crushing and bar buckling still occurs in the web of walls with boundary elements designed for full neutral axis depth. Therefore, anti-buckling ties in the web are recommended to help against bar buckling in the web as well as increasing the maximum compressive strain of concrete.

9.3.RECOMMENDATIONS FOR FUTURE RESEARCH

This study is one of the first steps towards understanding the behaviour of rectangular RC walls under more severe and realistic loading regimes. As the study was trying to answer some of the research gaps, further research questions were arousing. Therefore, future research recommendations are essential for the continuation of the research on this subject. Recommendations and suggestions for future researches are provided for some of the key parameters that influence the seismic performance of RC walls when subjected to bi-directional loading. These recommendations were categorized separately for experimental and numerical studies.

9.3.1. Recommendations for future experimental studies

- Experimental study conducted by Paulay and Goodsir (1985) on slender thin walls (walls with high slenderness ratio, H_w/t) subjected to cyclic in-plane loading showed the vulnerability of these walls to high axial load ratio as they observed a mixture of lateral instability and partial out-of-plane shear failures due to the combination of high axial load and out-of-plane deformations (out-of-plane deformations were due to out-of-plane buckling of the wall under in-plane loading). Due to the limitations with the number of specimens in this thesis, it was not possible to investigate thin walls with high axial load ratio under bi-directional loading. Therefore, additional experiments on thin walls with high axial load ratio under different loading regimes are required to fully understand the behaviour of walls prone to lateral instability when under high axial load ratio and bi-directional loading. This might affect the minimum thickness allowed by NZS3101 for preventing lateral instability failure. The test matrix should include thin walls with different section ductility levels (nominal ductile, limited ductile and ductile levels according to the latest NZS3101) subjected to high axial load ratio and bi-directional loading.

- Full rupture of the longitudinal bars along Wall D5-6 from Grand Chancellor Hotel in the February 2011 earthquake showed that the minimum longitudinal reinforcement ratio introduced by NZS3101: 2006–A3 (2017) might not be enough for walls with high axial load ratio (axial load can also significantly increase during the earthquake) when subjected to more complex loading regimes. However, due to the limitation with the number of specimens in this study, slender walls with low longitudinal reinforcement ratio under high axial load ratio and bi-directional loading were not investigated. The experiment's matrix should target slender walls prone to out-of-plane shear failure with different longitudinal reinforcement ratios subjected to bi-directional loading.
- Numerical results of the current study showed that a limited ductile or ductile wall designed for a medium axial load ratio would not fail in out-of-plane shear failure when subjected to higher axial load ratio (during the earthquake) and bi-directional loading. It would be beneficial to test this numerical finding in the laboratory for further confirmation.
- In the current experimental study a wall with 30% axial load ratio was tested under bi-directional loading and failed in out-of-plane shear. However, more experimental data is required to investigate the effects of axial load ratio in more details. The test matrix should target walls prone to out-of-plane shear failure with different axial load ratios subjected to bi-directional loading.
- Due to the limitations with the number of specimens, it was not possible to test walls prone to out-of-plane shear failure subjected to cyclic in-plane loading. Such experiments would help when investigating the effects of bi-directional loading on walls prone to out-of-plane shear failure (direct comparison of uni- and bi-directional loadings) and a better understanding of the out-of-plane shear failure's mechanism.

9.3.2. Recommendations for future numerical studies

There were some limitations with the Finite Element (FE) model used in this study that could have affected the capability of the model in simulating the behaviour of RC structural walls. In order to have a more realistic simulation of RC structural walls, it would be beneficial to consider these effects in the FE model. These limitations of the FE model are presented below.

- As was shown in Figure 6-2, the concrete material cyclic response did not account for the residual strain and the unloading/reloading loops always pass through the origin with secant stiffness.
- In the current version of DIANA, it was not possible to associate Menegotto-Pinto model with bar buckling and bar rupture.
- Perfect bond was considered between the reinforcement and the surrounding concrete in the FE model. The main reason was the limitation of the current version of DIANA in coupling the bond-slip for embedded reinforcement with the Menegotto-Pinto model.

10. REFERENCES

Acevedo, C. E., A. Creagh, J. Moehle, W. Hassan and A. Tanyeri (2010). "Seismic vulnerability of non-special boundary element of shear wall under axial force reversals." *Florida International University and University of California, Berkley, US*.

Akguzel, U. and S. Pampanin (2010). "Effects of variation of axial load and bidirectional loading on seismic performance of GFRP retrofitted reinforced concrete exterior beam-column joints." *Journal of Composites for Construction* 14(1), 94-104.

Alarcon, C., M. Hube and J. de la Llera (2014). "Effect of axial loads in the seismic behavior of reinforced concrete walls with unconfined wall boundaries." *Engineering Structures* 73, 13-23.

Almeida, J., O. Prodan, A. Rosso and K. Beyer (2017). "Tests on thin reinforced concrete walls subjected to in-plane and out-of-plane cyclic loading." *Earthquake Spectra* 33(1), 323-345.

ASCE41-13 (2013). Seismic Evaluation and Retrofit of Existing Buildings, American Society of Civil Engineers, Reston, Virginia.

Bathe, K.-J. (2006). *Finite element procedures*. Klaus-Jurgen Bathe.

Beckingsale, C. W. (1980). "Post elastic behaviour of reinforced concrete beam-column joints."

Behrouzi, A. A., A. Mock, L. Lowes, D. Lehman and D. Kuchma (2014). "Summary of large-scale C-shaped reinforced concrete wall tests."

Belarbi, A. and T. T. C. Hsu (1994). "Constitutive laws of concrete in tension and reinforcing bars stiffened by concrete." *Structural Journal* 91(4), 465-474.

Beyer, K., A. Dazio and M. Priestley (2008). "Quasi-static cyclic tests of two U-shaped reinforced concrete walls." *Journal of earthquake engineering* 12(7), 1023-1053.

Beyer, K., A. Dazio and N. Priestley (2011). "Shear deformations of slender reinforced concrete walls under seismic loading." *ACI Structural Journal* 108(EPFL-ARTICLE-162084), 167-177.

Beyer, K., M. Hube, R. Constantin, A. Niroomandi, S. Pampanin, R. Dhakal, S. Sritharan and J. W. Wallace (2017). Reinforced concrete wall response under uni-and bi-directional loading. *Proc., 16th World Conference on Earthquake Engineering*.

Bolong, Z. and C. Yuzhou (1991). "Behavior of exterior reinforced concrete beam column joints subjected to bi-directional cyclic loading." *Special Publication* 123, 69-96.

Bonet, J., M. Fernandez, M. Romero and P. Miguel (2005). "Capacity of RC rectangular sections subjected to biaxial bending: simplification to an increased uniaxial bending moment." *Magazine of Concrete Research* 57(8), 469-483.

Bonet, J., M. L. Romero and P. Miguel (2011). "Effective flexural stiffness of slender reinforced concrete columns under axial forces and biaxial bending." *Engineering Structures* 33(3), 881-893.

Bousias, S. N., G. Verzeletti, M. N. Fardis and E. Gutierrez (1995). "Load-path effects in column biaxial bending with axial force." *Journal of Engineering Mechanics* 121(5), 596-605.

Boys, A., D. Bull and S. Pampanin (2008). Seismic performance assessment of inadequately detailed reinforced concrete columns. *Proc., The New Zealand Society for Earthquake Engineering (NZSEE) Annual Technical Conference*.

Brueggen, B. L., C. E. French and S. Sritharan (2017). "T-shaped RC structural walls subjected to multidirectional loading: Test results and design recommendations." *Journal of Structural Engineering* 143(7), 04017040.

Campbell, K. W. and Y. Bozorgnia (2008). "NGA ground motion model for the geometric mean horizontal component of PGA, PGV, PGD and 5% damped linear elastic response spectra for periods ranging from 0.01 to 10 s." *Earthquake Spectra* 24(1), 139-171.

Cenedese, C., R. Nokes and J. Hyatt (2017). "Lock-exchange gravity currents over rough bottoms." *Environmental Fluid Mechanics*, 1-15.

Constantin, R. and K. Beyer (2016). "Behaviour of U-shaped RC walls under quasi-static cyclic diagonal loading." *Engineering structures* 106, 36-52.

Constantin, R. T. and K. Beyer (2012). Modelling of reinforced concrete core walls under bi-directional loading. *Proc., Proceedings of the 15th World Conference on Earthquake Engineering*.

Crisfield, M. A., J. J. Remmers and C. V. Verhoosel (2012). *Nonlinear finite element analysis of solids and structures*. John Wiley & Sons.

Dashti, F., R. P. Dhakal and S. Pampanin (2014). Numerical simulation of shear wall failure mechanisms. *Proc., The New Zealand Society for Earthquake Engineering (NZSEE) Annual Technical Conference*, Auckland, New Zealand.

Dashti, F., R. P. Dhakal and S. Pampanin (2017a). "Numerical Modeling of Rectangular Reinforced Concrete Structural Walls." *Journal of Structural Engineering* 143(6), 04017031.

Dashti, F., R. P. Dhakal and S. Pampanin (2017b). "Tests on slender ductile structural walls designed according to new zealand standards." *Bulletin of the New Zealand Society for Earthquake Engineering* 50(4), 504-516.

Deaton, J. B. (2013). Nonlinear finite element analysis of reinforced concrete exterior beam-column joints with nonseismic detailing, Georgia Institute of Technology.

DIANA (2015). DIANA Manual Release 9.6, TNO DIANA BV. Delft, the Netherlands.

Dunning Thornton (2011). Report on the structural performance of the Hotel Grand Chancellor in the earthquake on 22 February 2011. A report to the Department of Building and Housing (DBH), Dunning Thornton Consultants Ltd., Wellington, New Zealand.

Elwood, K., S. Pampanin and W. Y. Kam (2012). 22 February 2011 Christchurch earthquake and implications for the design of concrete structures. *Proc., The International Symposium on Engineering Lessons Learned from the 2011 Great East Japan Earthquake*, Tokyo, Japan.

Elwood, K. J. (2013). "Performance of concrete buildings in the 22 February 2011 Christchurch earthquake and implications for Canadian codes." *Canadian Journal of Civil Engineering* 40(3), 759-776.

Filippou, F. C., E. P. Popov and V. V. Bertero (1983). Effects of bond deterioration on hysteretic behavior of reinforced concrete joints. Earthquake Engineering Research Center, University of California, Berkeley, California.

Hilson, C., C. Segura and J. Wallace (2014). Experimental study of longitudinal reinforcement buckling in reinforced concrete structural wall boundary elements. *Proc., 10th US national conference on earthquake engineering. Anchorage, Alaska*.

Huang, Y.-N., A. S. Whittaker and N. Luco (2008). "Maximum spectral demands in the near-fault region." *Earthquake Spectra* 24(1), 319-341.

Hube, M. A. and K. M. Mosalam (2011). "Parametric study and design recommendations for in-span hinges in reinforced concrete box-girder bridges." *Journal of Bridge Engineering* 17(2), 334-342.

Ile, N. and J. Reynouard (2005). "Behaviour of U-shaped walls subjected to uniaxial and biaxial cyclic lateral loading." *Journal of Earthquake Engineering* 9(01), 67-94.

Johnson, B. (2010). Anchorage detailing effects on lateral deformation components of R/C shear walls. Master, University of Minnesota.

Junemann, R., J. C. de la Llera, M. A. Hube, J. Vásquez and M. Chacón (2016a). Inelastic finite element models to assess earthquake damage of RC wall buildings. *Proc., The New Zealand Society for Earthquake Engineering (NZSEE) Annual Technical Conference*, Christchurch, New Zealand.

Junemann, R., J. C. de la Llera, M. A. Hube, J. A. Vásquez and M. F. Chacón (2016b). "Study of the damage of reinforced concrete shear walls during the 2010 Chile earthquake." *Earthquake Engineering & Structural Dynamics* 45(10), 1621-1641.

Kabeyasawa, T., S. Kato, M. Sato, T. Kabeyasawa, H. Fukuyama, M. Tani, Y. Kim and Y. Hosokawa (2014). Effects of bi-directional lateral loading on the strength and deformability of reinforced concrete walls with/without boundary columns. *Proc., The Tenth U.S. National Conference on Earthquake Engineering*, Anchorage, Alaska, USA.

Kam, W. Y., S. Pampanin and K. J. Elwood (2011). "Seismic performance of reinforced concrete buildings in the 22 February Christchurch (Lyttelton) earthquake." *Bulletin of the New Zealand Society for Earthquake Engineering* 44(4), 239-278.

Kim, J.-K. and S.-S. Lee (2000). "The behavior of reinforced concrete columns subjected to axial force and biaxial bending." *Engineering Structures* 22(11), 1518-1528.

Kowalsky, M. J. (2000). "Deformation limit states for circular reinforced concrete bridge columns." *Journal of Structural Engineering* 126(8), 869-878.

Kurose, Y., G. Guimaraes, L. Zuhua, M. Kreger and J. Jirsa (1991). "Evaluation of Slab-Beam-Column Connections Subjected to Bidirectional lLoading." *Special Publication* 123, 39-68.

Lai, S.-S., G. T. Will and S. Otani (1984). "Model for inelastic biaxial bending of concrete members." *Journal of structural engineering* 110(11), 2563-2584.

Lai, T.-W. and J.-S. Chang (2001). Analysis of RC columns under cyclic axial compression with bidirectional eccentricities. *Proc., 26th Conference on OUR WORLD IN CONCRETE & STRUCTURES*, Singapore.

Leon, R. and J. O. Jirsa (1986). "Bidirectional loading of RC beam-column joints." *Earthquake spectra* 2(3), 537-564.

Li, K.-N., H. Aoyama and S. Otani (1988). Reinforced concrete columns under varying axial load and bi-directional lateral load reversals. *Proc., Proceedings of the 9th world conference on earthquake engineering, Tokyo-Kyoto, Japan*.

Litton, R. W. (1975). *A contribution to the analysis of concrete structures under cyclic loading*. University of California, Berkeley.

Low, S. S. and J. P. Moehle (1987). *Experimental study of reinforced concrete columns subjected to multi-axial cyclic loading*. University of California Berkeley, California.

Mahin, S. A. (1988). Inelsatic behaviour and modeling of reinforced concrete columns under multidirectional seismic excitations. *Proc., Ninth World Conference on Earthquake Engineering*, Tokyo-Kyoto, Japan.

Mander, J. B., M. J. N. Priestley and R. Park (1988). "Theoretical stress-strain model for confined concrete." *Journal of structural engineering* 114(8), 1804-1826.

Marante, M. and J. Flórez-López (2002). "Model of damage for RC elements subjected to biaxial bending." *Engineering Structures* 24(9), 1141-1152.

Maruyama, K., H. Ramirez and J. O. Jirsa (1984). "Short RC columns under bilateral load histories." *Journal of Structural Engineering* 110(1), 120-137.

Massone, L. M. and J. W. Wallace (2004). "Load-deformation responses of slender reinforced concrete walls." *Structural Journal* 101(1), 103-113.

Menegotto, M. and P. E. Pinto (1973). "Method of analysis for cyclically loaded reinforced concrete frames including changes in geometry and non-elastic behavior of elements under combined normal forces and bending moment." *IASBE Proceedings*.

NIST (2014). Recommendations for Seismic Design of Reinforced Concrete Wall Buildings Based on Studies of the 2010 Maule, Chile Earthquake.

Nokes, R. (2016). Streams 2.05—system theory and design. University of Canterbury, Christchurch.

NZS3101 (2006). Code of Practice for the Design of Concrete Structures, Standards Association of New Zealand.

NZS3101:2006-A3 (2017). Code of Practice for the Design of Concrete Structures, Standards Association of New Zealand.

NZSEE (2017). The Seismic Assessment of Existing Buildings, Ministry of Business, Innovation and Employment.

Oliva, M. G. and R. W. Clough (1987). "Biaxial seismic response of R/C frames." *Journal of Structural Engineering* 113(6), 1264-1281.

Orakcal, K., L. M. Massone and J. W. Wallace (2006). Analytical Modeling of Reinforced Concrete Walls for Predicting Flexural and Coupled–Shear-Flexural Responses. College of Engineering, Univ. of California, Berkeley, CA, Pacific Earthquake Engineering Research Center.

Padilla-Mora, P. and W. C. Schnobrich (1974). Non-linear response of framed structures to two-dimensional earthquake motion, University of Illinois Engineering Experiment Station. College of Engineering. University of Illinois at Urbana-Champaign.

Pallarés, L., J. Bonet, P. Miguel and M. F. Prada (2008). "Experimental research on high strength concrete slender columns subjected to compression and biaxial bending forces." *Engineering structures* 30(7), 1879-1894.

Parra, P. and J. Moehle (2014). Lateral buckling in reinforced concrete walls. *Proc., Tenth US Natl Conf Earthq Eng, Anchorage, Alaska*.

Paulay, T. and W. J. Goodsir (1985). "The ductility of structural walls." *Bulletin of the New Zealand Society for Earthquake Engineering* 18(3), 250-269.

Paulay, T. and M. J. N. Priestley (1992). *seismic design of reinforced concrete and masonry buildings*. John Wiley & Sons, Inc., New York, USA.

Paulay, T. and M. J. N. Priestley (1993). "Stability of ductile structural walls." *ACI Structural Journal* 90(4).

Pecknold, D. A. (1974). "Inelastic structural response to 2D ground motion." *Journal of Engineering Mechanics* 100(Proc. Paper 10846).

Priestley, M. J. N., M. C. Calvi and M. J. Kowalsky (2007). *Displacement-Based Seismic Design of Structures*. Pavia, Italy, IUSS Press.

Priestley, M. J. N., F. Seible and G. M. Calvi (1996). *Seismic design and retrofit of bridges*. New York, USA, John Wiley & Sons.

Qiu, F., W. Li, P. Pan and J. Qian (2002). "Experimental tests on reinforced concrete columns under biaxial quasi-static loading." *Engineering Structures* 24(4), 419-428.

Rodrigues, H., H. Varum, A. Arêde and A. G. Costa (2013). "Behaviour of reinforced concrete column under biaxial cyclic loading—state of the art." *International Journal of Advanced Structural Engineering* 5(1), 4.

Rots, J. G. and J. Blaauwendraad (1989). "Crack models for concrete, discrete or smeared? Fixed, multi-directional or rotating?" *HERON, 34 (1), 1989*.

SAP2000 Version 17.3.0 (2015). Integrated Finite Element Analysis and Design of Structures. Computers and Structures Inc, Berkeley, California, USA.

Segura, C. L. and J. W. Wallace (2017). "Seismic Performance Limitations and Detailing of Slender RC Walls." *ACI Structural Journal (accepted for publication)*.

Shegay, A., C. Motter, R. Henry and K. Elwood (2017). Experimental Study on Reinforced Concrete Walls with High Axial Loads. *Proc., 2017 NZSEE Annual Conference*, New Zealand Society for Earthquake Engineering.

Soleymani Ashtiani, M. (2013). Seismic Performance of High-Strength Self-Compacting Concrete in Reinforced Concrete Structures. PhD, University of Canterbury.

Soleymani Ashtiani, M., R. P. Dhakal and A. N. Scott (2014). Analytical Investigation on Seismic Performance of a High-Strength Self-Compacting Concrete Beam-Column Joint. *Proc., Tenth U.S. National Conference on Earthquake Engineering*, Anchorage, Alaska.

Su, R. and S. Wong (2007). "Seismic behaviour of slender reinforced concrete shear walls under high axial load ratio." *Engineering Structures* 29(8), 1957-1965.

Tatsuya, I. (1996). Post-yield behaviours of multi-story reinforced concrete shear walls subjected to bilateral deformations under axial loading. *Proc., The Eleventh World Conference on Earthquake Engineering*, Acapulco, Mexico.

Umehara, H. and J. O. Jirsa (1984). "Short rectangular RC columns under bidirectional loadings." *Journal of Structural Engineering* 110(3), 605-618.

Vecchio, F. J. and M. P. Collins (1986). "The modified compression-field theory for reinforced concrete elements subjected to shear." *ACI J.* 83(2), 219-231.

Wallace, J. W. and J. Moehle (2012). Behaviour and design of structural walls – lessons from recent laboratory tests & earthquakes. *Proc., International Symposium on Engineering Lessons Learned from the 2011 Great East Japan Earthquake*, Tokyo, Japan.

Wang, D., H.-N. Li and G. Li (2013). "Experimental tests on reinforced concrete columns under multi-dimensional dynamic loadings." *Construction and Building Materials* 47, 1167-1181.

Wong, Y.-L., T. Paulay and M. N. Priestley (1993). "Response of circular reinforced concrete columns to multi-directional seismic attack." *Structural Journal* 90(2), 180-191.

Yamamoto, N., Y. Sanada and S. Matsubara (2014). Tests and analyses for seismic performance evaluation of R/C shear walls fail in bending with concrete crushing. *Proc., Tenth U.S. National Conference on Earthquake Engineering*, Anchorage, Alaska.

Zeris, C. A. and S. A. Mahin (1991). "Behavior of reinforced concrete structures subjected to biaxial excitation." *Journal of structural engineering* 117(9), 2657-2673.

Zhang, Y. and Z. Wang (2000). "Seismic behavior of reinforced concrete shear walls subjected to high axial loading." *Structural Journal* 97(5), 739-750.